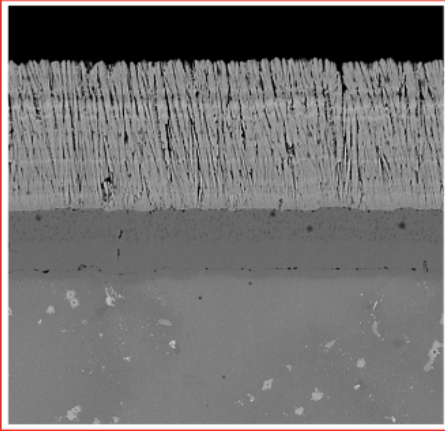


WOODHEAD PUBLISHING IN MATERIALS



Thermal barrier coatings

Edited by Huibin Xu and Hongbo Guo

WP
WOODHEAD
PUBLISHING

Thermal barrier coatings

Related titles:

Surface engineering of light alloys: Aluminium, magnesium and titanium alloys
(ISBN 978-1-84569-537-8)

This authoritative book provides a comprehensive review of the various surface engineering techniques employed to improve the properties of light alloys, focusing on titanium, magnesium and aluminium alloys. It examines surface related degradation of light alloys and covers surface engineering technologies in detail. The book includes chapters on corrosion behaviour of Mg alloys, anodising treatments of Mg alloys, micro-arc oxidation of light alloys, physical vapour deposition of light alloys, PIII/PSII of light alloys, laser surface modification of Ti alloys, plasma nitriding of Ti and Al alloys, duplex surface treatments of light alloys and biomedical devices using Ti alloys.

Electroless copper and nickel–phosphorus plating: Processing, characterisation and modelling
(ISBN 978-1-84569-808-9)

Compared with electroplating, electroless plating allows uniform deposits over different surfaces. Electroless copper and nickel–phosphorus deposits provide protective and functional coatings in industries as diverse as electronics, automotive, aerospace and chemical engineering. Written by leading experts in the field, this important book reviews the deposition process and the key properties of electroless copper and nickel–phosphorus deposits as well as their practical applications.

Nanostructured metals and alloys: Processing, microstructure, mechanical properties and applications
(ISBN 978-1-84569-670-2)

Nanostructured metals and alloys have enhanced tensile strength, fatigue strength and ductility and are suitable for use in applications where strength or strength-to-weight ratios are important. Part I of this important book reviews processing techniques for bulk nanostructured metals and alloys. Parts II and III discuss microstructure and mechanical properties, whilst Part IV outlines applications of this new class of material.

Details of these and other Woodhead Publishing materials books can be obtained by:

- visiting our web site at www.woodheadpublishing.com
- contacting Customer Services (e-mail: sales@woodheadpublishing.com; fax: +44 (0) 1223 832819; tel.: +44 (0) 1223 499140 ext. 130; address: Woodhead Publishing Limited, 80 High Street, Sawston, Cambridge CB22 3HJ, UK)

If you would like to receive information on forthcoming titles, please send your address details to: Francis Dodds (address, tel. and fax as above; e-mail: francis.dodds@woodheadpublishing.com). Please confirm which subject areas you are interested in.

Thermal barrier coatings

Edited by
Huibin Xu and Hongbo Guo



Oxford Cambridge Philadelphia New Delhi

Published by Woodhead Publishing Limited,
80 High Street, Sawston, Cambridge CB22 3HJ, UK
www.woodheadpublishing.com

Woodhead Publishing, 1518 Walnut Street, Suite 1100, Philadelphia,
PA 19102-3406, USA

Woodhead Publishing India Private Limited, G-2, Vardaan House,
7/28 Ansari Road, Daryaganj, New Delhi – 110002, India
www.woodheadpublishingindia.com

First published 2011, Woodhead Publishing Limited
© Woodhead Publishing Limited, 2011
The authors have asserted their moral rights.

This book contains information obtained from authentic and highly regarded sources. Reprinted material is quoted with permission, and sources are indicated. Reasonable efforts have been made to publish reliable data and information, but the authors and the publisher cannot assume responsibility for the validity of all materials. Neither the authors nor the publisher, nor anyone else associated with this publication, shall be liable for any loss, damage or liability directly or indirectly caused or alleged to be caused by this book.

Neither this book nor any part may be reproduced or transmitted in any form or by any means, electronic or mechanical, including photocopying, microfilming and recording, or by any information storage or retrieval system, without permission in writing from Woodhead Publishing Limited.

The consent of Woodhead Publishing Limited does not extend to copying for general distribution, for promotion, for creating new works, or for resale. Specific permission must be obtained in writing from Woodhead Publishing Limited for such copying.

Trademark notice: Product or corporate names may be trademarks or registered trademarks, and are used only for identification and explanation, without intent to infringe.

British Library Cataloguing in Publication Data
A catalogue record for this book is available from the British Library.

ISBN 978-1-84569-658-0 (print)
ISBN 978-0-85709-082-9 (online)

The publisher's policy is to use permanent paper from mills that operate a sustainable forestry policy, and which has been manufactured from pulp which is processed using acid-free and elemental chlorine-free practices. Furthermore, the publisher ensures that the text paper and cover board used have met acceptable environmental accreditation standards.

Typeset by Toppan Best-set Premedia Limited, Hong Kong
Printed by TJI Digital, Padstow, Cornwall, UK

Contents

<i>Contributor contact details</i>	<i>xi</i>
<i>Preface</i>	<i>xv</i>
Part I Materials and structure	1
1 Thermal barrier coatings prepared by electron beam physical vapor deposition (EB-PVD)	3
D. ZHANG, North China Electric Power University, China	
1.1 Introduction	3
1.2 Preparation process and parameters	6
1.3 Preparation processes of two-layered thermal barrier coatings (TBCs)	8
1.4 Factors affecting thermal cyclic behaviour of TBCs	11
1.5 Preparation of graded thermal barrier coatings (GTBCs)	16
1.6 Failure mechanism	19
1.7 Conclusion	20
1.8 References	20
2 Ceramic thermal barrier coating materials	25
W. MA and H. DONG, Inner Mongolia University of Technology, China	
2.1 Introduction	25
2.2 State-of-the-art ceramic thermal barrier coating (TBC) material – yttria stabilized zirconia (YSZ)	26
2.3 Zirconia doped with one or more oxides	31
2.4 Yttria stabilized hafnia and other alternative ceramic TBC materials	35
2.5 Lanthanum compounds, silicates and rare earth oxides	38
2.6 $(Ca_{1-x}Mg_x)Zr_4(PO_4)_6$ (CMZP), perovskite oxides and metal–glass composite	41
2.7 Future trends	43
2.8 References	44

vi	Contents	
3	Metallic coatings for high-temperature oxidation resistance	53
	X. PENG, Chinese Academy of Sciences, China	
3.1	Introduction	53
3.2	Oxidation-resistant metallic coatings and their fabrication techniques	55
3.3	Metallic coatings as bond coats for thermal barrier coatings (TBCs)	64
3.4	Conclusions	68
3.5	Acknowledgements	69
3.6	References	69
4	Nanostructured thermal barrier coatings	75
	C. G. ZHOU and Q. H. YU, Beihang University, China	
4.1	Introduction	75
4.2	Spray-drying process making powders	76
4.3	Phase composition and microstructure of nanostructured thermal barrier coatings (TBCs)	78
4.4	Mechanical properties	82
4.5	Thermophysical properties and the failure behavior	87
4.6	Conclusion	92
4.7	References	93
	Part II Processing and spraying techniques	97
5	Plasma spraying for thermal barrier coatings: processes and applications	99
	J. L. XU and K. A. KHOR, Nanyang Technological University, Singapore	
5.1	Introduction	99
5.2	Basic plasma concepts	100
5.3	Plasma spraying	102
5.4	Applications of plasma spraying	104
5.5	Conclusions	111
5.6	Acknowledgements	111
5.7	References	111
6	Processing, microstructures and properties of thermal barrier coatings by electron beam physical vapor deposition (EB-PVD)	115
	S. GONG and Q. WU, Beihang University, China	
6.1	Introduction	115
6.2	Description of the physical principles of electron beam physical vapor deposition (EB-PVD)	116

6.3	Manufacturing of thermal barrier coatings (TBCs) by EB–PVD	118
6.4	EB–PVD TBC microstructure and its advantages over plasma-sprayed coatings	120
6.5	Hot-fatigue behavior and failure mechanisms of TBCs	125
6.6	References	128
7	Processing, microstructures and properties of thermal barrier coatings (TBCs) by plasma spraying (PS) L. CHEN, China University of Petroleum, China	132
7.1	Introduction	132
7.2	Processing of thermal barrier coatings (TBCs) by plasma spraying (PS)	134
7.3	Microstructures of TBCs processed by PS	141
7.4	Properties of TBCs processed by PS	151
7.5	Conclusion	156
7.6	References	157
8	Plasma-sprayed thermal barrier coatings with segmentation cracks H. GUO, R. YAO and L. ZHOU, Beihang University, China	161
8.1	Introduction	161
8.2	Manufacturing of segmented thermal barrier coatings (TBCs)	162
8.3	Microstructure of segmented TBCs	165
8.4	Thermophysical and mechanical properties of segmented TBCs	166
8.5	Thermal shock resistance and associate failure mechanism	167
8.6	Future trends	172
8.7	References	172
9	Detonation gun sprayed thermal barrier coatings P. L. KE, Y. N. WU and C. SUN, Chinese Academy of Sciences, China	175
9.1	Introduction	175
9.2	Detonation gun (D-gun) sprayed thermal barrier coatings (TBCs)	177
9.3	TBCs deposited through arc ion plating (AIP)/D-gun two-step technology	181
9.4	Future trends	185
9.5	Conclusion	187
9.6	References	187

Part III Performance of thermal barrier coatings	191
10 Oxidation and hot corrosion of thermal barrier coatings (TBCs)	193
C. G. ZHOU and Y. X. SONG, Beihang University, China	
10.1 Introduction	193
10.2 Oxidation of thermal barrier coatings	194
10.3 Failure mechanisms of TBCs	198
10.4 The degradation mechanisms experienced by TBC systems exposed to deposits	202
10.5 Conclusions	208
10.6 References	208
11 Failure mechanism of thermal barrier coatings by electron beam physical vapor deposition (EB-PVD) under thermomechanical coupled loads	215
C. ZHANG, Baosteel Group Corporation, China and C. CHEN, AVIC Commercial Aircraft Engine Co., Ltd, China	
11.1 Introduction	215
11.2 Establishment of gas turbine service environment simulation system	217
11.3 Failure mechanism of EB-PVD TBC under in-plane thermal gradient coupled with mechanical loading	221
11.4 Failure mechanism of EB-PVD TBC under 3-D thermal gradient coupled with mechanical loading	233
11.5 Conclusions	240
11.6 References	241
12 Non-destructive evaluation (NDE) of the failure of thermal barrier coatings	243
G. CHEN, Northwestern Polytechnical University, China	
12.1 Introduction	243
12.2 Failure of thermal barrier coatings (TBCs)	245
12.3 Development of failure inspection methods	247
12.4 Future trends	258
12.5 References	258
13 Substrate and bond coat related failure of thermal barrier coatings	263
R. T. WU, National Institute for Materials Science (NIMS), Japan	

13.1	Introduction	263
13.2	Substrate related failure of thermal barrier coatings (TBCs)	265
13.3	Compatibility issues of nickel-based single-crystal superalloys with thermal barrier coating systems	276
13.4	Bond coat related failure of TBCs	278
13.5	Effect of bond coat on the TBC degradation mechanisms	286
13.6	Conclusions and future trends	288
13.7	References	290
14	Life prediction of thermal barrier coatings H. Y. QI and X. G. YANG, Beihang University, China	294
14.1	Introduction	294
14.2	The mechanical behavior of thermal barrier coating (TBC) systems under elevated temperatures	295
14.3	Life prediction for TBCs	305
14.4	Future trends	314
14.5	Conclusion	315
14.6	References	315
15	New materials, technologies and processes in thermal barrier coatings H. XU and J. WU, Beihang University, China	317
15.1	Introduction	317
15.2	Chemically modified yttria stabilized zirconia (YSZ)	318
15.3	Alternate low thermal conductivity (κ) materials	319
15.4	Microstructure modification	321
15.5	Advanced processing technologies	322
15.6	Future trends	325
15.7	References	325
	<i>Index</i>	329

Contributor contact details

(* = main contact)

Editors

H. Xu and H. Guo
School of Materials Science and
Engineering
Beihang University
37 Xueyuan Road
Beijing 100191
China

E-mail: xuhb@buaa.edu.cn
guo.hongbo@buaa.edu.cn

Chapter 1

D. Zhang
School of Energy, Power and
Mechanical Engineering
North China Electric Power
University
Beijing 102206
China

E-mail: zhangdb@ncepu.edu.cn

Chapter 2

W. Ma* and H. Dong
School of Materials Science and
Engineering
Inner Mongolia University of
Technology
49 Aimin Road
Xincheng district
Hohhot 010051
China

E-mail: wma@imut.edu.cn

Chapter 3

X. Peng
State Key Laboratory for
Corrosion and Protection
Institute of Metal Research
Chinese Academy of Sciences
72 Wenhua Road
Shenhe district
Shenyang 110016
China

E-mail: xpeng@imr.ac.cn

Chapter 4

C. G. Zhou* and Q. H. Yu
School of Materials Science and
Engineering
Beihang University
37 Xueyuan Road
Beijing 100191
China

E-mail: cgzhou@buaa.edu.cn

Chapter 5

J. Xu* and K. A. Khor
School of Mechanical and
Aerospace Engineering
Nanyang Technological University
50 Nanyang Avenue
Singapore 639798

E-mail: jlXu@ntu.edu.sg

Chapter 6

S. Gong* and Q. Wu
School of Materials Science and
Engineering
Beihang University
37 Xueyuan Road
Beijing 100191
China

E-mail: gongsk@buaa.edu.cn

Chapter 7

L. Chen
Department of Material Science
and Engineering
China University of Petroleum
18 Fuxue Road
Changping
Beijing 102249
China

E-mail: liqiang_chen@sohu.com

Chapter 8

H. Guo*, R. Yao and L. Zhou
School of Materials Science and
Engineering
Beihang University
37 Xueyuan Road
Beijing 100191
China

E-mail: guo.hongbo@buaa.edu.cn

Chapter 9

P. Ke*
Surface Engineering
Ningbo Institute of Materials
Technology and Engineering
Chinese Academy of Sciences
519 Zhuangshi Road
Zhenhai district
Ningbo 315201
China

E-mail: plkeimr@hotmail.com
kepl@nimte.ac.cn

Y. Wu and C. Sun*
State Key Laboratory for
Corrosion and Protection
Institute of Metal Research
Chinese Academy of Sciences
72 Wenhua Road
Shenhe district
Shenyang 110016
China

E-mail: yingnawu@gmail.com
csun@imr.ac.cn

Chapter 10

C. G. Zhou and Y. X. Song
 School of Materials Science and
 Engineering
 Beihang University
 37 Xueyuan Road
 Beijing 100191
 China
 E-mail: cgzhou@buaa.edu.cn

Chapter 11

C. Zhang*
 Baosteel Group Corporation
 Pu Dian Road 370
 Pudong New District
 Shanghai 200122
 China
 E-mail: zcx_buaa@163.com

C. Chen
 AVIC Commercial Aircraft Engine
 Co., Ltd
 Building 3
 Dongchuan Road 555
 Minhang District
 Shanghai 200241
 China
 E-mail: chenchen@mse.buaa.edu.cn

Chapter 12

G. Chen
 Shaanxi Key Laboratory of
 Friction Welding Technologies
 Northwestern Polytechnical
 University
 127 Youyi Xilu
 Xi'an
 Shaanxi Province 710072
 China
 E-mail: gfchen@gmail.com

Chapter 13

R. T. Wu
 International Center for Young
 Scientists (ICYS)
 National Institute for Materials
 Science (NIMS)
 1-2-1 Sengen
 Tsukuba
 Ibaraki 305-0047
 Japan

E-mail: wu.rudder@nims.go.jp

Chapter 14

H. Y. Qi* and X. G. Yang
 School of Jet Propulsion
 Beihang University
 37 Xueyuan Road
 Beijing 100191
 China

E-mail: qhy@buaa.edu.cn

Chapter 15

H. Xu* and J. Wu
 School of Materials Science and
 Engineering
 Beihang University
 37 Xueyuan Road
 Beijing 100191
 China

E-mail: xuhb@buaa.edu.cn

Thermal barrier coatings (TBCs) are finding increasing application in the most demanding high-temperature environment of aircraft and industrial engines. They have the capability to improve the durability of engines by reducing the surface temperature of the underlying components. The use of TBCs, along with internal cooling of the underlying superalloy components, has thus enabled advanced gas turbine engines to operate at temperatures even above the melting temperature of the superalloy, thus achieving a remarkable increase in the efficiency and performance of engines. This technology has been regarded as one of the most important and effective developments in efforts to improve the propulsion efficiency of advanced aero engines.

The TBC components must withstand the harsh environment coupled with high temperature, large temperature gradient, complex stress condition and corrosive atmosphere. No single coating component is able to satisfy these multifunctional requirements. As a result, a complex TBC structure has been developed. Research since the 1970s has been focused on a preferred coating system primarily comprising three separate layers on the substrate, so as to achieve long-term effectiveness in oxidative and corrosive environment at high temperatures, i.e. a ceramic top coat layer with low thermal conductivity to provide excellent thermal insulation for the hot components, a bond coat layer above the substrate to hold the ceramic coat on the substrate, and a thin thermally grown oxide (TGO) layer to provide adhesion between the ceramic top coat and the bond coat. The TBC component is expected to last over thousands of take-offs and landings in aero engines. However, the complexity and diversity of TBC structures and the severity of operating conditions give rise to premature TBC failure. This premature failure has slowed down the use of TBCs and compromised the ability to take full advantage of the energy efficiency and service lifetime potentially offered by TBCs. In view of this, fundamental investigations into TBC materials and processing principles and assessments of TBC performance, lifetime prediction and failure mechanisms

have been systematically conducted. The multidisciplinary subjects of materials science, physics, chemistry, mechanics, computation science and thermodynamics are involved in this research field.

At present, the TBC industry is key in the field of aero engines worldwide. It is necessary to make the theory and the applications of TBCs known to both researchers and graduate students, and this is the purpose of this book. The aim is not only to provide a clear and thorough presentation of both fundamental principles and applications of TBC systems in the aero engine industry, but also to prepare the way for future TBC systems by reviewing previous achievements. There are 15 independent chapters in this book, in which progress in TBC materials, advanced processing technologies, physical and chemical phenomena such as oxidation, diffusion, fatigue, thermal conduction and sintering, failure mechanisms and non-destructive evaluation of TBCs and their life prediction have been described.

A general description of the background, processing technology of electron beam physical vapor deposition (EB-PVD), oxidation and thermal cycling performance of TBCs manufactured by EB-PVD is given in Chapter 1. The selection principles and the progress of ceramic top coat materials in TBC systems are introduced in Chapter 2. Several proposals on the development trends in ceramic top coats are raised in this chapter. In Chapter 3, the emphasis is placed on a comparison of the processing and oxidation resistance of various metallic coatings. As a newly developed TBC system, the nanostructured TBCs are introduced in Chapter 4, including the fundamental principle of formation of nanostructure, microstructure features and associated properties, and several potential applications of nanostructured TBCs are suggested.

Two main processing technologies are generally used in the manufacture of TBCs, namely plasma spraying (PS) and electron beam physical vapor deposition (EB-PVD). The principles, microstructure characteristics and applications of PS and EB-PVD are addressed in Chapters 5 and 6, respectively, giving guidance in the selection of processing technology for the production of TBCs to meet different industrial purposes. In Chapter 7, plasma-sprayed TBCs are presented with the emphasis on thermal physical properties, mechanical properties, durability and failure mechanisms. The properties of plasma-sprayed TBCs can be further improved by modifications to the TBC structure. This fact was particularly evident in Chapter 8, in which a modified TBC structure with high segmentation crack density is proposed. In Chapter 9, the structure, characteristics and properties of TBC systems prepared by a so-called detonation plasma spray method are presented.

One of the primary tasks for TBCs is to effectively protect the underlying superalloy substrate from hot corrosion and high-temperature oxidation. The high-temperature oxidation and hot-corrosion behaviors of TBCs are

described in Chapter 10. The emphasis is focused on failure mechanisms of TBCs associated with cracking of TGO grown on the metallic bond coat and comparison of several kinds of metallic bond coating materials which are practical use in engineering design. In Chapter 11, the behaviors of TBCs under thermal-mechanical coupled loads are presented, and a failure mechanism is also put forward. Recently, non-destructive evaluation (NDE) methods have been used for the premature failure detection of TBC systems. Chapter 12 reviews the fundamentals and application of different NDE methods with particular emphasis on the latest results in the promising area of emission spectroscopy NDE used for in situ TBCs failure inspection. The inter-diffusion between the bond coat and the underlying substrate under high temperatures has significant influence on the mechanical properties of superalloy, oxidation resistance and durability of TBCs. This is clearly stated in Chapter 13.

Chapter 14 deals with life prediction of TBCs. The ability to foresee, theoretically, the lifetime of TBCs is fundamental in improving the safety of TBC components in industrial applications. In this chapter, three viscoplastic constitutive models are developed for TBC systems. Failure mechanisms of TBCs are discussed and a fatigue life model is set up for life prediction of TBC vanes.

In the final chapter, new TBC materials and processing technologies are reviewed and some possible directions for the development of TBCs in the future are suggested.

The author acknowledges all the contributors to the successful completion of this book. The author would also like to thank Dr Dongbo Zhang in North China Electric Power University (NEPU) for his contribution to Chapter 1, Dr Wen Ma in Inner Mongolia University of Technology (IMUT) for his contribution to Chapter 2, Dr Xiao Peng in Institute of Metal Research (IMR) in Chinese Academy of Science (CAS) for his contribution to Chapter 3, Professor Chungen Zhou and Dr Qinghe Yu in BUAA for their contribution to Chapter 4, Dr Jinlin Xu and Professor K.A. Khor in Nanyang Technological University (NTU) for their contribution to Chapter 5, Professor Shengkai Gong and Dr Qiong Wu in Beihang University (BUAA) for their contribution to Chapter 6, Dr Liqiang Chen in China University of Petroleum (CUP) for his contribution to Chapter 7, Professor Hongbo Guo, Miss Rui Yao and L. Zhou in BUAA for their contribution to Chapter 8, Drs Yingna Wu, Peiling Ke and Chao Sun in IMR of CAS for their contribution to Chapter 9, Professor Chungen Zhou and Dr Yinxue Song for their contribution to Chapter 10, Dr Chunxia Zhang in Baosteel Group Corporation (BGC) and Dr Chen Chen in BUAA for their contribution to Chapter 11, Dr Guofeng Chen in the Northwestern Polytechnical University, China, for his contribution to Chapter 12, Dr Rudder Wu in National Institute for Materials Science (NIMS) Japan for his contribution

to Chapter 13, Professors Hongyu Qi and Xiaoguang Yang in BUAA for their contribution to Chapter 14, and Mrs J. Wu for her contribution to Chapter 15. The authors will be grateful for all readers' comments.

Huibin Xu
Beihang University, China

Thermal barrier coatings prepared by electron beam physical vapor deposition (EB-PVD)

D. ZHANG, North China Electric Power University, China

Abstract: Thermal barrier coatings (TBCs), which offer excellent properties in terms of high-temperature operating, thermal barrier and flow- and wear-resistance, have been developed for application in hot-section components of gas turbines. Research in this area has become a new direction in the surface engineering field. Electron beam physical vapor deposition (EB-PVD) has received much research attention in recent years since it offers many advantages for TBCs.

This chapter introduces the structure and preparation processes of TBCs. Two-layer structured TBCs were prepared by EB-PVD on superalloy IC10/IC6. The behavior of TBCs under thermal cycling was investigated. The roughness of the bond coat was found to have a significant effect on the lifetime of TBCs, the lifetime clearly decreasing during thermal cyclic testing as the roughness average (Ra) of the bond coat increased. The thickness of the pre-oxide layer also affected the lifetime of TBCs, the lifetime decreasing during thermal cyclic testing as the pre-oxide layer thickness increased. Graded thermal barrier coatings were prepared by EB-PVD on superalloy and the thermal cycling behavior was investigated.

Key words: thermal barrier coating, EB-PVD, thermal cycled, two-layer structured TBCs, GTBCs.

1.1 Introduction

There are many methods of preparing thermal barrier coatings (TBCs), such as electron beam physical vapor deposition (EB-PVD), plasma spray, high-velocity oxy-fuel (HVOF), sol-gel, laser chemical vapor deposition, and so on.¹⁻⁸ At the time of writing EB-PVD and plasma spray have become popular preparation methods. Plasma spray has a simpler equipment structure than EB-PVD, and thermal spray has a higher spray rate than EB-PVD.

For plasma spray, it is not necessary to heat the substrate, and the deposition rate is much faster than that of EB-PVD. However, coatings prepared by EB-PVD are different from those prepared by plasma spray. EB-PVD TBCs have better surface roughness than those produced by plasma spray, which means that EB-PVD TBCs have good aerodynamics. EB-PVD TBCs have a columnar crystal microstructure and those produced by plasma

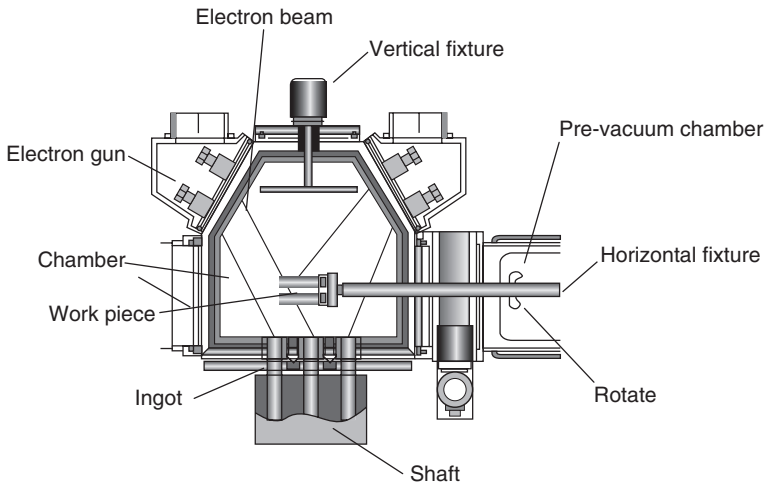
spray a laminated structure. Due to good resistance to spallation from the substrate, TBCs with the columnar structure obtained by EB–PVD have a longer lifespan than those with the laminated structure obtained by plasma spray during thermal cycling. Therefore, EB–PVD TBCs are likely to become popular in the future.

1.1.1 Electron beam physical vapor deposition (EB–PVD) technology and its equipment

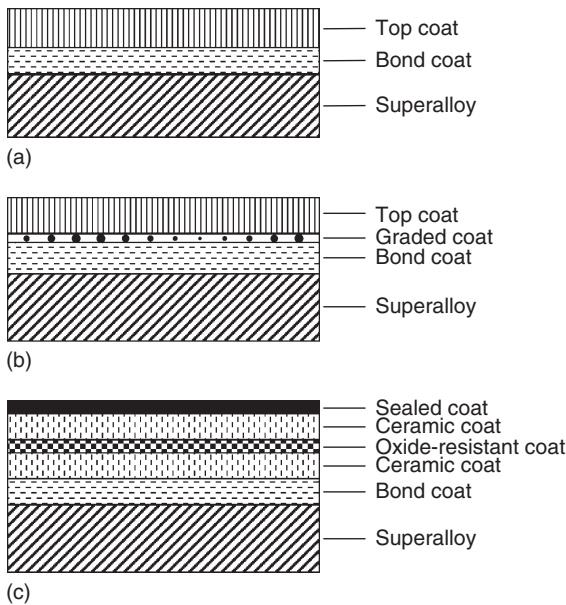
Since the 1980s, EB–PVD has been investigated for preparation of TBCs. A significant development in the 1990s was the invention by Paton Electric Institute of Welding in Ukraine of a new EB–PVD technology which decreased the preparation cost of EB–PVD TBCs. This technology has been widely applied in the production of TBCs.

The electron beam has a very important role as the thermal source of EB–PVD technology. EB–PVD is capable of depositing any type of material. The deposition mechanism consists of an electron beam formed at 2000 °C in an electron gun (either a Pierce gun or an electromagnetism deflexion gun), followed by acceleration of thermal electrons under high voltage. When the high-speed electrons hit materials in the ingot, energy is generated sufficient to melt and convert material into vapor and then deposit it onto the substrate. Compared to other preparation methods, this method has a higher deposition rate. Moreover, deposition parameters can be easily controlled and the surface is very smooth with a Ra surface value of about 1–2 μm. There is a strong adhesion between the substrate and coatings after deposition by EB–PVD. Process parameters are easily modified and the deposition rate can be accurately controlled.

The EB–PVD equipment is more complex compared to other methods. Figure 1.1 gives a diagram of EB–PVD equipment (UE205). There are four electron guns, two sets of sample fixtures (one vertical and one horizontal), three ingots, and two chambers (one of which is a pre-vacuum chamber) in this EB–PVD system. Three electron guns are used to heat the materials in the ingots, respectively, and one electron gun to heat the substrate (work-piece) to achieve the right deposition condition which is able to ensure good adhesion between substrate and coatings. During depositing, the sample fixture keeps rotating to get a stable substrate temperature and uniform coating thickness. Three ingots can deposit from one to three types of material and prepare coatings of different structures. There is a shaft below the material in the ingot. During depositing, the shaft pushes the material up to the ingot, thus increasing the deposition rate. EB–PVD equipment of different types with different structures can prepare TBCs of different shapes and structures. For example, some EB–PVD equipment (UE-206, UE204U) has six electron guns and more power.



1.1 EB-PVD equipment (UE205).



1.2 TBC structures: (a) two-layered; (b) graded; (c) multi-layered.

1.1.2 Thermal barrier coatings (TBCs): structure

There are three types of EB-PVD TBCs: two-layered, graded, and multi-layered. As shown in Fig. 1.2, two-layered structured TBCs are traditional TBCs comprising a bond coat with $M\text{CrAlY}$ ($M = \text{Ni, Co}$) and a ceramic

top coat with 6–8 wt% Y_2O_3 stabilized ZrO_2 . Graded TBCs (GTBCs) can relax the stress between the top coat and the bond coat which is brought by different coefficients of thermal expansion. In the GTBCs system, there is a transition layer with Al_2O_3 between the bond coat and the top coat. Multi-layered TBCs are usually used for specialist applications. In the future, it is likely that nanostructure TBCs will have an important role because they have the capacity to enhance the effectiveness of the thermal barrier.

1.2 Preparation process and parameters

TBCs should be prepared under optimum preparation conditions and parameters. Many preparation parameters can affect the quality of TBCs. Amongst these, three – vacuum pressure, substrate temperature, and deposition rate – can have a significant effect.

1.2.1 Vacuum pressure

O_2 pressure dictates the vacuum pressure in the chamber. If O_2 exists in the chamber, it will decrease the background vacuum. This is because O_2 can result in filament oxidation of the electron gun which will affect its lifetime. If the background vacuum pressure is low during MCrAlY depositing, oxygen will enter into the bond coat, inducing inter-oxidation which will decrease the effectiveness of the bond coat. The background vacuum pressure should be in the range 10^{-2} – 10^{-3} Pa during deposition.

1.2.2 Substrate temperature

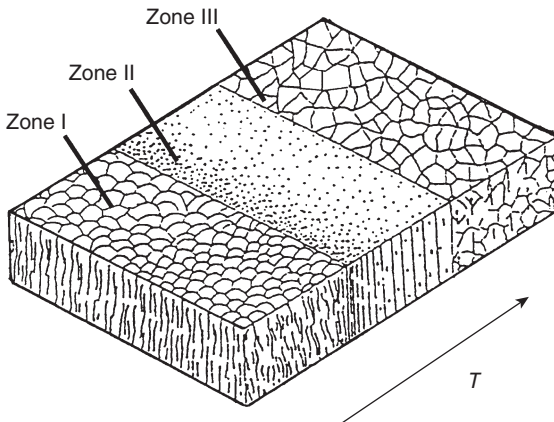
When the electron beam strikes the materials, the resultant transfer of high energy will generate sufficient heat to create vapor which rises and is deposited on the substrate. There are two possible states during solidification of liquid phase on the substrate. One is that material vapor deposits, adheres, and then diffuses into the substrate, and the fine coating forms after deposition. The other is that material vapor deposits onto but debonds with the substrate. In that case, the coating cannot combine with the substrate. Substrate temperature is an important factor in obtaining the fine coating. To increase the adhesion between coatings and the substrate, the substrate should be heated to a high temperature during depositing. Substrate temperature can also affect the crystal structure. Palatnik *et al.* investigated the relationship of substrate temperature and coating crystal structure. If the substrate temperature (T_s) is lower than $2/3$ of the melting point (T_m) of the material, the depositing material solidifies immediately. When it is higher than $2/3$ of the melting point, the depositing material vapor changes into the liquid state, then crystallizes, and finally changes into the solid

state.⁹ Movchan and Demchishin investigated the relationship between substrate temperature and coating crystal structure, then created a model of substrate temperature and coating crystal structure^{10,11} as shown in Fig. 1.3.

When the relationship of substrate temperature and the melting point of the depositing material is $T_s/T_m < 0.3$ (Zone I), the coating has a structure of columnar crystals with a round top surface. Because of the 'self-shadow effect' and uniform diffusion, there are a lot of holes between the grain boundaries. If the substrate temperature is low, the coating has a large cooling rate during depositing. The result is that the size of the columnar crystals in the coating system is small. As shown in Zone I in Fig. 1.3, there is a transitional region between zone I and Zone II, which is composed of columnar crystals with fibrillation.

When the relationship of substrate temperature and the melting point of the depositing material is $0.3 < T_s/T_m < 0.5$ (Zone II), the coating has a structure of compacted columnar crystals. Due to diffusion and concreting on the surface, compacted columnar crystals are formed as shown in Zone II in Fig. 1.3. In the range $0.3 < T_s/T_m < 0.5$, the columnar crystals will grow with the increasing T_s .

When the relationship between substrate temperature and the melting point of the depositing material is $0.5 < T_s/T_m < 1$ (Zone III), the recrystallization structure resulting from diffusion at high temperature can be seen in zone III. As the substrate temperature increases, the cooling rate of the coating decreases and large columnar crystals are formed. In order to obtain the desired crystal structure, the substrate temperature should be between 800 and 900 °C during TBCs deposition.



1.3 Relationship between substrate temperature and coating structure.

1.2.3 Deposition rate

For EB-PVD, both the voltage and the current are important parameters of the deposition rate. Deposition rate affects the size of the columnar crystals and the size and number of holes between the grain boundaries. As the deposition rate increases, the size of the columnar crystals and the holes between the grain boundaries also increase. For example, UE205, subject to 20 KV and 2 A, has a deposition rate of 1 $\mu\text{m}/\text{min}$, which is the optimum deposition condition needed to obtain the desired crystal structure in TBC systems.

1.3 Preparation processes of two-layered thermal barrier coatings (TBCs)

Traditional EB-PVD TBCs have a two-layered structure, comprising a 8YSZ top coat and a MCrAlY bond coat. Due to their simple structure and stability, they are currently used in turbine systems. The preparation process is described in detail below.

1. **Treatment of substrate surface:** To achieve good surface roughness and adhesion, EB-PVD requires a smooth surface to deposit coatings. The substrate surface is treated with different types of abrasive paper to ensure that R_a is about 1–3 μm before deposition. Since surface cleanliness can affect the adhesion between substrate and coatings, substrates are cleaned using acetone and alcohol in an ultrasonic bath.
2. **Preparation of MCrAlY:** To avoid oxidation, the background vacuum is about 10^{-3} Pa before deposition. Substrates should be uniformly heated to 800–900 °C. Substrate temperature plays an important role in obtaining perfect coatings. If it is not suitable for deposition, the bond coat will debond from the substrate. During deposition, sample holders should rotate to achieve uniform thickness and deposition rate. The deposition rate should be 1 $\mu\text{m}/\text{min}$ and the thickness of bond coat about 60–90 μm .
3. **Anneal for diffusion:** After the bond coat is deposited, bond coat and substrate have an extremely weak adhesion. To make it stronger, samples should be annealed at high temperature for several hours. For NiCo-CrAlY, the required temperature is 1050 °C and the annealing time is 2 h. At the high temperature, elements diffuse between the coating and the substrate, after which the interface between the coating and the substrate becomes a metallurgical bond. During annealing, the background vacuum should be at 10^{-3} Pa to avoid oxidation, and the rate of heating and cooling should be about 3 °C/min.
4. **Shot peening:** After annealing, samples should be shot blast in order to make the crystal structure more compact. There are two reasons for this.

First, grains grow during annealing and this decreases resistance to oxidation. To increase oxidation resistance the grain size needs to be small, and shot blast with suitable pressure (shot rate) and ball size can achieve this. Second, coatings prepared by EB-PVD have a lot of holes which allow oxygen ingress. After samples are shot blast, some of these holes are closed and hence oxidation resistance increases. The size of blast ball should be about $\Phi 250 \mu\text{m}$ and the pressure 3 atm.

5. **Pre-oxide step:** Thermal grown oxides (TGO) comprise a compacted Al_2O_3 film formed between the top coat and bond coat which prevents oxygen from entering the bond coat and protects the bond coat from oxidizing. The film should be about 1–2 μm thick.
6. **Top coat deposition:** A top coat with ZrO_2 –8wt.% Y_2O_3 is deposited on the surface of the bond coat. During depositing, the substrate is heated to 800–900 °C and the background vacuum should be at 10^{-2} Pa. Since there is oxygen in the ZrO_2 –8wt.% Y_2O_3 , the background vacuum is not very high. The deposition rate is 1–2 $\mu\text{m}/\text{min}$, and the top coat should be about 120 μm thick.

Thermal cycling tests are carried out to evaluate the resistance of coatings to thermal shock using the following method: the specimens are exposed to air for 0.5 h at 1323 K or 1373 K, and then cooled to room temperature within 5 min by forced air cooling.

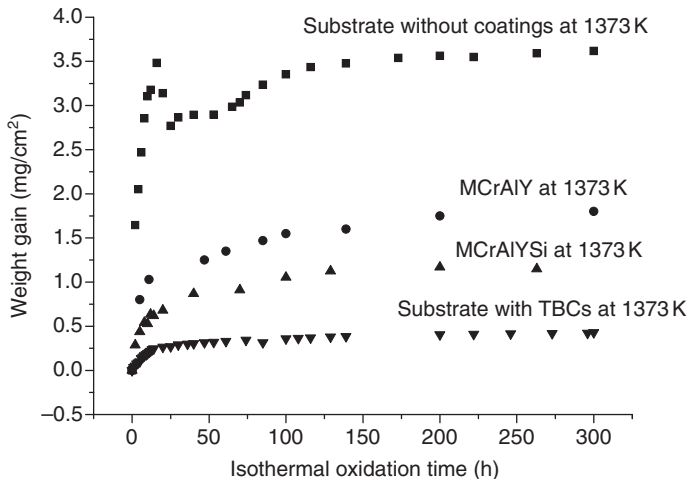
1.3.1 Traditional TBCs

As an example, traditional two-layered structured TBCs are prepared by EB-PVD equipment comprising four electron guns heating Ni_3Al -based alloy IC6.¹² Intermetallic compound (IC) based alloys have been the subject of research for potential application in hot-section components^{13–15} and a high-performance cast Ni_3Al base alloy, alloy IC6, has recently been developed for turbine blades, vanes of advanced aero-engines, and other high-temperature structural components.¹⁶ The sample of alloy IC6 used was rectangle-shaped with dimensions about 15 mm \times 10 mm \times 3 mm. The TBCs top coat was 8wt.% Y_2O_3 stabilized ZrO_2 (YSZ) about 150 μm thick. Both bond coats were about 50 μm thick. Isothermal oxidation was carried out at 1373 K in air, and a thermal cycling test was performed by exposing the sample to air at 1373 K for 30 min followed by forced air-cooling to room temperature within 5 min. A TG-328A thermal analytical balance was used to measure the weight gain of the specimens during oxidation. Scanning electron microscopy (SEM) with energy disperse spectrum (EDS) was employed to study the microstructure of the coatings and the composition distribution across the bond coat and the interface between the bond coat and the alloy IC6.

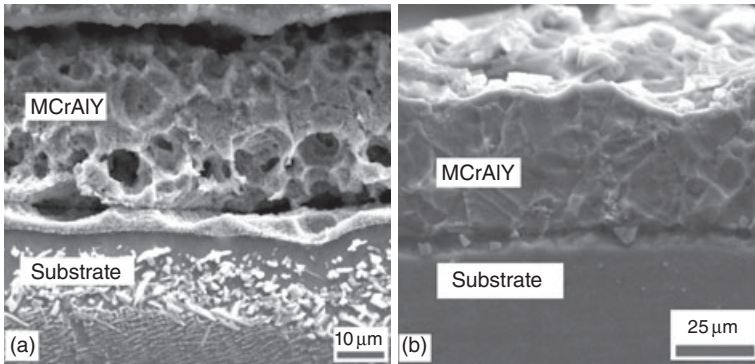
Oxidation of TBCs

Figure 1.4 shows the isothermal oxidation curves of the alloy IC6 with and without coatings. Being exposed to air at 1373 K for 300 h, the weight gain is only about 0.359 mg/cm² for the alloy with TBCs, which is much less than that for the alloy without coatings. This indicates that the current TBC system forms an excellent oxidation protection layer. On the other hand, even though it is well known that only the bond coat in a TBCs system has a role in oxidation protection, the oxidation weight gain for the alloy with TBCs is also lower compared to that coated with only a MCrAlY layer. Therefore, the alloy with TBCs results in lower oxidation weight gain.

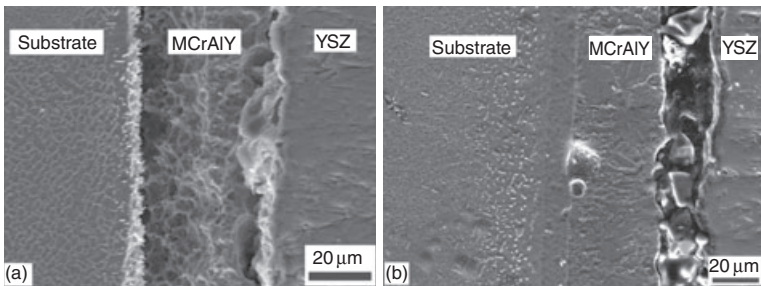
Figure 1.5 is a set of cross-sectional SEM images of alloy IC6 coated with MCrAlY after being isothermally oxidized at 1373 K for 0 h and 60 h. The Mo content in the coatings is 1.3wt.%. From Fig. 1.5(a) and the EDS results, it can be seen that, even in the as-deposited state, a clear interdiffusion zone can be observed between the substrate and the MCrAlY layer. Moreover, some cavity-like images were also observed, which might be brittle phase caused by the diffusion and action of Mo, Ni, and Si.^{16,17} The composition analysis also shows that the Mo content in the MCrAlY layer was about 1.3wt.%. After being isothermally oxidized for 60 h, as shown in Fig. 1.5(b), the interdiffusion zone thickened to as much as ca 20 μm . However, cavity-like images observed in the as-deposited coatings disappeared. The EDS results show that Mo diffused into the MCrAlY layer not only in the interdiffusion zone, but also in the outer layer where the content was higher than 7wt.%. It is considered that such a high Mo content will be one of the causes of the spallation of the ceramic top coat.



1.4 Isothermal oxidation curves of alloy IC6 with and without coatings.¹²



1.5 Cross-sectional SEM images of alloy IC6 coated with MCrAlY: (a) as-deposited; (b) after isothermal oxidation at 1373 K for 60 h.



1.6 SEM cross-sectional micrographs of two-layered TBCs: (a) after thermal cycle testing at 1373 K for 30 h; (b) after thermal cycle testing at 1373 K for 300 h.

Figure 1.6 shows a cross-sectional SEM image of TBCs with MCrAlY as the bond coat after a thermal cycling test at 1373 K for 30 h and 300 h. From Fig. 1.6(a), it can be seen that a thin and uniform TGO layer formed at the interface between YSZ and MCrAlY after the thermal cycling test at 1373 K for 30 h. Figure 1.6(b) shows the cross-sectional SEM image of TBCs after the thermal cycling test at 1373 K for 300 h. It can be seen that a thick TGO layer formed at the interface between YSZ and MCrAlY, which would result in the spallation of YSZ.

1.4 Factors affecting thermal cyclic behavior of TBCs

1.4.1 Effects of pre-oxide layer thickness on thermal cyclic behavior of TBCs

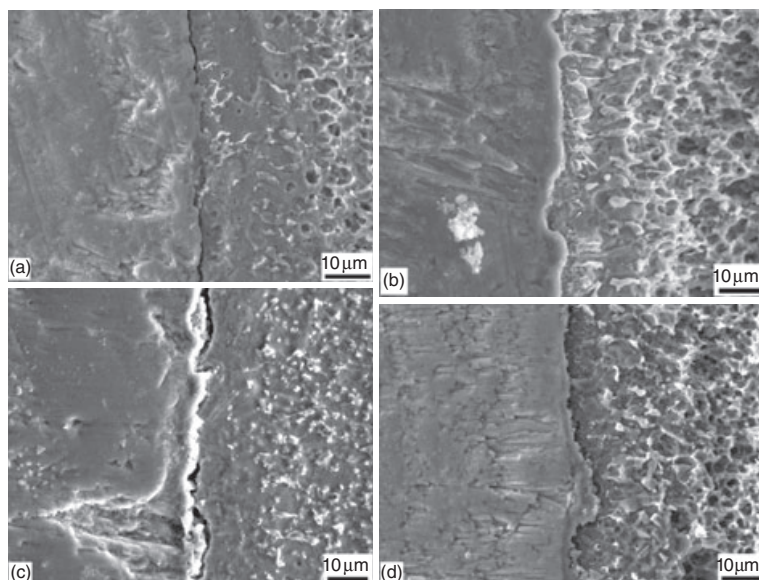
Typical TBCs consist of a MCrAlY bond coat and an yttria stabilized zirconia (YSZ) ceramic top coat.¹⁸ In such two-layered TBC systems, a TGO

layer always forms at the surface of the bond coat, because the YSZ is transparent to oxygen at high temperatures. The TGO layer plays an important role in TBCs performance.^{17,19–21} It is recognized that the failure of TBCs prepared by EB–PVD almost always occurs at the TGO layer with a critical TGO layer thickness of about 5 μm .^{22,23} The spallation of the YSZ top coat from the bond coat is reported to be caused by stresses arising from the formation of the TGO layer and a thermal mismatch between the metallic bond coat and the YSZ top coat.²⁴ However, the thermal cycling test is not only a process for the accumulation of internal stress, but also a process that causes fatigue of the oxide layer and changes the interfacial adhesion, which would affect the thermal cyclic lifetime of TBCs. Conventional two-layered TBCs were prepared by EB–PVD. The substrate material in this study was a Ni-based superalloy. After vacuum annealing at 1323 K for 2 h and before ceramic deposition, the bond coat was heated to 1323 K in air for different times to obtain pre-oxide layers of about 2.5 μm , 3.0 μm , and 3.1 μm measured from SEM images. TBCs vacuum annealed for 2 h were also prepared with a pre-oxide layer about 1 μm thick. Two-layered TBCs, with pre-oxide layers of different thicknesses, were prepared by EB–PVD to investigate the effect of pre-oxide layer thickness and TGO layer microstructure on the thermal cyclic lifetime.

Figure 1.7(a) is a typical cross-sectional SEM image of the as-deposited conventional two-layered TBCs with the bond coat vacuum-annealed for 2 h. A thin pre-oxide layer about 1 μm thick can be seen between the top coat and the bond coat. Figures 1.7(b), (c), and (d) show the cross-sectional SEM images of as-deposited TBCs with pre-oxide layers about 2.5 μm , 3.0 μm , and 3.1 μm thick after exposure to air for 6 h, 14 h, and 20 h, respectively. The interface between the bond coat and the pre-oxide layer is smooth and the pre-oxide layer is intact. By comparing with Fig. 1.7(a), it can be seen that there is no distinct difference with the images except that the thickness of the pre-oxide layer is different.

Figure 1.8 is a set of cross-sectional SEM images of TBCs with different pre-heating times after they had been thermally cycled at 1323 K for 100 h. The TGO layer thickened in all specimens but at different growth rates which accelerates with increasing pre-oxide layer thickness. The uniformity and the degree of intactness of the TGO layer did not show changes in samples with a pre-oxide layer less than 3.0 μm thick. However, cracks near the interface of TGO layer and the bond coat were observed, and the TGO grains became quite coarse in the sample with pre-oxide layer about 3.1 μm thick as shown in Fig. 1.8(d), implying that the TGO layer is very brittle.

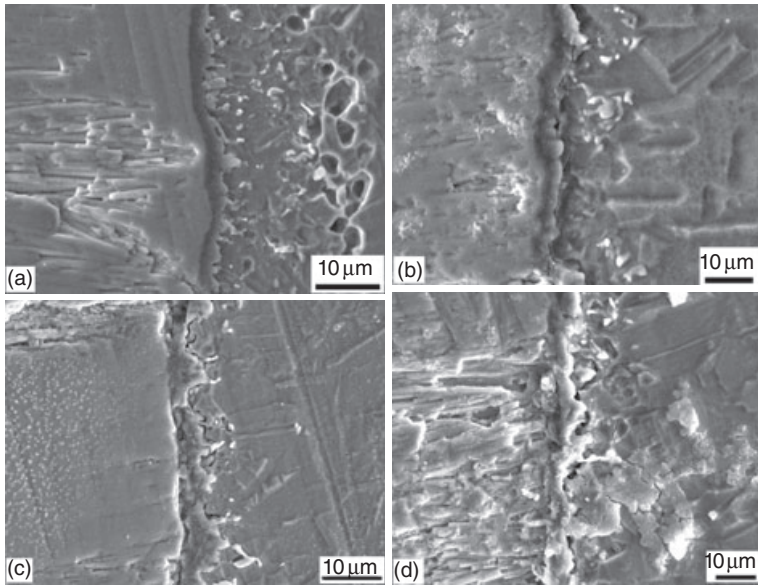
After the coatings had been thermally cycled, the thermal cycling lifetime changed with pre-oxide layers of different thickness. The thermal cyclic lifetime decreased from 730 h (1460 cycles) to 400 h (800 cycles) and the increment in TGO layer thickness for TBCs samples thermally cycled to



1.7 SEM cross-sectional micrographs of two-layered TBCs as-deposited: (a) a pre-oxide layer thickness of 1 μm ; (b) a pre-oxide layer thickness of 2.5 μm ; (c) a pre-oxide layer thickness of 3.0 μm ; (d) a pre-oxide layer thickness of 3.1 μm .

failure increased from 5.6 μm to 6.7 μm with the increasing pre-heating time. The mean growth rates were about $2.1 \times 10^{-12} \text{ m}\cdot\text{s}^{-1}$, $3.0 \times 10^{-12} \text{ m}\cdot\text{s}^{-1}$, $3.9 \times 10^{-12} \text{ m}\cdot\text{s}^{-1}$, and $4.7 \times 10^{-12} \text{ m}\cdot\text{s}^{-1}$ for the TBCs with pre-oxide layers 1.0 μm , 2.5 μm , 3.0 μm , and 3.1 μm thick, respectively. The higher mean growth rate implies that cracks or fracture were easily formed in the thicker TGO layer. The total TGO layer thickness increased from 6.6 μm to 9.8 μm . The increment of oxide layer thickness results in an increase in internal stress during the thermal cycling test, and the internal stress caused by the increment of the TGO layer increased with the increase in the pre-oxide layer thickness. Given that the total oxide layer of the TBCs thermally cycled to failure also increased its thickness with the pre-heating time, at the thermal cycling to failure stage, the total internal stress would be higher for the TBCs pre-heated for a longer time compared with those pre-heated for a shorter time. If the TGO thickness were the only reason for the failure, the thermal cyclic lifetime would be much shorter than the present result (for example, 400 h). Therefore, other factors for failure have to be taken into account.

Figure 1.9 is a set of cross-sectional SEM images of Ni-based superalloy coated with TBCs with different pre-oxides after thermal cycling to spallation at 1323 K. After thermal cycling, the three kinds of TBCs had



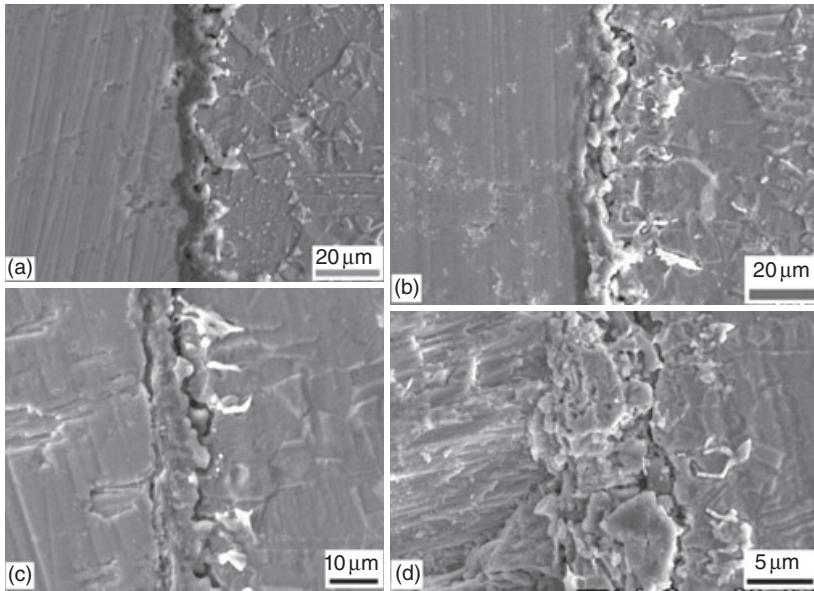
1.8 SEM cross-sectional micrographs of two-layered TBCs after thermal cycling testing at 1323 K for 100 h: (a) a pre-oxide layer thickness of 1 μm ; (b) a pre-oxide layer thickness of 2.5 μm ; (c) a pre-oxide layer thickness of 3.0 μm ; (d) a pre-oxide layer thickness of 3.1 μm .

different lifespans. From Fig. 1.9, it can be seen that the thickness of the TGO layer increased, evidently along with the increase in thermal cycling time among the three kinds of TBCs. For the thinner pre-oxide layer, the TGO layer structure was dense, even, and intact, and, with a thicker pre-oxide layer thickness, the TGO layer had a loose, uneven, and cracked structure.

Two-layered TBCs with pre-oxides of different thickness were prepared by EB-PVD on Ni-based superalloy. As the pre-oxide thickness increased from 1 μm to 3.1 μm , the thermal cyclic lifetime of TBCs decreased from 730 h to 400 h. The growth rate of the TGO layer increased during the thermal cycling test as the pre-oxide layer thickness increased.

1.4.2 Effect of bond coat surface roughness on thermal cyclic behavior of TBCs

The TGO layer plays an important role in TBC performance.^{25,26} It is well recognized that EB-PVD TBCs almost always fail at the TGO layer near the bond coat. In the present study, two-layered thermal barrier coatings were prepared by EB-PVD. The rectangle-shaped specimens of Ni-based

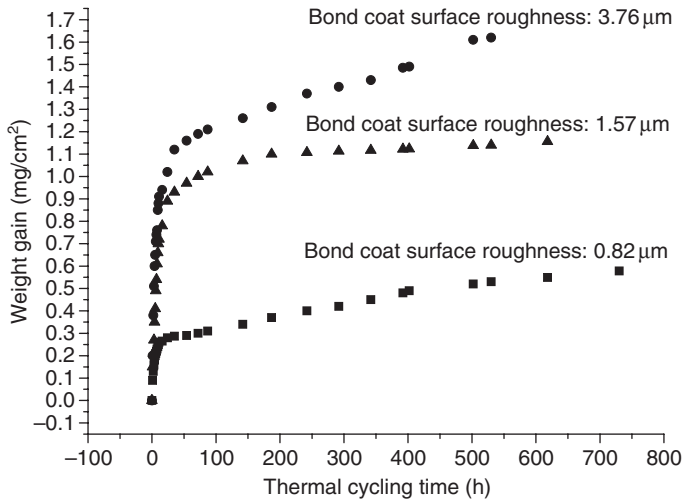


1.9 SEM cross-sectional micrographs of two-layered TBCs after thermally cycled to spallation at 1323 K: (a) a pre-oxide layer thickness of 1 μm ; (b) a pre-oxide layer thickness of 2.5 μm ; (c) a pre-oxide layer thickness of 3.12 μm ; (d) a pre-oxide layer thickness of 4.25 μm .

superalloy DD3 with dimensions 15 mm \times 10 mm \times 3 mm were used as substrate materials. The YSZ (8wt.% Y_2O_3 -stabilized ZrO_2) top coat and MCrAlY (Ni-24Co-15Cr-8Al-1Y, in wt.%) bond coat were about 120 μm and 60 μm thick, respectively. Before ceramic deposition, three different values of surface roughness (R_a) – 0.82 μm , 1.57 μm and 3.76 μm – were created by blasting the surface of the bond coat with different sizes of Al_2O_3 sands.

After ceramic deposition, the R_a values of the top coat were 1.51 μm , 1.71 μm , and 2.93 μm , respectively. Due to the growth of ceramic columns, the surface roughness of the top coat changed during ceramic deposition. Surface roughness of the top coat was not consistent with that of the bond coat.

Figure 1.10 shows the weight gain of TBCs vs the thermal cycling time for the specimens with surface roughness of 0.82 μm , 1.57 μm and 3.76 μm . It can be seen that the weight gain increases and the thermal cycling lifetime decreases with the increase in surface roughness. Higher roughness gives a larger surface area which results in larger weight gain during the cyclic testing. Generally, a rougher surface will increase the net area. Therefore, with the same oxidation rate, the weight gain per unit area will become



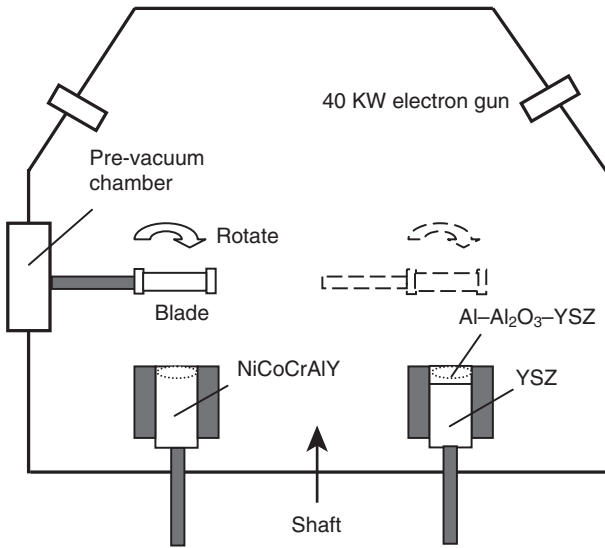
1.10 Thermal cyclic weight gain curves for three types of TBCs.²⁵

larger because the area used for the calculation was fixed according to the shape of the specimen. This means that the TGO thickness does not significantly increase with surface roughness. Compared with the lifetime of 730 h (1460 cycling times) for the specimen with bond coat surface roughness of 0.82 μm , the thermal cycling lifetime for the specimen with bond coat surface roughness of 3.76 μm was only 530 h (1060 cycling times).

1.5 Preparation of graded thermal barrier coatings (GTBCs)

Traditional two-layered structured TBCs for turbine blades consist of an oxidation protective bond coat and a thermally insulating YSZ top coat.^{27,28} The coating is thermally unstable under long exposure at elevated temperatures due to a TGO scale caused by the formation of alumina at the bond coat/YSZ top coat interface during selective oxidation of the bond coat.^{29–32} Stresses arising from different thermal coefficients between the TGO and the bond coat lead to coating failure along the interface between the TGO and the bond coat. Compared with the traditional two-layered coating, a continuously graded coating has the advantage of forming a continuous microstructure along the cross-section of the coating and consequently avoiding stress concentrations in the coating.

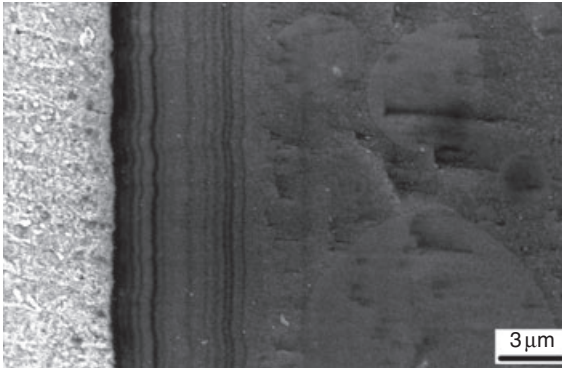
There are many traditional approaches preparing GTBCs. For example, they have been prepared by the co-deposition of a tablet comprising a mixture of Al_2O_3 –YSZ and YSZ onto NiCoCrAlY bond coat by means of



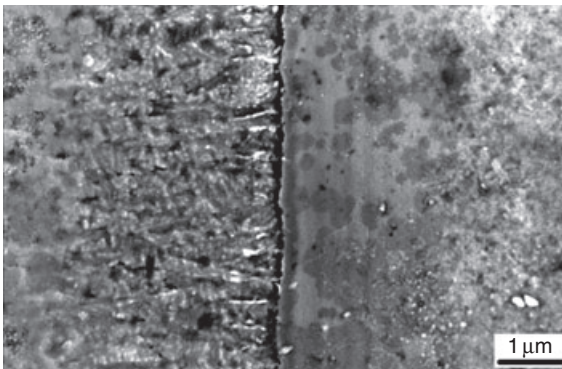
1.11 Preparation of graded TBCs.

EB-PVD. A Ni-22Co-21Cr-8Al-1Y coating about 40 μm thick was first deposited onto the substrate. Subsequently, a tablet pressed from a mixture of powders of Al_2O_3 -YSZ and an ingot of ZrO_2 -8wt% Y_2O_3 was evaporated by EB-PVD. As the vapor pressures of the tablet ingredients varied at the evaporation temperature, selective evaporation of the molten tablet of Al_2O_3 -YSZ took place: first Al_2O_3 and then YSZ. Figure 1.11 shows the preparation diagram. As-deposited coatings were heat-treated for 4 h at 1323 K. EM with EDS was used to analyze the composition distribution across the thickness of the coating and transmission electron microscopy (TEM) to observe the microstructures. The phases in the gradient coating were analyzed by X-ray diffraction (XRD) with $\text{CuK}\alpha$ radiation.

Figure 1.12 shows the SEM micrograph across the thickness of the GTBC along with the EDS analysis. In the gradient coating, the left side is a NiCoCrAlY bond coat, followed by a transition layer about 10 μm thick. In the YSZ top coat, a typical columnar microstructure was observed. The EDS analysis revealed that the distribution of elements such as Ni, Al, O, and Zr changed continuously across the thickness of the coating. The transition layer consists of t - ZrO_2 phase and α - Al_2O_3 phase. In addition, $\gamma + \gamma'$ phases from Ni-based solid solution in the NiCoCrAlY bond coat can be detected. Figure 1.13 is a magnification of a cross-sectional micrograph of the transition layer. In the transition layer, a thin Al_2O_3 layer, less than 2 μm thick, and a two-phase $\text{ZrO}_2/\text{Al}_2\text{O}_3$ region, about 5 μm thick, are observed and the outer layer is YSZ top coat. The microstructure of the GTBC moves



1.12 Cross-section micrograph of the as-deposited gradient coating.



1.13 SEM cross-sectional micrograph of the transition layer in the as-deposited gradient coating.

gradually from the metallic bond coat to the YSZ top coat, due to the formation of the transition layer.

1.5.1 New investigations on bond coat

For new generation engines with a high thrust ratio, the turbine inlet temperature (TIT) could reach up to 2000 K.³³ In such a case, the traditional TBC materials, including YSZ as the ceramic top coat and MCrAlY as the metallic bond coat, might not be adequate. Recently, many efforts have been made to explore new TBC materials that can work at higher temperatures than traditional TBC materials. As a promising high-temperature material with the potential capability of working at 1473 K, NiAl could be exploited as the bond coat material in TBC systems to replace the currently used MCrAlY (M: Ni/Co or Ni+Co) bond coat.^{34–38} Besides high-

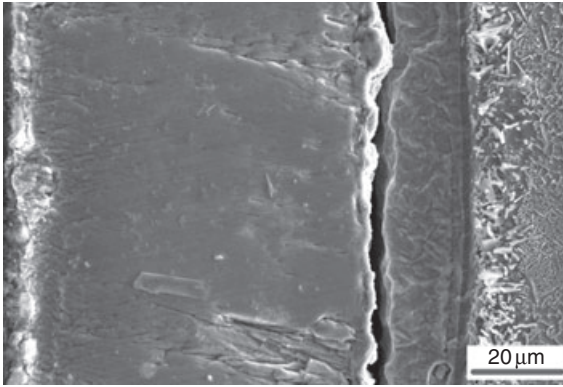
temperature oxidation resistance, inter-diffusion between the bond coat and the superalloy substrate should be well controlled in order to prevent the formation of the so-called secondary reaction zone (SRZ), especially in the case of Ni-based single-crystal superalloy substrate. In view of this, NiAl coatings have been modified by adding doping elements such as Pt and Hf.^{35,37} Also, a double-layered structure was applied, where the NiAl was used as the outer layer, while PtAl, RuAl, and Cr formed the interlayer between the NiAl and the substrate.³⁹⁻⁴³

1.5.2 New investigations on top coat

6–8 wt% yttria-partially stabilized zirconia (YSZ) has been widely used as the top coat material for TBC in past decades due to its low thermal conductivity and high thermal expansion coefficient (TEC) which is compatible with that of the underlying superalloy substrate.^{44,45} Recently, new ceramic candidates⁴⁶⁻⁵⁸ for TBC application to replace the current YSZ have been increasingly studied, with the aim of developing TBCs with a higher temperature capability, a lower thermal conductivity, and longer life time. The microstructure of YSZ TBCs has also been modified to improve these properties.^{59,60} The thermal conductivity of zirconia TBCs is significantly lowered by adding as dopants yttria and niobia.⁶¹ Also, La_2O_3 has been selected as an additive to YSZ because it can significantly suppress densification of YSZ. The EB-PVD La_2O_3 -YSZ coating demonstrates an extremely low thermal conductivity as well as high resistance to sintering, and the coating is characterized by feather-like sub-columns and nanopores, which contribute to limiting thermal transport.⁶² It has been suggested that a thermodynamic database be established for the ZrO_2 - Y_2O_3 - Gd_2O_3 - Al_2O_3 system in order to explore its implications for TBCs.⁶³

1.6 Failure mechanism

The failure mechanism for TBCs can be considered to be the combination of internal stress accumulation as the TGO layer thickness increases and fatigue of the TGO layer during thermal cycle testing. It is believed that sintering of the ceramic top coat is also one of the reasons for failure of EB-PVD TBCs. The formation of a TGO layer and sintering of the top coat will increase residual stress and brittleness of the coating and weaken the adhesion of the top coat to the bond coat. Two-layered TBCs prepared by EB-PVD always fail between the bond coat and the TGO layer. As shown in Fig. 1.14, the SEM image indicates that the bond coat and the TGO layer debonded. When the TGO layer thickness exceeds some certain value, the interface adhesion weakens and cracks form between the bond coat and the TGO layer.



1.14 The typical cross-sectional SEM of two-layered TBCs failure.

1.7 Conclusion

Thermal barrier coatings prepared by EB–PVD have a very important role in protecting superalloys operating in high-temperature environments. Different top coat (ceramic coat) and bond coat materials will come into use in order to improve high-temperature performance. Rare earth materials with lanthanum and cerium being doped into zirconate are being investigated as elements for incorporation into EB–PVD-prepared top coat. The composition, crystal structure, and cyclic oxidation behaviour of these coatings are being studied. For the bond coat, NiAl, PtAl, and RuAl are prepared by EB–PVD and their resistance to oxidation when subjected to high temperatures is being investigated.

1.8 References

1. J.R. NICHOLLS, M.J. DEAKIN, D.S. RICKERBY, A comparison between the erosion behaviour of thermal spray and electron beam physical vapour deposition thermal barrier coatings, *Wear* **233–235** (1999) 352–361.
2. R. VABEN, H. KABNER, A. STUKE, F. HAULER, D. HATHIRAMANI, D. STÖVER, Advanced thermal spray technologies for applications in energy systems, *Surface and Coatings Technology* **202** (2008) 4432–4437.
3. Y. WANG, G. SAYRE, Commercial thermal barrier coatings with a double-layer bond coat on turbine vanes and the process repeatability, *Surface and Coatings Technology* **203** (2009) 2186–2192.
4. M. MOVCHAN, YU. RUDOY, Composition, structure and properties of gradient thermal barrier coatings (TBCs) produced by electron beam physical vapor deposition (EB–PVD), *Materials and Design* **19** (1998) 253–258.
5. P.S. ANDERSON, X. WANG, P. XIAO, Impedance spectroscopy study of plasma sprayed and EB–PVD thermal barrier coatings, *Surface and Coatings Technology* **185** (2004) 106–119.

6. C. VIAZZI, J.P. BONINO, F. ANSART, Synthesis by sol-gel route and characterization of yttria stabilized zirconia coatings for thermal barrier applications, *Surface and Coatings Technology* **201** (2006) 3889–3893.
7. F. TANG, J.M. SCHOENUNG, Local accumulation of thermally grown oxide in plasma-sprayed thermal barrier coatings with rough top-coat/bond-coat interfaces, *Scripta Materialia* **52** (2005) 905–909.
8. T. GOTO, Thermal barrier coatings deposited by laser CVD, *Surface and Coatings Technology* **198** (2005) 367–371.
9. L.S. PALATNIK, Y.F. KOMNIK, *Phys. Metal and Metallogr.* **10** (1960) 141–142.
10. B.A. MOVCHAN, A.V. DEMCHISHIN, Study of structure and properties of thick vacuum condensates of nickel, titanium, tungsten, aluminum oxide and zirconium dioxide, *Fizika Metallovi Metallovedeie* **28** (1969) 83–90.
11. R.F. BUNSHAH, Structure/property relationships in evaporated thick films and bulk coatings, *Journal of Vacuum Science and Technology* **11** (1974) 633–638.
12. D. ZHANG, S. GONG, H. XU, H. ZHANG, Y. HAN, Thermal cycling behaviors of thermal barrier coatings on intermetallic Ni₃Al based superalloy, *Surface and Coatings Technology* **168** (2003) 78–83.
13. T. NODA, Application of cast gamma TiAl for automobiles, *Intermetallics* **6** (1998) 709–713.
14. M. YAMAGUCHI, H. INUI, K. ITO, High-temperature structural intermetallics, *Acta Materialia* **48** (2000) 307–322.
15. Z.P. XING, Y.F. HAN, Z.Y. CHENG, TEM study on the microstructure of the NiCrAlYSi coating/IC6 alloy substrate, *Acta Metallurgica Sinca* **134** (1998) 1149–1152 (in Chinese).
16. Y.F. HAN, Z.P. XING, M.C. CHATURVEDI, In: *Structural Intermetallics* (1997) 713; M.V. Nathal, R. Darolia, C.T. Liu, P.L. Martin, D.B. Miracle, R. Wagner, M. Yamaguchi (eds); The Minerals, Metals and Materials Society, Warrendale, PA.
17. X.F. BI, H.B. XU, S.K. GONG, Investigation of the failure mechanism of thermal barrier coatings prepared by electron beam physical vapor deposition, *Surface and Coatings Technology* **130** (2000) 122–127.
18. D. ZHANG, S.K. GONG, H.B. XU, Effects of pre-oxide layer thickness on thermal cyclic behavior of thermal barrier coatings, *Key Engineering Materials* **326–328** (2007) 1746–1749.
19. F. JAMARANI, M. KOROTKIN, Compositionally graded thermal barrier coatings for high temperature aero gas turbine components, *Surface and Coatings Technology* **54/55** (1992) 58–63.
20. K.S. FANCEY, A. MATTHEWS, Ionisation assisted PVD of zirconia thermal barrier coatings. Proceedings of the International Conference on Metallurgical Coatings, *Journal of Vacuum Science Technology A* **4**(6) (1986) 2656–2660.
21. H.B. XU, H.B. GUO *et al.*, Development of gradient thermal barrier coatings and their hot-fatigue behavior, *Surface and Coatings Technology* **130** (2000) 133–139.
22. A.G. EVANS, D.R. MUMM, J.W. HUTCHINSON *et al.*, Mechanisms controlling the durability of thermal barrier coatings, *Progress in Materials Science* **46** (2001) 505–553.
23. A. RABIEI, A.G. EVANS, Failure mechanisms associated with the thermally grown oxide in plasma-sprayed thermal barrier coatings, *Acta Materialia* **48** (2000) 3963–3976.

24. M. KOIZUMI, K. URABE, *Funct. Gradient Compos.* **75**(6) (1989) 887–893.
25. D. ZHANG, S. GONG, H. XU, Z. WU, Effect of bond coat surface roughness on the thermal cyclic behavior of thermal barrier coatings, *Surface and Coatings Technology* **201** (2006) 649–653.
26. M.Y. ALI, S.Q. NUSIER, G.M. NEWAZ, Mechanics of damage initiation and growth in a TBC/superalloy system, *International Journal of Solids and Structures* **38** (2001) 3329–3340.
27. H. GUO, X. BI, S. GONG, H. XU, Microstructure investigation on porous thermal barrier coating prepared by EB–PVD, *Scripta Materiala* **44** (2001) 683–687.
28. H. GUO, S. GONG, C. ZHOU, H. XU, Investigation on hot-fatigue behaviors of gradient thermal barrier coatings by EB–PVD, *Surface and Coatings Technology* **148** (2001) 110–116.
29. B.A. MOVCHAN, I.S. MALASHENKO, K. YU. YAKOVCHUK, Two- and three-layer coatings produced by deposition in vacuum for gas turbine blade protection, *Surf. Coat. Technol.* **67** (1994) 55–63.
30. R.A. MILLER, C.E. LOWELL, Failure mechanisms of thermal barrier coatings exposed to elevated-temperatures, *Thin Solid Films* **195** (1982) 265–273.
31. S.M. MEIER, D.M. NISSLEY, K.D. SHEFFLER, T.A. CRUSE, Thermal barrier coating life prediction model development, *Trans. ASME* **114** (1992) 258–263.
32. KH. G. SCHMITT-THOMAS, Thermal barrier coatings with improved oxidation resistance, *Surf. Coat. Technol.* **68/69** (1994) 113–115.
33. H. GUO, L. SUN, H. LI, S. GONG, High temperature oxidation behavior of hafnium modified NiAl bond coat in EB–PVD thermal barrier coating system, *Thin Solid Films* **516** (2008) 5732–5735.
34. C. LEYENS, B.A. PINT, I.G. WRIGHT, Effect of composition on the oxidation and hot corrosion resistance of NiAl doped with precious metals, *Surf. Coat. Technol.* **133–134** (2000) 15–22.
35. Y. ZHANG, J.A. HAYNES, B.A. PINT, I.G. WRIGHT, W.Y. LEE, Martensitic transformation in CVD NiAl and (Ni,Pt)Al bond coatings, *Surf. Coat. Technol.* **163–164** (2003) 19–24.
36. B.A. PINT, J.R. DISTEFANO, I.G. WRIGHT, Oxidation resistance: one barrier to moving beyond Ni-base superalloys, *Mater. Sci. Eng. A* **415** (2006) 255–263.
37. B.A. PINT, K.L. MORE, I.G. WRIGHT, Effect of quaternary additions on the oxidation behavior of Hf-doped NiAl, *Oxid. Met.* **59** (3–4) (2003) 257–283.
38. B.A. PINT, The role of chemical composition on the oxidation performance of aluminide coatings, *Surf. Coat. Technol.* **188–189** (2004) 71–78.
39. D. YOSHIDA, Y. SHIBATA, S. HAYASHI, T. NARITA, Changes of an outer beta-NiAl and inner alpha-Cr coating on Ni-40 at% Cr alloy during oxidation at 1373 K in air, *Oxid. Met.* **64** (1–2) (2005) 119–130.
40. J. RIETHMUELLER, G. DEHM, E.E. AFFELDT, E. ARZT, Microstructure and mechanical behavior on of Pt-modified NiAl diffusion coatings, *J. Mater. Res.* **97** (6) (2006) 689–698.
41. B. TRYON, T.M. POLLOCK, Experimental assessment of the Ru–Al–Ni ternary phase diagram at 1000 and 1100 °C, *Mater. Sci. Eng. A*, **430** (1–2) (2006) 266–276.
42. B. TRYON, T.M. POLLOCK, M. GIGLIOTTI, *et al.*, Thermal expansion behavior of ruthenium aluminides, *Scripta Mater.* **50** (2004) 845–848.
43. Q. WEI, H. GUO, S. GONG, H. XU, Novel microstructure of EB–PVD double ceramic layered thermal barrier coatings, *Thin Solid Films* **516** (2008) 5736–5739.

44. Q. WEI, H. GUO, S. GONG, H. XU, Novel microstructure of EB-PVD double ceramic layered thermal barrier coatings, *Thin Solid Films* **516** (2008) 5736–5739.
45. D.R. CLARKE, Materials selection guidelines for low thermal conductivity thermal barrier coatings, *Surface and Coatings Technology* **163–164** (2003) 67–74.
46. J.R. NICHOLLS, K.J. LAWSON, A. JOHNSTONE, D.S. RICKERBY, Methods to reduce the thermal conductivity of EB-PVD TBCs, *Surface and Coatings Technology* **151–152** (2002) 383–391.
47. X.Q. CAO, R. VABEN, D. STÖVER, Ceramic materials for thermal barrier coatings, *Journal of the European Ceramic Society* **24** (2004) 1–10.
48. M. GELL, L. XIE, X. MA, E.H. JORDAN, N.P. PADTURE, Highly durable thermal barrier coatings made by the solution precursor plasma spray process, *Surface and Coatings Technology* **177/178** (2004) 97–102.
49. D.L. YOUCHISON, M.A. GALLIS, R.E. NYGREN, J.M. MCDONALD, T.J. LUTZ, Effects of ion beam assisted deposition, beam sharing and pivoting in EB-PVD processing of graded thermal barrier coatings, *Surface and Coatings Technology* **177/178** (2004) 158–164.
50. S. RAGHAVAN, H. WANG, Thermal properties of zirconia co-doped with trivalent and pentavalent oxides, *Acta Materialia* **49** (2001) 169–179.
51. S. RAGHAVAN, H. WANG, Ta₂O₅/Nb₂O₅ and Y₂O₃ co-doped zirconias for thermal barrier coatings, *Journal of the American Ceramic Society* **87** (3) (2004) 431–437.
52. M. MATSUMOTO, N. YAMAGUCHI, H. MATSUBARA, Low thermal conductivity and high temperature stability of ZrO₂-Y₂O₃-La₂O₃ coatings produced by electron beam PVD, *Scripta Materialia* **50** (2004) 867–871.
53. D. ZHU, R.A. MILLER, Thermal conductivity and sintering behavior of advanced thermal barrier coatings, *Ceramic Engineering and Science Proceedings* **23** (2002) 457–468.
54. R. GADOW, M. LISCHKA, Lanthanum hexaaluminate – novel thermal barrier coatings for gas turbine applications – materials and process development, *Surface and Coatings Technology* **151–152** (2002) 392–399.
55. X. CAO *et al.*, Lanthanum-cerium oxide as a thermal barrier-coating material for high-temperature applications *Advanced Materials* **15** (2003) 1438–1442.
56. Q. XU, W. PAN *et al.*, Preparation and thermophysical properties of Dy₂Zr₂O₇ ceramic for thermal barrier coatings, *Materials Letters* **59** (22) (2005) 2804–2807.
57. D. MARKUS, R. VABEN, D. STÖVER, LaYbO₃, a candidate for thermal barrier coating materials, *Ceramic Engineering and Science Proceedings* **24** (3) (2003) 637–643.
58. J. WU, X. WEI *et al.*, Low-thermal-conductivity rare-earth zirconates for potential thermal-barrier-coating applications, *Journal of the American Ceramic Society* **85** (12) (2002) 3031–3035.
59. S. GU, T.J. LU, D.D. HASS, H.N.G. WADLEY, Thermal conductivity of zirconia coatings with zig-zag pore microstructures, *Acta Materialia* **49** (2001) 2539–2547.
60. X. CAO, R. VABEN, F. TIETZ, D. STÖVER, New double-ceramic-layer thermal barrier coatings based on zirconia-rare earth composite oxides, *Journal of the European Ceramic Society* **26**(3) (2006) 247–251.
61. M. MATSUMOTO, N. YAMAGUCHI, H. MATSUBARA, La₂O₃ doped Y₂O₃ stabilized ZrO₂ TBC prepared by EB-PVD, *Key Engineering Materials* **317–318** (2006) 501–504.

62. D.S. ALMEIDA, C.R.M. SILVA, M.C.A. NONO, C.A.A. CAIRO, Thermal conductivity investigation of zirconia co-doped with yttria and niobia EB-PVD TBCs, *Materials Science and Engineering, A* **443** (1–2) (2007) 60–65.
63. O. FABRICHNAYA, S. LAKIZA, C. WANG *et al.*, Thermodynamic database for the ZrO₂-YO₃/2-GdO₃/2-AlO₃/2 system and application to thermal barrier coatings, *Journal of Phase Equilibria and Diffusion* **27** (4) (2006) 343–352.

W. MA and H. DONG, Inner Mongolia University
of Technology, China

Abstract: This chapter gives a summary of the use of ceramic materials such as the standard yttria stabilized zirconia (YSZ) and some further candidate materials, Al_2O_3 , TiO_2 , mullite, $\text{CaO/MgO} + \text{ZrO}_2$, $\text{CeO}_2 + \text{YSZ}$, $\text{Y}_2\text{O}_3 + \text{HfO}_2$, zircon, $\text{La}_2\text{Zr}_2\text{O}_7$, $\text{La}_2\text{Ce}_2\text{O}_7$, $\text{LaMgAl}_{11}\text{O}_{19}$, SrZrO_3 , etc. as TBC materials. The thermophysical properties and corrosion-resistance characteristic of the TBC candidate materials and their thermal cycling behavior are discussed. The primary future development directions for ceramic TBC materials are also given in this chapter.

Key words: ceramic TBC material, YSZ, thermal conductivity, thermal expansion coefficient, thermal cycling.

2.1 Introduction

Some ceramic materials possessing low thermal conductivities have been used as thermal barrier coating (TBC) materials to increase turbine inlet temperatures since the 1960s. With increasing engine efficiency, they can reduce metal surface temperatures and prolong the lifetime of the hot sections of aero-engines and land-based turbines. The first application of TBCs in aerospace was developed by the National Advisory Committee for Aeronautics (NACA) and the National Bureau of Standards (NBS). The coating of calcia stabilized zirconia on the exhaust nozzle of the X-15 manned rocket plane in 1960s was believed to be the first use of TBCs in manned flight.¹ The ceramic coatings were first successfully applied to turbine section components in research engines in the mid-1970s,^{2,3} and by the 1980s they were applied in the turbine section components of certain commercial gas turbine engines.⁴ With further development, several ceramic materials such as YSZ (yttria stabilized zirconia), Al_2O_3 , TiO_2 , mullite, $\text{CaO/MgO} + \text{ZrO}_2$, $\text{CeO}_2 + \text{YSZ}$, $\text{Y}_2\text{O}_3 + \text{HfO}_2$, zircon, $\text{La}_2\text{Zr}_2\text{O}_7$, $\text{La}_2\text{Ce}_2\text{O}_7$, $\text{LaMgAl}_{11}\text{O}_{19}$, SrZrO_3 , etc. have been evaluated as TBC materials. Some detailed reviews on ceramic materials for TBCs have been contributed by Cao *et al.*,⁵ Levi,⁶ Schulz *et al.*^{7,8} and Clarke and Phillot.⁹

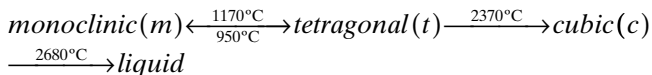
The selection of TBC materials is restricted by some basic requirements, such as high melting point, no phase transformation between room temperature and operating temperature, low thermal conductivity, chemical

inertness, thermal expansion matching with the metallic substrate, good adherence to the metallic substrate and low sintering rate of the porous microstructure.^{10,11} So far, no one material can fulfill all the requirements mentioned above; instead, only some of them can be satisfied. The properties of some ceramic materials which have been evaluated as TBC materials are listed in Table 2.1. Thermal expansion coefficient (TEC) and thermal conductivity seem to be the most important properties for TBC materials selection. These data are collected from different references and hence may not be complete. The number before YSZ represents the weight percentage of Y_2O_3 in ZrO_2 . The advantages and disadvantages of some TBC materials are listed in Table 2.2.

2.2 State-of-the-art ceramic thermal barrier coating (TBC) material – yttria stabilized zirconia (YSZ)

Prior to 1975, pure zirconia (ZrO_2) was of very limited interest as a structural or engineering ceramic, and its use was restricted to refractory applications.¹² This is attributed to the displacive tetragonal (*t*) to monoclinic (*m*) phase transformation, which occurs at $\sim 950^\circ C$ on cooling in pure ZrO_2 and is accompanied by a shear strain of ~ 0.16 and a volume expansion of $\sim 4\%$. The change of shape with the transformed volume can result in catastrophic fracture and hence structural unreliability of fabricated components. However, ZrO_2 has other intrinsic physical and chemical properties, including high hardness, good wear resistance, low coefficient of friction, chemical inertness, ionic conductivity, low thermal conductivity and high melting point, which make it attractive as an engineering material. The focus of continued effort is to understand and improve its mechanical behavior.¹³ The dramatic increase in its industrial applicability has been brought about by the discovery that the $t \rightarrow m$ phase transformation can be controlled by suitable materials processing to become the source of transformation plasticity and transformation toughening in tailored, two-phase microstructures.¹⁴

Pure ZrO_2 experiences the following phase transformations:



Pure ZrO_2 at ambient pressure is polymorphic, exhibiting cubic (*c*) (fluorite) structure ($Fm\bar{3}m$) at high temperatures ($>2370^\circ C$), tetragonal (*t*) structure ($P4_2/nmc$) at intermediate temperatures ($1200^\circ C$ – $2370^\circ C$) and monoclinic (*m*) symmetry ($P2_1/c$) at low temperatures ($<950^\circ C$). The $t \rightarrow m$ phase transformation in pure ZrO_2 commences at $\sim 950^\circ C$ (referred to as M_s) on cooling and is reversible at $\sim 1150^\circ C$ on heating.¹⁵ The *t* and *m*

Table 2.1 The properties of TBC materials⁵

Materials	T_m (K)	$D_{th}(m^2s^{-1}) \times 10^{-6}$	λ ($Wm^{-1}K^{-1}$)	α (K^{-1}) $\times 10^{-6}$	E (GPa)	C_p ($Jg^{-1}K^{-1}$)	ν
ZrO ₂	2953	0.43	2.17	15.3	21		0.25
3YSZ	2973	0.58	2.12	11.5(293–1273 K)		0.64	
8YSZ (APS)				10.7(293–1273 K)	40		0.22
18YSZ				10.53			
5 wt% CaO + ZrO ₂	2558 (soften)			9.91	149.3		0.28
3Al ₂ O ₃ ·2SiO ₂	2123		3.3	5.3(293–1273 K)	30		0.25
Al ₂ O ₃	2323	0.47	5.8	9.6	30		0.26
Al ₂ O ₃ (TGO)				8(293–1273 K)	360		0.22
Al ₂ O ₃ + TiO ₂				5.56(1073 K)			
CeO ₂	2873	0.65	2.77	13(293–1500 K)	172	0.47	0.27–0.31
La ₂ Zr ₂ O ₇	2573	0.86	1.56	9.1(293–1273 K)	175	0.49	
La ₂ Ce ₂ O ₇		0.19	0.6	12.3(573–1473 K)		0.43	
BaZrO ₃	2963	1.25	3.42	8.1(293–1273 K)	181	0.45	
SrZrO ₃	2883	1.4	2.08(1273 K)	10.9(473–1373 K)	170	0.46	0.25
YBa ₂ ZrO ₆	1973		0.37(543 K)		120	2.8	
CaTi _{1/2} ZrO ₇			2.1	9.04		0.7	
TiO ₂	2098	0.52	3.3	9.4(293–1500 K)	283		0.28
Y ₂ Ti ₂ O ₇	>2173			11.0(293–1293 K)			
Y ₃ Al ₅ O ₁₂	2243		3.0	9.1			
LaMgAl ₁₁ O ₁₉			1.7	10.1(298–1473 K)		0.86	
LaPO ₄	2343		1.8	10.5	133		0.28
CePO ₄	2318	1.4		9–11		0.43	
2MgO·NiO	2573		1.9				
BaNd ₂ Ti ₃ O ₁₀ (BNT) (Applied Thin Film, Inc.)	>1800		0.5 (1573 K)	11.5			
NiCoCrAlY (bond coat)				17.5(293–1273 K)	86		0.3
IN737 superalloy (substrate)				16(293–1273 K)	197		0.3

Symbols have the following meanings: D_{th} , thermal diffusivity; E, Young's modulus; α , thermal expansion coefficient; λ , thermal conductivity; C_p , heat capacity; ν , Poisson's number; T_m , melting point; TGO, thermally grown oxide on bond coat.

Table 2.2 Some TBC materials and their characteristics⁵

Materials	Advantages	Disadvantages
7–8 YSZ	<ul style="list-style-type: none"> (1) high thermal expansion coefficient (2) low thermal conductivity (3) high thermal-shock resistance 	<ul style="list-style-type: none"> (1) sintering above 1473 K (2) phase transformation (1443 K) (3) corrosion (4) oxygen-transparent (1) crystallization (1023–1273 K) (2) very low thermal expansion coefficient
Mullite (3Al ₂ O ₃ ·2SiO ₂)	<ul style="list-style-type: none"> (1) high corrosion resistance (2) low thermal conductivity (3) good thermal-shock resistance below 1273 K (4) not oxygen-transparent 	<ul style="list-style-type: none"> (1) phase transformation (1273 K) (2) high thermal conductivity (3) very low thermal expansion coefficient
Alumina (Al ₂ O ₃)	<ul style="list-style-type: none"> (1) high corrosion resistance (2) high hardness 	<ul style="list-style-type: none"> (1) increased sintering rate (2) CeO₂ precipitation (>1373 K) (3) CeO₂-loss during spraying
YSZ + CeO ₂	<ul style="list-style-type: none"> (3) not oxygen-transparent (1) high thermal expansion coefficient (2) low thermal conductivity (3) high corrosion resistance (4) less phase transformation between <i>m</i> and <i>t</i> than YSZ (5) high thermal-shock resistance 	
La ₂ ZrO ₇	<ul style="list-style-type: none"> (1) very high thermal stability (2) low thermal conductivity (3) low sintering rate 	<ul style="list-style-type: none"> (1) relatively low thermal expansion coefficient
La ₂ Ce ₂ O ₇	<ul style="list-style-type: none"> (4) not oxygen-transparent (1) very high thermal stability (2) high thermal expansion coefficient (3) low thermal conductivity 	<ul style="list-style-type: none"> (1) CeO₂-loss during spraying (3) relatively high sintering rate (>1523 K)
Silicates	<ul style="list-style-type: none"> (4) high corrosion resistance (1) cheap, readily available (2) high corrosion resistance 	<ul style="list-style-type: none"> (1) decomposition into ZrO₂ and SiO₂ during thermal spraying (2) very low thermal expansion coefficient
SrZrO ₃	<ul style="list-style-type: none"> (1) high thermal expansion coefficient (2) low thermal conductivity (3) low sintering rate 	<ul style="list-style-type: none"> (1) phase transformations (2) SrO-loss during spraying

structures can be described in terms of distortions of the fluorite structure, with the major distortion associated with the $t \rightarrow m$ phase transformation corresponding to a shear of $\sim 9^\circ$ parallel to the basal plane of the t unit cell, to define a monoclinic β angle of $\sim 81^\circ$. It is the apparent displacive nature of the structural change, together with the morphology of the m product, which has invited the application of the theory of martensite crystallography to the transformation.

The suitable addition of the stabilizing oxides such as CaO, MgO, Y_2O_3 , CeO_2 and selected rare earth oxides, combined with relatively high cooling rates from sintering and solution treatment temperatures, permits metastable tetragonal ZrO_2 (t') to be retained at room temperature in the form of an equiaxed polycrystalline aggregate. Y_2O_3 stabilized ZrO_2 (YSZ) is discussed in this section while other oxides stabilized ZrO_2 are discussed in other sections. The mechanism of phase transformation toughening in ZrO_2 involves two aspects, both related to the difficulty of nucleating the martensitic transformation.¹⁶ First, the M_s of t - ZrO_2 can be reduced to below room temperature by controlling the stabilizer concentration in this phase. More importantly, the M_s of the particle or grain size of this phase decreases with decreasing size. Zhu and Yan¹⁷ and Basu *et al.*¹⁸ have reported that $0.4 \mu\text{m}$ is the critical grain size for the thermally induced phase transformation of the YSZ ceramics, and that no thermally induced transformation is observed in the t - ZrO_2 materials having grain size finer than $0.4 \mu\text{m}$.

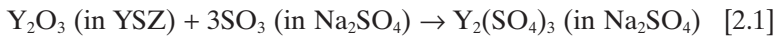
Second, however, such fine particles undergo martensitic transformation in the stress field of propagating cracks. The volume change resulting from the stress-induced transformation in these fine t - ZrO_2 particles in a zone around the crack creates favorable tractions on the crack faces, which impedes further crack propagation and significantly increases the fracture toughness. For increasing fracture toughness, the t -phase transformability is the critical factor. The key is to maximize the retention of t - ZrO_2 at room temperature or application temperature with sufficient transformability in a tensile stress field. According to the above idea, partially stabilized ZrO_2 , a mixture of the c and m phases, is produced by controlling the amount of stabilizer added (about 6–8 wt% Y_2O_3) with a consequence of an obvious improvement of the thermal-shock resistance compared with pure and fully stabilized zirconia materials.^{19,20}

The initial YSZ TBCs contained from 12 to 20 wt% of Y_2O_3 , which was added to fully stabilize the c -phase. Later, Stecura²¹ showed that better performance could be achieved by lowering the Y_2O_3 level to between 6 and 8 wt%. So far, 7–8YSZ has been the TBC material studied and used most widely. It has a lot of good properties such as: a high melting point of $\sim 2680^\circ\text{C}$ which makes it suitable for high-temperature applications; low thermal conductivity of ~ 2.1 – $2.2 \text{ W m}^{-1} \text{ K}^{-1}$ in bulk material at 1000°C ; high TEC of $\sim 11 \times 10^{-6} \text{ K}^{-1}$; low density of $\sim 6.4 \text{ g/cm}^3$ which can reduce the

weight of the turbine components; low elastic modulus of ~40 GPa; high hardness of ~14 GPa which enables the turbine components to possess a better erosion resistance. Consequently, 7–8YSZ has been used frequently in turbine and diesel engines.^{22,23} Furthermore, it has been proved that 7–8YSZ coating is more resistant against the corrosion of Na₂SO₄ and V₂O₅ compared with CaO or MgO stabilized ZrO₂ coating.²⁴

Although 7–8YSZ has plenty of advantages for TBC applications, there are also some disadvantages. First, a major disadvantage of 7–8YSZ is the limited operating temperature (<1200°C) for long-term operation. At higher temperatures, phase transformations from metastable tetragonal (*t'*) to tetragonal and cubic (*t + c*) and then to monoclinic (*m*) occur, giving rise to the formation of cracks in the coating.^{10,25}

Second, 7–8YSZ is sensitive to the hot corrosion.^{26–28} It has a better corrosion resistance if the clean fuel is used, whereas the corrosion problem becomes more serious when using fuel containing a certain amount of S, Na and V elements. The chemical reactions between Na₂O, SO₃ or V₂O₅ in the fuel and the stabilizer of Y₂O₃ in 7–8YSZ result in the degradation of the coating. In particular, the deposit salt of V₂O₅ reacts with Y₂O₃ to get a product of YVO₄, resulting in depleting Y₂O₃ and degrading 7–8YSZ TBCs, and preventing its applications in marine gas turbine engines. The reactions may be summarized as follows:



Third, the SiO₂ impurity (even as low as 1 wt%) in 7–8YSZ coating has a strong detrimental effect on the thermal cycling lifetime.²⁹ Firstly, in bulk ZrO₂-base ceramics, SiO₂ segregates at grain boundaries with excessive amounts collecting at triple points. SiO₂ at the grain boundaries leads to changes in the size and shape of grains and it may also dissolve Y₂O₃ from the 7–8YSZ grain boundaries leading to a localized degradation. Secondly, SiO₂ can also cause ZrO₂ polycrystal superplasticity, dramatic increase in sintering rates and decrease in electrical conductivity. Thirdly, it may also lead to increased creep rates, as what has been observed within ZrO₂-base ceramics.

Furthermore, these coatings possess a high concentration of oxygen ion vacancies, which at high temperatures assist oxygen transport and the oxidation of the bond coat at the ceramic bond/coat interface, namely the formation of thermally grown oxide (TGO) on the bond coat surface. This leads to a spallation of the ceramic, and such failure mechanism of the TBC is predominant when the coatings are thin as in gas turbines. This problem has been overcome to a large extent by providing oxidation-resistant bond coats such as alumina and mullite.³⁰

2.3 Zirconia doped with one or more oxides

In addition to Y_2O_3 stabilized ZrO_2 , other oxides, such as CaO , MgO , CeO_2 , Nd_2O_3 or Sm_2O_3 , are also investigated as the stabilizers for ZrO_2 . First, CaO (3–5 wt%) stabilized ZrO_2 (CaO – ZrO_2) coating prepared by atmospheric plasma spraying (APS) has between four and three times lower thermal diffusivity compared with that of a sintered ZrO_2 at a temperature below $1027^\circ C$.³¹ This coating experiences a sintering effect above $1027^\circ C$, resulting in a remarkable decrease of the thermal insulation effect. CaO – ZrO_2 did not prove to be a viable material for the more advanced TBC applications. The problem with this material is related to ‘destabilization’ from c – ZrO_2 that is observed in the as-sprayed coating to m – ZrO_2 . Although the CaO is added to ZrO_2 with the intent of extending the high-temperature c -phase field down to room temperature, it is now known that the c -phase is actually not stable below $1140^\circ C$.³² However, it proves that the addition of CeO_2 in the CaO – ZrO_2 system conveys excellent thermal-shock resistance at $1000^\circ C$ and $1200^\circ C$, which is superior to that of 5 wt% CaO – ZrO_2 coatings.³³ Moreover, no destabilization of c/t – ZrO_2 phase occurred during thermal shock tests.

Second, MgO (15–24 wt%) stabilized ZrO_2 (MSZ) has an ability to avoid the detrimental $t \rightarrow m$ phase transformation of ZrO_2 ,³⁴ with the equilibrium phases of c – ZrO_2 and MgO . MgO (24 wt%)– ZrO_2 has a relatively high TEC of $12.3 \times 10^{-6} K^{-1}$.¹⁵ For diesel engines operating with low-quality fuels, which yield liquid salt deposits on the ceramic-coated components, the MSZ system has better properties than the YSZ system in these environments in which the corrosion resistance to vanadate attack is better, but problems with sulphidation of the MgO cannot be ruled out. The MgO reacts readily with SO_3 to form the melt-soluble $MgSO_4$, with the reaction of MgO in contact with molten $NaVO_3$ even at very low partial pressures (10^{-7} bar) of SO_3 .³⁵ Extensive formation of $MgSO_4$ leading to the degradation of the MSZ TBCs in low-quality fuel burner rig tests has also been reported.³⁶ Moreover, thermal cycling to only $1000^\circ C/1050^\circ C$ has revealed a progressive destabilization of the MSZ coatings, apparently as the result of rapid coarsening of the tetragonal MSZ grains followed by spontaneous $t \rightarrow m$ phase transformation.³⁷ In addition, the MSZ system has a lower strength and erosion resistance.³⁸ Although the MgO is added to ZrO_2 with the intent of extending the high-temperature c -phase field down to room temperature, it proves that the c -phase is actually not stable below $1400^\circ C$.³² Toriz *et al.* gave $950^\circ C$ as the practical upper-use temperature for MSZ in gas turbine applications.³⁹ Therefore, these shortcomings combine to make MSZ an unpromising candidate for naval ship engine applications.

Third, stabilization of t – ZrO_2 in the CeO_2 – ZrO_2 system ($CeSZ$) can be kept over a wide range of compositions, 16–26 wt% CeO_2 , with the

preferred composition being 25 wt% CeSZ. CeSZ displays considerably greater moisture stability than YSZ under similar environmental conditions.^{40,41} Although the attainable fracture strength of (21 wt%) CeSZ is not as high as that of YSZ, the toughness can be considerably greater (maximum fracture toughness for YSZ is $\sim 10 \text{ MPa}\cdot\text{m}^{1/2}$, whereas that for CeSZ is $\sim 17 \text{ MPa}\cdot\text{m}^{1/2}$).⁴² Some tests also indicate that CeO_2 reacts less readily than Y_2O_3 with molten vanadate–sulfate systems.^{35,43,44} Miller⁴⁵ has reported that 12–20 wt% CeO_2 stabilized ZrO_2 exhibited instability, indicating they could never be realistically considered as TBC materials for gas turbines. The CeO_2 (25 wt%)– ZrO_2 material offered some benefits as its thermal and mechanical properties were reasonable, but independent erosion tests showed that its erosion resistance was significantly inferior to that of the YSZ systems. However, the plasma-sprayed CeO_2 (25 wt%)– ZrO_2 yields t' -phase which is retained even after 100 h annealing at 1600 °C, and does not undergo a $t \rightarrow m$ phase transformation under low-temperature cycling.⁴⁶

Furthermore, Lee *et al.* has reported the same system with some different results.⁴⁷ CeSZ TBCs prepared by APS with 16 and 18 wt% CeO_2 consist of only t' -phase with high CeO_2 content, whereas the CeSZ coatings with 20–26 wt% CeO_2 consist of a mixture of t' -phase with high CeO_2 content and some amount of metastable cubic (c') phase with low CeO_2 content. During thermal cycling at 1130 °C, the t' -phase and the mixture of the t' -phase and the c' -phase decompose to c -phase with high CeO_2 content and t -phase with low CeO_2 content. Some of the t -phase transforms to the m -phase on cooling. More m -phase is observed to develop in the CeSZ coatings with 16 wt% CeO_2 than those with 18–26 wt% CeO_2 , and the CeSZ coatings lifetimes with 18–26 wt% CeO_2 are longer than those with 16 wt% CeO_2 . The tolerable amount of CeO_2 in ZrO_2 alloy required for TBCs is $>16 \text{ wt}\%$. This material is proposed for ultra-high temperature TBCs, although it may be lacking in erosion resistance as compared to YSZ. Another disadvantage for this material as a TBC material is that CeO_2 has a potential to be reduced to Ce_2O_3 with much decreased melting point.

However, it appears that even in melts such as NaVO_3 where the V_2O_5 activity is too low for direct reaction, CeSZ may nonetheless be destabilized by a mineralization effect. In burner rig tests with Na, S and V impurity additions, CeSZ suffered chemical attack, forming both cerium sulfates (mostly in the lower temperature tests at 700 °C) and CeVO_4 ; it was difficult to be certain, perhaps because of the high V and S levels used, that CeSZ was significantly more resistant than YSZ to hot corrosion in these particular tests.³⁶

YSZ coating doped with CeO_2 is supposed to bring an improvement in thermal cycling lifetime, due to the higher TEC and the lower thermal conductivity of CeO_2 compared with that of YSZ. A remarkable improvement in thermal shock tolerability was attained by the addition of CeO_2

into YSZ.^{48–50} The CeO₂-doped YSZ coating has a better thermal-shock resistance mainly because of⁵¹: (i) little phase transformation between the *t*-phase and *m*-phase in this coating; (ii) a smaller stress generated by the bond coat oxidation in this coating due to the better thermal insulation; (iii) a larger TEC in this coating. However, the addition of CeO₂ into YSZ has some negative effects similar to those found in the CeSZ system, such as the decrease of hardness and the stoichiometry change of the coating due to the vaporization of CeO₂,⁵⁰ the reduction of CeO₂ into Ce₂O₃ and the accelerated sintering rate of the coating.^{52,53}

Fourth, some rare earth oxides have also been reported as the stabilizers of ZrO₂ besides Y₂O₃ and CeO₂, which are Dy₂O₃,⁸ Nd₂O₃, Er₂O₃, Sm₂O₃,⁵⁴ Yb₂O₃,^{8,55} Sc₂O₃,^{56–58} Gd₂O₃,⁵⁹ Ta₂O₅, Nd₂O₅^{60,61} and so on. The different stabilizers have various levels of the stabilizing ability, together with the varied stabilizing mechanisms, that are closely correlated with cation migration at high temperatures. The stabilization ability of different oxides has been summarized by Raghavan *et al.*,⁶⁰ and it has an increasing tendency with the cation radius increase from Sc³⁺ to Y³⁺, whereas it decreases with further increase of the cation radius from Y³⁺ to La³⁺.

Rare earth oxide stabilizers such as Dy₂O₃ and Yb₂O₃ behave similarly to Y₂O₃; a 4 mol.% addition creates a *t*'-phase while a 12 mol.% addition creates a *c*-phase. A reduction of ~40% in thermal conductivity was achieved with an optimized version of 12 mol.% DySZ. The cyclic lifetimes of these new electron beam physical vapor deposition (EB-PVD) TBCs were comparable to that of YSZ.⁸ Zhang *et al.*⁵⁵ have studied the thermal cycling behavior of a ZrO₂ coating stabilized by Yb₂O₃, and proved that the cyclic lifetime of the 2.6 mol.% Yb₂O₃-ZrO₂ coating is increased by ~30% compared with that of YSZ (3.4 mol.% Y₂O₃) under the same conditions.

Khor and Yang^{54,62,63} have studied coatings of ZrO₂ stabilized by Nd₂O₃ (NdSZ), Er₂O₃ (ErSZ) and Sm₂O₃ (SmSZ), respectively. Grinding of the three plasma-sprayed coatings in the 4–6 mol.% Nd₂O₃, Er₂O₃ or Sm₂O₃ revealed no *t* → *m* phase transformation. In the 2–3 mol.% Nd₂O₃, Er₂O₃ or Sm₂O₃ composition, there is *t*'-phase in different levels, respectively. Due to the fast cooling effect of the APS process, all the three coatings mainly have the *t*'-phase which would not transform into the other phases after mechanical treatment in contrast with *t*-ZrO₂. The stabilization ability of the *t*'-phase against heat treatment has the order of NdSZ < ErSZ < SmSZ, and it is supposed that this phenomenon may result from the fast diffusion speed of Nd³⁺ and the low diffusion speed of Sm³⁺ at high temperatures.⁵⁴

Compared with the YSZ coating, the ScSZ coating (Sc₂O₃-ZrO₂) has a higher corrosion resistance against the vanadates and sulfates, and the *t*'-phase is more stable at high temperatures.⁵⁶ Jones *et al.*^{57,58} have demonstrated that the Sc₂O₃, Y₂O₃-stabilized ZrO₂ (SYSZ) with 7 mol.% of total amount of stabilizer (the stabilizer contains 2.5–20 mol.% Y₂O₃) gives

significantly better t' -phase stability at 1400 °C than either pure Y_2O_3 - or Sc_2O_3 -stabilized ZrO_2 . Sc_2O_3 -rich SYSZ powder shows 5–10 times better resistance to vanadate-induced destabilization and better high-temperature phase stability than YSZ powder. This suggests that SYSZ could be a possible candidate for ultra-high temperature TBC application.

Wu⁵⁹ has explored the Gd_2O_3 - ZrO_2 (GdSZ) system (with chemical composition of $0.15GdO_{1.5} \cdot 0.85ZrO_2$) as a TBC candidate material. The thermal conductivity of GdSZ is ~30% lower than that of 7YSZ, and it is chemically stable at high temperatures in contact with α - Al_2O_3 (main composition in TGO). However, the thermal cycling lifetime of EB-PVD GdSZ TBC is shorter than that of 7YSZ.

Raghavan *et al.*^{60,61} have investigated ZrO_2 - Y_2O_3 - Ta_2O_5 / Nb_2O_5 as the TBC candidate materials. After choosing specific compositions, single-phase (t -phase) and dual-phase (t -phase + c -phase) compositions that are stable despite ageing at 1500 °C for 200 h and having a thermal conductivity as low as the 6–8YSZ were synthesized. In particular, a 16.6 wt% $YO_{1.5}$ + 16.6 wt% $TaO_{2.5}$ stabilized ZrO_2 composition was insensitive to the $t \rightarrow m$ phase transformation upon thermal cycling, and it also showed only slight evidence of corrosion in vanadate-sulfate melts after 500 h, compared with the extensive attack and spallation within much shorter time (50–100 h) for 7YSZ. Properly designed co-doping thus circumvents the problems of thermal and chemical destabilization in 7YSZ.⁶⁴

Matsumoto *et al.*^{65,66} have studied the influence of some oxides additives, namely Al_2O_3 , CoO, SrO, La_2O_3 , Pr_2O_3 , Nd_2O_3 and Er_2O_3 , on the densification of YSZ compacted powder, and found that the addition of Al_2O_3 or CoO gives significant increase in density. In terms of sintering, these compounds will be deleterious for YSZ TBC if they are used in secondary phase. In contrast, the addition of SrO, La_2O_3 , Pr_2O_3 and Nd_2O_3 decreases density. Among those, La_2O_3 has the greatest effect on suppression of densification, followed by SrO, Pr_2O_3 and Nd_2O_3 . The addition of Er_2O_3 has little effect on densification. The La_2O_3 doped YSZ plasma-sprayed coating has been investigated and reveals a low thermal conductivity even after high-temperature annealing. However, too much La_2O_3 addition leads to decreased t' -phase stability and cyclic lifetime of the coating; the optimum amount of La_2O_3 is about 1 mol. %.

Zhu and Miller⁶⁷ have investigated the thermal properties of ZrO_2 -based TBCs stabilized by co- or multi-dopants, namely YSZ-Nd, YSZ-Yb, YSZ-Nd-Yb, YSZ-Gd-Yb and YSZ-Sm-Yb. YSZ and YSZ with one more dopant show typically higher thermal conductivities than the YSZ coatings with paired dopant additions. The total dopant concentration affects thermal conductivity as well. A low thermal conductivity regime was observed for plasma-sprayed TBCs in the range 6–15 mol. % total dopant concentration and about 10 mol. % for the EB-PVD coatings. Multi-component cluster

oxide coatings were thermal cyclic tested at 1160 °C and showed longer cyclic lifetimes than YSZ at given dopant concentrations. The coating cyclic lifetime generally decreased as the total dopant concentration was increased. Ternary additions of Gd/Yb/Sc and Nd/Yb/Sc did not further improve the thermal insulation property.

2.4 Yttria stabilized hafnia and other alternative ceramic TBC materials

2.4.1 Yttria stabilized hafnia

HfO₂-Y₂O₃ (in ~19 mol.%, ~25 mol.% and ~38 mol.%) coatings prepared by EB-PVD have been studied by Singh *et al.*,⁶⁸ and the thermal conductivity of HfO₂-25 mol.% Y₂O₃ was found to be the lowest (1.1 W/mK) among the three compositions. HfO₂-25 mol.% Y₂O₃ exhibited a relatively low conductivity rate increase at high temperatures due to its good sintering resistance as compared with 8YSZ. In addition, the HfO₂-25 mol.% Y₂O₃ plasma-sprayed coating also has a better sintering resistance than YSZ coating.⁶⁹ Zhu *et al.*⁷⁰ compared the 1650 °C sintering and cyclic behavior of the HfO₂-18 mol.% (Y, Gd, Yb)₂O₃ coating with that of HfO₂-5 mol.% Y₂O₃ and HfO₂-15 mol.% Y₂O₃ coatings. The advanced multi-component HfO₂-based coating had a relatively slow conductivity increase during the first 20 h of steady-state testing, as well as a good water-vapor-stability. It also showed essentially no cracking and delamination during subsequent testing of 100 30-min cycles at 1650 °C, indicating excellent sintering resistance and cyclic durability.

Ibegazene *et al.*⁷¹ have studied the influence of HfO₂-addition on the structure and mechanical properties of 8YSZ coatings prepared by APS. In the coating, only the *t'*-phase existed; this phase transformed into the mixture of *t* + *c* phases during annealing at 1200 °C and the *t*-phase would further transform into the *m*-phase. Young's modulus increased with increase in the HfO₂ content.

2.4.2 Al₂O₃

Al₂O₃ did not prove to be a viable material for the more advanced TBC applications, primarily because of its relatively high thermal conductivity and low TEC compared with YSZ.⁷² The plasma-sprayed Al₂O₃ coating contains mainly unstable phases such as γ - and δ -Al₂O₃. These unstable phases will transform into stable α -Al₂O₃ during thermal cycling, accompanied by a significant volume change ($\gamma \rightarrow \alpha$, ~15%) which results in micro-crack formation in the coating.^{73,74} The doping of transition metal oxides such as Cr₂O₃, Fe₂O₃ or TiO₂ into Al₂O₃ can only partially stabilize the

α - Al_2O_3 . Even though Al_2O_3 alone is not a good TBC candidate, its addition to YSZ can improve the hardness and bond strength without substantial modification of Young's modulus and toughness, as well as the oxidation resistance of the substrate.^{75–77} A gradient coating of 8YSZ– Al_2O_3 has a much longer thermal cycling lifetime than that of the 8YSZ coating.⁷⁸

2.4.3 Mullite

Mullite ($3\text{Al}_2\text{O}_3 \cdot 2\text{SiO}_2$) is an important ceramic material because of its low density, high thermal stability, high chemical stability in severe environments, low thermal conductivity and favorable strength and creep behavior.⁷⁹ Compared with YSZ, mullite has a much lower TEC and a higher thermal conductivity, and is much more oxygen-resistant than YSZ. Mullite contains a larger amount of amorphous phase resulting from the rapid cooling of molten mullite on a cold substrate during the APS process.⁸⁰ The amorphous phase in the coating crystallizes in a subsequent exposure to high temperature (750–1000 °C), accompanied by a volume contraction, causing cracking and debonding.³⁰ For applications such as diesel engines where the surface temperatures are lower than those encountered in gas turbines and the temperature variations across the coating are large, mullite is an excellent alternative to ZrO_2 as a TBC material. Engine tests performed with both materials show that the lifetime of the mullite coating in the engine is significantly longer than that of the YSZ coating.^{81,82} Above 1000 °C, the thermal cycling lifetime of the mullite coating is much shorter than that of YSZ.³⁰ Furthermore, mullite is the most promising coating material for SiC substrate because their TECs are similar.⁸⁰

Gilbert *et al.*^{83,84} have investigated the thermal fracture of mullite–YSZ composite TBCs under thermal shock by both experimental and numerical studies. They demonstrated that the mullite–YSZ composite coatings reduced the driving force for coating delamination. When compared to the monolithic YSZ coatings, the composite coatings have a higher threshold temperature for both surface and horizontal crack initiation. Since the mullite–YSZ composite coating has a higher thermal resistance compared to the monolithic mullite coating, it is an excellent candidate for applications where high temperature and temperature gradients are present.

2.4.4 Pyrochlore oxides ($\text{A}_2\text{B}_2\text{O}_7$)

Pyrochlore oxides ($\text{A}_2\text{B}_2\text{O}_7$) are relatively new TBC candidate materials and have been paid much attention recently, because several zirconate pyrochlores have lower thermal conductivities than YSZ.⁸⁵ The crystal structure of pyrochlores consists of the corner-shared BO_6 octahedra forming the backbone of the network and A ions fill the holes which are

formed by six BO_6 octahedra. It can largely tolerate vacancies at the A , B and O sites without phase transformation. Both A and B sites can be substituted by a lot of other elements with similar ionic radii when the electrical neutrality is satisfied, resulting in the potential to tailor their thermal properties. The pyrochlores are also attractive because many are refractory up to temperatures well in excess of 1500°C and thermally stable. Of particular interest are the zirconates of the larger lanthanides ($\text{Gd} \rightarrow \text{La}$) – an increased level of substitution relative to the co-doped compositions (from $<15\%$ to $50\% \text{MO}_{1.5}$) and the use of cations with a much higher atomic mass contrast with Zr than Y^{86} are expected to yield a substantial reduction in thermal conductivity to 7YSZ .⁸⁵ Thermal conductivities ranging from $\sim 1.1 \text{ Wm}^{-1}\text{K}^{-1}$ to $\sim 1.7 \text{ Wm}^{-1}\text{K}^{-1}$ at temperatures between 700°C and 1200°C have been reported for zirconates of Gd , Eu , Sm , Nd and La .^{87–92} Co-doping of pyrochlores on both A and B sites has been proposed to further reduce their thermal conductivities and also to modify their TECs. Some success has been achieved, at least up to $\sim 800^\circ\text{C}$, as exemplified by studies in which $\text{La}_2\text{Zr}_2\text{O}_7$ was doped with 30 at.% of Nd , Eu or Gd and the thermal conductivities were reduced from $\sim 1.55 \text{ Wm}^{-1}\text{K}^{-1}$ to $\sim 0.9 \text{ Wm}^{-1}\text{K}^{-1}$ for Gd doping.⁹² Similar results for single- or double-oxide doped $\text{La}_2\text{Zr}_2\text{O}_7$ have also been reported by Zhu *et al.*⁷⁰ who found that $\text{La}_{1.7}\text{Yb}_{0.3}\text{Zr}_2\text{O}_7$ and $\text{La}_{1.7}\text{Gd}_{0.15}\text{Yb}_{0.15}\text{Zr}_2\text{O}_7$ had lower thermal conductivities than the undoped $\text{La}_2\text{Zr}_2\text{O}_7$ and that the Gd_2O_3 and Yb_2O_3 co-doped materials showed the lowest thermal conductivity.

Although $\text{La}_2\text{Zr}_2\text{O}_7$ has a lower thermal conductivity than YSZ , its coating did not give a longer thermal cycling lifetime than YSZ which might be explained by its relatively low TEC and poor toughness.⁹³ However, the double-ceramic-layer coating of $\text{YSZ}/\text{La}_2\text{Zr}_2\text{O}_7$ has increased thermal cycling lifetime and can even be used in higher temperatures compared with YSZ coating.^{94,95} It has been proved that $\text{La}_2\text{Zr}_2\text{O}_7$ can be toughened by addition of $\text{Y}_3\text{Al}_5\text{O}_{12}$ or BaTiO_3 (both volume percent up to 20%),^{96,97} which might give a positive influence for TBC applications. The addition of CeO_2 into $\text{La}_2\text{Zr}_2\text{O}_7$ ($\text{La}_2(\text{Zr}_{0.7}\text{Ce}_{0.3})_2\text{O}_7$) can improve its sintering resistance, reduce its thermal conductivity to some extent, as well as prolong its thermal cycling lifetime by applying the $\text{La}_2(\text{Zr}_{0.7}\text{Ce}_{0.3})_2\text{O}_7/\text{La}_2\text{Zr}_2\text{O}_7$ coating.⁹⁸ Unfortunately, even though $\text{Nd}_2\text{Zr}_2\text{O}_7$, $\text{Eu}_2\text{Zr}_2\text{O}_7$ and $\text{Gd}_2\text{Zr}_2\text{O}_7$ have larger TECs than $\text{La}_2\text{Zr}_2\text{O}_7$, the thermal cycling lifetimes of their single-layer coatings are very short, similar to that of the $\text{La}_2\text{Zr}_2\text{O}_7$ coating.^{95,99}

The zirconates of Dy , Er and Yb with fluorite structure are also listed here, because they are very similar to the above-mentioned rare earth zirconates with pyrochlore structure. The thermal conductivities of $\text{Dy}_2\text{Zr}_2\text{O}_7$, $\text{Er}_2\text{Zr}_2\text{O}_7$ and $\text{Yb}_2\text{Zr}_2\text{O}_7$ range from $\sim 1.3 \text{ Wm}^{-1}\text{K}^{-1}$ to $\sim 1.6 \text{ Wm}^{-1}\text{K}^{-1}$, which are comparable to the other zirconates with pyrochlore structure, allowing them to be considered as TBC candidate materials.¹⁰⁰

2.5 Lanthanum compounds, silicates and rare earth oxides

2.5.1 Lanthanum cerium oxide

Lanthanum cerium oxide ($\text{La}_2\text{Ce}_2\text{O}_7$) has been proposed as a new TBC material, which has a higher TEC and a lower thermal conductivity than YSZ.^{101,102} $\text{La}_2\text{Ce}_2\text{O}_7$ is a solid solution of La_2O_3 in CeO_2 having fluorite-type structure with 1/8 O sites as vacancies. It has a good phase stability either from room temperature to 1400°C or after annealing at 1400°C even for 384 h. The higher TEC of $\text{La}_2\text{Ce}_2\text{O}_7$ ($\sim 12.3 \times 10^{-6} \text{ K}^{-1}$, 300–1200°C) compared with that of 8YSZ ($10.5\text{--}11.5 \times 10^{-6} \text{ K}^{-1}$, 30–1000°C)⁵⁰ makes it possible to relieve thermal stress during thermal cycling. The thermal expansion improvement can be attributed to the large size of Ce^{4+} and the partial reduction of Ce^{4+} to Ce^{3+} at elevated temperatures. The minimum TEC of $\text{La}_2\text{Ce}_2\text{O}_7$ at $\sim 250^\circ\text{C}$ is a result of the formation of oxygen vacancies. The addition of some oxides, such as Ta_2O_5 and WO_3 , results in an increase in the TECs of $\text{La}_2\text{Ce}_2\text{O}_7$ below 400°C.¹⁰³ The thermal conductivities of $\text{La}_2\text{Ce}_2\text{O}_7$ range from $\sim 0.5 \text{ Wm}^{-1}\text{K}^{-1}$ to $\sim 0.6 \text{ Wm}^{-1}\text{K}^{-1}$ due to the varied densities, which are obviously much lower than those of YSZ.

Thermal cycle testing of $\text{La}_2\text{Ce}_2\text{O}_7$ coating at 1250°C has indicated that this coating has a much better thermal-shock resistance than the $\text{La}_2\text{Zr}_2\text{O}_7$ coating and even better than the 8YSZ coating.¹⁰¹ Moreover, it has been proved that double-ceramic-layer coating system of $\text{La}_2\text{Ce}_2\text{O}_7/8\text{YSZ}$ has a much longer thermal cycling lifetime than the $\text{La}_2\text{Ce}_2\text{O}_7$ coating alone.¹⁰⁴

It is worth noting that proper control of coating composition is critical for a good thermal cycling behavior, because the coating with a composition more close to stoichiometric $\text{La}_2\text{Ce}_2\text{O}_7$ has a better thermal-shock resistance.

Another fluorite structure material, namely neodymium cerate ($\text{Nd}_2\text{Ce}_2\text{O}_7$), has also been proposed as a new TBC material.¹⁰⁵ It is thermally stable in the temperature range of interest for TBC applications (1200–1400°C). The TEC of $\text{Nd}_2\text{Ce}_2\text{O}_7$ is higher than that of YSZ, and even more interesting is the TEC change as a function of temperature paralleling that of the superalloy bond coat. Moreover, the thermal conductivity of $\text{Nd}_2\text{Ce}_2\text{O}_7$ is $\sim 30\%$ lower than that of YSZ. The thermal-shock resistance of $\text{Nd}_2\text{Ce}_2\text{O}_7$ coating prepared by APS is inferior to that of $\text{La}_2\text{Ce}_2\text{O}_7$.

2.5.2 Silicates

There are few reports on silicates as TBC materials rather than as environmental barrier coatings. Only the spraying of zircon (ZrSiO_4),¹⁰⁶ natural zircon sand¹⁰⁷ and wollastonite (CaSiO_3)¹⁰⁸ have been reported. Zircon has

a low TEC ($4.99 \times 10^{-6} \text{ K}^{-1}$, 25–1400 °C) and a high thermal conductivity ($3.46 \text{ Wm}^{-1}\text{K}^{-1}$, 90–1500 °C).¹⁵ It is chemically very stable especially at lower temperatures. With the exception of concentrated hydrofluoric acid, zircon is not generally attacked by acids but by basic materials at elevated temperatures. Zircon has a dissociation line at 1676 °C from phase diagram of the $\text{ZrO}_2\text{-SiO}_2$ system,¹⁰⁹ so that it is not possible for zircon to form from liquid phase, but via solid–solid reaction of zirconia and silica. During plasma spraying, zircon dissociates and consequently its coatings are composed of a mixture of crystalline ZrO_2 and amorphous SiO_2 . When zircon is used as TBC for diesel engines, the decomposed SiO_2 in the coating may cause problems due to the evaporation of SiO and Si(OH)_2 .¹¹⁰ Ramaswamy *et al.*¹⁰⁷ have studied both natural zircon and a combination of zircon and Y_2O_3 . The $t\text{-ZrO}_2$ phase substantially destabilized when the as-sprayed zircon coatings were annealed at 1200 °C, followed by recombination of ZrO_2 and SiO_2 to form ZrSiO_4 . However, the $t\text{-ZrO}_2$ phase was completely stabilized in the coatings of the zircon and Y_2O_3 mixture upon annealing at 1400 °C. A greater amount of Y_2O_3 addition (up to 20 mol.%) into zircon decreases the zircon formation in the coatings, resulting in less porosity in the coating even after annealing at 1400 °C, thereby improving coating stability and adhesion.¹¹¹ Both coatings exhibited good thermal-shock resistance and thermal barrier characteristics and are supposed to be suitable for TBC applications.

As to CaSiO_3 coating,¹⁰⁸ crystalline CaSiO_3 , glassy phase and tridymite (SiO_2) were observed in the as-sprayed coating. Tridymite (SiO_2) likely reacted with other composites such as CaO and glassy phase to form crystalline CaSiO_3 when the coating was heated at about 882 °C. After the first thermal cycle (from 20 and 1000 °C), the TECs and the thermal diffusivities of the coatings are $6.3\text{--}8.5 \times 10^{-6} \text{ K}^{-1}$ and $3.24\text{--}3.72 \times 10^{-3} \text{ cm}^2/\text{s}$, respectively. Therefore, the APS CaSiO_3 coating may be used as TBC on substrate such as titanium and titanium alloys.

2.5.3 Rare earth oxides

The melting points of rare earth oxides are above 2200 °C. Except for the valence-changeable elements such as Ce, Pr, Eu and Tb, the other rare earth oxides have similar chemical, physical and mechanical properties. Coatings of rare earth oxides (La_2O_3 , CeO_2 , Pr_2O_3 and Nb_2O_5 as main phases) have lower thermal diffusivities and higher TECs than ZrO_2 .¹¹² No further reports about these materials are available. Most of the rare earth oxides are polymorphic at elevated temperatures,¹¹³ and the phase instability will certainly affect the thermal-shock resistance of their coatings to some extent. Rare earth oxides are commonly used as dopants or partial starting materials of TBC materials with the consequences of reducing their thermal

conductivities, improving phase stability as well as increasing thermal cycling lifetimes.^{5,6,9}

2.5.4 $Y_3Al_5O_{12}$

$Y_3Al_5O_{12}$ (YAG) has a rather complex cubic structure with 160 atoms per unit cell ($Z = 8$) with the chemical formula $A_3B_2(CO_4)_3$, where the A cation (Y^{3+}) is in a dodecahedral coordination site, the B cation (Al^{3+}) is in an octahedral site and the C cation (Al^{3+}) is in a tetrahedral site.¹¹⁴ Padture and Klemens¹¹⁵ were the first to propose YAG as an oxygen barrier in a TBC system due to its low oxygen diffusivity ($\sim 10^{10}$ lower than that in YSZ) and its comparably low thermal conductivity ($3.2 \text{ Wm}^{-1}\text{K}^{-1}$, 1000°C) at high temperatures. YAG also possesses a low creep rate, a low electrical conductivity, a phase/thermal stability (up to its melting point of 1970°C) and an isotropic thermal expansion. Therefore, it is a promising candidate as TBCs, or as oxidation and erosion-resistant material, which can be used in gas turbine engines.¹¹⁶ However, the relatively low TEC ($9.1 \times 10^{-6} \text{ K}^{-1}$) and the low melting point of this material seem to be the major problems. The YAG coatings prepared by different processes are reported extensively.¹¹⁷⁻¹²⁰

2.5.5 Lanthanum aluminates

Oxides with magnetoplumbite structure of the general composition, $\text{LnMgAl}_{11}\text{O}_{19}$ ($\text{Ln} = \text{La to Gd}$; $\text{M} = \text{Mg, Mn to Zn}$), have high melting points, high thermal expansion and low thermal conductivities which make them suitable for applications as high-temperature TBCs. Also, sintering in these oxides is suppressed due to the low ionic diffusion in magnetoplumbites.¹²¹⁻¹²⁴ In particular, the values of average TECs of $\text{LaMgAl}_{11}\text{O}_{19}$, $\text{SmMgAl}_{11}\text{O}_{19}$ and $\text{GdMgAl}_{11}\text{O}_{19}$ are about $\sim 9.5-9.7 \times 10^{-6} \text{ K}^{-1}$ from room temperature to 1500°C .¹²⁴ Thermal expansion behavior of all these oxides appears to be independent of the composition, indicating that the thermal expansion of these oxides is controlled by their basic magnetoplumbite crystal structure rather than having a composition based on the individual rare earth elements present. The thermal conductivities of these materials range from $2-3 \text{ Wm}^{-1}\text{K}^{-1}$ from room temperature to 1150°C exhibiting little temperature dependence. The $\text{SmMgAl}_{11}\text{O}_{19}$ and $\text{GdMgAl}_{11}\text{O}_{19}$ compositions have lower thermal conductivities than $\text{LaMgAl}_{11}\text{O}_{19}$. Doping with Yb in the Ln site in $\text{GdMgAl}_{11}\text{O}_{19}$ can effectively reduce its thermal conductivity. Thermal conductivities of plasma-sprayed $\text{LaMgAl}_{11}\text{O}_{19}$ and $\text{LaMnAl}_{11}\text{O}_{19}$ coatings after 20 h exposure to temperatures up to 1600°C did not change, indicating good sintering resistance. The microhardness of all $\text{LnMgAl}_{11}\text{O}_{19}$ coatings is higher than that of hardened steel but is below the hardness of ZrO_2 , and the elastic behavior of the coatings is superior to YSZ because of the lower

indentation modulus.¹²² However, the La-containing magnetoplumbites are not highly stable at elevated temperatures in water-containing atmosphere, such as in the combustion environment of turbine engines, and show significant continuous weight loss.⁷⁰

2.5.6 LaPO₄

Lanthanum phosphate (LaPO₄) has a monoclinic structure with four formula units of LaPO₄ in the P2₁/n unit cell. This material has been proposed as a TBC candidate material by Morgan and Marshall¹²⁵ and Sudre *et al.*,¹²⁶ because it has a high-temperature stability (melting point, ~2070 °C), a high TEC (9–10 × 10⁻⁶ K⁻¹) and a low thermal conductivity (~1.8 Wm⁻¹K⁻¹ at 700 °C), as well as a low Young's modulus (133 GPa). In addition, LaPO₄ is expected to be relatively inert to molten salts containing sulfate or vanadate because the basic lanthanum cation is strongly bonded to the acidic phosphate group. It does not react with alumina, which is a positive attribute, but bonds poorly to it, which is a limitation on its application. In contrast, LaPO₄ is a line compound that melts congruently, but small deviations from stoichiometry change its solidus temperature from ~2070 °C to 1580 °C on the La-rich side or to 1050 °C on the P-rich side. From this point of view, much attention must be paid to controlling the coating process parameters and/or starting material compositions (feedstock for the plasma-spraying process and target material for the EB-PVD process) to get the desired coating composition.

Another monazite-type material CePO₄ has very similar properties to those of LaPO₄.¹²⁷ The linear TEC and thermal conductivity of the CePO₄ ceramics are 9–11 × 10⁻⁶ K⁻¹ (200–1300 °C) and 1.81 Wm⁻¹K⁻¹ (500 °C), respectively. Such properties make it suitable for consideration as a TBC candidate material. However, the CePO₄ ceramics are cracked or decomposed by acidic or alkaline aqueous solutions at high temperatures, which is a limitation in TBC applications.

2.6 (Ca_{1-x}Mg_x)Zr₄(PO₄)₆ (CMZP), perovskite oxides and metal-glass composite

2.6.1 (Ca_{1-x}Mg_x)Zr₄(PO₄)₆

(Ca_{1-x}Mg_x)Zr₄(PO₄)₆ (CMZP) is synthesized by incorporating Mg²⁺ with CaZr₄(PO₄)₆ and belongs to a well-known NZP family possessing an ultra-low TEC.¹²⁸ The crystal structure of NZP is a hexagonal structure with a $R\bar{3}c$ space symmetry, and is built up of PO₄ tetrahedra and ZrO₆ octahedra which are linked at corners to form a strong three-dimensional network. CMZP has a lower thermal conductivity (lower than ZrO₂ by a factor of

approximately two) and its TEC is near zero.^{129–131} Furthermore, this material is less dense than ZrO_2 with theoretical density of 3.2 g/cm^3 . Moreover, no strength-loss after air quenching from temperatures up to 1500°C was observed, showing a good thermal-shock resistance. Therefore, the light-weight ceramic could be used as thermal protection systems for space shuttles and for filter systems such as the filtration system for molten metals and hot gas clean-up, rather than as a TBC material in turbine engines.

2.6.2 Perovskite oxides (ABO_3)

The ideal perovskite ABO_3 is cubic symmetry, in space group $Pm\bar{3}m$. The structure is commonly visualized as a three-dimensional network of regular corner-linked BX_6 octahedra, the B cations being at the center of these octahedra and the A cations being centrally located in the spaces between them. The most commonly occurring distortion in perovskites is octahedral tilting. This means the tilting of the BX_6 octahedra about one or more of their symmetry axes, maintaining both regularity of the octahedral (approximately) and their corner connectivity (strictly). Such tilting allows greater flexibility in the coordination of the A cation, while leaving the environment of the B cation essentially unchanged. It is also a major contributor to structural variability in perovskites.¹³²

Such perovskites are usually characterized by a melting point higher than 2000°C . Furthermore, the TEC has values typically greater than $8.5\text{--}9 \times 10^{-6} \text{ K}^{-1}$ and thermal conductivity of less than $2.2 \text{ Wm}^{-1}\text{K}^{-1}$, which are advantageous for being used as a heat insulating layer.¹³³ Perovskites additionally offer the potential for extensive substitution of ions at A and/or B site, which enables the properties of the materials to be selectively influenced.¹³⁴

So far, only some materials with perovskite structure have been studied as TBC candidates, such as SrZrO_3 and BaZrO_3 , as well as two complex perovskites $\text{Ba}(\text{Mg}_{1/3}\text{Ta}_{2/3})\text{O}_3$ (BMT) and $\text{La}(\text{Al}_{1/4}\text{Mg}_{1/2}\text{Ta}_{1/4})\text{O}_3$ (LAMT).^{89,135–137} The TECs of SrZrO_3 , BaZrO_3 , BMT and LAMT are $8.7\text{--}10.8 \times 10^{-6} \text{ K}^{-1}$ ($200\text{--}1100^\circ\text{C}$), $\sim 7.9 \times 10^{-6} \text{ K}^{-1}$ ($30\text{--}1000^\circ\text{C}$), $9.6\text{--}11.3 \times 10^{-6} \text{ K}^{-1}$ ($200\text{--}1200^\circ\text{C}$) and $8.2\text{--}10.6 \times 10^{-6} \text{ K}^{-1}$ ($200\text{--}1200^\circ\text{C}$), respectively, which are comparable to that of YSZ except BaZrO_3 . The thermal conductivities of these materials (except BaZrO_3) are below $2.8 \text{ Wm}^{-1}\text{K}^{-1}$ at 1000°C , with the sequence of $\text{BMT} > \text{YSZ} > \text{SrZrO}_3 > \text{LAMT}$. The fracture toughness of SrZrO_3 is half of that of YSZ, whereas the values of BMT and LAMT are four times lower than that of YSZ. Finally, the Young's moduli of the above-mentioned materials are all lower than that of YSZ.

Some preliminary thermal cycling results indicate that the single-layer-coatings of these materials have shorter cycling lifetime, whereas the

double-ceramic-layer coatings of SrZrO₃/YSZ and LAMT/YSZ have similar cycling lifetime compared with YSZ at the surface temperature of ~1250 °C. Doping Yb₂O₃ or Gd₂O₃ in SrZrO₃ can reduce the thermal conductivity of SrZrO₃,¹³⁸ and a very promising result is that the double-ceramic-layer coating of Yb₂O₃ doped SrZrO₃ in combination with YSZ has ~25% longer cycling lifetime than that of the optimized YSZ coating at the surface temperature of ~1350 °C.

2.6.3 Metal–glass composite

A new concept for TBC systems based on a mixture of metal and glass is called metal–glass composite (MGC).^{139–141} In the MGC system, the TEC depends on the metal–glass ratio and varies from $9.5\text{--}12.3 \times 10^{-6} \text{ K}^{-1}$. Another advantage of the gas-tight composite coatings is their ability to protect the bond coat from severe oxidation with a consequence of long lifetimes in oxidation tests. The MGC coatings have long thermal cycling lifetimes, which are supposed to be due to their high TECs, good adherence to the bond coat and the absence of open porosity. Such a coating does not have open pores, preventing the oxidation of bond coat from corrosive gases.

2.7 Future trends

The quest for new ceramic TBC candidate materials possessing low thermal conductivities is a major research area. This can be fulfilled by means of reducing phonon conduction of the materials. In real crystal structures, scattering of phonons occurs when they interact with lattice imperfections in the ideal lattice. Such imperfections include vacancies, dislocations, grain boundaries, atoms of different masses and other phonons. Ions and atoms of different ionic radius may also scatter phonons by locally distorting the bond length and thus introducing elastic strain fields into the lattice. The effects such imperfections cause can be quantified through their influence on the phonon mean free path. Moreover, materials having a large mean atomic mass, a low Young's modulus and randomly distributed point defects at a sufficiently high density favor reducing the phonon mean free path with the consequence of low thermal conductivity. In addition, materials with fine grain size in nanometer dimensions have proved to have a lower thermal conductivity resulting from much intensified grain-boundary scattering.

It is a time- and cost-consuming process to investigate the vast range of chemical compositions of all refractory oxides and minerals in order to identify promising compositions. The most rapid progress will probably only

be made by using a combination of intuition about crystal structures and complementary atomic-level simulations to guide experiments. This is well practiced by Schelling *et al.*¹⁴²

2.8 References

1. HJELM L N and BORNHORST B R (1961), 'Development of improved ceramic coatings to increase the life of XLR999 thrust chamber', in: *Research-Airplane-Committee Report on Conference on the Progress of the X-15 Project*, NASA Tech Memo X-57072, 227–253, National Aeronautics and Space Administration, Washington DC.
2. STECURA S (1976), *Two-Layer Thermal Barrier Coating for Turbine Airfoils – Furnace and Burner Rig Test Results*, NASA Tech Memo X-3425, National Aeronautics and Space Administration, Washington DC.
3. LIEBERT C H, JACOBS R E, STECURA S and MORSE C R (1976), *Durability of Zirconia Thermal-Barrier Ceramic Coatings on Air-Cooled Turbine Blades in Cyclic Jet Engine Operation*, NASA Tech Memo X-3410, National Aeronautics and Space Administration, Washington DC.
4. DEMASI J T and SGEFFKER K D (1986), *Thermal Barrier Coating Life Prediction Model Development*, NASA Contract Rep 175087, National Aeronautics and Space Administration, Washington DC.
5. CAO X, VABEN R and STÖVER D (2004), 'Ceramic materials for thermal barrier coatings', *J Eur Ceram Soc*, **24**, 1–10.
6. LEVI C G (2004), 'Emerging materials and processes for thermal barrier systems', *Curr Opin Solid State Mater Sci*, **8**, 77–91.
7. SCHULZ U, SARUHAN B, FRITSCHER K and LEYENS C (2004), 'Review on advanced EB–PVD ceramic topcoats for TBC applications', *Int J Appl Ceram Technol*, **1**(4), 302–315.
8. SCHULZ U, RAMOND B S and LAVIGNE O (2004), 'Low thermal conductivity ceramics for turbine blade thermal barrier coating application', in: Curzio E L and Readey M J (eds), *28th International Conference on Advanced Ceramics and Composites B*, Wiley, Hoboken, NJ, **25**(4), 375–380.
9. CLARKE D R and PHILLOT S R (2005), 'Thermal barrier coating materials', *Mater Today*, **8**(6), 22–29.
10. VABEN R, TIETZ F, KERKHOFF G and STÖVER D (1998), 'New materials for advanced thermal barrier coatings', in: Lecomte-Beckers J, Schuber F and Ennis P J (eds), *Proceedings of the 6th Liège Conference on Materials for Advanced Power Engineering*, Forschungszentrum Jülich, Jülich, Germany, 1627–1635.
11. CERNUSCHI F, BIANCHI P, LEONI M and SCARDI P (1999), 'Thermal diffusivity/microstructure relationship in Y-PSZ thermal barrier coatings', *J Therm Spray Technol*, **8**(1), 102–109.
12. RYSHKEWITCH E (1960), *Oxide Ceramics: Physical Chemistry and Technology*, Academic Press, New York.
13. HANNINK R H J, KELLY R M and MUDDLE B C (2000), 'Transformation toughening in zirconia-containing ceramics', *J Am Ceram Soc*, **83**(3), 461–487.
14. GARVIE R C, HANNINK R H J and PASCOE R T (1975), 'Ceramic steel?', *Nature*, **258**, 703–704.

15. GARVIE R C (1970), 'Zirconium dioxide and some of its binary systems', in: Alper A M (ed.), *High-temperature oxides*, Vol. 5-II, Academic Press, New York, 117–166.
16. CHEN L B (2006), 'Yttria-stabilized zirconia thermal barrier coatings – a review', *Surf Rev Lett*, **13**(5), 535–544.
17. ZHU W Z and YAN M (1997), 'Effect of grain size on the kinetics of isothermal tetragonal to monoclinic transformation in ZrO_2 (2 mol.% Y_2O_3) ceramics', *J Eur Ceram Soc*, **17**, 1729–1739.
18. BASU B, VLEUGELS J and BIEST O V D (2004), 'Transformation behaviour of tetragonal zirconia: role of dopant content and distribution', *Mater Sci Eng A*, **366**, 338–347.
19. ALVAREZ M R and TORRALVO M J (1996), 'Textural evolution of zirconia and yttria-doped zirconia on thermal treatment under different conditions', *Colloids Surf A: Physicochem Eng Aspects*, **113**, 165–174.
20. KELLY P M and ROSE L R F (2002), 'The martensitic transformation in ceramics – its role in transformation toughening', *Prog Mater Sci*, **47**, 463–557.
21. STECURA S (1978), *Effects of Compositional Changes on the Performance of a Thermal Barrier Coating System*, NASA TM-78976, National Aeronautics and Space Administration, Washington DC.
22. SLIFKA A J, FILLA B J, PHELPS J M, BANCKE G and BERNDT C C (1998), 'Thermal conductivity of a zirconia thermal barrier coating', *J Therm Spray Technol*, **7**(1), 43–46.
23. LIMA C R C and TREVISAN R DA E (1999), 'Temperature measurements and adhesion properties of plasma sprayed thermal barrier coatings', *J Therm Spray Technol*, **8**(2), 323–327.
24. KASPAR J and AMBROZ O (1988), 'Plasma spray coatings as thermal barriers based on zirconium oxide with yttrium oxide', in: Eschnauer H, Huber P, Nicoll A R and Sandmeier S (eds), *The 1st Plasma-Technik-Symposium*, Plasma-Technik AG, Wohlen, Switzerland, **2**, 155–166.
25. THORNTON J and MAJUMDAR A (1995), 'Ceria precipitation and phase stability in zirconia based thermal barrier coatings', in: Ohmori A (ed.), *Proceedings of the 14th International Thermal Spray Conference: Thermal Spray – Current Status and Future Trends*, ASM International, Materials Park, OH, 1075–1080.
26. KVERNES I, SOLBERG J K and LILLERUD K P (1979), 'Ceramic coatings on diesel engine components', in: Fairbanks J W and Stringer J (eds), *Proceedings of the 1st Conference on Advanced Materials for Alternative Fuel Capable Directly Fired Heat Engines*, Maine Maritime Academy, Castine, ME, US Department of Energy, 233–257.
27. JONES R L (1991), 'Development of hot-corrosion-resistant zirconia thermal barrier coatings', *Mater High Temp*, **9**, 228–236.
28. JONES R L (1997), 'Some aspects of the hot corrosion of thermal barrier coatings', *J Therm Spray Technol*, **6**(1), 77–84.
29. MILLER R A, BRINDLEY W J, GOEDJEN J G, TIWARI R and MESS D (1994), 'The effect of silica on the cyclic life of zirconia-yttria thermal barrier coating', in: Berndt C C and Sampath S (eds), *Proceedings of the 7th National Thermal Spray Conference: Thermal Spray in Industrial Applications*, ASM International, Materials Park, OH, 49–54.

30. RAMASWAMY P, SEETHARAMU S, VARMA K B R and RAO K J (1999), 'Thermal shock characteristics of plasma sprayed mullite coatings', *J Therm Spray Technol*, **7**(4), 497–504.
31. MANARA J, BRANDT R, KUHN J, FRICKE J, KRELL T, SCHULZ U, PETERS M and KAYSSER W A (2000), 'Emittance of Y_2O_3 stabilised ZrO_2 thermal barrier coatings prepared by electron-beam physical-vapour deposition', *High Temp-High Press*, **32**(3), 361–368.
32. STUBICAN V S (1986), 'Phase equilibria and metastabilities in the systems ZrO_2 -MgO, ZrO_2 -CaO and ZrO_2 - Y_2O_3 ', *Adv Ceram*, **24A**, 71–82.
33. RAMASWAMY P, SEETHARAMU S, VARMA K B R and RAO K J (1999), 'Evaluation of CaO-CeO₂-partially stabilized zirconia thermal barrier coatings', *Ceram Inter*, **25**, 317–324.
34. BENNETT A (1986), 'Properties of thermal barrier coatings', *Mater Sci Technol*, **2**, 257–261.
35. JONES R L (1992), 'Thermogravimetric study of the 800 °C reaction of stabilizing oxides with SO_3 - $NaVO_3$ ', *J Electrochem Soc*, **139**, 2794–2799.
36. NAGARAJ B A and WORTMAN D J (1990), 'Burner rig evaluation of ceramic coatings with vanadium-contaminated fuels', *Trans ASME*, **112**, 536–542.
37. KVERNES I (1987), 'Ceramic coatings as thermal barriers in diesel and gas turbine engine components', in: Vincenzini P (ed.), *High Tech Ceramics: Part C – Materials Science Monographs*, Elsevier, Amsterdam, 2519–2536.
38. KVERNES I (1981), 'Problems encountered in developing and using thermal barrier coatings on diesel engine components', in: Fairbanks J W and Stringer J (eds), *Proceedings of the 2nd Conference on Advanced Materials for Alternative Fuel Capable Heat Engines*, EPRI Report RD-2369-SR, Palo Alto, CA, 1–21.
39. TORIZ F C, THAKKER A B and GUPTA S K (1988), 'Thermal barrier coating for jet engines', *ASME Gas Turbine Aeroengine Congress and Exposition*, American Society of Mechanical Engineers, New York, 88-GT-279.
40. TSUKUMA K and SHIMADA M (1985), 'Strength, fracture toughness, and Vickers hardness of CeO₂-stabilized tetragonal- ZrO_2 polycrystals (Ce-TZP)', *J Mater Sci*, **20**(4), 1178–1184.
41. TSUKUMA K (1986), 'Mechanical properties and thermal stability of CeO₂-containing tetragonal-zirconia polycrystals', *Am Ceram Soc Bull*, **65**(10), 1386–1389.
42. SWAIN M V (1985), 'Inelastic deformation of Mg-PSZ and its significance for strength-toughness relationship of zirconia-toughened ceramics', *Acta Metall*, **33**(11), 2083–2091.
43. JONES R L, WILLIAMS C E and JONES S R (1986), 'Reaction of vanadium compounds with ceramic oxides', *J Electrochem Soc*, **133**, 227–230.
44. REIDY R F and JONES R L (1995), 'Thermogravimetric analysis of the reaction of CeO₂ with the $NaVO_3$ - SO_3 system', *J Electrochem Soc*, **142**, 1353–1357.
45. MILLER R A (1984), 'Introduction to life modeling of thermal barrier coatings' in: *Turbine Engine Hot Section Technology Conference*, NASA CP-2339, National Aeronautics and Space Administration, Washington DC, 149–154.
46. BRANDON J B, TAYLOR R and MORRELL P (1991), 'Microstructure, composition and property relationships of plasma-sprayed thermal barrier coatings', *Surf Coat Technol*, **50**, 141–149.

47. LEE E Y, SOHN Y, JHA S K, HOLMES J W and SISSON R D (2002), 'Phase transformations of plasma-sprayed zirconia-ceria thermal barrier coatings', *J Am Ceram Soc*, **85**(8), 2065–2071.
48. HOLMES J W and PILSNER B H (1987), 'Cerium oxide stabilized thermal barrier coatings', in: Houck D L (ed.), *Proceedings of the national thermal spray conference: thermal spray – advances in coatings technology*, ASM International, Materials Park, OH, 259–270.
49. HEINTZE G N and MCPHERSON R (1987), 'Fracture toughness of plasma-sprayed zirconia coatings', in: Houck D L (ed.), *Proceedings of the National Thermal Spray Conference: Thermal Spray – Advances in Coatings Technology*, ASM International, Materials Park, OH, 271–275.
50. SODEKA S, SUZUKI M, INOUE T, UENO K and OKI S (1996), 'Thermal and mechanical properties of plasma sprayed ZrO_2 - CeO_2 - Y_2O_3 coatings', in: Berndt C C (ed.), *Proceedings of The 9th National Thermal Spray Conference: Thermal Spray – Practical Solutions for Engineering Problems*, ASM International, Materials Park, OH, 295–302.
51. KIM H K, CHOI H S and LEE C H (1999), 'Failure analysis of plasma sprayed ZrO_2 - CeO_2 - Y_2O_3 thermal barrier coatings', in: Lugscheider E and Kamer P A (eds), *Proceedings of the United Thermal Spray Conference*, Verlag für Schweißen und Verwandte Verfahren, Düsseldorf, Germany, 740–746.
52. ROUANET A, PERAUDEAU G, SIBIEUDE F, PRIEM T, RANC R, RIGAL E and CORNU A (1995), 'Chemical and structural characterization of quenched ceria (yttria) stabilized zirconia or hafnia ceramics for plasma coatings', in: Ohmori A (ed.), *Proceedings of the 14th International Thermal Spray Conference: Thermal Spray – Current Status and Future Trends*, High Temperature Society of Japan, Osaka, Japan, 507–512.
53. THORNTON J, MAJUMDAR A and MCADAM G (1997), 'Enhanced cerium migration in ceria-stabilized zirconia', *Surf Coat Technol*, **94/95**, 112–117.
54. KHOR K A and YANG J (1997), 'Rapidly solidified neodymia-stabilised zirconia coatings prepared by DC plasma spraying', *Surf Coat Technol*, **96**, 313–322.
55. ZHANG Y H, WITHERS P J and FOX M D (1999), 'Damage mechanisms of coated systems under thermomechanical fatigue', *Mater Sci Technol*, **15**, 1031–1036.
56. LEONI M, JONES R L and SCARDI P (1998), 'Phase stability of scandia-yttria-stabilized zirconia TBCs', *Surf Coat Technol*, **108**(1–3), 107–113.
57. JONES R L, REIDY R F and MESS D (1996), 'Scandia, yttria-stabilized zirconia for thermal barrier coatings', *Surf Coat Technol*, **82**, 70–76.
58. JONES R L and MESS D (1996), 'Improved tetragonal phase stability at 1400 °C with scandia, yttria-stabilized zirconia', *Surf Coat Technol*, **86/87**, 94–101.
59. WU J (2004), *Novel Low-Thermal-Conductivity Ceramics for Thermal Barrier Coating*, PhD thesis University of Connecticut, Storrs, CT.
60. RAGHAVAN S, WANG H, PORTER W D, DINWIDDIE R B and MAYO M J (2001), 'Thermal properties of zirconia co-doped with trivalent and pentavalent oxides', *Acta Mater*, **49**, 169–179.
61. RAMASWAMY P, WANG H, DINWIDDIE B, POTER W D, VABEN R, STÖVER D and MAYO M J (2004), ' Ta_2O_5/Nb_2O_5 and Y_2O_3 co-doped zirconias for thermal barrier coatings', *J Am Ceram Soc*, **87**(3), 431–437.

62. KHOR K A and YANG J (1997), 'Lattice parameters tetragonality (c/a) and transformability of tetragonal zirconia phase in plasma sprayed ZrO_2 - Er_2O_3 coatings', *Mat Lett*, **31**(1/2), 23–28.
63. KHOR K A and YANG J (1997), 'Plasma sprayed ZrO_2 - Sm_2O_3 coatings: lattice parameters, tetragonality (c/a) and transformability of tetragonal zirconia phase', *J Mater Sci Lett*, **16**(12), 1002–1004.
64. PITEK F M and LEVI C G (2007), 'Opportunities for TBCs in the ZrO_2 - $YO_{1.5}$ - $TaO_{2.5}$ system', *Surf Coat Technol*, **21**, 6044–6050.
65. MATSUMOTO M, YAMAGUCHI N and MATSUBARA H (2004), 'Low thermal conductivity and high temperature stability of ZrO_2 - Y_2O_3 - La_2O_3 coatings produced by electron beam PVD', *Scripta Mater*, **50**, 867–871.
66. MATSUMOTO M, AOYAMA K, MATSUBARA H, TAKAYAMA K, BANNO T, KAGIYA Y and SUGITA Y (2005), 'Thermal conductivity and phase stability of plasma sprayed ZrO_2 - Y_2O_3 - La_2O_3 coatings', *Surf Coat Technol*, **194**, 31–35.
67. ZHU D and MILLER R A (2004), 'Development of advanced low thermal conductivity thermal barrier coatings', *Int J Appl Ceram Technol*, **1**(1), 86–94.
68. SINGH J, WOLFE D E, MILLER R A, ELDRIDGE J I and ZHU D (2004), 'Tailored microstructure of zirconia and hafnia-based thermal barrier coatings with low thermal conductivity and high hemispherical reflectance by EB-PVD', *J Mater Sci*, **39**, 1975–1985.
69. ZHU D and MILLER R A (1998), 'Sintering and creep behavior of plasma-sprayed zirconia- and hafnia-based thermal barrier coatings', *Surf Coat Technol*, **108/109**, 114–120.
70. ZHU D, FOX D S, BANSAL N P and MILLER R A (2004), *Advanced Oxide Material Systems for 1650 °C Thermal and Environmental Barrier Coating Applications*, NASA/TM-2004-213219, National Aeronautics and Space Administration, Washington DC.
71. IBEGAZENE H, ALPERINE S and DIOT C (1995), 'Yttria-stabilized hafnia-zirconia thermal barrier coatings: the influence of hafnia addition on TBC structure and high-temperature behaviour', *J Mater Sci*, **30**(4), 938–951.
72. WILKES K E and LAGEDROST J F (1973), *Thermophysical Properties of Plasma Sprayed Coatings*, NASA CR-121144, National Aeronautics and Space Administration, Washington DC.
73. CHRASKA P, DUBSKY J, NEUFUSS K and PISACKA J (1997), 'Alumina-base plasma-sprayed materials-part I: phase stability of alumina and alumina-chromia', *J Therm Spray Technol*, **6**(3), 320–326.
74. ILAVSKY J, BERNDT C C, HERMAN H, CHRASKA P and DUBSKY J (1997), 'Alumina-base plasma-sprayed materials-part II: phase transformation in alumina', *J Therm Spray Technol*, **6**(4), 439–444.
75. FOUJANET M C, LUMET J P and DEREPI J L (1988), Structural analysis of zirconia-alumina plasma sprayed coatings, in: Eschnauer H, Huber P, Nicol A R and Sandmeier S (eds), *The 1st Plasma-Technik-Symposium*, Plasma-Technik AG, Wohlen, Switzerland, **2**, 357–366.
76. SAINTE-CATHERINE M C, DEREPI J L and LUMET J P (1991), 'Zirconia-alumina plasma sprayed coatings: correlation between microstructure and properties', in: Sandmeier S, Eschnauer H, Huber P and Nicoll A R (eds), *The 2nd Plasma-Technik-Symposium*, Plasma-Technik AG, Wohlen, Switzerland, **2**, 131–140.
77. KRISHNAMOORTHY P R, RAMASWAMY P and NARAYANA B H (1991), 'Evaluation of multilayer ZrO_2 and Al_2O_3 thermal barrier coatings', in: Sandmeier S, Eschnauer

- H, Huber P and Nicoll A R (eds), *The 2nd Plasma-Technik-Symposium*, Plasma-Technik AG, Wohlen, Switzerland, **3**, 263–272.
78. XU H, GUO H, LIU F and GONG S (2000), ‘Development of gradient thermal barrier coatings and their hot-fatigue behaviour’, *Surf Coat Technol*, **130**, 133–139.
 79. BRUNAUER G, FERY F, BOYSEN H and SCHNEIDER H (2001), ‘High temperature thermal expansion of mullite: an in-situ neutron diffraction study up to 1600 °C’, *J Eur Ceram Soc*, **21**, 2563–2567.
 80. LEE K N, MILLER R A and JACOBSON N S (1995), ‘New generation of plasma-sprayed mullite coatings on silicon carbide’, *J Am Ceram Soc*, **78**(3), 705–710.
 81. KOKINI K, TAKEUCHI Y R and CHOULES B D (1996), ‘Surface thermal cracking of thermal barrier coatings owing to stress relaxation: zirconia vs mullite’, *Surf Coat Technol*, **82**, 77–82.
 82. YONUSHONIS T M (1997), ‘Overview of thermal barrier coatings for diesel engines’, *J Therm Spray Technol*, **6**(1), 50–56.
 83. GILBERT A, KOKINI K and SANKARASUBRAMANIAN S (2008), ‘Thermal fracture of zirconia–mullite composite thermal barrier coatings under thermal shock: an experimental study’, *Surf Coat Technol*, **202**, 2152–2161.
 84. GILBERT A, KOKINI K and SANKARASUBRAMANIAN S (2008), ‘Thermal fracture of zirconia–mullite composite thermal barrier coatings under thermal shock: a numerical study’, *Surf Coat Technol*, **203**, 91–98.
 85. MALONEY M J (2000), *Thermal Barrier Coating Systems and Materials*, US Patent 6 117 560.
 86. KLEMENS P G (1955), ‘The scattering of low-frequency lattice waves by static imperfections’, *Proc Phys Soc*, **A68**, 1113–1128.
 87. SURESH G, SEENIVASAN G, KRISHNAIAH M V and MURTI P S (1997), ‘Investigation of the thermal conductivity of selected compounds of gadolinium and lanthanum’, *J Nucl Mater*, **249**, 259–261.
 88. SURESH G, SEENIVASAN G, KRISHNAIAH M V and MURTI P S (1998), ‘Investigation of the thermal conductivity of selected compounds of lanthanum, samarium and europium’, *J Alloy Compd*, **269**, L9–L12.
 89. VABEN R, CAO X, TIETZ F, BASU D and STÖVER D (2000), ‘Zirconates as new materials for thermal barrier coatings’, *J Am Ceram Soc*, **83**(8), 2023–2028.
 90. MALONEY M J (2001), *Thermal Barrier Coating Systems and Materials*, US Patent 6 1177 200B.
 91. WU J, WEI X, PADTURE N P, KLEMENS P G, GELL M, GARCIA E, MIRANZO P and OSENDI I (2002), ‘Low-thermal-conductivity rare-earth zirconates for potential thermal barrier coating applications’, *J Am Ceram Soc*, **85**(12), 3031–3035.
 92. LEHAMN H, PITZER D, PRACHT G, VABEN R and STÖVER D (2003), ‘Thermal conductivity and thermal expansion coefficient of the lanthanum rare-earth element zirconate system’, *J Am Ceram Soc*, **86**(8), 1338–1344.
 93. CAO X, VABEN R, TIETZ F, JUNGEN W and STÖVER D (2001), ‘Thermal stability of lanthanum zirconate plasma-sprayed coating’, *J Am Ceram Soc*, **84**(9), 2086–2090.
 94. VABEN R, DIETRICH M, LEHMANN H, CAO X, PRACHT G., TIETZ F, PITZER D and STÖVER D (2001), ‘Development of oxide ceramics for an application as TBC’, *Mater Sci Eng Technol*, **32**(8), 673–677.
 95. VABEN R, TRAEGER F and STÖVER D (2004), ‘New thermal barrier coatings based on pyrochlore/YSZ double-layer systems’, *Int J Appl Ceram Technol*, **1**(4), 351–361.

96. LI J, DAI H, ZHONG X, ZHANG Y, MA X, MENG J and CAO X (2007), 'Effect of the addition of YAG ($Y_3Al_5O_{12}$) nanopowder on the mechanical properties of lanthanum zirconate', *Mater Sci Eng*, **A460/461**, 504–508.
97. LI J, DAI H, ZHONG X, ZHANG Y, MA X, MENG J and CAO X (2008), 'Lanthanum zirconate ceramic toughened by $BaTiO_3$ secondary phase', *J Alloy Compd*, **452**, 406–409.
98. CAO X, VABEN R, TIETZ F and STÖVER D (2006), 'New double-ceramic-layer thermal barrier coatings based on zirconia–rare earth composite oxides', *J Eur Ceram Soc*, **26**, 247–251.
99. CAO X (2007), 'Application of rare earths in thermal barrier coating materials', *J Mater Sci Technol*, **23**(1), 15–35.
100. XU Q, PAN W, WANG J, WAN C, QI L and MIAO H (2006), 'Rare-earth zirconate ceramics with fluorite structure for thermal barrier coatings', *J Am Ceram Soc*, **89**(1), 340–342.
101. CAO X, VABEN R, FISCHER W, TIETZ F, JUNGEN W and STÖVER D (2003), 'Lanthanum–cerium oxide as a thermal barrier coating material for high-temperature applications', *Adv Mater*, **15**(17), 1438–1442.
102. MA W, GONG S, XU H and CAO X (2006), 'The thermal cycling behavior of Lanthanum–Cerium Oxide thermal barrier coating prepared by EB–PVD', *Surf Coat Technol*, **200**, 5113–5118.
103. MA W, GONG S, XU H and CAO X (2006), 'On improving the phase stability and thermal expansion coefficients of lanthanum cerium oxide solid solutions', *Scripta Mater*, **54**, 1505–1508.
104. MA W, GONG S, LI H and XU H (2008), 'Novel thermal barrier coatings based on $La_2Ce_2O_7/8YSZ$ double-ceramic-layer systems deposited by electron beam physical vapor deposition', *Surf Coat Technol*, **202**, 2704–2708.
105. DAI H, ZHONG X, LI J, MENG J and CAO X (2006), 'Neodymium–cerium oxide as new thermal barrier coating material', *Surf Coat Technol*, **201**, 2527–2533.
106. CHRASKA P, NEUFUSS K, KOLMAN B and DUBSKY J (1997), 'Plasma spraying of silicates', in: Berndt C C (ed.), *Proceedings of the 1st United Thermal Spray Conference: Thermal Spray – a United Forum for Scientific and Technological Advances*, ASM International, Materials Park, OH, 477–481.
107. RAMASWAMY P, SEETHARAMU S, VARMA K B R and RAO K J (1999), 'Thermal barrier coating application of zircon sand', *J Therm Spray Technol*, **8**(3), 447–453.
108. LIU X and DING C (2002), 'Thermal properties and microstructure of a plasma sprayed wollastonite coating', *J Therm Spray Technol*, **11**(3), 375–379.
109. BUTTERMAN W C and FOSTER W R (1953), 'Zircon stability and ZrO_2 – SiO_2 phase diagram', *Am Mineral*, **52**, 880–888.
110. KVERNES I, LUGSCHEIDER E and LADRU F (1998), 'Lifetime and degradation processes of TBCs for diesel engines', in: Lecomte-Beckers J, Schuber F and Ennis P J (eds), *Proceedings of the 6th Liège Conference on Materials for Advanced Power Engineering*, Forschungszentrum Jülich GmbH, Jülich, Germany, 997–1001.
111. SUZUKI M, SODEOKA S and INOUE T (2008), 'Zircon-based ceramics composite coating for environmental barrier coating', *J Therm Spray Technol*, **17**(3), 404–409.
112. DING C, XI Y, ZHANG Y, QU J and QIAO H (1991), 'Thermophysical properties of plasma sprayed rare earth oxide coatings', in: Sandmeier S, Eschnauer H,

- Huber P and Nicoll A R (eds), *The 2nd Plasma-Technik-Symposium*, Plasma-Technik AG, Wohlen, Switzerland, **3**, 27–32.
113. WARSHAW I and ROY R (1965), ‘Polymorphism of the rare earth sesquioxides’, *J Phys Chem*, **65**, 2048–2051.
 114. FLORIAN P, GERVAIS M, DOUY A, MASLOT D and COUTURES J P (2001), ‘A multi-nuclear multiple-field nuclear magnetic resonance study of the Y_2O_3 – Al_2O_3 phase diagram’, *J Phys Chem*, **B105**, 379–391.
 115. PADTURE N P and KLEMENS P G (1977), ‘Low thermal conductivity in garnets’, *J Am Ceram Soc*, **80**(4), 1019–1020.
 116. PARTHASARATHY T A, MAH T and MATSON L E (1993), ‘Deformation behavior of an Al_2O_3 – $Y_3Al_5O_{12}$ eutectic composite in comparison with sapphire and YAG’, *J Am Ceram Soc*, **76**(1), 29–32.
 117. SU Y J, TRICE R W, FABER K T, WANG H and PORTER W D (2004), ‘Thermal conductivity, phase stability, and oxidation resistance of $Y_3Al_5O_{12}$ (YAG)/ Y_2O_3 – ZrO_2 (YSZ) thermal barrier coatings’, *Oxid Metals*, **61**(3/4), 253–271.
 118. WU Y, DU J and CHOY K L (2006), ‘Novel deposition of columnar $Y_3Al_5O_{12}$ coatings by electrostatic spray-assisted vapor deposition’, *J Am Ceram Soc*, **89**(1), 385–387.
 119. WEYANT C M and FABER K T (2008), ‘Processing-microstructure relationship for plasma-sprayed yttrium aluminum garnet’, *Surf Coat Technol*, **202**, 6081–6089.
 120. SARAVANAN S, SRINIVAS G H, JAYARAM V, PAULRAJ M and ASOKAN S (2008), ‘Synthesis and characterization of $Y_3Al_5O_{12}$ and ZrO_2 – Y_2O_3 thermal barrier coatings by combustion spray pyrolysis’, *Surf Coat Technol*, **202**, 4653–4659.
 121. VABEN R, CAO X, DIETRICH M and STÖVER D (2001), ‘Improvement of new thermal barrier coating system using layered or graded structure’, in: Singh M and Jessen T (eds), *The 25th Annual International Conference on Advanced Ceramics and Composites: an Advance Ceramics Odyssey*, American Ceramic Society, Westerville, OH, 435–442.
 122. FRIDRICH C, GADOW R and SCHIRMER T (2001), ‘Lanthanum hexaaluminate – a new material for atmospheric plasma spraying of advanced thermal barrier coatings’, *J Therm Spray*, **10**(4), 592–598.
 123. GADOW R and LISCHKA M (2002), ‘Lanthanum hexaaluminate – novel thermal barrier coatings for gas turbine applications – materials and process development’, *Surf Coat Technol*, **151/152**, 392–399.
 124. BANSAL and ZHU (2008), ‘Thermal properties of oxides with magnetoplumbite structure for advanced thermal barrier coatings’, *Surf Coat Technol*, **202**, 2698–2703.
 125. MORGAN P, MARSHALL D B (1995), ‘Ceramic composites of monazite and alumina’, *J Am Ceram Soc*, **78**(6), 1553–1563.
 126. SUDRE O, CHEUNG J, MARSHALL D, MORGAN P and LEVI C G (2001), ‘Thermal insulation coatings of $LaPO_4$ ’, *Ceram Eng Sci Proc*, **22**(4), 367–374.
 127. HIKICHI Y, NOMURA T, TANIMURA Y, SUZUKI S and MIYAMOTO M (2005), ‘Sintering and properties of monazite-type $CePO_4$ ’, *J Am Ceram Soc*, **73**(12), 3594–3596.
 128. LIU D M and BROWN J J (1993), ‘Thermal expansion of porous $(Ca_{1-x}Mg_x)Zr_4(PO_4)_6$ ceramics’, *Mater Chem Phys*, **33**, 43–49.

129. HIRSCHFELD D A, LIU D M and BROWN J J (1992), 'CMZP – a new high temperature thermal barrier material', in: Carlsson R, Johansson R and Kahlman L (eds), *The 4th International Symposium on Ceramic Materials and Components for Engines*, Elsevier Applied Science, London, UK, 372–380.
130. LIU D M and BROWN J J (1992), 'Lightweight $(\text{Ca}_{1-x}\text{Mg}_x)\text{Zr}_4(\text{PO}_4)_6$ ceramics', *Mater Chem Phys*, **32**, 161–167.
131. LIU D M (1994), 'Thermal diffusivity, specific heat, and thermal conductivity of $(\text{Ca}_{1-x}\text{Mg}_x)\text{Zr}_4(\text{PO}_4)_6$ ceramic', *Mater Sci Eng*, **B23**, 94–97.
132. HOWARD C J and STOKES H T (2005), 'Structures and phase transformations in perovskites – a group-theoretical approach,' *Acta Cryst*, **A61**, 93–111.
133. VABEN R, SCHWARTZ-LUCKGE S, JUNGEN W and STÖVER D *heat-insulating layer made of complex perovskite*, US Patent 20050260435 A1.
134. HEIMBERG B, BEELE W, KEMPTER K, BAST U, HAUBOLD T, HOFFMANN M, ENDRISS A, GREIL P, HONG C, ALDINGER F and SEIFERT H, *Process for Producing a Ceramic Thermal Barrier Layer for Gas Turbine Engine Component*, US Patent 6602553 B2.
135. MA W, MACK D E, VABEN R and STÖVER D (2008), 'Perovskite-type strontium zirconate as a new material for thermal barrier coatings', *J Am Ceram Soc*, **91**(8), 2630–2635.
136. MA W, JARLIGO M O, MACK D E, PITZER D, MALZBENDER J, VABEN R and STÖVER D (2008), 'New generation perovskite thermal barrier coating materials', *J Therm Spray Technol*, **17**(5/6), 831–837.
137. JARLIGO M O, MACK D E, VABEN R and STÖVER D (2009), 'Application of plasma-sprayed complex perovskites as thermal barrier coatings', *J Therm Spray Technol*, **18**(2), 187–193.
138. MA W, MACK D, MALZBENDER J, VABEN R and STÖVER D (2008), 'Yb₂O₃ and Gd₂O₃ doped strontium zirconate for thermal barrier coatings', *J Eur Ceram Soc*, **28**, 3071–3081.
139. DIETRICH M, VERLOTSKI V, VABEN R and STÖVER D (2001), 'Metal-glass based composites for novel TBC-systems', *Mater Sci Eng Technol*, **32**(8), 669–672.
140. STÖVER D, PRACHT G, LEHMANN H, DIETRICH M, DÖRING J E and VABEN R (2004), 'New material concepts for the next generation of plasma-sprayed thermal barrier coatings', *J Therm Spray Technol*, **13**(1), 76–83.
141. MACK D E, GROSS S M, VABEN R and STÖVER D (2006), 'Metal-glass based composites for application in TBC-systems', *J Therm Spray Technol*, **15**(4), 652–656.
142. SCHELLING P K, PHILLIPOT S R and GRIMES R W (2004), 'Optimum pyrochlore compositions for low thermal conductivity', *Philos Mag Lett*, **84**(2), 127–137.

Metallic coatings for high-temperature oxidation resistance

X. PENG, Chinese Academy of Sciences, China

Abstract: This chapter reviews metallic coatings with the ability to thermally grow a protective layer of chromia or alumina, together with the coating techniques. First generation coatings are developed using chemical vapour deposition techniques (CVD); adding small amounts of reactive elements (e.g., Ce, Y, La) or adding noble elements such as Pt can further enhance performance. Second-generation coatings of the alumina-forming M–Cr–Al–Y overlay type bring the advantages that composition can be tailored to specific environments and to match the composition of matrix alloy, in order to minimize the interdiffusion between coatings and matrix.

Key words: diffusion coating, chromized coating, aluminized coating, overlay coating, nanocrystalline coating, Pt modification, reactive element effect, high temperature oxidation.

3.1 Introduction

On being exposed to a high-temperature environment, almost all kinds of metals will spontaneously form a scale of thermally grown oxides (TGOs), which functions as a barrier between the underlying metals and environmental corrosive substances. A TGO scale with the desired degree of protectiveness will have high thermal stability, good compactness and slow growth rate, as well as strong adhesion to the metallic matrix. If a non-protective scale forms, the oxidation will cause rapid metal recession, which greatly reduces the mechanical properties and service lifetime of the metallic workpieces. Among the TGO oxides, chromia and alumina are two kinds which kinetically and thermodynamically meet the requirement of resistance to high-temperature oxidation. In general, chromia scale is ideal against oxidation below 1000°C and Type II hot corrosion (700–800°C), and alumina scale (particularly in its α phase form) is best against high-temperature oxidation above 1000°C and Type I hot corrosion (800–950°C).

Unfortunately, most conventionally coarse-grained (CG) commercial alloys cannot ensure the formation of chromia or alumina scales, because of some limitation of the Cr and Al content (e.g., high content would

increase the brittleness of alloy and decrease its hot strength or creep resistance). To improve the oxidation resistance of alloys, the addition of high Cr and/or Al coatings has become a preferred choice in most cases. The first generation of these coatings comprises well-known diffusion chromizing and aluminizing coatings, which are usually manufactured by chemical vapor deposition (CVD) pack cementation.^{1,2} The second-generation coatings are so-called overlay coatings, the majority of which are of M–Cr–Al type (M = Fe, Ni, Co, or their combinations) containing a small amount of yttrium. Compared to the diffusion coatings, overlay coatings have the advantage that their composition can be specifically designed and manufactured to match specific environment conditions.³ For a M–Cr–Al coating to be resistant to high-temperature oxidation, the chromium content is normally in the range 16–24 wt% and that of aluminum in the range 13–18 wt%.³ M–Cr–Al overlay coatings, which will be explained in more detail later, have been fabricated using various techniques.^{4–10}

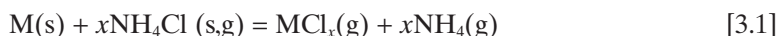
Recently, grain refinement, without any increase in Cr or Al, has been considered to be another approach to increasing the oxidation resistance of alloys because, in some specific cases, it can promote the formation of a protective scale of chromia or alumina.¹¹ Since the late 1990s, oxidation of nanocrystalline (NC) coatings has received considerable attention.^{12–23} Most investigators agree that the promotion of the selective formation of chromia or alumina scales is a primary reason for the superior oxidation resistance of NC coatings. So far, the intrinsic reason for the rapid formation of chromia or alumina scales during the initial oxidation period has not been experimentally established. However, the greatly enhanced diffusion of the corresponding oxide-forming component through the numerous grain boundaries in NC coatings during oxidation is believed to be one of the main causes.

So far, the maximum temperature for practical applications of metallic coatings is generally below 1100 °C. For metals which need to be exposed to higher temperatures, such as the nickel- or cobalt-based superalloys used as structural materials in gas turbine engines, thermal barrier coatings (TBCs) are normally used.^{24–27} A typical TBC is yttria-stabilized zirconia (YSZ). The application of TBCs, of which the thickness traditionally ranges from 100–500 µm, along with internal cooling of the underlying superalloy component, offers a 100–300 °C reduction in the surface temperature of the superalloy. This allows the superalloy-made workpieces to be operated at environmental temperatures above the melting temperature of the superalloy (~1300 °C), thereby improving the engine efficiency and performance. The YSZ is not applied directly onto the superalloy but deposited onto an oxidation-resistant metallic bond coat which is pre-treated on the superalloy. The bond coat is typically M–Cr–Al–Y-type overlay coating or Pt-modified aluminide diffusion coating.^{24,25,27}

3.2 Oxidation-resistant metallic coatings and their fabrication techniques

3.2.1 Diffusion coatings

Diffusion coatings are fabricated using CVD. This involves the dissociation and chemical reactions of gaseous reactants in a stimulant (heat, light, plasma) environment, which is followed by the formation of a stable solid product. The deposition involves homogeneous gas phase reactions that occur in the gas phase, and heterogeneous chemical reactions which occur on a heated surface and result in the formation of powders or films, respectively.²⁸ Pack cementation is a variation of CVD where the volatile gaseous reactants are generated within the powder packing as compared to the usual vapor generation routes in CVD. Metals for pack cementation are usually embedded in a powder mixture of a pure metal or alloy source (e.g., Al, FeAl, Cr, Si, depending on what element will be coated), a halide salt activator (e.g., NaCl, NaF, NH₄Cl) and an inert filler material (e.g., Al₂O₃). A controllable atmosphere, usually Ar or H₂/Ar, surrounds the pack as it is heated to a temperature at which the master metallic powder reacts with the halide salt activator to form volatile metal halide species of significant partial pressures. Suppose NH₄Cl is used as the activator, the reaction will be given below:



where M is the element to be coated. Several different vapor substances may be formed for aluminizing (e.g., Al, AlCl, AlCl₂ and AlCl₃) and for chromizing (e.g., Cr, CrCl₂, CrCl₃ and CrCl₄). Afterwards, partial pressure gradients are established between the powder and the metal for coating, which support vapor transport for each of the vapor substances to the metal matrix surface. On the surface, deposition of the desired coating element occurs via dissociation or disproportionation of the halide molecules, or by a displacement reaction with the matrix. Finally, the coating element interdiffuses and reacts with the matrix, bringing some specific phase, composition and microstructure on the surface. On this basis, the pack cementation can be summarized as four interrelated steps:²⁹ (i) a thermodynamic equilibrium between the activator and the powder of the master metal or alloy, which determines the vapor pressures of the active gaseous substances in the pack; (ii) the gaseous diffusion of the metal halides from the pack to the alloy matrix surface; (iii) reactions on the surface to deposit the coating elements and form the products with vapor substances; and (iv) solid-state diffusion of the coating elements into the matrix. Aluminized coatings and chromized coatings are two traditional diffusion coatings that have been extensively used for almost a century.

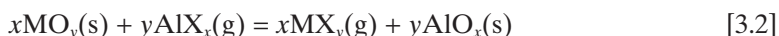
Aluminized coatings

Aluminized coatings are used to extend the life of metals in service in high-temperature environments by thermally growing a protective scale of alumina, a process which conventionally uses the pack-cementation method. The powder mixtures for pack aluminizing are usually composed of a pure metal or alloy (e.g., Al, FeAl), an activator (typically, a halide salt) and an inert alumina filler. The first public description of pack-cementation aluminizing was by Van Aller in a US patent filed in 1911 and in a 1914 presentation by Allison and Hawkins, all of whom are from the General Electric Research Laboratory.²⁴ In the 1940s, pack-cementation aluminizing low-alloy steel for a combustion chamber was reported by Franz in Germany, and pack aluminizing of cobalt-based alloy for gas turbine vane airfoils was reported around the 1950s.²⁴ Diffusion aluminized coatings were also fabricated by hot dip aluminizing,³⁰ slurry aluminizing³¹ and vacuum pulse aluminizing,³² etc. Since 1970, most vane and blade coatings have been applied by pack cementation and the more recently developed 'out-of-contact' CVD processes.^{24, 32–35}

For aluminized coatings formed by pack aluminizing, it is generally accepted that their growth mechanisms can be divided into two categories:³⁶ (i) inward growth under the condition of low-temperature, high-activity pack; and (ii) outward growth under the condition of high-temperature, low-activity pack. The transformation temperature for the growth of aluminides from inward to outward is not easily measured, and it is affected by pack chemistry. In general, when the temperature is below 950 °C, the aluminide coating grows inwardly, forming a M_xAl_y matrix ($y \geq x$; M = Ni, Fe or Co depending on what metal matrix is used for coating). At a higher temperature, the aluminide coating grows outwardly, forming a MAI matrix (e.g., β -NiAl on Ni-base metals).

When exposed to high-temperature environments, the thermally grown alumina scale on the aluminized coatings always suffers stresses which are induced by thermal cycling and oxide formation and growth. These can result in loss of the adherence and spalling of the scale. However, a small concentration of a reactive element (e.g., Y, La, Hf, Ce) can improve the adherence of alumina scale. This phenomenon is referred to as the 'reactive element effect' (REE). Theories associated with the REE have been reviewed elsewhere.^{37–39} It is generally accepted that the addition of RE or RE oxide particles improves the oxidation resistance of alumina formers through enhancing the alumina scale adhesion to the underlying metals by means of several mechanisms: (i) 'pegging' alumina scale to the underlying metal; (ii) preventing the coalescence of vacancies at the scale–metal interface; and (iii) eliminating dissociated sulfur at the scale–metal interface.

Different routes have been used to add reactive element into aluminized coatings. LePrince *et al.*⁴⁰ used a highly active process with a powder mixture of pure source elements to co-deposit Al and Hf onto Ni-base fibers, developing an aluminide coating (β -NiAl) with the precipitation of Ni₅Hf. The Ni₅Hf-precipitated aluminide coating showed improved oxide scale adherence during cyclic oxidation testing. Rapp *et al.*^{41,42} proposed two methods which can be used for doping of a minor element (e.g., Zr or Y) onto the surface of an aluminide diffusion coating produced by a single-step pack process. One is to add a small amount of an oxide source of the desired element (e.g., ZrO₂ or Y₂O₃) into the pack powder mixture, instead of some inert filler. In this case, the oxide dopant must be converted into high halogen activity within the pack to produce additional metal halide species according to the following equation:



where M is Zr or Y. The other is to add certain amounts of reactive element chlorides (e.g., ZrCl₄, YCl₃, or HfCl₄) as activator source. The chlorides can react with the master metal (or alloy) to produce AlCl_x species according to the equation given by:



where RE indicates a reactive element. Applying the single-step pack cementation at 1150°C for 24 h, RE-doped aluminide coatings were developed on IN 713LC matrix. The isothermal oxidation at 1100°C in air showed that the RE-doped aluminide coatings compared to RE-free coatings had formed α -Al₂O₃ scale with decreased growth rate but increased resistance to cracking and spalling.⁴³

Tu *et al.*⁴⁴ produced a Y-modified aluminide coating by aluminizing followed by yttrizing. The coating consisted of an external aluminide layer with Y enrichment near the surface and along the grain boundaries. Yttrium was deposited in a pack powder mixture of pure Y, NH₄Cl activator and an Y₂O₃ filler which was heated at 1050°C for 4 h. Through a 'two-step' method (Ni-La₂O₃ co-electroplating followed by aluminizing at 930°C for 2.5 h), Peng *et al.*⁴⁵ fabricated a La₂O₃-dispersed β -NiAl coating. Compared to the La₂O₃-free β -NiAl developed on electrodeposited pure Ni, this coating exhibited decreased oxidation kinetics at 1000°C in air. It has been proposed that during oxidation lanthanum ions from the La₂O₃ particles would incorporate the growing θ -alumina scale, where the lanthanum ions prevented the formation of microcracks in the scale by retarding the θ - α transformation, and suppressed outward aluminum diffusion for the scale growth by the segregation to the scale grain boundaries.

β -NiAl coatings developed on Ni or Ni-base alloys have low oxidation kinetics because they exclusively grow an external scale of alumina. It was

found in the 1970s that addition of Pt can further improve the adhesion of the scale to the coating matrix.⁴⁶ Some recent studies have contributed an enhanced understanding of the effect of Pt addition on scale adhesion. Pt addition has been found to decrease the number of voids formed at the oxide/metal interface⁴⁷ and to minimize the segregation at the interface of sulfur (which, as a common impurity in metals, typically 1–10 ppm, usually segregates to the interface during oxidation and consequently weakens the interfacial bonding).^{48,49}

Pt-modified nickel–aluminide coatings, which typically have a surface layer of either PtAl_2 or $(\text{PtAl}_2 + (\text{Ni,Pt})\text{Al})$, are normally fabricated by means of a ‘two-step’ method (Pt electroplating followed by pack aluminizing).^{50–52} A low-Al-activity CVD processing enabled a single-phase (Pt,Ni)Al coating to be developed.⁵³ Compared to the Pt–Al coatings, the available results^{53,54} indicated that the single-phased (Pt,Ni)Al coating fabricated by pack cementation exhibited improvements in cyclic oxidation and hot corrosion resistance, thermal stability and ductility. First-principle calculations show that the presence of Pt in the B2-type NiAl intermetallic compound brings the surface electronic energies to a higher state, which results in an increased surface energy. This will increase the void nucleation energy, thus making void formation a more difficult process,⁵⁵ which may explain the beneficial effect of Pt on cyclic oxidation. Some studies also showed that the Pt-modified aluminide coatings were much more resistant to hot corrosion than the Pt-free aluminide coatings,^{56–58} a result which is not yet fully understood. Some investigators have indirectly attributed it to the beneficial effect on the scale adhesion of Pt.^{57,58}

Chromized coatings

Kelley first produced chromized steels by means of pack cementation in 1923.⁵⁹ Samuel and Lockington⁶⁰ and Drewett⁶¹ published a comprehensive review of chromized coatings on steel in the early 1950s. In 1953, Gibson patented aluminizing of chromized steels with aluminum paints and heat treatment to improve high-temperature oxidation resistance.²⁴ In general, chromized coatings on nickel-base metals have good oxidation resistance, which can be further improved by the introduction of CeO_2 particles by the ‘two-step’ method (Ni– CeO_2 co-electroplating followed by pack chromizing).^{62–64} However, chromized ferritic steels do not have the desired oxidation resistance, particularly in the thermal cyclic condition. One important reason is that the chromization of the steels inevitably causes the formation of a surface chromium carbide layer,^{62–67} because carbon has a strong chromium affinity, which has a detrimental effect on the oxidation resistance of chromized steels.^{63,64} To mitigate or exclude the carbon effect, one promising route that has been suggested but not yet fully reported is the design of a

precursor film on the steels as an electrodeposited Ni-RE_xO_y film (RE = Ce, Y, La, etc.).⁶²⁻⁶⁴

M-Cr-Al type diffusion coatings

M-Cr-Al-type diffusion coatings, which have a composition similar to that of overlay coatings fabricated by means of the other techniques (see below), may be developed through pack-cementation methods such as simultaneous chromizing-aluminizing, aluminizing followed by chromizing (or vice versa). Geib and Rapp⁶⁸ simultaneously chrome-aluminized low-alloy steels and got a coating with a surface composition of 11–20 wt%Cr and 4–9 wt% Al. However, reports on the oxidation of M-Cr-Al type diffusion coatings are still rare.

Low-temperature pack cementation

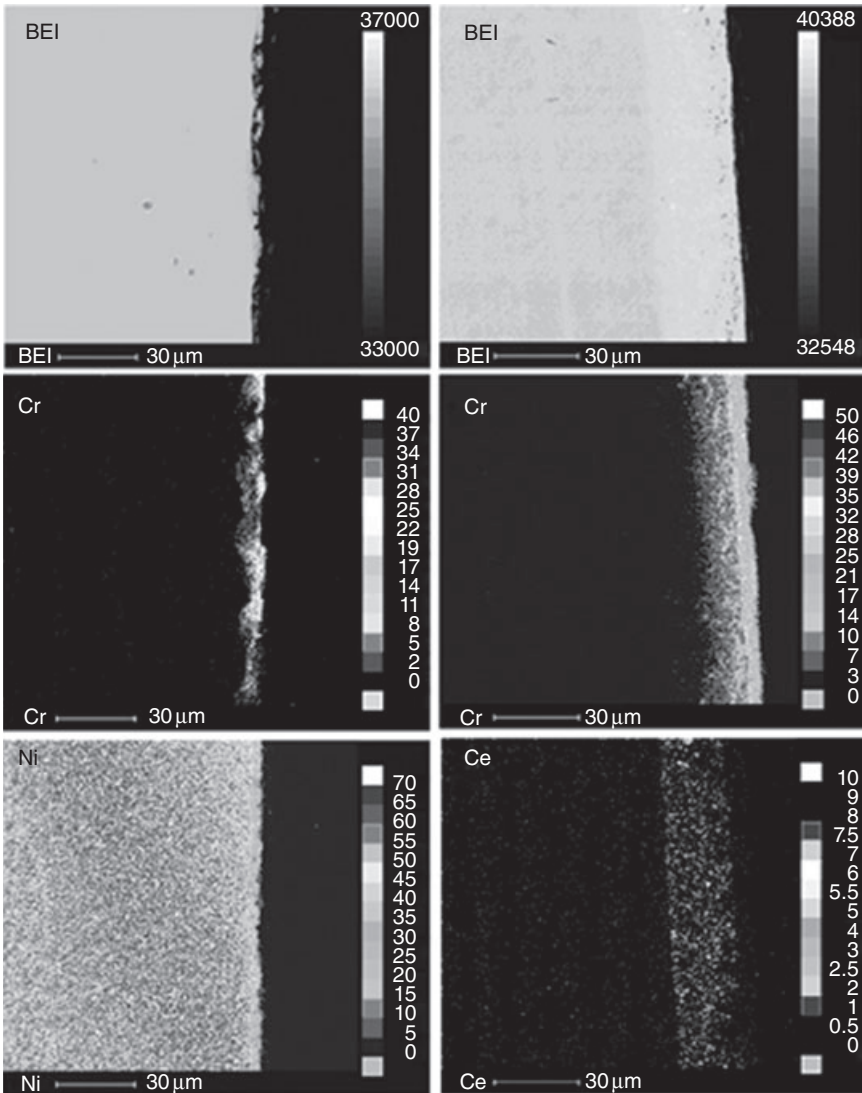
The temperatures at which conventional oxidation-resistant chromized and aluminized coatings are developed by pack cementation are very high (>1000 °C for chromization and >900 °C for aluminization). Such high temperatures significantly exceed the heat treatment temperatures for ferritic steel workpieces (normally below 700 °C), resulting in noticeable grain growth and carbide precipitation which has a detrimental impact on the mechanical properties, particularly in decreasing their high-temperature strength and creep resistance. Therefore, reducing the pack-cementation temperature is generally required for widespread application of these coatings to the steels. To achieve this goal, it is essential to enhance low-temperature chromizing and aluminizing kinetics, which are mainly determined by the diffusion of the coating element in the metal matrix. Metal grain boundaries (GBs) normally act as ‘short-circuit’ diffusion paths because of a reduced atomic density compared to the perfect crystal lattice. NC metals consist of a large volume fraction of GBs. Even when GB diffusion is dominant in the latter,⁶⁹⁻⁷¹ metallic diffusion in a nano-grained polycrystalline metal would be enhanced by orders of magnitude in comparison to the diffusion in its conventionally coarse-grained (CG) counterparts with the same chemical compositions at a given temperature. The enhancement lies in a different structure which comes from an enhanced diffusivity along the triple junctions between three GBs, and a reduced concentration of impurities in comparison to the GB in CG metals. Therefore, the nanostructure of steels is likely to be a promising approach for fabricating chromized and aluminized coatings at the desired low temperatures.

Recently, Zhang *et al.*⁷² developed an oxidation-resistant, low-temperature chromized coating on a mild carbon steel using the ‘two-step’ method: first, electrodeposition of NC Ni matrix film with dispersion of CeO₂

nanoparticles; second, pack cementation at 700 °C in a traditionally halide-activated pack mixture. The positive effects of the CeO₂ nanoparticles during chromization may be summarized as follows: (i) retarding the growth of the nickel nanograins at high temperatures by anchoring the movement of GBs; (ii) producing numerous Ni/oxide interphase boundaries, which would be additional 'short-circuit' paths other than GBs for chromium transport during chromization; and (iii) distributing the oxide more homogeneously with the particles in nano-scale instead of in micron range. Figure 3.1 shows the electron probe microanalysis (EPMA) of cross-sections of chromized coatings on a CG Ni (mean grain size: 30 μm) and CeO₂-dispersed NC Ni film (mean grain size: 56 nm). Clearly, the chromized CG Ni cannot form a continuous chromium coating on the surface. In contrast, the chromized Ni–CeO₂ film formed a surface layer 25 μm in thickness with a uniform distribution of Cr. Thus, the chromizing kinetics on the nanograined metal was greatly promoted. Moreover, CeO₂ particles are found to randomly disperse in the chromized coating, which tends to decrease the oxidation rate of the coating through the REE mentioned above.⁷²

Compared to chromizing, aluminizing has greatly increased coating growth rate at low temperatures when the reaction of Al with the metal matrix such as Ni, Fe and Co increases the inward diffusion of Al. However, the temperature of aluminizing kinetics is still quite low. For example, Xiang and Datta⁷³ developed aluminized coatings 30 μm in thickness (η -Fe₂Al₃) on P92 ferritic steels at 650 °C for 8 h in a pack of 4Al–2AlCl₃–Al₂O₃ (wt%). Zhan *et al.*⁷⁴ reported that the thickness of the aluminized coating reached ~50 μm when prepared in a pack of Al–NH₄Cl–Al₂O₃ for only 30 min at 560 °C with the assumption of the steel matrix nanograined by ball milling through a severe plastic deformation mechanism. Recent studies have also shown that, for 5 h pack cementation at 600 °C in a powder mixture of 45Al–5NH₄Cl–Al₂O₃ (wt%), the aluminide (δ -Ni₂Al₃) coating formed on a ~20 μm-grained Ni 18 μm in thickness, while the thickness of the aluminide on a ~60 nm-grained Ni–CeO₂ film was increased to ~58 μm. Moreover, the low-temperature aluminized coating on the NC Ni matrix had a dispersed CeO₂ and ultrafine-grained structure,⁷⁵ which exhibited excellent spalling resistance during cyclic oxidation in air at 1000 °C.⁷⁵ It was suggested that this result occurs because the dispersed CeO₂, together with the ultrafine-grained coating structure, helped prevent the formation of cavities at the coating interface.

Pack cementation is a simple, inexpensive and reproducible method for uniformly coating metallic components of different sizes and with complex shapes. However, the method has some limitations summarized follows:^{24,42} (i) easy incorporation of contaminants; (ii) labor-intensive with respect to cleaning the coated components after pack cementation; (iii) large amount of pack powder wasted together with the cost of powder disposal; and (iv) relatively long processing time.



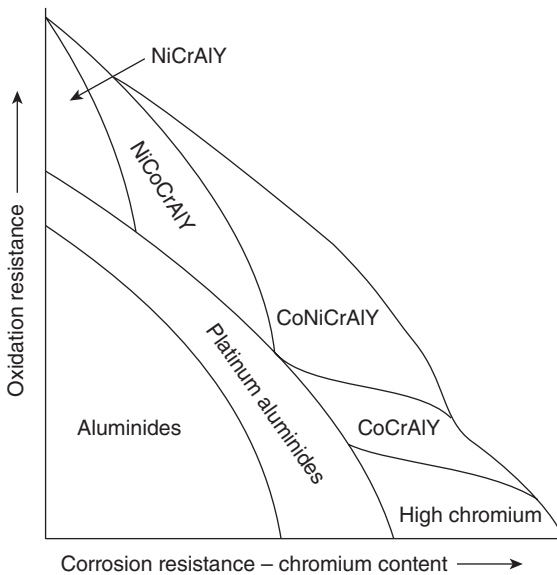
3.1 The back-scattered image, the corresponding elemental X-ray mappings of cross-sections for chromized samples on a coarse-grained Ni (left) and nanocrystalline Ni-base with dispersion of CeO₂ nanoparticles (Ni X-ray mapping not presented) (right).⁷²

3.2.2 M–Cr–Al(–Y) overlay coatings

M–Cr–Al–Y overlay coatings emerged in 1960s, probably beginning with an alloy having the composition Fe–25%Cr–4%Al–1.0%Y, from G.E. nuclear programs, that exhibited exceptional alumina adherence in cyclic oxidation.²⁴ A model composition Fe–Cr–Al–Y, with 10–15% aluminum,

was applied as a coating to Ni-base superalloys by electron beam physical vapor deposition (EB-PVD).⁷⁶ Because workpieces in industrial turbines are conventionally made of Ni- or Co-base structural superalloy, Ni-, Co- and NiCo-based M–Cr–Al–Y overlay coatings have been widely investigated, with the focus on oxidation and hot corrosion properties.^{8–10,18,24,77–83} Compared to the Ni–Cr–Al–Y-type overlay coating, the Co–Cr–Al–Y-type overlay coating has generally decreased oxidation resistance but increased hot corrosion resistance. For this reason, NiCo-base overlay coatings with a compromise in oxidation and hot corrosion performance were developed. For example, the nominal composition Ni–23%Co–15%Cr–12.5%Al–0.5%Y had adequate oxidation and hot corrosion properties which proved to be satisfactory for the protection of blade airfoils in the current Pratt and Whitney commercial aircraft engines.²⁴ In industry, many more complex Ni–Co–Cr–Al–Y compositions containing additions of Ta, W, Ti, Nb, Re, Zr, etc., singly or in combination, have been developed for specific purposes. A comparison between oxidation and hot corrosion resistance of overlay coatings of various types is presented in Fig. 3.2.^{3,84}

Oxidation and hot corrosion resistance also depend on the concentration of Cr. 16–24 wt%Cr in the overlay coatings favors not only an increase in low-temperature hot corrosion (Type II corrosion in a temperature of 650–800°C) resistance but also oxidation and Type I hot corrosion (800–950°C) resistance by promoting the formation of Al₂O₃ scale, through the



3.2 Dependence of oxidation resistance on corrosion resistance for various high-temperature coating systems.^{3,84}

so-called third element effect according to Wagner theory.⁸⁵ Therefore, the overlay coatings exhibit greatly enhanced resistance to oxidation and corrosion compared with the simple and Pt-modified aluminide coating of the first generation. The overlay coatings can be specifically developed through various coating techniques, including EB-PVD,^{18,76} plasma spray,⁸⁰ magnetron sputtering,^{81,82} high-velocity oxyfuel (HVOF),^{8,20,83} laser cladding,¹⁰ etc. A typical Ni-base commercial overlay coating is EB-PVD ATD10 (Ni-20Cr-11Al-0.3Y).

M-Cr-Al-Y overlay coatings always contain a small amount of yttrium. The purpose of adding yttrium is to increase the resistance of the protective scale (mostly alumina) to oxidation through the so-called REEs which have been explained in detail above.³⁷⁻³⁹ Interestingly, it was found that nanocrystallization of M-Cr-Al-based alloys without yttrium has an influence which is somewhat similar to that of yttrium additions in that it increases the adhesion of the developed alumina scale by means of several mechanisms as summarized by Peng *et al.*,¹¹ including forming interfacial 'oxide micropegs', minimizing the concentration of condensed cation vacancies and the segregation of sulfur at the scale/metal interface and increasing oxide diffusion creep by favoring the formation of a fine-grained scale structure. The alloy's nanocrystallization may also favor an exclusive development of a protective scale (mainly alumina), without increasing the contents of Cr and Al. This has made the synthesis of oxidation-resistant NC coatings an active field of research since the 1990s.¹¹⁻²³

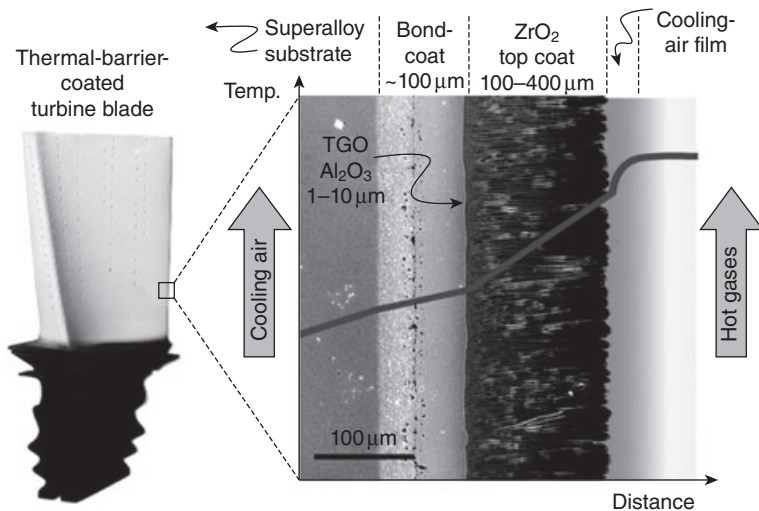
Several researchers have studied the oxidation of Ni-Cr-Al-type NC coatings prepared by sputtering. Chen and Lou⁸⁶ found that a three-component NC coating containing concentrations of both Cr and Al as low as 5 wt% can develop into alumina scales. For the Ni-20Cr-*x*Al NC coating, only 2.4 wt% Al is needed for selective development to an α -alumina scale at 1000 °C, while the minimum content for conventionally coarse-grained three-component alloys is 6 wt% Al. Below this concentration limit, the CG alloys form an external layer of Cr₂O₃ and NiCr₂O₄ spinel with deep internal Al₂O₃ particles underneath.¹⁷ An increased ability to selectively form alumina scales was also repeated for the oxidation of NiCrAl-type NC coatings prepared by HVOF using cryomilling-produced NC powders.²⁰

The M-Cr-Al-type NC coatings are mostly fabricated by magnetron sputtering. The coating species (mainly atoms), which are randomly sputtered by Ar ions from the target material, are deposited onto the anode in a vacuum chamber. Due to the high-temperature state of the sputtered atoms, those arriving at the much cooler anode surface can be effectively quenched at a rate approaching 10¹⁵ °C/s.⁸⁷ Such a high quenching rate, together with a quick reduction of the stored energy of the sputtered atoms by collision in the flying track or on the sample surface, does not permit adequate time to rearrange the adatoms on the metal matrix through

surface diffusion to form an alloy whose phase composition can be predicted according to bulk thermodynamic criteria. Therefore, the adatoms are locally accommodated to assemble a NC solid solution. In other words, the non-equilibrium characteristic of sputtering deposition fabricates a NC alloy coating with a chemical composition similar to, but phase composition dissimilar to, the target alloy. Most recently, a nanograined Ni–Cr–Al coating was fabricated by co-electrodeposition of NC Ni matrix and nanoparticles of Cr and Al.⁸⁸ Compared to ternary composites assembled with Cr and Al microparticles and conventionally coarse-grained alloys of similar composition, the nanocomposites exhibited a greatly increased ability to thermally develop chromia or alumina scales. The result constitutes a frame of reference for manufacturing novel oxidation-resistant Ni–Cr–Al-type coatings through simple electrochemical deposition, which is a sophisticated technique with the merits of simple processing, low expense, high productivity and good compositional control.

3.3 Metallic coatings as bond coats for thermal barrier coatings (TBCs)

Figure 3.3 shows a normal and practical TBC system,²⁵ which has three layers made of different materials with specific properties and functions; from bottom to top, they are (i) bond coat, (ii) TGO (normally Al_2O_3) and (iii) ceramic top coat (mostly YSZ). The bond coat is an oxidation-resistant



3.3 Cross-sectional morphology of an EB-PVD TBC coating onto a turbine blade, which consists of a top ceramic coat (YSZ), a TGO layer (alumina) and a bond coat. (Reprinted from reference [25] with permission from Copyright Clearance Center. INC)

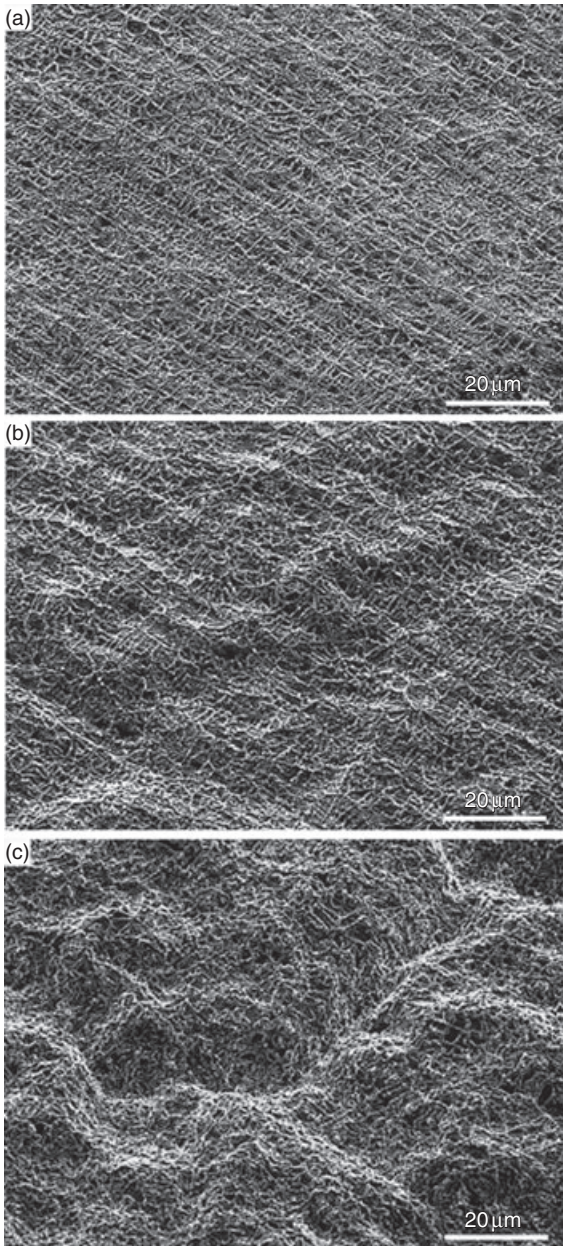
metallic layer 100–200 μm in thickness. Currently, two typical bond coats are M–Cr–Al–Y alloy (such as Ni–Cr–Al–Y or Ni–Co–Cr–Al–Y), which is deposited using plasma spray or EB–PVD, and Pt-modified aluminides, which are deposited by Pt electroplating in combination with pack aluminization or CVD. In many cases, the TBC damage is correlated with the oxidation and mechanical properties of the bond coat and the TGO. Driven by compressive stresses in the TGO, brought about by oxidation-induced volume increase following the Pilling–Bedworth ratio (growth stress) or by differences in the coefficient of thermal expansion (CTE) between TGO and bond coat (thermal stress), the TGO may crack and the TGO/bond coat interface may delaminate, which is currently the key reason for spallation failure of the TBC system.^{25,89}

3.3.1 Pt-modified aluminide bond coats

Contemporary commercial gas turbines usually have more advanced coating systems, e.g. platinum aluminides (or M–Cr–Al–Y, etc.), on first stage blades, and it is estimated that more than 80% of airfoils are coated by pack cementation or CVD aluminizing or chromizing processes.²⁴ Since the 1990s, aluminide coatings have been recognized as useful bond coats for some types of TBCs, capable of offering oxidation resistance.⁹⁰

Pt-modified Ni–Al coatings are susceptible to the development of surface undulations (surface ‘rumpling’) when thermally cycled at elevated temperatures.^{90–93} Figure 3.4 shows a typical evolution of surface rumpling of a Pt-modified Ni–Al coating on René N5 single crystal superalloy by platinum electroplating followed by a low-activity CVD aluminizing during cycling in air at 1200 °C.⁹¹ The rumpling was considered to be local volume reduction of the aluminide due to the depletion of Al by oxidation.⁹¹ This surface rumpling could cause premature coating failure during service, which normally occurs in the form of cracking and spallation of the protective oxide scale along the rumpled ridges and accelerated oxidation.

For a Pt-modified Ni–Al bond coat/EB–PVD YSZ TBC system, the growth of the TGO and the mechanical behavior of the bond coat are believed to play an extremely important role in determining the life of the system. The rumpling of the bond coat can lead to significant out-of-plane displacement of the bond coat/TGO interface, which is associated with local separations and delamination of the top ceramic coat and overall TBC failure. Moreover, other factors, such as surface roughness and defect size as well as sulfur impurity of a (Pt,Ni)Al bond coat, can influence the damage to the top YSZ.^{25,89} Pt-modified Ni–Al bond coats fabricated by different routes will have different structure, chemical composition and surface morphology, which causes damage to the TGO/bond coat according to different mechanisms.



3.4 Rumpling of the bond coat surface polished with 400-grit under cyclic loads in air at 1200°C (1 h cycles): (a) 1 cycle; (b) 10 cycles; (c) 50 cycles.⁹¹

3.3.2 M–Cr–Al–Y bond coats

In M–Cr–Al–Y overlay coating systems, Ni–Cr–Al–Y or Ni–Co–Cr–Al–Y are two typical coatings used as bond coats. They are normally deposited with low-pressure plasma spray (LPPS) or EB–PVD.^{25,89} The bond coats usually consist of γ -Ni solid solution matrix and β -NiAl phases, although minor precipitates of γ' -Ni₃Al and σ -(Cr, Co) phases have additionally been shown to exist.^{89,94–96} The concentration of the yttrium added is normally around or below 1.0 wt%. The yttrium addition can improve the adhesion of the TGO, mainly through scavenging the interface sulfur segregants, which would promote the growth of exiting interface voids⁹⁷ or weaken interface bonding.⁹⁸

The failure mechanism of the Ni–Cr–Al–Y or Ni–Co–Cr–Al–Y bond coat/YSZ TBC system is less well understood, because the YSZ top layer often fails catastrophically by large-scale delamination.^{94,99} The dominant delamination mode has been reported as separation along the TGO/bond coat interface after high-temperature exposure.^{89,94,99} The interface separation depends on the synergistic effect of several factors or parameters, such as the amount of stored energy in the TGO, the interface chemistry (e.g. sulfur concentration), the interface imperfections (e.g., physical defect size, yttrium-rich oxide protrusions) and the mechanical behavior of the bond coat. The original interface defect is normally considered as one important reason for the separation of the TGO from the bond coat. When the interface defect (e.g., void and delamination) grows to a critical size, local TGO buckling occurs. The critical interface flaw (\bar{c}) of buckling can be given by^{100,101}

$$\bar{c} = \frac{\pi h_{\text{ox}}}{2\sqrt{3}} \sqrt{\frac{E_{\text{ox}}}{(1-\nu_{\text{ox}}^2)\sigma_{\text{ox}}}} \quad [3.4]$$

where h_{ox} , E_{ox} , ν_{ox} are the thickness, elastic modulus and Poissons' ratio of the TGO, respectively, and σ_{ox} is the stress generated in the TGO. It has also been reported that oxide intrusions (normally containing reactive element such as yttrium) with a range of size and wavelength can be the source of the initial oxide delamination.¹⁰² In addition, it is noteworthy that a continuous γ -Ni layer can form at the TGO/bond coat interface because of the depletion of Al from the β -NiAl during oxidation. The evolution of the γ layer strongly depends on the oxidation temperature as well as the number of thermal cycles.⁹⁴ The alumina scale/ γ -Ni interface has low toughness, especially when segregation or contamination is present in combination with moisture in the surroundings.^{103,104} In most cases, the failure mechanism of the TGO/bond coat system follows a route of interface delamination, TGO buckling and finally the failure of the TBC system.

3.4 Conclusions

Metallic chromia- or alumina-forming diffusion coatings, which are referred to as the first-generation coatings, have been extensively used in gas turbine engines for aero-jet propulsion, land-based industrial power generation and in industrial boilers for electric generation to prevent oxidation of the structural metals in service in high-temperature environments. Compared to chromized coatings, aluminized coatings have more application advantages because they can form alumina scales that not only grow slowly but are also more thermodynamically stable at high temperatures (over $>1000^{\circ}\text{C}$) as well as in wet atmospheres. To further improve the oxidation resistance, composition modification of aluminized coatings by addition of specified elements has been extensively investigated. Compared to conventional NiAl coatings, platinum- and RE_xO_y ($\text{Re} = \text{Y, La, etc.}$)-modified nickel–aluminide coatings exhibit excellent resistance in thermal cyclic oxidation and hot corrosion. The enhanced adhesion of the alumina scales has been proposed as one of the main reasons. Grain refinement through structural tailoring may be another approach to further increase the adhesion of the alumina scales on aluminide coatings, by preventing the formation of large cavities at the oxide/metal interface, an effect for which the fundamental reason has not yet been fully explored. Fine-grained aluminide coatings can be developed on metals which are nanograined through special surface treatment or pre-deposited with a nanocrystalline metallic film such as Ni, by means of conventional pack aluminization but at much lower temperatures than normal. This processing method enables the fabrication of aluminide coatings on ferritic steels at the temperatures below the maximum temperature allowed by conventional heat treatment.

Compared to alumina-forming diffusion coatings, alumina-forming M–Cr–Al–Y overlay coatings (second-generation coatings) have the advantages that their composition can be specifically designed and manufactured to match not only the particular environment conditions but also the main compositions of matrix alloys, making it possible to minimize the inter-diffusion between coatings and matrix. Inter-diffusion can be best avoided by adding nanocrystalline M–Cr–Al-type coatings, because an alumina-forming M–Cr–Al NC coating may have concentrations of Cr and Al which are close to those in conventional M–Cr–Al-base alloys used as the matrix for coating. Oxidation of M–Cr–Al NC coatings has been widely investigated since the mid-1990s. For engineering applications, more works on the thermal stability and long-term oxidation performance of NC coatings should be conducted in the future.

TBCs (typically YSZ) are the third-generation coatings and have the most complex structure. The YSZ coat is normally deposited onto a bond coat, a metallic coating that is preferentially coated onto the matrix alloys

to increase the adhesion of the ceramic during oxidation. The bond coat is normally an alumina former, because the alumina TGO has a very low growth rate at high temperatures and is phase compatible with YSZ. Two major categories of bond coats which have been developed are the Pt-modified Ni–Al and M–Cr–Al–Y alloys. The rumpling of Pt-modified Ni–Al bond coat and TGO buckling of M–Cr–Al–Y bond coat are the major mechanisms for damage to the TGO/bond coat interface, which is considered as an important reason for the mechanical failure of the TBC system at high temperatures.

3.5 Acknowledgements

We acknowledge the financial support by the National Science Foundation of China (NSFC) project under Grant No. 51071162 and 50571108.

3.6 References

1. FITZER E, MAURER H J, 'Diffusion and precipitation phenomena in aluminized and chromium-aluminized iron- and nickel-based alloys', in: *Materials and Coatings to Resist High Temperature Corrosion* (Ed. Holmes D R, Rahmel A), London, UK, Applied Science, 1978, 253–269.
2. RESTALL J E, MALIK M, SINGHEISER L, 'Metallic diffusion and overlay coatings', in: *Proceeding of High Temperature Alloys for Gas Turbines and Other Applications* (Ed. Betz W), Dordrecht, Germany, Reidel, 1986, 357.
3. NICHOLLS J R, SIMMS N J, CHAN W Y, EVANS H E, 'Smart overlay coatings – concept and practice', *Surf Coat Technol*, 2002, **149**(2–3), 236–244.
4. NICHOLLS J R, HANCOCK P, AL YASIRI L H, 'Optimising oxidation resistance of MCrAl coating systems using vapor phase alloy design', *Mater Sci Technol*, 1989, **5**, 799–805.
5. WANG F, LOU H, ZHU S, WU W, 'The mechanism of scale adhesion on sputtered microcrystallized CoCrAl films', *Oxid Met*, 1996, **45**(1–2), 39–51.
6. LIU Z, GAO W, DAHM K L, WANG F, 'Oxidation behaviour of sputter-deposited Ni–Cr–Al micro-crystalline coatings', *Acta Mater*, 1998, **46**(5), 1691–1700.
7. WAKI H, KOBAYASHI A, 'Development of lateral compression method of circular tube thin coating for mechanical properties of plasma sprayed CoNiCrAlY', *Mater Trans*, 2006, **47**(7), 1626–1630.
8. BRANDL W, TOMA D, KRUGER J, GRABKE H J, MATTHAUS G, 'The oxidation behaviour of HVOF thermal-sprayed MCrAlY coatings', *Surf Coat Technol*, 1997, **94–5**(1–3), 21–26.
9. LI C J, LI W Y, 'Effect of sprayed powder particle size on the oxidation behavior of MCrAlY materials during high velocity oxygen-fuel deposition', *Surf Coat Technol*, 2003, **162**(1), 31–41.
10. HIROSE A, KOTANI H, KOBAYASHI K, 'Surface modification by laser cladding of Ni–Cr–Al–Y alloy', *Iron Steel Inst Jpn*, 1993, **79**(1), 105–112.
11. PENG X, WANG F, 'Oxidation resistant nanocrystalline coatings', in: *New developments in high temperature corrosion* (Ed. Gao W, Li Z), Cambridge, UK, Woodhead, 2008, 456–475.

12. WANG F, LOU H, 'Oxidation Behaviour and scale morphology of normal-grained CoCrAl alloy and its sputtered microcrystalline coating', *Mater Sci Eng*, 1990, **A43**, 279–285.
13. WANG F, 'Oxidation resistance of sputtered Ni-3(AlCr) nanocrystalline coating', *Oxid Met*, 1997, **47**(3/4), 247–258.
14. WANG F, YOUNG D J, 'Effect of nanocrystallization on the corrosion resistance of K38G superalloy in CO + CO₂ atmospheres', *Oxid Met*, 1997, **48**(5/6), 497–509.
15. CHEN G, LOU H, 'Oxidation behavior of a sputtered Ni-5Cr-5Al nanocrystalline coating', *Oxid Met*, 2000, **53**(5/6), 467–479.
16. LIU Z, GAO W, DAHM K L, WANG F, 'The effect of coating grain size on the selective oxidation behaviour of Ni-Cr-Al alloy', *Scripta Mater*, 1997, **37**(10), 1551–1558.
17. LIU Z, GAO W, DAHM K L, WANG F, 'Oxidation behaviour of sputter-deposited Ni-Cr-Al micro-crystalline coatings', *Acta Mater*, 1998, **46**(5), 1691–1700.
18. STRAUSS D, MULLER R, SCHUMACHER G, ENGELKO V, STAMM W, CLEMENS D, QUADDAKERS W J, 'Oxide scale growth on MCrAlY bond coatings after pulsed electron beam treatment and deposition of EBPVD-TBC', *Surf Coat Technol*, 2001, **135**(2–3), 196–201.
19. YANG S, WANG F, SUN Z, ZHU S, 'Influence of columnar microstructure of a sputtered NiAl coating on its oxidation behavior at 1000 °C', *Intermetallics*, 2002, **10**(5), 467–471.
20. AJDELSZTAJN L, PICAS J A, KIM G E, BASTIAN F L, SCHOENUNG J, PROVENZANO V, 'Oxidation behavior of HVOF sprayed nanocrystalline NiCrAlY powder', *Mater Sci Eng A*, 2002, **338**(1–2), 33–43.
21. MROWEC S, 'New generation of nanocrystalline coating materials resistant to high temperature corrosion', *High Temp Mater Proc*, 2003, **22**(1), 1–24.
22. PENG X, YAN J, ZHOU Y, WANG F, 'Effect of grain refinement on the resistance of 304 stainless steel to breakaway oxidation in wet air', *Acta Mater*, 2005, **53**(19), 5079–5088.
23. KHANNA A, BHAT D G, 'Nanocrystalline gamma alumina coatings by inverted cylindrical magnetron sputtering', *Surf Coat Technol*, 2006, **201**(1–2), 168–173.
24. GOWARD G W 'Progress in coatings for gas turbine airfoils', *Surf Coat Technol*, 1998, **108–109**(1–3), 73–79.
25. PADTURE N P, GELL M, JORDAN E H, 'Thermal barrier coatings for gas turbine engine applications', *Science*, 2002, **296**(5566), 280–284.
26. CLARKE D R, LEVI C G, 'Materials design for the next generation thermal barrier coatings', *Annu Rev Mater Res*, 2003, **33**, 383–417.
27. FEUERSTEIN A, KNAPP J, TAYLOR T, ASHARY A, BOLCAVAGE A, HITCHMAN N, 'Technical and economical aspects of current thermal barrier coating systems for gas turbine engines by thermal spray and EBPVD: a review', *J Therm Spray Technol*, 2008, **17**(2), 199–213.
28. CHOY K L, 'Chemical vapor deposition of coatings', *Prog Mater Sci*, 2003, **48**(2), 57–170.
29. KUNG SC, RAPP RA, 'Kinetic-study of aluminization of iron by using the pack cementation technique', *J Electrochem Soc*, 1988, **135**(3), 731–741.
30. NICHOLS E S, BURGER J A, HANINK D K, 'Protective coatings for turbine parts', *Mech. Eng.*, 1965, **87**, 52–56.

31. GALMICHE P M, 'Production of surface diffusion alloys', US Patent, 1975, No 3,900,613.
32. RESTALL J E, WOOD M I, 'Alternative processes and treatments (for gas turbine protective coating deposition)', *Mater Sci Tech*, 1986, **2**, 225–231.
33. PARZUKOWSKI R S, 'Gas-phase deposition of aluminum on nickel alloys', *Thin Solid Films*, 1977, **45**, 349–355.
34. GAUJE G, MORBIOLI R, 'Vapor phase aluminizing to protect turbine aerofoils', in: *High Temperature Protective Coatings* (Ed. Singhal SC), The Metallurgical Society of AIME, Atlanta, GA, 1983, 13–26.
35. WARNES B M, PUNOLA D C, 'Clean diffusion coatings by chemical vapor deposition', in: *24th International Conference on Metallurgical Coatings and Thin Films Surf. Coat. Technol.* (Ed. Khobaib M and Krutenat R C), 1997, Metallurgical Society, Warrendale, PA, **94–95**(1–3), 1–6.
36. GOWARD G W, BOONE D H, 'Mechanisms of formation of diffusion aluminide coatings on nickel-base superalloys', *Oxid Met*, 1971, **3**(5), 475–495.
37. WHITTLE D P, STRINGER J, 'Improvements in high temperature oxidation resistance by additions of reactive elements or oxide dispersions', *Philos Trans R Soc London Ser. A*, 1980, **295**(1413), 309–329.
38. MOON D P, 'Role of reactive elements in alloy protection', *Mater Sci Technol*, 1989, **5**(8), 754–764.
39. HOU P Y, STRINGER J, 'The effect of reactive element additions on the selective oxidation, growth and adhesion of chromia scales', *Mater Sci Eng A*, 1995, **202**(1–2), 1–10.
40. LEPRINCE G, ALPÉRINE S, VANDENBULCKE L, WALDER A, 'New high temperature-resistant NiCrAl and NiCrAl +Hf felt materials', *Mater Sci Eng*, 1989, **120–121**(Part II), 419–425.
41. RAPP R A, WANG D, WEISERT T, in: *Metallurgical Coatings* (Ed. Hobaid M and Krutenat R), TMS-AIME, Warrendale, PA, 1987, 131–141.
42. BIANCO R, RAPP R A, 'Pack cementation aluminide coatings on superalloys: codeposition of Cr and reactive elements', *J Electrochem. Soc*, 1993, **140**(4), 1181–1190.
43. BIANCO R, RAPP R A, SMIALEK J L, 'Chromium and reactive element modified aluminide diffusion coatings on superalloys: environmental testing', *J Electrochem Soc*, 1993, **140**(4), 1191–1203.
44. TU D C, LIN C C, LIAO S J, CHOU J C, 'A study of yttrium-modified aluminide coatings on IN 738 alloy', *J Vac Sci Technol*, 1986, **A4**(6), 2601–2608.
45. PENG X, LI T, PAN W P, 'Oxidation of a La₂O₃-modified aluminide coating', *Scripta Mater*, 2001, **44**(7), 1033–1038.
46. FELTEN E J, PETTIT F S, 'Development, growth, and adhesion of Al₂O₃ on platinum-aluminum alloys', *Oxid Met*, 1976, **10**, 189–223.
47. ZHANG Y, HAYNES J A, LEE W Y, WRIGHT I G, PINT B A, COOLEY K M, LIAW P K, 'Effects of Pt incorporation on the isothermal oxidation behavior of chemical vapor deposition aluminide coatings', *Metall Mater Trans A*, 2001, **32A**, 1727–1741.
48. HOU P Y, MCCARTY K F, 'Surface and interface segregation in beta-NiAl with and without Pt addition', *Scripta Mater*, 2006, **54**, 937–941.
49. HOU P Y, TOLPYGO V K, 'Examination of the platinum effect on the oxidation behavior of nickel-aluminide coatings', *Surf Coat Technol*, 2007, **202**(4–7), 623–627.

50. LEHNARDT G, MEINHARDT H, 'Present state and trend of development of surface coating methods against oxidation and corrosion at high temperatures', *Electrodeposition Surf Treatment*, 1972, **1**(1), 71–76.
51. FARRELL M S, BOONE D H, STREIFF R, 'Oxide adhesion and growth characteristics on platinum-modified aluminide coatings', *Surf Coat Technol*, 1987, **32**, 69–84.
52. GÖBEL M, RAHMEL A, SCHÜTZE M, SCHORR M, WU W T, 'Interdiffusion between the platinum-modified aluminide coating RT22 and nickel-based single-crystal superalloys at 1000 and 1200 °C', *Mater High Temp*, 1994, **12**(4), 301–309.
53. WARNES B M, PUNOLA D C, 'Clean diffusion coatings by chemical vapor deposition', *Surf Coat Technol*, 1997, **94–95**(1–3), 1–6.
54. WARNES B M, PUNOLA D C, 'Development of diffusion coatings for gas turbines', in: *Power Generation Technology: The International Review of Preliminary Power Production* (Ed. Knox R), Sterling Publications Limited, London, UK, 1995, 207–210.
55. YU R, HOU P Y, 'First-principles calculations of the effect of Pt on NiAl surface energy and the site preference of Pt', *Appl Phys Lett*, 2007, **91**(1), 011907-1–3.
56. WU W T, RAHMEL A, SCHORR M, 'Role of platinum in the Na₂SO₄-induced hot corrosion resistance of aluminum diffusion coatings', *Oxid Met*, 1984, **22**(1–2), 59–81.
57. SCHAEFFER J, KIM G M, MEIER G H, PETTIT F S, 'The effects of precious metals on the oxidation and hot corrosion of coatings', in: *The Role of Active Elements in the Oxidation Behavior of High Temperature Metals and Alloys* (Ed. Lang E), Elsevier, Amsterdam, the Netherlands, 1989, 231–267.
58. LEYENS C, PINT B A, WRIGHT I G, 'Effect of composition on the oxidation and hot corrosion resistance of NiAl doped with precious metals', *Surf Coat Technol*, 2000, **133–134**, 15–22.
59. KELLY F C, 'Chromizing', *Trans. Electrochem. Soc.*, 1923, **43**, 351.
60. SAMUEL R L, LOCKINGTON N A, 'Metal Treatment and Drop Forging', 1951, **18**, 354–359, 407–414, 440–444, 495–506, 543–548, and 1952, **19**, 27–32, 81–85.
61. DREWETT R, 'Diffusion coatings for the protection of iron and steel', *Anti-Corrosion Methods Mater*, 1969, **16**, 543–548.
62. PENG X, YAN J, XU C, WANG F, 'Oxidation at 900 °C of the chromized coatings on A3 carbon steel with the electrodeposition pretreatment of Ni or Ni-CeO₂ film', *Metall Mater Trans*, 2008, **39A**, 119–129.
63. YAN J, PENG X, WANG F, 'Oxidation of a novel CeO₂-dispersion-strengthened chromium coating in simulated coal-combustion gases', *Mater Sci Eng A*, 2006, **426A**(1–2), 266–273.
64. ZHU L, PENG X, YAN J, WANG F, WU W, 'Oxidation of a novel chromium coating with CeO₂ dispersions', *Oxid Met*, 2004, **62**(5–6), 411–426.
65. MAZIASZ J, SWINDEMAN R W, 'Selecting and developing advanced alloys for creep-resistance for microturbine recuperator applications', *J Eng Gas Turbines Power*, 2003, **125**(1), 310–315.
66. SAUNDERS S R J, NICHOLLS J R, 'Coatings and surface treatments for high temperature oxidation resistance', *Mater Sci Technol*, 1989, **5**(8), 780–798.
67. MEIER G H, CHENG C, 'Diffusion chromizing of ferrous alloys', *Surf Coat Technol*, 1989, **39–40**, 53–64.

68. GEIB F D, RAPP R A, 'Simultaneous chromizing-aluminizing coating of low-alloy steels by a halide-activated, pack-cementation process', *Oxid Met*, 1993, **40**(3–4), 213–228.
69. ENNIS P J, ZIELINSKA-LIPIEC A, WACHTER O, CZYRSKA-FILEMONOWICZ A, 'Micro-structural stability and creep rupture strength of the martensitic steel P92 for advanced power plant', *Acta Mater*, 1997, **45**(12), 4901–4907.
70. GLEITER H, 'Nanocrystalline materials', *Prog Mater Sci*, 1989, **33**(4), 223–315.
71. WÜRSCHUM R, HERTH S, BROSSMANN U, 'Diffusion in nanocrystalline metals and alloys – A status report', *Adv Eng Mater*, 2003, **5**(5), 365–372.
72. ZHANG H, PENG X, ZHAO J, WANG F, 'Prior electrodeposition of nanocrystalline Ni–CeO₂ film fabricating an oxidation-resistant chromized coating on carbon steels', *Electrochem Solid ST*, 2007, **10**(3), C12–C15.
73. XIANG Z D, DATTA, P K, 'Relationship between pack chemistry and aluminide coating formation for low-temperature aluminisation of alloy steels', *Acta Mater*, 2006, **54**, 4453–4463.
74. ZHAN Z L, HE Y D, WANG D R, GAO W, 'Low-temperature processing of Fe–Al intermetallic coatings assisted by ball milling', *Intermetallics*, 2006, **14**(1), 75–81.
75. XU C, PENG X, WANG F, 'Cyclic oxidation of an ultrafine-grained and CeO₂-dispersed δ -Ni₂Al₃ coating', *Corros Sci*, 2010, **52**(3), 740–747.
76. TALBOOM F P, GRAFWALLNER J, *Nickel or Cobalt Base with a Coating Containing Iron Chromium and Aluminum*, US Patent, 1970, No 3,542,530.
77. EVANS D J, ELAM R C, *Cobalt Base Coating for the Superalloys*, US Patent, 1972, No 3,676,085.
78. HECHT R J, GOWARD G W, ELAM R C, *High Temperature NiCoCrAlY Coating*, US Patent, 1975, No 3,928,026.
79. GIL A, SHEMET V, VASSEN R, SUBANOVIC M, TOSCANO J, NAUMENKO D, SINGHEISER L, QUADAKKERS W J, 'Effect of surface condition on the oxidation behavior of MCrAlY coatings', *Surf Coat Technol*, 2006, **201**(7), 3824–3828.
80. YANAR N M, MEIER E M, PETTIT F S, MEIER G H, 'The effect of yttrium content on the oxidation-induced degradation of NiCoCrAlY coatings and the influence of surface roughness on the oxidation of NiCoCrAlY and platinum aluminide coatings', *Mater High Temp*, 2009, **26**(3), 331–338.
81. WANG F H, LOU H Y, WU W T, 'Influence of defects on properties of sputtered CoCrAlY coating', *Acta Metall Sin*, 1992, **28**(10), B443–448.
82. TANIGUCHI S, ASANUMA N, SHIBATA T, WANG F H, LOU H Y, WU W T, 'Oxidation resistance of TiAl improved by CoCrAl and CoCrAlY coating', *J Jpn Inst Met*, 1993, **57**, 781–789.
83. BRANDLA W, TOMAA D, GRABKE H G, 'The characteristics of alumina scales formed on HVOF-sprayed MCrAlY coatings', *Surf Coat Technol*, 1998, **108–109**(1–3), 10–15.
84. MOM A J A, *High Temperature Coatings for Gas Turbines, an Overview*, NLR Report, MP 81003U, Amsterdam. 1981.
85. WAGNER C, 'Passivity and inhibition during the oxidation of metals at elevated temperatures', *Corros Sci*, 1965, **5**(11), 751–764.
86. CHEN G F, LOU H Y, 'Predicting the oxide formation of Ni–Cr–Al alloys with nano-sized grain', *Mater Lett*, 2000, **45**(5), 286–291.

87. SHIN S M, RAY M A, RIGSBEE J M, GREENE J E, 'Growth of metastable $\text{Cu}_{1-x}\text{Cr}_x$ solid solutions by ion mixing during bias-sputter deposition', *Appl Phys Lett*, 1983, **43**(3), 249–251.
88. YANG X, PENG X, CU C, WANG F, 'Electrochemical assembly of novel Ni-xCr-yAl nanocomposites with excellent high temperature oxidation resistance', *J Electrochem Soc*, 2009, **156**, C167–C175.
89. EVANS A G, MUMM D R, HUTCHINSON J W, MEIER G H, PETTIT F S, 'Mechanisms controlling the durability of thermal barrier coatings', *Progr Mater Sci*, 2001, **46**(5), 505–553.
90. DEB P, BOONE D H, MANLEY T F, 'Surface instability of platinum modified aluminate coatings during 1100°C cyclic testing', *J Vac Sci Technol*, 1987, **A5**(6), 3366–3372.
91. TOLPYGO V K, CLARKE D R, 'Surface rumpling of a (Ni, Pt)Al bond coat induced by cyclic oxidation', *Acta Mater*, 2000, **48**, 3283–3293.
92. TOLPYGO V K, CLARKE D R, 'On the rumpling mechanism in nickel-aluminide coatings: Part I: an experimental assessment', *Acta Mater*, 2004, **52**(17), 5115–5127.
93. TOLPYGO V K, CLARKE D R, 'Rumpling of CVD (Ni,Pt)Al diffusion coatings under intermediate temperature cycling', *Surf Coat Technol*, 2009, **203**, 3278–3285.
94. CAO F, TRYON B, TORBET C J, POLLOCK T M, 'Microstructural evolution and failure characteristics of a NiCoCrAlY bond coat in "hot spot" cyclic oxidation', *Acta Mater*, 2009, **57**, 3885–3894.
95. GOWARD G W, BOONE D H, 'Mechanisms of formation of diffusion aluminide coatings on nickel-base superalloys', *Oxid Met*, 1971, **3**(5), 475–495.
96. BAUFELD B, SCHMUCKER M, 'Microstructural evolution of a NiCoCrAlY coating on an IN100 substrate', *Surf Coat Technol*, 2005, **199**(1), 49–56.
97. GRABKE H J, WIEMER D, VIEFHAUS H, 'Segregation of sulfur during growth of oxide scales', *Appl Surf Sci*, 1991, **47**(3), 243–250.
98. HOU P Y, 'Segregation phenomena at thermally grown Al_2O_3 /alloy interfaces', *Annu Rev Mater Res*, 2008, **38**, 275–298.
99. SERGO V, 'Observation of subcritical spall propagation of a thermal barrier coating', *J Am Ceram Soc*, 1998, **81**(12), 3237–3242.
100. HUTCHINSON J W, SUO Z, 'Mixed mode cracking in layered materials', *Adv Appl Mech*, 1992, **29**, 63–191.
101. EVANS A G, CANNON R M, 'Stresses in oxide films and relationships with cracking and spalling', *Mater Sci Forum*, 1989, **43**, 243–268.
102. HUTCHINSON J W, HE M Y, EVANS A G, 'The influence of imperfections on the nucleation and propagation of buckling driven delaminations', *J Mech Phys Solid*, 2000, **48**(4), 709–734.
103. EVANS A G, HUTCHINSON J W, WEI Y, 'Interface adhesion: effects of plasticity and segregation', *Acta Mater*, 1999, **47**(15–16), 4093–4113.
104. BONNELL D A, KIELY J, 'Plasticity at multiple length scales in metal-ceramic interface fracture', *Phys Status Solid A*, 1998, **166**(1), 7–17.

Nanostructured thermal barrier coatings

C. G. ZHOU and Q. H. YU, Beihang University, China

Abstract: Thermal spray zirconia–8 wt% yttria (YSZ) deposits have been employed as thermal barrier coatings (TBCs) in the hot sections of gas turbines. The use of nanostructured YSZ represents an alternative for improving the performance of these coatings. Before spraying, finely dispersed particles must be agglomerated. Air plasma-sprayed nanostructured zirconia coatings consist of only the non-transformable tetragonal phase and the microstructure is composed of nanozones (unmelted or partially melted particles), splats, microcracks and high-volume spheroidal pores. The results indicate that the microhardness, elastic modulus and roughness of the nanostructured zirconia coatings exhibit the following trends: the smoother the roughness, the higher the microhardness and elastic modulus. The decrease of thermal diffusivity of the nanostructured coating was attributed to the increase of grain boundaries, micropores and defective crystal structure. The smaller the micropores are, the more interfaces are produced, and the effect on the phonon scattering is higher, resulting in the reduction of thermal diffusivity. Meanwhile, the nanostructured TBC also exhibits the promising thermal cyclic oxidation resistance.

Key words: nanostructured YSZ coating, air plasma spraying, agglomeration, mechanical performance, thermal property.

4.1 Introduction

Since the late 1990s, nanostructured zirconia TBCs have become a hot research field due to their low thermal conductivity, high coefficient of thermal expansion and excellent mechanical properties.^{1–7} These improved properties are caused by the modification to the structure.^{8–16} The microstructure and the properties of plasma spray coatings depend on various process parameters, and are markedly affected by the characteristics of the feeding powder, because the nanostructured powders clearly improve the deposit efficiency, coherence strength and hardness of the coatings.^{17,18} However, the individual nanoparticle is so fine that it cannot be used for plasma spray. Before spraying, finely dispersed particles must be agglomerated to a size of about 30–100 μm . The microstructure, density and grain size of the powders determine the quality of the coating.^{19,20} Meanwhile, phase transformation of as-sprayed zirconia coatings in the service environment is believed to be an important factor affecting the durability of the coating.^{21–23}

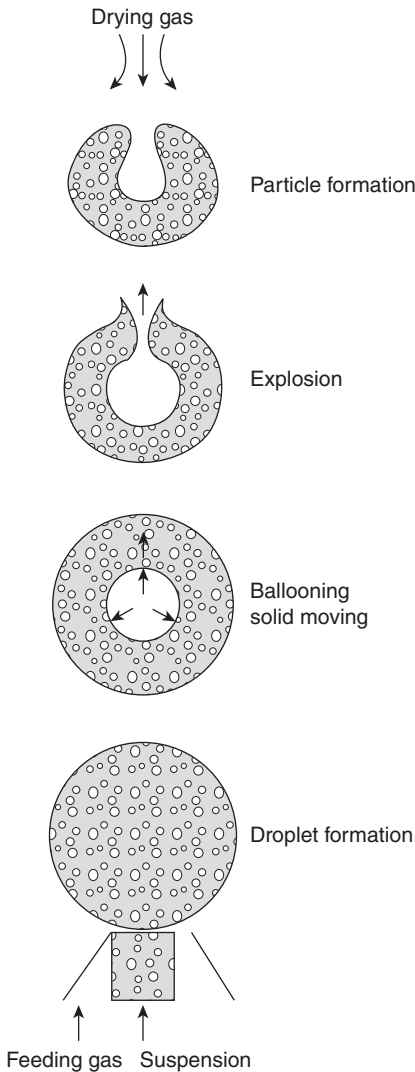
The spray drying process of compositing the powders, the phase stability and the mechanical and thermal properties of the nanostructured YSZ coating are discussed in this chapter. The first section is about the spray drying process of compositing the ceramic powders. In the following section, the phase composition and microstructure characterization of the nanostructured as-sprayed zirconia coatings are studied; the influence of annealing temperature and time on the phase stability and grain growth are also discussed. In the next section, the mechanical properties of nanostructured YSZ coating are discussed. In the last section, the thermophysical properties and the failure behavior of the plasma-sprayed nanostructured TBCs are illustrated.

4.2 Spray-drying process making powders

Due to its lower inertia force, the nanopowder cannot penetrate the hot gas downstream. Even if it can penetrate into the plasma plume, particles will be easily vaporized because of the low mass. This is the reason why the particle needs to be agglomerated. Spray-drying is a process by which a fluid feed material is transformed into a dry powder by spraying the feed into a hot medium.

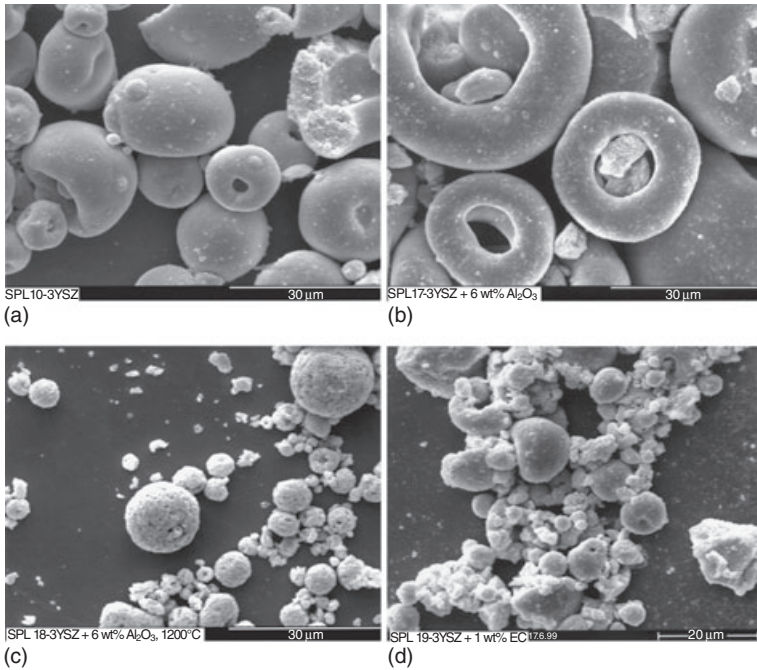
Spray-drying is a complex process, but we now propose a simple mechanism to describe the spray-drying process of ceramics with four steps as illustrated in Fig. 4.1:²⁴ (i) droplet formation; (ii) evaporation and ballooning; (iii) explosion; (iv) particle formation. The drying gas is introduced through the ceiling to the drying chamber. When the suspension is pumped into the drying chamber, it is separated into small droplets immediately by the compressed feeding gas. Then, the droplet shrinks because of the fast evaporation of the solvent. During the process of liquid moving from the inside to the outside of the droplet, the solid particles are carried along. Inside the droplet, a void is produced when the evaporation rate inside the droplet is higher than the diffusion rate through the droplet surface. When the pressure inside the droplet reaches a certain level, explosion is unavoidable. In the fourth step, the particle is plasticized by the loss of solvent and the addition of organic binder. The plasticized droplet shrinks continuously due to the effect of surface tension until it is totally dried. The particle size should be mainly determined by the third step at which most of the solvent has been lost and a soft shell is formed.

Figure 4.2 shows microphotographs of some spray-dried powders.²⁴ SPL10 (3YSZ) (Fig. 4.2a) has a smooth surface, explaining why this powder has a good flowability. The particle is an agglomeration of a large amount of small particles which are tightly combined with each other by organic binder. Figure 4.2b shows the microstructure of SPL17 (3YSZ + 6 wt%



4.1 Spray-drying process of ceramics.

Al_2O_3). Particles of this powder have much larger hollow centres than those of SPL10 (3YSZ) with a low bulk density (1.56 g/cm^3) and large mean size ($39.8 \mu\text{m}$). Although its particle size is large, this powder is not suitable for plasma-spraying because of its low density. Figure 4.2c shows SPL18 (3YSZ + 6 wt% Al_2O_3) with its starting powder densified by calcination at 1200°C for 10 h before drying. The particles are much smaller and more spherical than those of other powders. Figure 4.2d shows SPL19 (3YSZ + 1.8 wt%



4.2 Scanning electron micrographs of spray-dried powders: (a) SPL10 (3YSZ); (b) SPL17 (3YSZ + 6 wt% Al_2O_3); (c) SPL18 (3YSZ + 6 wt% Al_2O_3 , starting powder calcined at 1200 °C, 10 h); (d) SPL19 (3YSZ + 1.8 wt% PEI + 1 wt% ethylcellulose).

PEI + 1 wt% ethylcellulose). Most of the particles are not spherical having a cotton-like appearance due to the swelling or crack of cellulose. The mean particle size and bulk density of this powder are 7.3 μm and 1.27 g/cm^3 , respectively. The controlling factor of the property of spray-dried powders is the suspension preparation. In order to prepare a powder with high density, large particle size and good flowability, the solid content in the suspension should be high enough, and the starting powder should be densified at an appropriate temperature before drying if it is porous.

4.3 Phase composition and microstructure of nanostructured thermal barrier coatings (TBCs)

4.3.1 Phase composition

The mean grain sizes of the matrix $t\text{-ZrO}_2$ phase in heat-treated coatings were roughly estimated using the Scherrer equation^{25–26}

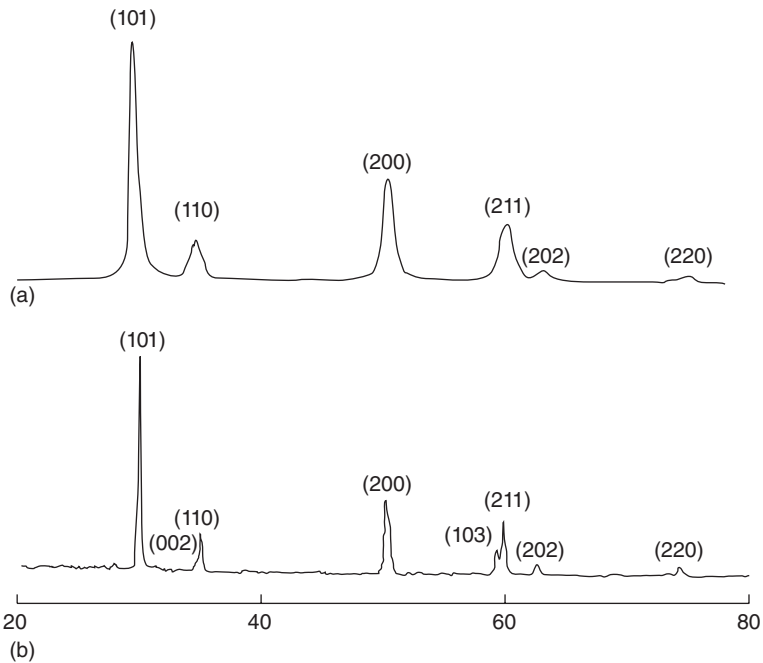
$$B_p(2\theta) = \frac{0.9\lambda}{D\cos\theta} \quad [4.1]$$

where D is the average dimension of crystallite, $B_p(2\theta)$ the broadening of the diffraction line measured at half maximum intensity and λ (0.154 nm) and θ denote the wavelength of the X-rays and the Bragg diffraction angle. The correction for instrumental broadening is taken into consideration in the measurement of the peak broadening by comparing the widths at half maximum intensity of X-ray reflection of the sample with the single crystalline Si standard, and then Gaussian correction is used to remove the instrumental broadening to obtain the true crystal broadening

$$B_p^2(2\theta) = B_h^2(2\theta) - B_i^2(2\theta)$$

where $B_p(2\theta)$ is the true half maximum width and $B_h(2\theta)$ and $B_i(2\theta)$ are the half maximum widths of the sample and the single crystalline Si standard.²⁷ The theta value of $2\theta = 30^\circ$ is selected to calculate the crystallite size and the peaks belong to ZrO_2 .

Figure 4.3 shows the X-ray diffraction patterns of the powder and as-sprayed coating.²⁸ It can be seen that there is no new phase in the coating and no clear difference in the peak intensities between the powder and coating. Both the powder and coating are composed of pure tetragonal zirconia, which is the stable phase in the middle temperature. However, the X-ray pattern of the coating has two more peaks than that of the powder,



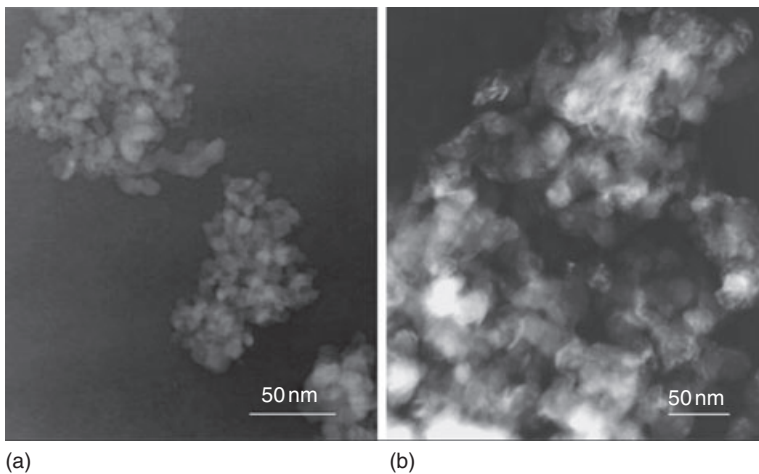
4.3 XRD patterns of (a) starting ZrO_2 powder and (b) as-sprayed ZrO_2 coating.

which indicates that the coating has a better crystal structure than the powder.

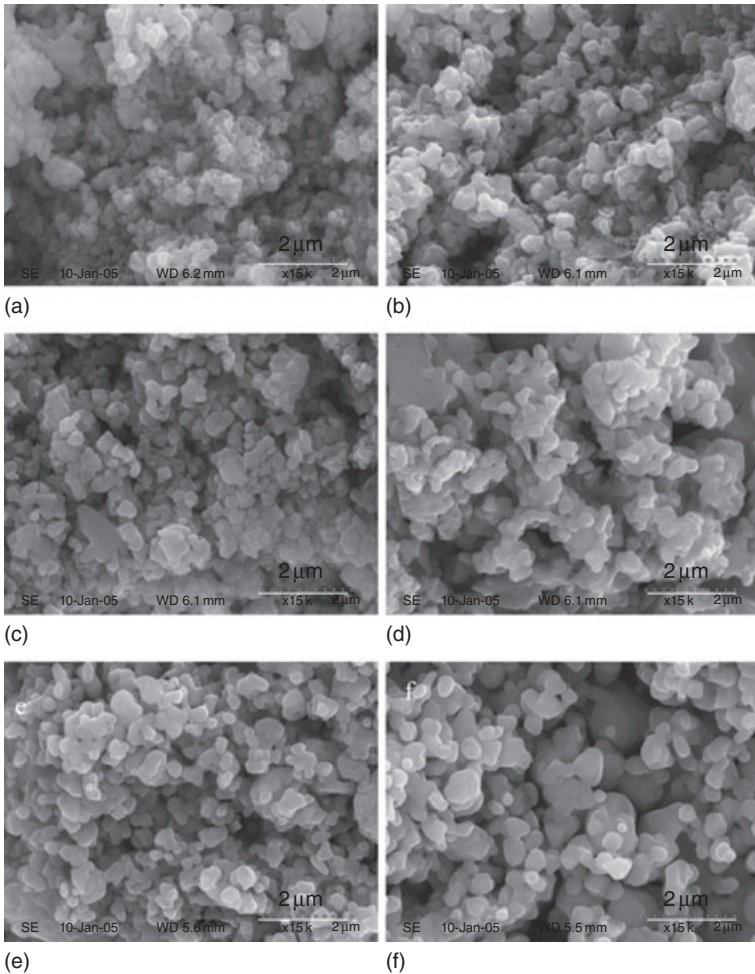
4.3.2 Microstructure

The transmission electron microscopy (TEM) image reveals the grain size of primitive particles and the as-sprayed coating, as shown in Fig. 4.4.²⁹ It can be seen that the non-molten phase of the coatings is composed of fine grains with sizes ranging from 30–50 nm. No smaller grains were found in the TEM image. Details of the microstructural features before and after annealing were examined through scanning electron microscopy (SEM) observation on the surface of top coat.²⁹ Figure 4.5 presents the surface morphology of nanostructured zirconia coatings in the as-sprayed state and after 15 h heat-treating at different temperatures. The as-sprayed microstructure is composed of the nanopowders and micropores between the nanopowders. The size of the nanopowders increases after annealing at different temperatures for 15 h. Further details of the microstructural features of the nanostructured zirconia coating after annealing were examined through fractured surfaces of coating.

The measured surface-connected porosity of the freestanding nanostructured zirconia coating is 13% and the median pore diameter (volume) is 0.3524 μm .³⁰ Figure 4.6a shows the cumulative porosity distribution of the coating measured by mercury intrusion porosimetry. Figure 4.6b illustrates the compositions of porosity based on the result of the porosity measurement in Fig. 4.6a. The result reveals a bimodal pore size distribution, similar

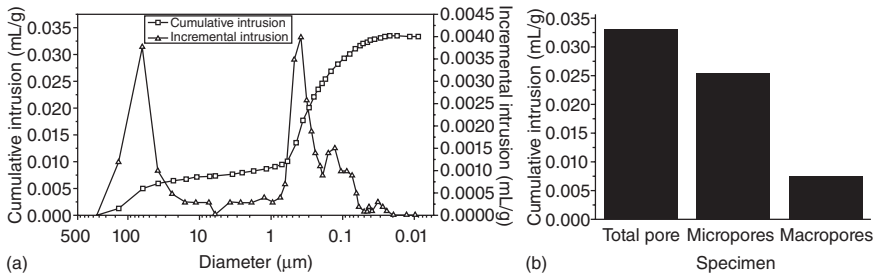


4.4 TEM image of the primitive nano YSZ particles (a) and the as-sprayed coating (b).



4.5 Surface morphology of the nano YSZ coatings at different temperatures after heat treatment for 15 h: (a) as-sprayed state; (b) 600°C; (c) 800°C; (d) 900°C; (e) 1000°C; (f) 1150°C.

to that in the conventional zirconia coatings.^{31,32} Micropores contribute a larger percentage of the total porosity than macropores. The fine micropores, with diameters smaller than 1 μm, include intraplate microcracks, intersplat gaps resulting from poor adhesion and small voids originating from the unmelted particles. A spot of macropores or large defects, with pore sizes of even up to 100 μm, are also present in the coating, which could be mainly attributed to macrocracks such as branching cracks, interlamellar pores due to improper adhesion and globular pores as a result of gas entrapment. The level of coating porosity is significantly connected with the spray conditions



4.6 Porosity distribution of the as-sprayed nanostructured zirconia coating (a), and composition of the total porosity (b).

such as powder sizes, spray distance, spray angle, etc. To some extent, the unmelted powders in the nanostructured coating help increase the number of micropores.

4.4 Mechanical properties

4.4.1 Hardness and elastic modulus

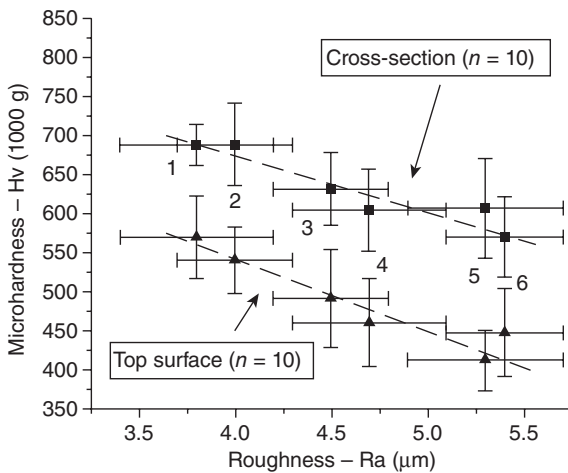
The nanostructured PSZ (ZrO_2 -7 wt% Y_2O_3) experimental powder Nanox 4007 (Inframat Corp., North Haven, CT, USA) was plasma sprayed under different parameters in air on mild steel substrates with a 40 kW, standard SG100 plasma torch (Praxair, Appleton, WI, USA). The substrates were grit-blasted with alumina just before thermal spraying ($R_a = 4.1 \pm 0.3 \mu\text{m}$). The substrates were not pre-heated. Typical coating thickness was 0.9–1.1 mm. The spray parameters applied are listed in Table 4.1.³³

Vickers microhardness measured on cross-section and top surface for 1000 g is shown in Fig. 4.7.³³ The value measured at top surface has slightly lower values than that measured at cross-section. Microhardness measurements in thermal spray coatings with respect to the planar or cross-sectional aspects of individual splats will correspond with area measurements on circles or ellipses. The planar hardness values were normalized with respect to the cross-section hardness values for indenting loads of 1000 g. Knoop microhardness values measured using 1000 g on the cross-sectional area are given in Fig. 4.8.³³ The Knoop values are lower than the Vickers values at the same load. In addition, the variation in Knoop values is higher than that in Vickers. Both phenomena are probably related to the difference in geometry of the two indenters, which provide different force fields in the coatings.

Observing Figs 4.7 and 4.8, leads to the following trend. Following the R_a axis from left to right, from spray parameter 1 to spray parameter 6, the torch power is decreasing and the spray distance is increasing. When the

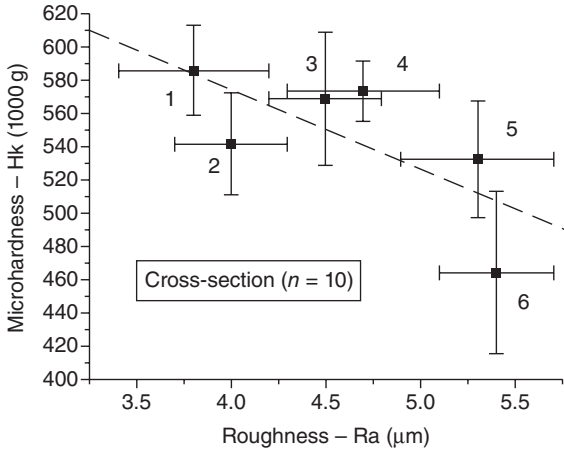
Table 4.1 Spraying parameters used for PSZ coatings

Parameters	Set 1	Set 2	Set 3	Set 4	Set 5	Set 6
Power (kW)	40	40	40	40	32	24
Current (A)	800	800	800	800	800	600
Voltage (V)	50	50	50	50	40	40
Ar flow plasma (slpm)	48	38	48	38	48	48
H ₂ flow plasma (slpm)	5	5	5	5	4	4
Ar flow carrier gas (slpm)	5	5	5	5	5	5
RPM-Hopper (%)	30	30	30	30	30	30
Spray distance (cm)	6	6	8	8	8	8

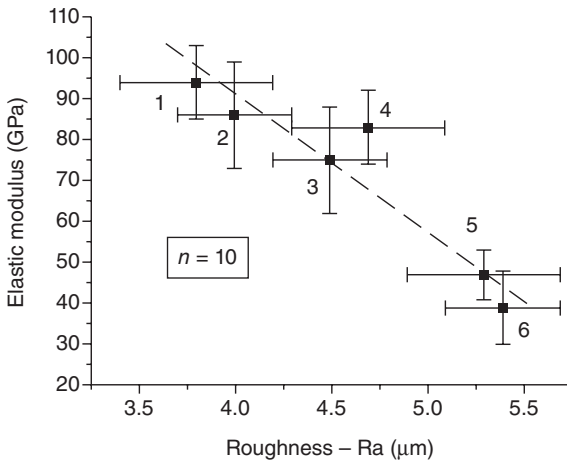


4.7 Vickers microhardness–roughness relationship (1000 g load) for different sets of spray parameters (Table 4.1).

plasma torch power is decreased, particle temperature and velocity will tend to drop, which will impede a larger spreading of the sprayed droplet. The values of elastic modulus and their relationship with roughness are shown in Fig. 4.9. Again the same trend is observed: the smoother the coating is, the higher the Knoop microhardness and elastic modulus are. A dashed line was placed in Figs 4.8 and 4.9 as a ‘guideline for eye’ to show this trend. The elastic modulus slightly changes from spray parameters 1 to 4, where the same plasma power was applied for different H₂/Ar ratios and a difference in spray distance of 2 cm. This experimental observation agrees with the elastic modulus measurements of PSZ coatings via the four-point bending method, which shows that the PSZ coatings did not present a significant change in elastic modulus values as varying the spray distance by 2 cm maintained the same plasma power.



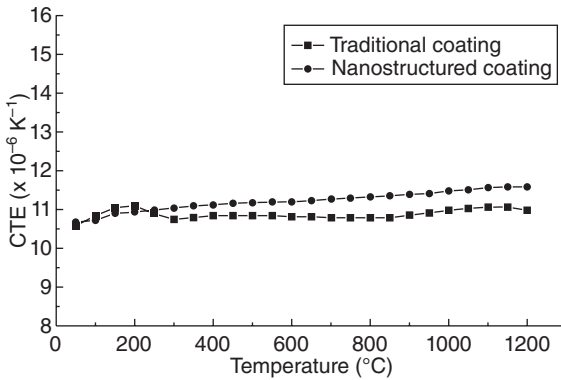
4.8 Knoop microhardness-roughness relationship (1000 g load) for different sets of spray parameters (Table 4.1).



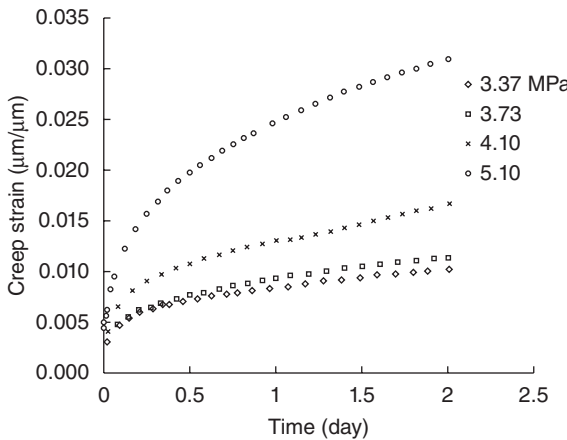
4.9 Elastic modulus-roughness relationship for different sets of spray parameters (Table 4.1).

4.4.2 Coefficients of thermal expansion (CTE)

Figure 4.10 shows the thermal expansion coefficient of nanostructured zirconia coating.³⁴ The average thermal expansion coefficient of the zirconia coatings at the first thermal cycle and second thermal cycle from room temperature to 1200°C are 11.0 and $11.6 \times 10^{-6} \text{ } ^\circ\text{C}^{-1}$, respectively. The thermal expansion coefficient of the zirconia coating increased in the beginning and then decreased from room temperature to 300°C in the first



4.10 Coefficient of thermal expansion (CTE) of the nanostructured zirconia coating.

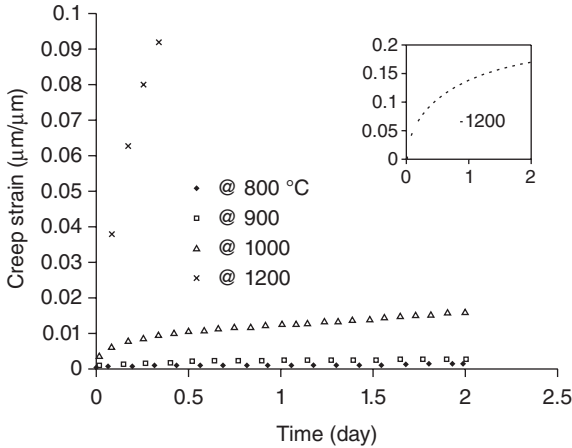


4.11 Compression creep strain of nanostructured samples under different stresses at 1000 $^{\circ}\text{C}$.

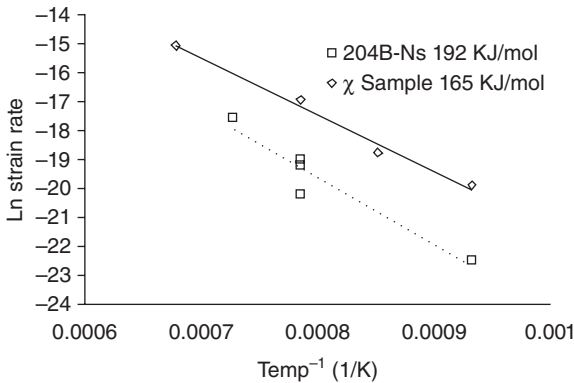
thermal cycle. This behavior is ascribed to the oxygen loss phenomenon in ceramic coatings prepared by atmospheric plasma spraying. When the as-sprayed zirconia coating was heated in atmosphere, the oxygen atoms were added to the vacancies of the coating again. The phenomenon disappeared in the second thermal cycle. During the second thermal cycle, the coefficient of thermal expansion increased linearly according to the increasing temperature.

4.4.3 Creep

Figures 4.11 and 4.12 show the creep strain of nanostructured coatings under a range of stresses and temperatures over two days.³⁵ It is clear that



4.12 Creep strain of nanostructured samples at different temperatures under ~4 MPa compressive stress.



4.13 Calculation of activation energy of nanostructured and hollow spherical YSZ samples, 165 ± 40 and 192 ± 25 KJ/mol, respectively.

this nanostructured coating, in spite of applying much lower stresses, exhibits an order of magnitude higher creep strain than the hollow spherical YSZ deposits. As was observed for the hollow spherical YSZ samples, the nanostructured deposits exhibit primary and secondary creep. As load and temperature of the test conditions are increased, the amount of creep strain rises accordingly. Again, temperature has a more significant effect than load, as is clear in Fig. 4.12.

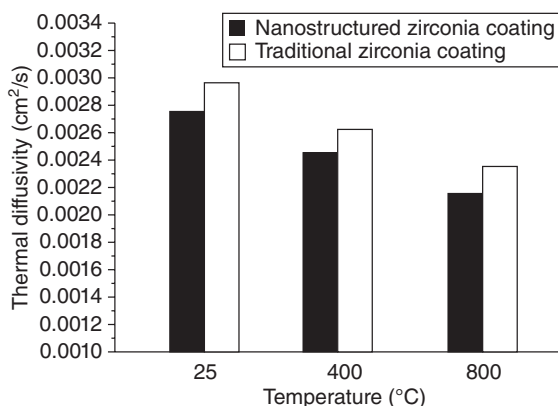
From the creep data, using the power-law creep ($\dot{\epsilon} = A\sigma^n$) and Arrhenius ($\epsilon = A\exp - Q/RT$) equations, stress exponents and activation energies for the coatings were calculated where $\dot{\epsilon}$ is creep strain rate, A a constant, σ applied stress in MPa, ϵ strain rate, Q activation energy, R gas constant and T temperature in Kelvin (Fig. 4.13).³⁵ The nanostructured deposit shows a slightly

lower activation energy of 165 ± 40 KJ/mol compared with 192 ± 25 KJ/mol for the hollow spherical YSZ sample; however, as to the interval of values, they may not be very different.

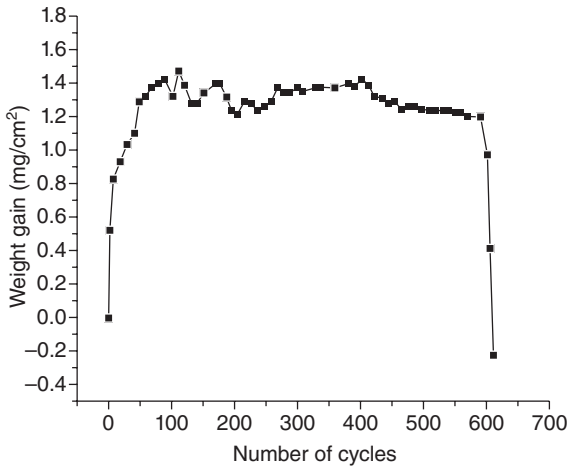
4.5 Thermophysical properties and the failure behavior

4.5.1 Thermal diffusivity

Figure 4.14 presents the thermal diffusivity of the as-sprayed nanostructured zirconia coatings and conventional zirconia coating as the temperature rises from room temperature to 800 °C. It can be seen that the thermal diffusivity of both coatings decreases slightly as the temperature increases. The thermal diffusivity of the as-sprayed nanostructured zirconia coating was in the range $2.15\text{--}2.75 \cdot 10^{-3}$ cm²/s during the temperature change from room temperature to 800 °C, while the thermal diffusivity of conventional zirconia coating was $2.35\text{--}2.96 \cdot 10^{-3}$ cm²/s. The thermal diffusivity of the plasma-sprayed nanostructured zirconia coating is lower than that of conventional zirconia coating. The decrease in the thermal diffusivity is attributed to the micropores in the nanostructured zirconia and the decreased grain size of nanostructured zirconia coatings. When the temperature is below 1200 °C, phonon transport dominates the heat conduction through zirconia. For conventional materials, the grain boundary contribution to phonon scattering is thought to be small.^{36,37} However, when the grain size is of the same order as the mean free path for phonon scattering, grain boundaries can have a significant effect. Kabacoff³⁷ investigated the influence of nanograin size on the phonon conductivity of zirconia-7 wt% yttria as a function of temperature. It was found that the thermal conductivity is



4.14 Thermal diffusivity of the as-sprayed nanostructured zirconia coating and conventional zirconia coating.



4.15 Kinetics of nanostructured TBC during 1 h cycles at 1050 °C.

drastically reduced for fine-grained materials, particularly when the grain size is of nanometer dimensions.

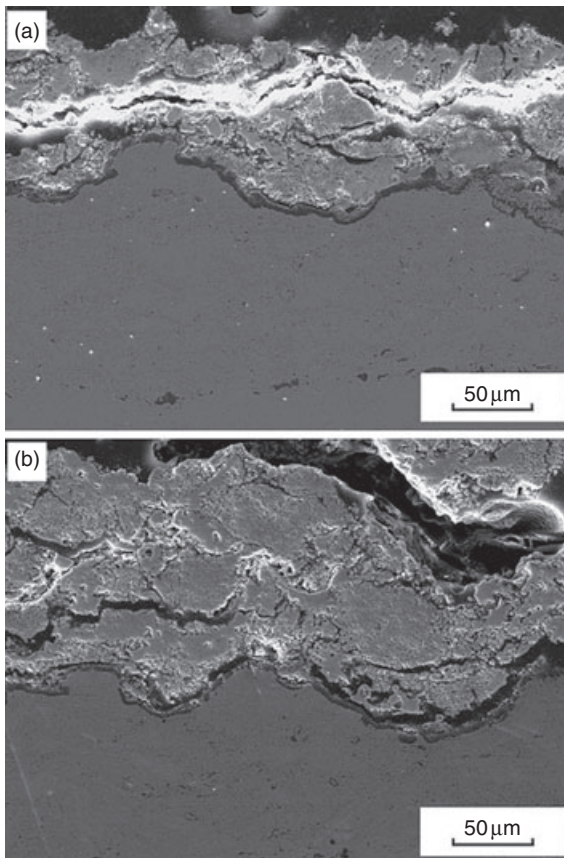
A cyclic oxidation test was performed to investigate the cyclic oxidation kinetics of nanostructured TBC. Figure 4.15 shows a plot of the weight change per unit area vs number of cycles for the test performed at 1050 °C in static air.³⁸ The nanostructured TBC had a weight gain of approximately 1.2–1.6 mg/cm² after 300 cycles, indicating a low oxidation rate. Moreover, the abrupt loss in weight for the nanostructured TBC did not occur until after approximately 600 cycles. The result indicates that the thermal cyclic lifetime of the nanostructured TBC is about 600 h for 1 h cycles at 1050 °C. The nanostructured TBC exhibits promising thermal cyclic oxidation resistance.

4.5.2 Failure mechanism

Table 4.2 shows the thermal cyclic life of two different TBCs under different thermal cyclings. It was found that the number of thermal shock cycles to failure at 1150 °C of the nanostructured TBCs was about two to four times larger than that of the conventional TBCs after thermal cyclic testing for 300 cycles at 1000 °C, and exhibited little increase after the isothermal oxidation for 100 h at 1000 °C.³⁹ These facts indicate that the influence of the low-temperature thermal cycling on the thermal cyclic lifetime is larger for the conventional TBCs than for the nanostructured TBCs. Figure 4.16 shows the cross-sectional micrograph of the failed nanostructured TBCs subjected to thermal cyclic testing at 1150 °C. The sample shown in

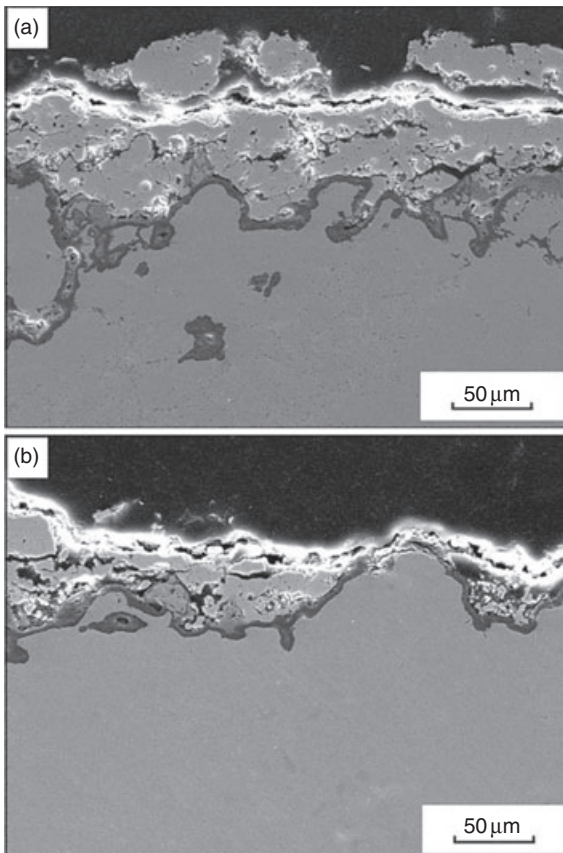
Table 4.2 Thermal cycles of nanostructured and conventional TBCs

Type	Nanostructured TBCs						Conventional TBCs					
Pre-treatment	1000°C × 300 cycles			1000°C × 100 h			1000°C × 300 cycles			1000°C × 100 h		
Life	19	38	38	23	36	45	7	10	10	24	29	35
Mean life	32			34			9			29		



4.16 Cross-sectional micrograph of the failed nanostructured TBCs. (a) The sample experienced 38 cycles at 1150°C after 300 cycles at 1000°C; (b) the sample experienced 36 cycles at 1150°C after isothermal oxidation for 100 h at 1000°C.

Figure 4.16a has experienced thermal cyclic testing for 300 cycles at 1000 °C before the thermal cyclic test at 1150 °C, while the sample in Fig.4.16b experienced isothermal oxidation testing at 1000 °C for 100 h. The two nanostructured TBCs samples withstood a further 38 and 36 thermal cycles at 1150 °C, respectively. The failure of the coatings in two nanostructured TBC samples occurred within the top coat through spalling of the YSZ within YSZ coating close to the YSZ/thermal growth oxide interface. The failed cross-sectional microstructure of the conventional TBCs is shown in Fig. 4.17. It was noted that the failure also occurred within the top coat above thermal grown oxide (TGO), which indicates that the failure of the nanostructured TBCs is similar to the failure scenario of the conventional TBCs.^{40–42} However, it was found that the TGO adheres well to the underlying bond coat. Possibly, such



4.17 Cross-sectional micrographs of failed conventional TBCs. The sample experienced 29 cycles at 1150 °C after isothermal oxidation for 100 h at 1000 °C. (a) and (b) taken at different zones in the failed interface.

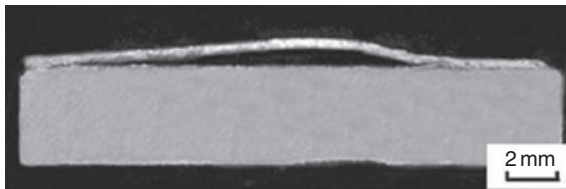
well-adhered TGO can be attributed to the nanostructure of the bond coat, which promotes the rapid formation of a uniform Al_2O_3 scale on the bond coat surface during the pre-heat treatment.^{43–47}

Moreover, it can be seen in Fig. 4.18 that the buckling of the nanostructured YSZ top coat occurred before it spalled out. The buckling may suggest the possible sealing of the YSZ top coat surface through sintering. Although the failure mechanism of the TBC deposited by nanostructured YSZ in the present study is not yet clear, it is possible that the sintering of the nanosized YSZ fraction in the coating during high-temperature cyclic testing is responsible for the failure of the top YSZ coat.^{48,49} This effect is possibly associated with the influence of the thermal cycling at 1000°C on the thermal shock life of two different TBCs owing to much less sintering and possibly sustainable higher strain tolerance of the nanostructured TBCs.

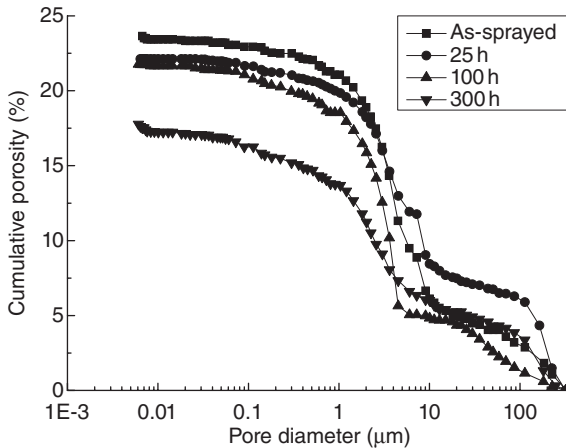
4.5.3 Sintering of nanostructured Al_2O_3 -yttria stabilized zirconia (YSZ) coating

Figure 4.19 shows the cumulative porosity distribution of the free-standing coating specimens which is determined by mercury porosimetry (MP). Cumulative porosity is the pore content normalized to the volume of the sample. In Fig. 4.19, it is clearly shown that the sintering of the coating leads to a lower porosity, as the annealing treatment time increased from 0 to 300 h, and the cumulative porosity decreased from 23.8 to 18%. The porosity is composed of micropores (diameter $< 4\ \mu\text{m}$) and macropores (diameter $> 4\ \mu\text{m}$). The presence of macropores above $4\ \mu\text{m}$ in the coating reduced fractionally from 5.9 to 5.8% after heat treatment at 1100°C over 0–300 h. However, the micropores below $4\ \mu\text{m}$ reduced from 17.8 to 12.2% after annealing at 1100°C over 0–300 h. After heat treatment at 1100°C for 25 h and 100 h, the percentage of the small pores in the sintered sample is 14% and 17%, respectively.

The sintering resistance of the nanostructured Al_2O_3 -YSZ coating can be understood by the shrinkage of the porosity.⁵⁰ During the sintering process,



4.18 Cross-sectional micrograph of the failed nanostructured TBCs showing the overview of a buckle. The samples experienced 36 cycles at 1150°C after isothermal oxidation of 100 h at 1000°C .



4.19 The cumulative porosity variation of the nanostructured 13AlYSZ coating before and after heat treatment at 1100°C for 25 h, 100 h and 300 h.

due to the presence of nanostructured particles and porosity, the porous nanozones are under a higher driving force for sintering and densification,⁵¹ which leads to a fast sintering. Therefore, the nanozones tend to densify rapidly and the porosity of the coating decreased from 23.8 to 22.1% after annealing treatment for 25 h. With the annealing treatment ongoing, the velocity of sintering is reduced, and the porosity dropped to 21.8% after annealing treatment for 100 h. This is caused by the grain growth and the precipitation of Al_2O_3 . The grain growth leads to a lower driving force for sintering and the precipitation of Al_2O_3 pins the boundaries, making sintering difficult. When the annealing time increases to 300 h, the porosity decreased to 18%. The slightly greater reduction in porosity per unit time from 100 to 300 h may simply be an experimental error since it is very difficult to measure the porosity level in a coating very accurately. Usually, an accelerated sintering occurs in the early stage, i.e. 25 h in this work, because the initial higher porosity and finer particle sizes contributed to sintering. As a result, an apparent shrinkage is observed at this stage. In this study, about 6% porosity decreased in the sintering process, similar to the tendency for the sintering of traditional 7 wt% Y_2O_3 -stabilized ZrO_2 ceramic coating.⁵²

4.6 Conclusion

Studies on nanostructured air plasma-sprayed YSZ coatings have shown that it is paramount to carefully control the spray parameters in order to

avoid the complete melting of the nanostructured YSZ agglomerates in the plasma jet, thus preserving and embedding part of the nanostructure of the agglomerates into the coating microstructure. Those coatings were produced from microscopic porous spray-dried particles formed via the agglomeration of individual nanosized YSZ particles. The semi-molten agglomerates, once embedded in the coating microstructure, created a bimodal feature, which consisted of a structure formed by the resolidification of agglomerates that had been fully molten in the spray jet combined with zones resulting from the incorporation of semi-molten material. By controlling the amount of previously molten and porous semi-molten particles embedded in the coating microstructure, it was possible to change considerably the mechanical response of the coating. Therefore, this bimodal microstructure affected the mechanical behavior of the coating. In recent years, new classes of ceramic materials having very low thermal conductivity and better high-temperature stability have been identified as potential successors to YSZ. In order to lower thermal conductivity, YSZ coatings have been modified by doping with several additives, such as Al_2O_3 , NiO, Nd_2O_3 , Er_2O_3 , Yb_2O_3 . However, these new materials have not yet been matured for practical application because of their poor mechanical and/or chemical properties. In the future, nanostructured YSZ coatings modified by Al_2O_3 , La_2O_3 , HfO_2 , etc. will be extensively investigated.

4.7 References

1. M. GELL, Application opportunities for nanostructured materials and coatings, *Mater. Sci. Eng. A* **204** (1995) 246–251.
2. Y.Y. ZENG, S.W. LEE, L. GAO, C.X. DING, Atmospheric plasma sprayed coatings of nanostructured zirconia, *J. Eur. Ceram. Soc.* **22** (3) (2002) 347–351.
3. R.S. LIMA, A. KUCUK, C.C. BERNDT, Evaluation of microhardness and elastic modulus of thermally sprayed nanostructured zirconia coatings, *Surf. Coat. Technol.* **135** (2001) 166–172.
4. H. CHEN, C.X. DING, Nanostructured zirconia coating prepared by atmospheric plasma spraying, *Surf. Coat. Technol.* **150** (1) (2002) 31–36.
5. C.G. ZHOU, N. WANG, S.K. GONG, H.B. XU, Thermal cycling life and thermal diffusivity of a plasma-sprayed nanostructured thermal barrier coating, *Scripta Mater.* **51** (2004) 945–948.
6. J. KARTHIKEYAN, C.C. BERNDT, J. TIKKANEN, S. REDDY, H. HERMAN, Plasma spray synthesis of nanomaterial powders and deposits, *Mater. Sci. Eng. A* **238** (1997) 275–286.
7. C.B. LIU, Z.M. ZHANG, X. L. JIANG, M. LIU, Z.H. ZHU, Comparison of thermal shock behaviors between plasma-sprayed nanostructured and conventional zirconia thermal barrier coatings, *Trans. Nonferrous Met. Soc. China* **19** (2009) 99–107.
8. R.S. LIMA, A. KUCUK, U. SENTURK, C.C. BERNDT, Integrity of nanostructured partially stabilized zirconia after plasma spray processing, *Mater. Sci. Eng. A* **313** (1/2) (2001) 75–82.

9. R.S. LIMA, A. KUCUK, U. SENTURK, C.C. BERNDT, Properties and microstructures of nanostructured partially stabilized zirconia coatings, *J. Thermal Spray Technol.* **10** (1) (2001) 150–152.
10. H. CHEN, C.X. DING, Nanostructured zirconia coatings prepared by atmospheric plasma spraying, *Surf. Coat. Technol.* **150** (1) (2002) 31–36.
11. C.G. ZHOU, N. WANG, Z.B. WANG, Thermal cycling life and thermal diffusivity of a plasma-sprayed nanostructured thermal barrier coating, *Scripta Mater.* **51** (10) (2004) 945–948.
12. B. LIANG, C.X. DING, Microstructure of nanostructure zirconia coating and its thermal shock resistance, *J. Inorg. Mater.* **21** (1) (2006) 250–256.
13. F. LIN, Y.G. YU, X.L. JIANG, K. L. ZENG, X.J. REN, Z.D. LI, Microstructures and properties of nanostructured TBCs fabricated by plasma spraying, *Chin. J. Nonferrous Met.* **16** (3) (2006) 482–487. (in Chinese).
14. M.R. GOLD, R.S. LIMA, A. KUCUK, C.C. BERNDT, Scratch testing and acoustic emission of nanostructured partially stabilized coatings, in: K. Ravi-Chandar, B.L. Karihaloo, T. Kishi, R.O. Ritchie, A.T. Yokobori Jr, T. Yokobori (Eds), *Proceedings of the 10th International Conference on Fracture*, Elsevier Science, Oxford, UK, 2001 (Paper #ICF1001074, pdf format).
15. B. LIANG, C. DING, Thermal shock resistances of nanostructured and conventional zirconia coatings deposited by atmospheric plasma spraying, *Surf. Coat. Technol.* **197** (2005) 185–192.
16. W.Q. WANG, C.K. SHA, D.Q. SUN, X.Y. GU, Microstructural feature, thermal shock resistance and isothermal oxidation resistance of nanostructured zirconia coating, *Mater. Sci. Eng. A* **424** (2006) 1–5.
17. Z. SHUI, B. WANG, A. LEVY, Erosion-corrosion of thermal spray coatings, *Surf. Coat. Technol.* **43/44** (1990) 859–874.
18. G. BARBEZAT, R. NICOLL, A. SICKINGER, Abrasion, erosion and scuffing resistance of carbide and oxide ceramic thermal sprayed coatings for different applications, *Wear* **162/164** (1993) 529–537.
19. N. BERGER-KELLER, G. BERTRAND, C. FILIATRE *et al.*, Microstructure of plasma-sprayed titania coatings deposited from spraydried powder, *Surf. Coat. Technol.* **168** (2003) 281–290.
20. R.S. LIMA, B.R. MARPLE, Thermal spray coatings engineered from nanostructured ceramic agglomerated powders for structural, thermal barrier and biomedical applications: a review, *J. Thermal Spray Technol.* **16** (1) (2007) 40–63.
21. F. TARASI, M. MEDRAJ, A. DOLATABADI, J.O. BERGHAUS, C. MOREAU, Phase formation and transformation in alumina/YSZ nanocomposite coating deposited by suspension plasma spray process, *J. Therm. Spray. Technol.* **19** (4) (2010) 787–795.
22. W.B. GONG, C.K. SHA, D.Q. SUN, W.Q. WANG, Microstructures and thermal insulation capability of plasma-sprayed nanostructured ceria stabilized zirconia coatings, *Surf. Coat. Technol.* **201** (2006) 3109–3115.
23. B. LIANG, C.X. DING, H.L. LIAO, C. CODDET, Phase composition and stability of nanostructured 4.7 wt.% yttria-stabilized zirconia coatings deposited by atmospheric plasma spraying, *Surf. Coat. Technol.* **200** (2006) 4549–4556.
24. X.Q. CAO, R. VASSEN, S. SCHWARTZ, W. JUNGEN, F. TIETZ, D. STÖVER, Spray-drying of ceramics for plasma-spray coating, *J. Eur. Ceram. Soc.* **20** (2000) 2433–2439
25. H.P. KLUG, L.E. ALEXANDER, *X-ray Diffraction Procedures for Polycrystalline and Amorphous Materials*, Wiley, London, UK, 1954.

26. L.L. SHAW, D. GOBERMAN, The dependency of microstructure and properties of nanostructured coatings on plasma spray conditions, *Surf. Coat. Technol.* **130** (2000) 1–8.
27. H. ZHOU, B. HE, J. WANG, B.D. SUN, Nanostructured yttria stabilized zirconia coatings deposited by air plasma spraying, *Trans. Nonferrous Met. Soc. China* **17** (2007) 389–393.
28. Y. ZENG, S.W. LEE, L. GAO, C.X. DING, Atmospheric plasma sprayed coatings of nanostructured zirconia, *J. Eur. Ceram. Soc.* **22** (2002) 347–351.
29. N. WANG, C.G. ZHOU, S. K. GONG, H. B. XU, Heat treatment of nanostructured thermal barrier coating, *Ceram. Int.* **33** (2007) 1075–1081.
30. H. ZHOU, F. LI, J. WANG, B.D. SUN, Microstructure analyses and thermophysical properties of nanostructured thermal barrier coatings, *J. Coat. Technol. Res.* **6** (3) (2009) 383–390.
31. H.B. GUO, R. VABEN, D. STÖVER, Thermophysical properties and thermal cycling behavior of plasma sprayed thick thermal barrier coatings, *Surf. Coat. Technol.* **192** (2005) 48–56.
32. D. CHEN, M. GELL, E.H. JORDAN, E. CAO, X. MA, Thermal stability of air plasma spray and solution precursor plasma spray thermal barrier coatings, *J. Am. Ceram. Soc.* **90** (2007) 3160–3166.
33. R.S. LIMA, A. KUCUK, C.C. BERNDT, Evaluation of microhardness and elastic modulus of thermally sprayed nanostructured zirconia coatings, *Surf. Coat. Technol.* **135** (2001) 166–172.
34. H. CHEN, X.M. ZHOU, C.X. DING, Investigation of the thermomechanical properties of a plasma-sprayed nanostructured zirconia coating, *J. Eur. Ceram. Soc.* **23** (2003) 1449–1455.
35. R. SOLTANI, E. GARCIA, T.W. COYLE, J. MOSTAGHIMI, R.S. LIMA, B.R. MARPLE, C. MOREAU, Thermomechanical behavior of nanostructured plasma sprayed zirconia coatings, *J. Thermal Spray Technol.* **15** (4) (2006) 657–662.
36. K.J. LAWSON, J.R. NICHOLLS, D.S. RICKERBY, The effect of coating thickness on thermal conductivity of CVD and PVD coatings, in: R.K. Datta, J.S. Gray (eds), *Advances in Surface Engineering*, Royal Society of Chemistry, Cambridge, UK, 1993, Vol. 1, 83–92.
37. L.T. KABACOFF, Thermal sprayed nano-structured thermal barrier coatings, *NATO Workshop on Thermal Barrier Coatings*, Aalborg, Denmark, AGARD-R-823, 1998, paper 12.
38. C.G. ZHOU, N. WANG, Z.B. WANG, Thermal cycling life and thermal diffusivity of a plasma-sprayed nanostructured thermal barrier coating, *Scripta Mater.* **51** (2004) 945–948.
39. Q. ZHANG, C.J. LI, S.L. ZHANG, X.R. WANG, G.J. YANG, C.X. LI, Thermal failure of nanostructured thermal barrier coatings with cold-sprayed nanostructured NiCrAlY bond coat, *J. Thermal Spray Technol.* **17** (2008) 838–845.
40. K.W. SCHLICHTING, N.P. PADTURE, E.H. JORDAN, M. GELL, Failure modes in plasma-sprayed thermal barrier coatings, *Mater. Sci. Eng. A* **342** (1–2) (2003) 120–130.
41. A. RABIEI, A.G. EVANS, Failure mechanisms associated with the thermally grown oxide in plasma-sprayed thermal barrier coatings, *Acta Mater.* **48** (15) (2000) 3963–3976.
42. E.P. BUSSO, J. LIN, S. SAKURAI, A mechanistic study of oxidation-induced degradation in a plasma-sprayed thermal barrier coating system: Part II: life prediction model, *Acta Mater.* **49** (9) (2001) 1529–1536.

43. H. LAU, C. LEYENS, U. SCHULZ, C. FRIEDRICH, Influence of bond coat pre-treatment and surface topology on the lifetime of EB-PVD TBCs, *Surf. Coat. Technol.* **165** (3) (2003) 217–223.
44. M. MATSUMOTO, T. KATO, K. HAYAKAWA, N. YAMAGUCHI, S. KITAOKA, H. MATSUBARA, The effect of pre-oxidation atmosphere on the durability of EB-PVD thermal barrier coatings with CoNiCrAlY bond coats, *Surf. Coat. Technol.* **202** (12) (2008) 2743–2748.
45. R. DAROLIA, Post-deposition oxidation of a nickel-base superalloy protected by a thermal barrier coating, US Patent 6,607,611, 19 August 2003.
46. T.J. NIJDAM, L.P.H. JEURGENS, J.H. CHEN, W.G. SLOOF, On the microstructure of the initial oxide grown by controlled annealing and oxidation on a NiCoCrAlY bond coating, *Oxid. Met.* **64** (5–6) (2005) 355–377.
47. O. RACEK, C.C. BERNDT, D.N. GURU, J. HEBERLEIN, Nanostructured and conventional YSZ coatings deposited using APS and TTPR techniques, *Surf. Coat. Technol.* **201** (1–2) (2006) 338–346.
48. R.S. LIMA, B.R. MARPLE, Nanostructured YSZ thermal barrier coatings engineered to counteract sintering effects, *Mater. Sci. Eng. A* **485** (1–2) (2008) 182–193.
49. O. RACEK, C.C. BERNDT, D.N. GURU, J. HEBERLEIN, Nanostructured and conventional YSZ coatings deposited using APS and TTPR techniques, *Surf. Coat. Technol.* **201** (1–2) (2006) 338–346.
50. Q.H. YU, C.G. ZHOU, H.Y. ZHANG, F. ZHAO, Thermal stability of nanostructured 13 wt% Al₂O₃-8 wt% Y₂O₃-ZrO₂ thermal barrier coatings, *J. Eur. Ceram. Soc.* **30** (2010) 889–897.
51. R.S. LIMA, B. R. MARPLE, Nanostructured YSZ thermal barrier coatings engineered to counteract sintering effects, *Mater. Sci. Eng. A.* **485** (2008) 182–193.
52. B. SIEBERT, C. FUNKE, R. VABEN, D. STÖVER, Changes in porosity and Young's modulus due to sintering of plasma sprayed thermal barrier coatings, *J. Mater. Process. Technol.* **92–93** (1999) 217–223.

Plasma spraying for thermal barrier coatings: processes and applications

J. L. XU and K. A. KHOR, Nanyang Technological
University, Singapore

Abstract: Plasma spraying processes are utilized for a wide range of industrial applications. This chapter reviews some fundamental aspects of plasma-spraying technology with the aim of understanding and controlling particular processes and mechanisms governing the formation and properties of plasma-sprayed coatings. The chapter mainly highlights the current status of plasma spraying in the biomedical field and the problems associated with plasma spray coating of hydroxyapatite which has shown promising effects on rapid bone remodeling and suitable functional life in orthopedic and dental applications.

Key words: plasma, plasma spraying, coating, biomaterials, hydroxyapatite, in vitro.

5.1 Introduction

Thermal plasma spraying is a process whereby a powder feedstock is injected into a high temperature plasma jet in which finely divided metallic and non-metallic materials are deposited in a molten or semi-molten state on prepared substrate.^{1,2} It has been used as an effective and economical method for producing ceramic coatings on metallic substrates and production of bulk powders from spheroidisation. This has been motivated mainly by the strong drive for high-performance materials and the growing need for new material-processing technologies. Particles injected into plasma zone will experience extreme heating rates and temperatures as high as 10000 K. Since plasma spraying is a very high-temperature process, the injected particles with varying size distribution will melt to yield an aerosol of molten droplets. Particles above critical size range may experience only partial melting while small particles may have a layer of vaporised materials surrounding the liquid droplets.³ Hence the plasma processing of a material with its stringent requirements needs to be carefully controlled to produce the desired results. Thus, the full potential of plasma technology depends on our ability to achieve the optimal match between the process requirements and the characteristics of the plasma source and reactor design used.

The plasma process has evolved over the years into a highly flexible coatings system capable of applying a wide range of materials. A major application of plasma spraying is to protect aircraft engine components by deposition of aerospace coating such as thermal barriers of zirconium/magnesium or alumina on metal substrates. Recently, it has also been used as a tool to process bio-ceramic materials such as hydroxyapatite (HA) as both coatings and powders.⁴⁻¹² In this chapter, a brief review of applications of plasma processing in biomaterials will be presented.

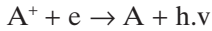
5.2 Basic plasma concepts

When we use the term plasma in daily life, normally plasma TV will come to mind, but what is plasma and how does it work? Apart from its application in plasma flat panel display, plasma processing has actually been used in many areas such as plastic bags, automobile bumpers, airplane turbine blades, artificial joints and semiconductor circuits. In physics and chemistry, plasma is defined as the fourth state of matter, the other three being solid, liquid and gas. Plasma is a partially ionised gas consisting of charged particles which have high kinetic energy and are normally at very high temperatures, of the order of $\sim 10\,000$ K.^{1,2} A better understanding of the plasma beam can be obtained from a simplistic explanation of the plasma from gas mechanics. The properties of a gas are primarily dependent on the movement of its molecules. During this movement, the molecules continually exchange energy and pulse through collisions with one another. When a certain amount of energy is supplied to a gas, the velocity of its molecules increases, the collisions become more frequent and the temperature of the gas increases. If the velocity is increased sufficiently, the molecules of the gas disintegrate into atoms upon mutual collisions, a process known as dissociation. When higher energy is applied, for example from a high electrical field, even the electrons forming the atomic shells are forced out. This process is known as ionisation. Upon ionisation, the electron released is in a higher state of energy and will soon return to its original path to minimise its energy. This stabilises the electron and releases energy in the form of kinetic or electromagnetic energy, which is the difference between the energy of the ionised electron and the energy of the electron in its original path.

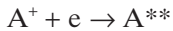
The final result of the whole dissociation and ionisation process is plasma, which contains electrically charged particles. However, the plasma is outwardly neutral as it will contain the same number of electrically positive and negative charges. Also, the processes of dissociation and ionisation are thermally balanced. This means that it is dependent on temperature, where equilibrium between the dissociation and ionisation processes and the appropriate reverse reactions are achieved. Another reaction, known as the

recombination process, also takes place continuously in the plasma. Depending on the way energy is released in the recombination process, several basic mechanisms of electron recombination can be categorised. Some of these are:¹²

1. Recombination with emission of radiation



2. Recombination with doubled excitation, when releasing energy causes displacement of two electrons with the formation of a neutral atom



3. Recombination at triplex, which is collision with electron, charged particle and neutral particle



To start the whole dissociation and ionisation process, it is first necessary to supply an external force. This can be in the form of high temperature or by the action of a high electric field.

A plasma jet can be generated by passing a gas through an electric arc. Ionisation of the gas then takes place and this gas stream is in turn converted into an extremely hot plasma jet once a process called ‘electrical breakdown’ takes place. The output, temperature and velocity are the main characteristics of the plasma beam. The temperature is dependent on the ionisation degree, which is then dependent on the kind of plasma gas and the parameters employed in the plasma torch. As an approximation, the mean temperature of the plasma can be calculated by dividing the mean enthalpy of the plasma by the gas volume, assuming that all heat is uniformly distributed over the gas volume.

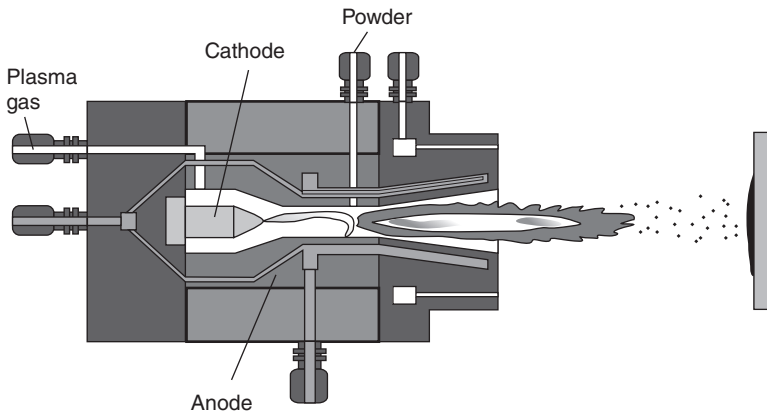
The velocity of the plasma beam can be approximated by applying fundamental gas mechanics laws for gas flow through a cylindrical tube, during its simultaneous heating. The dependence of velocity after heating can then be approximated from the equation of constant flow rate and the state equation of the gas, provided the gas pressure is assumed constant. Due to the kinetic and thermal effects of the plasma beam, the source material entering the plasma is accelerated and, depending on the input of thermal energy, conditions arising from plasma–particle interactions such as a great variety of phase changes take place. The first phase change takes place after the solid powder is injected into the plasma torch, i.e., melting. It has been pointed out that the degree of melting is very important for the final density of deposits. When the particles leave the plasma, they quench very quickly to produce, depending on different working conditions, non–equilibrium and different amounts of both crystalline and amorphous phases.¹² From

the practitioner's point of view, these phase changes can sometimes be beneficial; at other times, they are detrimental. Hence, it is important to study all of the possible phase changes occurring during plasma spraying.

5.3 Plasma spraying

There are several principal plasma generating devices currently used in material processing. These include direct current (DC) plasma torches, DC transferred arcs, radio frequency inductively-coupled plasma torches and hybrid combinations of them. DC plasma torches are the most commonly used plasma generation devices (about 99% of the market). In most cases (about 95% of the plasma spray market), DC plasma guns are working in air at atmospheric pressure. Ar, He, N₂ and their mixtures are the most commonly used gases. Figure 5.1 shows a typical DC plasma jet generated by striking a DC electric arc between two electrodes within the torch. Gas flowing between the electrodes can be heated up to temperatures of 6000–10000 K. The electric arc partially ionises the gas to form the plasma.

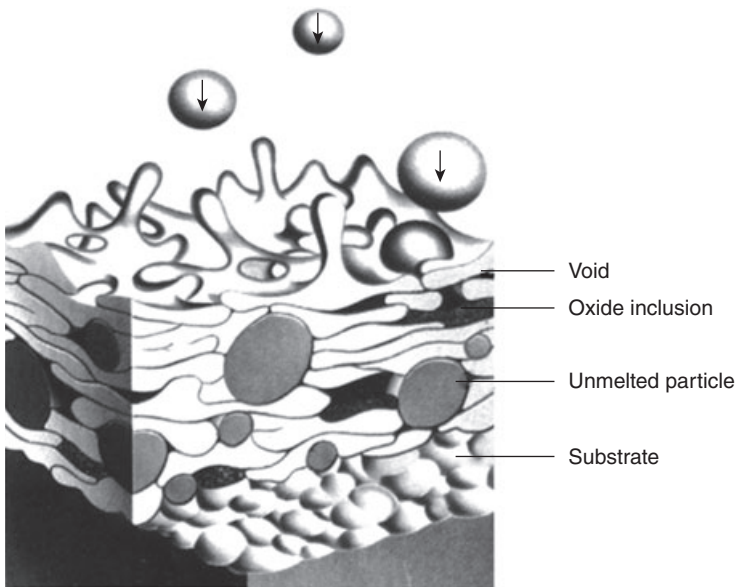
In a material processing through plasma spraying, the material to be deposited (feedstock), typically in powder form but sometimes a liquid or suspension or wire, will be injected through an external feed-port or internally in the high-temperature plasma. Melting takes place almost instantaneously. The molten particles are then accelerated rapidly towards the substrate. The deposits consist of a multitude of pancake-like lamellae called 'splats', formed by flattening of the liquid droplets. As the feedstock powders typically have sizes from micrometers to above 100 μm , the lamellae have thickness in the micrometer range and lateral dimension from several to hundreds of micrometers. Due to the significant difference in the



5.1 Schematic of plasma-spraying system.

temperature of the liquid droplet and the substrate, the spreading of the droplet on impact will be limited mainly by the solidification process that is taking place simultaneously. Typically, the cooling rate of the droplets is $\sim 10^6 \text{ Ks}^{-1}$ or greater. Adherence of the adjacent discs will likely take place through various contact points made prior to complete solidification. The microstructure of the coatings is therefore related to the nature of the interface between randomly stacked lamellae and the internal structure with each lamella produced by the rapid solidification process.

Some of the inherent defects of plasma-sprayed coating are voids, inclusions and poor adhesion of the lamellae. These may have arisen due to variation in the plasma-spraying process. Among them are fluctuations in powder feedrate, spraying cross-head speed and spraying distance. Other causes are incomplete melting of large particles and splashing of droplets on impact. In addition, due to the extreme conditions, transformations involved with feedstock related to physical and even both physical and chemical changes involving melting and rapid solidification, vaporisation, condensation and other chemical reactions might take place. A popular application for plasma-spraying processes is to produce a coating material on a substrate, depending on its composition and desired coating performance. Figure 5.2 shows a schematic diagram of particles impinging onto a substrate during the process of building up a coating. Examples of plasma-sprayed coatings can be found in a wide range of industry types where



5.2 Process of building up a coating.

coatings are used to provide protection against various forms of wear and corrosion or to give thermal protection or some desired physical characteristics such as electrical insulation.

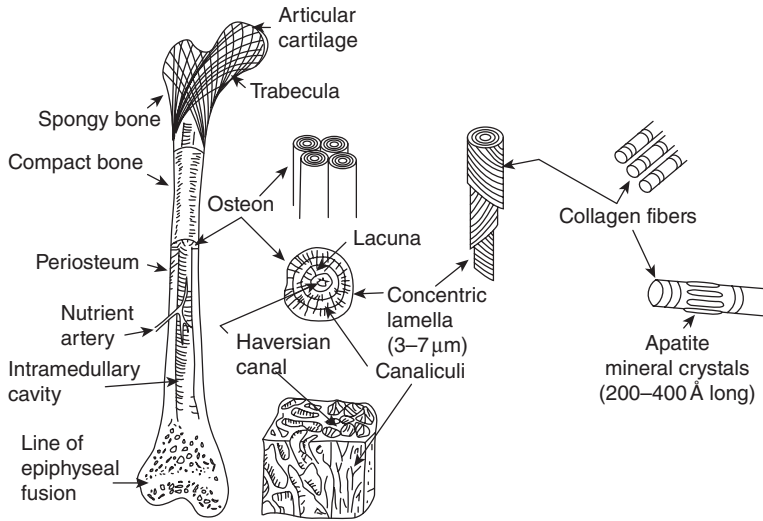
5.4 Applications of plasma spraying

5.4.1 Application in biomaterials

A biomaterial is a material in contact with fluids, cells and tissues of the living body utilised to evaluate, repair or replace any tissue or organ of the body.¹³ A prerequisite for any synthetic material implanted in the body is that it should have good mechanical strength, high chemical stability, high corrosion resistance, very low toxicity and high biocompatibility.¹³ Metals such as titanium, titanium alloys, stainless steel and CoCr-based alloys are popularly used as implant materials for their superior properties in terms of static and dynamic mechanical strength. In the past few years, researchers have been trying to improve on these mechanical properties and to develop new series of materials that can guarantee not only superior mechanical performance but also an excellent biological response. For this purpose, different materials have been produced to meet almost every conceivable need. Yet not all the problems connected with these implants, such as distance cell migration, breakage, stress shielding, reactivities and growth restriction, have been solved.¹⁴ Moreover, the surface of the metal implant can become corroded and discolored and in some instances release metallic elements to the surrounding tissues when used in the corrosive environment of a human body. Ti-6Al-4V alloys show many desirable features, such as biocompatibility, high corrosion resistance, excellent strength-to-weight ratio and so on, and they have been widely used in aerospace and orthopedic applications. Their corrosion resistance can be attributed to a passivation layer on the surface. However, it can be easily worn out and wear-corrosion failure can occur because of electric cell reactions between the passivated and non-passivated layers.¹⁵

Biomedical coatings generally have to satisfy specific requirements such as high crystallinity, high coating adhesion and suitable porosity.¹⁶ It is necessary to enhance biocompatibility, accelerate post-operative healing and improve adhesions. Coatings have specific functions ranging from improving fixation by establishing strong interfacial bonds, shielding the metallic implant from environmental attack or leaching effects, promoting fast tissue growth and interaction by the presence of a catalyst material and minimising adverse reaction by the provision of a biocompatible material.

Bone is mainly composed of mineral components, water and collagen fibers. A schematic anatomical view of a long bone is shown in Fig. 5.3.¹⁷ The major subphase of the mineral consists of submicroscopic crystals of

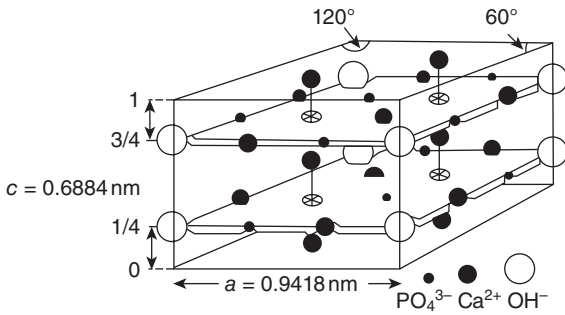


5.3 Organization of a typical bone.

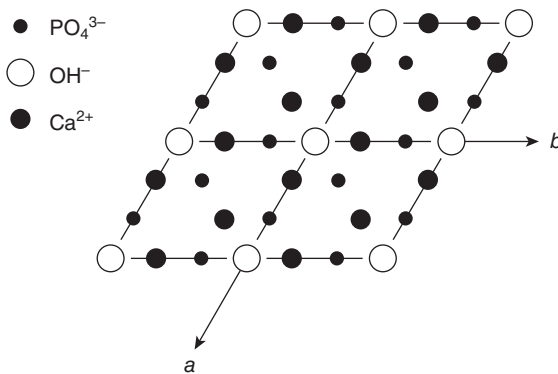
an apatite of calcium and phosphate, resembling HA in its crystal structure. A typical wet cortical bone is composed of 22 wt% organic matrix, 69 wt% mineral and 9 wt% water. It has been known that HA can form strong biological bonds with bony tissue without the presence of soft fibrous tissues. The provision of a high-calcium and phosphorus-rich environment promotes rapid bone formation within the vicinity of the HA implant. HA also establishes strong interfacial bonds with titanium implants. Its excellent biointegration makes it an ideal choice for use in orthopedic and dental applications.¹⁸ Some authors claimed that HA may act as a biological barrier to reduce toxic responses caused by the release of metallic ions from the metal substrate into the bone.¹⁹

The chemical formula of HA is presented as $\text{Ca}_4(\text{I})\text{Ca}_6(\text{II})(\text{PO}_4)_6(\text{OH})_2$ ($\text{Ca}_{10}(\text{PO}_4)_6(\text{OH})_2$). The Ca(I) atoms are on the fourfold symmetry $4(f)$ position and the Ca(II) atoms are in the sixfold symmetry $6(h)$ position.¹⁹ The OH groups occupy disordered positions above and below the triangles formed by the Ca(II) atoms. The disorder of the OH groups gives rise to a ‘macroscopic’ space group $\text{P}6_3/m$ (as determined by X-ray diffractometry), which is lost at the level of the individual columns.²⁰

As shown in Figs 5.4 and 5.5, biological HA has a hexagonal lattice with the space group of $\text{P}6_3/m$ ²¹ with dimension $a = b = 9.432 \text{ \AA}$ and $c = 6.881 \text{ \AA}$. The apatite structure of HA is represented by two sets of hexagonal cells shown in Fig. 5.5: OH atoms, represented by the solid dots, form the HA unit cell and Ca atoms, represented by the open dots, form a smaller hexagonal cell (without an indentical point in the center). The size ratio of



5.4 Crystal structure of HA:²¹ $a = b = 9.418 \text{ \AA}$ and $c = 6.884 \text{ \AA}$.



5.5 (0001)-plane of HA at $z = 3/4$.

the HA unit cell to the Ca cell is about $\sqrt{3}$. The crystal data of HA and some other physical properties are shown in Table 5.1. The ideal Ca:P ratio of HA is 10:6 and the calculated density is 3.21 g/cm.

HA promotes rapid bone growth and bonding between bony tissue and implant surfaces. Thermodynamically, HA is the most stable calcium phosphate compound at any given pH, temperature and composition of physiological fluid. However, the poor mechanical properties of bulk HA ceramics have provided impetus to research in HA coatings on metallic substrates in order to maintain biocompatibility and to improve mechanical properties. Thermal-spraying processes with their wide array of operating parameters are flexible manufacturing tools in production of bioactive HA coatings. Direct current (DC) plasma spraying of HA, in particular, since 1980s has been carried out by many researchers.²²⁻²⁹ However, many challenges have been met. HA, in the light of its biomedical application, demands stringent processing conditions before a successful outcome is achieved. Consequently, several critical issues have been recognised concerning the

Table 5.1 Physical properties of HA

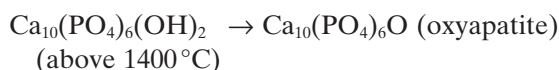
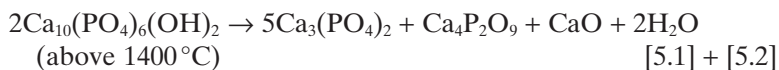
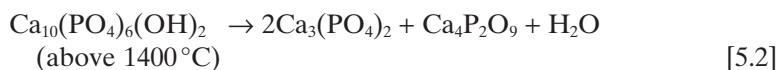
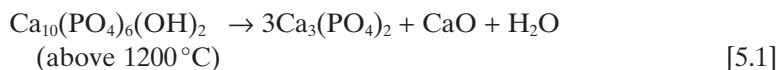
Molecular weight	1004.8
Space group	P6 ₃ /m
Lattice constants	$a = 0.9423\text{--}0.9418$ nm, $c = 0.6881\text{--}0.6884$ nm
Chemical unit number	$Z = 1$
Theoretical density	~ 3.156 g/cm ³
Thermal diffusivity	$\sim 5 \times 10^{-3}$ cm ² /s

plasma spraying of HA. Some have been extensively studied, thus overcoming the problem and establishing new knowledge and understanding of this class of calcium phosphates. However, many remain to be addressed. Some concerns regarding the plasma spraying of HA include:

1. induced chemical changes resulting in deviation from stoichiometry and decomposition;
2. amorphisation upon spraying;
3. induced stresses due to rapid heating and cooling;
4. full quantification of phases (including amorphous phase) after spraying.

5.4.2 Decomposition and chemical changes

Plasma spraying, being a non-equilibrium process, is bound to produce changes to the starting material after processing. When HA is introduced into the plasma, which is typically $15\text{--}20 \times 10^3$ K, it generally undergoes decomposition, melting and even vaporisation. The degree of these processes depends on a large number of factors, including initial size and size distribution of feedstock powders, chemical purity, pressure, feed rate, the power used for spraying and stand-off distance (for coatings). Even though the residence time of particles in the plasma is approximately 2–3 milliseconds, the heat input is high enough to cause decomposition and partial melting of HA. Decomposition of HA after plasma spraying has been noted by several authors:^{30–34}



There are also findings that the formation of the higher temperature phases such as α -tricalcium phosphate (TCP) and tetracalcium phosphate (TTCP) occurs subsequent to the formation of oxyapatite (OAp).³⁴ The loss of water is also thought to produce a solid solution of HA and OAp in which the chains of OH^- are replaced by O^{2-} and vacancies. The formation of CaO in the as-sprayed HA also suggests that P_2O_5 depletion occurs during the powder-spraying process.

Other than decomposed phases, the as-sprayed HA also contains amorphous material. This amorphous material has been seen as a problem by some in HA coatings, especially when the amorphous content is concentrated at the interface between implant and coating.^{35,36} It is also the view of several researchers that the presence of the amorphous phase in plasma-sprayed HA coatings is detrimental not only to the interface between the coating and substrate but the coating and the implanted area in the biological environment.^{37,38} Others such as Gross and Berndt, however, believe that the presence of the amorphous can be useful for absorbing mechanical mismatch and the promotion of bone remodeling.^{34,39} In DC plasma spraying, the formation of the amorphous phase is thought to be related to the rapid heating and cooling experienced by material undergoing plasma spraying. It was noted too that formation of the amorphous phase is also related to the partial dehydroxylation of HA during spraying.³⁹ Gross and Berndt have presented a model to highlight the changes to HA after plasma spraying which gives an idea of what phases can be present in the as-sprayed powders.³⁹

It is also known that the cooling rate has an important role in the formation of the various calcium phosphates. In plasma processing the cooling rate is so high that equilibrium phase transformations are a near impossibility. However, depending on the thermal treatment, different amounts of decomposition and amorphisation can take place. Other than temperature (thermal treatment), partial water vapor pressure also determines the thermal stability of HA, and hence the level of decomposition it experiences.^{39,40}

It was reported that the comparative dissolution behavior of different monophasic calcium phosphates in increasing order is as shown below:



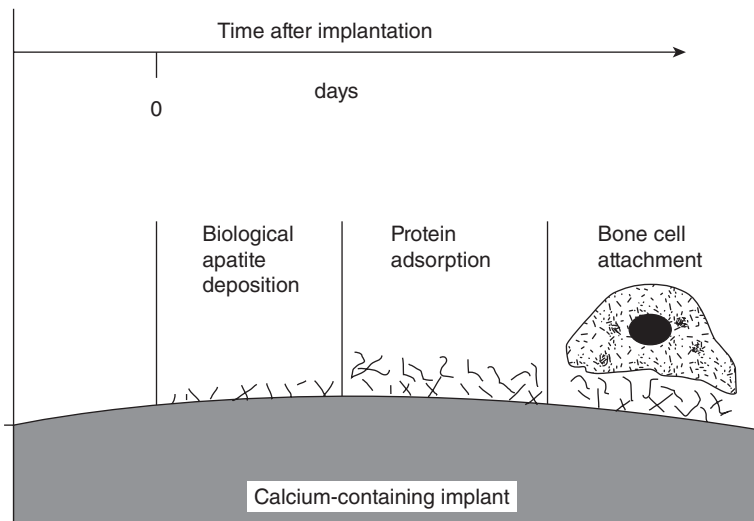
where ACP is amorphous calcium phosphate. Since the dissolution behavior of the coatings reflects their phase distribution, the presence of metastable components (e.g., TCP, TTCP) in turn leads to an increase in instability of the coatings. Therefore the phase balance of the plasma-sprayed coating may affect its long-term behavior under *in vivo* conditions.

5.4.3 *In vitro* tests

The growth of apatite crystals on the surface determines the characteristics and performance of a number of biomaterials. Because body fluid is highly supersaturated with respect to apatite, apatite deposition may occur on the surface of any biomaterial immersed in body fluid. For biomaterials that could be used in contact with bone, it is desirable to enhance growth of apatite on the implant surface. This will subsequently result in the formation of a chemical bond between bone and biomaterial. Figure 5.6 presents the proposed bonding between bone and implant. The precipitated apatite layer will serve as a substrate for subsequent protein adsorption and bone cell attachment. The proteins from the body serve as cell receptors, and adsorb onto the apatite surface (cell ligand), thus enabling cells to attach onto the implant.

These biological properties of biomaterials should be tested before medical application. However, considering the inconvenience involved in testing within the living organism (*in vivo* test), many studies seeking a comprehensive understanding of the factors that control the biomechanical properties have been conducted through *in vitro* studies. Actually, *in vitro* (Latin: *within the glass*) testing refers to the technique of performing a given procedure in a controlled environment outside of a living organism.

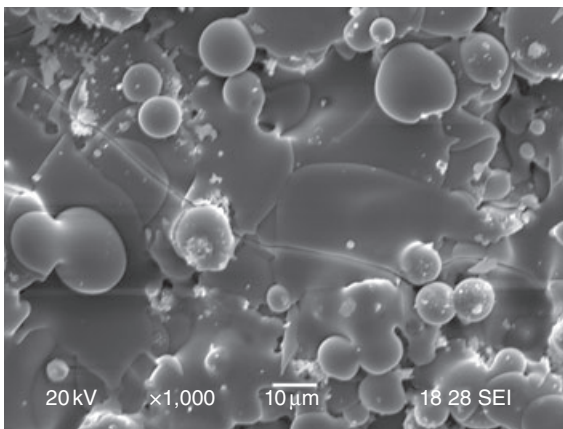
In some *in vitro* studies, the material is immersed in a protein-free and acellular solution that has an ion concentration nearly equal to that of



5.6 Schematic showing the proposed mechanism facilitating the bonding of bone to certain implants.⁴¹

human blood plasma; i.e., simulated body fluid (SBF). Because its chemical composition is close to that of human blood plasma, the bioactivity of an artificial material can be evaluated by examining the formation of apatite on its surface following immersion in SBF. It has been suggested that the efficacy of apatite nucleation is dependent not only on the composition of the biomaterial, but also on its concentration and structural arrangements. After soaking in SBF for a period, an HA sample is negatively charged immediately due to OH^- and PO_4^{3-} and the positively charged Ca^{2+} ions in the fluid. As the calcium ions accumulate, the surface imparts a positive charge, and thus combines with negatively charged phosphate ions in the fluid to form ACP. This phase is metastable, and eventually transforms into stable bone-like apatite. The apatite layer formed incorporates carbonate ions from the solution into its lattice by substituting phosphate groups. This substitution promotes the differentiation of marrow stromal stem cells into osteoblasts (bone-producing cells) that are responsible for the formation of bone. After immersion in SBF for 12 days, Yu *et al.*⁴² reported the formation of a dune-like layer consisting of small granules on the as-sprayed HA coating (Fig. 5.7). With continued immersion, the layer became denser and the granules gradually grew.⁴³

Cell culture is another *in vitro* technique in cellular biology that is carried out in a Petri dish. It is used not only to test material cytotoxicity (cell poisoning), but also to investigate surface-dependent responses of bone-forming cells. The quality of the bone where cell cultures are to be grown is taken into account in *in vitro* study. This kind of approach concerning *in vitro* research requires models that simulate the *in vivo* conditions: the study of primary osteoblast (bone-forming cell) behavior seems relevant to this purpose. Such a cell culture experiment provides evidence of enhanced



5.7 SEM micrograph of as-sprayed HA coating.

adhesion of osteoblasts on the nanophase HA. Moreover, cell culture work provides information on cell proliferation, alkaline phosphatase activity and concentration of calcium in the extracellular matrix. *In vitro* cellular models have been used to determine the efficacy of HA to serve as bone prostheses.^{44,45} A study by Khor *et al.* shows that the osteoblasts proliferated well on a HA coating surface.⁴⁶ All cells spread well and grew favorably across the coating surfaces. As observed, the cells are seen to be flattened and to attach tightly onto coating surfaces with their filopodium and lamellipodium, suggesting good cell viability on HA coatings.

5.5 Conclusions

Investigation of the current state-of-the-art in plasma-spraying technology has indicated that opportunities exist to significantly improve upon modern plasma-spraying systems. One such opportunity is the tailoring of pore morphologies to improve the insulative properties of the coatings. Schematically, based on the current studies on CaP biomaterials, potential future development of new CaP biomaterials will mainly be obtained via nanotechnologies. There are several recommendations for future studies in this field:

1. Future researchers should give careful consideration to selecting the appropriate approach to synthesise nanostructured CaP materials. This judicious selection would help to transfer the technology from laboratory- to industrial-scale application.
2. In addition to the currently required characterisation, broader assessments of the new biomaterials should be conducted. For example, an evaluation of the strengths and weaknesses, short-term and long-term successes and failures through *in vivo* study would be extremely helpful with respect to medical application within the human body.

5.6 Acknowledgements

We would like to thank Nanyang Technological University for funding support. J.L. Xu is a research fellow in School of Mechanical & Aerospace Engineering, Nanyang Technological University.

5.7 References

1. X. FAN, T. ISHIGAKI, Mo₅Si₃-B and MoSi₂ deposits fabricated by radio frequency induction plasma spraying, *Journal of Thermal Spray Technology*, **10**(4) (2001), 611–617.
2. K.A. KHOR, Y. MURAKOSH, M. TAKAHASHI, T. SANO, Plasma spraying of titanium aluminide coatings: Process parameters and microstructure, *Journal of Materials Processing Technology*, **48** (1995), 413–419.

3. S. MALMBERG, J. HEBERLEIN, Effect of plasma spray operating conditions on plasma jet characteristics and coating properties, *Journal of Thermal Spray Technology*, **2**(4) (1993), 339–344.
4. P. CHEANG, K.A. KHOR, Thermal spraying of hydroxyapatite (HA) coatings: effects of powder feedstock, *Journal of Materials Processing Technology*, **48** (1995), 429–436.
5. P. CHEANG, K.A. KHOR, Addressing processing problems associated with plasma spraying of hydroxyapatite coatings, *Biomaterials*, **17** (1996), 537–544.
6. E. CHANG, W.J. VHANG, B.C. WANG, C.Y. YANG, Plasma spraying of zirconia-reinforced hydroxyapatite composite coatings on titanium Part I: Phase, microstructure and bonding strength, *Journal of Materials Science: Materials in Medicine*, **8** (1997), 193–200.
7. Y.C. TSUI, C. DOYLE, T.W. CLYNE, Plasma sprayed hydroxyapatite coatings on titanium substrates Part 1: Mechanical properties and residual stress levels, *Biomaterials*, **19** (1998), 2015–2029.
8. H. LI, K.A. KHOR, P. CHEANG, Titanium dioxide reinforced hydroxyapatite coatings deposited by high velocity oxy-fuel (HVOF) spray, *Biomaterials*, **23** (2002), 85–91.
9. I.-S. LEE, H.-E. KIM, S.-Y. KIM, Studies on calcium phosphate coatings, *Surface and Coatings Technology*, **131** (2000), 181–186.
10. P.K. CHU, J.Y. CHEN, L.P. WANG, N. HUANG, Plasma-surface modification of biomaterials, *Materials Science and Engineering*, **R36** (2002), 143–206.
11. Y.C. TSUI, C. DOYLE, T.W. CLYNE, Plasma sprayed hydroxyapatite coatings on titanium substrates Part 2: optimization of coating properties, *Biomaterials*, **19** (1998), 2031–2043.
12. D. MATEJKA, B. BENKO, *Plasma Spraying of Metallic and Ceramic Materials*, Wiley, Chichester, UK, (1989).
13. A.M. EKTESSABI, M. HAMDI, Characterization of calcium phosphate bioceramic films using ion beam analysis technique, *Surface and Coatings Technology*, **153** (2002), 10–15.
14. M. MATTIOLI BELMONTE, A. DE BENEDITTIS, R.A.A. MUZZARELLI, P. MENGUCCI, G. BIAGINI, Bioactivity modulation of bioactive materials in view of their application in osteoporotic patients, *Journal of Materials Science: Materials in Medicine*, **9** (1998), 485–492.
15. S.Y. WANG, P.K. CHU, B.Y. TANG, X.C. ZENG, Y.B. CHEN, X.F. WANG, Radio-frequency plasma nitriding and nitrogen plasma immersion ion implantation of Ti–6Al–4V alloy, *Surface and Coating Technology*, **93** (1997), 309–313.
16. K.A. GROSS, C.C. BERNDT, Structural changes of plasma sprayed hydroxyapatite coatings during in vitro testing, in: E. Horowitz, J.E. Parr (eds), *Characterization and Performance of Calcium Phosphate Coatings for Implants*, Philadelphia, PA: ASTM, (1993): 256–268.
17. P. LUO, T.G. NIEH, Synthesis of ultrafine hydroxyapatite particles by a spray dry method, *Materials Science and Engineering*, **C3** (1995), 75–78.
18. P. CHEANG, K.A. KHOR, Addressing processing problems associated with plasma spraying of hydroxyapatite coatings, *Biomaterials*, **17** (1996), 537–544.
19. R.L. REIS, F.J. MONTEIRO, Crystallinity and structural changes in HA plasma-sprayed coatings induced by cyclic loading in physiological media, *Journal of Materials Science: Materials in Medicine*, **7** (1996), 407–411.

20. G. PENEL, G. LEROY, C. REY, B. SOMBRET, J.P. HUVENNE, E. BRES, Infrared and Raman microspectrometry study of fluor-fluor-hydroxy and hydroxy-apatite powders, *Journal of Materials Science: Materials in Medicine*, **8** (1997), 271–276.
21. T. NAKANO, T. AWAZU, Y. UMAKOSHI, Plastic deformation and operative slip system in mineral fluorapatite single crystal, *Scripta Materialia*, **44** (2001), 811–815.
22. D.P. RIVERO, J. FOX, A.R. SKIPOR, R.M. URBAN, J.O. GALANTE, Calcium phosphate coated porous titanium implants for enhanced skeletal fixation, *Journal of Biomedical Materials Research*, **22** (1988), 191–201.
23. P.S. PREVEY, X-Ray diffraction characterization of crystallinity and phase composition in plasma sprayed hydroxyapatite coatings, *Journal of Thermal Spray Technology*, **9** (2000), 369–376.
24. J.C. KNOWLES, K. GROSS, C.C. BERNDT, W. BONFIELD, Structural change of thermally sprayed hydroxyapatite investigated by Rietveld analysis, *Biomaterials*, **17** (1996), 639–645.
25. E. BOUYER, M. MULLER, R.H. HENNE, G. SCHILLER, Thermal plasma processing of nanostructured Si-based ceramic materials, *Journal of Nanoparticle Research*, **3** (2001), 373–378.
26. C.F. FENG, K.A. KHOR, Y.W. GU, P. CHEANG, Analysis of phase changes in plasma-sprayed Ti-6Al-4V/hydroxyapatite composite coating by DSC, *Materials Letters*, **51** (2001), 88–93.
27. E. PARK, R.A. CONDRATE SR, D. LEE, K. KOCIBA, P.K. GALLAGHER, Characterization of hydroxyapatite: before and after plasma spraying, *Journal of Materials Science: Materials in Medicine*, **13** (2002), 211–218.
28. L. SUN, C.C. BERNDT, K.A. KHOR, H.N. CHEANG, K.A. GROSS, Surface characteristics and dissolution behavior of plasma-sprayed hydroxyapatite coatings, *Journal of Biomedical Materials Research*, **62** (2002), 228–236.
29. J. WENG, Q. LIU, J.G.C. WOLKE, X. ZHANG, K. DE GROOT, Formation and characteristics of the apatite layer on plasma-sprayed hydroxyapatite coatings in simulated body fluid, *Biomaterials*, **18** (1997), 1027–1035.
30. A.C. TAS, F. KORKUSUZ, M. TIMUCIN, A. AKKAS, An investigation of the synthesis and high-temperature sintering behavior of calcium hydroxyapatite (HA) and tricalcium phosphate (TCP) bioceramics, *Journal of Materials Science: Materials in Medicine*, **8** (1997), 91–96.
31. E. CHANG, W.J. VHANG, B.C. WANG, C.Y. YANG, Plasma spraying of zirconia-reinforced hydroxyapatite composite coatings on titanium Part I: Phase, microstructure and bonding strength, *Journal of Materials Science: Materials in Medicine*, **8** (1997), 193–200.
32. P. CHEANG, K.A. KHOR, Addressing processing problems associated with plasma spraying of hydroxyapatite coatings, *Biomaterials*, **17** (1996), 537–544.
33. J. MOSTAGHIMI, M. PASANDIDEH-FARD, S. CHANDRA, Dynamics of splat formation in plasma spray coating process, *Plasma Chemistry and Plasma Processing*, **22** (2002), 59–84.
34. K.A. GROSS, C.C. BERNDT, In vitro testing of plasma-sprayed hydroxyapatite coatings, *Journal of Materials Science*, **5** (1994), 219–224.
35. R. MCPHERSON, N. GANE, T.J. BASTOW, Structural characterization of plasma-sprayed hydroxyapatite coatings, *Journal of Materials Science: Materials in Medicine*, **6** (1995), 327–334.

36. R. KUMAR, P. CHEANG, K.A. KHOR, Phase composition and heat of crystallization of amorphous calcium phosphate in ultra-fine radio frequency suspension plasma sprayed hydroxyapatite powders, *Acta Materialia*, **52** (2004), 1171–1181.
37. C.F. KOCH, S. JOHNSON, D. KUMAR, M. JELINEK, D.B. CHRISEY, A. DORAISWAMY, C. JIN, R.J. NARAYAN, I.N. MIHAILESCU, Pulsed laser deposition of hydroxyapatite thin films, *Materials Science and Engineering C*, **27** (2007), 484–494.
38. Z. ZYMAN, J. WENG, X. LIU, X. ZHANG, Z. MA, Amorphous phase and morphological structure of hydroxyapatite plasma coatings, *Biomaterials*, **14** (1993), 225–228.
39. K.A. GROSS, C.C. BERNDT, Thermal processing of hydroxyapatite for coating production, *Journal of Biomedical Materials Research*, **39** (1998), 580–587.
40. D.H. HARRIS, Overview of problems surrounding the plasma spraying of hydroxyapatite coatings, in: T.F. Bernacki (ed.), *Proceeding of the Third National Thermal Spray Conference*, Materials Park, OH: ASM International, 1990: 419–423.
41. M. SPECTOR, Basic principles of tissue engineering, in: S.E. Lynch, R. J. Genco, R.E. Marx (eds), *Tissue Engineering: Applications in Maxillofacial Surgery and Periodontics*, Carol Stream, IL: Quintessence, (1998): 3–16.
42. L.G. YU, K.A. KHOR, H. LI, P. CHEANG, Effect of spark plasma sintering on the microstructure and in vitro behavior of plasma sprayed HA coatings, *Biomaterials*, **24** (2003), 2695–2705.
43. X.B. ZHENG, C.X. DING, Characterization of plasma-sprayed hydroxyapatite/TiO₂ composite coatings, *Journal of Thermal Spray Technology*, **9** (4) 2000, 520–525.
44. S. ZHANG, K.E. GONSALVES, Preparation and characterization of thermally stable nanohydroxyapatite, *Journal of Materials Science: Materials in Medicine*, **8** (1997), 25–28.
45. S. SARIG, F. KAHANA, Rapid formation of nanocrystalline apatites, *Journal of Crystal Growth*, **237–239** (2002), 55–59.
46. K.A. KHOR, H. LI, P. CHEANG. Nanostructures and osteoblast behavior of thermal sprayed calcium phosphate splats, *Advances in Technology of Materials and Materials Processing*, **8**(2) (2006), 130–133.

Processing, microstructures and properties of thermal barrier coatings by electron beam physical vapor deposition (EB–PVD)

S. GONG and Q. WU, Beihang University, China

Abstract: Thermal barrier coatings (TBCs) produced by electron beam physical vapor deposition (EB–PVD) have exhibited some advantages over those produced by plasma spraying, being the most promising protective coatings for hot components used in rotation condition. In this work, the physical principles of EB–PVD technology are described. Processing, microstructures and properties of EB–PVD TBCs are reviewed. The failure mechanisms of EB–PVD TBCs subjected to thermal cyclic loads are also discussed.

Key words: thermal barrier coatings (TBCs), electron beam physical vapor deposition (EB–PVD), microstructure, property, processing.

6.1 Introduction

The major objectives of the turbine industry are to increase the engine combustion temperature, to double the thrust to weight ratio, and to improve the thermal efficiency of turbine components under severe environmental conditions at elevated temperatures.^{1,2} The use of nickel-based superalloy materials has resulted in an increase of almost 100 °C in engine operational temperature in the past 50 years.³ However, the limits of thermal stability have been reached. It has been suggested that a reduction in metallic temperature of 30–60 °C can produce a twofold increase in the life of turbine components. Thermal barrier coating (TBC) systems, as a means of protecting metallic substrates from high temperatures, can decrease the metallic temperature and improve the service life of turbine components. Therefore, through reducing the thermal conductivity of the TBCs by altering the microcomposition or by microstructural modifications, the life of turbine components can be prolonged.⁴

The typical TBC consists of two layers: an outer insulated ceramic top coat (TC), with its main function of reducing the heat transfer to the metallic substrate; and a metallic bond coat (BC) which mainly affects oxidation-resistance and is the actual thermal barrier. These are deposited directly onto the surface of the metallic components, BC first followed by TC.

During operational service, a thermally grown oxide (TGO) is formed between BC and TC as a result of oxidation of the BC at high temperatures. Since the top ceramic layer can endure a higher temperature than the metallic substrate, the engine operating temperatures can rise, prolonging the life of metal components when subjected to high temperature and pressure and reducing their cooling requirements, thus providing benefits in performance, efficiency and durability of the engine.⁵⁻¹⁰

Thermal barrier coatings deposited onto turbine components using the electron beam–physical vapor deposition (EB–PVD) process usually have unique columnar structures capable of narrowing the technological gap between insulation/life extension and reliability.⁵

The TBC materials and structures, processing techniques, properties and associated failure mechanisms have been briefly demonstrated in this chapter. Herein, we would present the processing, microstructures and properties of TBCs by EB–PVD in detail.

6.2 Description of the physical principles of electron beam physical vapor deposition (EB–PVD)

EB–PVD is widely used in the preparation of thick coatings as one of a variety of coating manufacturing methods in vacuum. In this method, a high-energy electron beam which is able to achieve rapid melting and evaporation is focused on target materials. Then the vapor is deposited onto certain substrates where it can evaporate both metals and ceramics. The high rate of deposition makes it popular in a wide range of application markets, such as optical prisms, filters, semiconductors and a high-value thermal barrier coating device, etc. The first system for the preparation of thermal barrier-coated EB–PVD in gas turbine blades was developed by the German company Leybold-Heraeus in the late 1960s.¹¹

Since the 1980s, the USA, the UK, Germany and the former Soviet Union countries have been investigating the physical vapor method of deposition to prepare TBC. The early EB–PVD technology is mainly used for the preparation of MCrAlY coatings. As the equipment is expensive and the production cost is relatively high, the development of EB–PVD technology has had to cease. In the early 1980s, the American company, Airco Temescal, prepared a reproducible, high-quality TBC in the laboratory using EB–PVD technology for the first time. In the mid-1980s, P & W, GE and other companies began to utilize the EB–PVD method for the processing of TBCs in rotor blades and guide vanes in aviation turbine engines. During the same period, the Soviet Union also used the EB–PVD techniques and successfully made TBCs for rotor blades in military aircraft. In the mid-1990s, the Paton Welding Institute in Ukraine produced low-cost EB–PVD

equipment, which was applied in the USA and Europe, and the EB-PVD TBC technology reached a new peak.

The electron beam is used as a heat source in EB-PVD. Since the evaporating rate is high, almost all the materials can be evaporated, and the interfacial bonding between the deposited coating and substrate is much stronger than plasma-sprayed coatings. As the processing parameters, such as electron beam power, beam spot size and location, can be controlled accurately, it is feasible to obtain a uniform coating thickness. Reactions between evaporation materials and crucible at high temperature can be avoided since the crucible is water-cooled, and it will not contaminate the coatings. The main processing procedures in the EB-PVD method are as follows: the electron beam with high energy density focuses on the target surface under magnetic or electric field and heats the target to a sufficiently high temperature to cause evaporation, then the evaporative atoms from the melted target move to the substrate surface and finally solidify to form films in a low-pressure environment.

The substrate is usually heated during the process of preparing the coating, in order to activate the surface of the substrate and then to improve the bonding between coating and substrate. When the atoms of the vapors impinge on the surface of the substrate, they may exist in several states: completely depositing onto the substrate, diffusing into the substrate and reacting with elements of the substrate, or re-evaporating from the substrate. All of these states can be controlled by changing the conditions of the substrate or the processing parameters of EB-guns.

The variable parameters include substrate temperature (T_s), shape, structure, composition and cleanliness as well as the electrical potential difference between the source of evaporation and the substrate. The substrate temperature plays a key role among these parameters. When the thickness of the films exceeds a few hundred nanometers, the crystal structure of the sediments depends on the substrate temperature. If the temperature of the substrate is $T_s < 2/3T_m$ (T_m —metal melting point, K), the metal atoms directly condense from vapor into solid phase; when $T_s > 2/3T_m$, the metal atoms change from vapor into a liquid phase (droplets); once the droplets reach a certain size they can be crystalloid.¹²

The following relationship exists between the substrate temperature and the microstructure of the coating, which is recognized as the classic EB-PVD coating-structural relationship model.

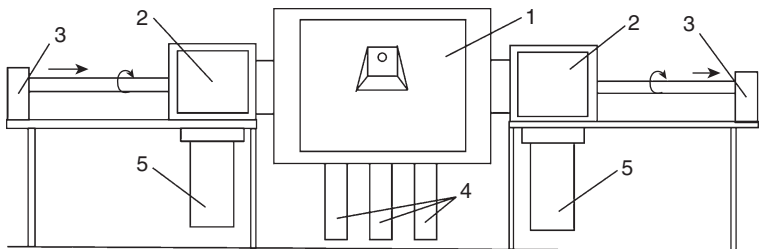
1. When $T_s/T_m < 0.3$, the coating presents as a dome of columnar structure due to a self-shadowing effect and an inadequate diffusion of the deposited atoms in the surface of the substrate. The grain boundary has more pores.

2. When $0.3 < T_s/T_m < 0.5$, a dense columnar grain structure forms and the coating structure forms owing to the condensation controlled by the surface diffusion. In this context, as T_s increases, the grain size of the columnar crystal also increases. A transition zone exists between zones I and II, which comprises close-packed fibrous grains.
3. When $0.5 < T_s/T_m < 1$, a recrystallization structure forms which is mainly controlled by volume diffusion.

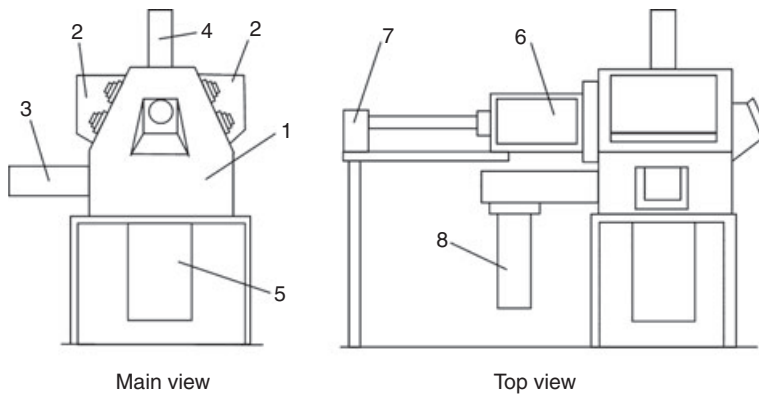
6.3 Manufacturing of thermal barrier coatings (TBCs) by EB-PVD

The EB-PVD method (illustrated in Fig. 13.1) is mainly used for the preparation of gas turbine engine blades, and its industrial production system consists of a central vapor deposition chamber (main chamber) and two target storage rooms (pre-vacuum chambers), equipped with a total of 2–6 electronic guns; one gun is used to pre-heat the substrate and other guns are used for heating target materials and causing evaporation of the materials. There are three water-cooled copper crucibles in the main vacuum chamber. The target material (bar) can be fed slowly by the lower transmission components. Three guns can heat three individual crucibles, respectively. In the evaporation chamber, the substrate can rotate or tilt simultaneously according to the needs of the workpiece geometry and coating thickness distribution. There are valves between the deposition chamber and the pre-vacuum room, so that the workpiece can be fed into the deposition chamber. While one workpiece is being deposited, the other is kept in a warm condition. When the deposition is finished, another pre-heated workpiece passes into the deposition chamber, thereby achieving continuous production.

Multipurpose EB-PVD equipment is illustrated in Fig. 6.2. There are six electron guns and four water-cooled crucibles equipped in the main vacuum



6.1 Industrial production system of EB-PVD:¹³ 1. main chamber; 2. pre-vacuum chamber; 3. horizontal transmission and rotation components of workpiece; 4. transmission components for target material; 5. vacuum chamber.



6.2 Multi-purpose EB-PVD equipment:¹³ 1. main chamber; 2. electron guns and housing; 3. horizontal transmission for shielding; 4. vertical transmission for workpiece; 5. transmission for target material; 6. pre-vacuum chamber; 7. horizontal transmission for workpiece; 8. vacuum chamber.

chamber, and the device has only a pre-vacuum chamber, which is different from the industrial production system. This device also has a workpiece-supported structure which could rotate around the vertical axis and feed a frame used for vacuum melting in the horizontal direction. Therefore, it can be used not only in coating but also in preparing multi-layer film and a variety of coatings, including depositing coatings in the C/C fibers, depositing superconducting coatings in conventional wire and preparing a new alloy or melting metals and alloy with electron beam.

The coating processing is finished in the vapor deposition chamber. Because coating material vapor needs to be uniformly distributed, the speed of coating materials, the activated gas pressure and electron beam scanning on the target must be precisely controlled.

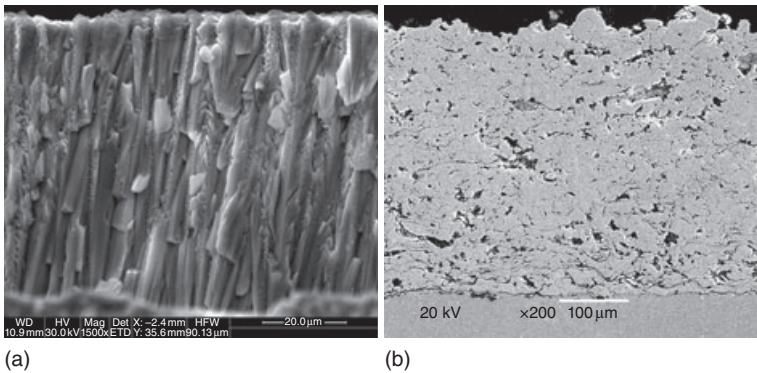
It is very important to pre-heat the vanes before the deposition of the coatings.¹⁴ The pre-oxidation of the bond coat before deposition of the ceramic coating can not only improve the combinational strength between the ceramic coating and the bond coat, but can also decrease the oxidation rate. The metal substrate temperature strongly influences the microstructure and life of the coating. Vanes are usually heated to 1073–1323 K before deposition. Since the sizes and qualities in various parts of the blade are different, and more heat is absorbed in the thick roots, the electron guns for warming should stay in the roots longer. Pre-heating procedures are designed according to the size and quality of a blade in order to ensure that the temperature of every part is uniform, rising to 1323 K within 15 min. Pre-heating blades with electron guns could heat one part precisely and achieve a uniform temperature field. It could increase the heating speed,

which boosts the rate of deposition in the coating. If the conditions are well-controlled, the blade surface temperature fluctuation will be ~ 10 K.

6.4 EB-PVD TBC microstructure and its advantages over plasma-sprayed coatings

The state-of-the-art TBCs consist of a ceramic top coat, typically 7 wt% yttria-stabilized zirconia (7YSZ), which has low thermal conductivity, is chemically inert in the combustion condition and has a relatively high coefficient of thermal expansion which is reasonably compatible with Ni-based superalloys.¹⁵ There are two main categories of metallic bond coat: one is the NiCoCrAlY-based system and the other is the Pt-modified diffusion aluminide. As 7YSZ is essentially transparent to oxygen at a high temperature, a TGO layer, mainly comprising thin, dense and continuous α -Al₂O₃, is formed between the bond coat and the YSZ top coat, thus providing oxidation protection.¹⁶ The top coats can be deposited by EB-PVD or by atmospheric plasma spraying (APS). The highly porous microstructures presented in EB-PVD and APS top coats reduce the inherent thermal conductivity. Thus, the differences in shape, orientation and pore distribution are the cause of the different values of thermal conductivity between EB-PVD and APS coatings.^{17,18}

Strain-tolerant TBCs are deposited with two methods, namely EB-PVD and APS. EB-PVD evaporates the oxide and directs the vapor onto the pre-heated component from an ingot. A columnar grain structure is formed during EB-PVD deposition (Fig. 6.3a).⁶ In the case of plasma spray, the raw material powders are melted and accelerated until they impinge upon the substrate at very high speed, rapidly solidifying to form a 'splat' (a flattened particle). The successive impingement of the molten particles and inter-



6.3 SEM micrographs of cross-sections of EB-PVD coating (a) and APS coating (b).

bonding among the splats develops to deposit coatings.^{19,20} The deposition is designed to incorporate inter-splat porosity with a network of crack-like voids that provide strain tolerance again, while lowering the thermal conductivity (Fig. 6.3b). Plasma spray (PS) deposition is a lower cost alternative.⁶

In the EB-PVD process, the coatings developed by vapor condensation offer superior strain tolerance and thermal shock resistance. The resistance to oxidation and corrosion is also better than APS coatings, and thus service life is prolonged.^{21,22} The interface in EB-PVD is integrated mainly by chemistry bonding. Furthermore, the surface finishing is smoother, cooling hole closure is avoided and an aerodynamic design of the blades is maintained. The columnar microstructure of EB-PVD coatings has been found to offer the superior performance and durability necessary for gas turbine blade applications.^{1,2} However, one disadvantage of EB-PVD coatings arises from the columnar structure, which leads to high thermal conductivity compared to that of APS coatings. APS coatings have a splat-based layered structure which offers advantages over EB-PVD in terms of insulation and cost-effectiveness.²⁴

Plasma spray TBCs have been applied to commercial parts of jet engines since the 1980s because of the relatively simple and inexpensive equipment required. Plasma-sprayed coatings are still used in combustors and other hot-gas path components although they have a porous and extensive cracked structure. Studies have shown that during thermal loading, the coating integrity could be lost as a result of damage propagation within the coatings.²

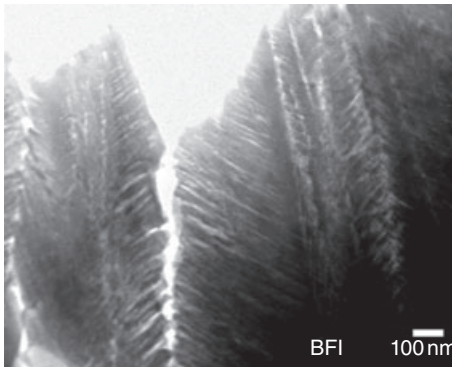
All major gas turbine engine manufacturers have used EB-PVD to produce TBCs. With further understanding of TBC systems, we would be able to improve maintenance scheduling, allow more positive usage and design systems with improved reliability and capability. Deposition parameters such as chamber pressure, substrate temperature and rotation speed have influenced the morphology and density of the columnar microstructure of EB-PVD TBCs accordingly.²⁵ The low thermal conductivity and high values of strain tolerance in the ceramic top coat are due to its intrinsic columnar microstructure. The efficiency of thermal insulation is closely related to the porosity of TBC materials. In the EB-PVD process, an electron beam heats the source material, then the vapor is produced and the evaporated atoms condense onto the substrate. Crystal nuclei form on the favored sites, growing either laterally or in the through-thickness direction, so as to form individual columns, resulting in a high degree of inter-columnar porosity.^{26,27} This specific coating structure provides more stress release with low in-plane Young's modulus under thermomechanical loading. Also, the structure can adapt to thermal stresses due to the coefficient of thermal expansion (CTE) mismatch. In addition, the microstructure and

texture throughout the thickness of the coating are variable during deposition, since growth depends on competitive processes.²⁸

6.4.1 Typical microstructure of the conventional TBCs

Due to its intrinsic columnar microstructure, the EB-PVD TBC exhibits low thermal conductivity and high values of strain tolerance. It has a unique microstructure containing individual primary columns, which grow on the substrate in a preferred crystallographic direction by adding atoms to the vapor phase. The growth of this column produces an inter-columnar open porosity which provides the TBCs with high strain tolerance. Substrate rotation during vapor deposition-processing produces an additional intracolumnar closed porosity. Furthermore, a feather-like subcolumnar structure forms at the periphery of each primary column with surfaces 45–60° inclined toward their growing axis due to over-shadowing (Fig. 6.4). The total porosity increases and therefore the thermal conductivity of the material is low. Finally, the secondary columns, so-called feather-arms, lie inside the columns due to the rotation of the specimens during the vapor deposition process, and an additional intracolumnar closed porosity inside the primary columns is produced as well (Fig. 6.4).^{25,28}

The YSZ-TBC shows a typical columnar structure which is normal to the BC surface. One column is generally believed to be a single crystal that grows continuously from the substrate. A single column consists of several different misorientated fine subcolumns, with nanopores along subcolumn boundaries. The YSZ plate-like grains in each subcolumn are stacked periodically along the growing direction of the subcolumn with a constant spacing. The nanopores at the subcolumn boundaries are perpendicular to



6.4 TEM showing the feather-like microstructure of EB-PVD YSZ coating.

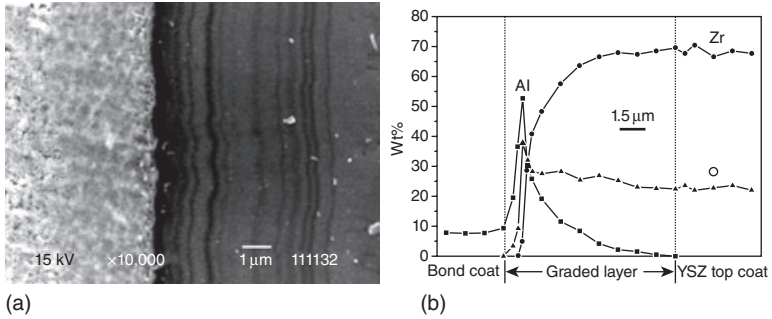
the growth direction of the subcolumns. Such nanopores are formed due to the misorientations of YSZ plate-like grains between subcolumns.^{25,29}

It is well accepted that the deposition parameters such as chamber pressure, substrate temperature and rotation speed can accordingly influence the morphology and density of the columnar microstructure of EB-PVD TBCs. Schulz and Schmucker³⁰ investigated microstructural properties of $\text{ZrO}_2\text{-4at\% Y}_2\text{O}_3$ coatings deposited with different thicknesses and at different substrate rotation speeds. The 0 rpm specimen consisted of simple, straight columns. The 1 rpm specimen had a wavy microstructure. In contrast, specimens deposited at higher rotation speeds consisted of straight columns with banded structures. Nanosized pores less than 50 nm in diameter could be observed in the columnar grains. All the coatings had a columnar microstructure with gaps between columnar grains. The grain size of the columns increased with increasing coating thickness and speed of rotation. The total porosity of the coating layers increased with increasing substrate rotating speed.

6.4.2 Multi-layered and graded TBCs

To overcome the disadvantages of YSZ, candidate materials that can withstand higher gas-inlet temperatures have been investigated, and multi-layered and graded structures have been produced. It has been shown that the thermal cycling lifetimes of the multi-layered coatings are two or three times longer than those of the single ceramic layer coatings.³¹ The multi-layered and graded structures are introduced below.

- **Multi-layer system:** Since thermal barrier coatings must endure arduous environments, such as corrosion, oxidation and thermal shock, it is necessary to develop a multi-layer system with several functions. Multi-layer systems generally consist of bonding layer, ceramic thermal barrier layer, anti-corrosion layer and diffusion barrier layer. The dense layer and barrier layer on the outside protect the inner layer from the diffusion of corrosive salts and other deposits into the metallic bond coat. Since there are a series of problems that remain unsolved in this multi-system, it has not yet been put into practical use. However, it is quite promising if the design of the system can be optimized.
- **Gradient-layer system:** In this system (shown in Fig. 6.5), the transition from metal layer to the ceramic layer is continuous and gradual.³² The sharp interface between metal and ceramic disappears. As a result, the premature spalling of TBCs due to the metal/ceramic thermal expansion coefficient mismatch is avoided. This coating structure design is considered to be the best solution in prolonging the thermal cycling lifetime

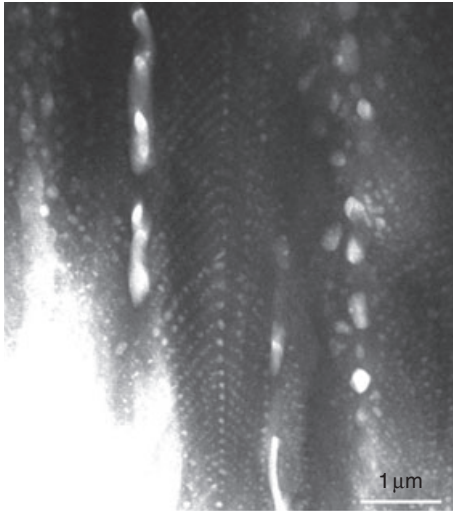


6.5 SEM micrograph of cross-section of gradient thermal barrier coating (GTBC) produced by EB-PVD (a) and related element profile across the thickness of the GTBC (b).³⁴

while ensuring thermal barrier insulation.³³ According to G. Zinsmeister's theory, when the electron beam evaporation power is constant, the vapor pressure of each phase in the mixture is dependent on the fraction of each phase in the mixture. Following this idea, a NiCoCrAlY/NiAl/Al₂O₃/YSZ gradient TBC was produced by co-evaporation and deposition of the mixture of Al–Al₂O₃–ZrO₂.^{33–37} During the processing, since $P_{\text{Al}} > P_{\text{Al}_2\text{O}_3} > P_{\text{ZrO}_2}$, the Al phase was first evaporated from the source of the mixture. As the temperature increased, the evaporation rate of Al₂O₃ increased gradually. Finally, the evaporation of ZrO₂ phase was also finished. As a consequence, a continuous structure and the transition of the composition between the bond coat and YSZ topcoat were realized. Afterwards, the deposited coatings were annealed in vacuum. During annealing, inter-diffusion between the bond coat and the transition layer occurred, resulting in the elimination of the interface.

On thermal exposure during service, the porous coatings will sinter, caused by ageing under service conditions, bringing about changes in the distribution and morphology of the open and closed porosity. The driving force for this process is the decrease in surface energy. The gaps between the individual columns were narrowed and even disappeared. The number of gaps between the subcolumns decreased. The sharp gaps observed in the as-deposited coating became blunted, as shown in Fig. 6.6. Also, the nanopores inside each column revealed spheroid morphology.

There are two important factors which affect the performance of the entire system. The first is that the thermal conductivity as one of the key functional properties of TBC will increase. Both inter- and intra-columnar porosity decrease as a result of sintering inducing reduction of the surface area. The columns join together to form blocks separated by cracks perpendicular to the interface. The cracks originate near the substrate/coating



6.6 TEM image of EB-PVD YSZ coatings after 100 h heat-treatment at 1373 K.

interface and run parallel to the interface, affecting the thermal conductivity. Thermal conductivity increases due to the alteration of the porosity distribution, size and morphology and the decrease in the amount of porosity.²⁸ Additionally, the in-plane strain tolerance is reduced after the columns sinter together to form bridges at the contacting points. The phases also change from the initial metastable tetragonal phase into a mixture of tetragonal phase in the case of the Y-PSZ coatings at high temperature.³⁸

6.5 Hot-fatigue behavior and failure mechanisms of TBCs

Thermal cycling lifetime is one of the most important properties for TBCs, which actually governs the duration of hot components in engines. However, there is lacking a reliable and precise method for evaluating damage and predicting the service life of TBCs based on thermomechanical characteristics.³⁹ The unique columnar microstructure of EB-PVD ceramics exhibits a higher strain tolerance, but failure still occurs by spallation.^{40,41} The failure of TBC systems usually occurs near the vicinity of the TGO scale, at the TGO/bond coat interface, within the TGO and at the YSZ/TGO interface.^{16,42-45} The failure mechanism is typically associated with buckling and spallation of the ceramic top coat from the TGO or at the TGO/bond coat interface.⁴⁶⁻⁴⁹ Final spallation of the TBC involves edge-cracking resulting

from oxidation and stress singularity, buckling and a 'link-up' of microcracks at the TGO/bond coat interface with the pre-existing microcracks at the YSZ/TGO interface.^{49,50}

For EB-PVD TBCs with PtNiAl bond coats, several mechanisms leading to TBC failure have been observed, including buckling, accelerated grain boundary oxidation, excessive TGO thickness and interfacial instability such as rumpling and ratcheting.⁵¹ There are several phenomena responsible for the spallation of YSZ after thermal cyclic oxidation, including formation and thickening of TGO resulting from oxidation of the bond coat; formation of the spinel such as Ni, Co-rich oxides; phase destabilization of YSZ coating; densification of YSZ coating by sintering; sulfur segregation; formation of voids at the TGO/bond coat interface.⁴⁹

In general, the TGO plays a significant role in affecting the thermal cycling life of EB-PVD TBCs.^{38,49} The TGO layer has two types of morphologies: regular undulation and irregular imperfections of thickness. The growth of the TGO layer follows the kinetics of parabolic law. Rumpling of the TGO/bond coat interface could cause localized cracking at the YSZ/TGO interface. Surface rumpling of the TGO occurs due to formation of voids at the TGO/bond coat interface and phase transformation of the bond coat. Formation of spinel is attributed to depletion of Al in the bond coat. The stress distribution in the direction of the thickness of the TGO layer is not uniform. The stress near the ceramic top coat is smaller than that close to the metal bond coat due to the stress in the direction of thickness.

TBCs tend to spall when they are subjected to thermal cycling due to thermal stresses generated by thermal expansion mismatching with the underneath metal substrate as well as the temperature gradients, residual stresses during deposition, phase transformations, progressive sintering of the ceramic top coat and environmental corrosion and erosion.⁵³ The stress in the TGO layer is significantly affected by the composition and structure of the top coat and bond coat, the creeping behavior of the bond coat and the morphologies and phase constituents of the TGO.³⁸

TBCs reveal different failure modes when they suffer from different serving conditions. These serving conditions are usually combinations of temperature gradient, mechanical loads and atmospheres coupled with oxidation and hot corrosion. There are two predominant failure modes for EB-PVD TBCs on turbine airfoils according to the engine-operating conditions. TBC failure typically occurs by cracking at one of the divides by the TGO interfaces (TBC/TGO or TGO/BC) when the TGO reaches a critical thickness of more than 5 μm under long-cycle, low-temperature operating conditions (cyclic oxidation). Under short-cycle and high-temperature conditions (isothermal oxidation), the damage to the interface would accumulate and the TBC failure would finally occur when fragmentation takes place. This type of failure is named 'ratchet'. The TGO undergoes displace-

ment instability when the TBC system is subjected to thermal cycling, being manifested as a localized penetration of the TGO into the bond coat at periodic sites along the TGO/BC interface.⁵³ Cracks form and extend laterally, due to the normal strains induced by the cycles by the downward displacements after being cycled. The cracks eventually coalesce, and then failure happens at one or two of the critical TGO interfaces. There is typically around 25% oxide layer debonding in length once the oxide approaches a thickness of 5–6 μm . The thermal expansion mismatching between the TGO and the substrate becomes a governing contributory factor in determining the failure under thermal cycling conditions rather than isothermal conditions.⁵⁴

In Section 6.3 we have mentioned that the initial oxidation of the bond coat surface before deposition can improve bonding between ceramic layer and the bond coat, and decrease the oxidation rate in service. Experimental observations relating the effect of bond coat pre-oxidation to TBC life have been described.⁵⁵ It has been shown that pre-oxidation of the bond coat under a selected range of partial oxygen pressures can improve the TBC life by more than two-fold as compared to a TBC without pre-oxidation. However, in both cases, the TBCs reveal similar failure mechanism, and the final TGO thickness and the depth of TGO penetration into the bond coat are nearly the same.⁵⁴ One explanation is that pre-oxidation can reduce the rate of ratcheting, thus decreasing TGO growing rate. The grains of the oxide formed in pre-oxidation processing are finer than those formed in an uncontrolled condition. As a result, the TBC after pre-oxidation treatment exhibits lower oxidation rate and much prolonged life.⁵⁴

It is also recognized that the failure mechanism of TBC is dependent on the type of bond coat. For TBCs with β -PtNiAl bond coats, the TGO thickens and elongates under high-temperature oxidation, which will lead to displacement instabilities. If the bond coat is relatively soft, the displacements are concessional, which would cause cracks to form in the TBC part above the TGO. Thus, the instabilities and TBC cracks propagate on a cycle-by-cycle basis, by a ratcheting mechanism. Another common system comprises a two-phase ($\beta + \gamma'$) NiCoCrAlY bond coat, which reveals a different TGO-based failure mechanism.⁵⁶ More than five metal elements exist in this bond coat. As a consequence, the TGO develops thickness heterogeneities which are a main feature of this system. The TGO contains various oxides rather than pure α -Al₂O₃, such as yttrium aluminum garnet (YAG) and other spinels. Both the magnitude of the 'pegs' and related geometric imperfections are sensitive to the composition of the bond coat, the deposition condition and the porosity, as well as the surface condition. The infusion of Pt into the surface can ameliorate these imperfections. In some cases, spinel oxides occur within the 'pegs', often accompanied by localized TGO cracks. These cracks seem to be confined to the region around the imperfections. However,

whether these localized cracks can be extended beyond the imperfections to cause delamination still remains to be ascertained. The PtNiAl system delaminates primarily along the interface between the TGO and the bond coat. In the NiCoCrAlY bond coat system, the cracks extend through the TGO only at the locations of the ‘pegs’, which do not enter into the TBC layer. A dominant delamination-cracking not only extends along the interface between the TGO and the bond coat but also traverses the ‘pegs’, leaving the TGO islands embedded in the bond coat.⁵⁷ The delamination cracks nucleate at occasional large ‘edge’ imperfections. Once the imperfections are formed, they will extend along the interface and finally result in failure of the TBC during the subsequent thermal cycles.⁵⁷

6.6 References

1. A. MARICOCCHI, D. BARTZ, D. WORTMAN, PVD TBC experience on GE aircraft engines, in W.J. Brindley (ed.), *Thermal Barrier Coating Workshop*, NASA-CP-3312, 1995, 79–83, NASA, Washington DC.
2. R.A. MILLER, Thermal barrier coatings for aircraft engines – history and directions, in W.J. Brindley (ed.), *Thermal Barrier Coating Workshop*, NASA-CP-3312, 1995, 17–34, NASA, Washington DC.
3. P. SCARDI, M. LEONI, L. BERTINI, L. BERTAMINI, Residual stress in partially-stabilised-zirconia TBCs: experimental measurement and modelling, *Surf. Coat. Technol.*, **94–95** (1997) 82–88.
4. Data file for X-ray diffraction, JCPDS-ICDD 27-997, International Center for Diffraction Data, Swarthmore, PA.
5. A. KULKARNI, A. GOLAND, H. HERMAN, *et al.*, Advanced neutron and X-ray techniques for insights into the microstructure of EB–PVD thermal barrier coatings, *Mater. Sci. Eng. A*, **426** (2006) 43–52.
6. M. MARTENA, D. BOTTO, P. FINO, *et al.*, Modeling of TBC system failure: stress distribution as a function of TGO thickness and thermal expansion mismatch, *Eng. Fail. Anal.*, **13** (2006) 409–426.
7. H.B. GUO, S.K. GONG, K.A. KHOR, H.B. XU, Effect of thermal exposure on microstructure and properties of EB–PVD gradient thermal barrier coatings, *Surf. Coat. Technol.*, **168**(1) (2003) 23–29.
8. H.B. GUO, H.B. XU, S.K. GONG, A study on EB–PVD gradient thermal barrier coatings under high-temperature hot-corrosion, *J. Mater. Sci.*, **37**(24) (2002) 5333–5337.
9. H.B. GUO, S.K. GONG, C.G. ZHOU, H.B. XU, Evaluation of hot-fatigue behaviors of gradient thermal barrier coatings by EB–PVD, *Mater. Sci. Eng. A*, **325** (2002) 261–269.
10. H.B. GUO, H.B. XU, S.K. GONG, Preparation of Al₂O₃–YSZ composite coatings by EB–PVD, *Mater. Sci. Eng. A*, **325** (2002) 389–393.
11. H.B. GUO, *Thermal fatigue behavior and failure mechanism of gradient thermal barrier coatings by electron beam physical vapor deposition*, Beijing University of Aeronautics and Astronautics, PhD Thesis, 2001.
12. X.Q. CAO, *Materials in Thermal Barrier Coatings*, Beijing, China: Science Press, 2007.

13. H.B. XU, S.K. GONG, F.S. LIU, Electron beam physical vapor deposition technology in Barton Welding Institute of Ukraine, *Aviation Engineering & Maintenance*, **6** (1997) 6–8.
14. E. REINHOLD, C. NEUS, P. BOTZLER, B.D. WENZEL, *et al.*, EB-preheating of turbine blades – the completion of EB-technology for thermal barrier coating, *Surf. Coat. Technol.*, **111** (1999) 10–15.
15. C. LEYENS, U. SCHULZ, B.A. PINT, *et al.*, Influence of electron beam physical vapor deposited thermal barrier coating microstructure on thermal barrier coating system performance under cyclic oxidation conditions, *Surf. Coat. Technol.*, **120–121** (1999) 68–76.
16. R.A. MILLER, Oxidation-based model for thermal barrier coating life, *J. Am. Ceram. Soc.*, **67**(8) (1984) 517–521.
17. D.D. HASS, A.J. SLIFKA, H.N.G. WADLEY, Low thermal conductivity vapor deposited zirconia microstructures, *Acta Mater.*, **49** (2001) 973–983.
18. J.R. NICHOLLS, K.J. LAWSON, A. JOHNSTONE, D.S. RICKERBY, Methods to reduce the thermal conductivity of EB-PVD TBCs, *Surf. Coat. Technol.*, **151–152** (2002) 383–391.
19. S.H. HILLMAN, R.M. GERMAN, Constant heating rate analysis of simultaneous sintering mechanisms in alumina, *J. Mater. Sci.*, **27** (1992) 2641–2648.
20. D. SEN, *et al.*, Pore morphology in sintered ZrO₂-8% mol Y₂O₃ ceramic: a small-angle neutron scattering investigation, *J. Alloys Compd.*, **340** (2002) 236–241.
21. R.A. MILLER, Current status of thermal barrier coatings – an overview, *Surf. Coat. Technol.*, **30** (1987) 1–11.
22. M. GELL, K. VAIDYANATHAN, B. BARBER, *et al.*, Mechanism of spallation in platinum aluminide/electron beam physical vapour deposited thermal barrier coatings, *Metall. Trans.*, **30A** (1999) 427–435.
23. U. SCHULZ, K. FRITSCHER, C. LEYENS, Two-source jumping beam evaporation for advanced EB-PVD TBC systems, *Surf. Coat. Technol.*, **133–134** (2000) 40–48.
24. D.J. WORTMAN, B.A. NAGARAJ, E.C. DUDERSTADT, Thermal barrier coatings for gas turbine use, *Mater. Sci. Eng. A*, **121** (1989) 433–440.
25. F. RENTERIA, B. SARUHAN, U. SCHULZ, *et al.*, Effect of morphology on thermal conductivity of EB-PVD PYSZ TBCs, *Surf. Coat. Technol.*, **201** (2006) 2611–2620.
26. A.J. ALLEN, S. KRUEGER, G.G. LONG, *et al.*, Small-angle neutron scattering studies of ceramic nanophase materials, *Nanostruct. Mater.*, **7**(1–2) (1996) 113–126.
27. A.J. ALLEN, J. ILAVSKY, G.G. LONG, Microstructural characterization of yttria-stabilized zirconia plasma-sprayed deposits using multiple small-angle neutron scattering, *Acta Mater.*, **49**(9) (2001) 1661–1675.
28. F. RENTERIA, B. SARUHAN, Effect of ageing on microstructure changes in EB-PVD manufactured standard PYSZ top coat of thermal barrier coatings, *J. Eur. Ceram. Soc.*, **26** (2006) 2249–2255.
29. Y. JUNG, T. SASAKI, T. TOMIMATSU, *et al.*, Distribution and structures of nanopores in YSZ-TBC deposited by EB-PVD, *Sci. Technol. Adv. Mater.*, **4** (2003) 571–574.
30. U. SCHULZ, M. SCHMUCKER, Microstructure of ZrO₂ thermal barrier coatings applied by EB-PVD, *Mater. Sci. Eng. A*, **276** (2000) 1–8.
31. J. ILAVSKY, G.G. LONG, A.J. ALLEN, C.C. BERNDT, Evolution of the void structure in plasma-sprayed YSZ deposits during heating, *Mater. Sci. Eng. A*, **A272** (1999) 215–221.

32. W.J. BRINDLEY, R.A. MILLER, TBCs for better engine efficiency, *Adv. Mater. Process.*, **8** (1989) 29–33.
33. H.B. GUO, H.B. XU, X.F. BI, S.K. GONG, Preparation of Al₂O₃–YSZ composite coating by EB–PVD, *Mater. Sci. Eng. A*, **325** (2002) 389–393.
34. H.B. XU, H.B. GUO, S.K. GONG, Development of gradient thermal barrier coatings by EB–PVD and their hot-fatigue behaviors, *Surf. Coat. Technol.*, **130** (2000) 133–139.
35. H.B. GUO, X.F. BI, S.K. GONG, H.B. XU, Microstructure investigation on gradient porous thermal barrier coatings prepared by EB–PVD, *Scripta Mater.*, **44** (2001) 683–687.
36. H.B. GUO, H.B. XU, S.K. GONG, Investigation on hot-corrosion of functionally gradient thermal barrier coatings, *J. Mater. Sci. Technol.*, **18**(1) (2002) 27–30.
37. H.B. GUO, S.K. GONG, C.G. ZHOU, H.B. XU, Investigation on hot-fatigue behaviors of gradient thermal barrier coatings by EB–PVD, *Surf. Coat. Technol.*, **148** (2001) 110–116.
38. A. AZZOPARDI, R. MEVREL, B. SAINT-RAMOND, *et al.*, Influence of aging on structure and thermal conductivity of Y–PSZ and Y–FSZ EB–PVD coatings, *Surf. Coat. Technol.*, **177–178** (2004) 131–139.
39. T. TOMIMATSU, S. ZHU, Y. KAGAWA, Effect of thermal exposure on stress distribution in TGO layer of EB–PVD TBC, *Acta Mater.*, **51** (2003) 2397–2405.
40. K. GREEN, T.M. POLLOCK, R.C. REED, *et al.*, *Superalloys 2004*, Warrendale, PA: The Minerals, Metals and Materials Society, 2004.
41. C.G. LEVI, Emerging materials and processes for thermal barrier systems, *Curr. Opin. Solid State Mater. Sci.*, **8** (2004) 77–91.
42. T.E. STRANGMAN, Thermal barrier coatings for turbine airfoils, *Thin Solid Films*, **127** (1985) 93–105.
43. M.J. STIGER, N.M. YANAR, M.G. TOPPINGS, F.S. PETTIT, G.H. MEIER, Thermal barrier coatings for the 21st century, *Z. Met.kd.*, **90** (1999) 1069–1078.
44. A.G. EVANS, D.R. MUMMS, J.W. HUTCHINSON, G.H. MEIER, F.S. PETTIT, G.H. MEIER, Mechanisms controlling the durability of thermal barrier coatings, *Prog. Mater. Sci.*, **46** (2001) 505–553.
45. P.K. WRIGHT, A.G. EVANS, Mechanisms governing the performance of thermal barrier coatings, *Curr. Opin. Solid State Mater. Sci.*, **4** (1999) 255–265.
46. S.M. MEIER, D.K. GUPTA, The evolution of thermal barrier coatings in gas turbine engine applications, *J. Eng. Gas Turbines Power*, **116** (1994) 250–257.
47. D. ZHU, R.A. MILLER, Determination of creep behavior of thermal barrier coatings under laser imposed temperature and stress gradients, *J. Mater. Res.*, **14** (1999) 146–161.
48. A.G. EVANS, M.Y. HE, J.W. HUTCHINSON, Mechanics-based scaling laws for the durability of thermal barrier coatings, *Prog. Mater. Sci.*, **46** (2001) 249–271.
49. S. DAS, S. DATTA, D. BASU, *et al.*, Thermal cyclic behavior of glass-ceramic bonded thermal barrier coating on nimonic alloy substrate, *Ceram. Int.*, **35** (2009) 2123–2129.
50. E.W. DOUGLAS, S. JOGENDER, M.A. ROBERT, Tailored microstructure of EB–PVD 8YSZ thermal barrier coatings with low thermal conductivity and high thermal reflectivity for turbine application, *Surf. Coat. Technol.*, **190** (2005) 132–149.
51. B.W. KEMPSHALL, Y.H. SOHN, S.K. JHA, *et al.*, A microstructural observation of near-failure thermal barrier coating: a study by photostimulated luminescence spec-

- troscopy and transmission electron microscopy, *Thin Solid Films*, **466** (2004) 128–136.
52. E. MARK WALTER, B. EIGENMANN, The mechanical response of three EB-PVD thermal barrier coating microstructures, *Mater. Sci. Eng. A*, **282** (2000) 49–58.
 53. J.A. RUUD, A. BARTZ, M.P. BOROM, C.A. JOHNSON, Strength degradation and failure mechanisms of electron-beam physical-vapor-deposited thermal barrier coatings, *J. Am. Ceram. Soc.*, **84**(7) (2001) 1545–1552.
 54. I. SPITSBERG, K. MORE, Effect of thermally grown oxide (TGO) microstructure on the durability of TBCs with PtNiAl diffusion bond coats, *Mater. Sci. Eng. A*, **417** (2006) 322–333.
 55. I.T. SPITSBERG, D.R. MUMM, A.G. EVANS, On the failure mechanisms of thermal barrier coatings with diffusion aluminide bond coatings, *Mater. Sci. Eng. A*, **394** (2005) 176–191.
 56. G.M. KIM, N.M. YANAR, E.N. HEWITT, F.S. PETTIT, G.H. MEIER, The effect of the type of thermal exposure on the durability of thermal barrier coatings, *Scripta Mater.*, **46** (2002) 489–495.
 57. T. XU, S. FAULHABER, C. MERCER, Observations and analyses of failure mechanisms in thermal barrier systems with two phase bond coats based on NiCoCrAlY, *Acta Mater.*, **52** (2004) 1439–1450.

Processing, microstructures and properties of thermal barrier coatings (TBCs) by plasma spraying (PS)

L. CHEN, China University of Petroleum, China

Abstract: A review is given of the process, microstructure and properties of plasma-sprayed thermal barrier coatings (PS-TBCs). The chapter first summarizes the main process methods, parameters and model of PS-TBCs before introducing the basic microstructural characteristics – splat, porosity and microcrack – and main properties – modulus, bonding strength and thermal conductivity – of PS-TBCs. The chapter goes on to discuss the relationship between the microstructure and mechanical properties of PS-TBCs and plasma-spraying parameters. In conclusion, some likely future trends in the field of PS-TBCs are described.

Key words: plasma spray, thermal barrier coatings, process methods, process parameters, process model, splat, porosity, microcrack, modulus, bonding strength, thermal conductivity.

7.1 Introduction

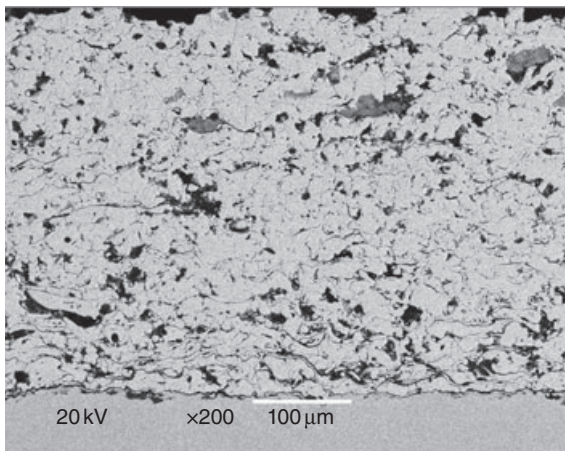
Plasma-sprayed thermal barrier coatings (PS-TBC) were invented in the 1960s to reduce the surface temperature of hot components by as much as 100–200 °C. Since then, they have been widely used in the fields of diesel, aerospace and land-based gas turbines and jet engines.^{1,2} Typical PS-TBCs usually consist of three layers, namely top coat (partially stabilized zirconia), an overlay of bond coat (MCrAlY) and the substrate. Partially stabilized zirconia (PSZ) containing 6–8 wt% of Y_2O_3 coatings (YSZ) demonstrates excellent thermal shock resistance, low thermal conductivity and relatively high coefficient of thermal expansion (CTE). The bond coat (MCrAlY) provides oxidation resistance.

The thermomechanical properties of TBCs are the key features making these materials useful. Notably, the porous, defected, layered microstructure of the plasma-sprayed coatings can substantially reduce the already low intrinsic thermal conductivity of YSZ by as much as 60% (typical thermal conductivities of plasma-sprayed YSZ are about 1 W/mK compared to the bulk value of 2.5 W/mK).^{3,4} Furthermore, the porosity, cracks and myriad arrays of interfaces also confer mechanical compliance on this system, enabling thermomechanical compatibility during cyclic thermal exposure

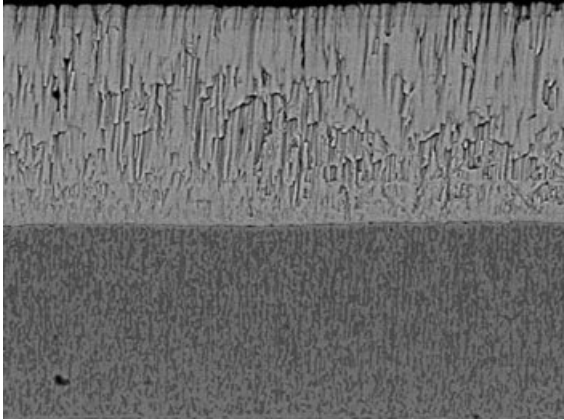
to operating temperatures between room temperature and over 1000°C. Finally, the YSZ system is also noted to have superior fracture toughness, adequate erosion resistance and thermochemical compatibility with the underlying bond coats and the dynamically evolving alumina scale at the interface.

By the 1990s, a second type of deposition process, electron beam physical vapor deposition (EB-PVD) TBC, had been successfully brought into commercial use. TBCs deposited by EB-PVD have been characterized as having a higher strain tolerance, smoother surface coating and better ability to control the microstructure of the deposited ceramics component to those deposited by plasma spraying. However, the PS-TBCs are currently the main preparation method in the fields of aerospace and power generation gas turbines because of their low cost, high production efficiency, adjustable and large range of coating thickness, easy control of ingredients and so on.⁵ The microstructure of a typical plasma-sprayed thermal barrier is illustrated in Fig. 7.1 and compared with that produced by EB-PVD, shown in Fig. 7.2.

Evolution of the complex microstructure and properties of plasma-sprayed coatings is related to a number of processing variables related to device, feedstock, process, deposition, etc. Despite scientific and technical progress on many fronts, the extraordinary complexity of the process and material variables has stymied both scientific understanding of the process-structure-property relationships and industry/application-related attributes, such as coating design, property characterization and, perhaps most importantly, reliability. In this chapter, the process, microstructure and properties and their relationship to PS-TBC will be mainly discussed.



7.1 Cross-sectional micrograph of a current state-of-the-art plasma-sprayed zirconia-yttria/MCrAlX TBC showing a porous and microcracked ceramic layer over a relatively dense metallic bond coat.



7.2 Cross-sectional photomicrograph of a current state-of-the-art EB-PVD YSZ/MCrAlX TBC showing a columnar ceramic over a relatively dense bond coat.

7.2 Processing of thermal barrier coatings (TBCs) by plasma spraying (PS)

Plasma-spray processing utilizes electrically generated plasma to heat and melt the feedstock material, a very intensive process requiring significant electrical power. It offers a method of depositing a feedstock material which is plasma-sprayed as a solid coating over an underlying target material. Deposits having a thickness from just a few micrometers up to several millimeters can be produced using a variety of feedstock materials, including metals and ceramics. In the plasma-spraying process, the material to be deposited, typically as a powder but sometimes as a liquid suspension, is introduced into the plasma jet emanating from a plasma torch. In the jet, where the temperature is about 10000 K, the material is melted and propelled towards a substrate. Then, the molten droplets flatten, rapidly solidify and form a deposit. Usually, the deposits remain adherent to the substrate as coatings. There are a large number of technological parameters influencing the interaction of the particles with the plasma jet and the substrate and therefore the deposit properties. These parameters include feedstock type, plasma gas composition and flow rate, energy input; torch offset distance, substrate cooling, etc. A typical plasma spray system consists of the following:

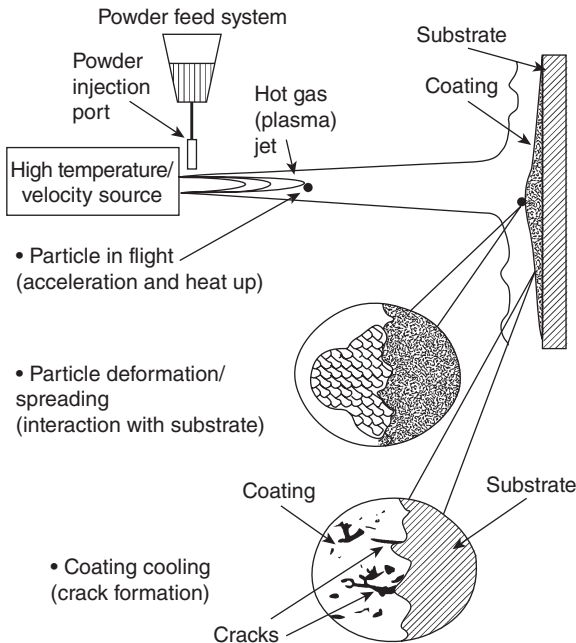
- spray torch (or spray gun) – the core device performing the melting and acceleration of the particles to be deposited;
- feeder – for supplying the powder or liquid to the torch;
- media supply – gases for generating the flame or plasma jet and carrying the powder, etc.

- robot – for manipulating the torch or the substrates to be coated;
- power supply – often for the torch only;
- control console(s) – either integrated or individual for all of the above.

7.2.1 Process method

The durability and failure mechanisms of PS-TBC are strongly dependent on the interfacial and microstructural features of the TBC system which are, in turn, linked to the method employed to deposit the individual layers. At present, there are several main processes for plasma spray preparation of TBC, such as atmospheric plasma spraying (APS), low-pressure plasma spraying (LPPS), laser cladding plus plasma spraying and solution precursor plasma spraying (SPPS), etc.

Atmospheric plasma spraying (APS) is a coating process carried out at normal pressure, which is usually applied to the ceramic coating on metallic structural components. In plasma-sprayed coating deposition, particles melt in the process of being deposited and when they impinge on the substrate, they flatten, undergo rapid solidification and form deposits known as splats, as shown schematically in Fig. 7.3.⁶ The high energy associated with the plasma-sprayed torches, and hence the impinging particles, gives rise to a



7.3 Schematic of air plasma spray process.⁶

rather rough and wavy interface which is fundamentally different from that produced by other methods such as EB-PVD. Furthermore, the presence of microstructural defects in the ceramics, i.e. porosities, generally introduces a long-term reliability problem as they tend to sinter after prolonged exposure at high temperatures leading to an increase in the coating elastic stiffness.

In order to overcome the limitations of APS, LPPS and vacuum plasma spray technologies are being developed. In the LPPS coating process, plasma spray gun, work piece and running machine are put in an airtight room with a low-vacuum environment. A low-pressure environment decreases the rate of oxidation of the feedstock powder as it melts in the plasma plume, and it also provides increased acceleration of the melted powder due to the decreased air resistance. The lower pressure also extends the length of the plasma arc, so that spray distances can be increased from 3–5 inches for normal plasma spray to 11–13 inches for LPPS. Compared with the ordinary APS coating, the LPPS coating is characterized by uniform and compact microstructure, low porosity, high purity, without oxide inclusion and smooth surface. The coating oxidation resistance performance is also distinctly enhanced.

At present, laser re-melting of the superficial layer of TBC prepared by PS may further remove the pores, inclusions, microcracks and other coating defects and enhance the coating quality and service life. Roughness results demonstrate a significant decrease after laser glazing.⁷

It is widely recognized that deposition of small, melted particles achieves a fine microstructure, which in turn leads to improvements in certain desirable mechanical properties such as strength and hardness. Unfortunately, it is generally impossible to feed powders finer than 5–10 μm due to the effects of surface forces on powder flow. Recently, the suspension plasma spray (SPS) process has been developed, partially to overcome this limitation. In this process, nano-sized particles are suspended in a liquid before being injected into the plasma plume, thus circumventing normal feeding problems.

Recently, a relatively new spraying technique, solution precursor plasma spray (SPPS), has been developed to deposit highly durable thermal barrier coatings. Similar to the existing plasma deposition methods, SPPS is based on the injection of liquid chemical precursors into a plasma jet and forming of a ceramic by pyrolysis in the plasma jet. In this process, an aqueous solution of the constituent metal salts (Zr and Y) is atomized and injected into a direct current (DC) arc plasma jet. The ceramic is formed by pyrolysis in the plasma jet before reaching the target material or, in some cases, after reaching the surface. This spray method is identical to APS deposition with the substitution of a solution atomizer for the solid powder feeder. The atomization characteristics can be varied, but it involves initial droplet sizes between 20 and 50 μm at various velocities up to 100 m/s. Plasma torch

operating power and gas flow rates are in the same range as used for depositing APS coatings.⁸

However, the primary difference attribute between SPPS and other methods is that the feedstock material is in the form of a liquid solution rather than a powder or a powder suspension. As a result, the SPPS process is able to deliver fine splats without the difficulties and limitations of both fabricating and feeding fine solid powders. Instead, SPPS has the challenges of formulating high-molarity solutions and engineering their chemical and physical properties.

7.2.2 Process parameters

The properties of TBC systems prepared by plasma-sprayed technology are dependent not only on the material being used and its microstructure but also on the process method and its parameters. There are many process parameters that influence plasma spray coating microstructure and properties. These parameters (summarized in Table 7.1.⁹) can be categorized into four groups: (i) plasma characteristics, such as plasma power, plasma gas flow rate, and plasma gas species, and geometry of the electrodes; (ii) powder feed parameters, such as size and shape of the powder, flow rate of the powder and carrier gas and powder injection site; (iii) plasma jet parameters, such as jet velocity and temperature, particle velocity and temperature, particle trajectories; (iv) particles at impact, such as particle velocity

Table 7.1 Processing parameters in plasma spraying⁹

Plasma characteristics	Power supply Plasma gas Mass flow rate plasma gas Cooling Mass flow rate cooling gas Nozzle geometry
Powder feed	Powder fraction and shape Thermal properties of powder material Carrier gas flow rate Injection geometry
Plasma jet	Jet velocity and temperature Particle velocity and temperature Particle trajectories
Particle impact	Particle velocity at impact Particle impact angle Molten state of particle at impact Substrate type Substrate temperature and roughness

at impact, particle impact angle, molten state of particle at impact, substrate type, roughness and temperature. Those parameters are not independent and they interact with one another.

Research has indicated that power input, substrate temperature, coating thickness and spray distance are closely correlated with the coating microstructure. The coating porosity may be reduced through enhancing power input, pre-heating substrate, reducing spray coating distance and adjusting appropriate spray angle. In order to reduce the hot corrosion attack of TBCs by oxidizing environments, some studies have tried to seal open pores on the TBC surface with organic materials, while others have used hot isostatic pressing (HIP) and laser remelting to post-treat the TBCs. These methods attempted to create a dense layer on the coating surface or a dense coating to prevent the oxidizing environment entering into the coating. On the other hand, studies have shown that inserting a graded coating between the ceramic and bond coat or changing the chemical composition of the ceramic coating can reduce the thermal stresses building up within the coating.

The average particle temperature and velocity distribution determine coating bond strength, porosity and coating inclusions such as oxides. It is generally accepted that higher velocities result in higher particle/droplet impact energy. This high kinetic energy leads to higher degree of particle deformation, producing better coating bonding strength and higher coating density. The temperature, velocity and environmental interactions of the particles are related to the particular jet velocity, temperature, resultant particle dwell time, all of which determine the subsequent coating microstructure and properties.

The dwell time of particles is controlled by gas velocity and powder particle characteristics. Gas velocity in turn is determined by the total gas flow through the nozzle and the gas characteristics. Particle velocity is then a function of jet velocity coupled with particle characteristics – that is, size, morphology and mass. The temperature of a given particle is thus a function of enthalpy, velocity, trajectory and its own physical and thermal properties.

The degree of melting particles in the plasma jet depends on their trajectories. The temperature and velocity vary considerably in the plasma jet, the most significant factor being the difference in temperature between the hot core of the jet and its relatively cold surrounding environment. The temperature drop from the jet core to the boundary is typically several thousand degrees over a few millimeters. This drop in temperature causes a corresponding drop in gas velocity and an increase in viscosity toward the outer boundaries. Temperature and velocity also decay as the jet exits the nozzle, so there are both radial and axial gradients of gas temperature, gas velocity and gas viscosity. Distributions of particles traveling in these

thermal jets are accelerated by the gas-velocity distributions through a distribution of temperature. Therefore, velocities and temperature of the particles in the plasma jet are dependent on the trajectories. Those particles injected into the core of the jet will melt and form splats to impact the substrate, while those with trajectories along the periphery of the jet will not melt or only partially melt. The unmelted or partially melted particles may be incorporated into the deposit causing lower deposit densities.

7.2.3 Process modeling

Due to the complexity of the phenomena, the process remains highly empirical, even after the practical use of plasma spraying for many years. The production of coatings is still based on trial and error approaches, depending on the experience and the instinctive feelings of the researchers. The irreproducibility of a high-quality plasma coating therefore continues to be a major problem for the rapid expansion of this technology. The main reason for this is the lack of understanding of the underlying physical processes during plasma spraying.

In order to create a higher reliability of coating production, it is necessary to gain a scientific understanding of different processes, namely the fluid dynamics of the plasma jet, the plasma-particle interactions and the particle impacts onto the surface. During the last years, many efforts by different authors have been made to gain knowledge of the interdependencies of plasma-spraying parameters and coating characteristics. However, the process is rather complex and only some of the phenomena involved were described sufficiently in the past. Reasonable tools to close this lack of understanding are simulation models as well as measuring and diagnostic techniques. Some comprehensive models that involve major physical mechanisms for plasma spray, i.e. transport phenomena of plasma flame, particle heating, acceleration, evaporation and oxidation, have been developed for predicting coating characteristics independent of selected spray parameters.⁹

7.2.4 Plasma jet modeling

A range of models has been proposed to calculate plasma jet temperature and velocity distributions. These models start with the results of the calculations described in the previous section or calculate temperature and velocity distributions at the nozzle exit consistent with the plasma gas flow rate and enthalpy. The codes consist of momentum and thermal energy equations for the multicomponent fluid mixture, continuity equations for each component of the mixture, taking into account the mixing with the surrounding atmosphere but usually neglecting chemical reactions, and state

relations for an ideal gas mixture with temperature-dependent specific heat, enthalpy and transport properties.¹⁰⁻¹²

The large velocity difference between the plasma jet and its surrounding atmosphere results in a large-scale engulfment of the outside gas which has been corroborated by shadowgraph, CARS spectroscopy measurements and probe sampling of the plasma jet. A multiphase model for turbulent flow could reproduce these effects. Such a model has been developed for an argon plasma jet flowing into an argon stagnant environment. The plasma jet is considered as a two-fluid mixture consisting of hot, out-moving fragments and cold, in-moving fragments. The results obtained for the axial distributions of temperature and velocity are in good agreement with measurements.¹²

7.2.5 Particle in flight modeling

The modeling of particle acceleration and heating in the flow uses the conventional equations for droplet motion in flows and heat transfer. However, some effects specific to the thermal plasma environment must be taken into account. The main effects are due to the high temperature gradient prevailing in the boundary layer surrounding the particles, strongly varying plasma properties, non-continuum conditions, thermophoresis, turbulent dispersion, evaporation and possible chemical reactions on the particle surface. The models based on the heat conduction equation are generally one-dimensional and allow the tracking of the melting, evaporation and possible resolidification front in a particle. However, recent work has shown that the large difference in velocity between the flow and particles can induce convective movements inside the particles.¹²

In the modeling of the plasma spray process, the injection conditions of the particles in the flow govern the particle trajectory distribution and therefore their treatment. Thus, these conditions must be as realistic as possible and involve the particle size, injection velocity and direction distribution at the injector exit. The description of powder injection that implicates a stochastic aspect is still a challenging problem.¹²

7.2.6 Splat formation modeling

With regard to splat formation, analytical models have been proposed for droplets impacting at 90° onto a smooth surface. They express the flattening degree as a function of dimensionless groups characteristic of the impact and spreading process: the Reynolds number that quantifies the viscous dissipation of the inertia forces, the Weber number that expresses the conversion of the kinetic energy into surface energy and a heat transfer parameter, the Peclet number, used to characterize the solidification rate. The

most popular analytical model provided by Madejski attempted to include viscous force, surface tension and crystallization kinetics. It can be simplified by assuming that the spreading is complete before solidification becomes significant and that the surface tension effects can be neglected. Surface tension effects are generally acknowledged to be minor under thermal spray conditions, except perhaps for droplet size $<10\ \mu\text{m}$ and at the end of the flattening process. Similar expressions with different constants have been established from analysis analogous to that of Madejski or from the fit of the results of numerical modeling.¹²

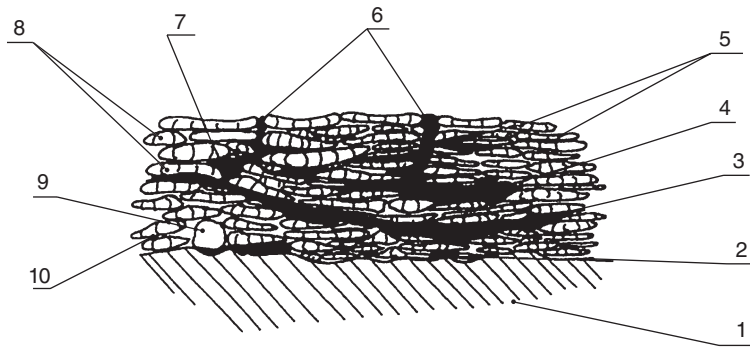
Over the last years, various numerical studies have dealt with the impact of a thermal-sprayed particle on a smooth surface. The majority assume a two-dimensional geometry and the most advanced solve the flow equations taking into account convective, viscous and surface tension effects. They track the material deformation during impact and involve the solidification process and heat interaction of the droplet with the underlying surface through an interfacial thermal contact. Such models enable the evaluation of the effect of particle parameters at impact on splat formation.^{12,13}

7.3 Microstructures of TBCs processed by PS

At present, the TBC topcoat is typically sprayed either by APS or LPPS. The plasma spraying process results in unique TBC microstructures which are greatly different from those of bulk materials and, consequently, many coating properties differ hugely from those of the corresponding bulk materials. The inherent complexity of the plasma spray process and the TBC microstructures represents a great challenge to the establishment of process–microstructure–property relations. A fundamental understanding of the microstructure properties is essential for process optimization and microstructural control.

The coating microstructures can be summarized as complex porous lamella structures consisting of a broad range of features, as shown Fig. 7.4. The pancake-shaped splat, about $1\text{--}50\ \mu\text{m}$ in thickness and $10\text{--}50\ \mu\text{m}$ in diameter, is the basic structural unit of a coating.¹⁴ A few layers of splats form a lamella which extends horizontally inside the coating, and distinct boundaries exist between lamellae. Inside a lamella, columnar grain structures which grow through splats can be observed. This indicates that the gradient direction of heat conduction is perpendicular to the spraying surface. An integral coating is made up of numerous lamellae.

Besides the layered structure, another prominent microstructural feature of a thermal spray coating is the ‘random’ distribution of a huge number of ubiquitous pores and voids of various sizes and shapes throughout the coating, which makes the coating appear sponge-like under scanning electron microscopy (SEM). To be precise, the pore distribution is actually



7.4 Schematics of typical plasma-sprayed coating: 1. Substrate; 2. Adherence defect; 3. Coating stratification (coherence defect) due to torch passes; 4. Coating stratification (coherence defect) due to relaxation of the residual stresses; 5. Cracks inside lamellae; 6. Vertical cracking resulting from residual stresses and open pores; 7. Closed pores; 8. Fully molten particles; 9. Unmelted particles; 10. Bad contact between lamellae.¹⁴

pseudo-random because the pores are more likely to be oriented close to the direction parallel or perpendicular to the deposition surface than to be at a much slanted angle. A truly random pore distribution will result in an isotropic coating with reduced stiffness.

Besides round, oval and elliptical pores, numerous long sharp crack-like horizontal delamination and vertical microcracks are visible. The delamination may lie either along the lamella boundaries (inter-lamella) or on the boundaries of splats in a lamella (infra-lamella). The vertical microcracks are caused by weak adhesion between lamellae or between splats. They usually initiate from the low-adhesive grain boundaries or some initial defects in the coatings and are believed to be caused by quenching and subsequent stress relaxation during the coating cool-down process when high biaxial tensile residual stresses are induced in the deposition surface.

This whole gamut of features encompasses a range of macro-, micro- and even nano-length scales. In this section, microstructural characterization across length scales of PS-TBCs will be discussed.

7.3.1 Splat formation

The basic characteristic of a PS-TBCs lies in its layered nature. As such, it is quite different from a bulk material. Since the deposit is a stack of layers, there is an inherent porosity associated with the structure. Also, this type of stacked structure introduces anisotropy in terms of microstructure and properties. The interfaces between layers play an important role in modify-

ing any property along the cross-sectional direction. Within a single spraying process, the differences in parameters generate a variety of particle temperature–velocity histories which in turn introduce a great amount of inhomogeneity within a coating. This layered coating structure is thus built up of a splat structure in which it is important to study an individual splat which is the building block.

Splats represent unit cells of plasma-sprayed coatings and their morphological and microstructural characteristics affect the properties of the coating. Many properties of the sprayed coatings, especially the adhesive strength to the substrate, depend remarkably on the splat behavior of the individual particles; hence splat morphologies become an important aspect. Splats are formed upon impact and flattening of molten droplets. The droplet size and impact velocity play important roles in the kinetics of the flattening and splat morphologies obtained. Flattening and cooling begin immediately after, and in some cases simultaneously with, droplet impingement. This flattening process includes spreading and solidification.

When a particle hits the substrate, the sudden deceleration causes a pressure build-up at the contact area. The high pressure forces melted material to jet laterally away from the point of impact. This causes fragmentation of splats and generates different morphologies. The liquid spreads outward from the point of impact and forms a splat. A very low kinetic energy means poor contact with the substrate and causes the splat to bounce off whereas a very high kinetic energy will cause it to splash. The arresting of spreading results from the conversion of particle kinetic energy into work of viscous deformation and surface energy, and it may also be effected through solidification. The spreading kinetics of the impacting droplet governs the splat shape and thickness.

Splat formation is also subject to the surface topography, wettability and reactivity of the substrate. Wetting affects the contact thermal resistance at the splat–substrate interface.¹² Under the same spray conditions, porosity increases if wetting is poor.¹⁵ If the surface of the substrate layer is rough, the flattening is also affected and the splats formed are thicker. The ability of the sprayed material to fill existing voids affects the quality of contact between the splat and the underlying layer, thereby controlling local cooling rate and overall heat transfer. Solidification and mechanical constraints can interfere with the flattening process.¹⁵

The study by Fukumoto *et al.* described the mechanisms of formation of fragmented splats and disk splats on room-temperature and high-temperature substrates.¹⁶ For a splash splat at room temperature, the bottom part of the splat solidifies rapidly after impacting onto the substrate and a porous microstructure is formed. This microstructure decreases the ability to transfer heat and acts as a heat insulator. Then the inside of the splat solidifies slowly and the viscosity increase is slow: therefore, the droplet flattens

rapidly with low viscosity. According to Raleigh–Taylor instability, the periphery of the splat becomes unstable and a splash splat forms. For a disk splat at high temperature, the contact condition is good owing to the good wettability and because the formation of the porous solidification layer is suppressed. Following this, the inside of the splat solidifies quickly. Therefore the viscosity of the droplet increases and most of the kinetic energy effectively is transferred to the viscous energy. The droplet thus flattens at lower velocity, resulting in the formation of a disk splat.

Splat morphology can be quantified in terms of properties such as splat flattening ratio and splat fragmentation index. Fragmentation degree in a way defines the degree of splashing and is given by $P^2/4\pi A$ where P is the perimeter of the splat and A is the splat area. Flattening degree describes how well the splat has undergone spreading and this is given by a ratio of diameter D of the splat over diameter d of the droplet.

Another important aspect of a single splat is the residual stresses that are generated upon its deposition and rapid solidification. Quenching of the impinging splat and restricted contraction lead to tensile stresses. Plasticity upon impact causes compressive stresses. Thermal mismatch between the coating and the substrate can be either tensile or compressive. Relaxation of these tensile stresses leads to microcracking of splats, a phenomenon more characteristic of ceramic splats than metallic splats.

An assemblage of millions of such splats consolidates to form the deposit. Therefore the coating structure is dependent on the details of solidification and resulting microstructure and morphology of splats. The physical phenomena involved in this process include heat and mass transfer, melt undercooling, selective nucleation of stable and metastable phases, non-equilibrium kinetics of crystalline growth, solidification, thermal resistance at the splats/substrate and splat/splat interfaces and substrate melting and resolidification.

In most cases, heterogeneous nucleation takes place at the contact between the molten splat and the colder substrate. The crystalline nuclei then grow into the undercooled melt in all directions and quickly form a solid layer covering the substrate surface followed by columnar growth normal to the substrate surface. A large temperature gradient exists in the solidified parts because of the high rate of heat transfer from the splat to the substrate. This rate can vary with substrate surface roughness, substrate temperature and substrate thermal properties, and also varying thickness regions of the substrate. Cooling rates in excess of 10^6 °C/sec result in solidification front velocities greater than 10 cm/sec with interface controlled heat transfer. This results in a stable solidification front leading to columnar solidification.¹⁷ Another study verifies that a stable planar interface does exist when the interfacial heat transfer coefficient across the melt and the substrate interface is large.¹⁸

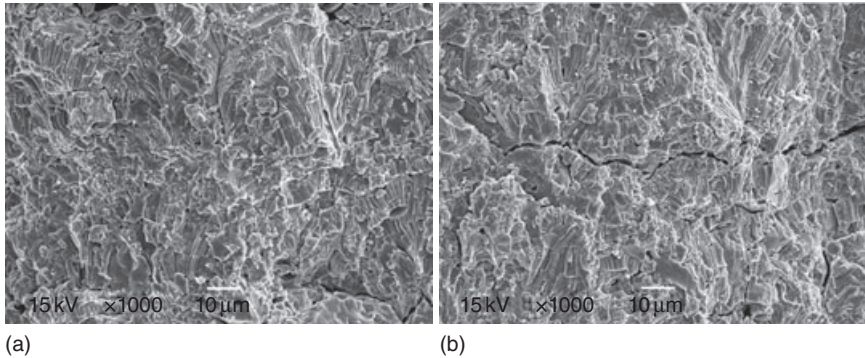
It has been shown before that spreading of a splat generates a core and a rim region. In the core region, where the particle droplet first comes in contact with the substrate, heat is extracted through the substrate and the solid liquid interface moves essentially upwards resulting in a columnar grain structure. In the case of the peripheral areas, the heat is extracted through the core region leading to radially elongated grains.¹⁹

Chraska and King studied single splats of YSZ using transmission electron microscopy (TEM), and a rapid solidification model was proposed for the observed narrow columnar grain structure: the heterogeneous nucleation and epitaxial growth mechanisms involved in the formation of first two splat layers are described for the YSZ ceramic coating. Nucleation in the second splat was seen to start at a significantly smaller undercooling than in the first splat.^{20,21}

7.3.2 Porosity

In addition to a 'brick-wall' structure, the thermal-sprayed coating also exhibits defect features such as globular pores, interlamellar pores, cracks, etc. Incomplete contact between successive splats and the presence of unmelted particles lead to the formation of voids. Rapid solidification and high-velocity impact of the molten particles give rise to inter-lamellar pores, while cracks are formed due to solidification thermal stresses and relaxation of tensile quenching stresses. Knowledge of the extent of these imperfections is critical since they may influence a wide range of coating properties and behaviors in service. Globular pores introduce porosity compliance which might be the origin of failure. Inter-lamellar pores enhance the thermal barrier effect but are also a source of delamination. The vertical microcracks in the splat relieve residual stresses, which are the first to sinter during thermal cycling. The sintering effects significantly change the pore architecture, with healing of intra-splat microcracks and enhanced inter-splat bonding. These are accompanied by pronounced grain growth. These changes lead to significant increases in both in-plane stiffness and through-thickness thermal conductivity. The latter is sensitive to increased inter-splat area, while the former is affected by both microcrack healing and improved inter-splat bonding.²² An illustration of how both inter-splat voids and intra-splat microcracks can coarsen and partially heal via sintering phenomena at elevated temperature is provided by the pair of micrographs shown in Fig. 7.5. While the temperature used for the heat treatment to which the coating in Fig. 7.5b was subjected was relatively high (1400 °C), the period concerned (10 h) was short compared to those common under service conditions.

Cipitria *et al.* have used a model to predict changes in pore architecture during sintering, and also the build-up and relaxation of global elastic



7.5 SEM micrographs of fracture surface of a YSZ coating produced by APS; (a) as-sprayed; (b) after heat treatment for 10 h at 1400 °C.

strains and stresses. While being stored, elastic strain energy levels in these coatings arising from (in-plane) inhibition of sintering shrinkage tend to remain low, while those from differential thermal expansion can be high immediately after a temperature change, particularly after being cooled to a temperature at which stress relaxation rates are slow. It has been shown that such strain energies, when converted to strain energy release rates per unit area for typical coating thicknesses, could exceed the fracture energy of the interface, and thus make spallation energetically favorable, particularly if the coating stiffness has been raised by sintering.²³

The amount of porosity, pore shape and distribution in TBC play an important role in its performance. Porosity is engineered into TBC to provide strain tolerance for the coating and to optimize thermal cycle life. If a TBC does not have adequate porosity then it may spall off because it cannot accommodate strains induced upon thermal cycling or by residue stress. If a TBC has too much porosity (by which the thermal resistivity is increased, but the mechanical bonding with the bond coat is decreased), then it has the potential to spall off due to oxidation of the bond coat. The pore shape (such as circular, oval, cylinder or cubic) and distribution (elongated transversely or longitudinally) also strongly affect the properties and performance of TBC. For example, if elongated pores are transversely distributed in TBC, the fracture energy is higher, thus TBC has higher resistance to spallation. However, TBCs with this kind of pore shape and distribution have higher thermal conductivity. Vice versa, if elongated pores are longitudinally distributed in the top layer, the TBC would be easier to delaminate due to lower fracture toughness, but may decrease the damage of the bond coat incurred by oxidation or hot corrosion and possess a lower thermal conductivity.²⁴

Many efforts have been made to classify the origin of different pores and estimate the pore size and shape distribution quantitatively.²⁵ The porosity rate of a coating is usually from 1 to 20%, varying largely with different coating methods. The porosity of APS ceramic coatings is, in general, between 3 and 20%. Generally, industry-standard TBC with 10–15% porosity is accepted. The existence of so many pores greatly reduces the elastic modulus and thermal conductivity of the coating. For example, the elastic modulus of a ceramic coating is only about one fourth or less of that of bulk ceramic, i.e. the ceramic coating is much more compliant.²⁶ Besides the reduced stiffness, many coatings also exhibit a certain degree of anisotropy or, to be precise, transverse isotropy. Five independent elastic constants exist for a transversely isotropic coating. The anisotropy is partially induced by the afore-mentioned pseudo-random distribution. Reduction of the coating stiffness in the direction perpendicular to the deposition surface is usually more significant, i.e. the effective modulus measured in that direction is often smaller than the effective modulus measured in the direction parallel to the deposition surface.

Microstructural characterization of thermal spray coatings involves quantitative measurements of geometrical features such as porosity (the form of voids, cracks and other defects) and analysis of material aspects in the coatings such as splat structure, interfaces, phases, etc. Various methods are employed for measurement of porosity, a prevalent feature in the microstructure.²⁷ Lavigne *et al.* and others have presented a reliable and reproducible procedure for characterization of porosity in PS–TBC using SEM and image acquisition (IA).²⁸ They have enlisted the methods used for metallographic preparation and SEM IA. Certain image analysis techniques have been employed to divide the net porosity into classes, such as globular pores and crack network.

7.3.3 Crack and fragment

As a key microstructure feature of PS–TBC, microcracks determine the performance and service lifetimes of the coatings by influencing their thermal conductivity and mechanical properties. In this section, crack formation in plasma-sprayed microstructures and its effects on mechanical and thermal properties are discussed.

Thin bonded layers on rigid surfaces show the familiar mud cracking pattern of meandering cracks intersecting to fragment the layer into independent pieces under biaxial stress. It is often seen on ceramic glazes, dry earth and tectonic plates. Three processes are involved in the formation of these features: vertical through-thickness cracking of the film, lateral elongation of this vertical crack and cracking parallel to the interface within the film, interface or substrate causing delamination.²⁹

The residual stresses induced in the fabrication process of PS–TBCs are associated with crack and fragment. In addition, they will strongly influence the coating adhesion strength, resistance to thermal shock, life under thermal cycling and erosion resistance.³⁰ Residual stresses are believed by many researchers to affect TBC integrity in high-temperature applications.³¹ Some experiments conducted show that the thermal fatigue lifetime of some TBCs is directly related to the magnitude of the residual stresses. As another example, the compressive residual stresses were sometimes thought to be the cause of coating spallation from the ceramic bond interface. The mechanisms which cause residual stresses in thermal spray coatings have been discussed extensively.³² Generally, three distinct processes have been singled out as the most conspicuous mechanisms active in inducing residual stresses in the coatings. These are (i) phase transformation of ceramic in the cooling process; (ii) primary cooling of the hotly melted spray particles from their impinging temperature to the elevated substrate temperature (deposition temperature), namely, the solidification process of splats; (iii) secondary cooling of the coating system, including substrate, from the elevated deposition temperature to room temperature, i.e. the thermal mismatch effect.

The first mechanism concerns phase transformations. For example, unstabilized pure zirconia which cools down from an impinging temperature well above 2500 °C to room temperature will transform from tetragonal phase to monoclinic phase. This phase transformation will bring about an internal volume increase of about 8% inside the zirconia and vice versa. Consequently, very large residual stresses will appear. However, in real applications, pure zirconia is rarely used. Instead, PSZ, for example, ZrO₂–6–8 wt% Y₂O₃ where yttria is added as stabilizer, is used.³³ The added stabilizer can minimize the phase transformation effect and keep the highly disruptive volume change at bay. Moreover, a small amount of phase transformation in the coating is thought to actually ‘toughen’ the coating and render major cracks less likely to form. This phenomenon is called the ‘transformation toughening effect’.³⁴ The benefit of transformation toughening is to render the PSZ coating superior to the fully stabilized zirconia coating, but there have been few theoretical analyses to explain the physics of such a phenomenon.

The second mechanism is the solidification process of the molten coating powder on top of its substrate after exiting from the nozzle of the spray gun. This process is usually called quenching or primary cooling. The temperature (T) of the molten powder is usually between 2500 and 3000 °C. Since the cooling rate of the spraying particle is very high, typically about 10⁶ °C/sec, it takes only about 1 μs for a very thin splat (a few micrometers in thickness) to contract and condense on the underlying material which is extremely thick relative to the splat. Therefore, the underlying substrate can

be regarded as rigid compared to the impinging and condensing thin layer of splat. Consequently, the ensuing residual stresses (quenching stress) in the condensing splats due to solidification are tensile stresses. The magnitude of the tensile residual stress from the above scenario can be estimated from $\sigma = E * \alpha (T - T_{\text{dep}})$, where E and α are the elastic modulus and the coefficient of thermal expansion (CTE) of the splat, respectively, and T_{dep} is the deposition temperature (200–400 °C). According to such a formula, the stress can reach as high as 200 MPa.

The above estimation is purely theoretical. In practice, residual stresses due to solidification are not so significant since other ongoing processes reduce the tensile residual stress. First, the tensile stress inside coatings will inevitably induce microcracking and other structural degradation which in turn can reduce the tension inside the coatings. This process is similar to stress relaxation and the stress relaxation of a NiCrAlY coating has been studied.³¹ On the other hand, the continual deposition of material on top of the previously deposited laminar coating will induce compressive stress underneath the current layer of deposition. As the coating thickness builds up, much of the tensile residual stress induced during solidification might be compensated by the compressive stress. These facts imply that the actual residual stress due to primary cooling is much smaller than that predicted theoretically. Some authors have even argued that solidification is quite insignificant in terms of generating residual stresses in coatings.³⁵

The third mechanism is secondary cooling where the coated substrate cools down from the deposition temperature to room temperature after thermal spraying is accomplished. The mismatch of the CTEs of different materials is the major reason that large residual stresses ensue after cooling. In fact, the thermal mismatch effect can be so great that it may constitute the major source of the residual stress in the coatings. Consider a common ceramic/bond coat/substrate system. The residual stress due to thermal mismatch will be largely compressive in the ceramic coating under ambient conditions because of the relatively low CTE possessed by the ceramic coating. Such compressive stress is in contrast with the tensile residual stress generated by the solidification/quenching process. It should be noted that the residual stress in the bond coat due to secondary cooling is also tensile. Secondary cooling is the only mechanism of residual stress generation.

Residual stresses develop in TBCs during processing and thermal cycling as a result of the thermal expansion mismatch between the thermal grown oxide (TGO) and the underlying metal and because of bond coat oxidation. These stresses provide the driving force for the failure of TBCs.

The residual stresses in TBCs can be distinguished according to their origin: stresses developing during oxidation at high temperature are called growth stresses; stresses which develop during cooling due to the difference

of the thermal expansion coefficient of the metallic substrate and the oxide are called mismatch stresses. The ambient stress status in each layer of a TBC will change with the variation of TGO thickness, TGO/bond coat interface morphology and material properties.^{36,37}

For APS TBCs, the coating usually fails within the ceramic top coat and near the YSZ/TGO interface.³⁸ Therefore, the stress state, especially the stress normal to the YSZ/TGO interface, in the APS YSZ coating is of great interest in the understanding of coating failure mechanisms and life prediction modeling. The stress distribution within the YSZ depends on TGO thickness, material properties of YSZ and YSZ/TGO/bond coat interfaces morphologies.^{39–43} When the TGO is thin, the YSZ on top of the peaks of the wavy interface is in tension, whilst the YSZ above the trough is in compression. With the thickening of TGO, the stress of YSZ above the peaks transforms from tension to compression, while the stress status of YSZ on top of the trough (about the same altitude of the peak) transfers from compression to tension. It was found that the maximum tensile stress occurred around the shoulder of the peak.^{43,50}

The stress in the TGO has an important influence on TBC failure. There are two main sources of stress: one from the thermal expansion misfit upon cooling and the other from TGO growth. Ambient temperature measured by the photo-stimulated laser piezo-spectroscopic technique indicates that the TGO is in compression (3–6 GPa).^{44–47} The stress in TGO may be alleviated by TGO creep or TGO/bond coat interface rumpling and redistributed in the vicinity of imperfections.^{48,49}

The stress normal to the YSZ/TGO and TGO/bond coat interfaces is related to TGO thickness and interface morphology. It has been shown that for a thin TGO layer, the stress at the YSZ/TGO interface is tensile at convex locations and compressive at concave locations.⁵⁰ With the thickening of TGO, the normal stress at the YSZ/TGO interface is usually compressive. For the TGO/bond coat interface, the convex locations are always in tension while the concave places are in compression.⁵⁰

Residual stresses can be measured by monitoring the bending curvatures of free-standing as-sprayed coatings.⁵¹ A more accurate method is X-ray diffraction. However, conventional X-ray diffraction is only able to measure the residual stresses at a depth within 10 μm of free surface. Any measurement of deep residual stresses requires chemical or mechanical removal of layers.

Bond strength and thermal fatigue life are strongly related to the thermal mismatch strains within the TBC and between the TBC and the substrate materials. One way of reducing the thermal mismatch strain is to form functionally graded materials (FGMs). The gradient layer can be continuous on a microscopic level. FGM coatings can be laminates comprising gradients of metals, ceramics or just a variation in porosity/density, etc. They

have superior properties to duplex coatings. The bond strengths for FGM and duplex coatings are about 18 MPa and 9 MPa, respectively. The thermal cycling resistance of the FGM coating is six times that of the duplex coating.⁵²

7.4 Properties of TBCs processed by PS

There are a number of mechanisms identified for the failure of TBC in service. Coating-delamination failure is closely related to the thermal stresses (including the internal stresses of the top coat, stresses inside TGO and mismatch in the coefficients of thermal expansion between top coat and bond coat) in the coating systems as well as the oxidation of the bond coat and substrate. Coating failure may be further accelerated by shrinkage-cracking and elastic-modulus increase from ceramic sintering and creep with an associated density increase at high temperatures.

Ceramic coating sintering and creep at high temperatures are among the most important issues for the development of advanced TBC. Sintering and creep not only can result in considerable coating thermal conductivity and elastic-modulus increase that will lead to reduced thermal insulation and increased thermal stresses, but they can also cause shrinkage-cracking, eventually leading to spallation of the coating. The densification and deformation of porous, microcracked ceramic TBC due to sintering and creep involve stress and thermally-activated diffusion and mechanical compaction processes. Faster shrinkage rates are observed initially, followed by slower but relatively constant rates for longer sintering times. Higher temperatures and compressive stresses will lead to a higher sintering/creep rate.

7.4.1 Modulus

The sintering densification process also results in an increase in the elastic modulus of the porous ceramic coating at high temperatures. Depending upon the actual temperatures and stresses experienced by the coating, a significant elastic modulus gradient will develop and evolve with time under high heat flux conditions. The surface of exposed TBC ceramic coating showed very fast modulus increase rate while much longer time is required for the inner layers of the ceramic coating to attain the maximum modulus value. The coating modulus increase results from the coating sintering and densification.

Measuring the properties as well as internal stresses of a thermal spray coating always represents a challenge since the coating itself is usually very thin and attached to a substrate. Any effort to separate the coating from its substrate may alter the internal stresses and even some properties of the coating. Only a brief introduction to various experimental methods for modulus and yield strength is presented here.

There are several methods for measuring Young's modulus of plasma-sprayed TBGs. These include indentation, four-point bending and ultrasonic techniques. Sub-sized and nano-indentation techniques are often used to measure mechanical properties at the surface of thin films. The nano-indentation technique was originally developed to measure Young's modulus and hardness of materials by interpreting the load–penetration response of the sample. It has subsequently been widely used for measuring properties of bulk materials and thin films.

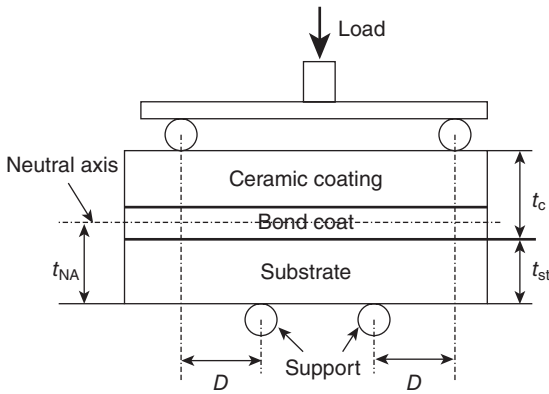
In combination with analytical and/or numerical models, a load–displacement curve formed by the load and penetration depth in a sub-sized indentation test can be used to estimate mechanical properties. As the area tested by nano-indentation only samples a very small region of material with a typical size of less than one grain, mechanical properties determined by this technique are in general in a probability distribution, affected by a variety of factors such as defects. To describe the consistency of materials, a Weibull distribution based on the weakest-link principle is usually adopted to interpret the nano-indentation results.

Using micro-/nano-hardness indentation to determine mechanical properties of materials such as modulus and yield strength is largely an empirical technique based on some well-derived data from known materials. In most cases, the correlation is realized in a form of $H-C \cdot \sigma$, where H is some micro-/nano-hardness measure, C is a constant or function of material property and σ is the material property of interest. When applied to an 'unknown' material, it becomes invalid. Moreover, as the indentation size is typically much less than the material grain size, the experimental results are sensitive to the microstructural characteristics in the vicinity of the tested area, which may cause a scattering of test results.

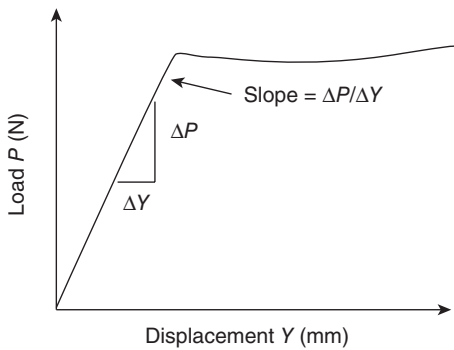
Although they are widely used to reveal materials properties, sub-sized and nano-indentation techniques are not suitable for characterizing the full range of desired mechanical properties of bond coats as a function of temperature. The Vickers microindentation technique has been used to estimate strengths of different bond coats at room temperature.

Four-point bending techniques have been used extensively in the characterization of various mechanical properties of metallic and ceramic materials, including Young's modulus, strength, fracture toughness, stress relaxation interfacial fracture resistance and fracture strain. Figure 7.6 is a schematic of four-point bend testers. Load and displacement of the cross-head are recorded for measurement of properties. A typical load–displacement curve obtained in a four-point bending test is shown in Fig. 7.7. Young's modulus and yield stress were derived from the following equations:

$$E = 2D^3 \Delta P / (3 I \Delta y) \quad [7.1]$$



7.6 Schematic of four-point bend testers.



7.7 Typical load–displacement curve obtained in a four-point bending test.

$$\sigma_y = P_y D t / (4 I) \quad [7.2]$$

where E is modulus, σ_y is the yield stress, D is the distance between the loading and supporting point, I is moment of inertia, $\Delta P / \Delta y$ is the slope of ‘elastic’ portion of the load–displacement curve, P_y is the yielding load and t is the thickness of the specimen.

Although four-point bending techniques are convenient to measure a variety of mechanical properties of different materials, their application on thin-foil layers ($<250 \mu\text{m}$) generally needs an addition of a much thicker substrate whose properties are well known. Moreover, the statistically determined properties are impinged on by various parameters such as residual stress, layer thickness and substrate temperature. All these factors mean that four-point bending techniques are not appropriate for accurate measurements of the properties of (Ni,Pt)Al bond coats, especially at elevated temperatures.

7.4.2 Bonding strength

Typically, grit-blasted, rough substrate surfaces are used for thermal spray coating deposition because of the established relationship between substrate surface roughness and coating adhesion.⁵³ The surface roughness effect on mechanical interlocking by calculations which show that a higher maximum pressure is generated at particle impact after increased substrate surface roughening. Alternatively, other researchers have demonstrated the importance of chemical bonding by showing comparable adhesion of thermal spray coatings onto smooth surfaces that were laser surface prepared, during deposition, to remove native oxides.

In general, the inter-atomic forces for particle bonding after impact during thermal spray deposition can range from weak van der Waals forces to strong chemical bonding forces, i.e., ionic, covalent or metallic bonding. For the case of air plasma spray deposited coatings, where complete particle melting leads to malleable particles impacting the substrate, mechanical interlocking must also be considered for long-range (1–10 μm) bonding.

Mechanical interlocking as a theory for thermal spray coating adhesion arises from the early observation that coatings adhered best to roughened substrates. Mechanical interlocking is evident as the penetration of impacted particles into valleys of the substrate or previously deposited layers. This is an especially important bonding mechanism for molten particles, which easily deform upon impact, even at the high strain rates occurring during thermal spray deposition.

While mechanical interlocking may be a primary bonding mechanism for molten powders, it does not adequately explain the adhesion of partially molten or non-molten ceramic YSZ particles. When unbonded surface zirconium, yttrium and oxygen sites on Y_2O_3 -stabilized ZrO_2 particles meet with other unbonded atoms within a 0.15 nm distance at elevated temperatures, a fraction of the unbonded sites will chemically bond. The close inter-atomic distance required for chemical bonding is considered to be traversed by solid-state and liquid phase diffusional transport of atoms.⁵⁴ The kinetics of diffusional transport must be evaluated in order to fully analyze the bonding mechanism.

Although there is no agreement on how to explain all observed coating failures, it is agreed that choosing an appropriate measurement to gauge the bonding strength of a thermal spray coating is of utmost importance in order to quantitatively calibrate aspects of coating integrity such as failure strength and fatigue lifetime. Such a bonding strength measurement will be essential for designing a thermal spray coating. So far, the widely accepted measurement of coating bonding strength has been the average debonding stress from the standard tensile adhesion test stipulated in ASTM C633-01.^{55,56}

The average debonding stress is without doubt simple to obtain, but it ignores the fact that a thermal spray coating is full of defects such as pores and cracks. It was found that there was a large variability in the bonding strength determined by the tensile adhesion test.⁵⁷ It is well known that existence of a crack will reduce the debonding stress, and the larger the crack the lower the debonding stress. Obviously, the difficulty of applying the debonding stress according to ASTM C633-01 is that it does not account for the structural defects inherent in the coating. Therefore, the debonding stress may not be an appropriate measurement of coating bonding strength. Instead, the fracture toughness which accounts for the interior coating defects is recommended as the measurement of coating bonding strength.

The fracture toughness of a YSZ coating has also been studied by Heintze and McPherson.⁵⁸ Coating toughness was found to be related to the composition of transformable tetragonal phase, i.e., addition of stabilizer such as yttria changed the toughness of zirconia coating.

The term 'fracture toughness' is sometimes ambiguous in context. It is often referred to as the critical stress intensity factor (SIF) since the SIF is an old and more understood fracture mechanics concept. However, by this reckoning, the fracture toughness implies the critical energy release rate which is more appropriate than the critical SIF because of the inherent mixed-mode situation encountered in the multi-layered thin coatings.

7.4.3 Thermal conductivity

The temperature- and time-dependent change in coating thermal conductivity is one of the most important parameters required for coating design and life prediction. The increase in thermal conductivity due to ceramic sintering can result in reduced coating thermal insulation and increased bond-coat/substrate oxidation.

There are three possible sources of heat conduction: lattice vibrations (phonons), photons and electrons. In dielectric materials, phonons dominate thermal transfer. They can be scattered by other phonons, crystal imperfections and surfaces. Phonon conductivity is the proportionality constant that relates the rate of heat flow per unit area and the temperature gradient. Thermal conductivity depends on the phonon mean path and the velocity as well as the lattice heat capacity. The phonon mean free path is the average distance traveled between scattering sites. Porosity, cracks and lattice defects all serve as phonon scattering centers, decreasing the phonon mean path and its conductivity. As discussed above, porosity and micro-cracking are typical microstructural features found in plasma-sprayed coating, which tend to lower thermal conductivity.

Pore shape and orientation, as well as percentage of porosity, affect coating properties such as thermal conductivity and elastic response.

Inter-splat porosity can be thought of as parallel cracks oriented perpendicular to the heat flow. Cracks oriented parallel to the direction of heat flow do not affect a material's thermal resistance, whereas those oriented perpendicular to the heat flow direction provide the maximum reduction in conductivity. It is clear that a low thermal conductivity coating should possess porosity oriented perpendicular to the temperature gradient, i.e., parallel to the substrate. Thus plasma-sprayed coatings are quite suitable for thermal barrier applications due to the lamellae structure.⁵⁹

There are two mechanisms by which thermal resistance can be enhanced via interfaces in multi-layer structures: (i) process of phonon reversal and (ii) interfacial resistance. The dominating operating mechanism depends on the individual layer's thickness. The process is only likely to occur given a layer thickness on the order of nanometers. For example, a TiO film on a fused silica substrate with a moderate interfacial resistance of $10^{-7} \text{ (m}^2\cdot\text{K)/W}$ was experimentally found to decrease the thermal conductivity in a 1 μm film by 50% relative to a bulk material.⁶⁰ There was further reduction in conductivity with thinner films on the order of 10 nm thick. On the other hand, interfacial resistance can contribute in systems with micron thick layers. Since boundaries serve as phonon scattering sites, the degree of scattering will theoretically increase with the number of interfaces in a given volume of material. This enhanced phonon scattering is the underlying source of interfacial resistance. The general theory of improving thermal resistance by layering has been studied using plasma-sprayed interfacial resistance. The theory is commonly determined experimentally by measuring the thermal conductivity of layered materials with varying numbers of interfaces.⁶¹

This interfacial phenomenon has also been observed for internal boundaries within a given material. Thermal conductivity of heat-treated plasma-sprayed YSZ coatings has been found to be higher than that of as-sprayed coatings.⁶¹ Microstructural evaluation indicates that sintering during heat treatment eliminates many inter-splat interfaces. The increase in thermal conductivity has been caused by a decrease in the number of boundaries between splats and pores.

7.5 Conclusion

Since the 1960s, the development of PS-TBC technology has made reasonable progress and achieved considerable economic efficiency. However, it is far from being able to meet the demand for technological progress in terms of spraying equipment conceptualization, spray craft optimization, coating evaluation and coating life forecast as well as functional coating. In the future, research in PS-TBCs technology should concentrate on the following aspects: (i) Online monitoring technology should be used to measure

the hydrodynamics characteristic of powder in plasma flame – this will assist in achieving a thorough understanding of the forming process of TBC and the mechanism by which various spray parameters influence TBC structure and performance. Multi-scale simulation and advanced test methods should be used to study the physical, chemical and mechanical behaviour of PS–TBC and to consolidate understanding of correlation failure theory for coating material and structure in a high-temperature environment. (ii) An established method and standard for PS–TBC is required along with development of testing technology for physical and chemical properties. (iii) The direction of progress in plasma-spraying equipment is likely to be in the development of high-energy and high-speed plasma spray along with powder feeding techniques, multi-purpose integrated technologies and real-time control technology. (iv) Establishment of a spray parameter database and model will allow the design and optimization of PS–TBC to continue. Functional gradient coating will develop and will enable controllability of coating performance. This new generation of TBC has evolved from an understanding of improvements to the structure, properties, processing and failure modes of earlier TBC systems. Such understanding will continue to improve TBC performance.

7.6 References

1. HODGE P.E., MILLER R.A., GEDWILL M.A. (1980), Evaluation of the hot corrosion behavior of thermal barrier coatings, *Thin Solid Films*, **73**, 447–453.
2. BENNET A., TORIZ F.C., THAKLEER A.B. (1987), A philosophy for thermal barrier coating design and its corroboration by 10000 h service experience on RB211 nozzle guide vanes, *Surf. Coat. Technol.*, **32**, 359–375.
3. CAO X.Q., VASSEN R., STÖVER D. (2004), New double-ceramic-layer thermal barrier coatings based on zirconia–rare earth composite oxides, *J. Eur. Ceram. Soc.*, **24** (1), 1–10.
4. CLARKE D.R., LEVI C.G. (2003), Materials design for the next generation thermal barrier coatings, *Annu. Rev. Mater. Res.*, **33**, 383–417.
5. MILLER R.A. (1997), Thermal barrier coatings for aircraft engines: history and directions, *J. Therm. Spray Technol.*, **6**, 35–42.
6. SEMENOV S.Y. (2002), Experimental diagnostics and modeling of thermal spray deposition processes of nano-structured wear resistant and thermal barrier coatings, UMI Number: 307671, 15.
7. BATISTA C., PORTINHA A., RIBEIRO R.M., TEIXEIRA V., COSTA M.F., OLIVEIRA C.R. (2005), Surface laser-glazing of plasma-sprayed thermal barrier coatings, *Appl. Surf. Sci.*, **247**, 313–319.
8. JORDAN E.H., XIE L., MA X., GELL M., PADTURE N.P., CETEGEN B., OZTURK A., ROTH J., XIAO T.D., BRYANT P.E.C. (2004), Superior thermal barrier coatings using solution precursor plasma spray, *J. Therm. Spray Technol.*, **13**(1), 57–65.
9. LUGSCHEIDER E., BARIMANI C., ECKERT P., ERITT U. (1996), Modeling of the APS plasma spray process, *Comput. Mater. Sci.*, **7**(1–2), 109–114.

10. DUSSOUBS B., FAUCHAIS P., VARDELLE A., VARDELLE M., THEMELIS N.J. (1997), Computational analysis of a threedimensional plasma spray jet, in: Berndt C.C. (ed.), *ThermalSpray: A United Forum for Scientific and Technological Advances*, ASM International, Materials Park, OH, 557–565.
11. PFENDER E., CHANG C.H. (1998), Plasma spray jets and plasma particulate interactions: modeling and experiment, in: Coddet C. (ed.), *Proceedings of ITSC 98*, ASTM International, Materials Park, OH, 315–327.
12. FAUCHAIS P., VARDELLE A. (2000), Heat, mass and momentum transfer in coating formation by plasma spraying, *Int. J. Therm. Sci.*, **39**, 852–870.
13. BUSSMANN M., AZIZ S.D., CHANDRA S., MOSTHAGIMI J. (1998), 3-D modelling of thermal spray droplet splashing, in: Coddet C. (ed.) *Proceedings of ITSC 98*, ASM International, Materials Park, OH, USA, 413–418.
14. MONTAVON G., SAMPATH S., BERNDT C.C., HERMAN H., CODDET C. (1995), Effects of vacuum plasma spray processing parameters on splat morphology, *J. Spray Technol.*, **4**, 67–74.
15. FAUCHAIS P., MONTAVON G., VARDELLE M., CEDELLE J. (2006), Developments in direct current plasma spraying, *Surf. Coat. Technol.*, **201**, 1908–1921.
16. FUKUMOTO M., NISHIOKA E., MATSUBARA T. (1999), Flattening and solidification behavior of a metal droplet on a flat substrate surface held at various temperatures, *Surf. Coat. Technol.*, **139**, 131–137.
17. SAMPATH S., HERMAN H. (1996), Rapid solidification and microstructure development during plasma spray deposition, *J. Therm. Spray Technol.*, **5**(4), 445–456.
18. WANG G.X., SAMPATH S., PRASAD V., HERMAN H. (1997), The stability of rapid planar solidification during melt substrate quenching, *Mater. Sci. Eng.*, **A226–A228**, 1035–1038.
19. HERMAN H. (1988), Plasma sprayed coatings, *Scientific American*, **259**(3), 112–117.
20. CHRASKA T., KING A.H. (2001), Transmission electron microscopy study of rapid solidification of plasma sprayed zirconia: part I First splat solidification, *Thin Solid Films*, **397**, 30–39.
21. CHRASKA T., KING A.H. (2001), Transmission electron microscopy study of rapid solidification of plasma sprayed zirconia: part II Interfaces and subsequent splat solidification, *Thin Solid Films*, **397**, 40–48.
22. PAUL S., CIPITRIA A., GOLOSNOY I.O., XIE L., DORFMAN M.R., CLYNE T.W. (2007), Effects of impurity content on the sintering characteristics of plasma-sprayed zirconia, *J. Therm. Spray Technol.*, **16**(5–6), 798–803.
23. CIPITRIA A., GOLOSNOY I.O., CLYNE T.W. (2009), A sintering model for plasma-sprayed zirconia thermal barrier coatings. Part II: Coatings bonded to a rigid substrate, *Acta Mater.*, **57**, 993–1003.
24. LEGER A.C., WIGREN J., HANSSON M.O. (1998), Development of a process window for a NiCoCrAlY plasma-sprayed coating, *Surf. Coat. Technol.*, **108–109**, 86–92.
25. HARDING J.H., MULHERAN P.A., CIROLINI S., MARCHESE M., JACUCCI G. (1997), Modeling deposition process of thermal barrier coating, *J. Therm. Spray Technol.*, **4**, 34–40.
26. MCPHERSON R. (1989), A review of microstructure and properties of plasma sprayed ceramic coatings, *Surf Coat. Technol.*, **39**, 173–181.
27. ANDREOLA F., LEONELLI C., ROMAGNOLI M., MISELLI P. (2000), Techniques used to determine porosity, *Am. Ceram. Soc. Bull.*, **79**, 49–52.

28. LAVIGNE O., RENOLLET Y., POULAIN M., RIO C., MORETTO P., BRANNVALL P., WIGREN J. (1999), Microstructural characterization of plasma sprayed thermal barrier coatings by quantitative image analysis, in: Strang A., Cawley J. (eds), *Quantitative Microscopy of High Temperature Materials Conference*, Institute of Materials, London, UK, 22–25.
29. KULKARNI A., WANG Z., NAKAMURA T., SAMPATH S., GOLAND A., HERMAN H., ALLEN A.J., ILAVSKY J., LONG G., FRAHM J., STEINBRECH R.W. (2003), Comprehensive microstructural and predictive property modeling of plasma-sprayed zirconia coatings, *Acta Mater.*, **51**(9), 2457–2475.
30. KURODA S., CLYNE T.W. (1991), The quenching stress in thermally sprayed coatings, *Thin Solid Film*, **200**, 49–66.
31. BRINDLEY W.J., WHITTENBERGER J.D. (1993), Stress relaxation of low pressure plasma-sprayed NiCrAlY alloys, *Mater. Sci. Eng.*, **A163**, 33–41.
32. HOBBS M.K., REITER H. (1988), Residual stresses in ZrO₂–8%Y₂O₃ plasma-sprayed thermal barrier coatings, *Surf. Coat. Technol.*, **34**, 33–42.
33. HARMSWORTH, P.D., STEVENS R. (1992), Phase transformation and properties of plasma-sprayed zirconia thermal barrier coatings, *J. Mater. Sci.*, **27**, 611–615.
34. HERMAN H., SHANKAR N.R. (1987), Survivability of thermal barrier coatings, *Mater. Sci. Eng.*, **88**, 69–74.
35. TAKEUCHI S.M., ITO M., TAKEDA K. (1990), Modeling of residual stress in plasma-sprayed coatings: effect of substrate temperature, *Surf. Coat. Technol.*, **43/44**, 426–436.
36. BUSSO E.P., LIN J., SAKURAI S., NAKAYAMA M. (2001), A mechanistic study of oxidation-induced degradation in a plasma-sprayed thermal barrier coating system. Part I: model formulation, *Acta Mater.*, **49**, 132–140.
37. CHENG J., JORDAN E.H., BARBER B., GELL M. (1998), Thermal residual stress in an electron beam physical vapor deposited thermal barrier coating system, *Acta Mater.*, **46**, 5839–5842.
38. MILLER R.A., LOWELL C.E. (1982), Failure mechanisms of thermal barrier coatings exposed to elevated temperatures, *Thin Solid Films*, **95**, 265–270.
39. ROSIER J., BAKER M., VOLGMANN M. (2001), Stress state and failure mechanisms of thermal barrier coatings: role of creep in thermally grown oxide, *Acta Mater.*, **49**, 3659–3662.
40. BUSSO E.P., LIN J., SAKURAI S. (2001), A mechanistic study of oxidation-induced degradation in a plasma-sprayed thermal barrier coating system. Part II: Life prediction model, *Acta Mater.*, **49**, 1529–1534.
41. TZIMAS E., MULLEJANS H., PETEVES S.D., BRESSERS J., STAMEN W. (2000), Failure of thermal barrier coating systems under cyclic thermomechanical loading, *Acta Mater.*, **48**, 18–20.
42. HSUEH C.H., FULLER E.R. (2000), Residual stresses in thermal barrier coatings: effects of interface asperity curvature/height and oxide thickness, *Mater. Sci. Eng.*, **A283**, 46–49.
43. BUSSO E.P., LIN J., SAKURAI S. (2001), A mechanistic study of oxidation-induced degradation in a plasma-sprayed thermal barrier coating system. Part I model formation, *Acta Mater.*, **49**, 1515–1528.
44. SCHLICHTING K.W., VAIDYANATHAN K., SOHN Y.H., JORDAN E.H., GELL M., PADTURE N.P. (2000), Application of Cr³⁺ photoluminescence piezo-spectroscopy to

- plasma-sprayed thermal barrier coatings for residual stress measurement, *Mater. Sci. Eng.*, **A291**, 68–72.
45. JORDAN E.H., SOHN Y.H., XIE W., GELL M., XIE L., TU F., PATTIPATI K.R., WILLET P. (2001), Residual stress measurement of thermal barrier coatings using laser fluorescence technique and their life prediction, in Autotestcon, Valley Forge, PA.
 46. GELL M., JORDAN E., VAIDYANATHAN K., MCCARRON K., BARBER B., SOHN Y.-H., TOLPYGO V.K. (1999), Bond strength, bond stress and spallation mechanisms of thermal barrier coatings, *Surf. Coat. Technol.*, **53**, 120–121.
 47. CHRISTENSEN R.J., LIPKIN D.M., CLARKE D.R., MURPHY K. (1996), Nondestructive evaluation of the oxidation stresses through thermal barrier coatings using Cr₃+piezospectroscopy, *Appl. Phys. Lett.*, **69**, 3754–3760.
 48. TOLPYGO V.K., CLARKE D.R. (2000), Surface rumpling of a (Ni, Pt)Al bond coat induced by cyclic oxidation, *Acta Mater.*, **48**, 3283–3288.
 49. HAYNES J.A., RIGNEY E.D., FERBER M.N., PORTER W.D. (1996), Oxidation and degradation of a plasma-sprayed thermal barrier coating system, *Surf. Coat. Technol.*, **86–87**, 102–108.
 50. BUSO E.P., LIN J., SAKURAI S. (2001), A mechanistic study of oxidation-induced degradation in a plasma-sprayed thermal barrier coating system. Part II: Life prediction model, *Acta Mater.*, **49**, 1529–1532.
 51. TSUI Y.C., HOWARD S.J., CLYNE T.W. (1994), The effect of residual stresses on the debonding of coatings – II. An experimental study of a thermally sprayed system, *Acta Mater.*, **42**, 2837–2844.
 52. KHOR K.A., DONG Z.L., GU Y.W. (1999), Plasma sprayed functionally graded thermal barrier, *Mater. Lett.*, **38**, 437–444.
 53. STÖVER D., FUNKE C. (1999), Directions of the development of thermal barrier coatings in energy applications, *J. Mater. Process. Technol.*, **92–93**, 195–202.
 54. SUN J.H., CHANG E., WU B.C. (1993), Performance of CVD A1203 intermediate layer between zirconia top coat and NiCrAlY bond coat, *Mater. Trans., JIM*, **34(7)**, 614–621.
 55. COBLE R.L. (1958), Initial sintering of alumina and hematite, *J. Am. Ceram. Soc.*, **41(2)**, 55–62.
 56. HAN W., RYBICKI E.F., SHADLEY J.R. (1992), Bond strength testing of thermal spray coatings using ASTM C633-79: Effect of specimen size on test results, Proceedings of the International Thermal Spray Conference, Orlando, FL, 28 May–5 June, 911–914.
 57. BERNDT C.C., LIN C.K. (1993), Measurement of adhesion for thermally sprayed materials, *Adhesion Sci. Tech.*, **7**, 1235–1264.
 58. HEINTZE G.N., MCPHERSON R. (1988), Fracture toughness of plasma-sprayed zirconia coatings, *Surf. Coat. Technol.*, **34**, 15–23.
 59. JENNIFER SU Y. (2001), *Processing and Performance of YSZ-Based Multilayer Thermal Barrier Coatings*, UMI Number: 3033564, 26–31.
 60. WU Z.L., KUO P.K., WRI L., GU L.S., THOMAS R.L. (1993), Photothermal characterization of optical thin films, *Thin Solid Film*, **236**, 191–198.
 61. RAVICHANDRAN K.S., AN K. (1999), Thermal conductivity of plasma-sprayed monolithic and multilayer coatings of alumina and yttria-stabilized zirconia, *J. Am Ceram. Soc.*, **82** (3), 673–821.

Plasma-sprayed thermal barrier coatings with segmentation cracks

H. GUO, R. YAO and L. ZHOU, Beihang University, China

Abstract: Plasma-sprayed thermal barrier coatings (TBCs) have been widely used on stationary components in turbine engines. The thermal shock resistance of such coatings is usually limited by their typical lamellar structure. In this work, a segmented structure was induced in the plasma-sprayed yttria stabilized zirconia (YSZ) coatings by using a 'hot' spraying condition. The thermophysical properties, mechanical properties and thermal cycling behaviors and associated failure mechanism of the segmented TBCs were addressed. The segmented TBCs exhibited very promising potential in improving the thermal cycling lifetime as compared to traditional non-segmented TBCs.

Key words: plasma spray, thermal barrier coatings (TBCs), segmentation cracks, thermal cycling, thermophysical property.

8.1 Introduction

Plasma-sprayed thermal barrier coatings (TBCs) have been extensively used to protect the components of gas turbines including combustion chambers, vanes and transition pieces from hot gases. The utilization of TBCs, accompanied by internal cooling, can achieve a temperature reduction of up to 300 K on the surface of the superalloy, which greatly extends the duration of its components.^{1,2} Moreover, this enables engines to operate at temperatures above the melting point of the superalloy, and thus their efficiency and energy performance are tremendously improved.

An increasing demand for engine efficiency and performance in a context of higher operating temperatures and lower emissions is propelling the rapid development of TBC technology. Current interests focus on plasma-sprayed TBCs that comprise an yttria stabilized zirconia (YSZ) top coat and a NiCoCrAlY bond coat. These are usually used in crucial hot sections of gas turbines to increase the turbine inlet temperature (TIT), hence enhancing the efficiency and performance of the turbines. However, sintering and progressive destabilization of the YSZ top coat caused by mismatched thermal stresses and the formation of thermally grown oxide (TGO) may lead to spallation failure of the plasma-sprayed TBCs.³⁻⁷

Although TBCs thicker than 1 mm have better thermal barrier capability than thinner ones, such as those with a thickness of only a few tenths of 1 mm, some critical problems remain to be solved in the present work.⁸⁻¹⁶ One serious problem is that thick TBCs present low thermal shock resistance when exposed to a high-temperature environment. An increase in coating thickness causes greater thermal gradients in the transient phase across the coating, and consequently leads to higher thermal stresses in the coating. Also, thick coatings will store more elastic strain energy, hence increasing the rate of energy release in a crack. These two factors have caused spalls of the thick TBCs, tensile cracks or chippings in the bulk of the coating materials. This failure mechanism is different from the conventional interface delamination failure that is mainly caused by thermal stresses resulting from differences in the thermomechanical properties between the coating and the substrate. Another factor that influences the performance of the thick coatings is the edge effect, defined as stress singularities resulting from moments and shear stresses at the coating edge. The stress will approach a singularity at the edge of the TBCs, especially those having a thickness of more than 500 μm . However, the edge effect might be avoided by optimization of the sample edge.

To improve the thermal shock performance of thick TBCs, some methods such as fabricating coatings with graded porosity or gradient layer structure have been attempted.¹⁷⁻¹⁹ Recently, macrocracks or segmentation cracks in TBCs that are perpendicular to the substrate have been reported to be conducive to an increase in the thermal shock resistance of plasma-sprayed TBCs, mainly because they can accommodate the stresses resulting from the different thermal expansions between the coating and the substrate.^{14,20-24} These macrocracks can be induced through post treatment such as laser glazing, or directly introduced during the deposition by applying large heat input to the substrate and using a high lamellar thickness.^{11,12}

Segmented TBCs have a higher amount of microcracks and lower Young's modulus and can tolerate greater strains.^{14,23} Those features that determine the thermal shocking behaviors of segmentation cracks TBCs are greatly ameliorated compared to the traditional non-segmented TBCs. This chapter addresses the manufacturing, thermophysical properties, mechanical properties and thermal cycling behaviors and associated failure mechanism of segmented TBCs.

8.2 Manufacturing of segmented thermal barrier coatings (TBCs)

When the coating is subjected to biaxial tensile stress, segmentation cracks may start and develop in the deposition phase because of stress relaxation.^{13,25,26} During spraying, the molten droplets impinge on the surface of

the substrate and quickly begin to solidify as a splat. When the solidified splat cools, shrinkage, usually associated with the decrease in temperature, is inhibited because the splat is attached closely to the substrate, and thus in-plane stresses are generated in the splat as a result. However, these stresses may be released immediately by the initiation of microcracks in the first splat.²⁵⁻²⁷

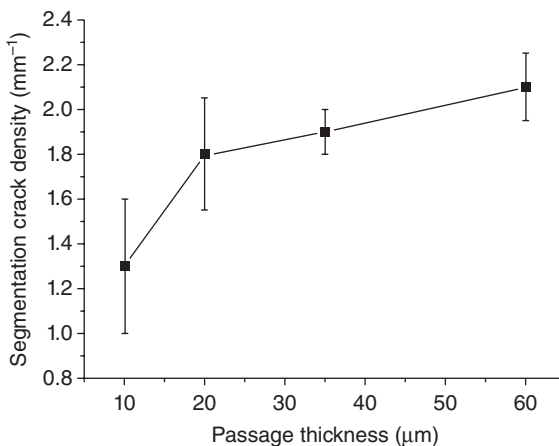
It is well accepted that the temperature of a substrate is the primary factor determining the development of segmentation cracks.^{13,20} When spraying is conducted on high-temperature substrate, the difference in temperature between the first splat and the following splats will be large enough to remelt the surface of the first splat, thereby creating good connections among the splats. Then, the tensile stresses developing in the second splat will be released by the proliferation of the microcracks pre-existing in the first splat. This circle continues until the spraying process is finished. In other words, the microcracks propagate in the first lamellae throughout the thickness. In the deposition of the second lamellae, contacting areas still exist between the first splat in the second lamellae and the final splat in the first lamellae, even if the heat input is not high enough to remelt the underlying splat. Because of these connections, some of the microcracks in the first lamellae propagate and penetrate into the next lamellae, and consequently initiate segmentation cracks. Such cracks remain all along the following processes and eventually develop into segmentation cracks.²⁰

Nevertheless, if the spraying is performed with low substrate or particle temperatures due to a long spraying distance, the heat from the new liquid splat is not high enough to create a good bonding to the underlying splat. Therefore, the real area of the connection between the splats is rather limited and estimated to be approximately 20%.²⁸ If so, a large number of horizontal cracks will present in the form of inter-splat or interlamellar delaminations, leading to obvious stress relaxation. Additionally, microcracks will form continuously within each splat and cause further tensile stresses, rather than propagating from splats to splats because of the poor bonding between the splats.^{13,20}

Passage thickness is another significant parameter affecting the density of the segmentation crack.^{20,27} The density is found to increase along with the increase in passage thickness. In one study, passage thickness is controlled by the plasma gun speed and the powder feed rate. It has been shown that segmentation cracks are much denser when the passage is fabricated thick by using a low plasma gun speed. It is generally accepted that when the plasma gun passes across the substrate materials at a low speed, more heat is transferred to the substrate resulting in a higher substrate temperature. Moreover, to a given coating thickness, the number of interlamellar delaminations decreases accordingly, owing to the increased lamellar thickness resulting from the low plasma gun speed. However, if controlled

by a powder feed rate, the segmentation crack density is not as sensitive to the passage thickness as that controlled by plasma gun speed. As shown in Fig. 8.1, the difference in segmentation crack density is not as much for the coatings sprayed with different passage thickness. A high feeding rate usually leads to thicker lamellae when hundreds of particles are deposited during one pass. These particles are probably still rather hot, so the cooling of the substrate leads to reduced tensile strain difference among the adjacent lamellae, thereby reducing the possibility of microcrack formation. However, it has been reported by Guo *et al.*²⁹ that an overhigh powdering rate tends to decrease the density of the microcrack slightly compared to the low powder feeding rate, which may be attributed to incomplete melt of the powders at such a high feed rate.

The particle sizes of the powder feedstock have critical effects on porosity and growth of segmentation cracks in the coatings.^{13,14} As discussed above, the coatings sprayed at a high plasma power and short spraying distance tend to have a high segmentation cracks density. It has been shown that since 20–45 μm powders have higher depositing efficiency and better capability of producing segmented coatings than commercially available, wide size distribution powders, they are considered to be preferable for processing segmented TBCs. Diagnostics of the in-flight particles demonstrates that the 20–25 μm powders yielded higher heat transmission because of their greater specific surface area compared to larger powders. This leads to more heat input to the substrate and a higher top coat temperature, as well as a higher velocity of the fine powders. Thus, the coatings sprayed from the fine powders exhibit a lower porosity, primarily due to the decrease of the volume of the inter-splat gaps and voids.



8.1 Segmentation crack densities of YSZ coatings sprayed with different feeding rates.

The type of feedstock tremendously influences the properties of the sprayed YSZ coatings because different powders interact diversely in a plasma flame, thus affecting the development of the microstructure.^{13,14,29} Generally, the coatings sprayed from hollow powders contain more unmelted particles because their particle size is broadly distributed. As a result, the sprayed coatings had a relatively higher segmentation crack density than the coating with high porosity because the origin and propagation of segmentation cracks are mainly hindered by delamination cracks and large defects. Therefore, the fused and crashed powder has greater capability of producing segmentation cracks in the coatings compared with the hollow powder.

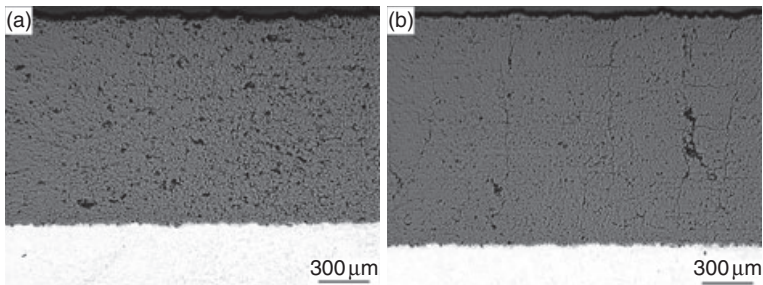
Cooling rate during deposition is also one of the main parameters determining the development of segmentation cracks. High cooling rate is conducive to the generation of segmentation cracks.

8.3 Microstructure of segmented TBCs

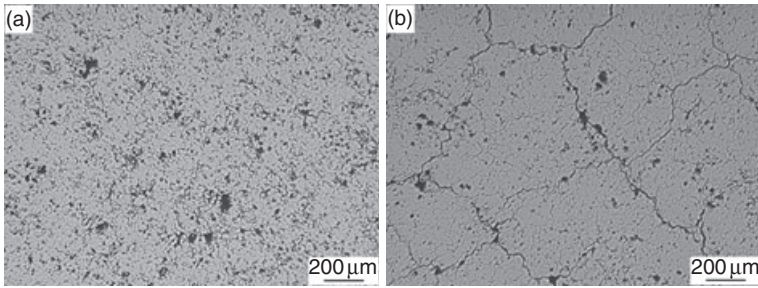
Figures 8.2a and b are the scanning electron microscope (SEM) micrographs of the cross-section of the YSZ coatings sprayed from the HOSP feedstocks. The number of segmentation cracks in the coating sprayed with a longer spraying distance and lower plasma power is rather limited (Fig. 8.2a). In contrast to this, the number of the segmentation cracks of the coating sprayed with a higher substrate temperature (Fig. 8.2b) increased enormously, with most passing throughout the coating thickness.

In Figures 8.3a and b, the polished surfaces of the above YSZ coatings are compared. From the surface appearance, the non-segmented coating contains a large amount of micrometer-sized pores, while the segmented coating has a fine segmentation crack network with a diameter in the order of $0.5 \mu\text{m}^{-1}$.

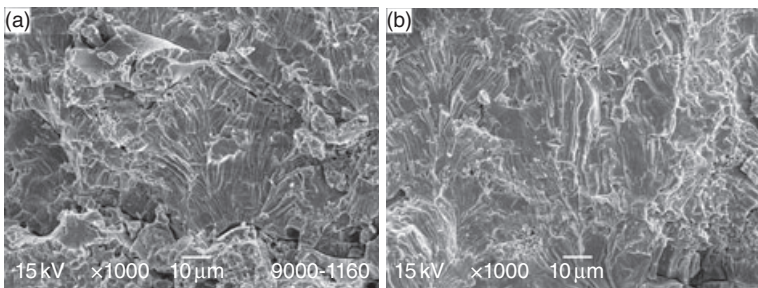
Figures 8.4a and b show the fracture surfaces of the cross-sections of the YSZ coatings. Some pores larger than $1 \mu\text{m}$ are presented in the non-



8.2 SEM micrographs of cross-sections of YSZ coatings: (a) traditional non-segmented; (b) highly segmented.



8.3 Surface morphologies of YSZ coatings: (a) traditional non-segmented; (b) highly segmented.



8.4 SEM micrographs of fracture cross-sections of YSZ coatings: (a) traditional non-segmented; (b) highly segmented.

segmented coating, as shown in Fig. 8.4a. These pores usually result from unmolten particles and gas entrapment during spraying. The segmented coating was apparently denser than the non-segmented coating, because fewer inter-splat gaps and voids are visible in the coating. Furthermore, the columnar grains go through several lamellae. Moreover, the contact between the lamellae is significantly improved, as shown in Fig. 8.4b.

8.4 Thermophysical and mechanical properties of segmented TBCs

The thermal diffusivities of the YSZ coatings were measured by laser flash apparatus. The thermal diffusivity values for the non-segmented coating range from $0.002\text{--}0.006\text{ cm}^2\text{ s}^{-1}$ between room temperature and 1200°C , while the segmented coating exhibits a perceptible increase in thermal diffusivity compared to the non-segmented coating. The difference indicates that the values of the thermal diffusivity largely depend on the microstructure of the coatings.

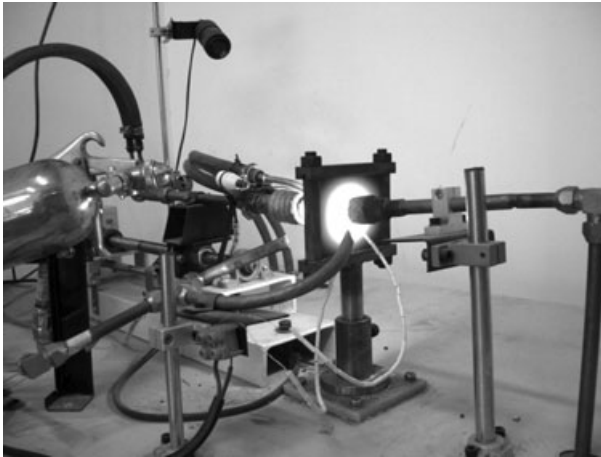
Thermal conductivity is calculated using the equation: $K(T) = \alpha(T) \cdot C_p \cdot \rho$ where $K(T)$ is the thermal conductivity, $\alpha(T)$ is the thermal diffusivity, C_p is the specific heat and ρ is the bulk density of the coating. The thermal conductivity of the segmented coating, with an increase of nearly 20% compared to that of the non-segmented coating,^{14,23} is approximately 1.75 W/mK.

Plasma-sprayed TBCs reveal a two-dimensional microcrack network: one is defined as a horizontal microcrack, resulting from the flawed contacts between the inter-splats of the coatings; the other is oriented vertically, primarily resulting from the microcracking of the splats during cooling. The former is particularly effective in reducing the thermal conductivity of the sprayed coatings, because the interfaces formed by such cracks are perpendicular to the main heat flux. Among the coatings mentioned above, the segmented coating has a lower porosity than the non-segmented coating, and thus has a better connection between the splats, which contributes to reducing the amount of horizontal microcracks. This explains why the segmented coating tends to have a slightly higher thermal conductivity compared to the non-segmented coating. Moreover, dispersed spheroid microporosity is also helpful in lowering the thermal conductivity of the YSZ coatings. It is worth noting that branching cracks are also introduced when the spraying is performed with thick lamellae, accompanying the generation of segmentation cracks. The branching cracks play a role in lowering the thermal conductivity of the segmented TBC.²⁰

Both the non-segmented and segmented coatings reveal very similar thermal expansion when heating to 1200 °C from room temperature, despite the different processing parameters and microstructure between the coatings. The average values of the thermal expansion coefficient (TEC) are in the range $10\sim 11.2 \times 10^{-6} \text{ K}^{-1}$.

8.5 Thermal shock resistance and associate failure mechanism

Thermal shock testing was conducted using a gas burner rig with natural gas and oxygen to evaluate the thermal shock resistance of the coatings (see Fig. 8.5). The temperatures of the coating surface and the back side (substrate) were measured using a pyrometer and a thermocouple fixed at the back of the substrate, respectively. During the test, the gas burner has a broad flame in order to produce a homogeneous temperature distribution in the center of the sample. The sample was heated to a desired temperature within 20 s, and then maintained at the temperature for 5 min. The back side of the sample was cooled by compressed air in order to keep a controlled temperature gradient across the thickness of the sample and, in this case, the temperature gradient was nearly $\sim 500^\circ\text{C}$. The burner was removed



8.5 Burner rig set-up for thermal shock testing.

automatically from the coating during the cooling, and the sample was cooled for 2 min using compressed air at a rate of more than $100^{\circ}\text{C}/\text{s}$. The lifetime of the coating is defined as the number of thermal cycles when the spallation of the coating is clearly visible to the naked eye.

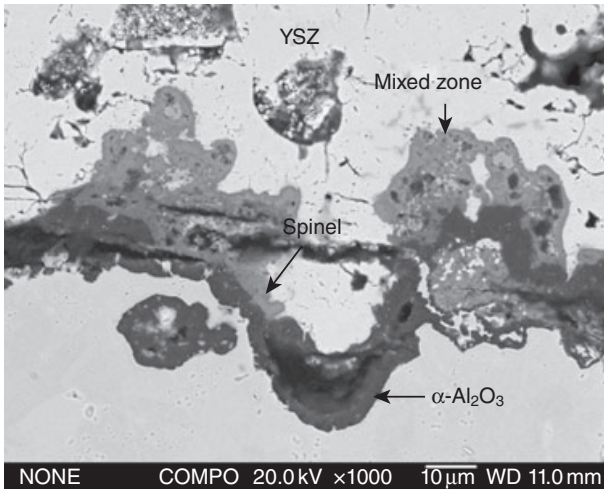
The segmented specimen had a thermal cycling lifetime of more than 2000 cycles at $1200 \pm 50^{\circ}\text{C}$ (surface)/ $1000 \pm 50^{\circ}\text{C}$ (substrate), while the non-segmented one had a lifetime of less than 500 cycles. The segmented coating exhibited a much improved thermal shock resistance. Figure 8.6 gives a photograph showing the surface morphology of the segmented TBC after 3200 cycles of thermal shock testing. Spallation of the YSZ coating occurred starting from the edge of the specimen, which is a typical failure mechanism caused by oxidation of the TBC, as shown in Fig. 8.7.

The traditional non-segmented specimen is usually spalled off from the substrate by cracking at the interface between the YSZ top coat and the bond coat.^{30–36} This is a typical failure mechanism of plasma-sprayed TBCs caused by thermal stresses deriving from the mismatch of thermal expansions between the ceramic top coat and the superalloy substrate. In the segmented specimen, some chippings on the surface of the top coat were observed before bulk spallation. The failure of the segmented coating then started from the edge of the specimen and propagated to the center. Finally, partial spallation of some segments rather than spallation of the whole coating occurred, which is quite different from the failure mechanism observed in traditional TBCs.^{13,20,31,37,38}

Segmented TBCs have a much longer thermal cycling lifetime than traditional non-segmented TBCs and a distinct failure mechanism, to which the contribution of the segmentation crack network should be attributed.



8.6 Photograph of the segmented TBC after thermal shock resistance of 3200 cycles.



8.7 SEM micrograph of cross-section of the segmented TBC after thermal shock testing, showing the morphology of TGO.

These cracks can improve the straining tolerance of the coatings by opening during tensile loading and closing during compressive loading, just like the behavior of the inter-column gaps of electron beam physical vapor deposition (EB-PVD) coatings. The straining tolerance may be seen as a reduction of the stress concentration that existed at various edges of a TBC specimen. In particular, at free edges, such as at the rim of a disk specimen or around the periphery of each segment in the segmented coating, shear stresses at the interface between the coating and the substrate will develop because of different thermal expansions, hence placing TBCs in lateral tension or compression depending on the instantaneous temperature as well as the specimen's thermal history. The thickness and the area of each coating are the geometrical factors that can determine the magnitude of the maximum shear stresses at the edges. To a constant coating thickness, a smaller area will lead to smaller stresses. Therefore, it is reasonable to anticipate that a highly segmented specimen can generate relatively small shear stresses compared to a non-segmented specimen, and hence the force to produce an interface crack is also significantly reduced.

Several factors, such as porosity and other horizontal cracks, may affect the thermal properties of TBCs, but it is found in the present study that segmentation cracks dominate the lifetimes of TBCs. Some other factors that are related to the changes of materials microstructure still need further investigation.

Plasma-sprayed 8YSZ coatings mostly consist of a non-equilibrium tetragonal phase (denoted as t') resulting from the rapid cooling during the spraying process.⁷ Nevertheless, exposure to high temperature leads to the decomposition of t' -phase. During the high-temperature stage, the t' -phase first transforms to the stable tetragonal phase (t) with low yttria content, and then to the monoclinic phase (m) during the cooling stage. The phase transformation of t' to m is associated with a volume expansion of up to 5%, which will deteriorate the integrity of the YSZ top coat and can hence cause the failure of TBCs.

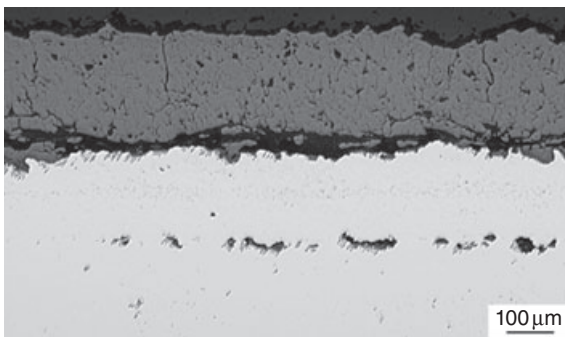
For the segmented coating sprayed under 'hot' condition, the issue of concern was the phase stability of the YSZ coating. Only a small amount of monoclinic phase was detected in both the as-sprayed coating and the coating after thermal shock testing.^{3,4,7,37} The presence of the monoclinic phase in the as-sprayed coating could be ascribed to the special processing condition for spraying highly segmented coatings, in which the substrate temperature could reach as high as 1273 K. It can be inferred that the coating surface temperature was even higher than the substrate temperature during the spraying. Therefore, it is possible that the phase transformation of t to m occurred just in the as-sprayed coating. As for the TBC specimen after thermal shock testing, the maximum temperature that the specimen was exposed to is lower than 1523 K. It is well recognized that

the decomposition of the γ' -phase in 8YSZ TBCs is very slow at temperatures below 1523 K. Therefore, it can be predicted that decomposition of TBC phase could not cause severe damage to the integrity of segmented TBCs.

As shown in Fig. 8.7, a TGO layer of about 5 μm thickness was formed on the bond coat and some horizontal cracks were developed in the top coat close to the TGO. The TGO consists of three zones: the $\alpha\text{-Al}_2\text{O}_3$ zone close to the NiCoCrAlY bond coat; the spinel zone above the $\alpha\text{-Al}_2\text{O}_3$ zone; and the mixed zone of spinel oxide and ZrO_2 . The formation of spinel oxides is related to depletion of Al in the bond coat.^{7,39–41} In the case of the segmented TBC, it usually survives hundreds of hours under a hot gas environment. As a result, severe oxidation inevitably occurs and a thick TGO is formed between the YSZ top coat and the bond coat. With the qualitative analysis given above, we currently believe that the geometrical effects of reducing stresses by segmentation cracks do indeed play a dominant role in prolonging the thermal cycling life of TBCs, but further quantitative investigations should be carried out in the near future.

Thick TBCs with different levels of segmentation crack densities can be produced by controlling the heat input to the substrate. The thermal cycling lifetimes of the sprayed TBC are strongly dependent on the segmentation crack density. Highly segmented TBCs achieve a significant improvement in thermal cycling lifetime as compared to TBCs without segmentation cracks. It has been shown that the segmentation crack network is quite stable during thermal cycling testing. No segmentation cracks disappear during sintering of YSZ coatings.

Segmentation cracks can be also applied to quite thin coatings. As shown in Fig. 8.8, a thin YSZ TBC with segmentation cracks was produced and exhibited a very satisfactory thermal shock resistance as compared to the traditional TBC. The failure of the thin coating was governed by the oxida-



8.8 Optical micrograph of cross-section of the thin TBC with segmentation cracks after 2320 cycles thermal shock testing.

tion of the bond coat because the temperature of the bond coat in the case of the thin TBC was almost 50–100 °C higher than that in the case of the thick TBC.

8.6 Future trends

With the development of technology, the production of highly segmented TBCs with high segmentation crack densities has become possible by using advanced processing methods. Even higher segmentation crack densities, as well as a high porosity level and hence low thermal conductivities, can be obtained by using suspensions as feedstock for the plasma-spraying process. One problem associated with the plasma-spraying process is the blocking of the cooling holes during deposition, and the search for solutions to overcome this problem is still in progress.

8.7 References

1. N.P. PADTURE, M. GELL, E.H. JORDAN, Thermal barrier coatings for gas-turbine engine applications, *Science*, **296** (2002): 280–284.
2. R.L. JONES, Thermal barrier coatings, in K.H. Stern (Ed.), *Metallurgical and Ceramic Coatings*, Chapman and Hall, London, UK, 1996, 194–253.
3. R. VASSEN, F. TIETZ, G. KERKHOFF, *et al.*, New materials for advanced thermal barrier coatings, in J. Lecomte-Becker, F. Schubert and P.J. Ennis (eds), *Materials for Power Engineering*, (1998), Forschungszentrum Jülich, Jülich, Germany, 1627–1635.
4. R.A. MILLER, Thermal barrier coatings for aircraft engines: history and directions, *J. Therm. Spray Technol.*, **6**(1) (1997): 35–42.
5. A. RABIEL, A.G. EVANS, Failure mechanisms associated with the thermally grown oxide in plasma-sprayed thermal barrier coatings, *Acta Mater.*, **48** (2000): 3963–3976.
6. K.W. SCHLICHTING, N.P. PADTURE, E.H. JORDAN, M. GELL, Failure modes in plasma-sprayed thermal barrier coatings, *J. Mater. Sci. Eng. A*, **342** (2003): 120–130.
7. H. GUO, H. MURAKAMI, S. KURODA, Thermal cycling behavior of plasma sprayed segmented thermal barrier coatings, *Mater. Trans.*, **47**(2) (2006): 306–309.
8. G. GUALCO, S. CORCORUTO, A. CAMPORA, Highly porous thick thermal barrier coatings produced by air plasma spraying of a plastic-ceramic mixed powder, in: C.C. Berndt (Ed.), *Thermal Spray: A United Forum for Scientific and Technological Advances, Proceedings of the 1st National Thermal Spray Conference*, ASM International, Materials Park, OH, 305–315.
9. H.-D. STEFFENS, Z. BABIAK, M. GRAMLICH, Some aspects of thick thermal barrier coating lifetime prolongation, *J. Therm. Spray Technol.*, **8**(4) (1999): 517–522.
10. R. TAYLOR, J.R. BRANDON, P. MORRELL, Microstructure composition and property relationships of plasma-sprayed thermal barrier coatings, *Surf. Coat. Technol.*, **50**(2) (1992): 141–149.
11. H. GUO, R. VABEN, D. STÖVER, Thermophysical properties and thermal cycling-behavior of plasma sprayed thick thermal barrier coatings, *Surf. Coat. Technol.*, **192** (2005): 48–56.

12. P. BENGTSSON, T. ERICSSON, J. WIGREN, Thermal shock testing of burner cans coated with a thick thermal barrier coating, *J. Therm. Spray Technol.*, **7**(3) (1998): 340–348.
13. H. GUO, H. MURAKAMI, S. KURODA, Effect of hollow spherical powder size distribution on porosity and segmentation cracks in thermal barrier coatings, *J. Am. Ceram. Soc.*, **89**(12) (2006): 3797–3804.
14. H. GUO, S. KURODA, H. MURAKAMI, Microstructures and properties of plasma-sprayed segmented thermal barrier coatings, *J. Am. Ceram. Soc.*, **89**(4) (2006): 1432–1439.
15. E.F. REJDA, D.F. SOCIE, T. ITOH, Deformation behavior of plasma-sprayed thick thermal barrier coatings, *Surf. Coat. Technol.*, **113** (1999): 218–226.
16. D. SCHWINGEL, R. TAYLOR, T. HAUBOLD, J. WIGREN, C. GUALCO, Mechanical and thermophysical properties of thick PYSZ thermal barrier coatings: correlation with microstructure and spraying parameters, *Surf. Coat. Technol.*, **108–109** (1998): 99–106.
17. M. TAMURA, M. TAKAHASHI, J. ISHII, K. SUZUKI, M. SATO, K. SHIMOMURA, Multilayered thermal barrier coating for land-based gas turbines, *J. Therm. Spray Technol.*, **8**(1) (1999): 68–72.
18. W.Y. LEE, D.P. STINTON, C.C. BERNDT, F. ERDOGAN, Y.D. LEE, Z. MUTA-SIN, Concept of functionally graded materials for advanced thermal barrier coating applications, *J. Am. Ceram. Soc.*, **79**(12) (1996): 3003–3012.
19. C. GUALCO, E. CORDANO, F. FIGNINO, C. GAMBARO, S. AHMANIEMI, S. TUURNA, T. MÄNTYLÄ, P. VUORISTO, An improved deposition process for very thick porous thermal barrier coatings, in: E. Lugscheider, C.C. Berndt (eds), *Tagungsband Conference Proceedings, Proceedings of the International Thermal Spray Conference*, DVS, Dusseldorf, Germany, 2002, 196–201.
20. H.B. GUO, R. VABEN, D. STÖVER, Atmospheric plasma sprayed thick thermal barrier coatings with high segmentation crack density, *Surf. Coat. Technol.*, **186** (2004): 353–363.
21. H.L. TSAI, P.C. TSAI, Performance of laser-glazed plasma-sprayed (ZrO₂-12wt.% Y₂O₃)/(Ni-22wt.% Cr-10wt.% Al-1wt.% Y) thermal barrier coatings in cyclic oxidation tests, *Surf. Coat. Technol.*, **71** (1995): 53–59.
22. S. AHMANIEMI, P. VUORISTO, T. MÄNTYLÄ, C. GUALCO, A. BONADEI and R. DIMAGGIO, Thermal cycling resistance of modified thick thermal barrier coatings, *Surf. Coat. Technol.*, **190** (2005): 378–387.
23. H. GUO, H. MURAKAMI, S. KURODA, Materials, effects of heat treatment on microstructures and physical properties of segmented thermal barrier coatings, *Mater. Trans.*, **46**(8) (2005): 1775–1778.
24. H. GUO, H. MURAKAMI, S. KURODA, Segmentation cracks in plasma sprayed thin thermal barrier coatings, *Advanced Ceramic Coatings and Interfaces: Ceramic Engineering and Science Proceedings*, **27**(3) (2007): 17–27.
25. S. KURODA, T.W. CLYNE, The quenching stress in thermally sprayed coatings, *Thin Solid Films*, **200** (1991): 49–66.
26. J.W. HUTCHINSON, Z. SUO, Mixed mode cracking in layered materials, in: J.W. Hutchinson, T.Y. Wu (eds), *Advances in Applied Mechanics*, Vol. 29(1992): Academic Press, New York, 1289–1298.
27. P. BENGTSSON, J. WIGREN, Segmentation cracks in plasma sprayed thick thermal barrier coatings, in: P.J. Maziasz, I.G. Wright *et al.* (eds), *Gas Turbine Materials*

Technology, Proceedings of ASM Materials Solutions, ASM International, Materials Park, OH, 1999, 92–101.

28. R. MCPHERSON, The relationship between the mechanism of formation, micro structure and properties of plasma sprayed coatings, *Thin Solid Films*, **83** (1981): 297–310.
29. H. GUO, S. KURODA, H. MURAKAMI, Segmented thermal barrier coatings produced by atmospheric plasma spraying hollow powders, *Thin Solid Films*, **506** (2006): 136–139.
30. Z.Z. MUTASIM, Y.L. NAVA, Development and performance evaluation of thick air plasma sprayed thermal barrier coatings, in: C.C. Berndt (Ed.), *Surface Engineering via Applied Research, Proceedings of the 1st International Thermal Spray Conference*, ASM International, Materials Park, OH, 2000, 1325–1330.
31. T.A. TAYLOR, D.L. APPLEBY, A.E. WEATHERILL, J. GRIFFITHS, Plasma-sprayed yttria-stabilized zirconia coatings: structure-property relationships, *Surf. Coat. Technol.*, **43/44** (1990): 470–480.
32. Y.W. GU, K.A. KHOR, Y.Q. FU, Y. WANG, Functionally graded ZrO₂-NiCrAlY coatings prepared by plasma spraying using pre-mixed, spheroidized powders, *Surf. Coat. Technol.*, **96**(2–3) (1997): 305–312.
33. K. KOKINI, J. DEJONGE, S. RANGARAJ, B. BEARDSLEY, Thermal shock of functionally graded thermal barrier coatings with similar thermal resistance, *Surf. Coat. Technol.*, **154** (2002): 223–231.
34. H.A. NIED, Edge crack stress intensity factors in layered ceramic-metal composites due to thermal mismatch, *Proceedings of the International Conference and Exhibits on Failure Analysis*, ASM International, Materials Park, OH, 1991, 59–68.
35. D. ZHU, R.A. MILLER, Investigation of thermal high cycle and low cycle fatigue mechanisms of thick thermal barrier coatings, *Mater. Sci. Eng. A*, **245** (1998): 212–223.
36. R.E. TAYLOR, X. WANG, X. XU, Thermophysical properties of thermal barrier coatings, *Surf. Coat. Technol.*, **120–121** (1999): 89–95.
37. Y. WANG, H. GUO, S. GONG, Thermal shock resistance and mechanical properties of La₂Ce₂O₇ thermal barrier coatings with segmented structure, *Ceram. Int.*, **35** (2009): 2639–2644.
38. R. VABEN, F. TRAEGER, D. STÖVER, Correlation between spraying conditions and micro crack density and their influence on thermal cycling life of thermal barrier coatings, in: B.R. Marple, C. Moreau (eds), *Advancing the Science and Applying the Technology, Proceedings of International Thermal Spray Conference*, ASM International, Materials Park, OH, 2003, 1455–1462.
39. T.J. NIJDAM, L.P.H. JEURGENS, W.G. SLOOF, Modeling the thermal oxidation of ternary alloys – compositional changes in the alloy and the development of oxide phases, *Acta Mater.*, **51** (2003): 5295–5307.
40. T.J. NIJDAM, L.P.H. JEURGENS, W.G. SLOOF, Promoting exclusive α -Al₂O₃ growth upon high-temperature oxidation of NiCrAl alloys: experiment versus model predictions, *Acta Mater.*, **53** (2005): 1643–1653.
41. H. GUO, H. MURAKAMI, S. KURODA, Thermal cycling and hot-corrosion behaviors of plasma sprayed segmented thermal barrier coatings, *Mater. Sci. Forum*, **546–549** (2007): 1713–1716.

Detonation gun sprayed thermal barrier coatings

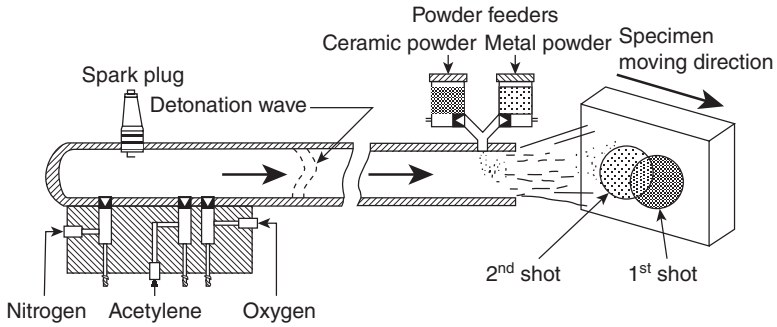
P. L. KE, Y. N. WU and C. SUN, Chinese Academy of Sciences, China

Abstract: Detonation gun spraying (D-gun spraying) is believed to be a promising new spraying technology in thermal barrier coatings (TBCs) for application to aircraft turbines. This chapter focuses mainly on two issues of aircraft turbine applications. It discusses first the low thermal conductivity of the new type of D-gun sprayed YSZ top coating. The failure mechanism of thermal shock cycling aimed at improving the lifetime of D-gun sprayed TBCs is then described.

Key words: thermal barrier coatings (TBCs), detonation gun spraying (D-gun spraying), thermal conductivity, thermal shock cycling, failure mechanism.

9.1 Introduction

Gas detonation gun (D-gun) technology and equipment were originally developed and patented in 1955 by Union Carbide (now Praxair).^{1,2} These approaches and capabilities, have not, however, been opened to the public until recently. Even so, in the 1960s, the Institute of Materials Science and Welding Institute of Ukraine, SSR managed to utilize D-gun technology, and eventually developed D-gun equipment. With the disintegration of the Soviet Union, D-gun spraying technology and equipment were offered for sale and thus made known to the research field. Since then, D-gun-sprayed coatings have found wide application, especially in the aircraft industries of the USA, Japan and the former Soviet Union.³⁻⁵ In light of this promising processing method, Beijing Institute of Aviation Materials, China, began to launch independent innovations in D-gun technology and equipment in 1985, but there remains a large gap compared with Ukraine. At the time of writing, there are about ten D-gun facilities in use in China, most of which were imported from Ukraine, and the technology has been studied systematically since the 1990s.⁶⁻¹¹ D-gun technology has now gained an ever-extending application in various engineering fields, such as the medical, aircraft, agricultural and machinery industries, especially for surface strengthening and modifying of machinery components.



9.1 Schematic illustration showing the principle of the D-gun spraying process.¹⁶

A schematic representation of a D-gun spraying device is given in Fig. 9.1. The main feature of D-gun spraying is that high-velocity particles, typically 800–1200 m/s, are accelerated by the detonation wave during spraying; therefore, higher bond strength, higher hardness and lower porosity of the coating can be achieved. This method allows the deposition of quality coatings for various purposes using various powder materials. Alloy(s), oxides, hard metal, carbide cermets as well as composite materials can be sprayed to form coatings with properties of wear-resistance, friction-reduction, thermal-resistance, insulation, conduction and thermal shock resistance. These are extensively used as wear-resistance coatings or seal coatings. The duration of parts can be extended several dozen fold by application of D-gun-sprayed coatings on the top coat.

The two processes in commercial use for thermal barrier coating (TBCs) are air plasma spraying (APS) and electron beam physical vapor deposition (EB-PVD). APS TBCs have lower cost and thermal conductivity compared with EB-PVD TBCs, but at the expense of durability.^{12–14} One means of improving the quality of TBCs, is to try to modify the current APS and EB-PVD techniques. The alternative is to develop a new generation of deposition technology, such as D-gun spraying. This might be a promising technology with the potential to solve some technical difficulties, such as the low torch temperature and very short heating time for $\text{ZrO}_2\text{-Y}_2\text{O}_3$ (YSZ) ceramic particles during the spraying process. Until 1999, Kim *et al.* had utilized D-gun spraying equipment to obtain TBCs successfully for the first time through optimizing the spray parameters, especially the ratio of C_2H_2 to O_2 .^{15–16}

9.2 Detonation gun (D-gun) sprayed thermal barrier coatings (TBCs)

9.2.1 Microstructure of as-sprayed D-gun TBCs

It is known that the D-gun-sprayed TBCs have a typical layer structure similar to that of coatings deposited using other thermal-spraying processes. D-gun spraying offers the highest particle velocity amongst all the thermal spraying technologies which means that it is able to achieve satisfactory lamellar bonding at the interfaces between the flattened particles. Based on the work of Wu and Ke,^{17–19} it is clear that as-sprayed D-gun YSZ top coats have a unique microstructure with vertical cracks, splats, unmelted particles and a rough bond coat surface with protrusions on the top coat. The unmelted particles, the porosity and especially the through-thickness cracks are all beneficial in imparting strain-tolerance to the TBC, while the porosity helps reduce the thermal conductivity. Moreover, it is generally agreed that a rough bond coat surface can increase the duration of a typical plasma-sprayed TBC system during thermal cycling. It has been assumed that the roughness of the bond coating provides mechanical interlocking at the interface between the top and bond coat; however, a recent theoretical analysis showed that periodic undulations of the surface of the bond coat can provide oscillatory energy-release rates, which would cause cracking in the top coat to be exposed locally, which, in turn, prevents or postpones TBC spallation. Inter-splat porosities and splat boundaries can also be seen under the protrusions in the bond coat around the interface. These can possibly provide a pathway for oxygen ingress into the bond coat when connecting to the interface of a relatively porous structure typical of the YSZ top coat.

9.2.2 Thermal conductivity

When designing a TBC, a thermally protective TBC layer with a low thermal conductivity is introduced to maximize the thermal drop across the thickness of the coating in order to protect the substrate alloy. Much research work focuses on how to further decrease the thermal conductance, especially from the initial ZrO_2 (between 2.5 and 4.0) to YSZ (2.3–2.6 in the dense form). Generally, there are three approaches to lowering the thermal conductivity of TBCs: (i) to lower the thermal conductivity of the coating material; (ii) to lower the thermal conductivity by increasing the porosity of the coating; and (iii) to increase the thickness of the coating. In this section, we will deal with two YSZ powder materials – normal solid ZrO_2 –8% Y_2O_3 (NSP–YSZ) and hollow spherical ZrO_2 –8% Y_2O_3 (HSP–YSZ) – sprayed by D-gun with a low thermal conductivity.

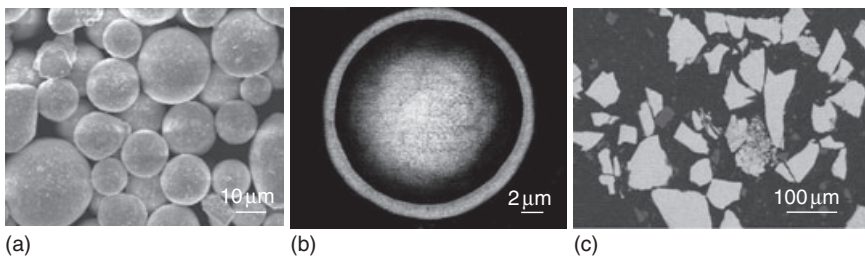
The thermal conductivity of TBCs is related to the microstructure and density of the YSZ. A relation which has been derived for calculation of the thermal conductivity (λ) values of YSZ coatings is²⁰

$$\lambda = \alpha \cdot \rho \cdot C_p \quad [9.1]$$

where α , C_p , ρ are thermal diffusivity, specific heat and density, respectively. With regard to the normal widely used solid powder of YSZ (NSP-YSZ), it has been reported that D-gun-sprayed YSZ free coatings had a thermal conductivity (1.0–1.4 W/mK) approaching that of the plasma-sprayed coatings (1.0–1.5 W/mK¹⁷), and much lower than their EB-PVD counterparts (>2.0 W/mK¹⁸).

In order to obtain a top coat with even better thermal insulation Ke *et al.*²¹ introduced HSP-YSZ as a new top coat powder material. Different from the NSP-YSZ, as shown in Fig. 9.2, HSP-YSZ has a high closed porosity (>10 vol. %), which is advantageous in increasing the effectiveness of thermal protection and enhancing thermal shock resistance. Correspondingly, the thermal conductivities of the freestanding NSP-YSZ and HSP-YSZ ceramic coatings were 1.0–1.4 W/mK and 0.8–1.2 W/mK from 200°C to 1200°C, respectively. In short, HSP-YSZ ceramic coating by D-gun spraying has lower thermal conductivity. Reducing thermal conductivity will help (i) to improve TBC durability by reducing the metal temperature and retarding the thermally-activated processes responsible for failure and/or (ii) to improve engine efficiency at higher temperatures.

Hasselmann analyzed the effect of cracks of various orientations on thermal conductivity and showed that the maximum reduction in thermal conductivity could be achieved when all cracks were oriented perpendicular to the direction of heat flow.²² Moreover, cracks oriented parallel to the direction of heat flow have negligible effects on thermal conductivity. Similar to a plasma-sprayed coating, a D-gun sprayed coating is formed by



9.2 SEM images of YSZ powders; (a) surface view of HSP; (b) cross-sectional view of HSP; (c) cross-sectional view of NSP.

a succession of molten and partly-molten droplets impacting on a substrate followed by lateral flattening, rapid solidifying and cooling, resulting in a ceramic top coat with a regular and thin lamellar microstructure. The lamellar intervals are applicable to the cracks oriented perpendicular to the direction of heat flow. As a result, the thermal conductivity of D-gun YSZ coatings is lower than that of bulk materials and EB-PVD YSZ coatings which have a columnar microstructure parallel to the direction of heat flow.

9.2.3 Failure mechanism of D-gun TBCs during thermal shock cycling

For plasma-sprayed TBCs with a rough bond coat, failure occurs during crack evolution in the TBC itself, which occurs on planes nominally parallel to the substrate. Conversely, EB-PVD coatings are deposited on smooth bond coats and failed, typically, by loss of adherence at the thermal grown oxide (TGO)/bond coat interface. In both cases, failure is initiated by the energy density in the TGO and exacerbated by sintering of the TBC. This occurs because a thin, highly stressed TGO develops beneath the TBC. The specific mechanisms that contribute to failure of D-gun TBCs are described in this section, with a view to enabling the design of TBCs with greater reliability and durability.

Stress within the TGO exerts a crucial influence on TBC failure.²³ Understanding the stress distributions is important to any failure mechanism model, and curvature and X-ray residual stress evaluation are the methods most commonly adopted.²⁴ However, curvature methods are not usually appropriate for stresses between alternate layers and thus may not lead to any bending of the multi-layer as a whole. Whether X-ray diffraction provides a measure of the stress in the top layer only, or an average over many layers, curvature methods depend largely on the layer thickness. Moreover, problems include peak broadening for very fine grained coatings, loss of peak intensity and a depth of penetration (some tens of micrometers) which can be on a scale equal to the surface roughness for thick coatings. Other methods such as Raman spectroscopy have also been used. One particularly promising method is photo-stimulated luminescence spectroscopy (PSLS)²⁵ since it is non-destructive and it produces a direct measure for local elastic strain energy in the TGO.

There are two main sources of the stresses.^{26,27} (i) thermal expansion mismatching upon cooling; and (ii) TGO growth. Studies have indicated that growth stresses range from near zero to about 1 GPa, and laser piezo-spectroscopic measurement shows that thermal expansion misfit results in compressive stresses ranging from 3–4 GPa. The stresses within the TGO layer are non-uniform, but all compressive stresses use Eq. [9.2] which is

similar to that given in reference²⁵ but modified to reflect one-axis stress within the cross-sectional TGO layer

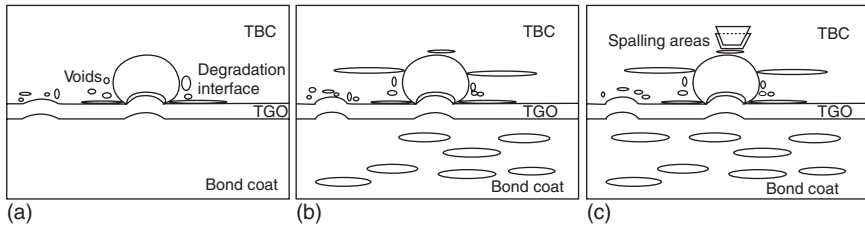
$$\Delta\nu = \frac{1}{3} \Pi_{ii} \sigma \quad [9.2]$$

where Π_{ii} is the trace of the piezo-spectroscopic coefficient tensor with a value of $7.6 \text{ cm}^{-1}/\text{GPa}$, $\Delta\nu$ is the frequency shift (cm^{-1}) of a Ruby (R2) line at about 14430 cm^{-1} and σ is the stresses in the TGO scale. Most of the stress values (thermal stresses together with growth stresses) ranged from 1–3 GPa. A low stress in these coatings provides little strain energy to drive failure and can be seen as the primary reason for their long spallation life under excessively severe thermal cycling conditions applied in D-gun-sprayed TBCs.

It should be noted that relatively higher stresses (4–5 GPa) were also found when measurements were taken where Ni, Cr-rich oxides were overlaid on the Al_2O_3 layer while 2–3 GPa was found in regions consisting of complete Al_2O_3 . This higher stress in the TGO with Ni, Cr-rich oxides is not well understood. A possible reason is that the measured stresses may cover not only the thermal stress, caused by thermal expansion mismatches between metals and oxides, and growth stresses but also phase stresses due to thermal expansion misfit between Al_2O_3 and Ni, Cr-rich oxides.

The combination of stress distributions in the TGO layer and damage which occurred during thermal shock cycling together with the proposed failure mechanism for the damage to D-gun TBCs, which occurs strictly in the ceramic layer and at the TGO/YSZ interface close to the Ni and Cr-rich oxides, is illustrated in Fig. 9.3.

- Undulated TGO formed at the interface during thermal shock cycling results in microcracking at the YSZ/TGO interface and the formation of voids, decreasing toughness between TGO and YSZ (Fig. 9.3a).
- As a result of depletion of Al due to severe internal oxidation within the bond coat, voluminous breakaway oxides containing Cr and Ni formed at the interface, especially around protrusions into the top coat (Fig. 9.3b). Strain caused by thermal expansion misfit during cooling and tensile stresses in the oxides resulted in formation of cracks and voids within the non-alumina oxides, leading to delamination of the outer ceramic layer and failure of the coating at the regions where chemical failure has occurred.
- The nucleation and propagation of the cracks in the ceramic coat along the splat boundary due to the D-gun intermittent spraying process as well as cracks normal to the interface will induce wedge-shaped spallation areas, even in the entire ceramic coat. (Fig. 9.3c)



9.3 Schematic illustrations showing progressive microstructural evolution and damage accumulation during thermal shock cycling leading to spallation failure of the TBC: (a) interface delamination due to undulation development-induced cracking at the YSZ/TGO interface and formation of voids; (b) internal oxidation in bond coat and formation of Ni/Cr-rich oxides due to Al depletion – crack initiation and voids formation within the non-alumina oxides caused by strain evolving from thermal expansion misfit and tensile stress in non-alumina oxides; (c) wedge-shaped spalling areas caused by the propagation and linkage of the cracks along the splat boundary and vertical cracks in the ceramic coat.

9.3 TBCs deposited through arc ion plating (AIP)/D-gun two-step technology

As noted above, the primary failure mechanism of D-gun TBCs involves the depletion of Al in the bond coat and formation of non-alumina break-down oxides within the TGO layer at the bond coat and ceramic top coat interface. With regard to durability and reliability, the challenge is to improve the oxidation resistance of the bond coat at high temperature. Many attempts have been made to deposit metallic coatings other than MCrAlY in order to improve substrate properties. Here we will give one example, an arc ion plated (AIP) NiCoCrAlYSiB alloy coating, designed to confer a better oxidation resistance.

Arc ion plating (AIP), also referred to arc plasma deposition (APD), is a well recognized method of producing protective coatings due to its high ionization efficiency and excellent film adhesion. It is a promising method for depositing oxidation-resistant coatings on gas turbine components. This novel composite two-step AIP/D-gun method has been designed to produce TBCs with better oxidation resistance and thus better thermal shock resistance.²⁸

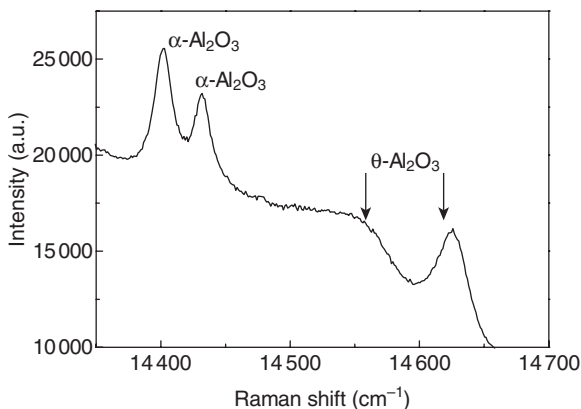
9.3.1 Bond coatings obtained by AIP

TGO growth is the dominant factor in controlling durability; therefore, the chemistry and microstructure of the bond coat are crucial, because of

their influence on the structure and morphology of the TGO. In this case, alloy coatings acting as bond coat deposited using AIP will be described below.

The provided NiCoCrAlYSiB bond coat has a relatively rough surface. Different sizes of particles were dispersed on the surface with smaller particles nucleating on larger ones. The larger particles were of different morphologies while smaller ones were globular. According to the X-ray diffraction (XRD) results, the as-deposited bond coat was composed mainly of γ' -Ni₃Al and γ -Ni phase. Within the as-deposited TBCs obtained by the AIP/D-gun two-step method, there was a uniform and dense NiCoCrAlY-SiB bond coat (generally 35–40 μm thick) with good adhesion to the substrate and the top coat.

As expected, the TGO scale is only Al₂O₃ phase during the thermal exposure of AIP/D-gun TBCs. Raman luminescence spectra on the TGO scale reveal additional peaks, together with α -Al₂O₃ peaks, after 1 h thermal exposure. These additional peaks are arrowed in Fig. 9.4, and reported to coincide with that of θ -Al₂O₃, indicating the co-existence of θ -Al₂O₃ and α -Al₂O₃ in the TGO at the early stage of oxidation. XRD analysis also confirmed this result. At 1100 °C, θ -Al₂O₃ and α -Al₂O₃ co-exist after 1 h oxidation. However, after 5 h oxidation only a weak θ -Al₂O₃ peak was identified, and α -Al₂O₃ was the dominant phase present in the oxide scale; extended oxidation causes no further change in phase composition of the TGO scale, only increasing the intensity of the α -Al₂O₃ peaks. This is borne out by Brumm and Grabke²⁹ who identified a region of phase co-existence at about 850–1200 °C.



9.4 Typical R1 and R2 fluorescence spectra for α -Al₂O₃, and an additional peak coinciding with θ -Al₂O₃.

9.3.2 Stress distributions of thermal grown oxide (TGO)

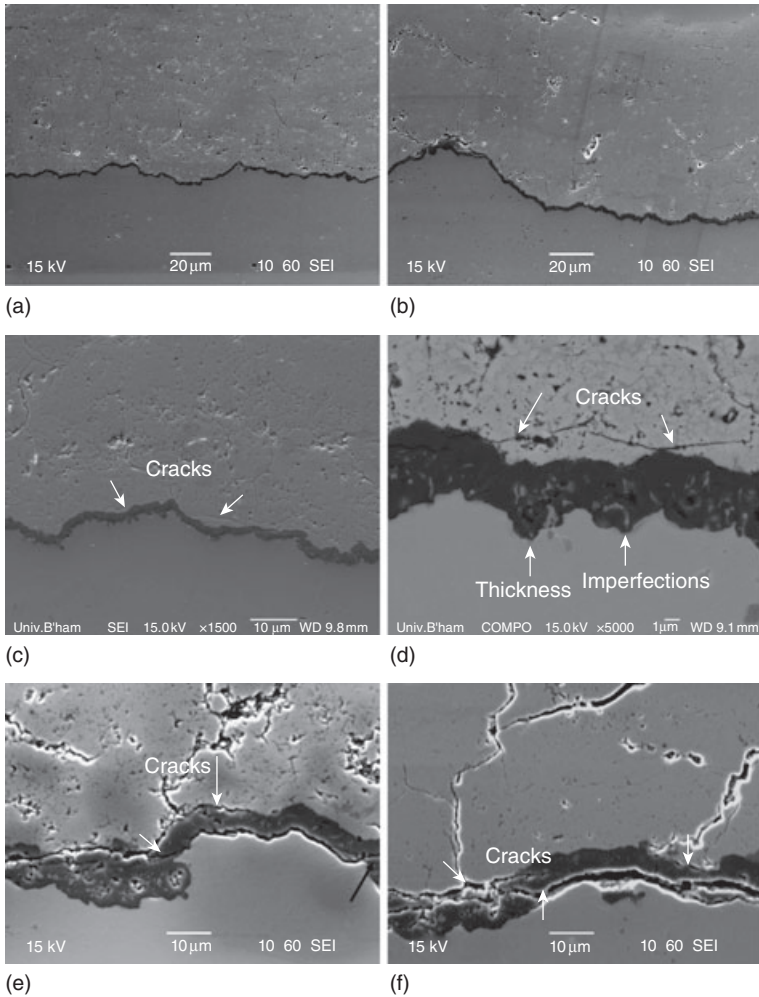
Equation [9.3]²⁵ is used to estimate internal stresses in the TGO when the TGO is assumed to be untextured and polycrystalline under biaxial-stresses:

$$\Delta v = \frac{2}{3} \Pi_{ii} \sigma \quad [9.3]$$

Spectra were recorded from samples that were thermally exposed for different times at 1100 °C. On the basis of the observed frequency shifts of the R2 line, the corresponding biaxial compressive stresses can be produced by inverting Eq. [9.3]. The measured stresses were varied. It should be noted that the transformation of metastable θ -Al₂O₃ to α -Al₂O₃ is generally accompanied by volume shrinkage of about 13%, creating a tensile stress (or decreasing compression). Therefore, compressive stresses of TGO during the transient oxidation period from the metastable θ -Al₂O₃ to the stable α -Al₂O₃ (~5 h) were at a lower level. After the transient period, the average stresses ranging from 0.5–1.5 GPa were almost independent of oxidation time. However, at long oxidation times (thermally exposed for 500 h), the stresses appeared to decrease due to the spallation failure.

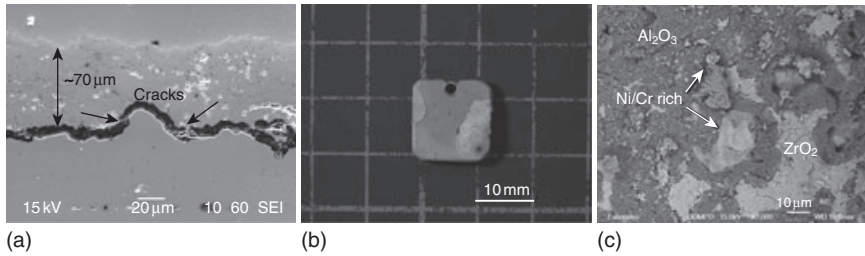
9.3.3 Microstructure evolution during thermal exposure

The changes in coatings microstructure with increasing oxidation time, especially at the TGO/TBC and TGO/bond coat interfaces shown in Fig. 9.5a–f have four features. (i) a more undulated and thickened TGO layer; (ii) separation between the bond coat and the TGO; (iii) cracks running across the TGO; and (iv) cracking within the top coat and along the TGO/bond coat interface. Initial cracking across the TGO was commonly observed around all undulation crests in those TBCs thermally exposed after 200 h, which can be seen from Fig. 9.5e. Meanwhile, the cracks within the top coat increased in length over time. It has been suggested that their eventual linkage would lead to the spallation of the lamellar TBC in the ceramic coat, which may account for the thinner top coat, with thickness of 70 μ m for the sample after 400 h thermal exposure (as shown in Fig. 9.6a) compared with ~200 μ m for the as-received samples. AIP/D-gun TBCs after 500 h decayed by instant peeling of the ceramic top coat from the substrate on cooling to room temperature (Fig. 9.6b). The ceramic top coat split into thin pieces and peeled off, although some YSZ still adhered to the substrate. Energy dispersive X-ray (EDX) composition analysis of the spallation area in the plan view (Fig. 9.6c) implied that the light region consisted of some remaining YSZ, while the area where TBC had been spalled off during cooling to room temperature was Al₂O₃ TGO layer (the grey black region)



9.5 Change of coating microstructure with thermal exposure at 1100°C for (a) 1 h; (b) 5 h; (c) 10 h; (d) 25 h; (e) 200 h; (f) 300 h, showing the TGO thickening and becoming more undulated, cracks running across the TGO and debonding damage along the bond coat/TGO interface.

and bare bond coat (Ni/Cr rich indicated by arrows). The fracture surface from the sample suggested that the failure of the AIP/D-gun TBCs occurred at the TGO/bond coat interface, leading to lamellar spallation of TBC and even peeling of the entire ceramic top coat.



9.6 (a) Cracking sequence caused by growth misfit, followed by cooling to ambient and the radial crack penetrating through the TGO at its inner edge. (b) Surface images of sample after 500 h cooling to ambient from macro-view. (c) Back scattered electron image of spallation area.

9.3.4 Failure mechanism of AIP/D-gun TBCs during thermal exposure

Compared with the thermal mismatch stresses (generally 3–4 GPa), the stresses in AIP/D-gun TGO were much lower. The exact cause for this was not well understood. Possible reasons could include different instrumentation as well as different methods of analyzing the recorded spectra. However, a reasonable deduction might be linked to greater strain tolerance of the HSP–YSZ top coat and better oxidation resistance in AIP/D-gun TBCs compared to D-gun TBCs with a NSP–YSZ top coat.

The fact that the stress values after the transient oxidation period did not change much with thermal exposure time, together with a slight decrease for the sample after 500 h thermal exposure, and the occurrence of catastrophic spallation failure at ambient temperature after cooling, suggests that spallation failure might be determined by an environmental-driven sub-critical crack along with the increase in the growth along the bond coat/TGO scale interface. Therefore, we could find that the decrease in biaxial stress at long oxidation times was a direct result of the growth of debonding damage at the TGO/bond coat interface which would result in stress relief as the materials expanded.

9.4 Future trends

Better thermal insulation of the hot path components is needed in state-of-the-art gas turbines and in diesel engines because of the increasing demands created by high process temperatures. As previously described, taking advantage of the higher closed porosity for HSP–YSZ, HSP–YSZ D-gun TBCs with HSP–YSZ have a lower thermal conductivity than those TBCs

with NSP–YSZ obtained by D-gun, PS and EB–PVD. Thus the next step in the development of D-gun TBCs should be aimed at lowering thermal conductivity and increasing coating thickness, thick TBCs being an attractive option. One problem in the application of thick coatings which needs addressing is the tensile stresses within a coating system. It is important to note that D-gun TBCs have been found to be a compressive stress state within the coatings system, which has potential for thick (TBCs).

It is a fact that the failure of the conventional duplex TBC systems is mainly caused by the thermal expansion mismatch between the ceramic top coat and metal bond coat of the systems. One method of solving this problem is to introduce the concept of functionally gradient material (FGM) into TBCs, which are referred to as ‘FGM–TBCs’; however, the fabrication of a fine mixture of ceramics and metals with a compositional gradient is quite difficult. Several processing techniques have been explored, such as plasma spraying, powder metallurgy, and *in situ* synthesis, but finding the optimum process for the fabrication of FGM–TBCs still remains a challenging task. Despite the difficulty, a new approach (a ‘shot control method’) in D-gun spraying with the potential to achieve an excellent FGM–TBC was successfully developed by the work of Kim *et al.*¹⁶ The FGM layer of the FGM–TBCs prepared using this method exhibited a well-mixed microstructure of metals and ceramics with a desired compositional gradient in the thickness direction. Microhardness measurements and XRD analyses revealed that the ceramics and metals mixed in the FGM layer maintained their individual properties without severe oxidation or phase transformation. The expected improvement in the thermal shock resistance due to the realization of a functionally graded layer between the ceramic and the metal coating layers in TBC systems was also proved, as shown by thermal shock tests using a burner rig tester.

Another viable method is to produce nano-structured coatings because of their extraordinary properties. Novel properties of nano-structures have been widely reported. For example, nano-sized powder materials, nano-composite or nano-scale multi-player thin films frequently exhibit novel properties that cannot be implemented in materials of conventional microstructures, demonstrating enhanced properties, including hardness, strength, ductility and toughness, and nano-structured YSZ coatings have low thermal conductivity, high coefficient of thermal expansion and excellent mechanical properties.^{30–32} Therefore, use of nano-structure materials is expected to improve the performance of TBCs.

One of the biggest challenges in thermal spraying of nano-materials is to retain the pre-existing nano-structure of the feedstock. During the plasma spraying of ceramics, it is necessary to partially melt the powder particles in order to achieve the necessary physical conditions for cohesion and adhesion. If nano-structured powder particles are fully melted during spraying,

then the traditional behavior of thermal spray particles, such as solidification, nucleation and growth, will take place. Such processes will destroy the original nano-structured features of the feedstock. D-gun spraying technology has advantages over both plasma spraying and high-velocity oxygen fuel (HVOF), since it has a moderate flame temperature for melting nano-materials instead of a high velocity to produce high-performance coatings.

9.5 Conclusion

In aircraft turbine applications, the spallation resistance and the thermal conductivity of the coating system are the main properties. This chapter focused on these two issues. The results showed that D-gun-sprayed TBCs with a lamellar structure had a low thermal conductivity, close to the thermal conductivity of the plasma-sprayed YSZ and much lower than their EB-PVD counterparts, due to microstructural difference.

Different process methods lead to different microstructure features which are associated with different failure mechanisms. Unlike PS where failure occurred due to crack evolution in the TBC itself and EB-PVD where failure, typically, occurred at the TGO/BC interface due to loss of adherence, the events that lead to the failure of D-gun sprayed TBCs are motivated by chemical failure and occur strictly in the ceramic layer and at the TGO/YSZ interface near Ni and Cr-rich oxides. Regarding TBCs modified by a two-step AIP/D-gun process, spallation failure might be determined by an environmental-assisted sub-critical crack with growth along the bond coat/TGO scale interface.

9.6 References

1. U. S. PATENT. 2714563, 1955.
2. ENGLISH PATENT. 742387, 1952.
3. R. C. TUCKER, JR. Structure property relationships in deposits produced by plasma spray and detonation gun techniques. *J. Vac. Sci. Technol.*, 1974 **11**(4):725–734.
4. Y. A. KHARLAMOV. Detonation spraying of protective coatings. *Mater. Sci. Eng.*, 1987 **93**:1–37.
5. X. Q. MA, Y. M. RHYIM, H. W. JIN, C. G. PARK and M. C. KIM. Application of fractal dimension to optimum deposition of NiCrAlY coating by D-gun spray. *Mater. Manu. Proc.*, 1999, **14**(2):195–204.
6. Y. N. WU. *Study on the High Temperature Properties and Failure Mechanisms of Protective Coatings for Blades of Gas Turbine*, Postdoctoral Research report, IMR, CAS, Shenyang, China, 2003.
7. P. L. KE. *Study on Thermal Shock Cycling Behaviors and Failure Mechanisms of Thermal Barrier Coatings Obtained by Detonation Gun Spraying*. Dissertation for degree of Doctor of Philosophy, IMR, CAS, Shenyang China., 2006.

8. Q. T. MI, J. P. CHEN and Y. K. FENG, Detonation gun spraying, *J. Mater. Eng.*, 1990, **6**:1–5.
9. S. LIU, Application of detonation gun spraying, *Welding and Joining*, 1997, **9**:2–5.
10. J. X. TANG, A. B. ZHANG, J. P. CHEN and Q. T. MI, Analysis on processing principle of detonation gun spraying, *Mater. Prot.* 2000, **9**(32):33–35.
11. G. H. LU, P. ZENG, H. P. HUANG, G. T. WANG, G. R. XIE, Z. P. PAN and S. J. HU, Microstructure and properties of Al_2O_3 ceramic gradient coatings deposited by detonation gun spraying, *J. Mater. Eng.*, 2000, **32**(4):30–33.
12. A. G. EVANS, D. R. MUMM, J. W. HUTCHINSON, G. H. MEIER and F. S. PETTIT, Mechanisms controlling the durability of thermal barrier coatings, *Prog. Mater. Sci.*, 2001, **46**(5):505–553.
13. N. P. PADTURE, M. GELL, and E. H. JORDAN, Thermal barrier coatings for gas-turbine engine applications, *Science*, 2002, **296**:280–284.
14. M. GELL, L. D. XIE, X. Q. MA, E. H. JORDAN and N. P. PADTURE, Highly durable thermal barrier coatings made by the solution precursor plasma spray process, *Surf. Coat. Technol.*, 2004, **177–178**:97–102.
15. X. Q. MA, Y. M. RHYIMN, H. W. JIN, C. G. PARK and M. C. KIM. Effect of aluminum oxide diffusion barrier layer on the oxidation behavior of detonation gun-sprayed thermal barrier coating at 1200°C , *Corrosion*, 1999, **55**:805–813.
16. J. H. KIM, M. C. KIM and C. G. PARK. Evaluation of functionally graded thermal barrier coatings fabricated by detonation gun spray technique, *Surf. Coat. Technol.*, 2003, **168**:275–280.
17. Y. N. WU, F. H. WANG, W. G. HUA, J. GONG, C. SUN and L. S. WEN, Thermal barrier coatings obtained by detonation spraying, *Surf. Coat. Technol.*, 2003, **166**:189–194.
18. P. L. KE, Y. N. WU, Q. M. WANG, J. GONG, C. SUN and L. S. WEN. Study on thermal barrier coatings deposited by detonation gun spraying, *Sur. Coat. Technol.*, 2005, **200**:2271–2276.
19. P. L. KE, Q. M. WANG, J. GONG, C. SUN and Y. C. ZHOU. Progressive damage during thermal shock cycling of D-gun sprayed thermal barrier coatings with hollow spherical $\text{ZrO}_2\text{--}8\text{Y}_2\text{O}_3$, *Mater. Sci. Eng. A*, 2006 **435–436**:228–236.
20. R. E. TAYLOR. Thermal conductivity determinations of thermal barrier coatings, *Mater. Sci. Eng. A*, 1998, **245**:160–167.
21. P. L. KE, Q. M. WANG, M. H. GUO, J. GONG, C. SUN and Y. C. ZHOU. Failure mechanism of D-gun sprayed thermal barrier coatings subjected to thermal shock cycling, *Mater. Sci. Forum*, 2005, **475–479**:3977–3980.
22. D. P. H. HASSELMAN. Effect of cracks on thermal conductivity, *J. Compos. Mater.*, 1978, **12**:403–407.
23. C. H. HSUEH and E. R. FULLER, Analytical modeling of oxide thickness effects on residual stresses in thermal barrier coatings, *Scripta Mater.*, 2000, **42**: 781–787.
24. P. J. WITHERS and H. K. D. H. BHADSHIA, Overview: residual stress Part 2 – Nature and origins, *Mater. Sci. and Technol.*, 2001, **17**:366–375.
25. R. J. CHRISTENSEN, D. M. LIPKIN and D. R. CLARKE. Nondestructive evaluation of the oxidation stresses through thermal barrier coatings using Cr^{3+} piezospectroscopy. *Appl. Phys. Lett.*, 1996, **69**:3754–3756.
26. D. M. LIPKIN and D. R. CLARKE. Measurements of the stress in oxide scales formed by oxidation of alumina-forming alloys, *Oxid. Met.*, 1996, **45**:267–280.

27. J. R. CHRISTENSEN, V. K. TOLPYGO and D. R. CLARKE, The influence of the reactive element yttrium on the stress in alumina scales formed by oxidation, *Acta Mater.*, 1997, **45**:1761–1766.
28. C. SUN, P. L. KE, Y. N. WU, W. G. HUA, J. GONG, L. S. WEN, Q. M. WANG, J. Q. XIAO, A. Y. WANG, A. L. JI, J. D. ZHENG and H. T. CAO. *A Method of Producing Thermal Barrier Coatings with Thermal Shock Resistance*, Chinese Patent No. 03133344.3, 2006.
29. H. J. GRABKE, M. W. BRUMM, and B. WAGEMANN, The oxidation of NiAl, *Mater. Corros.* 1996, **47**:675–677.
30. B. H. KEAR and G. SKAUDAN, Thermal spray processing of nanoscale materials, *Nanostruct. Mater.*, 1997, **8**:765–769.
31. M. GELL, Application opportunities for nanostructured materials and coatings, *Mater. Sci. Eng. A*, 1995, **204**:246–251.
32. G. SOYEZ, J. A. EASTMAN, L. J. THOMPSON, R. J. DIMELFI, G. R. BAI and P. M. BALDO, Grain-size-dependent thermal conductivity of nanocrystalline yttria-stabilized zirconia films grown by metal-organic chemical vapor deposition, *Appl. Phys. Lett.*, 2000, **77**:1155–1157.

Oxidation and hot corrosion of thermal barrier coatings (TBCs)

C. G. ZHOU and Y. X. SONG, Beihang University, China

Abstract: Thermal barrier coatings (TBCs) with a two-layered structure consisting of an oxidation protective bond coat and a thermally insulating yttria stabilized zirconia (YSZ) top coat are used to provide thermal insulation and oxidation resistance to metallic components from the hot gas stream in gas turbine engines used for aircraft propulsion, power generation and marine propulsion. The oxidation behavior of the bond coat, including both MCrAlY and Pt aluminide coating, has a major impact on the life of the TBCs. The oxidation behavior and failure mechanisms of TBC systems are summarized. In addition, the degradation mechanisms experienced by TBC systems exposed to deposits are also discussed.

Key words: thermal barrier coatings (TBCs), oxidation behavior, failure mechanism, degradation mechanism.

10.1 Introduction

Oxidation is a phenomenon whereby metallic elements of materials exposed to oxygen or oxygen-containing atmospheres at elevated temperatures are converted into their oxides.¹ The successful application of many materials requires excellent high-temperature properties. Surface stability of the candidate material is necessary in order to prevent rapid material consumption at high temperatures. In general, this indicates that the exposed material should be able to form a slow-growing, stable, adherent surface scale, which would protect the underlying substrate material. The most important and effective scales are oxides; they are easily produced through reaction with oxygen in the air or with oxygen-containing molecules such as H₂O, CO₂ or CO in other gaseous environments. The most sought-after oxide scales are Al₂O₃, Cr₂O₃ and SiO₂ because of their outstanding protective qualities. Many of the high-temperature components used in aircraft and ground power gas turbines rely on these scales for protection.²

When materials are exposed simultaneously to oxygen and some other environmental constituents such as CO₂ and SO₂, fused or molten salts and solid particles, the interaction between these environmental constituents

and the materials results in corrosion and erosion.¹ Hot corrosion is a serious problem in power generation equipment, gas turbines, internal combustion engines, fluidized bed combustion, industrial waste incinerators and the paper and pulp industries. This phenomenon has been noticed in boilers, internal combustion engines, gas turbines, fluidized bed combustion and industrial waste incinerators since the 1940s. However, it was not until the late 1960s, when gas turbine engines in military aircraft suffered severe corrosion while operating over sea water during the Vietnam conflict, that it became a topic of importance and general interest.^{3,4} Although there are some alloy compositions that require a long initiation time, during which the hot corrosion process moves from the initiation stage to the propagation stage, there is no alloy which is immune to hot corrosion attack indefinitely. Superalloys have been developed for high-temperature applications. However, these alloys are not always able to meet the requirements of both high-temperature strength and high-temperature corrosion resistance simultaneously. To achieve both strength and resistance to environmental degradation, these two functions should be separated. The load capability is provided by the substrate alloy, while the oxidation and corrosion resistance is achieved by the application of coatings. The high-temperature protection system has to meet several criteria, such as providing adequate environment resistance, being chemically and mechanically compatible with the substrate and being applicable in practice, reliable and economically viable.⁵

10.2 Oxidation of thermal barrier coatings

Typical TBCs have a two-layered structure consisting of an oxidation protective bond coat and a thermally insulating yttria-stabilized zirconia (YSZ) top coat.⁶ The metallic bond coat not only provides a surface for the top coat to bond to, but also prevents oxidation and corrosion of superalloy substrates as YSZ coating is essentially a porous layer that is transparent to oxygen penetration.

It has been determined that the oxidation behavior of the bond coat has a major impact on the life of the TBCs. Several factors can affect oxidation resistance of the bond coat, including: (i) bond coat and substrate materials; (ii) bond coat and substrate interdiffusion; (iii) characteristics and morphologies of the thermal grown oxides (TGO); (iv) phase transformation and cracking of the coating.⁷⁻¹² There are two different types of bond coats currently used in TBC systems, namely the MCrAlY bond coat, where M is a metal such as Ni and/or Co, and the platinum-modified nickel aluminides. The purpose of both coating types is to provide oxidation and corrosion resistance as metallic coatings. Thus, a brief overview of oxidation will be presented.

10.2.1 Oxidation mechanisms of metals and alloys

There are two means of oxidation of metals and alloys: metal atoms diffuse outwards from the metal and react with oxygen at the outer surface of the oxide, or oxygen diffuses and reacts with metal atoms at the metal oxide interface. Additionally, oxides can form subsurface precipitates instead of a discrete layer; this type of oxidation is especially common for high-temperature alloys exposed to an oxidation environment for extended time periods.¹³ In some cases, the diffusion of both metals and oxygen is significant and new oxides can form within the oxide layer.¹⁴ The growth of oxides thus forms a continuous, slow-growing scale.

In a binary alloy A–B, the more reactive element may be preferentially oxidized, either internally or externally, depending on content. It is possible that the oxidized element will form a protective scale on the surface of the alloy, so that the other elements will not be oxidized. The growth of a protective scale requires a sufficient supply of the metal that is oxidizing. In order to keep the protective scale growing, the rate of metal consumption due to oxide scale growth has to be slower or equal to the rate at which the metal atoms can diffuse to the scale.¹³

Stress can be generated in a metal/oxide system due to either the volume the oxide takes up being different from that of the metal it replaces, or differences in thermal expansion coefficients between the metal and the oxide, or more complicated mechanisms taking place, especially when alloys are considered. For an oxide that grows at the oxide/metal interface, the compressive stress slows down the flux of anion vacancies; thus the diffusion of oxygen ions to that interface¹⁵ can be slowed down. An additional oxidation mechanism may cause stress due to oxygen going into solution in the substrate. Some metals have a very high solubility for oxygen, causing a large dilational strain that can lead to tensile failure of the oxide.¹⁵

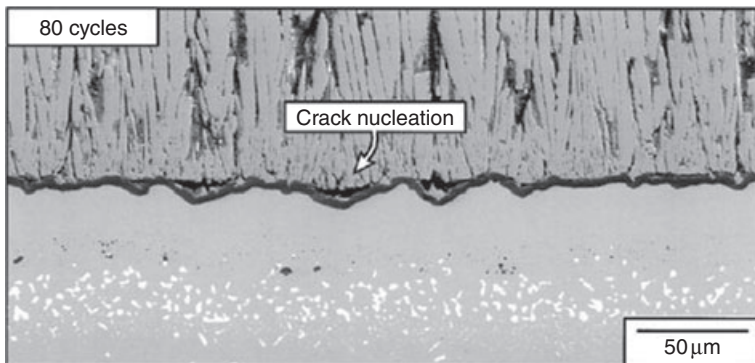
10.2.2 Oxidation behavior of thermal barrier coatings (TBCs)

When a MCrAlY bond coat is used, the TGO frequently exhibits an inhomogeneous morphology and/or composition, especially in the early stages of oxidation.¹⁶ This is caused by the multi-phase character of the MCrAlY coating, which generally consists of γ -Ni and β -NiAl; depending on composition and temperature, further phases, such as γ' -Ni₃Al, α -Cr, Ni–Y and/or σ -CoCr, may appear.¹⁷ By first exposing to a high temperature, i.e., during heat treatment, coating manufacturing and/or actual service, every individual phase prevailing in the coating will tend to form a different type of oxide, e.g., α -Al₂O₃, θ/γ -Al₂O₃, Cr₂O₃, NiO, (Ni,Co)(Cr,Al)₃O₄, etc.¹⁶ The transition of this heterogeneous scale into a stable α -Al₂O₃-based layer can lead to stress initiation and/or result in formation of cracks, which may be

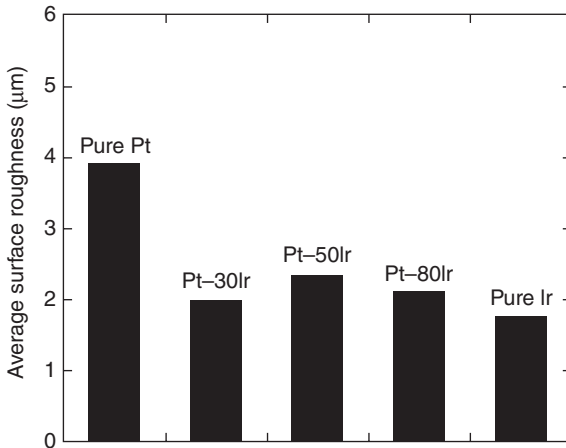
the starting points for failures during high-temperature service, especially during thermal cycling.

The addition of precious metals, such as Pt, Ru or Ir, to aluminide coating allows the formation of an adherent α -alumina scale and improves resistance to oxidation and hot corrosion. Since the early 1970s, Pt–aluminide diffusion layers have been successfully deposited as protective layers on high-temperature components.¹⁷ However, initially, these coatings served exclusively for protecting metals from high-temperature oxidation and hot gas corrosion, and therefore did not consist of a ceramic top coat for insulation. The application of Pt–aluminide coatings as a bond coat was first mentioned in 1993 in the patent of Duderstadt and Bangalore.¹⁸ These layers are normally produced by initial electrodeposition of a Pt layer 8–10 nm thick followed by a diffusion treatment, either as a separate thermal treatment or combined with the aluminizing step. The aluminization is performed using a pack cementation or a chemical vapor deposition (CVD) process.¹⁹ The outer layer of the modified aluminides comprises one of the intermetallic phases PtAl₂, Pt₂Al₃, PtAl²⁰ or Pt in solid solution, depending on the deposition parameters such as thickness of the Pt layer, duration and temperature of the thermal treatment or the activity of Al during the pack cementation process. According to Tawancy *et al.*,⁹ Pt excludes refractory metal strengthening elements out of the layer. This promotes the selective oxidation of Al.

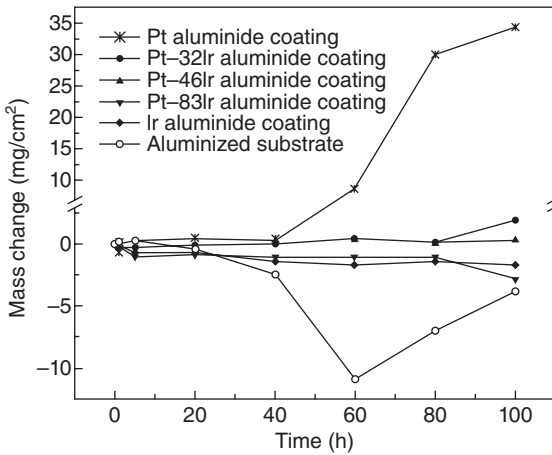
Pt-modified aluminide bond coats have shown substantially improved oxidation resistance for TBCs, but they are prone to ‘rumpling’, during which TGO can initiate cracks, leading to spallation of the top coat.^{20–24} A rumpled bond coat has a very negative effect on TBC adhesion as shown in Fig. 10.1.²⁵ In addition, Pt lacks adequate strength at high temperature,²⁶ and the cost of Pt is much higher than that of other noble metals. As



10.1 Rumpling on a NiAl bond coat after thermal cycling.²⁵



10.2 Average surface roughness of specimens measured by a surface profiler after cyclic oxidation.²⁷



10.3 Corrosion kinetics for Pt-Ir aluminide coatings and aluminized substrate at 1173K coated with 90% Na₂SO₄ + NaCl salts.²⁸

Fig. 10.2 illustrates, the addition of Ir to Pt-modified aluminide coating can be one means of retarding surface rumpling.²⁷ In addition, it was reported that PtIr-modified aluminide coating could enhance type I hot corrosion resistance, as shown in Fig. 10.3.²⁸ On the other hand, adding Ru to Pt-modified aluminide coating is of interest also because the addition of Ru to Ni-base superalloys has been proved to have the capacity to improve creep strength.²⁹

It has also been proposed that Pt group metals, such as Ru, can potentially act as diffusion barriers preventing the migration of detrimental elements toward the BC/TGO interface, thus possibly minimizing the interdiffusion effects.^{30–32} Recently, the replacement of Pt with Ru in the bond coat system has been investigated to fabricate a creep-resistant bond coat.³³ These experiments showed that Ru-modified aluminide bond coats offered less favorable oxidation resistance and oxide adherence in comparison with conventional Pt-modified aluminides.^{29,33}

In order to utilize the beneficial creep properties of RuAl^{34,35} without impairing the oxidation resistance of the bond coats, Tryon *et al.* investigated the hybrid Ru/Pt-modified bond coatings fabricated by electron beam physical vapor deposition (EB–PVD). It was found that these hybrid coatings exhibited comparable cyclic oxidation resistance and better creep properties compared with traditional Pt-modified coatings.³⁶ Three-layered Pt/Ru-modified aluminide coatings were developed by electrodeposition followed by the conventional aluminizing process. The Pt/Ru-modified aluminide coating showed better thermal cyclic oxidation resistance than Pt-modified aluminide coating since Ru provided an increase in the creep strength of the bond coat, with the result of retarding the rumpling phenomenon. The addition of Pt and Ru to aluminide has also been proved capable of increasing the surface concentration of Al and retarding the interdiffusion of the alloying elements.³⁷

10.3 Failure mechanisms of TBCs

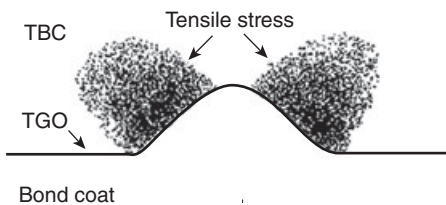
Experimental observations have shown that the failure of TBC systems is very complex and mostly affected by a superposition of different mechanisms. Previous experiments^{38–42} have demonstrated that oxidation of the bond coat and thermal mismatch stress^{43,44} contribute to the rapid degradation of TBCs. The major cause of TBC failure is delamination of the outermost coating layer from the bond coat to which it is applied.

The spallation of the TBC top coat is a very destructive event, as it will generally result in failure of the substrate in a relatively short time due to a large increase in the surface temperature of the metal. TBC spallation is initiated by cracking either at the TGO/bond coat interface or at or near the TGO/TBC interface.⁴⁵ It is widely accepted that once enough cracks form, they eventually coalesce into a crack large enough for the TBC to buckle and spall. In most cases, the cracking is attributed to the mechanical forces that result from the changing from a planar to a non-planar interface. During thermal cycling, progressive roughening of the bond coat/TGO/top coat interfaces occurs due to cyclic creep of the bond coat.⁴⁶ Such roughening, often termed ‘ratcheting,’ occurs only under thermal cycling, but not during isothermal exposures. It also requires an initial surface-geometry imperfection of some minimum dimension and the progressive lengthening

of the TGO caused by TGO cracking or in-plane growth during oxidation.^{47,48} For a nominally flat bond coat/TGO interface (EB–PVD TBC), this roughening is manifested in the form of TGO penetrating into the bond coat.^{25,49} In an already undulated interface, the undulation amplitude is amplified – atmospheric plasma spraying (APS) APS TBC.²⁰ All of these geometrical factors result in out-of-plane stresses normal to the metal/ceramic interface, the severity of which increases with thermal cycling. These stresses, in combination with the interfacial imperfections, are primarily responsible for the TBC failure. The relative locations of the tensile stresses that form around a perturbation are shown in Fig. 10.4.⁵⁰

Damage initiation and progression in the form of microcracks can occur in several different ways in TBCs, depending on the particularity of TBC, the portion of spallation life already consumed and the thermal cycling environment. The coalescence of these cracks results in the ultimate spallation failure of the TBC.⁵¹ The initiation of cracks close to the interface between the TBC and the bond coat seems to be fully explained by the residual stress calculations made by Chang *et al.*⁵² and others.^{25,53–55} Meanwhile, numerous models based on different conceptions have been proposed, which might qualitatively explain how cracks propagate.^{20,25,38,56} All models consider oxidation at the rough interface between TBC and bond coat as well as the phenomena resulting from reasons such as the redistribution of residual stresses induced by volume growth or morphological instability of the TGO layer^{15,56–60} as the driving force of crack propagation. A fracture mechanics approach was developed,⁶¹ by which cracks are modeled in the critical areas of the TBC system and assessed by using the modified crack closure integral method to determine the mode-dependent crack loading. The crack propagation capability is then predicted by using a recently-implemented mixed mode failure criterion and proper fracture toughness data.

The growth of the TGO during engine operation is the most important phenomenon responsible for the spallation failure of TBCs. TGO growth sometimes results in a constrained volume expansion that leads to compressive ‘growth’ stresses⁵⁹ persisting at all temperatures. Upon cooling, the thermal-expansion mismatch between the TGO and the bond coat leads



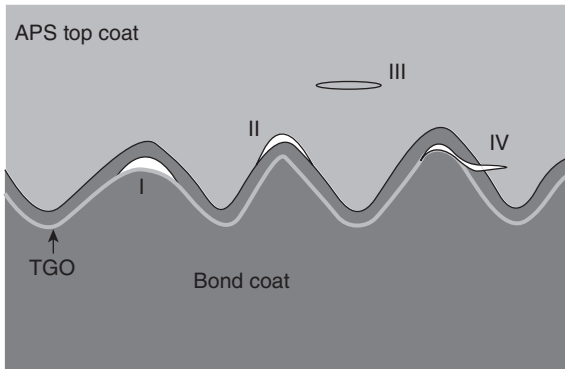
10.4 Tensile stresses in the TBC resulting from a surface imperfection.⁵⁰

to very high 'thermal' compressive residual stresses in the TGO which reach a maximum at ambient temperature.^{62,63} The strain energy in the TGO scales linearly with the TGO thickness and quadratically with the TGO stress, and drives fracture. In addition, a coefficient of thermal expansion mismatch between bond coat and ceramic topcoat can exacerbate a coating failure during thermal cycles.^{64,65} It is seen that bond coat exhibits a higher coefficient of thermal expansion than ceramic top coat.

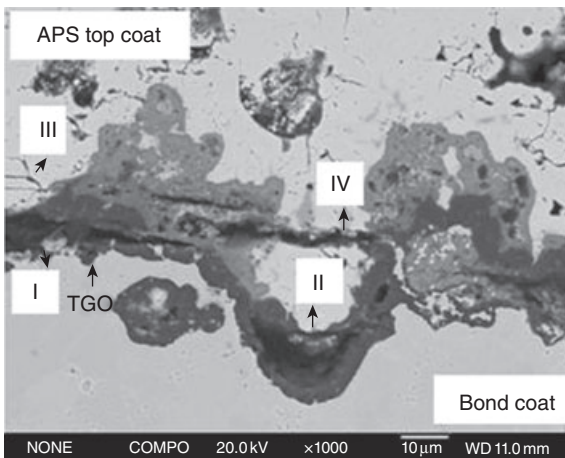
Evans *et al.*⁶⁶ provided an in-depth analysis of the various failure mechanisms of TBC systems. The mechanical failure mechanisms are the result of heterogeneities of TGO thickness in an otherwise planar interface, the formation of interface undulations or foreign object damage. The chemical failure mechanisms which result in the formation of Ni-rich oxides such as spinels are attributed to either Al-depletion, where the spinel forms below the alumina layer, or Ni diffusing through the alumina to form spinel on top of the alumina layer. In either case, the failure occurs within the spinel layer. The formation and growth of the α -Al₂O₃ TGO result in the depletion of Al in the bond coat. The Al depletion, if severe, results in the formation of other oxides, such as Ni- and Co-containing spinels, Y₃Al₅O₁₂ and Y₂O₃.^{67,68} The formation of these phases compromises the structural integrity of the TGO and accelerates localized oxidation by providing fast oxygen-diffusion paths.

The detailed failure mechanisms in the two classes of TBCs (APS and EB-PVD) are discussed separately.⁵¹ There are at least four primary failure mechanisms in APS TBCs driven by the out-of-plane stresses, which are shown schematically in Fig. 10.5a.^{38,69,70} As the TGO thickens, the tensile stress at the bond coat/TGO interface increases, which causes cracking at the bond coat/TGO interface at crests (mechanism I in Figs. 10.5 a and b).^{71,72} The thermal expansion mismatch between the top coat and the metal (bond coat/superalloy) puts the top coat in overall compression at room temperature. Because of the highly undulating nature of the metal/ceramic interface, out-of-plane stresses result in the vicinity of the TGO/top coat interface: tension at the crests and compression at the troughs.⁷³ The tension causes fracture along the TGO/top coat interface at the crests (mechanism II in Figs. 10.5 a and b) and cracking within the highly brittle top coat in the vicinity of the crests (mechanism III in Figs. 10.5 a and b).^{69,70} Beyond a certain TGO thickness, the thermal expansion coefficient of the bond coat/TGO composite becomes lower than that of both the top coat and the bond coat, which converts the compression force in the top coat undulation troughs into the tension force.^{70,74} This reversal causes cracking within the top coat in the 'valleys' between the crests (mechanism IV in Figs. 10.5 a and b).⁷⁰

There are three main types of failure mechanisms in EB-PVD TBCs, two of which are schematically shown in Fig. 10.6a. Mechanism I is the separa-



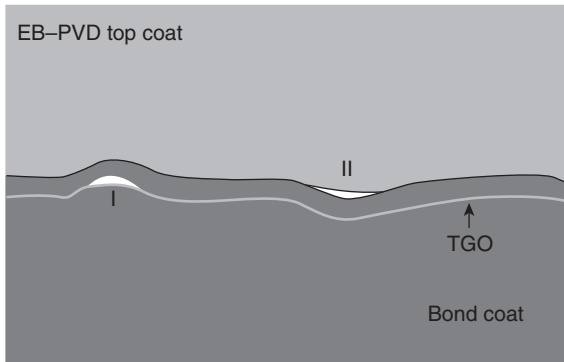
(a)



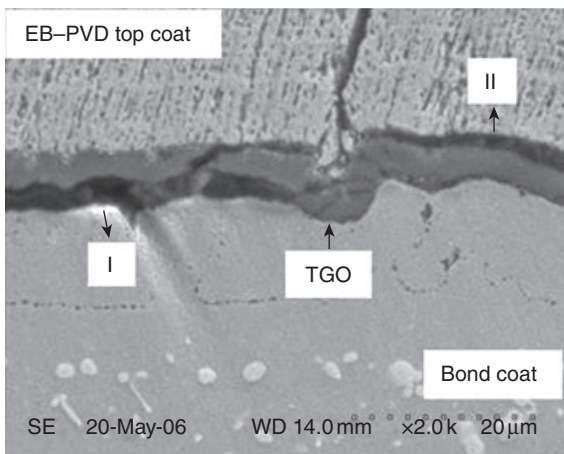
(b)

10.5 (a) Schematic diagram showing the four cracking mechanisms in APS TBC. (b) Cross-sectional SEM of a failed APS TBC showing the various cracking mechanisms illustrated in (a).⁵¹

tion of the bond coat/TGO interface, which is the same as that described in the APS TBC case (mechanism I in Fig. 10.5). The crests in the case of EB-PVD are ‘ridges’ present on the bond coat surface before top coat deposition (Fig. 10.6b).⁷⁵ Mechanism II in Fig. 10.6a is separation of the TGO/top coat interface and penetration of the TGO into the bond coat resulting from one or more of the following mechanisms: (i) progressive TGO roughening caused by bond coat cyclic creep (Fig. 10.6b);^{25,49} (ii) accelerated growth of embedded oxides due to localized TGO cracking;^{46,68,76} and (iii) cavity formation in the bond coat.⁴⁶ For EB-PVD TBCs with relatively flat and defect-free interfaces, the compression in the TGO causes large-scale buckling.^{75,77}



(a)



(b)

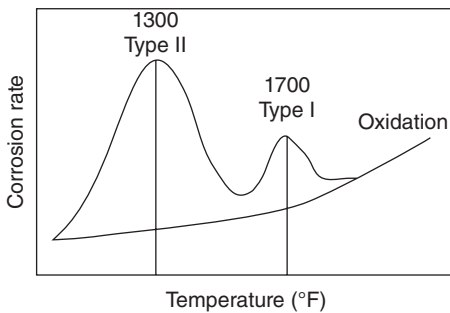
10.6 (a) Schematic diagram showing two of the three cracking mechanisms in EB-PVD TBC. (b) Cross-sectional SEM of a failed EB-PVD TBC showing the cracking mechanisms illustrated in (a).⁵¹

10.4 The degradation mechanisms experienced by TBC systems exposed to deposits

Corrosion induced by molten salts in an oxidizing gas at elevated temperatures is called 'hot corrosion'.^{78–81} It occurs when metals and alloys are covered with salt films at a temperature typically between 700 and 925 °C. According to Hancock⁸² and Eliaz *et al.*,⁸³ hot corrosion is an accelerated form of oxidation that occurs when metals are heated in the temperature range 700–900 °C in the presence of sulphate deposits, which are formed as a result of the reaction between sodium chloride and sulphur compounds in the gas phase surrounding the metal.

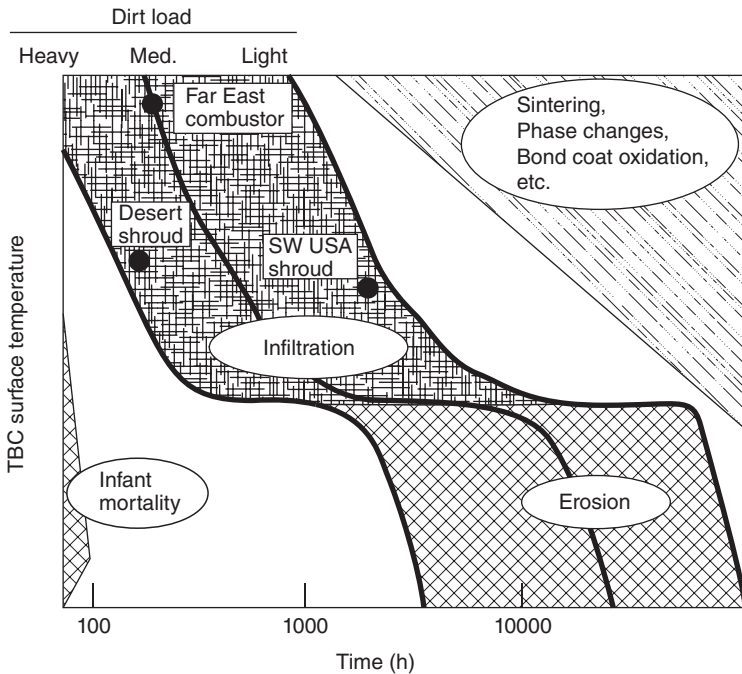
Corrosion which occurs above the melting point of the salt is called ‘type I hot corrosion’, while the corrosion at the lower end of the temperature range is called ‘type II hot corrosion’.¹ The range of the two types of hot corrosion measured in terms of metal loss under the impact of temperature is schematically illustrated in Fig. 10.7.¹ In both types of hot corrosion, fluxing with corroding salts defeats the protective oxide scale that formed on superalloys and coatings. Once the protective scale is rendered ineffective, the substrate alloy or coating becomes vulnerable to internal oxidation and sulphidation. There are generally two stages of hot corrosion. The first stage is the initiation stage that involves the breakdown of protective oxide scale. The second stage is known as the propagation stage, in which the salts have access to the unprotected metal and corrosion continues deteriorating at exceedingly high rates.

The degradation mechanisms experienced by TBC systems exposed to deposits during service may be manifold. Deposits may affect both the zirconia top coat and the bond coat, and their effect may be predominantly either chemical or mechanical in nature. Molten salt can penetrate into the YSZ coatings along pores and cracks in YSZ and it reacts with the metallic bond coat.^{84–88} The formation of monoclinic zirconia and/or the accelerated sintering of zirconia in the presence of oxides resulting from the chemical reaction of the deposits with the stabilizing phases in the zirconia top coat lead to the degradation of TBCs.^{89–93} Basically, both the formation of monoclinic zirconia and enhanced sintering contribute to the increased stress build-up within the zirconia layer. Transformation of metastable tetragonal zirconia into the monoclinic phase results in a volume expansion of approximately 4% which, given a significant occurrence in a coating, can lead to significant degradation of the structural integrity of the ceramic coating. Sintering of the zirconia coating increases its Young’s modulus, and thus adversely affects its mechanical properties.⁹⁴ In addition, infiltration of



10.7 Schematic illustration of temperature effect on rate of damage to superalloys based on type I and II hot corrosion superimposed on contribution due to oxidation.¹

molten deposits into the microstructure of a YSZ porous coating would cause additional stresses because of a thermal expansion mismatch between the deposits and the zirconia.^{95,96} It has been suggested that TBC damage from the deposits will only be significant if the deposits melt and infiltrate the ceramic coating. Non-infiltrating deposits were considered benign as they do not impose additional stress on the TBC. However, it is possible for a chemical reaction of yttria from the YSZ coating to give rise to a tetragonal-to-monoclinic phase transformation. Borom *et al.*⁹⁶ proposed a damage map consisting of four in-service failure regimes for APS YSZ TBCs (Fig. 10.8). They categorized the regimes as infant mortality, particle erosion, infiltration of molten particles and thermochemical phenomena, such as sintering, phase changes and bond coat oxidation, etc. Notably, for APS TBCs, hot corrosion attack of the bond coat seemed to play a significant role only after a very long operating period. In comparison, infiltration could affect the integrity of the ceramic coating in the range of several hundred to a few thousand hours, depending on TBC surface temperature and extent of deposit load.



10.8 Hypothetical in-service failure regimes for air plasma-sprayed YSZ TBCs shown schematically on a plot of TBC surface temperature vs log of hours to failure.⁹⁶

For sustained hot corrosion, a model that requires a negative solubility gradient has been proposed by Rapp and Goto,⁹⁷ i.e.,

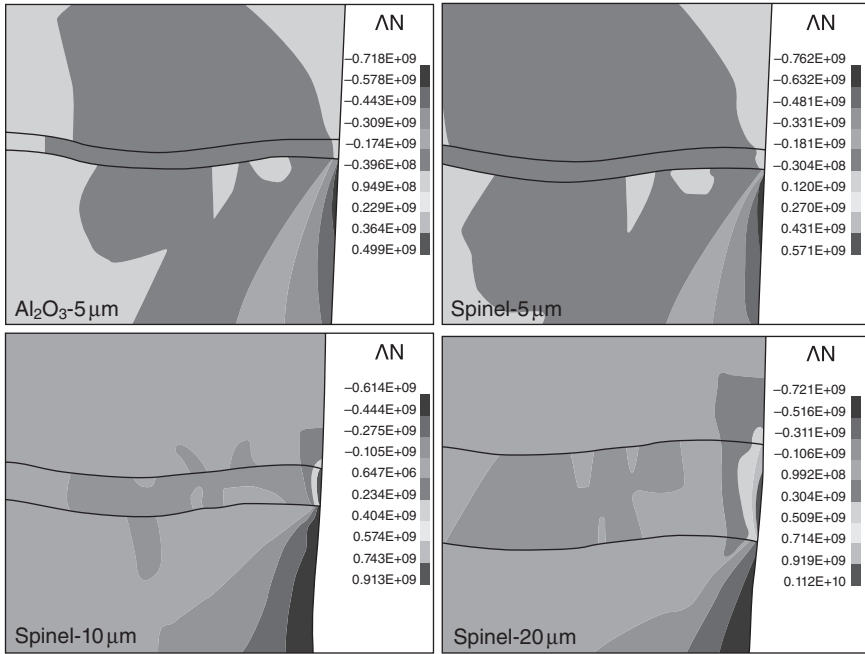
$$\{d(\text{oxide solubility})/dx\}_{\text{at the oxide-salt interface}} < 0$$

where x is the distance from the oxide-salt interface. This mechanism does not consume the molten salt and therefore will not be sustained until either the melt becomes more basic and oxide ions are not produced or the oxide scale is completely removed and the metal becomes accessible to the salt. The self-sustaining corrosion process can prevent the formation of continuous and protective Al_2O_3 .

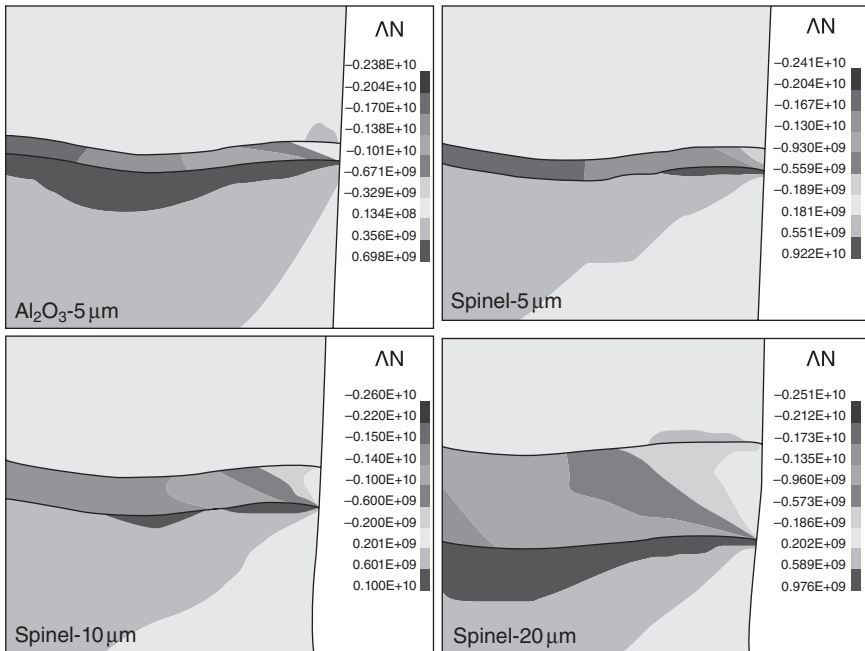
The salts involved in hot corrosion are typically alkali and alkaline earth sulphates. The exact composition of the salts depends on the particular industrial process, impurities involved and the fuel, air and coolant compositions. Khanna and Jha⁹⁸ reported on the chemistry of formation of salt during the combustion of coal/fuel. According to them, the sulphur present in coal and fuel oils yields SO_2 on combustion, which can be partially oxidized to SO_3 . NaCl (either impurity in the fuel or in the air) reacts with SO_3 and water vapor at the combustion temperature to yield Na_2SO_4 , which deposits on the metal/alloy surfaces and would be present as liquid at a sufficiently high temperature. Small amounts of vanadium present in the fuel, on combustion, form V_2O_5 , which can react with Na_2SO_4 to form low melting sodium vanadates which are highly corrosive. At high temperatures, deposits of Na_2SO_4 are molten (m.p. 884°C) and can cause accelerated attack on the Ni and Co-base superalloys.

Accelerated corrosion can also be caused by other salts, viz. vanadates or sulphates-vanadate mixtures or in the presence of solid or gaseous salts, such as chlorides.⁹⁹ Vanadium and sodium are common impurities in low-grade petroleum fuels. Molten sulphate-vanadate deposits resulting from the condensation of combustion products of such fuels are extremely corrosive to high-temperature materials in combustion systems.¹⁰⁰ DeCrescente and Bornstein⁸⁶ were the first to demonstrate that a sodium sulphate deposit must be fused rather than solid in order to cause a significant attack. With regard to experiments conducted in air, Goebel *et al.*¹⁰¹ found that basic fluxing in combination with sulphidation could cause the hot corrosion of Ni. The cyclic oxidation behavior of TBC exposed to NaCl vapor shows that the failure of the TBC occurs within the top coat and close to the YSZ/TGO interface. The formation of voluminous and non-protective oxide scales and the increased TGO thickness may be responsible for the accelerated failure of TBC.¹⁰²

A finite element analysis was employed to analyze the stress distribution in the coatings.¹⁰³ The computed result showed that: (i) maximum stresses occurred at the bond coat/TGO interface near the edge of the sample; (ii) the increased TGO thickness caused an increase in stress in the TGO/



(a)

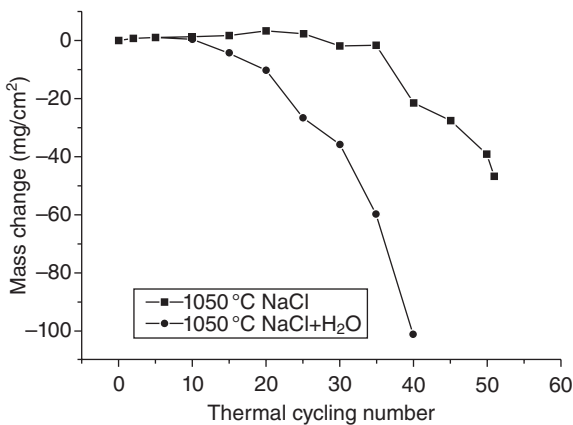


(b)

10.9 Typical contour plot of (a) axial and (b) radial stress distribution of TBC with TGO consisting of Al_2O_3 or spinel.¹⁰³

YSZ interface, as shown in Fig. 10.9, and (iii) the spinel TGO resulted in significantly higher stresses than Al_2O_3 TGO, which implies that the formation of spinel plays a dominant role in shortening the coating cycling life-time. Reese and Grabke¹⁰⁴ investigated the effect of NaCl on the oxidation of high-Cr and Ni-Cr steels. It has been found that the presence of NaCl(s) leads to the formation of voluminous, non-protective layers. The oxides grow according to the mechanism of active oxidation in which Cl plays a catalytic role.¹⁰⁴ Similar results have been found for Fe-Cr-Ni and Fe-Mn-Al alloys with NaCl deposits.¹⁰⁵⁻¹⁰⁷ After several cycles, depletion of Al in the coating surface occurs. Due to the depletion of Al, Ni and Cr react with oxygen to form NiO and Cr_2O_3 . The resultant NiO and Cr_2O_3 react with each other to form NiCr_2O_4 spinel. The oxide scale consisted of NiCr_2O_4 spinel, NiO and Al_2O_3 . Moreover, the TGO thickness is higher in the presence of NaCl (g) in dried air.¹⁰⁸ Therefore, the decrease in thermal cycling resistance for the TBC can be attributed to the increased TGO thickness and the significant formation of voluminous spinel, which result in higher residual stresses in the coating.

The synergistic effect of NaCl and water vapor shortened the cyclic oxidation life of NiCrAlY+YSZ coating at 1050 °C as illustrated in Fig. 10.10.¹⁰⁹ The failure of the coating mainly occurred near the interface between bond coat and YSZ. There was no phase transformation of ZrO_2 in NaCl plus water vapor. The thickness of the TGO became larger in the presence of water vapor and the amount of Cr and Ni in the TGO increased. The presence of water vapor accelerated the failure of TBC, which is in accordance with Wang *et al.*'s research into the corrosion behavior of Ti60 alloy,¹¹⁰ 1Cr11Ni2W2MoV steel,¹¹¹ pure Cr,¹¹² Fe-Cr alloy¹¹³ and K38G superalloy¹¹⁴ in O_2 plus water vapor.



10.10 Corrosion kinetics of TBC at 1050 °C in NaCl vapor and NaCl plus water vapor.¹⁰⁹

10.5 Conclusions

Oxidation is a common phenomenon when metallic elements are exposed to oxygen or oxygen-containing atmospheres at elevated temperatures. Thermal barrier coatings (TBCs) are used to provide thermal insulation and oxidation resistance to metallic components from the hot gas stream in gas turbine engines used for aircraft propulsion, power generation and marine propulsion. The oxidation behavior of the bond coat, including both MCrAlY and Pt-aluminide coating, has a major impact on the life of the TBCs. The failure of TBC systems is very complex and mostly affected by different mechanisms, wherein the oxidation of the bond coat and thermal mismatch stress contribute to the rapid degradation of TBCs. When metals and alloys are covered with salt films at elevated temperatures in an oxidizing gas, hot corrosion occurs. The degradation mechanisms experienced by TBC systems exposed to deposits were discussed.

10.6 References

1. B. SUDHANGSHU, *High Temperature Coatings*, Burlington, MA, Elsevier Science & Technology Books (2007).
2. J.L. SMIALEK, Advances in the oxidation resistance of high-temperature turbine materials, *Surf. Interface Anal.* **31** (7) (2001) 582–592.
3. R.A. RAPP, Chemistry and electrochemistry of the hot corrosion of metals, *Corrosion* **42** (10) (1986) 568–577.
4. R.A. RAPP, Hot corrosion of materials: a fluxing mechanism, *Corros. Sci.* **44** (2) (2002) 209–221.
5. T.S. SIDHU, R.D. AGRAWAL, S. PRAKASH, Hot corrosion of some superalloys and role of high-velocity oxy-fuel spray coatings – a review, *Surf. Coat. Technol.* **198** (1–3) (2005) 441–446.
6. D.M. ZHU, R.A. MILLER, Thermal conductivity and elastic modulus evolution of thermal barrier coatings under high heat flux conditions, *J. Therm. Spray Technol.* **9** (2) (2000) 175–180.
7. B.A. PINT, I.G. WRIGHT, W.Y. LEE, Y. ZHANG, K. PRÜBNER, K.B. ALEXANDER, Substrate and bond coat compositions: factors affecting alumina scale adhesion, *Mater. Sci. Eng. A* **245** (1998) 201–211.
8. B. LOWRIE, D.H. BOONE, Composite coatings of CoCrAlY plus platinum, *Thin Solid Films* **45** (3) (1977) 491–498.
9. H.M. TAWANCY, N. SRIDHAR, B.S. TAWABINI, N.M. ABBAS, T.N. RHYS-JONES, Thermal stability of a platinum aluminide coating on nickel-based superalloys, *J. Mater. Sci.* **27** (1992) 6463–6474.
10. H.M. TAWANCY, N.M. ABBAS, T.N. RHYS-JONES, Role of platinum in aluminide coatings, *Surf. Coat. Technol.* **49** (1–3) (1991) 1–7.
11. H.J. KIM, M.E. WALTER, Characterization of the degraded microstructures of a platinum aluminide coating, *Mater. Sci. Eng. A* **360** (1–2) (2003) 7–17.
12. G. NAVES, L. VILORIA, Laboratory and field corrosion behavior of coatings for turbine blades, *Surf. Coat. Technol.* **94–95** (1997) 161–167.

13. B. GLEESON, High-temperature corrosion of metallic alloys and coatings, in: M. Schutze (ed.), *Corrosion and Environmental Degradation, Vol. II*: Vol. 19 of the Materials Science and Technology Series, Weinheim, Germany Wiley-VCH (2000) 173–228.
14. C. WAGNER, Theoretical analysis of the diffusion processes determining the oxidation rate of alloys, *J. Electrochem. Soc.* **99** (1952) 369–380.
15. H.E. EVANS, Stress effects in high temperature oxidation of metals, *Int. Mat. Rev.* **40** (1995) 1–40.
16. D. CLEMENS, F. TIETZ, R. MUNOZ-ARROYO, R. ANTON, L. SINGHEISER, J. QUADAKKERS, Influence of composition and phase distribution on the oxidation behaviour of NiCoCrAlY Alloys, *Mat. Sci. Forum* **369–372** (2001) 165–172.
17. K. BUNGARDT, G. LEHNERT, H. MEINHARDT, German Patent 1 796 175, 1 July 1971.
18. E.C. DUDERSTADT, A.N. BANGALORE, U.S. Patent 5 238 752, 24 August, 1993.
19. Z. MUTASIM, W. BRENTNALL, Characterization and Performance evaluation of pack cementation and chemical vapor deposition platinum aluminide coatings, *J. Am. Soc. Mech. Eng.* 96-GT-436, 1996.
20. A.G. EVANS, D.R. MUMM, J.W. HUTCHINSON, G.H. MEIER, F.S. PETTIT, Mechanisms controlling the durability of thermal barrier coatings, *Prog. Mater. Sci.* **46** (5) (2001) 505–553.
21. V.K. TOLPYGO, D.R. CLARKE, Surface rumpling of a (Ni, Pt)Al bond coat induced by cyclic oxidation, *Acta Mater.* **48** (13) (2000) 3283–3293.
22. V.K. TOLPYGO, D.R. CLARKE, On the rumpling mechanism in nickel-aluminide coatings: Part I: an experimental assessment, *Acta Mater.* **52** (17) (2004) 5115–5127.
23. V.K. TOLPYGO, D.R. CLARKE, On the rumpling mechanism in nickel-aluminide coatings: Part II: characterization of surface undulations and bond coat swelling, *Acta Mater.* **52** (17) (2004) 5129–5141.
24. D.R. MUMM, A.G. EVANS, I.T. SPITSBERG, Characterization of a cyclic displacement instability for a thermally grown oxide in a thermal barrier system, *Acta Mater.* **49** (12) (2001) 2329–2340.
25. A.G. EVANS, M.Y. HE, J.W. HUTCHINSON, Mechanics-based scaling laws for the durability of thermal barrier coatings, *Prog. Mater. Sci.* **46** (2001) 249–271.
26. P.J. HILL, P. ELLIS, L.A. CORNISH, L.A. WITCOMB, I.M. WOLFF, The oxidation behaviour of Pt–Al–X alloys at temperatures between 1473 and 1623 K, *Proceedings of High Temperature Corrosion And Protection 2000*, Japan, (2000) 185–190.
27. A. SUZUKI, Y.N. WU, A. YAMAGUCHI, H. MURAKAMI, C.M.F. RAE, Oxidation behavior of Pt–Ir modified aluminized coatings on Ni-base single crystal superalloy TMS-82+, *Oxid Met* **68** (1–2) (2007) 53–64.
28. Y.N. WU, A. YAMAGUCHI, H. MURAKAMI, S. KURODA, Hot corrosion behavior of Pt–Ir modified aluminide coatings on the nickel-base single crystal superalloy TMS-82+, *J. Mater. Res.* **22** (1) (2007) 206–216.
29. B. TRYON, F. CAO, K.S. MURPHY, C.G. LEVI, T.M. POLLOCK, Ruthenium-containing bond coats for thermal barrier coating systems, *JOM*, **58** (1) (2006) 53–59.
30. I.T. SPITSBERG, R. DAROLIA, M.R. JACKSON, J. ZHAO, J.C. SCHAEFFER, U.S. Patent No. 6,306,524 B1, 2001.
31. P.K. DATTA, J.S. BURNELL-GRAY, K. NATESAN, Coating technology, in: J.H. Westbrook and R.L. Fleischer (eds), *Intermetallic Compounds*, Wiley, New York, **3** (2002) 561–588.

32. B. TRYON, Q. FENG, T. POLLOCK, Intermetallic phases formed by ruthenium–nickel alloy interdiffusion, *Intermetallics*, **12** (7–9) (2004) 957–962.
33. B. TRYON, Q. FENG, R.W. WELLMAN, K.S. MURPHY, J. YANG, C.G. LEVI, J.R. NICHOLLS, T.M. POLLOCK, Multilayered ruthenium-modified bond coats for thermal barrier coatings, *Metall. Mater. Trans. A* **37** (2006) 3347–3358.
34. T.K. NANDY, Q. FENG, T.M. POLLOCK, Elevated temperature deformation and dynamic strain aging in polycrystalline RuAl alloys, *Intermetallics*, **11** (10) (2003) 1029–1038.
35. T.K. NANDY, Q. FENG, D. BANERJEE, M.F.X. GIGLIOTTI, T.M. POLLOCK, Mechanical behavior of ternary and quaternary RuAl alloys, *Mater. Res. Soc. Symp. Proc.* **753** (2003) BB2.11.11.
36. B. TRYON, K.S. MURPHY, J.Y. YANG, C.G. LEVI, T.M. POLLOCK, Hybrid intermetallic Ru/Pt-modified bond coatings for thermal barrier systems, *Surf. Coat. Technol.* **202** (2007) 349–361.
37. Y. X. SONG, H. MURAKAMI, C. ZHOU, submitted to *J. Mater. Sci. Technol.*
38. R.A. MILLER, C.E. LOWELL, Failure mechanisms of thermal barrier coatings exposed to elevated temperatures, *Thin Solid Films*, **95** (3) (1982) 265–273.
39. C.C. BERNDT, H. HERMAN, Failure during thermal cycling of plasma-sprayed thermal barrier coatings, *Thin Solid Films*, **108** (4) (1983) 427–437.
40. B.C. WU, E. CHANG, D.C. TU, S.L. WANG, Microstructures, properties and failure analysis of (ZrO₂ – 8wt.% Y₂O₃)/((Co, Ni)-Cr-Al-Y) thermal barrier coatings, *Mater. Sci. Eng. A* **111** (1989) 201–210.
41. J.H. SUN, E. CHANG, B.C. WU, C.H. TSAI, The properties and performance of (ZrO₂ – 8 wt.% Y₂O₃) / (chemically vapour-deposited Al₂O₃) / (Ni – 22 wt.% Cr – 10 wt.% Al – 1 wt.% Y) thermal barrier coatings, *Surf. Coat. Technol.*, **58** (2) (1993) 93–99.
42. H.L. TSAI, P.C. TSAI, Microstructures and properties of laser-glazed plasma-sprayed ZrO₂-YO_{1.5}/Ni-22Cr-10Al-1Y thermal barrier, *J. Mater. Eng. Perform.* **4** (1995) 689–696.
43. H.L. TSAI, P.C. TSAI, Thermal cyclic response of laser-glazed plasma-sprayed ZrO₂ – 19.5 wt.% Y₂O₃ / Ni – 22 Cr – 10 Al – 1 Y thermal barrier coatings, *Mater. Sci. Eng. A* **177** (1–2) (1994) 227–232.
44. H.L. TSAI, P.C. TSAI, Performance of laser-glazed plasma-sprayed (ZrO₂ – 12 wt.% Y₂O₃) / (Ni – 22 wt.% Cr – 10 wt.% Al – 1 wt.% Y) thermal barrier coatings in cyclic oxidation tests, *Surf. Coat. Technol.*, **71** (1) (1995) 53–59.
45. H.E. EVANS, M.P. TAYLOR, Delamination processes in thermal barrier coating systems, *J. Corr. Sci. Eng.* **6** (Paper H011) (2003).
46. M. GELL *et al.*, Bond strength, bond stress and spallation mechanisms of thermal barrier coatings, *Surf. Coat. Technol.* **120–121** (1999) 53–60.
47. J.M. AMBRICO, M.R. BEGLEY, E.H. JORDAN, Stress and shape evolution of irregularities in oxide films on elastic–plastic substrates due to thermal cycling and film growth, *Acta Mater.* **49** (9) (2001) 1577–1588.
48. A.M. KARLSSON, A.G. EVANS, A numerical model for the cyclic instability of thermally grown oxides in thermal barrier systems, *Acta Mater.* **49** (10) (2001) 1793–1804.
49. Y.H. SOHN, J.H. KIM, E.H. JORDAN, M. GELL, Thermal cycling of EB–PVD/MCrAlY thermal barrier coatings: I. Microstructural development and spallation mechanisms, *Surf. Coat. Technol.* **146–147** (2001) 70–78.

50. B.J. ZIMMERMAN, *Rumpling phenomenon in platinum modified Ni-Al alloys*, Master Degree Thesis, Iowa State University, 2005.
51. N.P. PADTURE, M. GELL, E.H. JORDAN, Thermal barrier coatings for gas-turbine engine applications, *Science* **296** (2002) 280–284.
52. G.C. CHANG, W. PHUCHAROEN, R.A. MILLER, Behaviour of thermal barrier coatings for advanced gas turbine blades, *Surf. Coat. Technol.* **30** (1987) 13–28.
53. A.M. FREBORG, B.L. FERGUSON, W.J. BRINDLEY, G.J. PETRUS, Modeling oxidation induced stresses in thermal barrier coatings, *Mater. Sci. Eng. A* **A245** (1998) 182–190.
54. J. RÖSSLER, M. BÄKER, M. VOLGMANN, Stress state and failure mechanisms of thermal barrier coatings: role of creep in thermally grown oxide, *Acta Mater* **49** (2001) 3659–3670.
55. S.R. CHOI, J.W. HUTCHINSON, A.G. EVANS, Delamination of multilayer thermal barrier coatings, *Mech. Mater.* **31** (1999) 431–447.
56. A.G. EVANS, G.B. CRUMLEY, R.E. DEMARAY, On the mechanical behavior of brittle coatings and layers, *Oxid. Met.* **20** (1983) 193–216.
57. W.J. QUADAKKERS, A.K. TYAGI, D. CLEMENS, R. ANTON, L. SINGHEISER, The significance of bond coat oxidation for the life of TBC coatings, in: Hampikian JM, Dahotre NB (eds), *Elevated Temperature Coatings: Science and Technology III*, Warrendale, PA, The Minerals, Metals & Materials Society (1999) 119–130.
58. D.M. LIPKIN, D.R. CLARKE, M. HOLLATZ, M. BOBETH, W. POMPE, Stress development in alumina scales formed upon oxidation of (111) NiAl single crystals, *Corros. Sci.* **39** (2) (1997) 231–242.
59. E. SCHUMANN, C. SARIOGLU, J.R. BLACHERE, F.S. PETTIT, G.H. MEIER, High temperature stress measurements during the oxidation of NiAl, *Oxid. Met.* **53** (3–4) (2000) 259–272.
60. V.K. TOLPYGO, D.R. CLARKE, Competition between stress generation and relaxation during oxidation of an Fe–Cr–Al–Y alloy, *Oxid. Met.* **49** (1–2) (1998) 187–212.
61. J. AKTAA, K. SFAR, D. MUNZ, Assessment of TBC systems failure mechanisms using a fracture mechanics approach, *Acta Mater.* **53** (16) (2005) 4399–4413.
62. D.M. LIPKIN, D.R. CLARKE, Measurement of the stress in oxide scales formed by oxidation of alumina-forming alloys, *Oxid. Met.* **45** (3–4) (1996) 267–280.
63. K.W. SCHLICHTING *et al.*, Application of Cr³⁺ photoluminescence piezo-spectroscopy to plasma-sprayed thermal barrier coatings for residual stress measurement, *Mater. Sci. Eng. A* **291** (1–2) (2000) 68–77.
64. S. KURODA, T.W. CLYNE, The quenching stress in thermally sprayed coatings, *Thin Solid Films* **200** (1) (1991) 49–66.
65. J.D. LEE, H.Y. RA, K.T. HONG, S.K. HUR, Analysis of deposition phenomena and residual stress in plasma spray coatings, *Surf. Coat. Technol.* **56** (1) (1992) 27–37.
66. A.G. EVANS, D.R. MUMM, J.W. HUTCHINSON, G.H. MEIER, F.S. PETTIT, Mechanisms controlling the durability of thermal barrier coatings, *Prog. Mat. Sci.* **46** (2001) 505–553.
67. E.Y. LEE, R.R. BIEDERMAN, R.D. SISSON, Diffusional interactions and reactions between a partially stabilized zirconia thermal barrier coating and the NiCrAlY bond coat, *Mater. Sci. Eng. A* **120–121** (1989) 467–473.

68. D.R. MUMM, A.G. EVANS, On the role of imperfections in the failure of a thermal barrier coating made by electron beam deposition, *Acta Mater.* **48** (8) (2000) 1815–1827.
69. A. RABIEI, A.G. EVANS, Failure mechanisms associated with the thermally grown oxide in plasma-sprayed thermal barrier coatings, *Acta Mater.* **48** (18) (2000) 3963–3976.
70. K.W. SCHLICHTING, N.P. PADTURE, E.H. JORDAN, M. GELL, Failure modes in plasma-sprayed thermal barrier coatings, *Mater. Sci. Eng. A* **342** (1–2) (2003) 120–130.
71. X.Y. GONG, D.R. CLARKE, On the measurement of strain in coatings formed on a wrinkled elastic substrate, *Oxid. Met.* **50** (5–6) (1998) 355–376
72. D.R. CLARKE, W. POMPE, Critical radius for interface separation of a compressively stressed film from a rough surface, *Acta Mater.* **47** (6) (1999) 1749–1756.
73. C.H. HSUEH, P.F. BECHER, E.R. FULLER, S.A. LANGER, W.C. CARTER, Surface-roughness induced residual stresses in thermal barrier coatings: computer simulations, *Mater. Sci. Forum* **308–311** (1999) 442–449.
74. C.H. HSUEH, E.R. FULLER, Analytical modeling of oxide thickness effects on residual stresses in thermal barrier coatings, *Scripta Mater.* **42** (8) (2000) 781–787.
75. K. VAIDYANATHAN, M. GELL, E.H. JORDAN, Mechanisms of spallation of electron beam physical vapor deposited thermal barrier coatings with and without platinum aluminide bond coat ridges, *Surf. Coat. Technol.* **133–134** (2000) 28–34.
76. J. CHENG, E.H. JORDAN, B. BARBER, M. GELL, Thermal/residual stress in an electron beam physical vapor deposited thermal barrier coating system, *Acta Mater.* **46** (16) (1998) 5839–5850.
77. A.G. EVANS, J.W. HUTCHINSON, On the mechanics of delamination and spalling in compressed films, *Int. J. Solids Struct.* **20** (5) (1984) 455–466.
78. F.S. PETTIT, C.S. GIGGINS, Hot corrosion, in: C.T. Sims, N.S. Stoloff, W.C. Hagel (eds), *Superalloys II*, Wiley, New York (1987) 327–358.
79. G.W. GOWARD, Low-temperature hot corrosion in gas turbines: A review of causes and coatings therefor, *J. Eng. Gas Turbine Power, Tran ASME*, **108** (1986) 421–425.
80. R.A. RAPP, Y.S. ZHANG, Hot corrosion of materials: fundamental studies, *JOM*, **46** 47–55.
81. T.S. SIDHU, S. PRAKASH, R.D. AGRAWAL, Hot corrosion and performance of nickel-based coatings, *Curr. Sci.* **90** (1) (2006) 41–47.
82. P. HANCOCK, Vanadic and chloride attack of superalloys, *Mater. Sci. Technol.* **3** (1987) 536–544.
83. N. ELIAZ, G. SHEMESH, R.M. LATANISION, Hot corrosion in gas turbine components, *Eng. Fail. Anal.* **9** (1) (2002) 31–43.
84. J. STRINGER, *Hot Corrosion in Gas Turbines*, New York, Metals and Ceramics Information Center (1972) MCIC Report 72–08.
85. D.A. SHORES, K.L. LUTHRA, *Fundamentals of High-Temperature Corrosion*, New York, Academic Press (1992).
86. M.A. DECRESCENTE, N.S. BORNSTEIN, Formation and reactivity thermodynamics of sodium sulfate with gas turbine alloys, *Corrosion* **24** (1968) 127–133.

87. J.A. GOEBEL, F.S. PETTIT, G.W. GOWARD, Mechanisms for the hot corrosion of nickel-base alloys, *Metall. Trans.* **4** (1973) 261–278.
88. C. LEYENS, I.G. WRIGHT, B.A. PINT, Hot corrosion of an EB–PVD thermal-barrier coating system at 950 °C, *Oxid. Met.* **54** (5–6) (2000) 401–424.
89. I. GURRAPP, Thermal barrier coatings for hot corrosion resistance of CM 247 LC superalloy, *J. Mater. Sci. Lett.* **17** (1998) 1267–1269.
90. S.Y. PARK, J.H. KIM, M.C. KIM, Microscopic observation of degradation behavior in yttria and ceria stabilized zirconia thermal barrier coatings under hot corrosion, *Surf. Coat. Technol.* **190** (2–3) (2005) 357–365.
91. R.L. JONES, The development of hot-corrosion-resistant zirconia thermal barrier coatings, *Mater. at High Temp.* **9** (1991) 228–236.
92. H.E. EATON, N.S. BORNSTEIN, J.T. DEMASI-MARCIN, The effects of environmental contaminants on industrial gas turbine thermal barrier coatings, *Proc. Int. Gas Turbine Aeroengine Congress and Exhibition*, ASME, New York (1996) Paper 96-GT-283.
93. M.F. TRUBELJA, D.M. NISSLEY, N.S. BORNSTEIN, J.T.D. MARCIN, Pratt & Whitney thermal barrier coating development, *Proc. Advan. Turbine Systems Annu. Program Rev. Meet.*, U.S. Department of Energy, Washington, DC (1997).
94. C. LEYENS, U. SCHULZ, B.A. PINT, I.G. WRIGHT, Influence of electron beam physical vapor deposited thermal barrier coating microstructure on thermal barrier coating system performance under cyclic oxidation conditions, *Surf. Coat. Technol.* **120–121** (1999) 68–76.
95. F.C. TORIZ, A.B. THAKKER, S.K. GUPTA, Thermal barrier coating for jet engines, *Proceedings of the International Gas Turbine Aeroengine Congress*, ASME, Paper 88-GT-279 (1988).
96. M.P. BOROM, C.A. JOHNSON, L.A. PELUSO, Role of environment deposits and operating surface temperature in spallation of air plasma sprayed thermal barrier coatings, *Surf. Coat. Technol.* **86–87** (1996) 116–126.
97. R.A. RAPP, K.S. GOTO, Hot corrosion of metals by molten salts, in: J. Braustein, J.R. Selman (eds), *Molten Salts I*, Pennington, NJ, Electrochemical Society (1981) 159–177.
98. A.S. KHANNA, S.K. JHA, Degradation of materials under hot corrosion conditions, *Trans. Indian Inst. Met.* **51** (5) (1988) 279–290.
99. N.S. BORNSTEIN, M.A. DECRESCENTE, H.A. ROTH, The relationship between relative oxide ion content of Na₂SO₄, the presence of liquid metal oxides and sulfidation attack, *Metall. Trans.* **4** (1973) 1799–1810.
100. Y.S. HWANG, R.A. RAPP, Thermochemistry and solubilities of oxides in sodium sulfate-vanadate solutions, *Corrosion* **45** (11) (1989) 933–937.
101. J.A. GOEBEL, F.S. PETTIT, G.W. GOWARD, Mechanisms for the hot corrosion of nickel-base alloys, *Metall. Trans.* **4** (1973) 261–278.
102. C.G. ZHOU, Y.X. SONG, C.L. WANG, H.B. XU, Cyclic-oxidation behavior of thermal-barrier coatings exposed to NaCl vapor, *Oxid. Met.* **69** (1–2) (2008) 119–130.
103. C.G. ZHOU, C.L. WANG, Y.X. SONG, Evaluation of cyclic oxidation of thermal barrier coatings exposed to NaCl vapor by finite element method, *Mater. Sci. Eng. A* **490** (2008) 351–358.
104. E. REESE, H.J. GRABKE, Einfluß von natriumchlorid auf die oxidation von hochlegierten chrom- und chrom-nickel-stählen, *Mater. Corr.* **44** (1993) 41–47.

105. C.J. WANG, Y.C. CHANG, Y.H. SU, The hot corrosion of Fe–Mn–Al–C alloy with NaCl/Na₂SO₄ coating mixtures at 750 °C, *Oxid. Met.* **59** (2003) 115–133.
106. B.P. MOHANTY, D.A. SHORES, Role of chlorides in hot corrosion of a cast Fe–Cr–Ni alloy. Part I: Experimental studies, *Corr. Sci.* **46** (12) (2004) 2893–2907.
107. D.A. SHORES, B.P. MOHANTY, Role of chlorides in hot corrosion of a cast Fe–Cr–Ni alloy. Part II: thermochemical model studies, *Corr. Sci.* **46** (12) (2004) 2909–2924.
108. C.L. WANG, *High temperature Corrosion Behavior of Thermal Barrier Coating Exposed to NaCl Vapor*, Master Degree Thesis, Beijing University of Aeronautics and Astronautics, 2006.
109. Y.X. SONG, C.G. ZHOU, H.B. XU, Corrosion behavior of thermal barrier coatings exposed to NaCl plus water vapor at 1050 °C, *Thin Solid Films* **516** (16) (2008) 5686–5689.
110. Y. SHU, F. WANG, W. WU, Corrosion behavior of Ti60 alloy coated with a solid NaCl deposit in O₂ plus water vapor at 500–700 °C, *Oxid. Met.* **52** (1999) 463–473.
111. Y. SHU, F. WANG, W. WU, Synergistic effect of NaCl and water vapor on the corrosion of 1Cr-11Ni-2W-2Mo-V steel at 500–700 °C, *Oxid. Met.* **51** (1999) 97–110.
112. Y. SHU, F. WANG, W. WU, Corrosion behavior of pure Cr with a solid NaCl deposit in O₂ plus water vapor, *Oxid. Met.* **54** (2000) 457–471.
113. F. WANG, Y. SHU, Influence of Cr content on the corrosion of Fe–Cr alloys: the synergistic effect of NaCl and water vapor, *Oxid. Met.* **59** (2003) 201–214.
114. F. WANG, S. GENG, S. ZHU, Corrosion behavior of a sputtered K38G nanocrystalline coating with a solid NaCl deposit in wet oxygen at 600 to 700 °C, *Oxid. Met.* **58** (2002) 185–195.

Failure mechanism of thermal barrier coatings by electron beam physical vapor deposition (EB-PVD) under thermomechanical coupled loads

C. ZHANG, Baosteel Group Corporation, China and
C. CHEN, AVIC Commercial Aircraft Engine Co. Ltd, China

Abstract: This chapter discusses the failure mechanism of thermal barrier coatings (TBCs) in service in gas turbine engines. A service environment simulation system was established in order to examine the failure behaviour of TBCs subjected to a gradient temperature field coupled with complex mechanical loadings. The experiment took the form of a finite element analysis accompanied by non-destructive evaluation (NDE) in order to analyse the TBCs failure mechanism.

Key words: thermal barrier coatings, failure mechanism, thermomechanical loadings, non-destructive evaluation, service environment simulation.

11.1 Introduction

Ceramic coatings have emerged as vital constituents of hot section components in aero-propulsion systems. These act as both thermal (TBC) and environmental (EBC) barriers.^{1,2} Most coated components are actively cooled from the back side, resulting in temperature gradients along the through-thickness direction during operation.³⁻⁹ Moreover, during engine shut down, the surface of coatings can cool quite rapidly, which causes additional gradients. At the same time, the coating is also subject to temperature gradient along the surface direction due to the non-uniform heating of the combustion chamber. Therefore, TBCs in the service environment are subject to temperature gradient in both the through-thickness and the surface direction. Accompanied by non-uniform thermal loading, TBCs coated gas turbines also underwent complicated mechanical loading, including tension, compression, fatigue and so on.

However, most studies are focused on the degradation of TBCs subjected to either uniform temperature field or mechanical loading. Few investigations have been applied to the evaluation of TBCs subjected to coupled thermomechanical loading. Recent observations can be made only on

engine components which have been removed from service.^{10–12} In order to observe the failure mechanism of TBCs in service, an effective service environment simulation system is required and the corresponding failure mechanism of TBCs subjected to coupled thermomechanical loading must be studied.

Non-destructive evaluation (NDE) techniques, including acoustic emission (AE), photo-simulated luminescence spectroscopy (PSLS) and impedance spectroscopy (IS), are widely used to study the degradation of TBCs. IS, in particular, is an efficient, quick and powerful testing method for ceramic materials.^{13–15} Voltage and current responses, on application of an alternating current (a.c.) with varying frequency, relating to yttrium stabilized zirconia (YSZ), thermal grown oxides (TGO) and mixed oxide layers have been observed in the impedance spectra.^{13,15} The influence of changes in the thickness and conductivity of the TGO layer on the impedance spectra has been identified by both experimental and modelling results.¹⁶ In this investigation, TGO and interfacial microcracks were studied *in situ* using IS.

Due to the complexity of the thermomechanical coupled effect and non-uniform temperature field, finite element (FE) analysis was also introduced to simulate the stress fields in the whole experiment, including the heating, temperature dwell and cooling procedures. The simulation results are in good agreement with the NDE and scanning electron microscopy (SEM) observations during the degradation of TBCs. By this means, the failure mechanism of TBCs subjected to thermomechanical loading is attained.

11.1.1 Commentary

Thermal barrier coatings are widely used as the protective coating in gas turbine engines and their reliability is a matter of much concern. In order to predict the lifetime of TBCs during in-service operation, the first requirement is a thorough investigation of the failure mechanism of the coating. In the service environment, TBCs are subject to high temperature, non-uniform heating along both the through-thickness and the surface direction, fast heating and cooling, hot corrosion and complicated mechanical loadings. Due to the lack of effective service condition simulation, most investigations are focused on the failure mechanism of TBCs either in a uniform temperature field or subjected mechanical loading. Therefore, simulation of the coating and gas turbine engines in service and the corresponding failure mechanism is considered to be one of the most important directions for future research.

Some research has been carried out on failure mechanisms of TBC under a temperature gradient field.^{9–11} It has been reported that the failure mode in this circumstance is different from that which is found under isothermal

heat treatment.^{10,17} Subjected to a temperature gradient field, delamination occurred in the ceramic coating instead of the TBC bond coat interface. Subjected to a thermal gradient, isolated cracks parallel to the interface are envisaged, that experience an energy release rate and exfoliate.¹⁷ However, under conditions of isothermal oxidation, most failure occurred at the bond coat/TGO or TGO/TBC interface.⁸ A situation comprising three-dimensional temperature gradient fields is more close to the real service conditions of TBCs in gas turbine engines.^{10,12,17,18} This suggests that further study of the failure mechanism of TBCs under a temperature gradient field is required.

In order to obtain the temperature gradient field, some simulation systems have been reported, such as furnace cycling and burner rig testing.^{18–20} Using such equipment, a temperature gradient along the through-thickness direction can be obtained. However, very few reports are concerned with the 3D temperature gradient field, which encompasses a temperature gradient along both the through-thickness direction and the in-plane direction (parallel to the surface of the coating). In this investigation, hollow tube samples coated with EB-PVD TBC were employed to simulate turbine blades. Infrared light was focused on a very small area of the TBC surface, accompanied by compressed air through the tube to cool the substrate, by this means, thermal gradients along both the axial and radial directions were obtained.

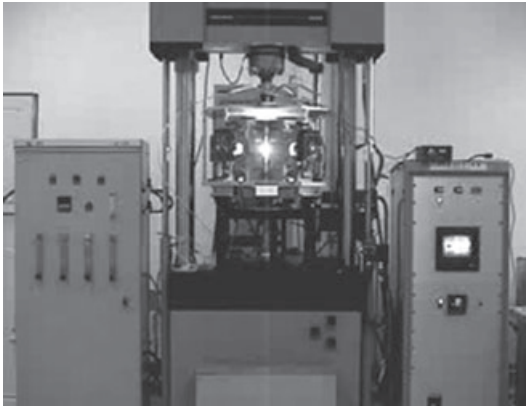
The usual procedure for heating furnaces is not capable of satisfying the high heating and cooling rates, which are considered to occur during engine start-up and shut-down, respectively.²⁰ In order to simulate the service temperature gradient field and high heating rate of a gas turbine, an infrared thermal shock testing system was employed in this investigation. Using the infrared heating system, an average heating rate of 55 °C/s was attained.

In this chapter, the results obtained from this gas turbine service environment simulation system are analyzed, accompanied by finite element (FE) modeling. Hence, the method of studying the failure mechanism of TBCs and the corresponding laws governing failure are established.

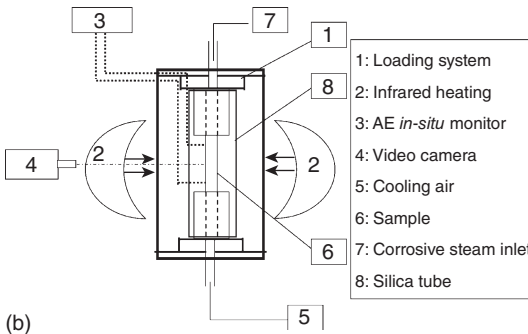
11.2 Establishment of gas turbine service environment simulation system

11.2.1 Thermomechanical loading test system

In the investigation, a thermomechanical loading system was employed in order to simulate the service condition of a gas turbine blade. The basis is a mechanical loading system coupled with a thermal shock system using focused infrared light. The photo and schematic of the system are shown in Fig. 11.1.



(a)



(b)

11.1 TBCs service environmental performance simulation test system: (a) photograph; (b) schematic diagram.

An Instron 8803 was employed in the mechanical loading system. The maximum load was 250 kN, while the maximum alternate loading frequency was 40 Hz. WaveMaker™ software was used to programme and apply the loading wave pattern in the experiment.

In the thermal shock system, the infrared light was generated by four 4 kW bulbs, and focused on the sample using concave mirrors. Therefore, the heated length of the sample which could be controlled was only 20 mm. Taking advantage of such a small heated area, the temperature gradient along the axial direction was obtained.

Heating and cooling took place in three stages:

- **Heating procedure:** the surface temperature is increased to 1100°C from room temperature – the high heating rate of the system (55°C/s on average) enables this to be done in less than 20 s;
- **Temperature dwell procedure:** the temperature is kept at 1100°C for 5 min;

- **Cooling procedure:** the infrared lights are switched off and the sample is cooled to room temperature using compressed air.

In the experiment, the surface temperature was controlled by the power of the infrared light, which was calibrated by thermocouple.

11.2.2 Sample description

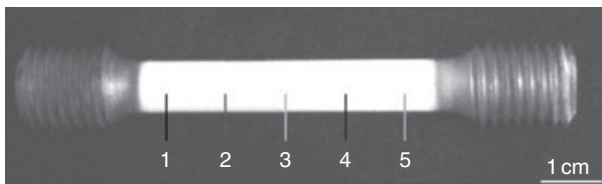
In this investigation, Ni-based superalloys were used as substrate materials. The specimens were fabricated into cylinders with both ends screwed to fit the grips of the mechanical loading machine, as shown in Fig. 11.2. The diameter of the specimen was 8 mm, and the length of the coated part 50 mm.

The samples were heated using an infrared heating system with a controllable heating rate. The heated length along the axial direction was 1.5 mm. In the specimen, the centre of the heated zone is indicated as No. 3, as marked in Fig. 11.2. The edges of the heated zone are indicated as Nos. 2 and No. 4, and the area far from the heated zone as Nos. 1 and 5. The desired temperature was reached in 20 s. In this case, the surface temperature of the specimen was around 1373 K. After holding at this temperature for 5 min, the heating power was reduced to 0 in 20 s, and then the specimen was cooled down to room temperature in 3 min by compressed air.

It can be seen from Fig. 11.2 that standard tensile samples have been used in order to facilitate fitting to the mechanical loading system. It should be noted that an acoustic probe can be also embedded at the end of the sample. Hence crack propagation during the experiment can be successfully monitored *in situ*. However, this is not included in this investigation.

11.2.3 Experimental parameters

Different mechanical loadings were applied to the sample, and the parameters and loading types are illustrated in Table 11.1. In this investigation, samples S1 and S2 denote the solid cylinder samples, while H1 and H2 denote the tube-shaped samples.



11.2 Photograph of the sample. In the thermal shock test, infrared light is focused on the area marked as No. 3.

Table 11.1 Experimental parameters for thermomechanical loading test

Sample code	S1	S2	H1	H2
Mechanical loading (MPa)*	99.5	119.4	143.3	132.3
Mechanical loading description	Constant tensile loading	Fatigue loading		
Temperature/power	45%	50%	50%	50%
Cycling in Section	1670 11.3.1	1670 11.3.2	660 11.4.1	180 11.4.1

* The mechanical loading value in fatigue loading denotes the peak value in the loading curve.

Table 11.2 Parameters for super alloy*¹⁹

T(K)	293	473	573	673	773	873	973	1073	1173	1273	1373
$k(\text{W}\cdot\text{m}^{-1}\cdot\text{K}^{-1})$		9.67	11.47	13.44	14.99	16.79	17.96	19.63	19.51	19.43	19.00
$c(\text{J}\cdot\text{Kg}^{-1}\cdot\text{K}^{-1})$		385	427	456	481	498	506	506	489	473	443
$\alpha(\times 10^{-6} \text{K}^{-1})$			12.36	12.91	13.15	13.41	13.98	14.49	15.01	15.93	16.94
$E(\text{GPa})$	127.6	124.0	121.0	118.0	114.0	110.0	105.0	100.0	93.5	84.0	
ν	0.33		0.33		0.34	0.34	0.36	0.36	0.37	0.38	

* T = testing temperature, k = thermal conductivity, α = thermal expansion coefficient, E = Young's modulus, ν = Poisson's ratio.

During mechanical loading, the samples were heated by focused infrared light. The highest thermal loading and mechanical loading were achieved at the same time in order to simulate the whole engine operation procedure, from engine start-up to temperature dwell and then shut-down.

In this investigation, FE analysis was performed using the ANSYS 9.0 software developed by ANSYS Inc., Canonsburgh, PA, USA. In the simulation, PLANE 13 (four-node quadrilateral element) was selected for coupled-field thermal structure analysis.

Material parameters employed in the simulation were assumed to be isotropic and temperature-dependent and are illustrated in Tables 11.2–11.5. It should be noted that in the simulation, only elastic deformation was considered. Material evaluation during thermal cycling was not included in the simulation.

Table 11.3 Parameters for NiCoCrAlY bond coat¹⁹

$T(K)$	293	473	673	873	1073	1273	1373
$k(W \cdot m^{-1} \cdot K^{-1})$	5.8	7.5	9.5	12.0	14.5	16.2	17.0
$\alpha(\times 10^{-6} K^{-1})$	13.6	14.2	14.6	15.2	16.1	17.2	17.6
$E(GPa)$	200	190	175	160	145	120	110
ν	0.30	0.30	0.31	0.31	0.32	0.33	0.33

Table 11.4 Parameters for TGO layer¹⁹

$T(K)$	293	473	673	873	1073	1273	1373
$k(W \cdot m^{-1} \cdot K^{-1})$	10	7.8	6.0	5.1	4.4	4.4	4.0
$\alpha(\times 10^{-6} K^{-1})$	8.0	8.2	8.4	8.7	9.0	9.3	9.6
$E(GPa)$	400	390	380	370	355	325	320
ν	0.23	0.23	0.24	0.24	0.25	0.25	0.25

Table 11.5 Parameters for YSZ top coat¹⁹

$T(K^{-1})$	293	473	673	873	1073	1273	1373
$k(W \cdot m^{-1} \cdot K^{-1})$	1.9	1.8	1.7	1.6	1.6	1.7	1.7
$\alpha(\times 10^{-6} K^{-1})$	9.0	10.0	9.7	9.8	10.0	10.3	10.3
$E(GPa)$	48	47	44	40	34	26	22
ν	0.10	0.10	0.10	0.11	0.11	0.12	0.12

11.3 Failure mechanism of EB-PVD TBC under in-plane thermal gradient coupled with mechanical loading

11.3.1 Failure mechanism of EB-PVD TBC under in-plane thermal gradient coupled with constant tensile loading

In this experiment, a constant load of 99.5 MPa was applied to the sample during testing. The test was carried out using INSTRON 8803. After 1670

cycles of thermal shock testing, the specimens were cut into five pieces corresponding to those parts marked in Fig. 11.2, respectively. The impedance spectroscopy of the cycled specimens was measured at 673 K using an impedance analyzer (Solatron® 1260 coupled with 1296). Zview software was used for impedance spectroscopy analysis. Platinum wire was fixed to the superalloy substrate as an electrode, and the silver paint on the top coat functions as another electrode.

Failure modes during thermal shock testing

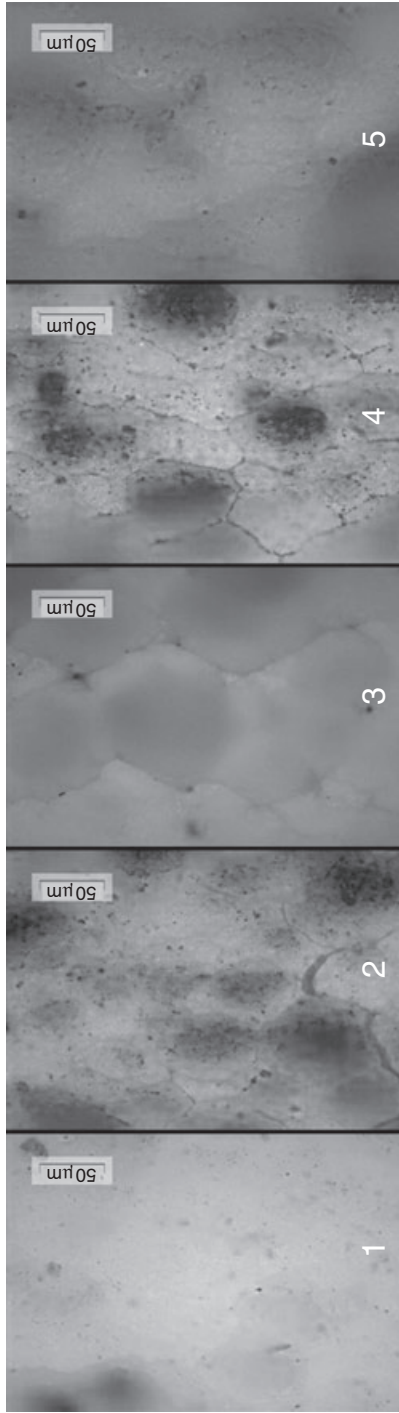
Figure 11.3 shows optical micrographs of the specimen. Surface morphology varies with the position of the sample along the axial direction. Few cracks can be observed on the coatings at the two ends of the specimens (Nos. 1 and 5). Crack networks are observed on the surfaces of the coatings at the edge of the heated zone and in the hottest zone. It should be noted that the coating surface in the hottest zone is denser and smoother than those at the edge of the heated zone, possibly due to sintering of YSZ coating at high temperature.

Figure 11.4 shows SEM micrographs of cross-sections from different parts of the specimen. It can be seen that in Parts 1 and 5 which are far away from the heated zone the YSZ top coats are still intact and well bonded to the bond coat. However, a large number of vertical cracks running perpendicular to the coating surface can be seen at the edge of the heated zone (Nos. 2 and 4). Moreover, some horizontal cracks propagated along the interface between YSZ top coat and bond coat. Cracks along the interface are not observed in the hottest zone (No. 3), although the coating was exposed to the highest temperature. This suggests that the surface temperature is not the dominant reason for the failure of TBC. The largest temperature gradient along the axis direction is attained at the edge of the hottest zone (Nos. 2 and 4), which causes higher thermal stresses. Consequently, cracks of the TBCs are initiated due to the thermal gradient coupled with the constant tensile mechanical loading.

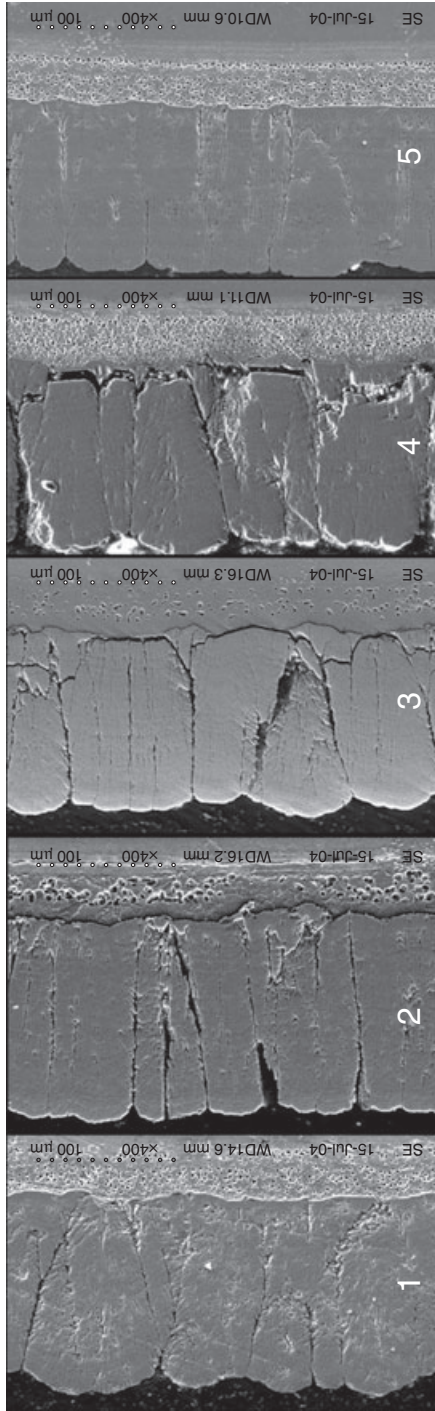
The formation of vertical cracks in the coatings can be attributed to the temperature gradient through the coating thickness. Transient tensile stresses were generated at the surface of the coatings on cooling from high temperature to room temperature. Generation of the horizontal cracks was partly caused by the temperature gradient along the axial direction.

Evaluation of impedance spectroscopy

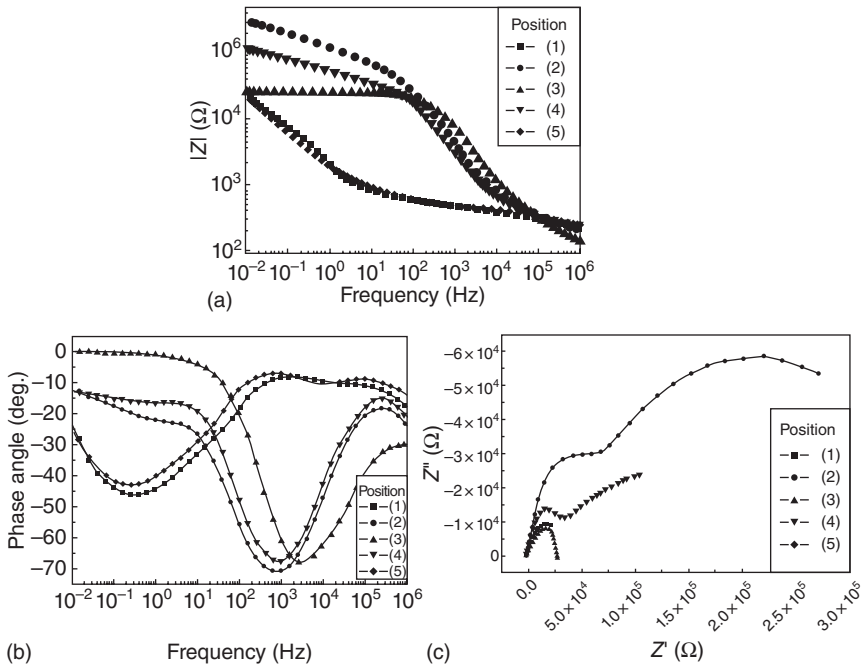
Figure 11.5 shows the impedance spectroscopy results for the specimen after thermal shock. Figure 11.5a shows the $\lg|Z|-\lg f$ curve of the Bode plot, Fig. 11.5b the $\theta-\lg f$ curve of the Bode plot and Fig. 11.5c is the Nyquist plot.



11.3 Surface morphology of the sample after thermomechanical loading test at different positions.²¹



11.4 Cross-sectional microstructure at different positions of the sample. The markers of different positions correspond with those shown in Fig. 11.3.²¹



11.5 Impedance spectra of different parts of the sample after thermomechanical loading:²¹ (a) |Z|–f; (b) phase angle–f; (c) Z''–Z'.

There are three kinds of zones in the specimen, as mentioned in Figs. 11.2 and 11.4. The impedance spectroscopies are rather different from each other, depending on the zones measured. In the low-frequency range, the resistance values obtained at the edge of the heated zone are the highest, while those from the far ends are the lowest. The resistance value in the low-frequency range (0.01 Hz–100 Hz) detected from the hottest zone is almost constant. Also, in the θ –lgf plot, the curve corresponding to the coating from the hottest zone is kept at zero degree. This means that the electrical characteristics make the largest contribution to the resistance value at the low end of the frequency range.

It can be seen from the SEM micrographs that the coating in the hottest zone shows the thickest TGO layer. Assuming all the coating structures to be the same, the resistance value of the coating corresponding to No. 3 should be the largest. However, the actual experimental results are different from those expected. There are three reasons for this:

1. Nos. 2 and 3 are at the edge of the heated zone. The surface temperature in these zones is around 1200 K. At this temperature, the bond coat was

oxidized. The TGO in these zones is only a little thinner than that in the hottest zone.

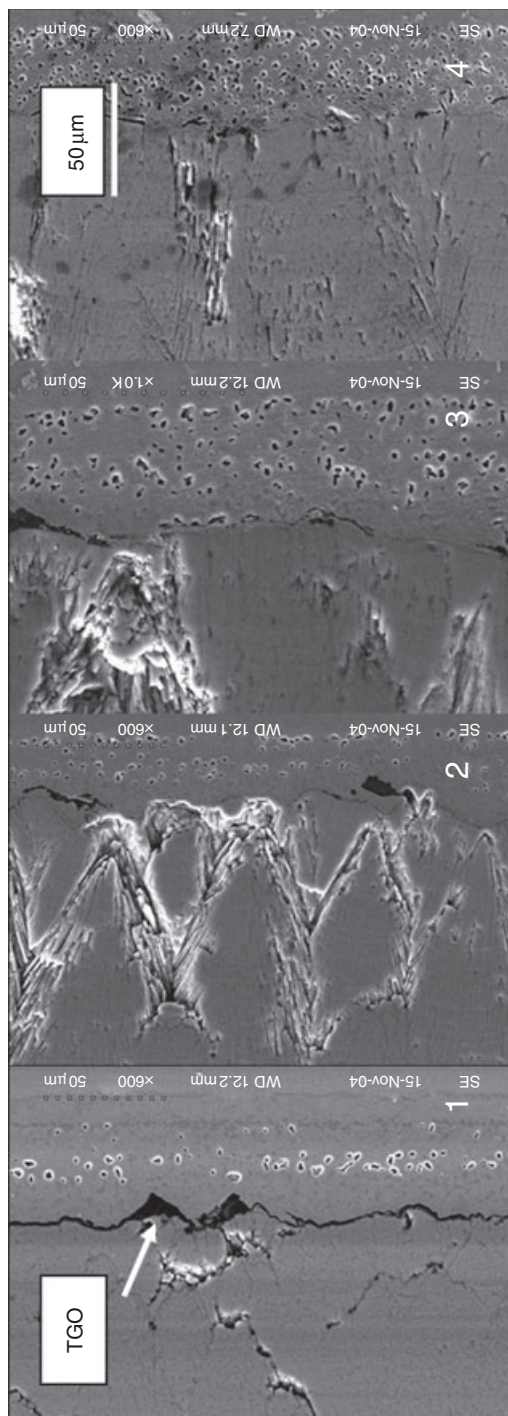
2. Sintering of the ceramic coating occurred at the centre of the heated zone. This gave rise to increased coating conductivity, with consequent decrease in the value.
3. Nos. 2 and 4 experienced the largest thermal gradient along the axial direction. As a result, more cracks and defects, such as horizontal cracks, were generated in the coating, which contributed to the increased resistance value.

It can be concluded that the failure mechanism of the TBC-coated cylinder specimens subjected to thermal load coupled with mechanical load was investigated. The failure modes of the TBC after thermal shock were evaluated by impedance spectroscopy together with SEM. Thermal gradients across the coating thickness and parallel to the coating plane, rather than coating surface temperatures, are the most important factors responsible for the formation of vertical and horizontal cracks which eventually led to the failure of the TBCs.

11.3.2 Failure mechanism of EB-PVD TBC under in-plane thermal gradient coupled with cycling fatigue loading

Failure modes

Cross-sectional microstructures of the sample after thermomechanical loading tests at different positions are shown in Fig. 11.6. The morphology varies greatly with different testing positions and temperatures. In the low-temperature zone (position 5 in Fig. 11.2, also position 1 in Figs 11.2 and 11.6) few cracks and little failure can be seen either in the ceramic coating or at the interface between the ceramic coating and the metallic coating. At the mid-temperature zone (position 2 or 4 in Figs 11.2 and 11.6), which is at the edge of the heated zone, vertical cracks are present in the ceramic coating and these emerged as horizontal cracks. It should be noted that, in this area, the vertical cracks emerged in the ceramic coating, rather than at the TBC/TGO interface, which has always been considered to be the weakest part in the TBC system. Compared to other positions, the highest crack density in the ceramic coating occurs in this area. At the same time, it can be seen in Fig. 11.6 that interfacial failure occurred at the highest temperature zone, with both delamination of the ceramic coating and TGO growth shown. At the low temperature zone, however, TGO is much thinner (hardly visible even) and no apparent interfacial failure occurs. It can be easily seen that TGO growth is correlated with testing temperature. TGO tends to attain a higher growth rate at the heated area, which results in



11.6 SEM images for the sample at different positions. The observation position is marked in the schematic. The position markers correspond with those shown in Fig.11.2.

thicker TGO in the higher temperature region. TGO growth coupled with mechanical loading caused dislocation and slipping of grains at the interface, which is considered to result in stress concentration.

Impedance evaluation

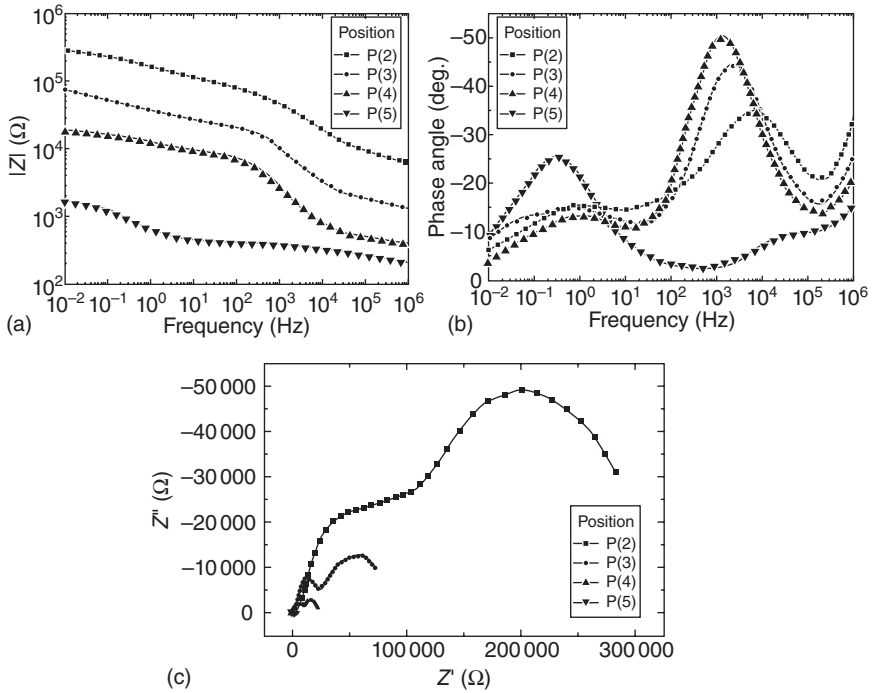
Interfacial failure after thermomechanical testing at different positions of the sample was evaluated using impedance spectroscopy. Figure 11.7b shows a Bode plot (phase angle vs frequency) and Figure 11.7c shows a Nyquist plot (imaginary impedance (Z'') vs real impedance (Z')) from impedance measurements of sample S1 at different positions subjected to thermomechanical loading. It was reported that the relaxation process is correlated with the electrical resistance and capacitance of each equivalent element, which is considered to represent the electrical properties of each layer.^{20,21} In the TBC system, the TGO relaxation process is presented as a Bode plot (phase angle vs frequency) at a frequency of around 10^3 Hz.²⁰

Fig. 11.7a illustrates the impedance resistance moduli at different positions, a clear trend of the resistance modulus increasing with testing positions can be seen. A higher electrical resistance modulus is obtained in the area tested at higher temperature. In Fig. 11.7b, different electrical responses are exhibited at different positions. From positions 2–4, which were subjected to higher temperature, a relaxation process at a frequency of around 10^3 Hz is observed, while in the positions at the low-temperature zone, position 5 in Fig. 11.7, no apparent relaxation process is observed. This suggests that the TGO at the low temperature zone is so thin that it makes little contribution to the electrical relaxation.

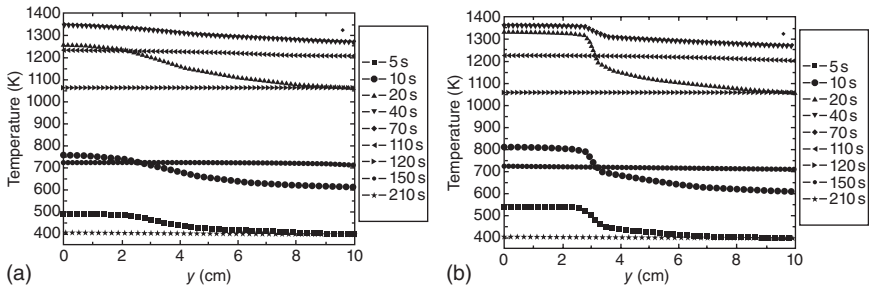
From Fig. 11.7c, it can also be seen that the electrical resistance measured at the high temperature zone is much higher compared to the low-temperature zone. From the low-temperature to the high-temperature zone, the increasing electrical resistance of the TGO denotes increasing TGO thickness. It is considered that thicker TGO tends to form at the high the temperature zone rather than at the low-temperature zone.

TGO growth

As the infrared heating light was focused on a small area of the sample, the temperature varied according to position during the thermomechanical loading test, resulting in the TGO thickness varying according to distance from the heated area. These phenomena can be seen from the cross-sectional microstructure of samples after the thermomechanical loading test – a result confirmed by the impedance measurements at different positions. The simulated temperature profiles along the axial direction at the TGO/TBC interface and the TBC layer are illustrated in Fig. 11.8. Comparing the



11.7 Impedance spectra of sample S2 obtained at different positions.



11.8 Simulated temperature profile at the TGO/TBC interface (a) and the TBC layer (b) along the axial direction during thermomechanical loading experiment. y on the x -axis denotes the distance from heated centre; the heated length in the model is 2.5 mm. Temperature profiles for each experimental stage are shown.

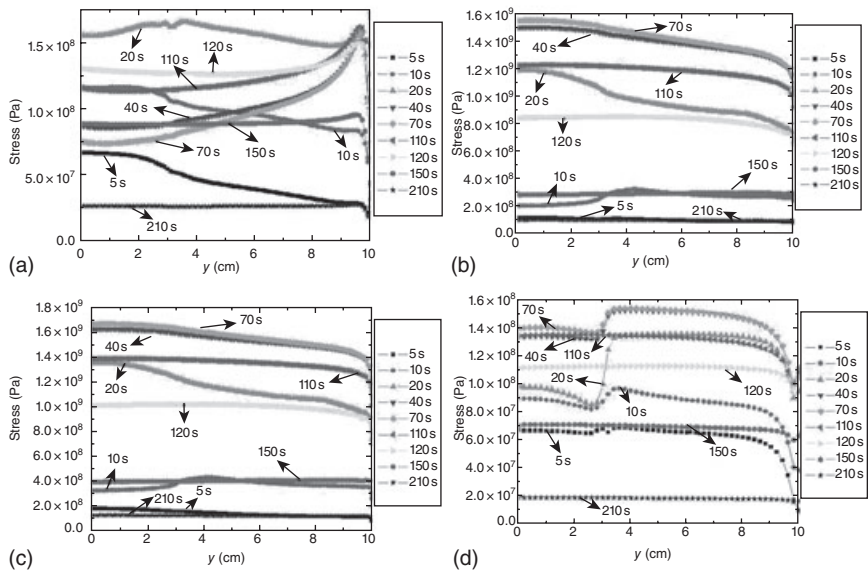
temperature profiles of both TGO/TBC interface and TBC layer at 70 s, which is also the temperature dwell procedure in the test, no apparent difference is obtained. This implies that the temperature gradient along the radius direction can be ignored, compared to that along the axial direction. At the same time, an obvious temperature drop takes place along the axial

direction in the range 70–200 °C. This is considered to be the dominant reason for TGO at the heated area being much thicker than that at the cold end. The higher growth rate of TGO at the heated zone is considered to be one of the reasons responsible for the failure of TBCs.

Stress analysis

The simulated equivalent stress distribution profile, as a function of distance from heated centre along the axial direction obtained from interfaces and TBC layer, is illustrated in Fig. 11.9. It can be seen from the figure that, except for the substrate/bond coat interface, the highest stress level is present at 70 s, which is the temperature dwelling procedure. No apparent stress drop along the axial direction is observed in each interface and metallic layer, which is considered to be a consequence the high thermal conductivity the metallic layers. However, in the TBC layer, a clear temperature drop is present at the edge of the heated centre, particularly during the heating procedure (at 20 s).

Stress profiles along the radial direction in each interface and ceramic coating are illustrated in Fig. 11.10. In each figure, a stress peak is present at the edge of the heated zone, which changes from tensile stress to com-

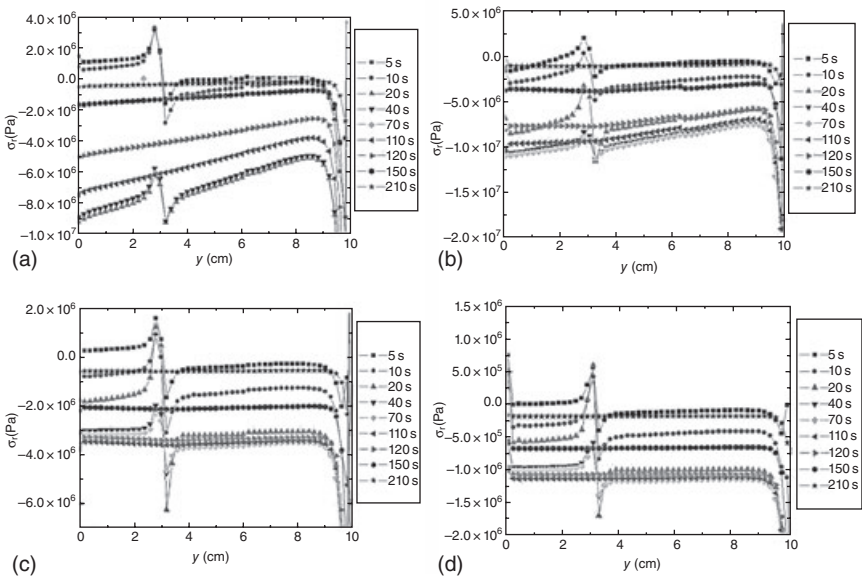


11.9 Stress spatial distribution at interfaces and in ceramic coating vs axial position at different periods of cycling: (a) substrate/bond coat; (b) bond coat/TGO; (c) TGO/YSZ; (d) YSZ layer.

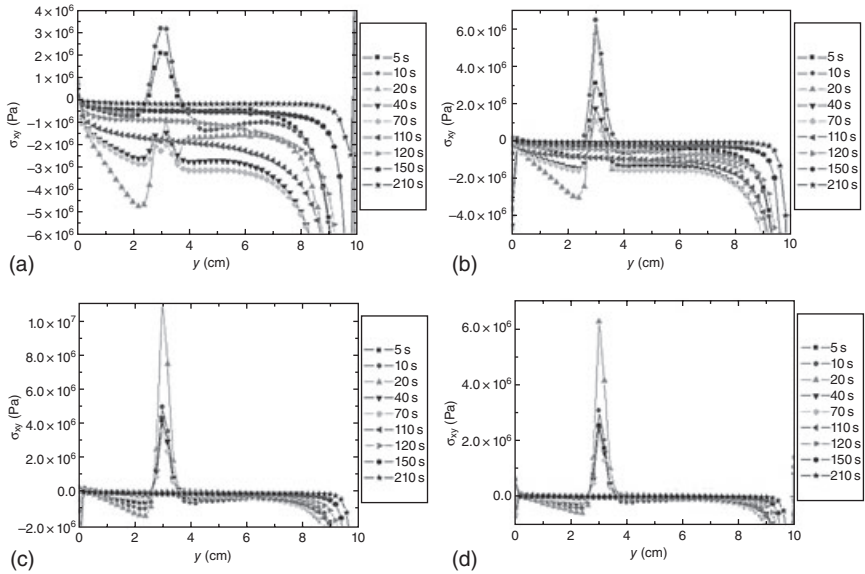
pressive stress. This implies that a large shear stress along the radial direction is present in this area. The shear stress profiles along the axial direction are shown in Fig. 11.11. It can be seen from Fig. 11.6 that, at the edge of the heated zone (position 3), a large number of cracks are present, particularly vertical cracks. This is considered to be induced by the shear stress along the radial direction in this area. With the emerging of vertical cracks, horizontal cracks are formed, which will finally result in delamination of the ceramic coating.

This stress trend is also illustrated in a normal stress profile along the axial direction in Fig. 11.12. Looking at the lowest testing temperature at the non-heated area, no failure or cracks should occur. However, it can be observed from the microstructure of the sample that a large number of vertical cracks are present in the area. This can be attributed to the large tensile stress applied on the coating, making it very likely that cracks will propagate along the through-thickness direction following mode I fracture.

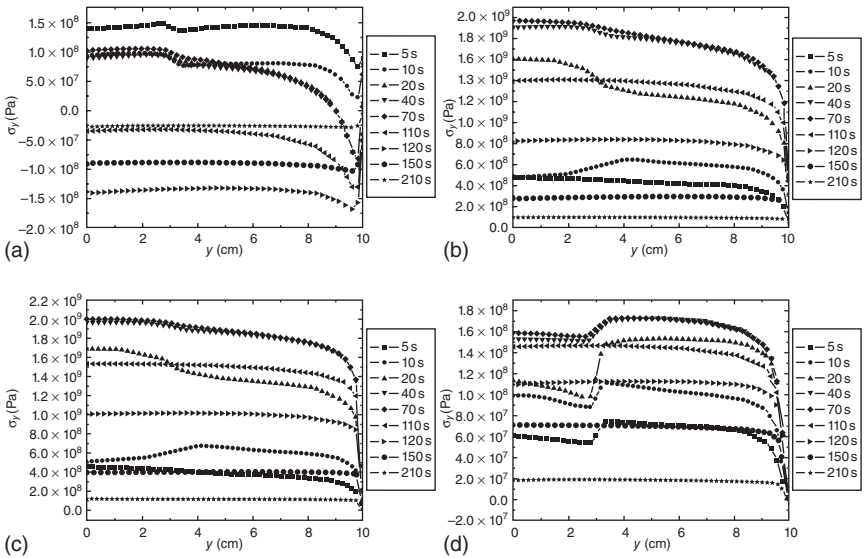
As is the case for the stress profile along the radial direction, a stress peak at the edge of the heated zone can also be seen in the shear stress profile along the axial direction. This might be responsible for the formation of horizontal cracks and the delamination of the coating.



11.10 σ_r spatial distribution of interfaces vs axial position at different times for cylinder specimen with loading: (a) substrate/bond coat; (b) bond coat/TGO; (c) TGO/YSZ; (d) YSZ layer.



11.11 σ_{xy} spatial distribution of interfaces vs axial position at different times for cylinder specimen with loading: (a) substrate/bond coat; (b) bond coat/TGO; (c) TGO/YSZ; (d) YSZ layer.



11.12 σ_y spatial distribution of interfaces vs axial position at different times for cylinder specimen with loading: (a) substrate/bond coat; (b) bond coat/TGO; (c) TGO/YSZ; (d) YSZ layer.

The shape of the stress profile in the TBC system suggested a possible failure mechanism of the coating. The shrinkage of the substrate is inevitable when it is subjected to tensile stress along the axial direction σ_y coupled with compressive stress along the radial direction, σ_r . It can be seen from the simulated stress profiles that the highest values of both σ_y and σ_r are obtained in substrate at the heated centre. Therefore, the shrinkage of the substrate in the radial direction will result in a defect between bond coat and substrate, which is also considered to be de-cohesion between bond coat and substrate.

Subjected to applied mechanical loading, due to the large thermal mismatch between TBC and bond coat, the stress concentration in the TGO layer is enormous. It can be seen from Fig. 11.11 that the shear stress level in TGO-related interfaces is much larger than in other layers. This enables the crack to propagate along the interface following mode II fracture. The interfacial failure is observed in the heated centre, where TGO is thickest in all positions due to high temperature during the thermomechanical test.

Failure mechanism

Subjected to in-plane thermal loading with mechanical loading, the substrate is under compression caused by the coupled effect of normal axial tensile stress σ_y and radial compressive stress σ_r . The highest values for the both are presented at the heated zone, which enhances the contraction of the substrate. Hence, defects occurred at the interface between substrate and bond coat, which is a possible reason for the de-cohesion of the interface.

Due to high temperature and mechanical fatigue loading, plastic deformation and slip bands occurred in the metallic bond coat. These defects in the ceramic coating gave rise to the formation of the oxidation penetration paths. Consequently, abnormal oxidation in the bond coat and oxidation at the surface of the bond coat are observed.

Stress concentration in the TGO layer is one of the most important reasons for the failure of TBCs. An order of 1 GPa is shown at both bond coat/TGO interfaces and TGO/TBC interfaces. Delamination and crash of the TGO are also observed.

11.4 Failure mechanism of EB-PVD TBC under 3-D thermal gradient coupled with mechanical loading

In this investigation, a tube-shaped sample was employed. Subjected to infrared heating at a local area of the sample surface coupled with cooling

air through the hollow in the sample, a temperature gradient field along both radius and axial directions was obtained.

11.4.1 Failure modes

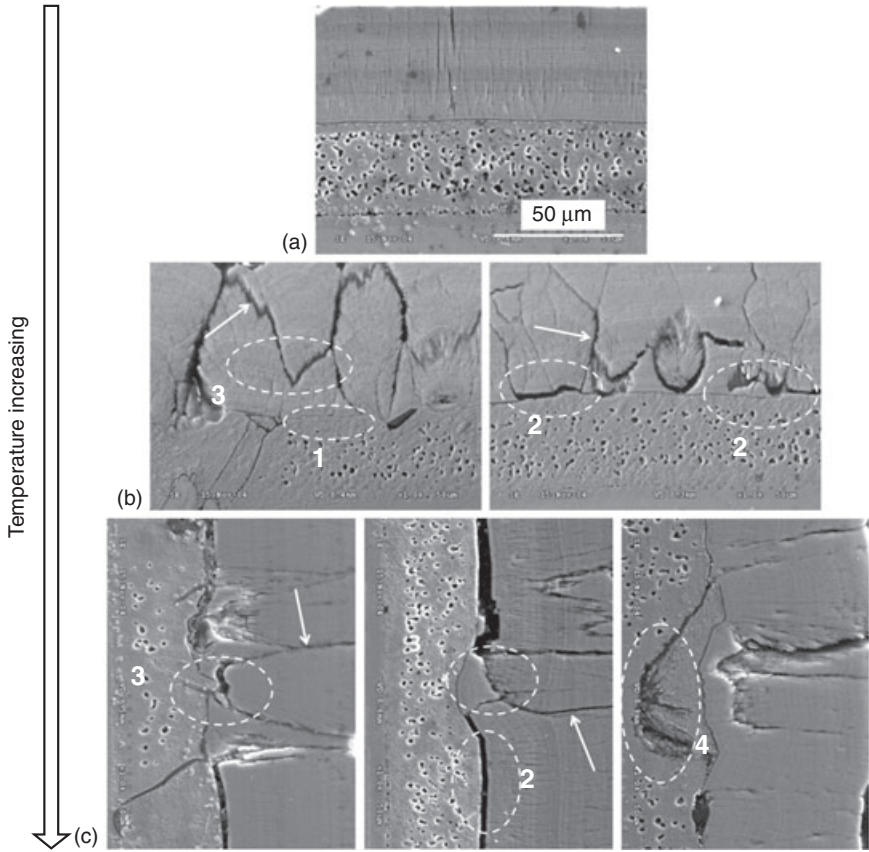
The cross-sectional microstructure of the sample at different positions is illustrated in Fig. 11.13. Failure mode varies according to the position of the sample along the axial direction.

It can be seen from Fig. 11.13 that at the area far away from the heated zone, no apparent damage can be observed in the coating. No obvious cracks are present in the ceramic coating and the interfaces. It can also be seen that the coating is well attached to the substrate by means of the bond coat. As the testing temperature at this area is relatively low, accompanied by a low stress level, failure hardly occurred in this area. The corresponding stress level details are discussed in Section 11.4.2.

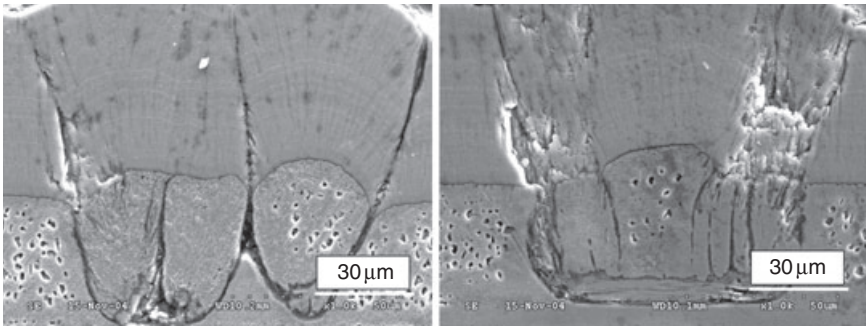
As the test area moves towards the heated centre, failures present in the TBC layer at the edge of the heated zone. The arrows in Fig. 11.13 denote the vertical cracks present in the ceramic coating in this area. The mechanism of nucleation and propagation of the vertical cracks will be discussed in detail using simulated stress analysis in Section 11.4.2. However, the figure clearly shows that vertical cracks emerged in both the ceramic coating (mark 3) and the TBC/bond coat interface (mark 2), and these are considered to result in the local delamination of TBC. In the low-temperature area and in the TGO layer (mark 1 in Fig. 11.13), very few interfacial failures can be observed. This suggests that in this situation, the ceramic coating has good adhesion with the metallic coating and the stress concentration in the TBC layer is of more concern.

At the heated centre, three kinds of failure mode are observed. At the edge of the heated centre, both vertical cracks (arrows denoted) and local spallation (mark 3) caused by vertical cracks emerging can be observed. At the same time, severe interface delamination occurs at this area (mark 2). Compared to the interfacial failure shown at the edge of the heated zone, the interface delamination shown in this area is induced by the decrease in interface adhesion rather than by the emerging of vertical cracks. The decrease in adhesion is considered to be induced by the growth of TGO during heat treatment. It should be noticed that, in the heated area, failure in the bond coat occurs (mark 4), which is different from that in other positions. The same phenomena are widely observed in this area and shown in Fig. 11.14.

It is well known that the fracture toughness of the bond coat is much higher than that of the ceramic coating. As a large number of slip bands are present in the metallic coating, plastic deformation occurs at the tip of the cracks, leading to a compressive stress field at the crack tip, and finally



11.13 Cross-sectional images for sample H2 at different positions along the radius direction.



11.14 Failure modes for sample H1 along the direction perpendicular to loading.

resulting in the inhibition of crack propagation. It is considered that when subjected to thermomechanical coupled loading, creep of the bond coat is accelerated. Therefore, the plastic deformation of the metallic coating is completed at a relatively early stage of the test. Consequently, during the following cycling test, there are insufficient slip bands in the metallic coating, which presents as a decrease in fracture toughness.

Compared to the failure mechanism of the solid cylinder sample subjected to the thermomechanical loading test, some differences are shown in the tube sample. In the tube sample, the outer surface is locally heated, while internal cooling is done using cooling air. Therefore, a thermal gradient along both the radial and the axial direction is obtained, which is considered to be responsible for the failure of TBCs. However, in the solid cylinder sample, the thermal gradient along the radius direction is ignored. Therefore, in the solid cylinder sample, only the thermal gradient along the axial direction is considered.

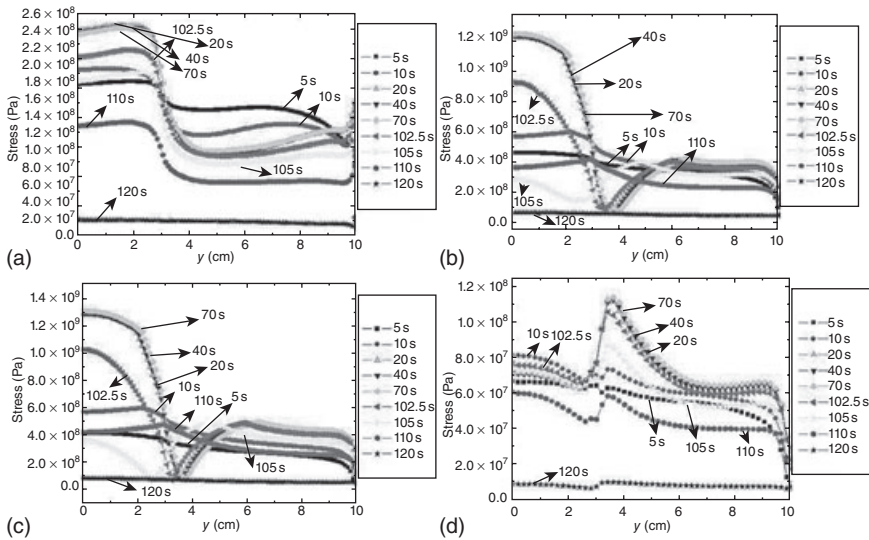
Consequently, different failure modes are present in the solid cylinder sample and the tube sample. In the solid cylinder sample, vertical cracks in the ceramic coating and the emerging of vertical cracks near the TBC/TGO interface are the dominant phenomena. However, in the tube sample, crack propagation along both the through-thickness direction and the interface direction are observed. This is considered to be responsible for the delamination of the coating.

11.4.2 Stress analysis

In the stress analysis, a tensile stress profile ranging from 0–160 MPa was applied to the sample, in accordance with the experimental parameters. The periodicity of the stress profile corresponds to that of the infrared heating. Equivalent stress profiles along the axial direction of each layer and interface are shown in Fig. 11.15. In each part of the figure, the heating procedure takes place over 0–20 s and the temperature dwell procedure over 20–70 s. Cooling to room temperature is reached at 120 s.

It can be seen from the stress profile in the bond coat/substrate interface that the highest stress occurred in the heated area and that stress increased with temperature. At the same time, the equivalent stress shows a large drop at the edge of the heated area. This can be attributed to the coupled effect of applied tensile stress and the temperature-induced thermal expansion.

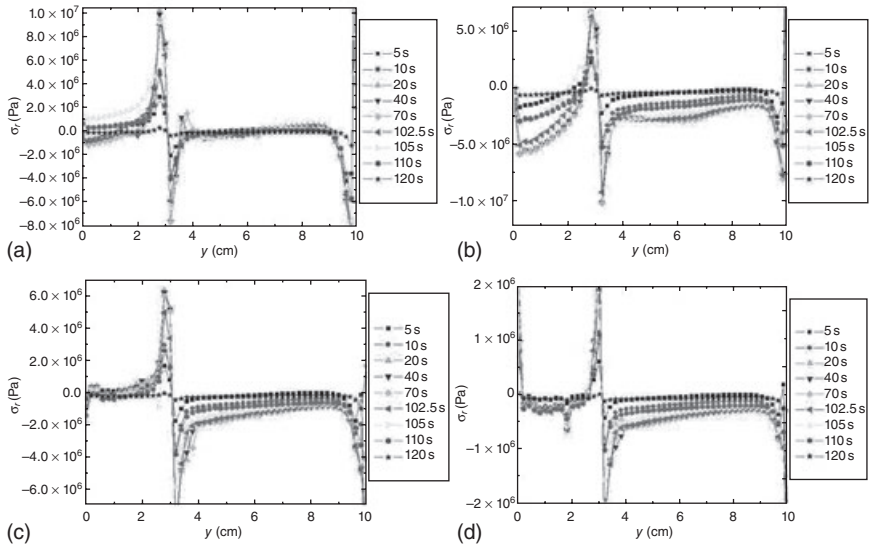
The highest stress level is shown in the TGO-related interfaces due to the high Young's modulus of the TGO layer, and the stress trend along the axial direction is similar to that which occurs in the substrate/bond coat interface. However, it can be seen in Fig. 11.15b that the stress level at the edge of the heated zone is the lowest in the whole profile. This explains why few interfacial failures are observed in this area (Fig. 11.13).



11.15 Stress spatial distribution of interfaces vs axial position at different times for hollow cylinder specimen with loading: (a) substrate/bond coat; (b) bond coat/TGO; (c) TGO/YSZ; (d) YSZ layer.

A different phenomenon is shown in the stress profile in the YSZ layer, where the highest stress peak value is present at the edge of the heated zone. In this layer in the heated area, the stress value is slightly decreased towards the edge of the heated area, and no obvious stress gradient is shown in the non-heated area along the axial direction in the whole experimental procedure. Comparing the stress value in the heated area with that in the non-heated area, no obvious difference can be seen. It should also be noted that in the whole experimental procedure, the stress level change is not so much as in other layers. This suggests that fatigue failure is not the dominant reason for the failure in the ceramic coating.

The stress distributions along the radial direction in each layer and the interface are illustrated in Fig. 11.16. A stress value peak is present at the edge of the heated zone, whereas a relatively low stress level is shown in other positions along the axial direction. It should be noted that the stress status changed from compression to tension at the edge of the heated zone, where the lattice distortion is much larger than at other positions, and hence large lattice strain energy was stored. Therefore, crack formation and subsequent propagation occurred releasing the induced strain energy. At the same time, it can be seen from the stress profiles along the axial direction that, except at the edge of the heated centre, the stress value is not high enough to cause any failure.



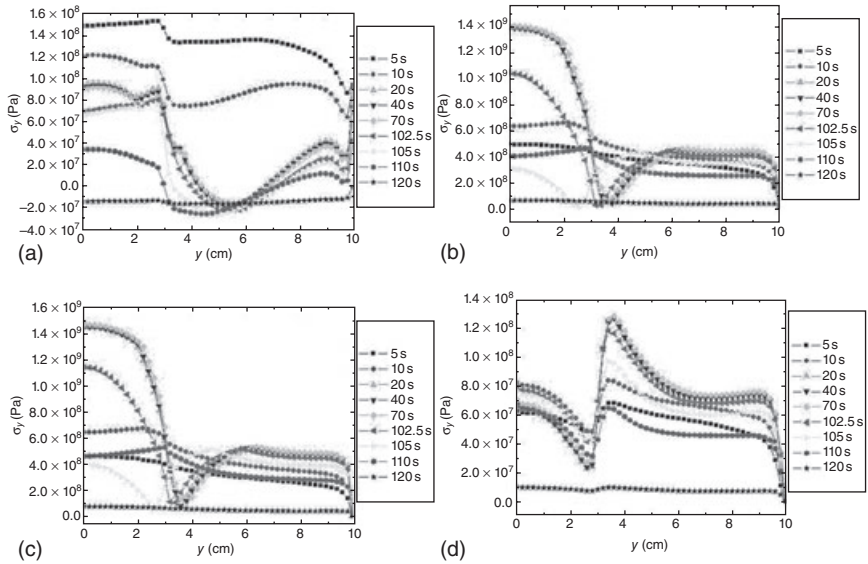
11.16 σ_r spatial distribution of interfaces vs axial position at different times for hollow cylinder specimen with loading: (a) substrate/bond coat; (b) bond coat/TGO; (c) TGO/YSZ; (d) YSZ layer.

The in-plane normal stress distribution along the axial direction is illustrated in Fig. 11.17, and the stress is of the same order as equivalent stress. This implies that σ_y is the dominant stress component in equivalent stress. Regarding the texture of EB-PVD TBC, the in-plane fracture toughness of the ceramic coating is lower than that in the through-thickness direction. Hence σ_y is of great concern as the dominant cause for cracks along the through-thickness direction. The presence of vertical cracks causes a moment to be applied on the ceramic column due to applied in-plane stress which acts as the driving force behind the propagation of horizontal cracks.

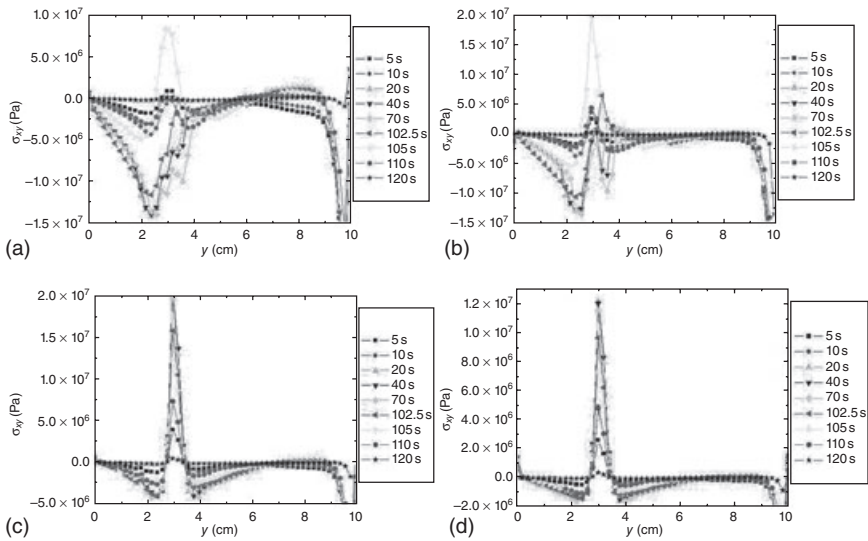
The shear stress profiles are illustrated in Fig. 11.18 which shows a trend similar to that of the stress distribution along the radius direction. The stress level is relatively low in most positions except at the edge of the heated zone, where a stress peak value is presented. This suggests that occurrence of fracture is highly possible at this area.

11.4.3 Failure mechanism

Subjected to high temperature coupled with fatigue load cycling, substrate and bond coat are under tension, σ_y , with the highest stress level being 150 MPa. At the edge of the heated area, the substrate and bond coat underwent shear stress over 10 MPa caused by non-uniform thermal



11.17 σ_y spatial distribution of interfaces vs axial position at different times for hollow cylinder specimen with loading: (a) substrate/bond coat; (b) bond coat/TGO; (c) TGO/YSZ; (d) YSZ layer.



11.18 σ_{xy} spatial distribution of interfaces vs axial position at different times for hollow cylinder specimen with loading:²² (a) substrate/bond coat; (b) bond coat/TGO; (c) TGO/YSZ; (d) YSZ layer.

loading. Therefore, slip bands formed in the bond coat at an angle of 45° from the interface. Cracks induced at these defects tend to propagate in the bond coat, since the slip bands will be blocked at the interface. Hence, the bond coat is internal oxidized.

Stress concentration in the TGO layer is one of the most important reasons for the failure of TBCs. An order of 1 GPa is shown at both bond coat/TGO interfaces and TGO/TBC interfaces. Delamination and crash of TGO is also observed.

Subjected to mechanical loading, normal stress, σ_y is at a relatively high level, accompanied by radius stress and shear stress, and residual stress in the ceramic coating increases. During the experiment, the coating is exposed to high temperature, so the strength of the ceramic coating decreases, particularly at the area with the highest temperature gradient. Therefore, vertical cracks and delamination in the ceramic coating are considered to be the most important reason for the failure of TBCs.

11.5 Conclusions

The failure mechanism of the sample subjected to thermomechanical loading was obtained using microstructure analysis and impedance spectroscopy accompanied by stress simulation. Some conclusions are drawn as follows.

Cracks initiated and propagated in ceramic coating are considered to be the dominant reason for the failure of TBCs. This is entirely different from the failure mechanism in a uniform temperature field without mechanical loading. It is also proved by FEM stress analysis that the degradation of the ceramic coating is accelerated under applied mechanical loading.

The highest crack density in ceramic coatings occurred at the edge of the heated area, which is also considered to be the area with the highest temperature gradient. According to the results obtained by impedance spectroscopy, the highest electrical resistance was presented at the area with the highest temperature gradient rather than the highest temperature. This is induced by the vertical crack density.

In the tube sample, the temperature gradient along both the radius and the axial directions was obtained. In this situation, vertical cracks occurred in the ceramic coating. At the same time, delamination of the ceramic coating was also observed. The emerging of vertical cracks and delamination of the coatings are considered to be responsible for the failure of TBCs.

In the solid cylinder sample, only the temperature along the axial direction was considered. Subjected to applied mechanical loadings, accompanied by thermal stress, cracks along the through-thickness direction are the dominant reason for the failure TBCs.

11.6 References

1. ANDERSON, P.S., X. WANG and P. XIAO, Impedance spectroscopy study of plasma sprayed and EB-PVD thermal barrier coatings. *Surface & Coatings Technology*, 2004. **185**(1): 106–119.
2. WANG, X. and P. XIAO, Characterisation of clay sintering process using impedance spectroscopy. *Journal of The European Ceramic Society*, 2002. **22**(4): 471–478.
3. MILLER, R.A., Oxidation-based model for thermal barrier coating life. *Journal of the American Ceramic Society*, 1984. **67**(8): 517–521.
4. STRANGMAN, T.E., Thermal barrier coatings for turbine airfoils. *Thin Solid Films*, 1985. **127**(1–2): 93–106.
5. EVANS, A.G., M.Y. HE and J.W. HUTCHINSON, Mechanics-based scaling laws for the durability of thermal barrier coatings. *Progress in Materials Science*, 2001. **46**(3–4): 249–271.
6. PADTURE, N.P., M. GELL and E.H. JORDAN, Thermal barrier coatings for gas-turbine engine applications. *Science*, 2002. **296**(5566): 280–284.
7. EVANS, A.G., *et al.*, Mechanisms controlling the durability of thermal barrier coatings. *Progress in Materials Science*, 2001. **46**(5): 505–553.
8. WRIGHT, P.K. and A. EVANS, Mechanisms governing the performance of thermal barrier coatings. *Current Opinion in Solid State and Materials Science*, 1999. **4**: 255–265.
9. BOROM, M.P., C.A. JOHNSON and L.A. PELUSO, Role of environmental deposits and operating surface temperature in spallation of air plasma sprayed thermal barrier coatings. *Surface and Coatings Technology*, 1996. **86–87**: 116–126.
10. EVANS, A.G. and J.W. HUTCHINSON, The mechanics of coating delamination in thermal gradients. *Surface & Coatings Technology*, 2007. **201**(18): 7905–7916.
11. MERCER, C., *et al.*, A delamination mechanism for thermal barrier coatings subject to calcium-magnesium-alumino-silicate (CMAS) infiltration. *ACTA Materialia*, 2005. **53**(4): 1029–1039.
12. KRAMER, S., *et al.*, Mechanisms of cracking and delamination within thick thermal barrier systems in aero-engines subject to calcium-magnesium-alumino-silicate (CMAS) penetration. *Materials Science and Engineering*, 2008. **490**(1–2): 26–35.
13. WANG, X., J.F. MEI and P. XIAO, Non-destructive evaluation of thermal barrier coatings using impedance spectroscopy. *Journal of The European Ceramic Society*, 2001. **21**(7): 855–859.
14. SONG, S.H. and P. XIAO, Relation of microstructural and compositional features to the electrical properties in degraded thermal barrier coating systems. *Journal of Materials Science*, 2003. **38**(8): 1661–1665.
15. DENG, L.F. and P. XIAO, Characterisation of alumina scales on FeCr alloy using impedance spectroscopy. *Thin Solid Films*, 2008. **516**(15): 5027–5031.
16. DENG, L.F., Y.S. XIONG and P. XIAO, Modelling and experimental study of impedance spectra of electron beam physical vapour deposition thermal barrier coatings. *Surface & Coatings Technology*, 2007. **201**(18): 7755–7763.
17. HUTCHINSON, J.W. and A.G. EVANS, On the delamination of thermal barrier coatings in a thermal gradient. *Surface & Coatings Technology*, 2002. **149**(2–3): 179–184.
18. HE, M.Y., D.R. MUMM and A.G. EVANS, Criteria for the delamination of thermal barrier coatings: with application to thermal gradients. *Surface & Coatings Technology*, 2004. **185**(2–3): 184–193.

19. ZHANG, D.B., *et al.*, Measurements of the thermal gradient over EB–PVD thermal barrier coatings. *Vacuum*, 2003. **70**(1): 11–16.
20. VASSEN, R., *et al.*, Recent activities in the field of thermal barrier coatings including burner rig testing in the European Union. *Advanced Engineering Materials*, 2008. **10**(10): 907–921.
21. CHEN, C., *et al.*, Failure of EB–PVD thermal barrier coatings subjected to thermo-mechanical loading. *Chinese Journal of Aeronautics*, 2006. **19**: s82–s85.
22. PENG, H., *et al.*, Numerical Analysis of EB–PVD Thermal barrier coatings under thermal-mechanical coupled environment. *Materials Science Forum*, 2007. **546–549**: 1795–1799.
23. ZHOU, Y.C. and T. HASHIDA, Coupled effects of temperature gradient and oxidation on thermal stress in thermal barrier coating system. *International Journal of Solids And Structures*, 2001. **38**(24–25): 4235–4264.

Non-destructive evaluation (NDE) of the failure of thermal barrier coatings

G. CHEN, Northwestern Polytechnical University, China

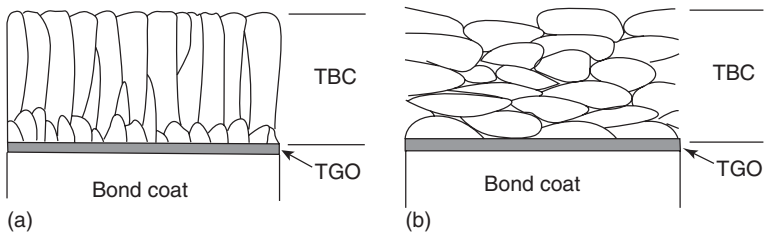
Abstract: This chapter discusses the development of non-destructive evaluation (NDE) methods used for the detection of premature failure of thermal barrier coatings (TBCs) systems. The fundamentals and application of different NDE methods are reviewed, with particular interest focused on the latest results with regard to the promising emission spectroscopy NDE method used for *in situ* TBCs failure inspection.

Key words: thermal barrier coatings (TBCs), non-destructive evaluation (NDE), high-temperature oxidation, gas turbine.

12.1 Introduction

A large number of coatings have been developed and are widely used to protect a variety of structural engineering materials from corrosion, oxidation, wear and erosion. Of them all, thermal barrier coatings (TBCs) have the most complex structure. TBCs are applied to the hot-section components of gas turbines and they are required to operate under the most demanding conditions encountered by the structural components. The demand for improved performance has led to the increasing use of TBCs in gas turbines, and they are the most important materials on the technology roadmap in that field. The function of TBCs is to provide thermal insulation and oxidation protection simultaneously, and TBCs have become the crucial element in the pursuit of improved efficiency, longer lifetime and reduced environmental impact.¹⁻⁹

The state-of-the-art TBCs consist of an yttria stabilized zirconia (YSZ) top coat, a thin thermally grown oxide (TGO) reaction layer and a metallic bond coat on a superalloy substrate. The thermal insulation is provided by an outer YSZ layer deposited by either electron beam physical vapor deposition (EB-PVD) or plasma-spraying (PS) techniques. The oxidation protection is provided by a thin TGO layer. Since superalloys are not generally optimized for oxidation resistance, a bond coat (BC) is usually used to develop a durable oxidation barrier, and it must be designed to maintain a stable TGO over the life of the system. The schematic representations of TBCs prepared by EB-PVD and PS are illustrated in Fig. 12.1, which shows



12.1 Schematic representation of TBCs obtained by EB-PVD (a) and PS (b).

the different structures obtained by EB-PVD and PS. In the modern TBCs system, the TGO layer is the source of the major strain incompatibility that leads to failure.^{2,6} Evolutionary processes in the surrounding layers have deleterious effects that converge on the TGO, further aggravating the problem. The adhesion and growth kinetics of a TGO layer and hence the system life can be strongly influenced by the composition and/or morphology of the bond coat.

The application of TBCs in conjunction with internal cooling of the underlying superalloy component can provide a surface temperature reduction of 50–150 °C, with potential of over 170 °C.⁹ This has enabled the operation of modern gas turbines having combustion gas temperatures in excess of 250 °C above the melting temperature of the protected superalloy components, thereby improving turbine efficiency and performance. Alternatively, TBCs help reduce metal temperature and make gas turbine components more durable at lower operating temperatures. Therefore, the growing reliance on TBCs to increase the gas inlet temperature of gas turbines requires that TBCs must be ‘prime reliant’, and must not fail over the life of the components. However, lack of reliability and concern over premature failure have slowed the general application of TBCs in gas turbines and, even where used, the benefits offered by TBCs, such as the temperature advantage, and hence energy efficiency and operating lifetime, have not yet been fully realized.⁴ The exact failure mechanisms of TBCs are still not clear due to the many contributing factors. The type and fabrication procedures of the bond coats, as well as the TBCs, may result in different behaviors that could complicate understanding of TBCs failure even more.²

Due to the severity of TBCs failure, early detection of TBCs degradation and failure is becoming critical to prevent catastrophic failure as more advanced gas turbines depend on TBCs for their high-temperature operation. TBCs on turbine hot-section components, therefore, require regular maintenance. A typical periodic maintenance is a visual inspection of the TBCs for cracks, spallation, erosion or other damage that will indicate the remaining TBCs life. These visual inspections require the gas turbine to be

taken out of service and to be partially disassembled to provide access to the TBCs by boroscope. This type of maintenance is costly because it requires skilled labor and the interruption of service. Moreover, in most cases only the regions with very large spalled area can be seen visually, and this is the basis for boroscope inspection today. Therefore, for the reliable application of TBCs, it is highly desirable to have non-destructive evaluation (NDE) methods that can detect the presence of small defects in TBCs at an early stage, monitor their growth and predict the remaining life of TBCs.

The present chapter summarizes the current status of understanding of TBCs failures and the development of failure detection methods; particular interest will be concentrated on the NDE methods and the latest development of *in situ* NDE of TBCs failure during gas turbine operation.

12.2 Failure of thermal barrier coatings (TBCs)

As mentioned above, the actual TBCs failure mechanisms are complex and difficult to understand due to the large number of contributing factors. Even so, some general failure models have been produced based on a large number of results.^{2,6,9,10} The present topic of NDE development for TBCs failure evaluation/detection does not allow the author to give a detailed introduction to each failure mechanism of TBCs, therefore, a general summary of TBCs failure will be presented in terms of TBCs materials, structure and application, in order to facilitate a basic understanding of the different NDE methods used in this chapter. For more information readers should refer to Chapters 8, 11 and 13.

12.2.1 Materials

Bond coat

Bond coat is recognized as the most crucial component in TBCs and a critical factor affecting the stability and durability of TBCs.^{4,6,9} Its chemistry and microstructure are dependent on the compositions and preparation processes, and then have significant influence on the durability through the structure and morphology of TGO formed in service. TBCs failure is often observed either at the interface between the bond coat and the TGO or between the TGO and the YSZ, or within the TGO or within the YSZ near the TGO, and the failure is dependent on the bond coat used. Thus, increasing the adhesion and integrity of the interfacial TGO layer may greatly contribute to the reliability of TBCs. Generally, the onset of TBCs spallation is triggered by some form of microstructural imperfections at or close to the TGO layer. These imperfections in or around the TGO convert

the misfit stress, which results from the different mechanical properties of different layers in the TBCs, into a driving force for failure by crack initiation, propagation at the interface and final large-scale buckling of TBCs. Two principal failure models have been proposed, even though the relative importance of these two mechanisms has not been established for different bond coats. One is the development of undulations with thermal cycling, in accordance with wrinkling and ratcheting mechanisms.^{11,12} Such imperfections develop primarily in bond coats most susceptible to viscoplastic deformation. They induce cracks in the superposed TBCs that extend laterally and link together to cause failure. The other is the extent of oxidation, which leads to heterogeneity of the TGO layer thickness.¹³ These imperfections give rise to failure by decohesion of the interface between the TGO and the bond coat, which may be accelerated by impurity segregation.^{14,15}

At present, bond coat materials are in two categories, one of which is based on NiCoCrAlY and the other is Pt-modified diffusion aluminide. Both of them result in distinct TGO features as well as differing tendencies to plastic deformation. Accordingly, the failure mechanisms are often different.¹⁶ Both TGO growth and inter-diffusion with the substrate contribute to the bond coat change in terms of chemistry and phase structures and have a similar effect. Undulations can be promoted by softening or local volume changes arising from phase transformations in the bond coat.^{11,17} Impurities migrating from the substrate can embrittle the interface or produce local oxide penetrations. In the extreme case, Al depletion from bond coat/substrate inter-diffusion can reduce the ability of bond coat to sustain protective Al_2O_3 growth and destabilize the Al_2O_3 layer by introducing unwanted elements in favor of the formation of inter-phases with lower toughness or adherence.¹⁸ Under some circumstances, thermal stress relaxation by plastic flow of the bond coat can lead to cracking of the TGO upon reheating, giving rise to local oxide penetrations.¹⁹

Yttria stabilized zirconia (YSZ) insulation layer

Durability and stability concerns in the YSZ layer arise primarily from the anticipated increases in surface temperature in advanced gas turbine technologies. The consequences are increased susceptibility to morphological changes of the pore structure as well as densification of the compliance-enabling features, i.e. the columnar structure YSZ produced by EB-PVD, with attendant degradation of the insulation efficiency and strain tolerance. Moreover, current YSZ layers are becoming more susceptible to destabilization of the 'non-transformable' tetragonal ZrO_2 structure (t') as the higher operating temperature reduces the diffusional hindrance to partitioning,²⁰ while the effect of the subsequent monoclinic transformation is

generally considered undesirable. The problem can be further aggravated by chemical reaction with molten salt deposits from the combustion environment, mostly vanadates, sulfates and silicates.^{21–23}

12.2.2 Structure

As seen in Fig. 12.1, two different TBCs microstructures can be produced by EB–PVD and PS methods. A columnar TBCs grain structure with multi-scale porosity produced by EB–PVD has much more strain tolerance capability than the splat structure produced by PS, while the inter-splat/intra-splat porosity and a network of crack-like voids in the PS TBCs can provide much lower thermal conductivity compared to that of EB–PVD TBCs. Both of them make different contribution to the failure of TBCs in the initiation or propagation of the defects/imperfections. A more detailed description of the failure from EB–PVD and PS TBCs can be found in Reference 6.

12.2.3 Application

TBCs applied in aero gas turbines for propulsion will experience numerous thermal cycles whereas TBCs in industrial gas turbines for power generation will have a long isothermal history. For the latter, much longer service lifetime will be demonstrated with the same TBCs, and the failure process model is also different. Another issue occasionally encountered is the mechanical degradation of TBCs by foreign object impact and/or erosion.²⁴ Usually this effect will contribute along with other factors to the failure.

12.3 Development of failure inspection methods

With the application of TBCs in the early 1980s, a method of evaluating TBCs failure has been sought, proposed and developed. The major impetus of this thrust for TBCs failure inspection was to improve the integrity and performance during service of the coatings. Acoustic emission (AE) was the first method applied to qualitative and quantitative evaluation of the cracking process within the YSZ in TBC systems.^{25–27} The AE method can be used for destructive and non-destructive testing. Indentation, tensile adhesion tests and four-point bending test coupled with AE can be taken as the destructive way. *In situ* AE evaluation can also be applied to the inspection of micro- and macrocracking initiation and propagation in TBCs. This method is focused only on the detection of the defects in the form of cracks due to the limited lifetime exhibited by the TBCs at that time.

However, there are numerous defects present in well-developed TBCs, such as delamination, spallation and TGO development. Thus, infrared (IR)

thermography was developed to evaluate effectively the delamination defects in TBCs.^{28,29} Besides the delamination defects, IR thermography was also used to inspect the degradation of YSZ in TBCs, because there existed a correlation between YSZ degradation and TBCs lifetime.^{30,31} For this technique, the sample is usually heated from front or back surfaces by a flash of radiation, and the thermal image is captured using an IR camera. Delaminations, large internal cracks or changes in thermal diffusivity all result in a non-uniform temperature distribution and hence image contrast.

With the development of TBCs materials and preparation processes, more and more results suggested that the TBCs lifetime has a close relation with the reaction layer of TGO. The evaluation of the formation of TGO is important and non-destructive evaluation and detection of these coating failures at the TGO layer is necessary. All the previously mentioned NDE methods, however, did not take the TGO layer into account. Therefore, some new NDE methods were developed, e.g. electrochemical impedance spectroscopy (EIS)^{32–35} and photo-stimulated luminescence spectroscopy (PSLS).³⁵ These methods consider the role of TGO in the determination of defects evolution and eventual failure of TBCs. EIS can determine the evolution of YSZ as well as TGO,³³ whereas PSLS focuses only on the state of TGO.³⁵ Recently, a new kind of NDE method has been proposed by doping marker ions in the YSZ layer in TBCs system; *in situ* evaluation of TBCs failure during engine operation could be made, demonstrating its key and promising role in determination of the failure of TBCs.^{36,37}

Based on the above-mentioned methods, the techniques used in NDE of failure of TBCs can be categorized into four groups based on different aspects of TBCs discussed in detail as follows:

1. crack or delamination development in TBCs;
2. thermal property change of TBCs;
3. TGO development and its interface with YSZ and bond coat;
4. doping ions in YSZ.

12.3.1 Inspection of crack or delamination in TBCs

In the early stage of TBCs development, crack development plays a major role in determining the lifetime of TBCs.^{26,27} Failure-related cracking in the YSZ is of great concern; its initiation and evolution can give rise to noise and so can be monitored by the AE technique, whereby the noise response can be correlated with the evaluation of the coating and its lifetime predicted. Acoustic emission (AE) is a term describing a class of phenomena whereby transient elastic waves are generated by the rapid release of energy from localized sources within a material.³⁸ Studies on AE responses during

the thermal cycling of plasma-sprayed TBCs have shown that the type of cracking and the AE responses may be influenced by a number of factors, such as the porosity, the presence of metastable phases, the thermal expansion mismatch between substrate and coating and the anisotropy of thermal expansion among the phases. A stable microcracking network can be generated for TBCs with good adhesion strength. These coatings remain effective even after the formation of a microcrack network. In contrast, catastrophic failure occurred because of unstable crack growth. A 'crack density function' (CDF),³⁹ considering both the number and size of cracks, has been proposed, and it is found that macrocracking events tend to occur at low values of the CDF. One of the shortcomings is that this method provides temporal information of cracking in the system, but no spatial information.

With the development of TBCs including material for TBCs as well as the process methods used in the preparation of TBCs and their increasingly wide application, crack detection no longer effectively predicts the failure of TBCs. Interest has moved to the delamination of the top YSZ coat at the interface or in itself which would lead to the spallation of the top layer partly or totally, eventually causing the TBCs failure. Harada *et al.*²⁸ and Saitoh *et al.*²⁹ proposed an evaluation method for delamination effects using infrared thermography, and further work has since been carried out to study the use of this technique to predict TBCs failure.^{30,31,40} The detection of the delamination in TBCs with the infrared thermography method is always coupled with measurement of the thermal properties of TBCs components; detailed information will be given in the following section.

12.3.2 Inspection of thermal property change of YSZ in TBCs

Changes in all kinds of coating properties after long-term operation may degrade the performance of the coatings. The thermal barrier performance of TBCs (in other words, the thermal resistance of TBCs) can be degraded by means of decreases in TBCs thickness, rises in TBCs density and peeling of TBCs. Thermal properties are usually treated as just basic material parameters and have not been utilized widely in TBCs characterization and failure analysis. This ageing process can alter the thermal properties of the coating (through phase transformation and microstructure change) and introduce defects like cracks, delaminations and spallations. Thermal transport properties such as thermal conductivity and thermal diffusivity are closely related to the microstructural changes of the TBCs. Therefore, it is highly desirable to have an evaluation technique sensitive to the coating properties as well as the thermal contact with the substrate.

A variety of measurement techniques have been developed to determine the thermal properties of coatings. Measurements are distinguished by a wide variety of methods employed for heating and temperature sensing. Several photothermal methods utilize front surface temperature sensing, and these include photoacoustic measurements,⁴¹ IR thermography,³¹ deflection method,⁴² etc. in which IR thermography can be used to non-destructively inspect the TBCs failure.^{43–46} In this method, a laser heats the part to be inspected and the surface temperature of the heated part is measured using a radiation thermometer or infrared camera. The thermal resistance of the TBCs is evaluated based on the measured temperature. An important requirement in this non-destructive inspection method is to divide the heating wavelength and measuring wavelength in order to remove the influence of the reflected light. Another requirement is to perform the heating and measurement of the target part continuously and at a fixed speed. This method is believed to be effective for complex-shaped metal parts of actual gas turbines coated with TBCs. Also, the TBCs thickness can be evaluated by the IR method.^{31,43–46} Further related information about optical NDE techniques for TBCs can be found in Ellingson *et al.*⁴⁷

Recently, a new generation of NDE IR method, phase of thermal emission spectroscopy, has been developed for TBCs failure analysis.⁴⁸ Phase of thermal emission spectroscopy is a technique whereby harmonic heating is induced in the coating by laser excitation and the resulting temperature field is detected through its thermal emission. The thermal emission comes from the volume of the coating experiencing transient temperature variation and carries information regarding heat transport through the TBCs related to the coating's thermal properties, thickness, the thermal contact (delamination) with the substrate and the substrate thermal properties. By changing the laser modulation frequency, the thermal penetration depth relative to the coating thickness is altered. Therefore, phase of thermal emission spectroscopy can be used for characterization of the coating properties over a large range of thermal penetration depths. A combination of features makes phase of thermal emission spectroscopy unique and potentially superior to existing IR techniques for coating property measurements. This technique does not require any special sample preparation and requires access only to the top surface of the coating, permitting non-destructive measurements to be made on coatings in almost any condition with arbitrary substrate shape and dimension. The method can simultaneously provide thermal conductivity and volumetric heat capacity of the coating as well as the thermal contact resistance of the interface. This method is not sensitive to environmental temperature, and therefore can be utilized at the high operating temperatures of the coating.

Impedance spectroscopy (IS) has also been used for NDE of TBCs.^{32,33,49} Impedance spectroscopy is a method for the evaluation of defects and

degradation of materials using the AC frequency response of the electrical impedance of a material. The impedance characteristic of a material depends on temperature, thickness or area of the coating, formation of reaction layer or delamination. These degradations and defects are evaluated by measuring the variation of impedance caused by these microstructural changes. Therefore, the IS method enables the thickness reduction of TBCs, initiation of defects, formation of oxide film and coating delamination to be detected by these resistance and capacitance data.³² Moreover, defects such as delamination, spalling and cracking and other forms of material damage can be detected using voltage and current response when alternating current with varying frequency is applied. Changes of both resistance and capacitance associated with the degradation can be measured. Thickness reduction of TBCs has already been successfully evaluated by IS.³³ Impedance spectroscopy is a cheap, quick and powerful testing method, which is particularly useful for ceramic materials. Voltage and current responses, on application of an alternating current with varying frequency, relating to YSZ, TGO and mixed oxide layers were observed in the impedance spectra.³⁴ These responses can be modeled using equivalent circuits software. In all, IS is a powerful NDE method capable of detecting different types of defects mentioned above; changes in other physical properties and even the formation, growth and thickness of the TGO can also be monitored by IS.^{49,50}

Compared to the 'dry' IS technique (tested at high temperatures of 200–350 °C, EIS was developed as a NDE technique for the life-remaining prediction and quality control of TBCs.^{51–53} Electrochemical impedance response was acquired at room temperature and analyzed with an AC equivalent circuit. EIS is an NDE technique that measures electrochemical impedance of materials using an applied voltage with varying frequency. The electrochemical impedance characteristics of TBCs may depend on the thickness and microstructure of the YSZ coating, the thickness and microstructure of the TGO and, potentially, the damage at critical interfaces in the vicinity of TGO.³⁵

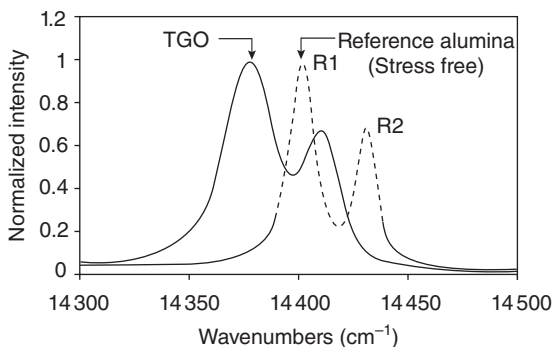
12.3.3 Inspection of thermal grown oxide (TGO) and its interface with YSZ and bond coat

Although these above-mentioned non-destructive inspection techniques can characterize the degradation of TBCs, studies on NDE of the detrimental influence of the TGO reaction layer are limited. Moreover, only a few attempts have been made at NDE of the TBCs lifespan. The formation of the TGO layer in TBCs and its evolution and damage play an important role in determining the life of TBCs in service. There is a real need for non-destructive tools to evaluate whether TBCs are damaged and, on the basis

of the damage detected, determine how much life remains before failure will occur. Once the TBCs have buckled or spalled they can generally be seen optically, but it is essential to develop a tool capable of detecting damage evolution before it reaches the critical buckling size. Thus, it is a prerequisite that the non-destructive tool is able to probe through the thickness of the TBCs to detect any damage related to the TGO. The evaluation of the TGO reaction layer can be realized by using the IS method.^{33,35,50} The physical properties, the formation and the thickness of the reaction layer can be evaluated using this method together with sensitivity analysis. The other promising method is PSLS since it is non-destructive and produces a direct measure of local elastic strain energy in the TGO.⁵⁴⁻⁶⁸ This process also provides a basis for the quantitative determination of the extent of local damage prior to the spalling from an analysis of the shape of the luminescence spectra.

The application of PSLS as a NDE technique for TBCs was pioneered by Clarke and refined by some other researchers.^{54,55} This technique is concentrated on the stress state of the TGO. Adhesion of the TBCs to the bond coat has been shown to be dependent upon a good bond being maintained between TGO and bond coat. The thermal expansion mismatch between the metallic bond coat and the alumina TGO is such that the TGO is under a large compressive stress (about 4 GPa) at room temperature. Laser excitation of small amounts of Cr ions in the TGO causes fluorescence to occur and the spectral response is pressure (stress) dependent. If the TGO becomes detached, the stress would be reduced and this in turn results in a peak shift in the fluorescent spectra, which is illustrated in Fig. 12.2.

In α -alumina the R-line fluorescence is split into a doublet (R1, R2) by crystal field effects. Of the two lines, it has been found that the R2 line has a more linear pressure dependence and is also more isotropic for different



12.2 The typical R1/R2 fluorescence spectra for chromium containing stress-free and stressed α -Al₂O₃.

crystallographic orientations. Hence, the stress measurements reported have been primarily based on measurements of R2. For polycrystalline materials where the sample volume probed is large compared with the grain size, the frequency shift, $\Delta\nu$, of the R2 line is given by:

$$\Delta\nu = 2.54 \text{ (cm}^{-1} \text{ GPa}^{-1})\sigma \quad [12.1]$$

and for the case of a scale which we take to be stressed in only two dimensions, Eq. (12.1) becomes:

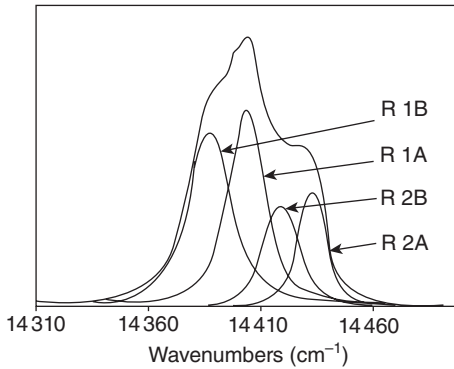
$$\Delta\nu = 5.07 \text{ (cm}^{-1} \text{ GPa}^{-1})\sigma_{2D} \quad [12.2]$$

where the biaxial stress, σ_{2D} , is taken to be homogeneous.

However, the spectra observed from aged TBCs were not usually similar to the clear doublet observed in single-crystal material. The shape and position of the R1R2 doublet for the measured TGO luminescence spectra changes with stress, temperature, oxidation time and even Cr^{3+} ion concentration,⁶⁹⁻⁷¹ and therefore allows quantitative information on these conditions to be extracted from analysis of the fluorescence spectrum.⁶⁷ Some spectra can be described as being due to two stress states in the material – physically interpreted as being due to bonded (stressed) and de-bonded (unstressed) material. More often, although there may be dominant contributions from two stress states, there is evidence that there may be a distribution of stressed states present. This makes the extraction of quantitative data complicated.

A program was developed to separate the contribution from the different stress states.⁷⁰ Each spectrum is considered to consist of an underlying linear baseline (due to background signal and instrumental effects) together with multiple R1R2 curves. The R1 peak is used to obtain an initial estimate of the parameters for fitting to a single doublet, and the optimization routine uses a sequential quadratic programming method combined with a line search to find the best-fit parameters subject to constraints on the intensity ratios, half-width ratios, R1 and R2 shapes and R1–R2 separation. If the fit to a single doublet is deemed unsatisfactory, a fit to two doublets is implemented, with the parameters from the fit to a single doublet utilized to obtain an initial estimate of the parameters for the optimization routine – the typical de-convoluted spectrum is demonstrated in Fig. 12.3. The appropriateness of the fitting program was compared in an international round-robin⁶⁷ and the present program was demonstrated to be in agreement with that used by other leading workers in the field.

Figure 12.4 shows the stress map for EB–PVD/Pt-aluminide after 400 1 h cycles at 1100 °C in the fast cool ageing test, EB–PVD/MCrAlY after 4000 h at 1000 °C in the slow cool ageing test and after 1175 1 h cycles at 1000 °C in the fast cool ageing test. Based on the stress analysis, the detachment of the top TBCs coat can be extrapolated. For example, the highly stressed



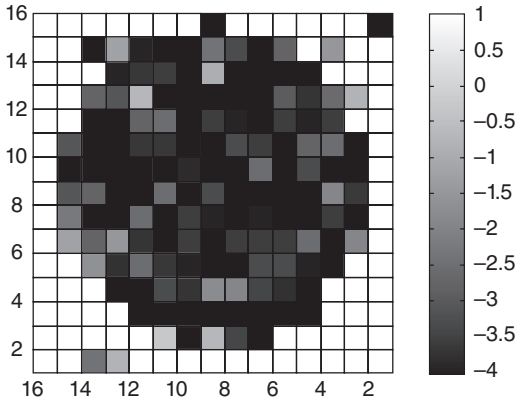
12.3 The de-convolution of the fluorescence spectrum.

regions with dark area represent the attached TBCs and low stressed regions are detached TBCs.

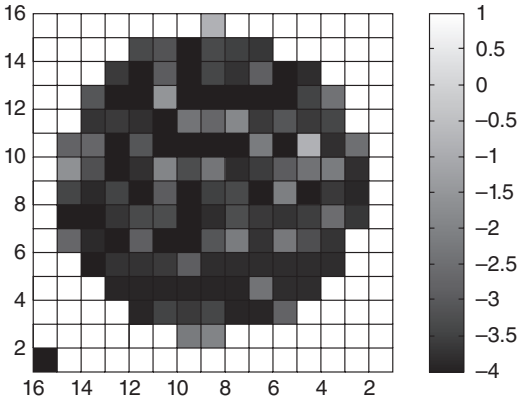
12.3.4 In situ inspection by doping in YSZ

Substantial savings in gas turbine maintenance could be obtained if the TBCs materials could be made to emit signals that contain information about their deterioration (cracking/spalling) and instrumentation could be developed to detect these signals *in situ* during gas turbine operation. An exciting development in rocket engine health monitoring shows great promise for application in *in situ*, real-time TBCs health monitoring.⁷² The technique consists of optical detection of species in the vapor phase inside the chemically reacting or expanding flow. Species originating from the deteriorating TBCs would appear as atomic vapor, oxides and/or hydroxide species in the engine flow path. During flow expansion through the turbine and nozzle, these species equilibrate, typically by collisional de-excitation or emission of radiation. This radiation can be monitored anywhere in the engine where optical access can be designed into the engine components. The use of fiber optics as light guides facilitates the optical access and could allow the design of low-cost, *in situ* TBCs health monitoring equipment.

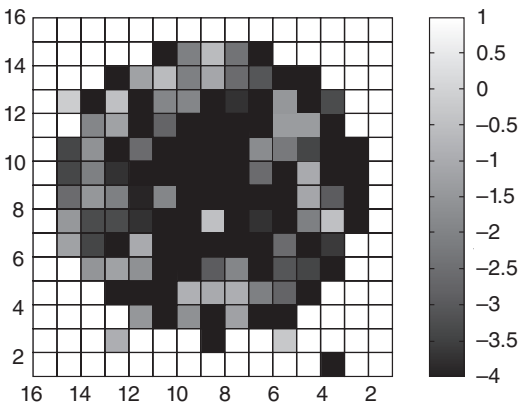
An ideal engine monitoring system would correctly identify the engine part before it fails. It is desirable to detect and track the TBCs failure throughout the life of the component. Therefore, TBCs can be doped with signature marker materials that can be monitored optically in the combustion gas or the exhaust. The marker materials can be incorporated in the area where the failure is generally initiated, which is the inner YSZ at the TGO/YSZ interface in the case of the plasma-sprayed TBCs. From the presence of the marker species in the combustion gas or the exhaust, deter-



(a)



(b)

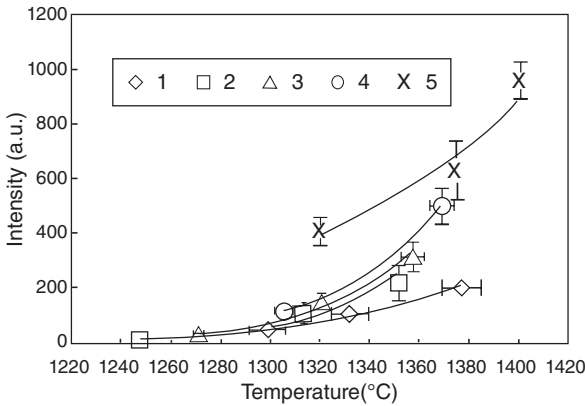


(c)

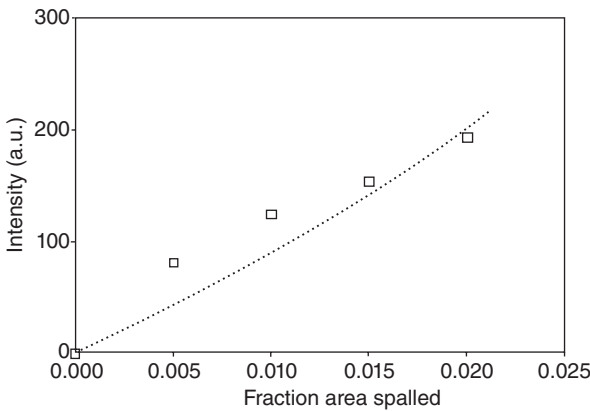
12.4 The stress map for EBPVD/Pt aluminate after 400 1-h cycles at 1100°C in the fast cool ageing test (a), EBPVD/MCrAlY after 4000 h at 1000°C in the slow cool ageing test (b) and after 1175 1-h cycles at 1000°C in the fast cool ageing test (c) in their high stress component (R2B).

mined by a spectroscopic interpretation of the observed optical emission, the mechanical condition and deterioration of TBCs can be inferred.

Our preliminary research demonstrated the feasibility of using spectroscopic *in situ* NDE to monitor the deterioration of Li₂O-doped TBCs.³⁶ The intensity of characteristic luminescence response of lithium ions at its wavelength of 670.8 nm can be used to extrapolate the degradation degree of TBCs, which is demonstrated in Figs 12.5 and 12.6. In these figures, the top YSZ layer was drilled out in the samples in order to expose the bottom Li₂O-doped layer and simulate coating spallation. The figures show a linear



12.5 Effect of flame temperature and number of 1 mm diameter holes on the intensity of slurry dip-processed 1 wt% Li₂O-doped YSZ/YSZ TBCs.



12.6 Emission intensity measured at 1320°C vs fraction area spalled (drilled out) for the slurry-dip processed 1 wt% Li₂O-doped TBCs.

increase in the emission intensity with increasing extent of spallation under the condition that there is a certain amount of Li dopant. It demonstrates the viability of using Li emission spectroscopy as a tool to monitor the health of TBCs.

However, this technique requires that the addition of Li_2O in the YSZ layer would not impair the performance of TBCs compared with the widely accepted normal plasma-sprayed TBCs during application, particularly regarding the stability and durability of TBCs in service. Therefore, the actual configuration design for the plasma-sprayed TBCs was also carried out. Plasma-sprayed TBCs with a Li_2O -doped YSZ inner layer and a regular YSZ outer layer configuration could be an option for the modified TBCs used in emission spectroscopic failure analysis. Thermal cycling tests at 1125 and 1150 °C indicated that the modified plasma-sprayed TBCs with a 1/9 (the thickness of the inner and outer YSZ layer in *mil*, 1 mil = 25.4 μm) configuration doped with medium Li_2O concentration of 1 and 3 wt% exhibited longer durability,³⁷ which can be seen in the Tables 12.1 and 12.2.

Another *in situ* doping NDE method has been proposed, but it is still in its infancy.⁷³ It consists of an inner layer of the coating doped with a chromophore adjacent to the bond coat. Where the coating is intact, the doped region is buried and so can only be probed with a laser wavelength to which the coating is transparent. Where the coating has spalled away or has been eroded, the doped layer is exposed and can be illuminated with a laser in the UV as well as in the visible. As the TBC erodes away, successive doped

Table 12.1 Thermal cycling results for the plasma-sprayed TBCs tested at 1115 °C

Configuration	0.3 wt% Li_2O	1 wt% Li_2O	3 wt% Li_2O	5 wt% Li_2O
5/5	2	2	Failed in annealing	Failed in annealing
1/9	NA	35	>75	NA

Note: Standard no Li_2O doped sample failed after 75 cycles and annealing was performed at 1150 °C in Ar + 5H₂ atmosphere for 4 h, all the samples were subject to annealing before thermal cycling.

Table 12.2 Thermal cycling results for the plasma-sprayed TBCs tested at 1150 °C

Configuration	1 wt% Li_2O	3 wt% Li_2O
1/9	22	>22
2/8	20	19
3/7	20	3

Note: Standard no Li_2O doped sample failed after 22 cycles.

layers will be removed and so the visible luminescence will characterize the remaining layers, enabling the remaining thickness of the coating to be assessed.

12.4 Future trends

With the development of TBCs, new kinds of materials will be applied in TBC systems to make the next generation of TBCs more reliable and durable. These include a more stable TBCs insulation layer with much lower thermal conductivity and, higher temperature capability as a substitute for the current YSZ^{8,74} and more reliable bond coat materials.⁹ In the mean time, a deeper and more comprehensive understanding of the failure of the new TBCs will be generated and the life of TBCs will be easier to predict. Concurrently, new kinds of NDE methods for assessing TBCs degradation will be developed and matured, for example, femtosecond laser-induced breakdown spectroscopy⁷⁵ and microwave⁷⁶ to detect thickness loss in TBCs. Even so, more issues will need to be addressed relating to the full development of currently proposed NDE methods and considerable attention should also be paid to NDE instrumentation and application for field inspection of the TBCs coated gas turbine vanes/blades.

12.5 References

1. STIGER M J, YANAR N M, TOPPING M G, PETTIT F S and MEIER G H (1999), 'Thermal barrier coatings for the 21st century', *Z Metallkd*, **90**, 1069–1078.
2. EVANS A G, MUMM D R, HUTCHINSON J W, MEIER G H and PETTIT F S (2001), 'Mechanisms controlling the durability of thermal barrier coatings', *Prog Mater Sci*, **46**, 505–555.
3. PETERS M, LEYENS C, SCHULZ U and KAYSSER W A (2001), 'EB-PVD TBCs for aeroengines and gas turbines', *Adv Eng Mater*, **3**, 193–204.
4. PADTURE N P, GELLM and JORDAN E H (2002), 'Thermal barrier coatings for gas-turbine engine applications', *Science*, **296**, 280–284.
5. SCHULZ U, LEYENS C, FRITSCHER K, PETERS M, SARUHAN-BRINGS B and LAVIGNE O (2003), 'Some recent trends in research and technology of advanced thermal barrier coatings', *Aerospace Sci Technol*, **7**, 73–80.
6. NICHOLLS J R (2003), 'Advances in coating design for high-performance gas turbines', *MRS Bull*, **28**, 659–670.
7. CLARKE D R and LEVI C G (2003), 'Materials design for the next generation thermal barrier coatings', *Ann Rev Mater Res*, **33**, 383–417.
8. LEVI C G (2004), 'Emerging materials and processes for thermal barrier systems', *Curr Opin Solid State Mater Sci*, **8**, 77–91.
9. GLEESON B (2006), 'Thermal barrier coatings for aeroengine applications', *J Propul Power*, **22**, 375–383.
10. SPITSBERG I T, MUMM D R and EVANS A G (2005), 'On the failure mechanisms of thermal barrier coatings with diffusion aluminide bond coatings', *Mater Sci Eng A*, **394**, 176–191.

11. HE M Y, EVANS A G and HUTCHINSON J W (2000), 'The ratcheting of compressed thermally grown thin films on ductile substrates', *Acta Mater*, **48**, 2593–2601.
12. EVANS A G, HE M Y and HUTCHINSON J W (1997), 'Convergent debonding of films and fibers', *Acta Mater*, **45**, 3543–3554.
13. MUMM D R and EVANS A G (2000), 'On the role of imperfections in the failure of a thermal barrier coating made by electron beam deposition', *Acta Mater*, **48**, 1815–1827.
14. HUTCHINSON J W, HE M Y and EVANS A G (2000), 'The influence of imperfections on the nucleation and propagation of buckling driven delaminations', *J Mech Phys Solids*, **48**, 709–734.
15. GAUDETTE F A, SURESH S, EVANS A G, DEHM G and RUHLE M (1997), 'The influence of chromium addition on the toughness of γ -Ni/ α -Al₂O₃ interfaces', *Acta Mater*, **45**, 3503–3513.
16. YANAR N M, PETTIT F S and MEIER G H (2006), 'Failure characteristics during cyclic oxidation of yttria stabilized zirconia thermal barrier coatings deposited via electron beam physical vapor deposition on platinum aluminide and on NiCo-CrAlY bond coats with processing modifications for improved performances', *Metal Mater Trans*, **37A**, 1563–1580.
17. TOLPYGO V K and CLARKE D R (2000), 'Surface rumpling of a (Ni, Pt)Al bond coat induced by cyclic oxidation', *Acta Mater*, **48**, 3283–3293.
18. SHILLINGTON E A G and CLARKE D R (1999), 'Spalling failure of a thermal barrier coating associated with aluminum depletion in the bond-coat', *Acta Mater*, **47**, 1297–1305.
19. TOLPYGO V K and CLARKE D R (1999), 'Tensile cracking during thermal cycling of alumina films formed by high-temperature oxidation', *Acta Mater*, **47**, 3589–3605.
20. JONES R L (1996), 'Thermal barrier coatings', in: Stern K H (ed.), *Metallurgical and Ceramic Protective Coatings*, Chapman & Hall, London, UK, 195–235.
21. JONES R L and WILLIAMS C E (1987), 'Hot corrosion studies of zirconia ceramics', *Surf Coat Technol*, **32**, 349–358.
22. STOTT F H, DE WET D J and TAYLOR R (1994), 'Degradation of thermal barrier coating at very high temperatures', *MRS Bull*, **19**, 46–49.
23. BOROM M P, JOHNSON C A and PELUSO L A (1996), 'Role of environment deposits and operating surface temperature in spallation of air plasma sprayed thermal barrier coatings', *Surf Coat Technol*, **86–87**, 116–126.
24. CHEN X, WAND R, YAO N, EVANS A G, HUTCHINSON J W and BRUCE R W (2003), 'Foreign object damage in a thermal barrier system: mechanisms and simulations', *Mater Sci Eng A*, **352**, 221–231.
25. SHANKAR R N, BERNDT C C, HERMAN H and RANGASWAMY S (1983), 'Acoustic emission from thermally cycled plasma-sprayed oxides', *Am Ceram Soc Bull*, **62**, 614–619.
26. BERNDT C C and HERMAN H (1983), 'Failure during thermal cycling of plasma-sprayed thermal barrier coatings', *Thin Solid Films*, **108**, 427–437.
27. BERNDT C C and MILLER R A (1984), 'Failure analysis of plasma sprayed thermal barrier coatings', *Thin Solid Films*, **119**, 173–184.
28. HARADA S, IKEDA Y, MIZUTA Y, SUGITA Y and ITO A (1995), 'The inspection of delaminated defects in ZrO₂-coated material by infrared thermography techniques', in: Sekine K (ed.), *Proceedings of the 1st Symposium on Thermographic NDT and E Techniques*, Tokyo, Japan, 27–28 Nov, 47–52.

29. SAITOH M, ITOH Y and ISHII J (1995), 'Evaluation of thermal barrier coating using infrared thermography', in: Sekine K (ed.), *Proceedings of the 1st Symposium on Thermographic NDT and E Techniques*, Tokyo, Japan 27–28 Nov, 53–58.
30. WANG H and DINWIDDIE R B (2001), 'Characterization of thermal barrier coatings using thermal methods', *Adv Eng Mater*, **3**, 465–468.
31. MANDELIS A (2001), 'Diffusion-wave laser radiometric diagnostic quality-control technologies for materials NDE/NDT', *NDT&E Int*, **34**, 277–287.
32. NAKAJIMA M, SHOJI T and HASUDA H (1995), 'Nondestructive characterization of silicon carbide by impedance spectroscopy method', *Trans Japan Soc Mech Eng*, **61**, 940–945.
33. OGAWA K, MINKOV D, SHOJI T, SATO M and HASHIMOTO H (1999), 'NDE of degradation of thermal barrier coating by means of impedance spectroscopy', *NDT&E Int*, **32**, 177–185.
34. ANDERSON P S, WANG X, XIAO P (2004), 'Impedance spectroscopy study of plasma sprayed and EB-PVD thermal barrier coatings', *Surf Coat Technol*, **185**, 106–119.
35. SOHN Y H, JAYARAJ B, LAXMAN S, FRANKE B, BYEON J W, KARLSSON A M (2004), 'The non-destructive and nano-microstructural characterization of thermal-barrier coatings', *JOM*, **56**, 53–57.
36. CHEN G F, LEE K N and TEWARI S N (2006), 'Emission spectroscopy analysis for the non-destructive evaluation of the health of thermal barrier coatings', *J Mater Sci*, **41**, 6855–6860.
37. CHEN G F, LEE K N and TEWARI S N (2007), 'The concept and development of emission spectroscopy for the non-destructive evaluation (NDE) of the failure of thermal barrier coatings', *NDT&E Int*, **40**, 265–270.
38. LIN C K and BERNDT C C (1998), 'Acoustic emission studies on thermal spray materials', *Surf Coat Technol*, **102**, 1–7.
39. BERNDT C C (1989), 'Failure processes within ceramic coatings at high temperature', *J Mater Sci*, **24**, 3511–3514.
40. IBARRA-CASTANEDO C, GOMZÁLEZ D, KLEIN M, PILLA M, VALLERAND S and MALDAGUE X (2004), 'Infrared image processing and data analysis', *Infrared Phys Technol*, **46**, 75–83.
41. ROSENCWAIG A and GERSHO A (1976), 'Theory of the photoacoustic effect with solids', *J Appl Phys*, **47**, 64–69.
42. BERTOLOTI M, LIAKHOV G, VOTI R L, MICHELOTTI F and SIBILIA C (1993), 'Method for thermal diffusivity measurements based on photothermal deflection', *J Appl Phys*, **74**, 7078–7084.
43. FUJII T and TAKAHASHI T (1998), *Estimation of Thermophysical Properties of Coating Layers for Gas Turbine Hot Parts – Part 1: Measurement of Thermophysical Properties of Coating Layer and Superalloy, and Comparison Between Virgin and Aged Material*, CRIEPI Report W97017, Central Research Institute of Electric Power Industry, Tokyo, Japan.
44. FUJII T and TAKAHASHI T (1999), *Estimation of Thermophysical Properties of Coating Layers for Gas Turbine Hot Parts – Part 2: Comparison Between Virgin and Aged Thermal Barrier Coatings in Terms of Plasma Spray Powder Size And Shape*, CRIEPI Report W98017, Central Research Institute of Electric Power Industry, Tokyo, Japan.

45. MORINAGA M, TAKAHASHI T and FUJII T (1998), *Development of Non-Destructive Inspection For The Performance Of Thermal Barrier Coating – Part 1 Numerical Analysis For TBC Thermal Resistance Detecting Method With Transient Heating*, CRIEPI Report W97021, Central Research Institute of Electric Power Industry, Tokyo, Japan.
46. MORINAGA M and TAKAHASHI T (1999), *Development of Non-destructive Inspection for the Performance of Thermal Barrier Coating – Part 2 Experimental Study for TBC Thermal Resistance Detecting Method with Transient Heating*, CRIEPI Report W99005, Central Research Institute of Electric Power Industry, Tokyo, Japan.
47. ELLINGSON W A, VISHER R J, LIPANOVICH R S, DEEMER C M (2006), 'Optical NDT techniques for ceramic thermal barrier coating: NDT of ceramic: an introduction to the technical focus issue', *Mater Eval*, **64**, 45–51.
48. YU F L and BENNETT T D (2005), 'Phase of thermal emission spectroscopy for properties measurements of delaminating thermal barrier coatings', *J Appl Phys*, **98**, 103501–103505.
49. WANG X, MEI J and XIAO P (2001), 'Non-destructive evaluation of thermal barrier coatings using impedance spectroscopy', *J Euro Ceram Soc*, **21**, 855–859.
50. WANG X, MEI J and XIAO P (2001), 'Determining oxide growth in thermal barrier coatings (TBCs) non-destructively using impedance spectroscopy', *J Mater Sci Lett*, **20**, 47–49.
51. JAYARAJ B, VISHWESWARAIAH S, DESAI V H and SOHN Y H (2004), 'Electrochemical impedance spectroscopy of thermal barrier coatings as a function of isothermal and cyclic thermal exposure', *Surf Coat Technol*, **177–178**, 140–151.
52. JAYARAJ B, DESAI V H, LEE C K and SOHN Y H (2004), 'Electrochemical impedance spectroscopy of porous ZrO_2 8 wt% Y_2O_3 and thermally grown oxide on nickel aluminide', *Mater Sci Eng A*, **372**, 278–286.
53. BYEON J W, JAYARAJ B, VISHWESWARAIAH S, RHEE S, DESAI V H and SOHN Y H (2005), 'Non-destructive evaluation of degradation in multi-layered thermal barrier coatings by electrochemical impedance spectroscopy', *Mater Sci Eng A*, **407**, 213–225.
54. MA Q and CLARKE D R (1993), 'Stress measurement in single-crystal and polycrystalline ceramics using their optical fluorescence', *J Am Ceram Soc*, **76**, 1443–1448.
55. CHRISTENSEN R J, LIPKIN D M, CLARKE D R and MURPHY K (1996), 'Non-destructive evaluation of oxidation stresses through thermal barrier coatings using Cr^{3+} piezospectroscopy', *Appl Phys Lett*, **69**, 3754–3756.
56. TOLPYGO V K, DRYDEN J R and CLARKE D R (1998), 'Determination of the growth stresses generated during the oxidation of Fe–22Cr–4.8Al–0.3Y alloy', *Acta Mater*, **46**, 927–937.
57. TOMIMATSU T, ZHU S and KAGAWA Y (2003), 'Effect of thermal exposure on stress distribution in TGO layer of EB–PVD TBC', *Acta Mater*, **51**, 2397–2405.
58. SERGO V and CLARKE D R (1998), 'Observation of sub-critical spall propagation of a thermal barrier coating', *J Am Ceram Soc*, **81**, 3237–3242.
59. SOHN Y H, KIM J H, JORDAN E H and GELL M (2001), 'Thermal cycling of EB–PVD/MCrAlY thermal barrier coatings: II. Evolution of photo-stimulated luminescence', *Surf Coat Technol*, **146–147**, 102–109.

60. XIE L, SOHN Y H, JORDAN E H and GELL M (2003), 'The effect of bond coat grit blasting on the durability and thermally grown oxide stress in an electron beam physical vapor deposited thermal barrier coating', *Surf Coat Technol*, **176**, 57–66.
61. GONG X Y and CLARKE D R (1998), 'On the measurement of strain in coatings formed on a wrinkled elastic substrate', *Oxid Met*, **50**, 355–376.
62. ATKINSON A, SELCUK A and WEBB S J (2000), 'Variability of stress in alumina corrosion layers formed in thermal barrier coatings', *Oxid Met*, **54**, 371–384.
63. SELCUK A and ATKINSON A (2002), 'Analysis of the Cr³⁺ luminescence spectra from thermally grown oxide in thermal barrier coatings', *Mater Sci Eng A*, **335**, 147–156.
64. SELCUK A and ATKINSON A (2003), 'The evolution of residual stress in the thermally grown oxide on Pt diffusion bond coats in TBCs', *Acta Mater*, **51**, 535–549.
65. WEN M, JORDAN E H and GELL M, 'Evolution of photo-stimulated luminescence of EB–PVD/(Ni, Pt)Al thermal barrier coatings', *Mater Sci Eng A*, **398**, 99–107.
66. PENG X and CLARKE D R (2000), 'Piezospectroscopic analysis of interface debonding in thermal barrier coatings', *J Am Ceram Soc*, **83**, 1165–1169.
67. MURPHY S (2003), 'NDE assessment of TBCs: an interim report of a photo-stimulated luminescence "round-robin" test', *Surf Coat Technol*, **163**, 87–94.
68. SRIDHARAN S, XIE L, JORDAN E H and GELL M (2004), 'Stress variation with thermal cycling in the thermally grown oxide of an EB–PVD thermal barrier coating', *Surf Coat Technol*, **179**, 286–296.
69. CHEN G F (2004), 'Cr-related luminescence in α -alumina prepared by sintering and oxidizing', *Mater Sci Eng B*, **113**, 106–109.
70. SAUNDERS S R J, BANKS J P, CHEN G F and CHUNNILALL C J (2004), 'Measurement of residual stress in thermally grown oxide layers in thermal barrier coating systems – development of non-destructive test methods', *Mater Sci Forum*, **383**, 461–464.
71. CHEN G F and RUHLE M (2005), 'Transient alumina transformation on a sputtered K38G nanocrystalline coating', *Surf Coat Technol*, **191**, 263–266.
72. MADZSAR G C, BICKFORD R L and DUNCAN D B (1992), 'An overview of in-flight plume diagnostics for rocket engines', in: *Proceedings of the 28th AIAA/ASME/SAE/ASEE Joint Propulsion Conference*, Nashville, TN, 6–8 July, 1–23.
73. GENTLEMAN M M and CLARKE D R (2004), 'Concepts for luminescence sensing of thermal barrier coatings', *Surf Coat Technol*, **188–189**, 93–100.
74. CLARKE D R, LEVI C G and EVANS A G (2006), 'Enhanced zirconia thermal barrier coating systems', *Proc IMechE Part A: J Power and Energy*, **220**, 85–92.
75. DAS D K, MCDONALD J P, LEVI C G, YALISOVE S M and POLLOCK T M (2008), 'Detection of a marker layer in a 7YSZ thermal barrier coating by femtosecond laser-induced breakdown spectroscopy', *Surf Coat Technol*, **202**, 3940–3946.
76. SAYAR M, SEO D and OGAWA K (2009), 'Non-destructive microwave detection of layer thickness in degraded thermal barrier coatings using K- and W-band frequency range', *NDT&E Int*, **42**, 398–403.

Substrate and bond coat related failure of thermal barrier coatings

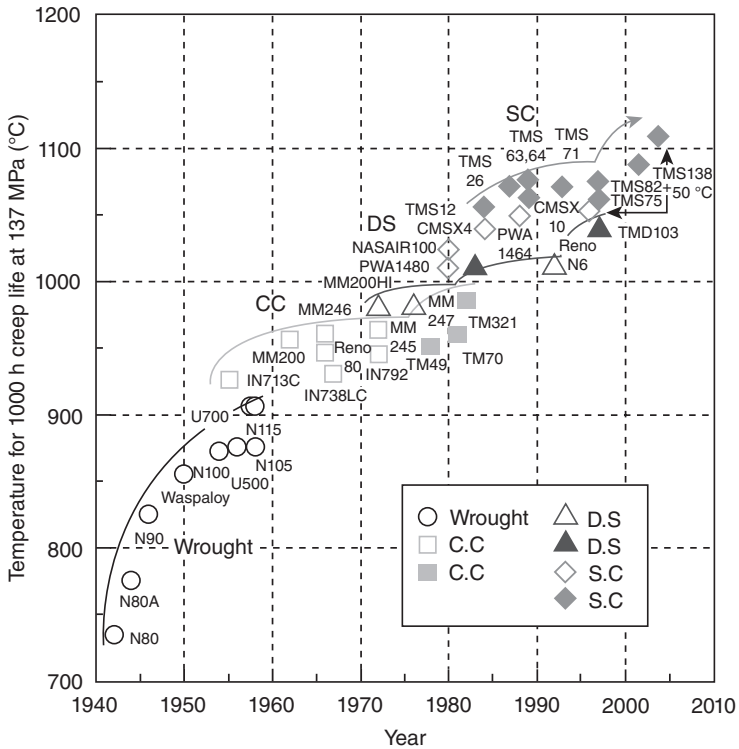
R. T. WU, National Institute for Materials Science (NIMS), Japan

Abstract: The current chapter describes research aimed at improving understanding of the high-temperature degradation mechanisms of thermal barrier coating (TBC) systems on different bond coats and single-crystal superalloys. The first part presents a systematic study aimed at demonstrating that the compatibility of modern nickel-base single-crystal superalloys with TBC systems is influenced strongly by the content of alloying element additions in the superalloy substrate. This is followed by a detailed study of the bond coat effect on TBC degradation, based on an electron beam physical vapour deposition (EB-PVD) yttrium stabilized zirconia (YSZ) top coat and a substrate material of CMSX-4 superalloy.

Key words: nickel-based single crystal superalloys, thermal barrier coatings, compatibility, oxidation, interface, residual stress, rumpling, interfacial adhesion, fracture toughness.

13.1 Introduction

The success of turbine technology can be largely attributed to the development and utilization of Ni-base superalloys as the material for hot-section turbine components. Following the Kyoto Protocol aiming at mitigating CO₂ emission to prevent global warming, there has been a considerable international effort aimed at improving the efficiency of the gas turbines used for jet propulsion and electricity generation, due to the price of fossil fuels and widespread environmental concerns about the effects of CO₂ emissions. As is widely known, high-temperature materials are important in this respect, since fuel economy and rate of emissions scale directly with the temperature of the hot gas stream exiting the combustor regions; this effect explains the incentive to raise the operating temperatures experienced by the turbomachinery in these engines. In fact, a substantial enhancement of the engine is based on the increase of the maximum turbine entry temperature over the years as shown in Fig. 13.1.¹ It is not surprising therefore that all the major original equipment manufacturers (OEMs) possess research programmes which seek to develop new grades of alloy for use in their engines.



13.1 Evolution of the high-temperature capability of the superalloys over a period of 60 years since their emergence in the 1940s.¹

Ni-base superalloys¹⁻⁴ play a vital role in this, since they have emerged as the materials of choice for the turbine blades, nozzle guide vanes and hot-section seals in the very hottest parts of these engines. These are amongst the most complex of the alloys produced by man, owing to the addition of many different alloying elements such as Co, Cr, Mo, W, Al, Ta, Re, Ru, which are added to provide a balance of properties, e.g. creep resistance, tensile strength, fatigue capability, oxidation resistance, corrosion resistance and castability. While the alloy designer must consider all of these properties in order to meet the turbine design specifications, advanced 4th and 5th generation Ni-base single crystal superalloys tend to exhibit improved creep resistance at a cost of sacrificing high-temperature oxidation resistance. Thus, advanced thermal barrier coatings (TBCs) – usually based on yttria stabilised zirconia (YSZ) – must now be applied to the surface of alloy components as a functional material to further enhance the temperature capability of the turbine blade aerofoils.

With the introduction of TBCs onto the surface of the alloy substrate being exposed to the high-temperature environment, the composite struc-

ture results in a complex interplay between the inter-diffusion and internal stresses due to mismatches in coefficients of thermal expansion (CTE). Thus, TBC-coated components are subjected to several potentially inter-related failure mechanisms due to their structural complexity.^{5–10}

In the first experimental section of this chapter, TBC systems on different single-crystal superalloys will be presented. This section will focus on substrate-related failure of TBCs, aiming at demonstrating that the compatibility of modern Ni-base single-crystal superalloys with TBC systems is influenced strongly by the content of alloying element additions in the superalloy substrate. The results can be explained by postulating that the fracture toughness parameters controlling de-cohesion are influenced strongly by small changes in composition arising from inter-diffusion with the bond coat, which itself inherits elemental changes from the substrate.

The second experimental section of this chapter involves a comparative study of different bond coats (two β -structured Pt–Al types and a γ/γ' Pt diffusion type) in TBC systems based on an electron beam physical vapour deposition (EB–PVD) YSZ top coat and a substrate material of CMSX-4 superalloy. Generation of stress in the thermally grown oxide (TGO) on thermal cycling, and its relief by plastic deformation and fracture, have been the subject of detailed experimental investigation.

13.2 Substrate related failure of thermal barrier coatings (TBCs)

Single-crystal (SC) superalloys¹ have traditionally been designed with the priority of optimising the creep, fatigue, oxidation and corrosion-resistant properties. However, as the demand for more fuel-efficient turbine systems continues, the substrate materials must now be coated with TBCs^{11,12} to enhance the high-temperature capability of critical turbine components such as turbine blades and guide vanes. Yet, it is known that TBC-coated Ni-base superalloys are prone to spallation;¹³ for this reason, several bond coat technologies have been developed as a means to enhance the mutual compatibility of the two by improving the oxidation resistance of the coated specimens.

Unfortunately, little work^{14,15} has been reported to elucidate the compatibility issues of superalloys with the TBCs. More importantly, the influence of the substrate composition on the TBC spallation life is not well understood. This is despite much progress which has been made to determine the micromechanics of the failure mode of TBCs.¹⁶ In particular, the approach in modeling TBC failure^{17–20} generally relies on the treatment of the oxidation-induced stresses that drive TBC spallation, despite the fact that it might reasonably be assumed that the TBC life and the modes of failure (i.e.

location of interfacial failure) are also influenced significantly by the inherited chemistry of the underlying superalloys.

In this section, the compatibility of a number of Ni-base SC superalloys with TBC systems will be discussed to demonstrate that the compositions of these alloys play an important role in determining TBC spallation resistance.

13.2.1 Experimental details and background information

Fully heat-treated (solution and primary-aged) SC alloys of SRR99, CMSX-4, TMS-82+, PWA-1484 and TMS-138A processed using conventional investment casting methods into cylindrical rods (10 mm in diameter), with the long axis of each aligned close ($\pm 5^\circ$) to the $\langle 001 \rangle$ axis, were used as substrate materials for this research. The chemical compositions of the alloys considered are given in Table 13.1 (major elemental additions) and Table 13.2 (trace elements). These chemical analyses were conducted by Cannon Muskegon Corporation using LECOTM Carbon & Sulfur Determinator, X-ray fluorescence (XRF) and inductively coupled plasma mass spectrometry (ICPMS) methods, to industry leading levels of precision (i.e. ppm levels). Three different bond coats, a high-temperature low-activity Pt–Al (HT Pt–Al), a low-temperature high-activity Pt–Al (LT Pt–Al) and

Table 13.1 Nominal chemical composition, wt%, of the Ni-based superalloys considered

Element	Co	Cr	Mo	W	Al	Ti	Ta	Hf	Re	Ru	C	Ni
SRR99	5.0	8.0	–	9.5	5.5	2.2	2.8	–	–	–	0.011	Bal.
TMS-82+	7.8	4.9	1.9	8.7	5.3	0.5	6.0	0.1	2.4	–	–	Bal.
PWA1484	10.0	5.0	2.0	6.0	5.6	–	8.7	0.1	3.0	–	–	Bal.
CMSX-4	9.6	6.5	0.6	6.4	5.6	1.0	6.5	0.1	3.0	–	–	Bal.
TMS-138A	5.8	3.2	2.8	5.6	5.7	–	5.6	0.1	5.8	3.6	–	Bal.

Note: – means that the element is not included in the chemical analysis.

Table 13.2 Levels of trace elements in the superalloy substrates examined, as determined by XRF, LECO and ICPMS methods (in ppm by weight)

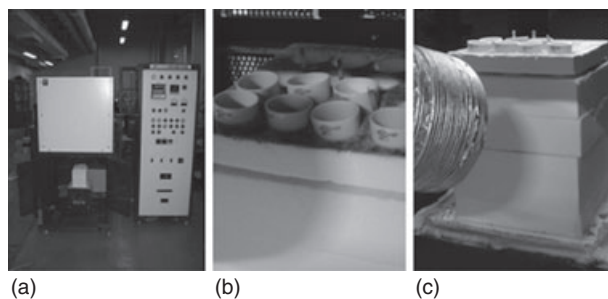
Element	S	B	O	N	P	Zr
SRR99	2	2	2	4	2	4
TMS-82+	2	1	2	2	11	13
PWA1484	3	2	2	1	6	19
CMSX-4	2	8	2	2	4	7
TMS-138A	2	3	2	1	18	3

a Pt-diffusion bond coat, were subsequently deposited onto the flat surfaces of all substrate materials.

The HT Pt–Al and the LT Pt–Al bond coat specimens were prepared by first electrodepositing a thin layer of platinum of 5 and 7 μm , respectively, followed by a vacuum heat treatment applied at 1100°C for 1 h. Next, 5 h vapour phase and 20 h pack-aluminisation processes were applied at 1080°C and 870°C, respectively. Both the vapour phase and pack processes involve the generation of vapours containing Al, which are usually halides due to their high vapour pressures. The vapours flow and react with the substrate surface upon contact forming the aluminide coating. In the aluminisation process, specimens are either embedded in a pack mix (i.e. LT Pt–Al) or suspended in a vapour-filled environment (i.e. HT Pt–Al) in a heated chamber.

The Pt-diffusion bond coat specimen was first electroplated with a 10 μm layer of platinum and then a vacuum heat treatment at 1150°C for 1 h was subsequently carried out. No aluminisation process was applied in this case. All specimens were further heat-treated for 1 h at 1100°C in an argon atmosphere and a ZrO₂/7 wt% Y₂O₃ (YSZ) top coat 175 μm in thickness was then deposited by EB–PVD. A further vacuum heat treatment (1100°C, 1 h) and ageing (870°C, 16 h) were applied to all specimens before testing.

The TBC coated disc-shape specimens were then subjected to cyclic oxidation testing in a purpose-built rig (see Fig. 13.2). Each thermal cycle involved 1 h at a furnace temperature of 1135°C (approximately 10 min to reach the peak temperature); after which, the specimens were removed automatically from the rig and fan-cooled by laboratory air for 1 h. Five individual specimens of each TBC system were cycled to failure to determine the average TBC spallation lifetime, in order to evaluate the scatter in the experimental results. In addition to the cycled to failure test, additional specimens were removed from the rig at specific intervals for



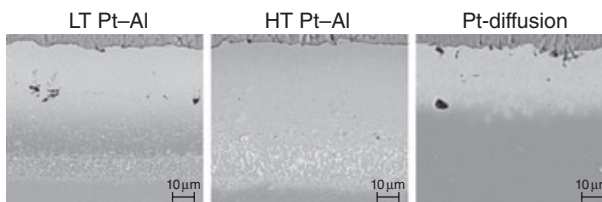
13.2 Pictures showing the use of the thermal cycling furnace (a), the placement of specimens on the sample stage (b) and the heating/cooling conditions (c).

luminescence measurements (see below) and then returned for further thermal cycling. Some specimens were withdrawn from cycling, mounted in epoxy, cut through by an abrasive alumina blade to reveal the cross-section and polished to mirror-finish for microstructural characterisation. An additional three coated disc-shape specimens were isothermally heated at 1135 °C in the same rig for 150 h.

Microstructure characterisation was carried out in a field emission gun scanning electron microscope (FEG-SEM) equipped with energy dispersive X-ray (EDX) using the secondary electron detection mode at a working distance of 15 mm and an accelerating voltage of 20 kV. For high-resolution quantitative elemental analysis, a prototype field emission electron probe microprobe analyser (FE-EPMA) was used for analysis by wavelength dispersive X-ray spectrometry (WDS). A probe current of 5.0×10^{-8} A was applied within a probe diameter of about 0.25 μm , at an accelerating voltage of 20 kV.

13.2.2 Characterisation of coating cross-sections – as received condition

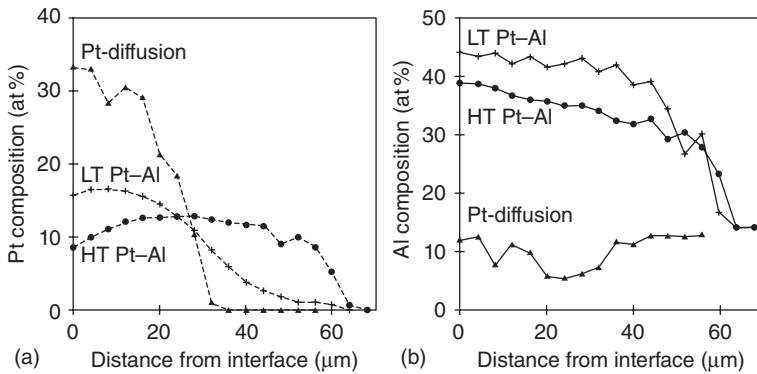
Scanning electron micrographs illustrating the microstructures of the three coatings in the as-received condition are given in Fig. 13.3. In all cases, the YSZ top coat layer had almost the same thickness. Discernible differences can be seen between the microstructures and the thicknesses of the bond coats. Pt-Al bond coat systems produce a single-phase β -(Pt,Ni)Al microstructure (i.e. NiAl with Pt in solid solution) next to the YSZ. Below the grit-line (residual Al_2O_3 particles remaining from the grit-blasting process prior to Pt plating) is the inner multi-phase layer of the coating consisting of precipitates rich in refractory metals (Ta, W, Mo) in the β phase matrix. The Pt-diffusion bond coat consists of a two-phase γ and γ' microstructure both above and below the grit-line; the β -NiAl phase is completely absent since the aluminisation step was absent. Al and Pt EDX concentration line-



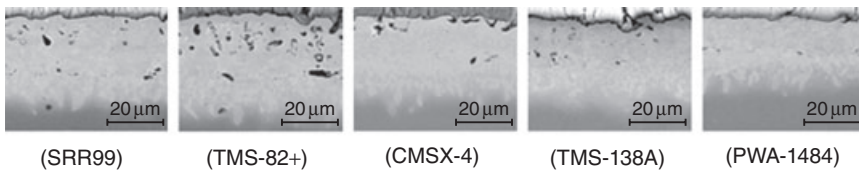
13.3 The cross-section microstructures of the bond coats (LT Pt-Al, HT Pt-Al and Pt-diffusion) in the as-received coatings on CMSX-4.

profiles of these coatings are shown in Fig. 13.4. As can be seen, the aluminisation process significantly increases both the Al concentration and the bond coat thickness in the Pt–Al systems. The main difference between the LT Pt–Al and HT Pt–Al bond coats is in the Pt profile. The LT Pt–Al has a higher Pt concentration within the first 20 μm , whereas the HT Pt–Al bond coat has a higher Pt concentration at 30–60 μm . The Pt-diffusion bond coat, on the other hand, inherits the original Al content from the superalloy substrate and has higher Pt concentration than the Pt–Al systems due to the thicker electroplated Pt prior to the diffusion-heat treatment process. In all cases, the post-processing heat treatment resulted in the formation of a thin thermally grown oxide (TGO) layer, which shows as a thin dark line between the bond coat and YSZ, even before any thermal cycling had taken place. The microstructures of Pt-diffusion coatings on superalloy substrates are also shown in Fig. 13.5.²¹ Again, the TBC top coats were prepared to similar thickness.

Based on the results of the thermal cycling experiment, it was found that coating life varied significantly with the composition of the superalloy substrate as illustrated in Fig. 13.6²¹ with the error bars indicating \pm one



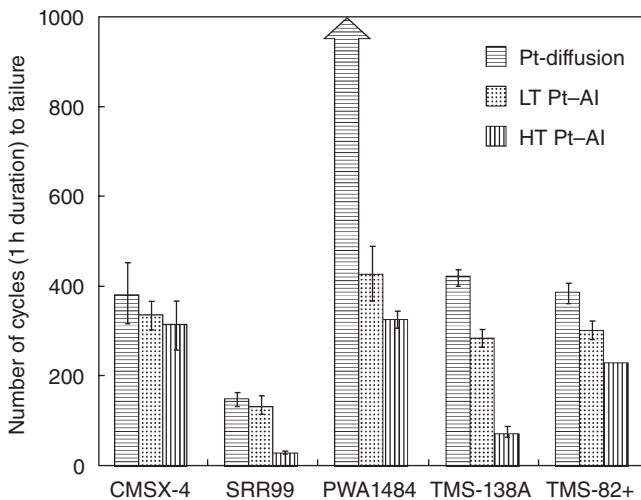
13.4 EDX concentration line-profile of Pt (a) and Al (b) in the as-received bond coats.



13.5 The microstructures of Pt-diffusion coatings on the superalloy substrates in the as-received condition.

standard deviation in the lifetimes of each set of five specimens. For instance, TBC-coated PWA1484 exhibited spallation lifetimes at least three times superior to those of first-generation superalloy SRR99 regardless of the type of bond coat being applied, suggesting that strong chemical effects were inherited from the substrate. In addition, the spallation resistance of TBC-coated fourth generation TMS-138A behaved significantly better than that of SRR99 and comparable to that the second-generation superalloy CMSX-4, suggesting that no detrimental effect is inherited from ruthenium addition to the substrate, at least for the Pt-diffusion coating. It should be noted here that the thermal exposure of PWA-1484 specimens coated with Pt-diffusion bond coat was interrupted at the 1000th cycle as the purpose of demonstrating TBC spallation resistance had been fulfilled. These findings confirm a dependence of the TBC spallation life on the superalloy composition, and can be explained only by the different degradation mechanisms taking place in the bond coat or near the TGO interfaces (since the bond coat and the ceramic top coat were prepared in the same way on all different substrates).

In terms of the bond coat technology, it was demonstrated in general that the type of bond coat being applied had less influence on the TBC spallation life than did the substrate. It was shown as well that Pt-diffusion bond coats outperformed both Pt–Al systems.



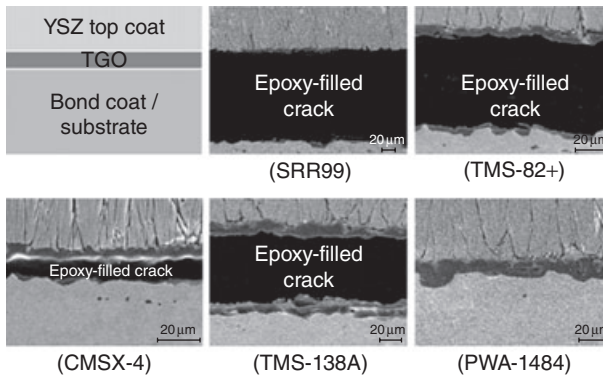
13.6 TBC spallation life for cyclic oxidation testing (1 h thermal cycling to peak temperature) of TBC coated superalloys. The error bars indicate \pm one standard deviation in the lifetimes of each set of five specimens.

13.2.3 Mechanism of TBC failure

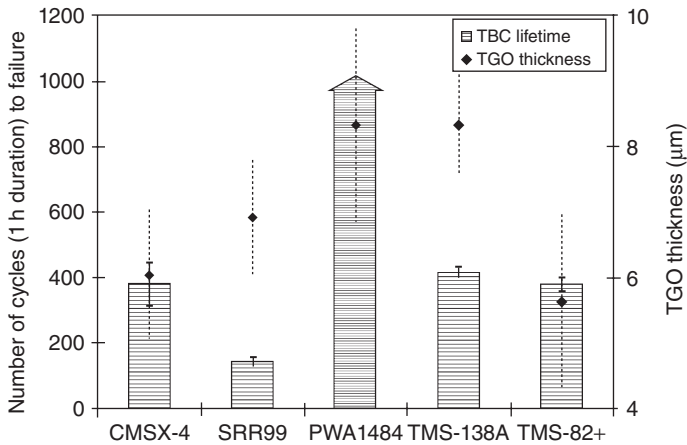
As previously demonstrated, the composition of the superalloy substrates has a larger influence on the TBC spallation life than that of the bond coat materials. For this reason, attention is focused in this section on how the substrate affects the mechanism of TBC failure, at a fixed TBC preparation condition. Pt-diffusion bond coat was chosen for this investigation as it showed the largest substrate effect on the coating spallation life.

SEM images of the fracture interface for each of the five substrates are shown in Fig. 13.7.²¹ It was found that de-cohesion occurred at a position which depended on the substrate composition. In particular, it was observed that specimens with shorter TBC spallation life tended to fail at the TGO/bond coat interface; while more spallation-resistant coatings failed within the TGO. In addition, by importing higher magnification files of these SEM images into imaging software, the thickness of the TGO at failure for each of the specimens could be quantised by making boundary selections (i.e. defining the top and bottom TGO interfaces) and calculated with reference to the scale bar of these images. These TGO thicknesses were plotted along with the TBC life for comparison as illustrated in Fig. 13.8.²¹

Based on these results, it can be seen that the TGO thickness at failure in TMS-138A is considerably thicker than that of the TMS-82+, even though TBC-coated TMS-138A offered slightly longer TBC spallation life than TMS-82+. Moreover, despite the fact that the TBC lifetimes of CMSX-4, TMS-138A and TMS-82+ were within a few cycles of each other, their TGO growth kinetics are very different. Thus, it seems that there is little correlation between the oxide growth kinetics and the TBC spallation life.



13.7 SEM micrographs illustrating the location of interfacial spallation failure of TBC (Pt-diffusion bond coat) coated superalloys.



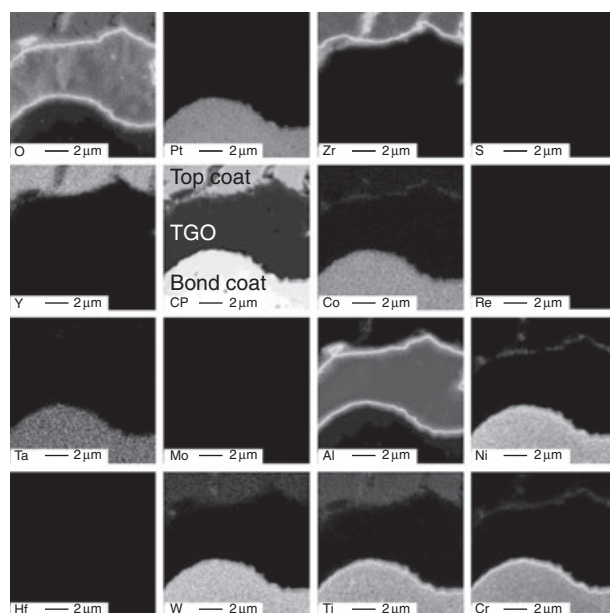
13.8 TBC spallation life vs the thickness of TGO upon failure; illustrating no clear correlation between the two.

13.2.4 High-resolution analysis and mapping by electron probe microprobe analyser/wavelength dispersive spectroscopy (EPMA/WDX)

Elemental compositions of the TGO layers on the three bond coats were characterized using WDS analysis (see Table 13.3). The results are quoted only for specimens with TGO thickness greater than the spatial resolution of the FE-EPMA/WDX technique ($\sim 1 \mu\text{m}$). Chemical mapping of the bond coat near the TGO interfaces was also carried out to determine the elemental chemical distributions on specimens after 100 cycles thermal exposure as shown in Figs 13.9–13.13. The results suggest that for all specimens, the oxide layers are primarily Al_2O_3 . However, it has also been observed for some specimens that either islands or continuous layers of Ni, Cr and or Co-rich oxides are present above the primarily Al_2O_3 layer. For example, CMSX-4, TMS82+, TMS-138A and PWA1484 all contain islands which are rich in Cr; while TMS82+, TMS138A and PWA1484 further contain islands rich in Ni. In addition, the presence of Co-rich regions has also been noticed on TMS-82+ and TMS-138A. For SRR99 specimens, fairly continuous Ni, Cr and Co-rich oxides are present. However, it should be recognised that the number of spinel phases in the TGO is very small in any of the TBC-coated systems; the TGO thickness upon failure varies between different alloys and is essentially a measure of the amount of alumina.

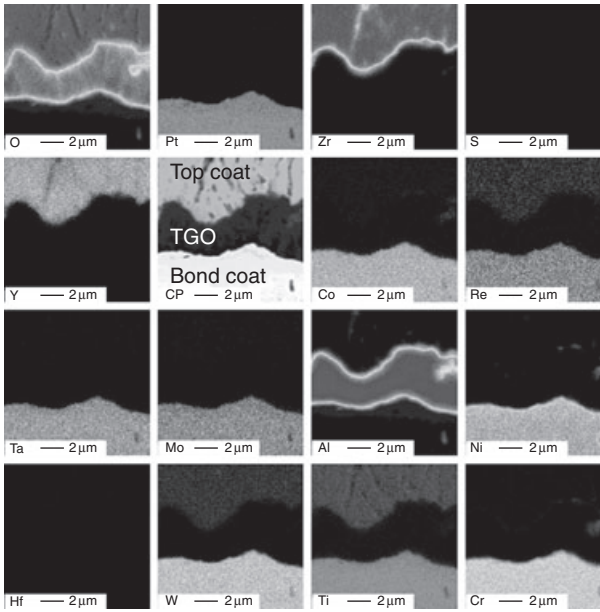
Table 13.3 Elemental compositions (wt%) of the TGO layers measured by WDS FE-EPMA analysis

Element	Pt	Zr	Y	Co	Re	Ta	Mo	Al	Ni	Ru	W	Ti	Cr	O
SRR99	0.3	0.8	0.1	0.1	–	0.0	–	51.6	0.5	–	0.1	0.0	0.2	46.2
TMS-82+	0.5	0.7	0.1	0.1	0.1	0.1	0.0	51.6	0.6	–	0.1	0.0	0.1	45.9
PWA1484	0.5	0.9	0.1	0.1	0.1	0.1	0.0	51.6	0.7	–	0.1	–	0.1	45.6
CMSX-4	0.3	0.9	0.1	0.1	0.1	0.1	0.0	48.8	0.7	–	0.0	0.0	0.1	48.7
TMS-138A	0.4	0.8	0.1	0.1	0.1	0.0	0.0	51.7	0.6	0.0	0.1	–	0.0	46.0

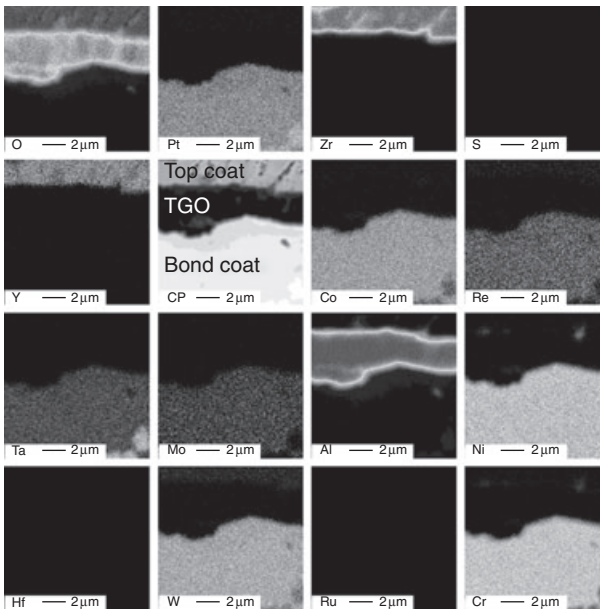


13.9 Quantitative WDX maps of the TBC coated SRR99–Pt-diffusion system following 100 cycle exposure at 1135°C.

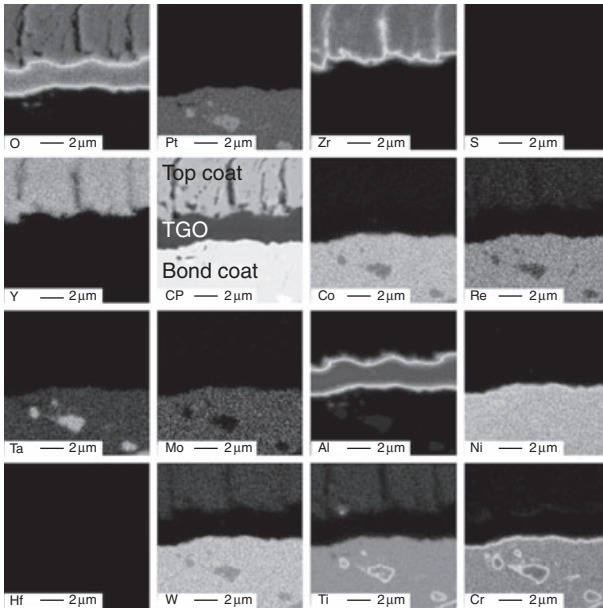
At the TGO/bond coat interface, an enriched layer (i.e. a bright line) of Ni, Cr, Al and Ti was observed in the SRR99 specimen. TMS-82+ and CMSX-4 also have enriched layers of Ni and Cr near the interface. Both TMS-138A and PWA1484, in contrast, had no noticeable enrichment of alloying constituents.



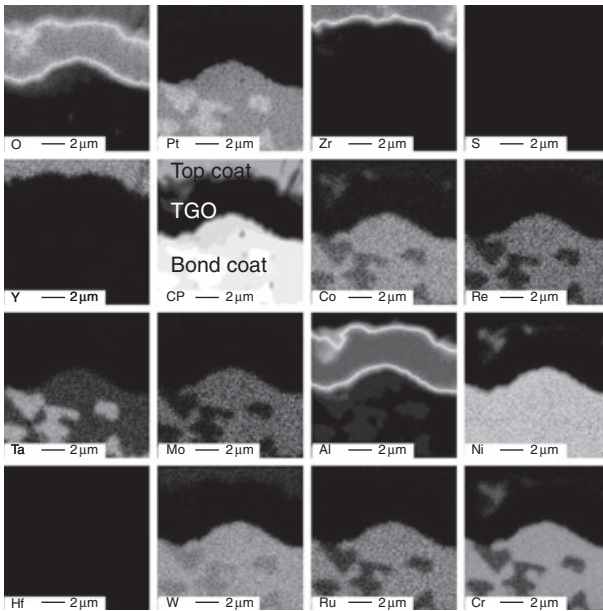
13.10 Quantitative WDX maps of the TBC coated TMS-82+-Pt-diffusion system following 100 cycle exposure at 1135°C.



13.11 Quantitative WDX maps of the TBC coated PWA1484-Pt-diffusion system following 100 cycle exposure at 1135°C.



13.12 Quantitative WDX maps of the TBC coated CMSX-4-Pt-diffusion system following 100 cycle exposure at 1135°C.



13.13 Quantitative WDX maps of the TBC coated TMS138A-Pt-diffusion system following 100 cycle exposure at 1135°C.

13.3 Compatibility issues of nickel-based single-crystal superalloys with thermal barrier coating systems

The studies presented here provide new insights into the current understanding of TBC systems. Traditionally, it is considered that TBC spallation occurs by the accumulation of local damage to form a weakly bonded area that can be susceptible to buckling.^{22–24} Choi *et al.*²² have studied the competing failure processes of TBCs, such as edge delamination and small/large-scale buckling. Their results show that the failure mechanism depends strongly on both the thickness and in-plane modulus of the YSZ top coat. Assuming the in-plane elastic modulus for the EB–PVD top coat is in the range 0.05–0.25 times the bulk modulus of dense YSZ²⁴ and taking the top coat to be approximately 175 μm in thickness as is the case in the current study, substantial suppression of TGO buckling is believed to be present. Therefore, the final failure mode is more likely to be associated with edge delamination or wedging²⁵ irrespective of the initiation process.

Consider that TBC spallation occurs as the stored elastic energy of the TGO and top coat, which stiffens with time due to sintering, exceeds the interfacial adhesion between the TGO and bond coat. In the case of the steady-state energy release rate, a driving force G exists for the delamination of the multilayer TBC as:²⁴

$$G = \frac{\left(\sum_i \sigma_0 h_i \right)^2}{2 \sum_i \frac{E_i}{(1 - \nu_i^2)} h_i}$$

where E_i , h_i and ν_i are the elastic modulus, thickness and Poisson's ratio of each layer i , respectively and σ_0 is the equi-biaxial residual plane stress. The general argument is that the driving force for spallation G increases as the TGO thickens; delamination occurs when G reaches the critical interfacial fracture toughness G_c . In fact, as the EPMA mapping has revealed, the segregation of Ni, Cr and Co-rich oxides above the Al_2O_3 increased the overall TGO thickness and, thus, further increased this misfit strain energy.

However, the findings have conclusively confirmed that the resistance of TBC to spallation during thermal cycling is strongly dependent upon the composition of the superalloy substrate upon which the TBC system is placed. Since there is little correlation between the oxide growth kinetics and the TBC spallation life and the levels of trace elements present (e.g. sulphur) do not vary substantially from alloy to alloy, any differences in TBC lives will be attributable to differences in major elemental additions rather than trace elements.

The presence of Ti as an alloying element in SRR99, TMS-82+ and CMSX-4 is suggested to have shortened the TBC life. EPMA mapping of

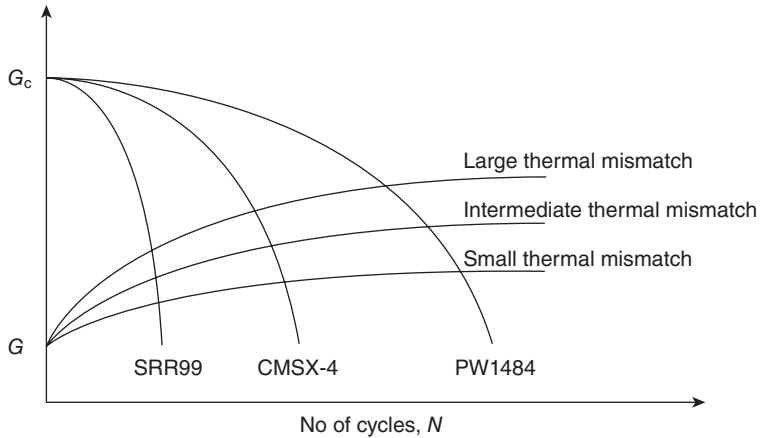
Ti shows a concentration-enriched layer (i.e. a bright layer) near the TGO/bond coat interface in the coated SRR99 system. In fact, previous studies^{26,27} have suggested that fast diffusion of Ti to the surface leads to the formation of Ti-rich oxides, potentially weakening the adhesive strength at the TGO/bond coat interface. In addition, Ti^{4+} ions, reported²⁸ to substitute for Al^{3+} ones to create Al vacancies within the alumina scale, may also degrade the properties of the TGO/bond coat interface. Thus, it is not difficult to rationalise the reason why SRR99, among the alloys considered, exhibits the fastest oxidation rate and the shortest TBC life. TMS-138A and PWA1484, in contrast, have no detected enrichment of alloy constituents at the TGO/bond coat interface and represent the two most spallation-resistant systems.

Regarding the spallation mechanisms as mentioned previously, it appears that the more spallation-resistant coatings failed at the top coat/TGO interface or tended to fail within the TGO; while specimens with shorter TBC spallation life preferentially failed at the TGO/bond coat interface, which again is the interface most likely to be affected by diffusion of harmful elements from the superalloys. This leads to a proposed argument that the TGO/bond coat interfacial adhesive strength of TBCs, which controls the TBC lifetime, is a dynamic materials property dependent on and influenced considerably by the composition of the substrate materials (i.e. superalloys). This situation can be qualitatively represented by a schematic drawing (Fig. 13.14) which illustrates the possible variation of the driving force G and the interfacial fracture toughness G_c with the time of thermal exposure.

Based upon the steady-state energy release rate equation for the delamination of the multi-layer TBC, the driving force G increases with TGO thickness, which is assumed to grow parabolically with time t , then thermal cycling at higher temperatures will accelerate the kinetics. The possible variation of G_c is also shown. At the beginning, for any choice of bond coat, G_c is assumed to be roughly the same for all alloy systems consistent with the identical processing conditions employed. However, upon thermal exposure, as the harmful elements such as Ti diffuse to the TGO interface, the value of G_c is believed to decrease – rapidly for a substrate system such as the SRR99 and modestly for PWA1484 with other alloys under consideration falling somewhere between the two.

It should be recognised that studies published so far have tended to consider just a single substrate composition with a TBC placed upon it; thus, any influence of the substrate chemistry is then factored out from the experiment. It would appear that the superalloy composition has a major influence on the lifetime of the systems, potentially due to the sensitivity of the interfacial fracture toughness to substitutional elements diffusing through the bond coat system from the superalloy substrate beneath it. These findings have implications for the design of TBC systems for the protection of the turbine blade aerofoils used for high-temperature applica-

Driving force for spallation, G
 Interfacial fracture toughness, G_c



13.14 Schematic illustration of the proposed variation of driving force G and interfacial fracture toughness G_c during thermal cycling.

tions. Traditionally, Ni-base SC superalloys have been designed with their mechanical properties – particularly in creep and fatigue – in mind. However, as the operating conditions of modern gas turbines continue to become more aggressive and use of TBCs for the provision of thermal insulation is increasing, a further property of the superalloy substrate is then required: that of compatibility with the TBC system which it is required to support. In particular, the influence of different alloying elements present in the superalloy on the TBC's interfacial fracture toughness needs to be better understood.

13.4 Bond coat related failure of TBCs

Traditionally, the study of TBCs has been focused on the investigation of individual bond coat systems.^{29–32} However, as the operating temperature of advanced gas turbines increases, new bond coats based on existing ones are required to meet this demand and suit different applications.^{33,34} Thus, it becomes necessary not only to understand how a coating system performs but also to know how and why existing coating systems behave differently.

Little work³⁵ has been reported in which the modes of degradation responsible for TBC spallation are compared for different bond coats. This is despite much progress that has been made on the micromechanics of the failure of aluminide bond coat systems.^{30,31} In particular, the usual approach

to modelling TBC failure^{36–41} concentrates on the treatment of the oxidation-induced stresses that drive TBC spallation-despite the fact that it is likely that the modes of failure^{33,42,43} and evolution of the residual stress are influenced considerably by the bond coat systems.

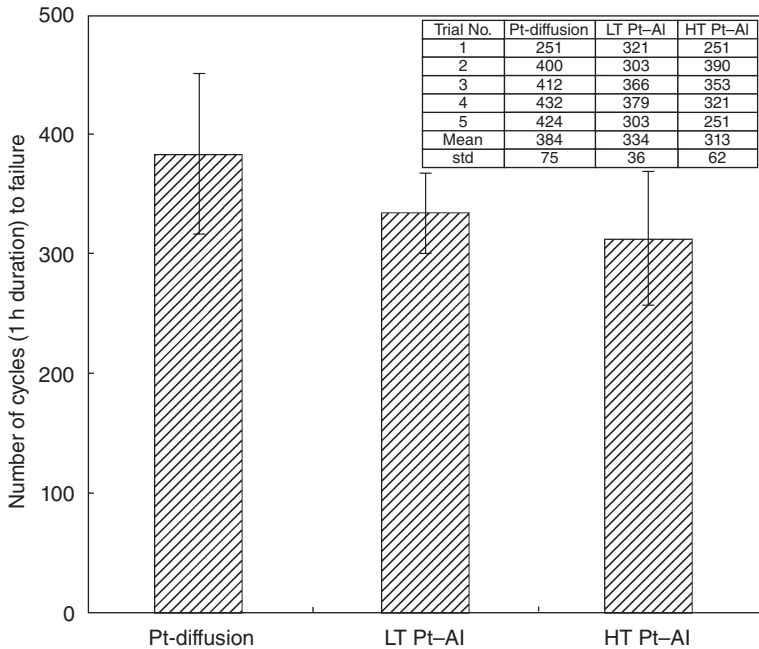
The work reported here was carried out with these factors in mind. Three different representative bond coat systems were deposited on SC CMSX-4 substrates and then subjected to identical (industry standard) EB-PVD YSZ coating processes. It has been shown that both the evolution of the residual stress in the TGO and the mode of TBC failure depend on the bond coat composition. FEG-SEM and EDX analysis were used to study the composition and microstructure changes occurring near the TGO/bond coat interface.

13.4.1 Experimental details and background information

The TBC spallation life (defined as detachment of top coat by approximately 20% in area) in thermal cycling conditions was found to be slightly dependent on the type of bond coat system used (see Fig. 13.15). Pt-diffusion bond coat specimens achieved a mean TBC life of 384 cycles; 15% and 23% longer than for LT and HT Pt–Al bond coats. It should be pointed out that, although the three bond coats differed significantly in composition and were prepared by different coating manufacturing processes, all three systems showed remarkably similar spallation life. However, it was found that depending on the type of bond coat, de-cohesion of the TBC occurred at different interfaces. Since the substrate and the ceramic top coat were prepared to be identical, this can only be explained by the different behaviours of the bond coats, as will be discussed later.

13.4.2 Residual stress measurement by luminescence spectroscopy

Residual stress in the TGO can be measured by piezospectroscopy which acquires Cr³⁺ luminescence spectra^{30–33} emitted from α -Al₂O₃ as a result of excitation by a laser beam. The details for luminescence experiments are given in Levi.³³ Luminescence spectra were acquired using a Renishaw Raman optical microprobe (model 2000) fitted with a motorised mapping stage. The luminescence from the TGO is due to the photo-stimulation of trace Cr³⁺ impurities present within the alumina. The spectrum has a featured intense doublet, the R1 and R2 lines, where R2 represents the peak with the higher wave number and lower integral peak area.³⁴ The characteristic R-line luminescence is a phenomenon resulting from the non-phonon radiative decay from the Cr³⁺ first excited state to the ground state within the *d* orbital.³⁵ The laser source was a green Ar+ laser with a



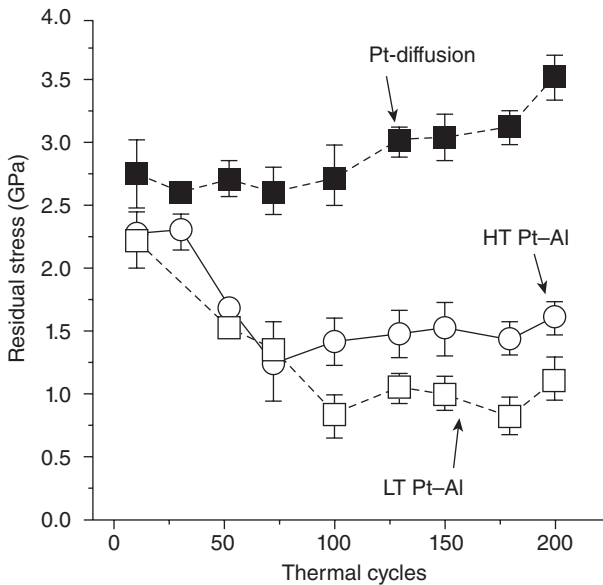
13.15 TBC spallation life for cyclic oxidation testing (1 h at 1135 °C) of TBC systems. The error bars indicate \pm one standard deviation in the lifetimes of each set of five specimens.

wavelength of 514.5 nm, which is focused on the specimen surface through an objective lens. The focused spot size can be adjusted by using different objective lens, with a minimum spot size of approximately 2 μm . However, upon incident on the specimen surface, the laser beam scatters within the YSZ top coat and consequently, results in an effective spot size at the TGO of approximately 20 μm .^{35,36} The light scattered back from the specimen was then collected by the objective lens, dispersed by a 1800 lines/mm grating and then received by a charge coupled device (CCD) detector.

An air conditioning unit was used to maintain a stable room temperature at 22 ± 0.3 °C. An acquisition time of 1 s was used for each spectrum. Measurements (121 per specimen) were taken on a square grid of 200×200 μm with a pitch of 20 μm located in the centre of the flat face of the disk specimen. Before and after each measurement, the spectrometer was calibrated by taking a spectrum from a strain-free SC sapphire sample. The residual stress in the TGO was estimated from the R2 peak shift assuming a planar equi-biaxial stress: $\sigma(\text{GPa}) = 5.07\Delta\nu$ (cm^{-1}). Transition phases of alumina (e.g., $\theta\text{-Al}_2\text{O}_3$) produced luminescence lines at 14260 cm^{-1} , 14330 cm^{-1} ,

14546 cm^{-1} and 14626 cm^{-1} , which are distinguishable from the R1 and R2 lines of $\alpha\text{-Al}_2\text{O}_3$.⁴⁴ However, no significant transition phases were seen in the TGO for all the cases in this study. Five individual specimens of each TBC system were used for the above analyses to ensure consistency of the experimental results.

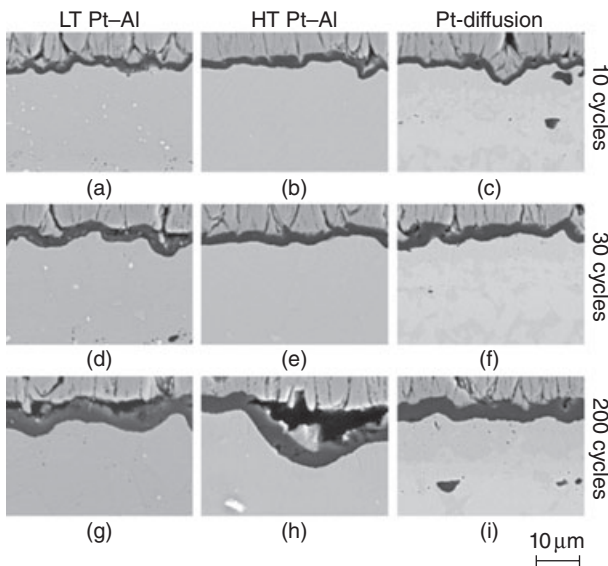
Luminescence measurements illustrating the evolution of residual stress in the TGO layer are given in Fig. 13.16. It was found that that the evolution of this stress was substantially different between the Pt-diffusion and the Pt-Al bond coat systems, despite the fact that they all had similar initial stress level in the as-coated condition. The Pt-diffusion bond coat systems began with a compressive stress of 2.8 GPa that gradually increased to 3.5 GPa over the coating lifetime, while those of the Pt-Al coatings decreased from an initial compressive stress of about 2.3 GPa to between 1 and 1.5 GPa during the first 75–100 thermal cycles, before maintaining a steady level to near the end of life. The error bars in Fig. 13.16 represent \pm one standard deviation of the 121 measurements made at each timestep. It is therefore notable that the standard deviation increases significantly for the Pt-diffusion bond coats just before failure.



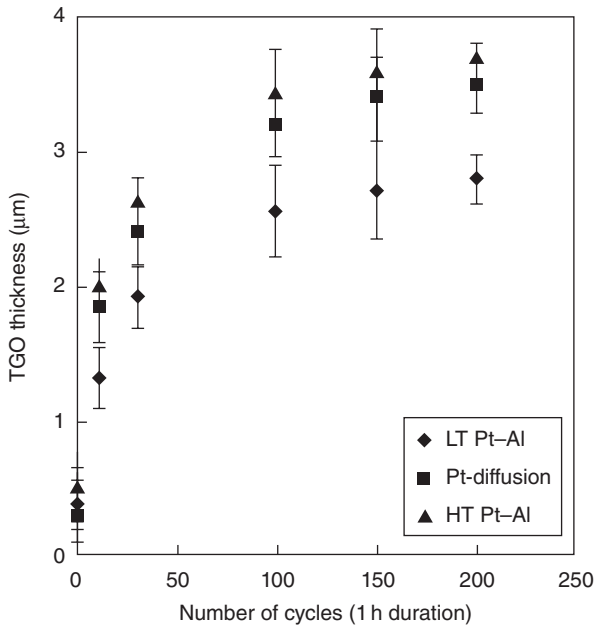
13.16 Compressive residual stress in the TGO shift vs number of cyclic oxidation tests of the bond coat systems.

13.4.3 Microstructure imaging of thermal cycled specimens using a field emission gun scanning electron microscope/energy dispersive X-ray (FE-SEM/EDX)

Cross-section scanning electron micrographs illustrating the microstructures of the three coatings after 10, 30 and 200 thermal cycles are shown in Fig. 13.17. Based on these SEM images, the oxidation kinetic (TGO thickness vs time) curve is plotted in Fig. 13.18. A few observations can be made with regard to the thermal-cycling-induced degradation. First, it can be seen that the TGO morphology evolved quite differently for the three bond coats. For example, the TGO interfaces in the Pt–diffusion system remained intact on thermal cycling for most of its spallation life. In contrast, local interfacial separation of the TGO in the Pt–Al systems occurred at less than 30% of their lifetimes. Furthermore, final spallation occurred at the TGO/YSZ interface for the LT Pt–Al bond coat but at the TGO/bond coat interface for the Pt–diffusion system. The HT Pt–Al bond coat system showed a mixture of the two failure modes. Finally, the waviness of the TGO layer in Pt–Al systems appears to amplify significantly upon thermal cycling.



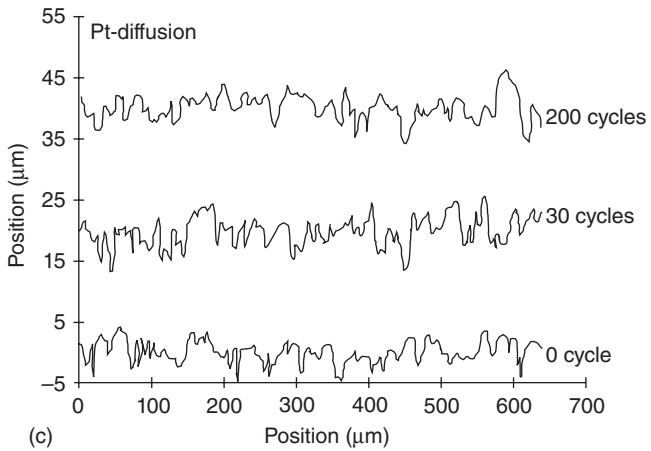
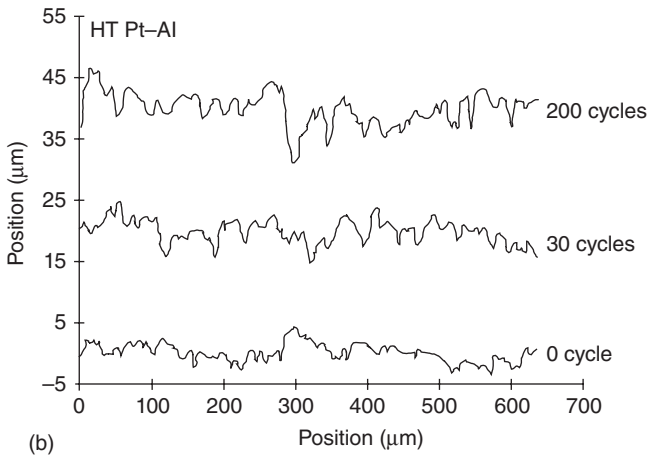
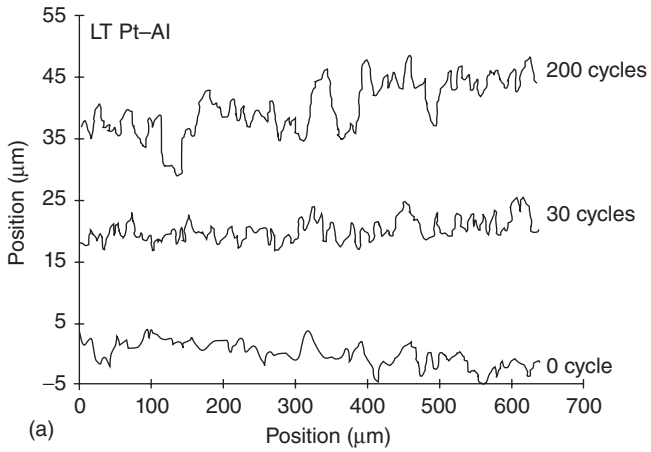
13.17 A series of SEM micrographs illustrating the near-TGO microstructure of the coatings after 10, 30 and 200 thermal cycles.



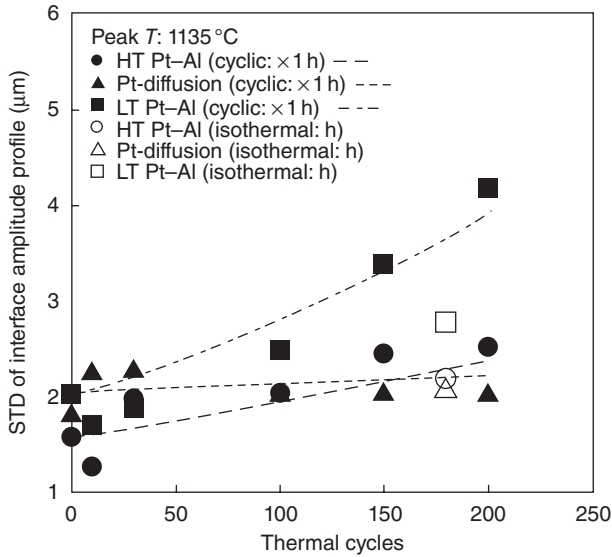
13.18 TGO thickness vs number of thermal cycles (1 h at 1135°C) for the three bond coat systems.

13.4.4 Quantification of rumpling at the thermally grown oxide (TGO)/bond coat interface

Measurement of the interfacial waviness was carried out by tracking the normal displacement along the TGO/bond coat interface in a cross-section SEM image over a distance of approximately 640 μm with a step size of 1 μm . Each position on the interface was represented by a pair of X (distance parallel to the specimen surface) and Y (distance normal to the specimen surface) co-ordinates. Figure 13.19 shows the evolution of the TGO/bond coat interface morphology for each of the three bond coat systems. The amplitude of waviness was quantified by determining the standard deviation (STD) of each profile. Figure 13.20 shows the standard deviation from the mean for each profile as a function of the number of thermal cycles. Results of isothermal tests were also plotted for reference. As can be seen in both Figs 13.19 and 13.20, the LT Pt–Al system exhibited a marked increase in TGO/bond coat interfacial waviness with thermal cycling. The HT Pt–Al bond coat also demonstrated a tendency to roughen with thermal cycling, but at a considerably slower rate. In contrast to the



13.19 TGO/bond coat interface profiles of: (a) LT Pt-Al; (b) HT Pt-Al; (c) Pt-diffusion bond coat at stages of the thermal cycling history.



13.20 Standard deviation of interface amplitude profile (i.e. magnitude of rumpling) as a function of the number of thermal cycles for the three different bond coat systems.

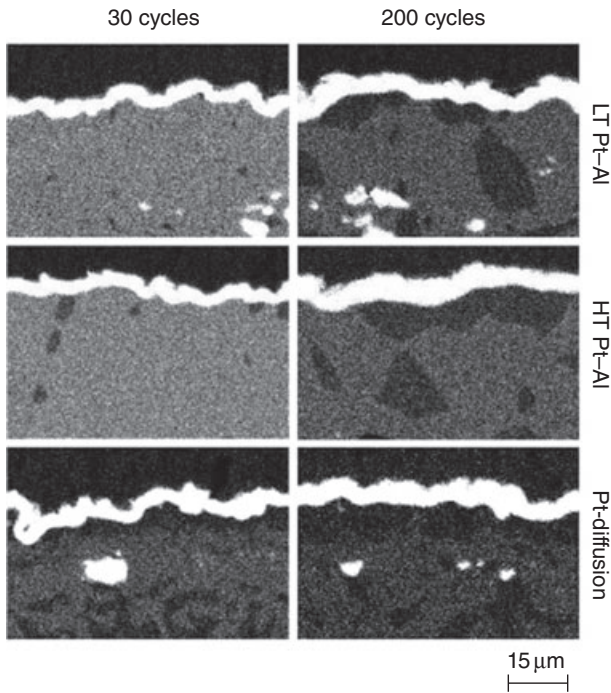
Table 13.4 Elemental compositions (at. %) taken using WSD FE-EPMA analysis of the TGO layer from specimens at 200 thermal cycles

Bond coat	Pt	Zr	Y	Co	Re	Ta	Al	Ni	Ti	Cr	O
LT Pt-Al	0.04	0.21	0.01	0.04	0.01	0.01	37.05	0.23	0.01	0.04	62.35
HT Pt-Al	0.02	0.20	0.02	0.04	0.00	0.02	38.60	0.29	0.02	0.04	60.75
Pt-diffusion	0.04	0.23	0.02	0.02	0.01	0.01	37.75	0.21	0.01	0.02	61.68

two Pt-Al systems, the Pt-diffusion bond coat showed no detectable roughening.

13.4.5 Chemical analyses of TGO layers and interfaces

Elemental compositions of the TGO layers on the three bond coats were characterised using WDS analysis after 200 thermal cycles (see Table 13.4). The results are quoted only for locations having TGO thickness greater than the spatial resolution of the FE-EPMA/WDS technique. The results show that for all specimens, the oxide layers consisted of more than 99 at% Al_2O_3 . Less than a total of 1 at% of other elements originating from the top coat, bond coat and substrate was detected in the oxide layer, possibly due to solid solution and particle segregation within the alumina scale. In



13.21 A series of Al EDX maps illustrating the microstructural evolution of the bond coat systems after 30 and 200 thermal cycles.

addition, high-resolution Al-mapping (Fig. 13.21) of the bond coat near the TGO interfaces using FE-SEM/EDX revealed how the different bond coats respond to the Al loss resulting from TGO growth and inter-diffusion with the substrate. Both Pt-Al bond coats showed a progressive phase transformation from the as-deposited single-phase β -(Pt,Ni)Al to a two-phase β -(Pt,Ni)Al and γ' -(Pt,Ni)₃Al microstructure. These images reveal that the phase transformation in the Pt-Al systems was detectable within the first 30 thermal cycles and the rate of transformation in the HT Pt-Al bond coat appeared to be faster. The Pt-diffusion bond coat, on the other hand, showed a distinct γ' to γ phase transformation near the TGO/bond coat interface. Upon thermal cycling, a continuous γ layer was eventually formed directly below the Al₂O₃ layer and thickened as the Al depletion continued.

13.5 Effect of bond coat on the TBC degradation mechanisms

The results presented here provide a detailed comparison of the progressive degradation of TBCs with three different bond coat systems upon thermal

exposure. The results show that the three TBC-coated bond coat systems failed with quite different characteristics, despite having similar lifetimes. In particular, the location of the TBC spallation interface varied strongly with type of bond coat employed. In addition, both the bond coat rumpling and the TGO residual stress measurements showed significantly different behaviour for the different bond coats. Since the substrate and the ceramic top coat were identical for all three systems, these differences can only be explained by the different processes taking place in the bond coats.

Quantification of the bond coat/TGO interfacial roughness indicated that rumpling was detectable within the first 30 cycles of thermal exposure in the Pt–Al systems. Upon further thermal cycling, the undulation in the TGO amplified in the LT Pt–Al system and resulted in localised vertical separation between the YSZ (which remained at its initial roughness) and the TGO, as can be clearly seen in Figs. 13.17g and k. TGO rumpling is capable of relieving the residual stress in the TGO by increasing its waviness,⁴⁵ which explains the reduction of the TGO residual stress in the Pt–Al coatings. In contrast, the absence of rumpling in the Pt-diffusion bond coat system helped in ensuring that the YSZ/TGO and the TGO/bond coat interfaces remained intact over the majority of the coating lifetime. Consequently, when there was significant rumpling (i.e. the LT Pt–Al system), coating de-cohesion took place primarily in the YSZ/TGO interface. In the absence of rumpling as in the case of the Pt-diffusion system, spallation eventually occurred at the bond coat/TGO interface. The HT Pt–Al bond coat system showed a mixture of these two failure modes, presumably due to the fact that its rate of rumpling was considerably less than that of the LT Pt–Al system.

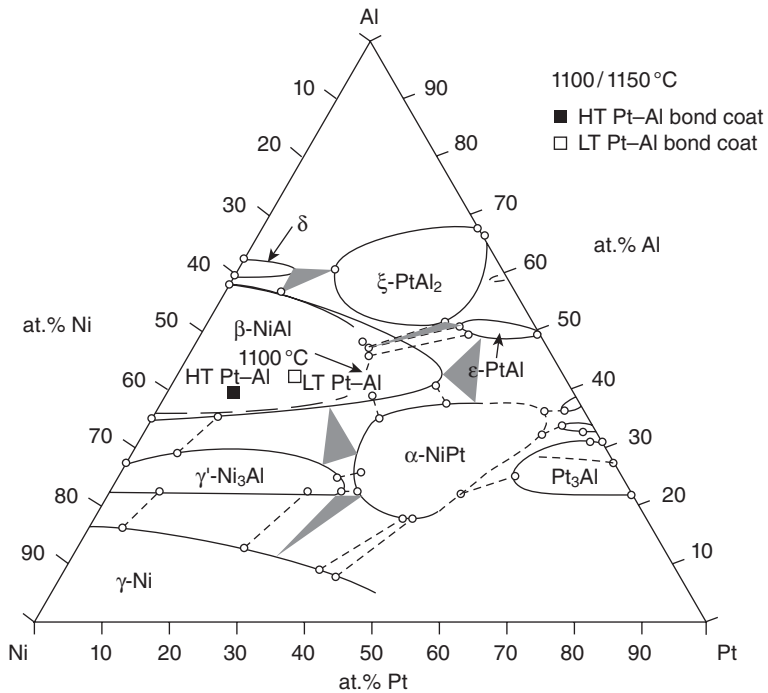
In addition to the observed consequences of rumpling, the mechanism by which rumpling occurs is also of importance. In particular, the dependence of rumpling on the properties of the bond coat materials must be considered. Upon depletion of Al, a phase transformation from the as-deposited single-phase β -(Pt,Ni)Al to a two-phase β -(Pt,Ni)Al and γ' -(Pt,Ni)₃Al microstructure takes place in Pt–Al bond coats. It has been proposed⁴⁶ that this phase transformation induces non-uniform volume changes of the bond coat and thus leads to rumpling.^{30,32,44,47–49} However, this mechanism does not appear to play a major role in inducing bond coat rumpling, at least in the current study, for two reasons. First, according to the proposed mechanism, the LT Pt–Al bond coat, which exhibited strongest rumpling behaviour in the current study, should correspondingly have the fastest oxidation kinetics (i.e. fastest Al-depletion rate). However, the present results showed that it had the slowest oxidation rate among the three systems studied. Second, the lower-Al containing Pt–Al bond coat (HT Pt–Al), according to the proposed mechanism, should be more sensitive to Al depletion and, thus, prone to the phase transformation-induced rumpling than its high-Al Pt–Al counterpart (LT Pt–Al). However, results showed the opposite, in

that the rate of rumpling in the HT Pt–Al system was considerably lower than that of the LT Pt–Al system.

Based on these considerations, it is suggested that rumpling is not primarily induced by the phase transformation associated with the Al-depletion, but depends on the high-temperature mechanical properties of the bond coats. Thus, it is hypothesised that the rumpling behaviour observed in this study may be controlled by the high-temperature resistance to plastic deformation of these bond coat materials. The fact that the magnitude of rumpling was lower in the isothermal conditions suggested that the rumpling mechanism may be mainly due to micromechanical interactions of the TBC systems and strongly related to the resistance of the bond coat materials to plastic deformation at elevated temperatures; but not the temperature and time-dependent phase transformation process. The Pt-diffusion bond coat, which inherited the two-phase γ and γ' microstructure of the superalloy, should be more resistant to plastic deformation at elevated temperatures than the single-phase β -(Pt,Ni)Al Pt–Al bond coats. Similarly in the Pt–Al system, a previous study⁵⁰ has suggested that a strengthening effect (i.e. high value creep index and activation energy) can be attributed to the precipitation of finely dispersed γ' within the β matrix. The extent of γ' phase precipitation depends not only on the Al depletion by inter-diffusion or oxidation, but primarily on how close the composition is to the $\beta/\beta + \gamma'$ phase boundary (Fig. 13.22)⁵⁰ at elevated temperatures. The HT Pt–Al system, leaner in both Pt and Al near its rumpling interface, is situated closer to the $\beta/\beta + \gamma'$ phase boundary than the LT Pt–Al system. Thus, one would expect the HT Pt–Al system to be stronger in creep than the LT Pt–Al system, due to a higher volume fraction of precipitated γ' . This explanation is consistent with the observation that the Al-rich Pt–Al (LT Pt–Al) bond coat exhibited a considerably faster rumpling rate than the low Al-containing one (HT Pt–Al). Clearly, further studies need to be done to clarify the role of high-temperature plasticity in the rumpling phenomenon.

13.6 Conclusions and future trends

The importance of superalloy substrate composition in determining the oxidation kinetics and the cycling life of TBC systems has been demonstrated here. The TBC spallation life was found to vary by a factor of up to three, depending upon the chemical composition of the superalloy substrate even though the bond coat and top coat were nominally the same. This effect implies that considerable chemical effects are at play. By comparison, the choice of bond coat among common types has a smaller effect in determining TBC spallation life. The experimental results can be explained only if the fracture toughness parameters controlling de-cohesion (i.e. the frac-



13.22 Ternary Ni–Al–Pt phase diagram at 1100 and 1150 °C²¹ showing the two Pt–Al bond coat systems considered in the current study.

ture toughness of the TGO and the fracture toughness of the interfaces bounding it) are influenced strongly by small changes in composition arising from inter-diffusion with the bond coat, such that they are degraded during thermal cycling. Chemical analysis shows that trace elements such as sulphur (on the basis of bulk chemical analysis) in the superalloy substrate are not responsible for the effects reported, indicating that major elemental additions, such as Ti in particular, are the cause.

Although results obtained here provide some insight to assist the design of advanced superalloys or oxidation-resistant coatings, further work needs to be carried out to elucidate more detailed mechanisms associated with the degradation of TBCs.

The importance of substrate composition on the lifetime of TBCs was highlighted. The relationship between substrate composition and the composition of the Pt-diffused layer is central to the beneficial effect of Pt-modification in the context of diffusion coating technology. The Pt-diffusion bond coat is resistant to rumpling and results in an enhanced TBC life, but this effect is diminished in alloys containing elements that have an adverse effect on adhesion at the bond coat/YSZ interface. In view of this,

future use of the Pt-diffusion bond coat requires a more considered approach towards the chemistry of the underlying superalloy and the composition of the Pt-diffused substrate prior to top coat application. For optimum turbine blade aerofoil characteristics in service, it may now be necessary to balance the mechanical behaviour of the substrate and its compatibility with the TBC systems in order to improve the performance of the system as a whole.

It is believed that with the development of more sophisticated models, the important phase transformations and oxidation behaviour which govern the degradation of coated superalloys will be modeled, with the goal of developing a predictive capability which is presently lacking; this activity will require the identification of the physical factors which dictate substrate/coating interactions – it will also provide the basis for a chemistry-based approach to coating life prediction.

In terms of the work on the study of bond coat rumpling, the current study showed the different rumpling behaviours between the Pt-diffusion and Pt–Al bond coats. Both Pt–Al systems exhibited rumpling behaviour, but the LT Pt–Al bond coat system showed a significantly faster rumpling rate than the HT Pt–Al bond coat system. The Pt-diffusion system, in contrast, showed no tendency to rumple. It would be of interest as a continuation of the current work to study the effect of the substrate composition on bond coat rumpling. If such an effect is apparent, it would be interesting to correlate the TBC spallation life with the magnitude of rumpling.

13.7 References

1. R.C. REED, *Superalloys: Fundamentals and Applications* (Cambridge, UK: Cambridge University Press 2006).
2. C.T. SIMS, N.S. STOLOFF and W.C. HAGEL (eds), *Superalloys II: High-Temperature Materials for Aerospace and Industrial Power* (New York: Wiley 1987).
3. K.A. GREEN, T.M. POLLOCK, H. HARADA *et al.* (eds), *Superalloys 2004, Proceedings of the Tenth International Symposium on the Superalloys* (Warrendale, PA: The Minerals, Metals and Materials Society (TMS), 2004).
4. W. BETTERIDGE and S.W.S. SHAW, 'Development of superalloys,' *Materials Science and Technology*, **3**, 1987, 682–694.
5. A.M. KARLSSON and A.G. EVANS, 'A numerical model for the cyclic instability of thermally grown oxides in thermal barrier systems,' *Acta Materialia*, **49**, 2001, 1793–1804.
6. N. CZECH, H. FIETZEK, M. JUEZ-LORENZO, V. KOLARIK and W. STAMM, 'Studies of the bond-coat oxidation and phase structure of TBCs,' *Surface and Coatings Technology*, **113**, 1999, 157–164.
7. V. LUGHI, V.K. TOLPYGO, and D.R. CLARKE, 'Microstructural aspects of the sintering of thermal barrier coatings,' *Materials Science & Engineering A*, **368**, 2004, 212–221.

8. K.T. VOISEV and T.W. CLYNE, 'Laser drilling of cooling holes through plasma sprayed thermal barrier coatings,' *Surface and Coatings Technology*, **176**, 2004, 296–306.
9. A. NUSAIR KHAN, J. LU and H. LIAO, 'Heat treatment of thermal barrier coatings,' *Materials Science & Engineering A*, **359**, 2004, 129–136.
10. M. ANDRITSCHKY, P. ALPUIM, D. STÖVER and C. FUNKE, 'Study of the mechanics of the delamination of ceramic functional coatings,' *Materials Science and Engineering A*, **271**, 1999, 62–69.
11. C.G. LEVI, 'Emerging materials and processes for thermal barrier systems,' *Current Opinion in Solid State and Materials Science*, **8**, 2004, 77–91.
12. N.P. PADTURE, M. GELL and E.H. JORDAN, 'Thermal barrier coatings for gas-turbine applications,' *Science*, **296**, 2002, 280–284.
13. V.K. TOLPYGO and D.R. CLARKE, 'On the rumpling mechanism in nickel-aluminide coatings, part I: an experimental assessment,' *Acta Materialia*, **52**, 2004, 5115–5127.
14. B.A. PINT, I.G. WRIGHT, W.Y. LEE, Y. ZHANG, K. PRUSSNER and K.B. ALEXANDER, 'Substrate and bond coat compositions: factors affecting alumina scale adhesion,' *Materials Science and Engineering A*, **245**, 1998, 201–211.
15. B.A. PINT, 'The role of chemical composition on the oxidation performance of aluminide coatings,' *Surface and Coatings Technology*, **188–189**, 2004, 71–78.
16. B.A. PINT, J.A. HAYNES, K.L. MORE and I.G. WRIGHT, 'The use of model alloys to understand and improve the performance of Pt-modified aluminide coatings,' in: *Superalloys 2004*, eds K.A. Green, T.M. Pollock, H. Harada, T.E. Howson, R.C. Reed, J.J. Schirra and S. Walston, (Warrendale, PA, USA: The Minerals, Metals and Materials Society (TMS), 2004), 597–606.
17. E.P. BUSO, J. LIN and S. SAKURAI, 'A mechanistic study of oxidation-induced degradation in a plasma-sprayed thermal barrier coating system: Part II: Life prediction model,' *Acta Materialia*, **49**, 2001, 1529–1536.
18. F. TRAEGER, M. AHRENS, R. VABEN and D. STÖVER, 'A life time model for ceramic thermal barrier coatings,' *Materials Science and Engineering A*, **358**, 2003, 255–265.
19. E.P. BUSO, L. WRIGHT, H.E. EVANS, L.N. MCCARTNEY, S.R.J. SAUNDERS, S. OSGERBY and J. NUNN, 'A physics-based life prediction methodology for thermal barrier coating systems,' *Acta Materialia*, **55**, 2007, 1491–1503.
20. M. BAKER, J. ROSLER and G. HEINZE, 'A parametric study of the stress state of thermal barrier coatings Part II: cooling stresses,' *Acta Materialia*, **53**, 2005, 469–476.
21. R.T. WU, K. KAWAGISHI, H. HARADA and R.C. REED, 'The retention of thermal barrier coating systems on single-crystal superalloys: effects of substrate composition,' *Acta Materialia*, **56**, 2008, 3622–3629.
22. S.R. CHOI, J.W. HUTCHINSON and A.G. EVANS, 'Delamination of multilayer thermal barrier coatings,' *Mechanics of Materials*, **31**, 1999, 431–447.
23. M.Y. HE, D.R. MUMM and A.G. EVANS, 'Criteria for the delamination of thermal barrier coatings; with application to thermal gradients,' *Surface and Coatings Technology*, **185**, 2004, 184–193.
24. A. SELCUK and A. ATKINSON, 'The evolution of residual stress in the thermally grown oxide on Pt diffusion bond coats in TBCs,' *Acta Materialia*, **51**, 2003, 535–549.

25. A. STRAWBRIDGE and H.E. EVANS, 'Mechanical failure of thin brittle coatings,' *Engineering Failure Analysis*, **2**, 1995, 85–103.
26. B.A. PINT, J.A. HAYNES, K.L. MORE, I.G. WRIGHT and C. LEYENS, 'Compositional effects on aluminate oxidation performance: objectives for improved bond coats,' in: *Superalloys 2000*, eds T.M. Pollock, R.D. Kissinger, R.R. Bowman, K.A. Green, M. McLean, S.L. Olson and J.J. Schirra, (Warrendale, PA, USA: The Minerals, Metals and Materials Society (TMS), 2000), 629–638.
27. A.L. PURVIS and B.M. WARNES, 'The effects of platinum concentration on the oxidation resistance of superalloys coated with single-phase platinum aluminide,' *Surface and Coatings Technology*, **146–147**, 2001, 1–6.
28. P. FOX and G.J. TATLOCK, 'Effect of tantalum additions on oxidation of overlay coated superalloys,' *Materials Science and Technology*, **5**, 1989, 816–827.
29. A.G. EVANS, D.R. MUMM, J.W. HUTCHINSON, G.H. MEIER and F.S. PETTIT, 'Mechanisms controlling the durability of thermal barrier coatings,' *Progress in Materials Science*, **46**, 2001, 505–553.
30. V.K. TOLPYGO and D.R. CLARKE, 'On the rumpling mechanism in nickel-aluminide coatings, part I: an experimental assessment,' *Acta Materialia*, **52**, 2004, 5115–5127.
31. V.K. TOLPYGO and D.R. CLARKE, 'On the rumpling mechanism in nickel-aluminide coatings, part II: characterisation of surface undulations and bond coat swelling,' *Acta Materialia*, **52**, 2004, 5129–5141.
32. M. GELL, K. VAIDYANATHAN, B. BARBER, J. CHENG and E. JORDAN, 'Mechanism of spallation in platinum aluminide/electron beam physical vapor-deposited thermal barrier coatings,' *Metallurgical and Materials Transactions A*, **30**, 1999, 427–435.
33. C.G. LEVI, 'Emerging materials and processes for thermal barrier systems,' *Current Opinion in Solid State and Materials Science*, **8**, 2004, 77–91.
34. N.P. PADTURE, M. GELL and E.H. JORDAN, 'Thermal barrier coatings for gas-turbine applications,' *Science*, **296**, 2002, 280–284.
35. R.C. PENNEFATHER, and D.H. BOONE, 'Mechanical degradation of coating systems in high-temperature cyclic oxidation,' *Surface and Coatings Technology*, **47**, 1995, 76–77.
36. E.P. BUSSO, J. LIN and S. SAKURAI, 'A mechanistic study of oxidation-induced degradation in a plasma-sprayed thermal barrier coating system: Part II: Life prediction model,' *Acta Materialia*, **49**, 2001, 1529–1536.
37. F. TRAEGER, M. AHRENS, R. VABEN and D. STÖVER, 'A life time model for ceramic thermal barrier coatings,' *Materials Science and Engineering A*, **358**, 2003, 255–265.
38. E.P. BUSSO, L. WRIGHT, H.E. EVANS, L.N. MCCARTNEY, S.R.J. SAUNDERS, S. OSGERBY and J. NUNN, 'A physics-based life prediction methodology for thermal barrier coating systems,' *Acta Materialia*, **55**, 2007, 1491–1503.
39. M. BAKER, J. ROSLER and G. HEINZE, 'A parametric study of the stress state of thermal barrier coatings Part II: cooling stresses,' *Acta Materialia*, **53**, 2005, 469–476.
40. M. JINNESTRAND and S. SJOSTROM, 'Investigation by 3D FE simulations of delamination crack initiation in TBC caused by alumina growth,' *Surface and Coatings Technology*, **135**, 2001, 188–195.

41. A.M. KARLSSON and A.G. EVANS, 'A numerical model for the cyclic instability of thermally grown oxides in thermal barrier systems,' *Acta Materialia*, **49**, 2001, 1793–1804.
42. A.G. EVANS, M.Y. HE and J.W. HUTCHINSON, 'Mechanics-based scaling laws for the durability of thermal barrier coatings,' *Progress in Materials Science*, **46**, 2001, 249–271.
43. J.S. WANG and A.G. EVANS, 'Measurement and analysis of buckling and buckle propagation in compressed oxide layers on superalloy substrates,' *Acta Materialia*, **46**, 1998, 4993–5005.
44. D.R. MUMM and A.G. EVANS, 'On the role of imperfections in the failure of a thermal barrier coating made by electron beam deposition,' *Acta Materialia*, **48**, 2000, 1815–1827.
45. G. LEE, A. ATKINSON and A. SELCUK, 'Development of residual stress and damage in thermal barrier coatings,' *Surface and Coatings Technology*, **201**, 2006, 3931–3936.
46. V.K. TOLPYGO and D.R. CLARKE, 'Surface rumpling of a (Ni, Pt)Al bond coat induced by cyclic oxidation,' *Acta Materialia*, **48**, 2000, 3283–3293.
47. D.R. MUMM, A.G. EVANS and I.T. SPITSBERG, 'Characterisation of a cyclic displacement instability for a thermally grown oxide in a thermal barrier coating system,' *Acta Materialia*, **49**, 2001, 2329–2340.
48. V.K. TOLPYGO and D.R. CLARKE, 'Morphological evolution of thermal barrier coatings induced by cyclic oxidation,' *Surface and Coatings Technology*, **163–164**, 2003, 81–86.
49. B. GLEESON, W. WANG, S. HAYASHI and D. SORDELET, 'Effects of platinum on the interdiffusion and oxidation behavior of Ni–Al-based alloy,' *Materials Science Forum*, **213**, 2004, 461–464.
50. M.P. TAYLOR, H.E. EVANS, E.P. BUSSO and Z.Q. QIAN, 'Creep properties of a Pt-aluminide coating,' *Acta Materialia*, **54**, 2006, 3241–3252.

H. Y. QI and X. G. YANG Beihang University, China

Abstract: Three viscoplastic constitutive models were developed for top coats and substrate. Some important material properties were tested and evaluated under high temperature, and thermal fatigue experiments for atmospheric plasma spraying (APS) and electron beam physical vapor deposition (EB-PVD) were designed and carried out. A fatigue life model was set up and the lifetime of a vane with thermal barrier coating (TBC) was predicted.

Key words: APS, EB-PVD, viscoplastic constitutive model, thermal fatigue, life prediction, vane.

14.1 Introduction

At time of writing, mainstream turbine manufacturers provide an initial gas temperature level of 960–1100 °C for basic service and 1065–1300 °C for peak service. In military aircraft turbines, the gas temperature rises to 1600 °C.¹ The application of thermal barrier coating (TBC) is an effective means of protecting aero-engine blades from hot gas. Currently, there are two methods used for depositing TBC on substrate, namely plasma spray (PS) and electron beam physical vapor deposition (EB-PVD). A typical TBC system consists of two thin coatings: a ceramic coating and a metallic bond coat (BC).

Since the 1980s, the failure mechanisms of atmospheric plasma spraying (APS) and EB-PVD have been analyzed and spallation and local buckling found to be major failure modes. TBC failure results in a combination of oxidation and thermal fatigue.^{2–4} Most life prediction models are based on NASA's initial work on phenomenological and macroscopic approaches.⁵ However, the potential of TBC cannot be fully utilized due to the lack of a reliable life prediction method and accurate stress–strain results.

In much of the literature, methods based on elastic–plastic theory using an axisymmetric model have been used to analyze failure mechanism and life prediction. Additionally, by adopting finite element method (FEM) theory and simulative technology, many models such as an axisymmetric and elastic–plastic model with realistic oxide growth and an elastic–plastic model with creep of the bond coating, have been simulated and analyzed.⁶ However, these ‘traditional’ models were not able to simulate exactly the

complex mechanical behaviours of TBC in a high-temperature environment. Some viscoplastic constitutive models, such as ‘Walker’ and ‘Willam–Warnke’, have been developed for TBC systems. Compared to the classical model, the viscoplastic constitutive models allow both cyclic plasticity and creep deformation to be modeled within the framework of continuum damage mechanics. Viscoplastic constitutive models cover all aspects of inelastic deformation, such as monotonic and cyclic plasticity, strain-rate sensitivity, creep and creep relaxation.

Ability to operate in an increasingly high-temperature environment is a key performance indicator in the development of jet engines. With the extensive application of advanced technology, such as directionally solidified superalloys on hot sections, investigation of methods of analyzing the structures of complex heterogeneous materials as well as their failure mechanisms are becoming increasingly urgent. Spallation of TBC in service, deformation analysis and thermal fatigue life prediction methods for a vane with TBC have been intensively investigated and discussed.

14.2 The mechanical behavior of thermal barrier coating (TBC) systems under elevated temperatures

14.2.1 Introduction

Modern methods for life prediction of structures are based on inelastic analyses, which lead to large numbers of cycles of computation, especially under high temperature and cyclic loadings. In order to achieve a higher level of accuracy without increasing the computing time required, better constitutive equations need to be employed to describe material behaviour.⁷

An advanced constitutive model based on the Willam–Warnke flow surface has been developed for concreteness.⁸ The model has ability to describe non-equal yield stresses in compression and tension and rate-independent features. Based on this model and the experimental data, Xie developed a genetic algorithm to optimize material constants. The FEM model for PWA 264 TBC with thermal grown oxide (TGO) has been simulated and analyzed successfully.⁹

Using experimental data from NASA’s Hot Section Technology (HOST) program, and based on the Walker viscoplastic material model, an alternative unified viscoplasticity constitutive model was adopted for EB–PVD coating. The substrate used is DZ40M, a kind of directionally solidified superalloy. Based on the Chaboche constitutive model, an advanced viscoplasticity constitutive model for orthotropic substrate was developed^{10,11} to describe behavior under high temperature.

14.2.2 Material constitutive laws

TBC generally comprises a multi-layer structure with a top coat of brittle material while the bond coat and substrate are ductile material. Thus, when evaluating material behaviour with regard to temperature, each layer has its own specific constitutive law. The Willam-Warnke model was used for the APS ceramic top coat while the Walker model was adopted for EB-PVD. The Chaboche constitutive law was used for the metal substrate.

Willam–Warnke model for the top coat by APS

A viscoplastic constitutive model based on the theory of finite deformation for PS TBCs able to describe characteristics of tension/compression asymmetry, strain rate sensitivity and hydrostatic stress dependency has been introduced. The APS TBC exhibits non-equal yield stresses in compression and tension and non-linear rate-dependent behaviour under high temperature. In order to simulate realistic deformation characteristics, the viscoplastic Willam–Warnke model was adopted for the top coat. The constitutive equations are as follows:^{8,9}

$$f = K^2 \left[\left(\frac{1}{2\mu} \right) \int F^n dF + \left(\frac{R}{H} \right) \int G^m dG \right] \quad [14.1]$$

$$\dot{\epsilon}_{ij}^I = c_0 \left[c_1 \delta_{ij} + c_2 (S_{ij} - a_{ij}) + c_3 \left((S_{iq} - a_{iq})(S_{qj} - a_{qj}) - \frac{2J_2 \delta_{ij}}{3} \right) \right] \quad [14.2]$$

$$\dot{a}_{ij} = h \left[\dot{\epsilon}_{ij}^I - c_4 \left(c_1 \delta_{ij} + c_5 a_{ij} + c_6 \left(a_{iq} a_{qj} - \frac{2J_2 \delta_{ij}}{3} \right) \right) \right] \quad [14.3]$$

where f is the viscoplastic potential function, F is the three-parameter Willam–Warnke yield criterion, G is the recovery function, σ_{ij} is a stress component; δ_{ij} is Kronecker delta, S_{ij} and S_{iq} are the deviatoric stress component and J_2 is the second stress invariant. Because the second and third invariants of the deviatoric part of the Cauchy stress tensor are adopted, this Willam–Warnke model features the non-equal yield stresses in compression and tension, rate and hydrostatic independence. $\dot{\epsilon}_{ij}^I$ indicates non-linear strain rate tensor, a_{ij} indicates internal variables of non-linear kinematic hardening, $C_0 \sim C_6$ indicate functions of the stress and back stress tensors and their invariants and K , R , H , m , n , h , and μ are material constants.

Walker model for the top coat by electron beam physical vapor deposition (EB–PVD)

Within the framework of unified viscoplasticity, the complete set of equations is given by Walker. This model offers a great deal of scope for the

description of temperature-dependent phenomena. The Walker model contains one scalar internal state variable K , called drag strength, and an internal variable Ω called back stress. The viscoplastic potential was as follows:^{12,13}

$$f = \frac{K}{n+1} \left[\frac{J(\sigma - X)}{k(\dot{p})} \right]^n \tag{14.4}$$

where K and n are material parameters and p is internal state variable. In this formula $J(\sigma - X)$ is the internal stress invariant. The viscoplastic strain rate was written as

$$\dot{\epsilon}_{ij}^I = \left[\frac{\sqrt{\frac{2}{3} \left(\frac{3}{2} S_{ij} - \Omega_{ij} \right) : \left(\frac{3}{2} S_{ij} - \Omega_{ij} \right)}}}{K_d} \right]^n \frac{\left(\frac{3}{2} S_{ij} - \Omega_{ij} \right)}{\sqrt{\frac{2}{3} \left(\frac{3}{2} S_{ij} - \Omega_{ij} \right) : \left(\frac{3}{2} S_{ij} - \Omega_{ij} \right)}} \tag{14.5}$$

The drag stress was written as

$$K = K_1 - K_2 e^{(-n_7 \dot{p})} \tag{14.6}$$

where \dot{p} is the rate of the accumulated inelastic strain:

$$\dot{p} = \sqrt{\frac{2}{3} \dot{\epsilon}_{ij}^I : \dot{\epsilon}_{ij}^I} \tag{14.7}$$

The evolution equation for the back stress tensor was shown as

$$\dot{\Omega}_{ij} = (n_1 + n_2) \dot{\epsilon}_{ij}^I - (\Omega_{ij} - \dot{\Omega}_{ij} - n_1 \epsilon_{ij}^I) \dot{G} \tag{14.8}$$

where K_1 , K_2 , n_1 , n_2 , and n_7 are temperature-dependent material parameters.

Chaboche model for the substrate

A modified Chaboche constitutive model for directionally solidified superalloy substrate able to describe characteristics of loading direction dependency, creep, cyclic hardening/softening and mean stress relaxation has been developed. A fourth-order tensor M_{ijkl} was induced for the viscoplastic constitutive law, which laid a foundation for achieving accurate stress and strain analysis on a turbine vane with PS TBC.

The substrate used for specimens and a vane in our work is DZ40M, a kind of directionally solidified superalloy. Based on the Chaboche constitutive model, an advanced constitutive model for orthotropic substrate has been developed.^{10,11} The constitutive relation is as follows:

$$f = \sqrt{\frac{3}{2} M_{ijkl} (\sigma'_{ij} - X'_{ij}) (\sigma'_{kl} - X'_{kl})} - R - K \tag{14.9}$$

$$\dot{\epsilon}_{ij}^I = \frac{\partial f}{\partial \sigma_{ij}} = \frac{3}{2} \left\langle \frac{f}{K} \right\rangle^n \frac{M_{ijkl} (\sigma'_{kl} - X'_{kl})}{\sqrt{\frac{3}{2} M_{ijkl} (\sigma'_{ij} - X'_{ij}) (\sigma'_{kl} - X'_{kl})}} \quad [14.10]$$

$$\dot{X}_{ij} = \frac{2}{3} ac \dot{\epsilon}_{ij}^I - c \left(\frac{J(X_{ij})}{a} \right)^m \dot{p} X_{ij} - \beta |J(X_{ij})|^{r-1} X_{ij} \quad [14.11]$$

$$\dot{R} = b(Q - R) \dot{p} \quad [14.12]$$

where f is the yield function, X_{ij} , X_{kl} and R indicate internal stresses for kinematic hardening and isotonic hardening, respectively, and $J(x_{ij})$ is the internal stress invariant. In the general case of an initially anisotropic material, a fourth-order tensor M_{ijkl} was introduced. To simplify M_{ijkl} , there are only three parameters, namely M_{11} , M_{33} and M_{55} . $\dot{\epsilon}_{ij}^I$ indicates the viscoplastic strain rate. The formula $\dot{p} = \sqrt{3/2} \dot{\epsilon}_{ij}^I M_{ijkl}^{-1} \dot{\epsilon}_{kl}^I$ is called the accumulated plastic strain rate. K , n , k , a_1 , c_1 , a_2 , c_2 , β , m , r_1 , b and Q in the equations are temperature-dependent parameters. This model is able to describe direction-dependent characteristics, hardening properties, relaxation of the mean stress and cyclic creep.

14.2.3 Material parameters of TBCs under high temperature

Measurement of Young's modulus for the top coat

While the thermal-sprayed coatings bring many advantages, there are still some aspects requiring further investigation and better understanding in order to improve performance and increase the scope of applications. One important property of thermal-sprayed coatings, which is difficult to determine, is Young's modulus. An accurate Young's modulus value is necessary to evaluate residual stresses, bond strength, fatigue crack growth rates and coating stress under in-service loading conditions.¹⁴

Because all coatings are used while they are bonded to a substrate, it is important to use a procedure capable of evaluating the Young's modulus *in situ*. One of the problems encountered is that the ceramic top coat is usually thin, and therefore it is difficult to obtain a specimen entirely made of coating material to conduct a modulus test. Nowadays, by using warm hydrochloric acid, the top coat specimen of TBCs can be detached. However, it is difficult to conduct the measurement of the applied load and displacement under high temperature.¹⁵

APS top coat was selected to measure the Young's modulus using the resonant frequency method. The Young's modulus of top coat under high temperature measured using the bending resonance method was the par-

ticular focus. The testing system included both hardware and software components.

Specimens were produced using a METCO-7M APS of a CoNiCrAlY bond coat and a top-coat of ZrO_2-6-8 wt% Y_2O_3 . The bond coat thickness was about 120 μm , while that of the top coat was about 240 μm . Some specimens for the resonant frequency method were deposited onto 1Cr18Ni9Ti stainless steel substrate. With approximate dimensions $120 \times 5 \times 1.5$ mm. The resonant flexural frequencies were tested by suspending the rectangular beam specimens from hanging string at the node positions for the fundamental flexural resonance.^{16,17} The modulus of the coating can be determined in a straightforward manner from the stiffness of the composite beam, which is equal to the sum of the stiffnesses of the components

$$E_{c+s}I_{c+s} = E_sI_s + E_cI_c \quad [14.13]$$

where E is the Young's modulus, I is the moment of inertia and subscripts $c + s$, c and s refer to the quantity for composite beam with both coating and substrate, for coating only and for substrate only, respectively. Young's modulus for a homogeneous rectangular beam is related to the resonant frequency by

$$E = 0.94642 \frac{TL^3}{h^3} \frac{mf^2}{t} \quad [14.14]$$

where L , h and t are the length, height and thickness of a homogenous specimen, respectively, T indicates a dimensionless shape factor (dependent on the specimen length, height and Poisson's ratio), m indicates the mass and f indicates the resonant frequency of the fundamental mode of vibration. The combination of the two equations leads to the following expression for the modulus of the coating, E_c :

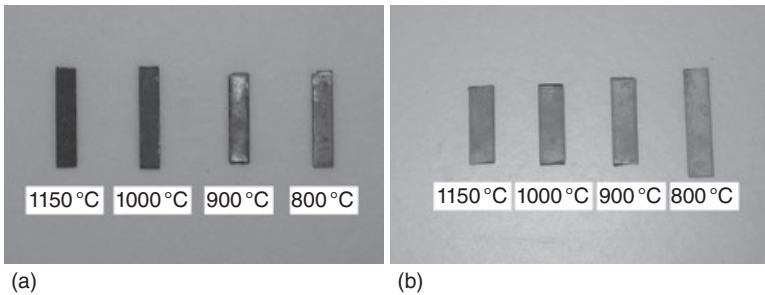
$$E_c = E_s \left[\frac{m_{c+s}}{m_s} \left(\frac{f_{c+s}}{f_s} \right)^2 - 1 \right] \frac{t_s}{t_{c+s} - t_s} \quad [14.15]$$

E_s is determined by the resonant frequency of the bar after the coating is removed and E_c could be deduced by the change in resonant frequency and sample dimensions between the composite beam with and without the coating.

A testing system was set up based on the resonant frequency and composite beam theory. The system, shown in Fig. 14.1, consists of a high-temperature furnace, a signal generator and a pair of hanging strings, together with DASP2005 signal processing software and so on. This system is able to measure the Young's modulus of the film of composite beam and laminate at room temperature or at high temperature. The highest temperature bearable for the furnace is up to 1300°C.



14.1 Young's modulus testing system.



14.2 Specimens for oxidation experiment: (a) 1Cr18Ni9Ti substrate with no TBC; (b) specimens with TBC.

Antioxidative properties are a key material parameter. If the substrate is oxidized, the resonance frequencies values will not be accurate. The substrate used for the TBC system was 1Cr18Ni9Ti stainless steel, which is a kind of austenitic refractory steel extensively applied in many fields.¹⁸ A 1Cr18Ni9Ti stainless steel plate was cut using a wire cutting machine, polished by abrasive paper for degreasing and derusting and treated by sand blasting so as to reach a specified roughness. These samples were shorter than those for measuring Young's modulus.

The oxidation of the substrate was designed and carried out at a temperature of 200°–1150 °C. The oxidation weight of the specimens was close to zero. The substrates after the oxidation experiment and without TBCs are shown in Fig. 14.2a. The experiment shows that, the 1Cr18Ni9Ti stainless steel could be manufactured for use as the TBC substrate material. Specimens with TBCs are shown in Fig. 14.2b. After 2 h of testing using resonance frequencies, the ceramic top coat did not detach from the substrate and the experiment could be considered a success.

Table 14.1 Young's modulus under different temperatures

T (°C)	20	100	200	300	400
E (GPa)	62.5	59.6	55.7	50.3	44.9
T (°C)	600	800	900	1050	1150
E (GPa)	29.8	22.2	21.5	19.8	18.6

Three specimens were fabricated with ceramic top coat. The resonance frequencies of the specimens were obtained at room temperature up to 1150°C, and every specimen was tested three times at each temperature. The average Young's modulus of the ceramic top coat is shown in Table 14.1, in which the Young's modulus decreases as the temperature increases. From room temperature to 800°C, the Young's modulus decreases rapidly. However, at temperatures above 800°C, it decreases slowly.

Evaluation of thermal conductivity for the top coat

Thermal spraying is a process whereby a stream of molten droplets impacts on the substrate followed by flattening, rapid solidification and cooling processes. The individual molten droplets spread to thin lamellae, the stacking of which constitutes the deposit.¹⁹ Thermally-sprayed coatings generally have a lamellar structure. The properties of a thermally sprayed coating depend on its microstructure which, in turn, depends on the spraying process used. The relationship between the properties and structure of a coating is of key importance in determining whether a desirable coating can be produced. For the top-coat of a TBC system, the fundamental microstructural property may be the porosity. Currently, evaluation of porosity volume is the major analytical method for TBC microstructure.^{20,21}

The TBC system under evaluation was a two-layer material system consisting of a 7–8% Y_2O_3 – ZrO_2 top coating insulator over a CoNiCrAlY bond coat. The substrate material was 1Cr18Ni9Ti stainless steel. The McPherson model was used to study the relationship between the deposit structure and thermal conductivity properties in this work. The relative thermal conductivities can be derived by the following equation:²²

$$\frac{\lambda_c}{\lambda} = \frac{2\alpha}{\pi} \frac{\delta}{a} \left(1 + \frac{2\alpha\delta}{a\pi} \right)^{-1} \quad [14.16]$$

where λ_c and λ are thermal conductivities of deposit and splat materials, α indicates the bonding ratio between lamellae, δ indicates the mean lamellae thickness and a indicates the size of bonding region. Obviously, the thermal conductivity also depends on the geometric dimensions of bond region.

Table 14.2 Thermal conductivity of topcoat under high temperature

T (°C)	20	800	900	1000	1100
λ_c (W/mK)	0.59	0.84	0.91	0.99	1.18

The relationship between the microstructural parameters and the thermal conductivity was demonstrated experimentally. The mean lamellar thickness $\delta = 9.12 \mu\text{m}$, can be obtained by microscopic image test using a scanning electron microscope. Some parameters of equation [14.16] are $\alpha = 0.32$ and $a = 3.62$. The thermal conductivity of 6–8% $\text{Y}_2\text{O}_3\text{-ZrO}_2$ is given in Table 14.2. The thermal conductivity at high temperature is higher than that at room temperature, the maximum relative value being 50%.

14.2.4 Finite element method (FEM) calculation and analysis

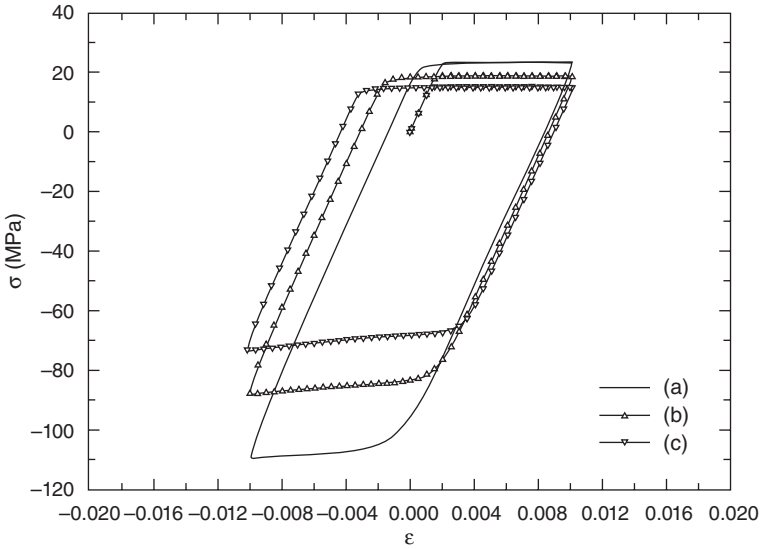
Although ABAQUS is a complete material library, the advanced constitutive equation cannot be modified in the ABAQUS/CAE interface. However, CAE software provides a development function allowing users to add a user-defined material model (UMAT) in order to find accurate solutions to their practical problems. Three constitutive equations were developed in FORTRAN for APS, EB-PVD and metallic substrate, respectively.

Simulation for the top coat

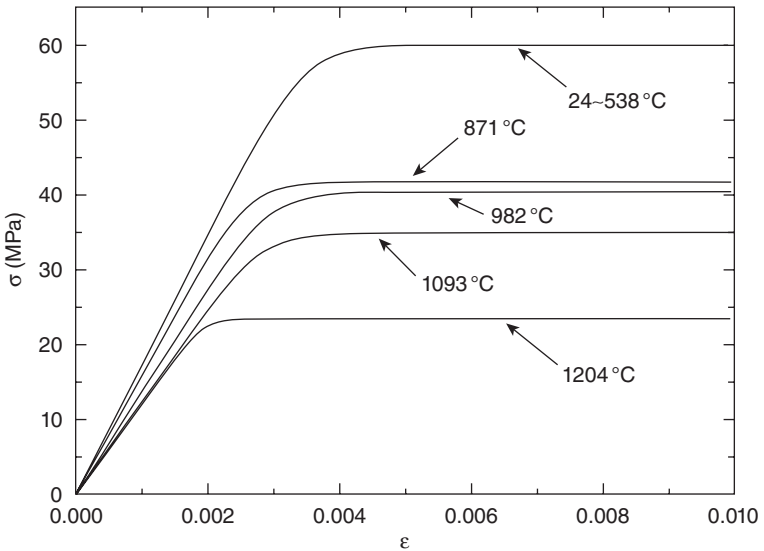
Regarding the APS top coat, the Willam–Warnke model has the ability to describe the non-equal yield stresses in compression and tension for the top coat while incorporating strain rate dependency under high temperature. A FORTRAN program was implemented for the UMAT subroutine in ABAQUS, and the resulting developed UMAT code was successfully applied to describe the complex mechanical behaviors of material under high temperature. The material constants were from references.⁸ Some simulation results are shown in Figs. 14.3, 14.4 and 14.5.

Simulation for DZ40M superalloy

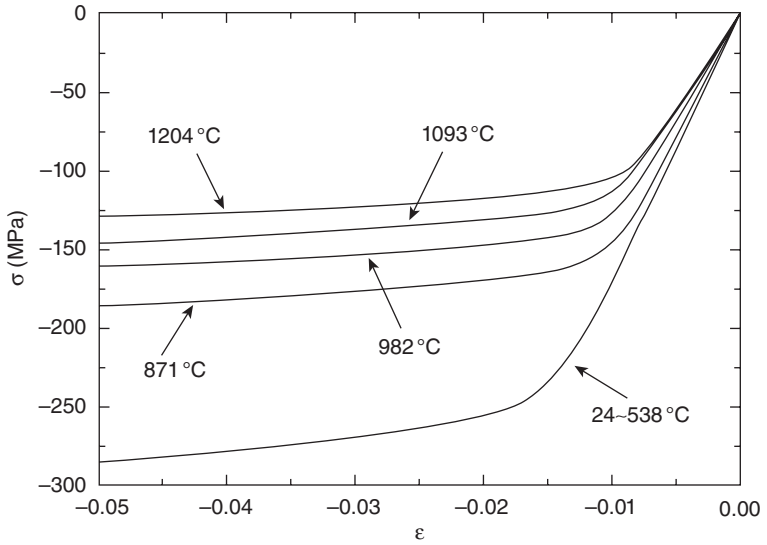
Because the Chaboche viscoplastic constitutive model is able to simulate the monotonic and cyclic behaviour of DZ40M relatively well, an ABAQUS UMAT subroutine was developed to implement it. Some comparisons are given in Figs. 14.6 and 14.7, which show advanced non-linear and anisotropic behaviour at 500°C and cyclic behavior at 900°C.



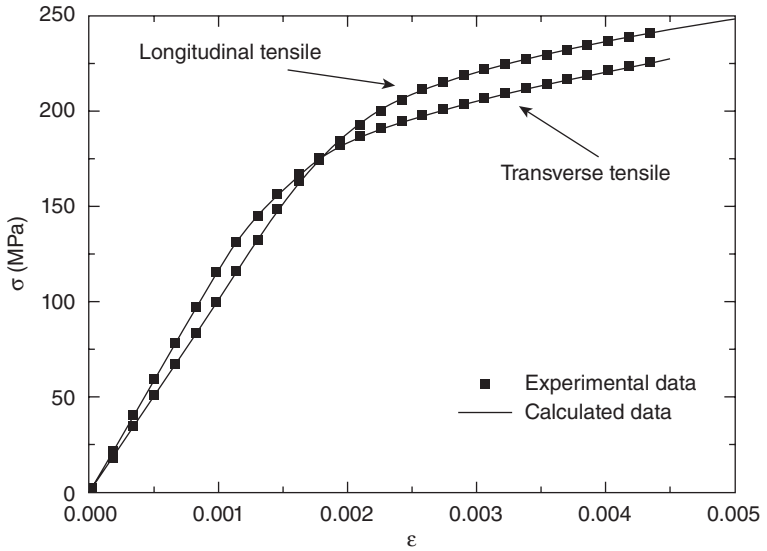
14.3 Stress–strain curves under incorporating strain rate dependency: (a) strain rate 1.0×10^{-3} ; (b) strain rate 1.0×10^{-4} ; (c) strain rate 1.0×10^{-5} .



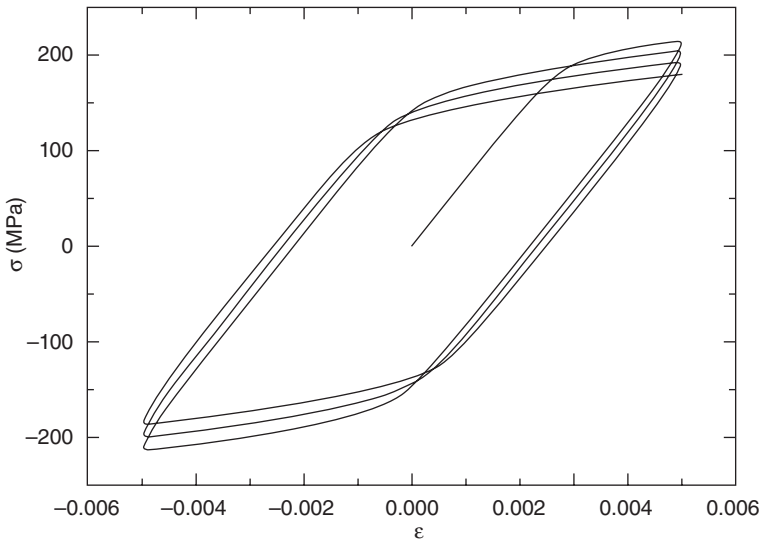
14.4 Monotonic tensile curves under strain rate 1.0×10^{-3} .



14.5 Monotonic compressive curves under strain rate 1.0×10^{-3} .



14.6 Monotonic tensile stress–strain curves under 500 °C.



14.7 Cyclic behaviour under 900 °C.

14.3 Life prediction for TBCs

14.3.1 Life prediction model

Phenomenological fatigue life model

Based on the Manson–Coffin model, the prediction model is as follows:

$$N_f = (\Delta\epsilon / \Delta\epsilon_f)^{-b} \tag{14.17}$$

where N_f is number of cycles to failure, $\Delta\epsilon$ is strain range, $\Delta\epsilon_f$ is critical strain range and b is a material parameter.

Oxidation will be considered in this model due to its key significance. When bond coating was oxidized for different lengths of time, $\Delta\epsilon_f$ decreased with the increase in TGO thickness and this value changed from $\Delta\epsilon_{f0}$ to $\Delta\epsilon_f$. The equation is as follows:²³

$$\Delta\epsilon_f = \Delta\epsilon_{f0} \left(1 - \frac{\delta}{\delta_c} \right)^c + \Delta\epsilon \left(\frac{\delta}{\delta_c} \right)^c \tag{14.18}$$

where δ is TGO thickness, δ_c is critical TGO thickness when TBC cracks are caused by oxidation only and c is a material parameter. Therefore, the life prediction model for TBCs is as follows:

$$N_f = \left[(\Delta\epsilon_{f0} / \Delta\epsilon) \left(1 - \frac{\delta}{\delta_c} \right)^c + \left(\frac{\delta}{\delta_c} \right)^c \right]^{-b} \tag{14.19}$$

For Eq. [14.19], the parameters with the exception $\Delta\epsilon_f$ and δ_c , are determined by thermal testing and $\Delta\epsilon$ is obtained by finite element analysis. The thermal fatigue life could be obtained by using Miner linear cumulative damage theory.

This approach, used by General Electric Company, employed time-dependent, non-linear finite element modeling of the stresses and strains present in the APS TBC. The modified model is expressed as:²⁴

$$\Delta\epsilon_{RZ} + 0.4\Delta\epsilon_R = 0.121N_f^{-0.486} \quad [14.20]$$

where $\Delta\epsilon_{RZ}$ is the shear strain range, $\Delta\epsilon_R$ is the normal strain range and N_f is the number of cycles to failure. The subscripts R and Z represent two directions for the cylindrical coordinate system. The model is the only one to consider failure induced by edges.

An EB-PVD ceramic has a columnar structure as a result of the vapor deposition process. Failure in an EB-PVD TBC occurs in the TGO layer adjacent to the metallic bond coating. Compared to the failure mechanism of APS TBC, this model has extended the life prediction of the EB-PVD coating. On the other hand, the strain range of TGO will be adopted as an important parameter in the fatigue model.

Fatigue model based on imperfections

With respect to the imperfections in TBC system, the driving stress used for predicting cracking and failure is written as follows:²⁵

$$\sigma_c = \frac{E(\epsilon_g - 1)}{2(1-\nu)\epsilon_g} \left(\frac{h}{R} \right) \quad [14.21]$$

where E is Young's modulus, h is the TGO thickness and ϵ_g is growth strain at highest temperature. By equating the crack diameter $2R$ to the spacing $2d$ between imperfections, a critical TGO thickness, h_c yields

$$h_c = \frac{2\sqrt{\pi}(1-\nu^2)\epsilon_g d^{3/2} K_{Ic}}{(\epsilon_g - 1)RE} \quad [14.22]$$

where K_{Ic} is the stress intensity factor. According to the kinetic oxidation model, the failure time is given by

$$t_f = h_c^2 / 2k_p \quad [14.23]$$

where k_p is the parabolic rate constant, which is a strong function of temperature and optimized using static oxidation experimentation. If the cyclic behavior $d\Delta_R/dN$ is specified, the fatigue model is as follows:

$$N_f \approx \frac{2\sqrt{\pi}(1-\nu^2)d^{3/2} K_{Ic}}{E(d\Delta_R/dN)L} \quad [14.24]$$

In this formula, E is the Young's modulus of the TBC with wavelength $2L$ imperfection and ν is Poisson's ratio. The fatigue model has two features: (i) the model is based on microstructural imperfection and renders the physical meaning of failure mechanism more obvious; (ii) the parameters such as $d\Delta_R / dN$ which are required for TBC thermal fatigue experimentation are difficult to obtain. Further study is required for thorough verification of the model.

Some other models based on fracture mechanics utilize such concepts as time-dependent interface toughness and strain energy release rate, with the emphasis placed within the TGO or at the TGO/bond coat interface. The durability of the TBC is controlled by the energy density in the TGO and the formation or presence of imperfections in the vicinity of the TGO.

Fatigue model based on damage mechanics

Busso quantified the effects of different microstructural variables and service conditions on the local stresses induced by oxidation, sintering processes and thermal cycling in a typical PS TBC system. The driving force $\sigma_{22\max}$ was combined with a damage mechanics approach. Two boundary conditions for this fatigue model were set as $D = 0$ at the beginning of thermal cycling and $D = 1$ at thermal fatigue failure. The continuous evolution of microscopic damage with thermal cycles is given by^{26,27}

$$dD = \hat{D}\{\sigma_{22\max}, \bar{\sigma}_{22\max}, D\}dn \quad [14.25]$$

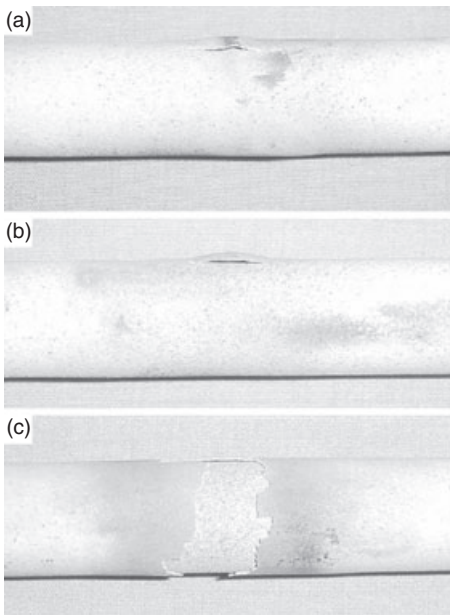
where n is the number of cycle under a load case, and can be expressed in functional form in terms of the maximum cycle stress, $\sigma_{22\max}$, the mean cycle stress, $\bar{\sigma}_{22\max}$, and the current microscopic damage state, D . This model was suitable only for measuring the thermal fatigue load.

14.3.2 Life prediction for plasma sprayed PS thermal barrier coatings

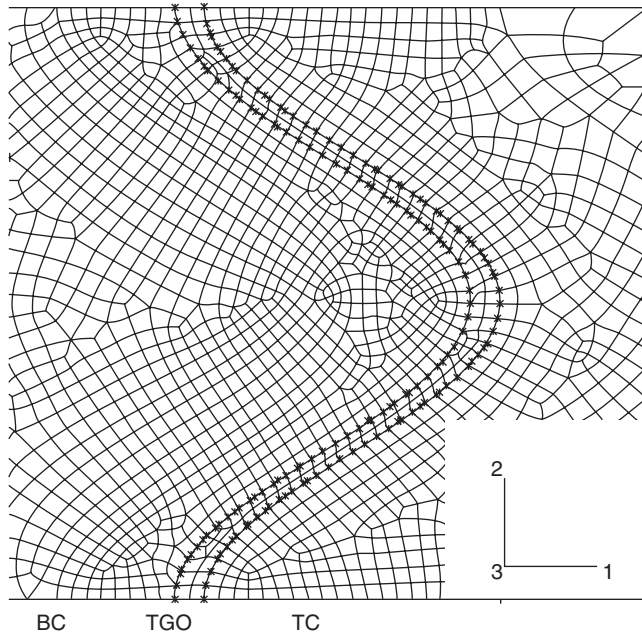
In order to set up a fatigue model for APS TBC, thermal fatigue experiments were designed. The load case was designed using rapid heating (120 s) and rapid cooling (300 s), simulating the shut down of a turbine engine. By using induction heating and air compressor technology, the APS TBC structure was heated to 1050 °C and cooled to 100 °C.

Instead of a vane, hollow cylindrical specimens were designed with internal radius 11 mm, external radius 15 mm and length 80 mm. The specimens were APS coated with the zirconia–yttria (6%–8% Y_2O_3 – ZrO_2) on a nickel–chromium–aluminum (Ni22Cr10Al1.0Y) bond coat. The metal substrate was Ni-based superalloy (DZ40M). The ceramic layer was 0.250 mm thick while the bond coat was 0.125 mm thick.

Using macroscopic images and FEM simulation, the damage evolution of the TBC could be summarized as follows. Under thermal fatigue load, cracks nucleated in the TBC, which were initially in-plane Mode I and Mode II or mixed-mode tangential cracks. The crack in the ceramic layer was driven primarily by the normal stress or the in-plane shear stress. If the compressive stress along the axial direction occurs at the same time, then these cracks link together and protrusion occurs as shown in Fig. 14.8a. Due to induction heating, the length of the heated specimen is finite. The part far away from the heated section will provide displacement constraint similar to plane-strain constraint. Meanwhile, a temperature gradient exists along the axial direction. An axial compressive stress results from the temperature gradient along the axis of the specimen and a mismatch in the structure. Based on the protrusion, the ceramic layer will buckle as shown in Fig. 14.8b. On the other hand, it should be noted that the circular stress in the specimen could be compressive stress. However, the temperature gradient along the circular direction is close to zero, so it is impossible for these specimens to be buckling. Simultaneously, the axial direction of the specimens is sufficiently long compared to the diameter (circular direction). The buckling phenomenon is not only a function of force but also of distance; thus the buckling does not occur along the circular direction. Finally, TBC spallation occurs along the axial direction as shown in Fig. 14.8c.



14.8 Failure mode of APS TBC under thermal fatigue: (a) protrusion; (b) buckling; (c) spallation.



14.9 FEM model for TBC.

In order to consider the TGO thickness and interface, the interface morphology is conceptualized as a periodic array of wavy-type segments characterized by co-sinusoidal interface in a FEM model. This interface between the bond coat and the ceramic top coat is introduced, with a period as well as peak-to-valley amplitude of 0.01 mm and peak-to-peak dimensions up to 0.04 mm. An axisymmetric model of this specimen was set up in Fig. 14.9. By introducing a co-ordinate system, an orthonormal basis {1, 2, 3} was defined, where directions 1, 2 and 3 denote the normal, axial and circular direction, respectively.

Many TBC life models were based on the assumption that oxidation and thermal strain range are important factors limiting the lifetime of the coating. The strain range was always defined as the equivalent strain range, such as axial strain or shear strain range. According to the failure mechanism and coupling different strain ranges, a life model for TBC was set up in the present work:

$$N = \left[\left(\frac{\Delta\epsilon_{t0}}{\Delta\epsilon_{RZ} + a\Delta\epsilon_Z} \right) \left(1 - \frac{\delta}{\delta_c} \right) + \left(\frac{\delta}{\delta_c} \right) \right]^b \quad [14.26]$$

where $\Delta\epsilon_{RZ}$ and $\Delta\epsilon_Z$ are the shear and axial strain range at critical location and δ is TGO thickness at any N th cycles. a , b , $\Delta\epsilon_{t0}$ and δ_c are parameters of this model. The fatigue life was predicted by the linear cumulative

damage hypothesis. According to this rule, the fatigue damage was $D_m = 1/N_m$ after one cycle. Applying n_m cycles with thermal fatigue load k and corresponding fatigue life endurance N_m is equivalent to overall damage $D = \sum_{m=1,k} n_m \cdot D_m = \sum_{m=1,k} n_m/N_m$. When the criterion $D \geq 1$, spallation failure of the top coat occurs. The parameters of the fatigue predictive model were optimized and are listed in Table 14.3 and the predicted lives for APS are listed in Table 14. 4.

14.3.3 Life prediction for EB–PVD thermal barrier coatings

EB–PVD specimens with the same geometry size as APS samples were coated with zirconia–yttria (6–8 % Y_2O_3 – ZrO_2) on a nickel–chromium–aluminum (Ni22Cr10Al1.0Y) bond coat. The metal substrate was Ni-based superalloy (DZ40M). The ceramic layer was 0.125 mm thick while the bond coat was 0.07–0.08 mm thick. The load-case consist of a 2.5 min heating from room temperature to 1150 °C, a holding time of 0.5 min and a cooling time of 4.5 min.

As a result, the EB–PVD coating was reported to be more strain-tolerant in the direction perpendicular to the columns (in-plane coating direction) and thus more resistant to crack growth compared with the PS coatings. Another difference was the morphology of the bond coat/top coat interface, mechanical adhesion for PS and chemical adhesion for EB–PVD. The top coat/bond coat interface has been modified by EB–PVD processing.

The failure location of EB–PVD TBCs was within the TGO (usually Al_2O_3) that formed between the ceramic coating and the bond coating. In

Table 14.3 Parameters for the fatigue life model

a	b	$\Delta\varepsilon_{f0}$	δ_c
2.202	3.751	0.087	0.058

Table 14.4 Thermal fatigue data of APS

Specimen	Pre-oxidation time (h)	Lifecycle	Predicted lifecycle
PL100a	100	430	398
PL100b	100	350	398
PL200a	200	280	306
PL200b	200	380	306

other literature, the failure location was in the TGO/bond coat interface. The failure mode of EB–PVD TBCs under cyclic thermal load is shown in Fig. 14.10. Compared with APS TBC, this difference in failure mechanism can primarily be attributed to the difference in the microstructure of the TBC. The EB–PVD TBC interface is relatively smooth, so the stress concentration is correspondingly small. Therefore, the stress or the strain state in the TGO is important and should be focused on. Because the TGO is very thin (less than 0.1 mm) and usually remains elastic during the load case, it is difficult to obtain the strain range from finite element analysis (FEA). It is assumed that the TGO has a negligible influence on mean stress/strain of the bond coating. The TGO strain will be determined based on the bond coating. The mean stress/strain can be obtained from FEA analysis. The formula for TGO strain calculation can be obtained as follows. First, the TGO expansion strain is given by:

$$\epsilon = \frac{\delta L(T)}{L} = \int_{T_{sf}}^T \alpha(T) dT \quad [14.27]$$

where T is temperature and T_{sf} is the stress-free temperature. Assuming that the expansion parameters of Al_2O_3 change linearly with temperature, the TGO strain is:

$$\epsilon_{(T)} = \epsilon_{ss(T)} - \epsilon \frac{\delta L(T)}{L} \quad [14.28]$$

Where $\epsilon_{ss(T)}$ is strain of bond coating. For a cyclic load, the evolution of bond coating strain at given temperature can be calculated using FEA analysis. Then by using Eqs. [14.27] and [14.28], the evolution of TGO strain and the strain range can be obtained. The predicted lives are listed in Table 14.5.



14.10 Failure mode of EB–PVD TBC under thermal fatigue.

Table 14.5 Thermal fatigue data of EB-PVD

Specimen	Pre-oxidation time (h)	Lifecycle	Predicted lifecycle
EB50a	50	202	226
EB50b	50	250	226
EB100a	100	145	173
EB100b	100	200	173

14.3.4 Life prediction for the vane with TBCs

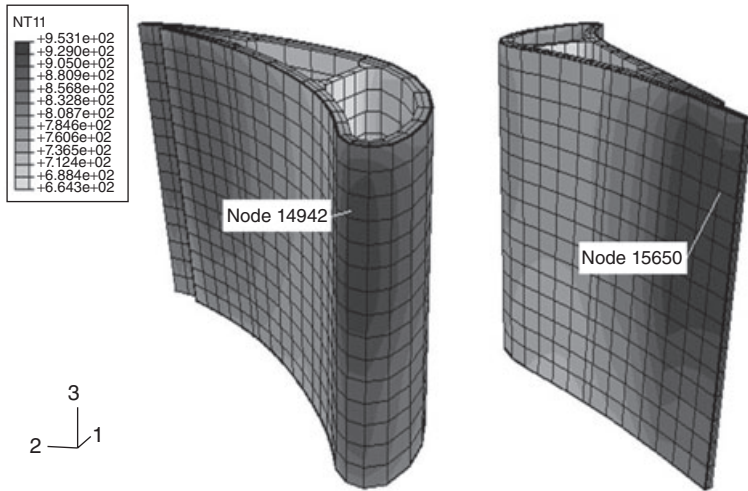
In order to analyze the local stress–strain field, a sub-model method, which is included in commercial FEM code, is always used for large and complicated structures such as a vane which has a twist in its shape from the root to the end and a body which is thin and uneven at different positions. However the sub-model is not suitable for a vane with TBC because the top coat and bond coat are meso-scale. The sub-model will comprise a great many meshes for a part of a vane with TBC. So it is necessary to establish an equivalent way in which macro-scale stress state and meso-scale will link each other.

First, a cylinder-shaped sample with different inner radius was simulated in meso-scale. The results showed that different radius could not affect the stress–strain fields close to the interface. In other words, the sections at the leading and trailing edge could be assumed as samples with different radius. Thus the stress–strain field at the leading and trailing edge could be neglected, which results in different radius.

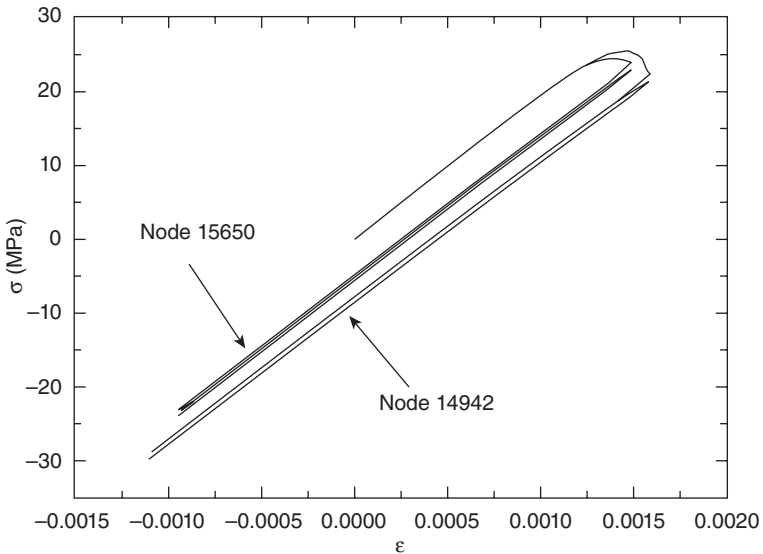
Secondly two interfaces (such as straight and cosine interface) between top coat and bond coat were simulated for TBC. The local field close to the interface and that far away from the interface were defined as ‘near-field’ and ‘far-field’, respectively. Compared to the results of macro-scale and different interfaces, there is a proportional factor to the strain range in near-field and far-field.

The vane TBC was modelled and meshed using solid elements. The ceramic top coat was meshed into two through-thickness layers with 1100 elements. The bond coat was meshed into one layer with 550 elements. Because the TGO thickness is very small, the interface between top coat and bond coat was neglected.

The initial state was set as 400°C, a temperature at which the vane is in a stress-free state. The boundary conditions were applied to fix the inner root of the vane. The heating and cooling times were 155 s and 109 s, respectively. The two cyclic thermal mechanical behaviors of the vane were simulated by the constitutive equation mentioned above.



14.11 Critical locations at leading and trailing edge.



14.12 Cyclic behavior of two critical locations.

The temperature field of the vane with TBC is shown in Fig. 14.11. Generally, failure will occur at the top coat. Nodes 14942 and 15650 at the leading and trailing edge were selected as the critical locations for the vane with TBC. The ceramic stress–strain behavior was calculated for two cycles as shown in Fig. 14.12. After the second cycle, the cyclic behavior is stable.

According to the fatigue model and Miner's law, the predicted life at the leading and trailing edge was 334 h and 255 h, respectively.

14.4 Future trends

1. Life prediction methodology for the failure of the PS TBC under thermal fatigue loading condition has been studied in the previous work. There are two primary goals in developing semi-empirical models: (i) to include correct variables such as mechanical strain range; (ii) to quantify models for some processes, especially with regard to oxidation behavior. The weight gained and thicknesses at high temperature were adopted by the NASA life model to describe oxidative damage. However, this describes only the diffusion of Al in bond coat towards the bond coat surface. In order to quantify oxidation damage totally, it is necessary to include the diffusion of Al towards the substrate. Our results confirm that microstructural evolution is controlled by the diffusion of Al towards the substrate as well as towards the TBC. A mathematical model of Al depletion has now been presented, which can provide a basis to develop a more accurate life prediction model in further work.
2. For most thermal fatigue experiments, inductive heating was selected for specimens with TBC. During the heating of the specimens, it is very difficult to detect the damage evolution online because the temperature gradient decreases from the outer to the inner edges of the specimens. Although acoustic emission (AE) technology has been used for online damage evaluation and measurement, operating environments are often very noisy and the acoustic emission signals are usually very weak. Thus, signal discrimination can be very difficult, yet it is extremely important for successful applications. The next step is likely to be the design of flame heating methods to reduce acoustic noise.
3. Based on the failure mechanism, the radial strain range was defined as an important parameter in the NASA life model. Presently, effective strain range is defined as axial strain, coupled shear and radial strain, respectively. In the future, more effective use will need to be made of strain range in life prediction.
4. For blades and vanes with APS or EB-PVD coating, different scales means that it is very difficult to measure the strain range at the critical location. Because sub-model technology comprises a great many meshes for a part of a vane and blade with TBC, it should be further studied to find how to calculate the stress-strain field at a critical location.

14.5 Conclusion

The TBC generally consists of a multi-layered structure. Every layer has different constitutive laws because the top coat is brittle material and the bond coat and substrate are ductile material. Viscoplasticity law for top coat and substrate has been developed and integrated in FEM code. The important parameters of the top coat, such as Young's modulus and thermal conductivity, have been tested and obtained at high temperature.

Generally, it has been shown in our work that the failure mechanism of APS TBC is mode I, mode II or mixed. The shear and axial strain range were selected as the parameters for the life model. Compared with the experimental data, the predicted life is considered adequate. For EB-PVD coating, the result is better. However, using those models for blade and vane, many important factors need to be studied further.

14.6 References

1. ZHANG H., SUN K., XU Q. (2009), 'Preparation and thermal conductivity of $\text{Sm}_2(\text{Zr}_{0.6}\text{Ce}_{0.4})_2\text{O}_7$ ceramic', *Journal of Materials Engineering and Performance*, Published online.
2. SHEFFLER K. (1988), 'Current status and future trends in turbine application of thermal barrier coatings', *ASME Journal of Engine for Gas Turbine and Power*, **110**, 605–609.
3. LI W., THOMAS S. (2004), 'An analysis of the indentation test to determine the interface toughness in a weakly bonded thin film coating–substrate system', *Acta Materialia*, **52**, 2989–2999.
4. GOWARD G. (1988), 'Progress in coatings for gas turbine airfoils', *Surface Coating Technology*, **156**, 73–79.
5. TRAEGER F., AHRENS M. (2003), 'A life time model for ceramic thermal barrier coatings', *Materials Science and Engineering*, **A358**, 255–265.
6. RÖSLER J., BÄKER M., VOLGMANN M. (2001), 'Stress state and failure mechanisms of thermal barrier coatings: role of creep in thermally grown oxide', *Acta Materialia*, **49**(18), 3659–3670.
7. CHABOCHE J.L. (1989), 'Constitutive equations for cyclic plasticity and cyclic viscoplasticity', *International Journal of Plasticity*, **5**, 247–302.
8. XIE W., WALKER K.P., JORDAN E.H. (2003), 'Implementation of a viscoplastic model for a plasma sprayed ceramic thermal barrier coating', *Journal of Engineering Materials and Technology*, **125**, 200–207.
9. JANOSIK L.A., DUFFY S.F. (1998), 'A viscoplastic constitutive theory for monolithic ceramics-I', *ASME Journal of Engineering for Gas Turbines and Power*, **120**, 155–161.
10. QI H., MA H. (2008), 'Thermal fatigue of thermal barrier coatings by atmospheric plasma spraying', *Journal of Key Engineering Materials*, **385–387**, 405–408.
11. HAN S.L., LI S.X., SMITH D.J. (2001), 'Comparison of phenomenological and crystallographic models for single crystal nickel base superalloys I analytical identification', *Mechanics of Materials*, **33**, 251–266.

12. GUNTHER H. (1990), 'Comparison of the uniaxial behaviour of the inelastic constitutive models of Miller and Walker by numerical experiments', *International Journal of Plasticity*, **6**, 189–206.
13. FREED A.D., WALKER K.P. (1993), 'Viscoplasticity with creep and plasticity bounds', *International Journal of Plasticity*, **9**, 213–242.
14. RYBICKI E.F., SHADLEY J.R. (1995), 'In situ evaluations of Young's modulus and Poisson's ratio using a cantilever beam specimen', in: Berndt C.C. and Sampath S. (eds), *Proceedings of the 8th National Thermal Spray Conference*, ASM, Materials Park, OH. 409–414.
15. POMEROY M.J. (2005), 'Coatings for gas turbine materials and long term stability issues', *Materials and Design*, **26**, 223–231.
16. JING B.-K., HIDEAKI M. (2005), 'Influence of porosity on hardness and Young's modulus of nanoporous EB-PVD TBCs by nanoindentation', *Materials Letters*, **59**, 3462–3466.
17. TAO L., CHEN F., DING H. (2005), 'Properties of plasma sprayed NiCrAlY + (ZrO₂ + Y₂O₃) coating on refractory steel surface', *Journal Central South University of Technology*, **12**, 246–249.
18. QI H., LI R., YANG X. (2007), 'Thermal fatigue life of thermal barrier coatings', *Journal of Rare Earths*, **25**, 370–374.
19. LI C. (2002), 'Relationship between the microstructure and properties of thermally sprayed deposits', *Journal of Thermal Spray Technology*, **11**, 365–374.
20. STRANGMAN T., RAYBOULD D. (2007), 'Damage mechanisms, life prediction, and development of EB-PVD thermal barrier coatings for turbine airfoils', *Surface and Coatings Technology*, **202**, 658–664.
21. DU Q., LIU X. (2005), 'Thermal barrier coating – thermal conductivity measurement and methods to reduce the thermal conductivity', *Journal of Functional Materials*, **36**, 1100–1106.
22. MCPHERSON R. (1984), 'A model for the thermal conductivity of plasma-sprayed ceramic coatings', *Thin Solid Films*, **112**, 89–95.
23. BOSE S. (2007), *High Temperature Coatings*, Oxford, UK, Butterworth-Heinemann.
24. MILLER R.A. (1988), *Life Modeling of Thermal Barrier Coatings for Aircraft Gas Turbine Engines*, NASA Technical Memorandum 100283, National Aeronautics and Space Administration, Washington DC.
25. EVANS A.G., MUMM D.R., HUTCHINSON J.W. (2001), 'Mechanisms controlling the durability of thermal barrier coatings', *Progress in Materials Science*, **46**, 505–553.
26. BUSSO E.P., LIN J., SAKURAI S. (2001), 'A mechanistic study of oxidation-induced degradation in a plasma-sprayed thermal barrier coating system. Part I: model formulation', *Acta Materialia*, **49**, 1515–1528.
27. BUSSO E.P., LIN J., SAKURAI S. (2001), 'A mechanistic study of oxidation-induced degradation in a plasma-sprayed thermal barrier coating system, Part II: life prediction model', *Acta Materialia*, **49**, 1529–1536.

New materials, technologies and processes in thermal barrier coatings

H. XU and J. WU, Beihang University, China

Abstract: To meet the demand for advanced turbine engines, new materials and new manufacturing technologies for thermal barrier coatings (TBCs) applications have been sought. Ceramic materials with high operating temperature capabilities and other excellent thermo-physical and mechanical properties have been investigated by materials researchers, with the purpose of replacing the currently used yttria stabilized zirconia (YSZ). Also, several novel processing methods have been proposed recently by researchers to develop more reliable and durable TBCs.

Key words: thermal barrier coatings (TBCs), turbine engines, temperature capability, thermo physical property.

15.1 Introduction

Thermal barrier coatings (TBCs) are widely used in gas turbines to increase the turbine inlet temperature (TIT) or to reduce cooling requirements, thus achieving higher engine efficiency, lowering emissions and increasing performance goals.¹⁻⁵ Currently, commercial standard TBCs are typically two-layered structures, consisting of a ceramic top coat and a metallic bond coat deposited onto a superalloy substrate. The actual thermal barrier is the ceramic top coat with the prime function of reducing the transfer of heat to the metallic substrate. Owing to its excellent mechanical, chemical and thermal properties, 7–8 wt% (4–4.5 mol%) yttria stabilized zirconia (YSZ) is the primary industrially employed TBC, usually applied either by plasma spraying (PS) or electron beam physical vapor deposition (EB-PVD), producing characteristic microstructures with certain desirable attributes.⁶⁻¹⁰ While PS leads to the pores between the splats being oriented parallel to the substrate surface, revealing lower thermal conductivity ($0.8\text{--}1.1\text{ W}\cdot\text{m}^{-1}\cdot\text{K}^{-1}$), the columnar grain microstructure created by the EB-PVD process contains channels between the columns and pores within the grains which are oriented perpendicular to the substrate surface, exhibiting a higher thermal conductivity ($1.5\text{--}1.9\text{ W}\cdot\text{m}^{-1}\cdot\text{K}^{-1}$). Conversely, the columnar distribution of the grains allows an increase strain tolerance and, hence, EB-PVD TBCs present greater durability compared to PS TBCs.

Nevertheless, the YSZ coatings, together with a considerable increase in these effects at 1200 °C and above, which affects the reliability and service life of the TBCs, suffer from both phase transformation and sintering, even at temperatures as low as 1100 °C.^{11–13} Therefore, different strategies are being investigated to replace the current YSZ coatings in order to develop more durable and reliable TBCs.^{14–17} The approaches can be broadly classified as chemically modified YSZ,^{18–30} novel alternate low thermal conductivity (κ) materials and microstructural modifications. Additionally, advanced processing technologies to produce TBCs with tailored microstructure are also essential. They will be addressed in more detail below.

15.2 Chemically modified yttria stabilized zirconia (YSZ)

A key physical property of the ceramic top coat is its thermal conductivity (κ). Use of an appropriate dopant introduces vacancies due to the different valences of the host atoms. It also strains the lattice because of different atomic sizes. Both of these phenomena reduce the mean free path of the phonon scattering. Instead of one (yttria), the addition of two or more dopants to stabilize zirconia, i.e. chemically modified YSZ, is then expected to incorporate a substantial amount of vacancies, providing an efficient source of scattering phonons with lower κ .

Schulz *et al.* prepared ZrO_2 -25 wt% CeO_2 -2.5 wt% Y_2O_3 (CeSZ) TBCs by EB-PVD. The CeSZ has a lower thermal conductivity than YSZ and, at the same time, presents good corrosion resistance and superior phase stability at high temperature. Cyclic tests carried out in a furnace at 1100 °C showed a higher thermocyclic resistance and a longer lifetime of CeSZ TBC compared to YSZ TBC.^{24–25}

Nicholls *et al.* evaluated dopants including nickel oxide (NiO), neodymia (Nd_2O_3), gadolinia (Gd_2O_3), erbia (Er_2O_3) and ytterbia (Yb_2O_3) as both ternary and quaternary additions. It was found that Gd_2O_3 , Nd_2O_3 , Er_2O_3 and Yb_2O_3 lowered κ of zirconia-4.5 mol% yttria (8 wt% yttria) when added at a 4 mol% level. NiO, the only divalent oxide addition used, produced only a small decrease. Er_2O_3 (4 mol%) reduced κ by 25% and colored the ceramic pink; Nd_2O_3 (4 mol%) lowered κ by 42% and colored the ceramic blue. The best system, Gd_2O_3 , resulted in a thermal conductivity of $0.88 \text{ W}\cdot\text{m}^{-1}\cdot\text{K}^{-1}$ (a 47% reduction), achieving thermal conductivities comparable to PS TBCs in an EB-PVD system. In all cases, the ceramic crystal structure remained t prime phase, and the modified EB-PVD TBCs had a columnar microstructure.^{26,28}

Zhu and Miller developed the multiple co-doping of TBCs, being designated as ‘defect cluster systems’ and typically comprising Y plus two other cations, one smaller (Yb, Sc) and one larger (Sm, Nd, Gd). They found that

YSZ and YSZ with one or more dopant show typically higher κ than the coatings of $\text{ZrO}_2\text{-Y}_2\text{O}_3$ with paired dopant additions. The total dopant concentration affects κ as well. A low κ regime was observed for the PS TBCs in the range 6–15 mol% total dopant concentration and about 10 mol% for the EB–PVD coatings. The multicomponent oxide clustering coatings were thermally cycled at 1160 °C and showed better cyclic lives than YSZ at the given dopant concentrations. The coating cyclic life generally decreases with increase in the total concentration. It was proposed that these added dopant oxides effectively promote the creation of thermodynamically stable, highly defective lattice structures with essentially immobile defect clusters and/or nanoscale ordered phases, thus reducing κ and improving coating sintering resistance.^{29,30}

15.3 Alternate low thermal conductivity (κ) materials

15.3.1 Fluorite oxides

Fluorite oxides as candidates of TBCs mainly include HfO_2 , CeO_2 and ThO_2 . Although CeO_2 is not a practical choice because of its volatilization, reduction of CeO_2 into Ce_2O_3 and the accelerated sintering rate of the coating at elevated temperatures,^{31–33} it has higher coefficient of thermal expansion (CTE) and lower (κ) than YSZ. Fluorite lanthanum cerate ($\text{La}_2\text{Ce}_2\text{O}_7$), which is a solid solution of La_2O_3 in CeO_2 , does not present phase transformation after long-term annealing at 1400 °C and, at the same time, has a large TEC that is close to that of the bond-coat layer even at high temperature. Thermal cycling testing indicated that the single $\text{La}_2\text{Ce}_2\text{O}_7$ (LC) coating has a thermal cycling life comparable to the conventional YSZ coating and in addition the $\text{La}_2\text{Ce}_2\text{O}_7/8\text{YSZ}$ double-ceramic-layer (DCL) systems showed improved thermal cycling life.^{34–36}

HfO_2 -containing compositions have been widely investigated, both ZrO_2 -based and ZrO_2 -free materials.^{37–39} It has been found that $\text{HfO}_2\text{-Y}_2\text{O}_3$ TBCs display thermal cycling resistance comparable to 7YSZ, but at higher Y_2O_3 compositions of up to 27 wt% when the crystal structure is fully cubic phase.³⁸ The lowest thermal conductivity determined at 1316 °C has been obtained for ZrO_2 -free 25 wt% Y_2O_3 -stabilized HfO_2 , with a value of $1.1 \text{ W}\cdot\text{m}^{-1}\cdot\text{K}^{-1}$, which also has a low rate of conductivity increase, and good sintering resistance, as compared with YSZ.³⁹

15.3.2 Zirconate pyrochlore oxides ($\text{RE}_2\text{Zr}_2\text{O}_7$)

Rare earth (RE) zirconate pyrochlores ($\text{RE}_2\text{Zr}_2\text{O}_7$) are of interest for use as TBCs due to their lower thermal conductivities than YSZ and thermal stability at high temperatures.^{16,40–43} It has been found that the thermal

conductivities at temperatures between 700 °C and 1200 °C for zirconates of Gd, Eu, Sm, Nd and La are in a range 1.1–1.7 W·m⁻¹·K⁻¹, which is significantly below that of 7YSZ.^{16,42,44–47} However, their CTEs are much lower than those of the metallic bond coat materials, which induced a reduction in the TBC thermal cycling properties. A double and graded layered TBC structure of La₂Zr₂O₇/YSZ has been developed to overcome that problem, offering the potential for TBCs at temperatures higher than 1250 °C.^{16,48,49}

15.3.3 Lanthanum hexaluminate (LaMgAl₁₁O₁₉, LHA)

Lanthanum hexaluminate (LaMgAl₁₁O₁₉, LHA), which displays the magnetoplumbite structure, crystallizes in the habit of platelets. The magnetoplumbite structure is characterized by the highly charged La³⁺ cation located in an oxygen position in the hexagonal close-packed structure of oxygen ions. Ion diffusion is strongly suppressed vertical to the crystallographic *c*-axis, thus hindering sintering densification. The low thermal conductivity of LHA is caused by its microstructure, i.e. a random arrangement of LHA platelets that build up a well-balanced microporous coating and the insulating properties of the material with its crystallographic feature. LHA is considered to be a promising competitor to YSZ for operations above 1300 °C since the crystalline phase is stable to at least 1300 °C and its plate-like structure enables excellent ageing behavior at 1300 °C (eight-fold less shrinkage than that of YSZ).^{50–52}

15.3.4 Nanocrystalline materials

Nanocrystalline materials offer the potential of limiting thermal conductivity by incorporating grain boundary scattering as an extrinsic phonon-scattering phenomenon. Additional benefits are provided for TBC applications because of the possibility of improving toughness and ductility compared to that of coarser-grained ceramics.^{53–55}

Soyez *et al.* evaluated the thermal conductivity of nanocrystalline YSZ films as prepared by metal-organic chemical vapour deposition (MOCVD). A significant reduction in thermal conductivity in these films compared to that of bulk YSZ is observed for grain sizes smaller than the phonon mean free path, and the observed changes in thermal conductivity are more likely to be attributable to the effects of grain size than the porosity.⁵⁶

Nanocrystalline YSZ TBCs were subsequently investigated using standard plasma-spraying technology.^{57–73} It was found that nanostructured YSZ TBCs possessed higher hardness, higher CTE, lower thermal diffusivity and better thermal shock resistance compared to conventional TBCs, although the grain size tended to increase during annealing at elevated temperatures, which could result in substantial degree of sintered density. These results

demonstrated potential benefits of grain refinement to the nanometer scale in TBC applications, but also indicated that extremely small grain sizes will need to be produced and stabilized against grain growth in order to obtain significant improvements in thermal property.

15.4 Microstructure modification

Considerable efforts have been made to develop EB-PVD TBCs with lower thermal conductivity and PS TBCs with improved strain tolerance by microstructural modification through advanced processing technologies. They are summarized below.

15.4.1 Electron beam physical vapor deposited thermal barrier coatings (EB-PVD TBCs)

EB-PVD TBCs have three main porosity features.⁷⁴ Columns and inter-columnar gaps (type I) lead to an in-plane anisotropy which has a significant impact on the strain tolerance of the EB-PVD TBC system.^{75–79} The other two arrangements of intra-columnar pores, aligned spherical pores (type II) and random spherical pores (type III), are much more effective at impeding heat flow through the coating as they are generally inclined to the heat flow direction.⁷⁴ According to this, the changes in the parameters of the deposition process lower the thermal conductivity of TBCs by modifying the pore microstructure in the top coat. For instance, a decrease of 15% in YSZ thermal conductivity has been obtained by increasing the chamber pressure and decreasing the substrate temperature.⁸⁰ More remarkable is the 40% reduction reached with a modified microstructure based on inclined columnar growth, known as the ‘zig-zag’ or ‘herringbone’ structures, varying the vapour incidence from the normal direction.^{81,82} Nevertheless, the erosion resistance decreases with the column angle and, therefore, depending on the specific application of the component, a compromise between the thermal conductivity and the erosion resistance will be necessary.

Recently, a new tailored microstructure of EB-PVD 8YSZ TBC has been proposed.⁸³ By periodically interrupting the condensing vapor during the deposition process to create strain fields, the phonon and photon scattering processes can be enhanced, leading to a lower thermal conductivity and a higher reflectance, respectively. The changes in the microstructure, mainly in the porosity and in the grain boundaries, lead to a reduction in thermal conductivity after 2 h testing at 1316 °C from 1.8 to 1.2 W·m⁻¹·K⁻¹ (~30% reduction), and also to an increase in the reflectance of up to 56%. Furthermore, an improvement of 100% in oxidation cyclic life as well as a better strain tolerance than the non-modified 8YSZ TBC structure has been attained. The new tailored YSZ is expected to offer the potential within the

turbine industry of longer turbine component life and reduced fuel consumption.

15.4.2 Plasma sprayed (PS) TBCs

In air plasma-sprayed (APS) coatings, inter-splat pores are roughly aligned parallel to the substrate surface and are accompanied by microcracks and a fine grain size.⁸⁴ This pore orientation is highly effective for impeding the flow of heat through the coating. Therefore, APS coatings have low thermal conductivities which are usually in the range 0.8–1.1 W/mK.¹⁴ However, this coating has less in-plane strain tolerance to accommodate the differences of strain between the metallic bond coat and the ceramic top layer during thermal cycling.^{84,85} This constrains their use in low thermal cyclic environments such as land-based power generation turbines. Modifications to the APS deposition conditions have enabled dense, vertically cracked (DVC) coatings to be deposited.^{86–93} The roughly equally spaced vertical cracks enable the coating to expand with the metal during heating, and they may become important for aero gas turbine applications in the years ahead. A new, potentially lower-cost, solution precursor plasma spray (SPPS) deposition process has also been recently proposed.^{94–96} It is claimed to have the potential for creating more durable TBCs with reduced strain compatibility limitations compared to conventional APS TBCs.

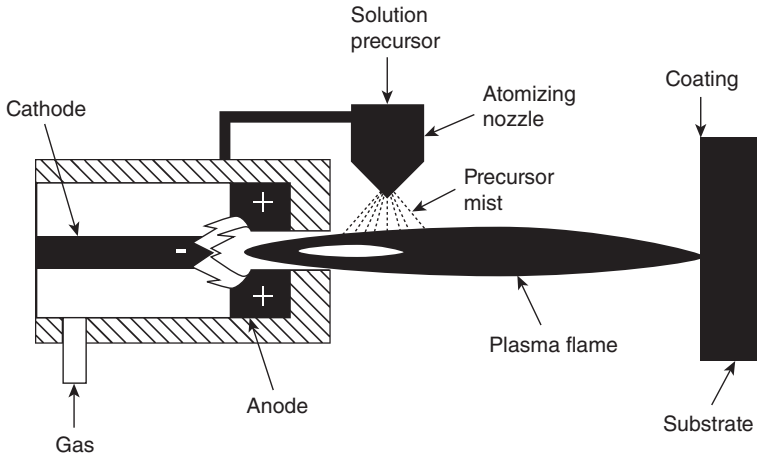
15.5 Advanced processing technologies

In order to develop ‘tailored’ microstructure, a processing approach must be identified or developed for which coating architecture can be manipulated and controlled. Several alternative methods have been proposed to develop more reliable and durable TBCs.

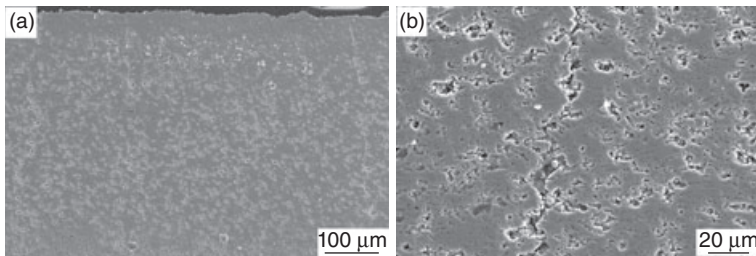
15.5.1 Solution precursor plasma spray (SPPS)

The SPPS process was first reported and applied in the synthesis and deposition of nano-powders and deposited by Herman *et al.*^{97–99} The process was then developed successfully in a joint effort by the researchers at the Institute of Materials Science and Mechanical Engineering Department at the University of Connecticut and the Inframat Corporation, making high-durability, low-thermal conductivity 7YSZ thermal barrier coatings needed for marine, aircraft and industrial engine applications.^{94–96,100–105}

The SPPS process, which is schematically illustrated in Fig 15.1, is fundamentally different in that, instead of ceramic powder, an aqueous solution of zirconium and yttrium salts is injected into the plasma gas environment.^{94–96,100–105} Upon entrainment into the plasma, the subsequent vaporiza-



15.1 Schematic illustration of the SPPS process.⁹⁶



15.2 SEM micrographs of polished cross-sections of the SPPS TBC: (a) low-magnification; (b) higher-magnification.

tion of the water in the droplets and decomposition of the acetate and nitrite groups result in the formation of ceramic material, which contains the desired nano-structure in the final coating structure.

The SPSS process enables the creation of some unique features and so makes it possible to manufacture high-strength TBCs, as shown in Fig. 15.2. The basic characteristics of the SPPS TBCs are: uniformly dispersed porosity, absence of unwanted coarse splat boundaries and straining tolerance providing evenly spaced vertical cracks. Thermal cyclic durability tests of TBCs deposited by APS, SPPS and EB-PVD demonstrated that the spallation times of SPPS coatings were 2.5 times longer than those by EB-PVD coatings and 1.5 times longer than the APS coatings under the same conditions. During these tests, vertical cracks and ultra-fine splats in the SPPS coatings were found to remain stable.

15.5.2 Electron beam directed vapor deposition (DVD)

Some of the limitations of the traditional EB–PVD process conducted in vacuum include low coating rates, difficulties in controlling and modifying microstructure and deposition limited to the line of sight.^{106,107} The last limitation is alleviated by rotation of the substrate so that every point on the surface to be coated has a chance to receive the deposit. Many engineering components, however, have design features that give rise to shadowing of some areas of the components, resulting in vapor molecules being unable to arrive at those sites. Either the shadowed areas get no coating, or the deposited coating is thin with poor column orientation.

Researchers at the University of Virginia in the USA and the Fraunhofer Institute for Electron Beam and Plasma Technology in Germany have devised a modification of the EB–PVD process called electron beam directed vapor deposition (DVD), which increases the deposition rate significantly by improved mixing of vapors from multiple ingot sources. Additionally, the process can modify the microstructure, vary porosity and direct some of the vapor to the other shadowed areas of the depositing surface.

In the DVD process, material is vaporized by using a continuous high-voltage/medium-power (60 kV/10kW) e-beam gun (modified to function in a low vacuum environment by incorporating differential pumping of the gun column and the use of a very small (~3 mm) e-beam exit opening). The vapor is entrained in a carrier gas stream and deposited onto a substrate at a high rate ($>10 \mu\text{m}\cdot\text{min}^{-1}$). Atoms in the carrier gas flow generate collisions with the vapor molecules. The collisions keep the vapor stream directed at the surface, including the shadowed regions to be coated. The collimating effect of the carrier gas has also been found to increase deposition rate. During processing of DVD, the carrier gas stream is created by a rarefied, inert gas supersonic expansion through a nozzle. The speed and flux of the gas atoms entering the chamber, the nozzle parameters and the operating chamber pressure can all be significantly varied to lead to a wide range of processing conditions. These changes are expected to affect the morphology of porous coating structures.

The supersonic carrier gas stream, which is maintained by achieving a high upstream pressure (i.e. the gas pressure prior to its entrance into the processing chamber) and a lower downstream pressure (or chamber pressure), is critical to the process. The ratio of the pressure from upstream to downstream along with the size and shape of the nozzle opening control the speed of the gas entering the chamber. The molecular weight of the carrier gas (compared to that of the vapor) and the speed of the carrier gas control its effectiveness in redirecting the vapor atoms via binary collisions towards the substrate. High molecular weight carrier gases are preferred, but they have a high electron scattering cross-section. Helium is therefore

used for entrainment. High gas speeds are thus required to redirect the vapor toward the substrate with a minimal amount of gas flow. High gas speeds also facilitate the formation of a wall jet (i.e. a component of the gas speed generally aligned parallel to the substrate surface) through the interaction of the carrier gas jet with the substrate.

Compared to conventional EB–PVD processing, two major differences exist in DVD conditions. The first is the use of an elevated chamber pressure. Typical chamber pressures in DVD are between 0.1 and 1 Torr which have higher order of magnitude than those found in EB–PVD. The second is the high-speed carrier gas stream used to alter the direction and speed of the vapor species. The presence of the carrier gas strongly affects the incident angle of the vapor species during deposition and can thus modify the growing process. Recently, e-beam multisource evaporation, a plasma activation system to ionize the vapor and the gas stream, together with electrical biasing of the substrate were incorporated into the DVD process, which opened new possibilities for the creation of more desirable film structures and compositions.

15.6 Future trends

To exploit the full potential of TBCs, further studies are required for substantial improvement of the TBC system. Up to now many of the newly developed EB–PVD TBCs have been introduced into service or ground testing with only an underlying standard YSZ ceramic layer. Future research must generate an increasing understanding of the processing–property interplay of these systems to provide reliable data for improved service life.

15.7 References

1. R.A. MILLER, *Surf. Coat. Technol.*, **30** (1987) 1.
2. R.A. MILLER, *J. Therm. Spray Technol.*, **6**(1) (1997) 35.
3. R.L. JONES, in *Metallurgical and Ceramic Coatings*, K. H. Stern, Ed., Chapman and Hall, London UK, 1996, 194.
4. N.P. PADTURE, M. GELL, E.H. JORDAN, *Science*, **296** (2002) 280.
5. S. BOSE, in *High Temperature Coatings*, S. Bose, Ed., Butterworth-Heinemann, Elsevier, Oxford, UK, 2007, 155.
6. S. STECURA, *Adv. Ceram. Mater.*, **1**(1) (1986) 68.
7. D.P.H. HASSELMAN, L.F. JOHNSON, L.D. BENTSEN, R. SYED, H.L. LEE, M.V. SWAIN, *Am. Ceram. Soc. Bull.*, **66** (1987) 799.
8. S. BOSE, J. DEMASI, *J. Therm. Spray Technol.*, **6**(1) (1997) 99.
9. W.A. NELSON, R.M. ORENSTEIN, *J. Therm. Spray Technol.*, **6**(2) (1997) 176.
10. J. THORNTON, *Mater. Sci. Forum*, **22** (1998) 159.
11. J. ILAVSKY, J.K. STALICK, *Surf. Coat. Technol.*, **127**(2–3) (2000) 120.
12. U. SCHULZ, *J. Am. Ceram. Soc.*, **83** (2000) 904.
13. D. R. CLARKE, C. G. LEVI, *Annu. Rev. Mater. Res.*, **33** (2003) 383.

14. J.R. NICHOLLS, *Mater. Res. Soc. Bull.*, **28**(9) (2003) 659.
15. C.G. LEVI, *Curr. Opin. Solid State Mater. Sci.* **8**(1) (2004) 77.
16. R. VASSEN, X. CAO, F. TIETZ, D. BASU, D. STÖVER, *J. Am. Ceram. Soc.* **83**(8) (1999) 2023.
17. D. STÖVER, C. FUNKE, *J. Mater. Process. Technol.*, **92–93** (1999) 195.
18. R.L. JONES, R.F. REIDY, D. MESS, *Surf. Coat. Technol.*, **82** (1996) 70.
19. R.L. JONES, D. MESS, *Surf. Coat. Technol.*, **86–87** (1996) 94.
20. P.D. HARMSWORTH, R. STEVENS, *J. Mater. Sci.*, **26** (1991) 3991.
21. D.J. KIM, *J. Am. Ceram. Soc.*, **73**(1) (1990) 115.
22. S. RAGHAVAN, H. WANG, W.D. PORTER, *et al.*, *Acta Mater.*, **49** (2001) 169.
23. R. VAŠEN, N. CZECH, W. MALLÉNER, *et al.*, *Surf. Coat. Technol.*, **141** (2001) 135.
24. U. SCHULZ, K. FRITSCHER, M. PETERS, *Surf. Coat. Technol.*, **82** (1996) 259.
25. C. LEYENS, U. SCHULZ, K. FRITSCHER, *Mater. High Temp.*, **20** (2003) 475.
26. Y.A. TAMARIN, E.B. KACHANOV, S.V. ZHERZDEV, *Mater. Sci. Forum*, **251–254** (1997) 949.
27. J.R. NICHOLLS, K.J. LAWSON, A. JOHNSTONE, D.S. RICKERBY, *Mater. Sci. Forum*, **369** (2001) 595.
28. J.R. NICHOLLS, K.J. LAWSON, A. JOHNSTONE, D.S. RICKERBY, *Surf. Coat. Technol.*, **151–152** (2002) 383.
29. D.M. ZHU, R.A. MILLER, *Ceram. Eng. Sci. Proc.*, **23** (2002) 457.
30. D.M. ZHU, Y.L. CHEN, R.A. MILLER, *Ceram. Eng. Sci. Proc.*, **24** (2003) 525.
31. S. SODEOKA, M. SUZUKI, T. INOUE, *et al.*, in: *Proceedings of the 9th National Thermal Spray Conference: Thermal Spray-Practical Solutions for Engineering Problems* C. C. Berndt Ed., ASM International, Materials Park, OH, 1996, 295.
32. J. THORNTON, A. MAJUMDAR, G. MCADAM, *Surf. Coat. Technol.*, **94/95** (1997) 112.
33. A. ROUANET, G. PERAUDEAU, F. SIBIEUDE, *et al.*, in: *The 14th international thermal spray conference: Thermal Spray-Current Status and Future Trends* A. Ohmori Ed., High Temperature Society of Japan, Osaka, 1995, 507.
34. X. CAO, R. VASSEN, W. FISCHER, *et al.*, *Adv. Mater.*, **15** (17) (2003) 1438.
35. W. MA, S.K. GONG, H.B. XU, X.Q. CAO, *Scripta Mater.*, **54** (2006) 1505.
36. W. MA, S.K. GONG, H.B. XU, X.Q. CAO, *Surf. Coat. Technol.*, **200** (2006) 5113.
37. D.M. ZHU, R.A. MILLER, *Surf. Coat. Technol.*, **108–109** (1998) 114.
38. K. MATSUMOTO, Y. ITOH, T. KAMEDA, *Sci. Technol. Adv. Mater.*, **4** (2003) 153.
39. J. SINGH, D. E. WOLFE, R. A. MILLER, *et al.*, *J. Mater. Sci.*, **39** (2004) 1975.
40. M.J. MALONEY, US Patent 6117560, 2000.
41. M.J. MALONEY, European Patent EP 0 992 603 A1, 2000.
42. J. WU, X. WEI, N.P. PADTURE, *et al.*, *J. Am. Ceram. Soc.*, **85** (2002) 3031.
43. M.J. MALONEY, US Patent 20030049470 A1, 2003.
44. G. SURESH, G. SEENIVASAN, M.V. KRISHNAIAH, P.S. MURTI, *J. Nucl. Mater.* **249** (1997) 259.
45. G. SURESH, G. SEENIVASAN, M.V. KRISHNAIAH, P.S. MURTI, *J. Alloys Compd.* **269** (1998) L9.
46. LEHMANN, H., *et al.*, *J. Am. Ceram. Soc.*, **86** (2003) 1338.
47. B. SARUHAN, P. FRANCOIS, K. KRITSCHER, U. SCHULZ, *Surf. Coat. Technol.*, **182** (2004) 175.
48. D. STÖVER, G. PRACTH, H. LEHMANN, *et al.*, *J. Therm. Spray Technol.*, **13** (2004) 76.
49. R. VASSEN, F. TRAEGER, D. STÖVER, *Int. J. Appl. Ceram. Technol.*, **1** (2004) 351.
50. R. GADOW, M. LISCHKA, *Surf. Coat. Technol.*, **151** (2002) 392.
51. X.Q. CAO, R. VASSEN, D. STÖVER, *J. Euro. Ceram. Soc.*, **24** (2004) 1.

52. X.Q. CAO, Y.F. ZHANG, J.F. ZHANG, *et al.*, *J. Euro. Ceram. Soc.*, **28** (2008) 1979.
53. M. GELL, *Nanostruct. Mater.*, **6** (1995) 997.
54. M. GELL, *Mater. Sci. Eng. A*, **204** (1995) 246.
55. U. BETZ, H. HAHN, *Nanostruct. Mater.*, **12** (1999) 911.
56. G. SOYEZ, A. EASTMAN, L.J. THOMPSON, G.R. BAI, P.M. BALDO, A.W. MCCORMICK, R.J. DIMELFI, A.A. ELMUSTAFA, M.F. TAMBWE, D.S. STONE, *Appl. Phys. Lett.*, **77**(8) (2000) 1155.
57. R.S. LIMA, A. KUCUK, C.C. BERNDT, *Surf. Coat. Technol.*, **135** (2001) 166.
58. R.S. LIMA, A. KUCUK, C.C. BERNDT, *Mater. Sci. Eng. A*, **313** (2001) 75.
59. R.S. LIMA, A. KUCUK, U. SENTURK, C.C. BERNDT, *J. Therm. Spray Technol.*, **15**(1) (2001) 150.
60. H. CHEN and C. X. DING, *Surf. Coat. Technol.* **150**(1) (2002) 31.
61. R.S. LIMA, A. KUCUK, C.C. BERNDT, *Mater. Sci. Eng. A*, **327** (2002) 224.
62. H. CHEN, X.M. ZHOU, C.X. DING, *J. Euro. Ceram. Soc.*, **23**(9) (2003) 1449.
63. H. CHEN, C.X. DING, S. LEE, *Mater. Sci. Eng. A*, **361**(1–2) (2003) 58.
64. C.G. ZHOU, N. WANG, Z.B. WANG, *Scripta Materi.*, **51**(9) (2004) 945.
65. R.S. LIMA, S.E. KRUGER, G. LAMOUCHE, B.R. MARPLE, *J. Therm. Spray Technol.* **14**(1) (2005) 520.
66. B. LIANG, C.X. DING, *Surf. Coat. Technol.*, **191** (2005) 267.
67. B. LIANG, C.X. DING, *Surf. Coat. Technol.*, **197**(2–3) (2005) 185.
68. B. LIANG, C. DING, H. LIAO, C. CODDET, *Surf. Coat. Tech.*, **200** (2006) 4549.
69. R.S. LIMA, B.R. MARPLE, *J. Therm. Spray Technol.*, **16**(1) (2007) 40.
70. C.G. ZHOU, N. WANG, H.B. XU, *Mater. Sci. Eng. A*, **452–453** (2007) 569.
71. N. WANG, C.G. ZHOU, S.K. GONG, H.B. XU, *Ceramics International*, **33** (2007) 1075.
72. R.S. LIMA, B.R. MARPLE, *Mater. Sci. Eng. A*, **485** (2008) 182.
73. J. WU, H.B. GUO, L. ZHOU, L. WANG, S.K. GONG, *Asian Thermal Spray Conference, Xi'an China, 22–24 Oct. 2009*.
74. T.J. LU, C.G. LEVI, H.N.G. WADLEY, A.G. EVANS, *J. Am. Ceram. Soc.*, **84** (2001) 2937.
75. S.G. TERRY, C.G. LEVI, *J. Am. Ceram. Soc.*, **84** (2001) 2937.
76. U. SCHULZ, K. FRITSCHER, C. LEYENS, M. PETERS, *Ceram. Eng. Sci. Proc.*, **22**(41) (2001) 347–356.
77. K. FRITSCHER, F. SZHCS, U. SCHULZ, *et al.*, *Ceram. Eng. Sci. Proc.*, **23**(4) (2002) 341–352.
78. C.A. JOHNSON, J.A. RUUD, R. BRUCE, D. WORTMAN, *Surf. Coat. Technol.*, **108–109** (1998) 80.
79. U. SCHULZ, K. FRITSCHER, C. LEYENS, M. PETERS, *J. Eng. for Gas Turbines Power*, **124**(2) (2002) 229–234.
80. D.V. RIGNEY, A.F. MARICOCCHI, A.J. WORTMANN, R.W. BRUCE, J.D. RIGNY, U.S. Patent 6 447 854, 2002.
81. U. SCHULZ, B. SARUHAN, K. FRITSCHER, C. LEYENS, *Int. J. Appl. Ceram. Technol.* **1** (2004) 302.
82. W. BEELE, G. MARIJNISSEN, E. VERGELDT, E. HURON, R. DAROLIA, in *Turbine Forum, Advanced Coatings for High Temp enraptures*, Nice, 17–19 Apr. 2002, 1.
83. D.E. WOLFE, J. SINGH, R.A. MILLER, J.I. ELDRIDGE, D.M. ZHU, *Surf. Coat. Technol.* **190** (2005) 132.
84. J.R. NICHOLLS, M.J. DEAKIN, D.S. RICKERBY, *Wear*, **233–235** (1999) 352.
85. T.E. STRANGMAN, *Thin Solid Films* **127** (1985) 93.
86. T.A. TAYLOR, U.S. Patent 5073433, 1991.

87. T.A. TAYLOR, D.L. APPELBY, A.E. WEATHERILL, J. GRIFFITHS, *Surf. Coat. Technol.*, **43/44** (1990) 470.
88. T.A. TAYLOR, in: N. B. Dahotre, R. J. Gaster, R. A. Hill and O. O. Popoola (Eds), *Heat Treating and Surface Engineering: Proceedings of the 22nd International Surface Engineering Conference*, ASM International, Materials Park, OH, 2003, 520.
89. R. VASSEN, F. TRAEGER, D. STOVER, *J. Therm. Spray. Technol.*, **13**(3) (2004) 396.
90. H.B. GUO, S. KURODA, H. MURAKAMI, *J. Am. Ceram. Soc.*, **89**(4) (2006) 1432.
91. H.B. GUO, S. KURODA, H. MURAKAMI, *Thin Solid Films*, **506–507** (2006) 136.
92. P. BENGTTSSON, J. WIGREN, in: P.J. Maziasz, I.G. Wright *et al.* (Eds), *Gas Turbine Materials Technology: Conference Proceeding from ASM Materials Solutions*, ASM International, Materials Park, OH, 1999, 92.
93. H.B. GUO, R. VASSEN, D. STÖVER, *Surf. Coat. Technol.*, **186** (2004) 353.
94. L. XIE, X. MA, E.H. JORDAN, N.P. PADTURE, T.D. XIAO, M. GELL, *J. Mater. Sci.*, **39** (2004) 1639.
95. L. XIE, X. MA, E.H. JORDAN, N.P. PADTURE, T.D. XIAO, M. GELL, *Mater. Sci. Eng. A.*, **362** (2003) 204.
96. L. XIE, X. MA, E.H. JORDAN, N.P. PADTURE, T.D. XIAO, M. GELL, *Surf. Coat. Technol.*, 177–178 (2004) 97.
97. J. KARTHIKEYAN, C.C. BERNDT, J. TIKKANEN, J.Y. WANG, A.H. KING, H. HERMAN, *Nanostruct. Mater.* **9**(1) (1997) 137.
98. J. KARTHIKEYAN, C.C. BERNDT, S. REDDY, J-Y. WANG, A.H. KING, H. HERMAN, *J. Am. Ceram. Soc.*, **81** (1998) 121.
99. H. HERMAN, S. SAMPATH, R. MCCUNE, *MRS Bull.*, **7** (2000) 17.
100. N.P. PADTURE, K.W. SCHLICHTING, T. BHATIA, A. OZTURK, B. CETEGEN, E.H. JORDAN, M. GELL, S. JIANG, T.D. XIAO, P.R. STRUTT, E. GARCIA, P. MIRANZO, M.I. OSENDI, *Acta Mater.*, **49** (2001) 2251.
101. E.H. JORDAN, L. XIE, C. MA, M. GELL, N. PADTURE, B. CETEGEN, J. ROTH, T. D. XIAO, P. E. C. BRYANT, *J. Therm. Spray*, **13**(1) (2004) 57.
102. A. JADHAV, N. PADTURE, F. WU, E. JORDAN, M. GELL, *Mater. Sci. Eng. A*, **405** (2005) 313.
103. X. MA, F. WU, J. ROTH, M. GELL, E. JORDAN, *Surf. Coat. Technol.*, **201** (2006) 3343.
104. X.Q. MA, T.D. XIAO, J. ROTH, L.D. XIE, E.H. JORDAN, N.P. PADTURE, M. GELL, X.Q. CHEN, J.R. PRICE, in: D. von Hofe (Ed.), *Thermal Spray 2004: Advances in Technology and Application*, ASM International, Materials Park, OH, 2004, 1103.
105. M. GELL, F. WU, E.H. JORDAN, N.P. PADTURE, B.M. CETEGEN, L. ZIE, A. OZTURK, E. CAO, A. JADHAV, D. CHEN, X. MA, in: *Proceedings of 2005, ASME Turbo Expo 2005*, ASME New York, 905.
106. J.F. GROVES, G. MATTAUSCH, H. MORGNER, D.D. HAAS, H.N.G. WADLEY, *Surf. Eng.*, **16**(6) (2000) 461.
107. Z. YU, D.D. HASS, H.N.G. WADLEY, *Mater. Sci. Eng. A*, **394**(1–2) (2005) 43.

-
- ABAQUS, 302
accumulated plastic strain rate, 298
acoustic emission, 247, 248–9
AIP *see* arc ion plating
air plasma spraying, 176, 322
 process schematic, 135
aluminised coatings, 56–8
aluminium oxide, 35–6
ANSYS 9.0, 220
APS *see* atmospheric plasma spraying
arc ion plating, 181
arc plasma deposition, 181
ASTM C633-01, 154–5
atmospheric plasma spraying, 120–1,
 135, 199
 William-Warnke model for the top
 coat, 296

back stress, 297
biomaterials, 104–7
bond coat related failure
 bond coat effect on the TBC
 degradation mechanisms,
 286–8
 ternary Ni–Al–Pt phase diagram,
 289
experimental details and background
 information, 279
 TBC spallation life for cyclic
 oxidation testing, 280
residual stress measurement by
 luminescence spectroscopy,
 279–81
residual stress evolution in TGO
 layer, 281

rumpling quantification at the TGO/
 bond coat interface, 283–5
 interface amplitude profile
 standard deviation, 285
 TGO/bond coat interface profiles,
 284
TGO layers and interfaces chemical
 analyses, 285–6
 bond coat systems microstructural
 evolution, 286
 elemental compositions taken
 using TGO layer WSD
 FE-EPMA analysis, 285
thermal barrier coatings failure,
 245–6, 278–86
thermal cycled specimens
 microstructure imaging, 282
 near-TGO microstructure, 282
 TGO thickness vs thermal cycles,
 283
bond coats, 18–19, 194
 M–Cr–Al–Y, 67
 platinum-modified aluminide, 65–6
 thermal barrier coatings, 64–7
branching cracks, 167

CAE software, 302
calcium magnesium zirconium
 phosphate, 41–2
cell culture, 110–11
ceramic thermal barrier coating
 materials, 25–44
 advantages and disadvantages, 28
 CMZP, perovskite oxides and
 metal–glass composite, 41–3

- calcium magnesium zirconium phosphate, 41–2
- metal–glass composite, 43
- perovskite oxides, 42–3
- future trends, 43–4
- lanthanum compounds, silicates and rare earth oxides, 38–41
- lanthanum aluminates, 40–1
- lanthanum cerium oxide, 38
- lanthanum phosphate, 41
- rare earth oxides, 39–40
- silicates, 38–9
- yttrium aluminium garnet, 40
- properties, 27
- yttria stabilised hafnia and other alternative materials, 35–7
- aluminium oxide, 35–6
- mullite, 36
- pyrochlore oxides, 36–7
- yttria stabilised hafnia, 35
- yttria stabilised zirconia, 26–30
- zirconia doped with one or more oxides, 31–5
- Chaboche constitutive model, 295, 297–8, 302
- change coupled device (CCD) detector, 280
- chemical vapour deposition (CVD), 55, 196
- chromised coatings, 58–9
- CMZP *see* calcium magnesium zirconium phosphate
- coefficient of thermal expansion (CTE), 84–5, 319
- nanostructured zirconia coating, 85
- cooling rate, 165
- crack density function (CDF), 249
- creep, 85–7, 151
- D-gun *see* detonation gun
- D-gun spraying, 177
- defect cluster systems, 318–19
- detonation gun, 175
- detonation gun sprayed thermal barrier coatings, 175–87
- as-sprayed D-gun TBCs microstructure, 177
- D-gun spraying process principle, 176
- failure mechanism during thermal shock cycling, 179–81
- microstructural evolution and damage accumulation, 181
- future trends, 185–7
- TBC deposited through air ion plating D-gun two-step technology, 181–5
- bond coatings obtained by AIP, 181–2
- coating microstructure change with increasing oxidation time, 184
- failure mechanism during thermal exposure, 185
- fluorescence spectra for α -Al₂O₃, 182
- lamellar TBC spallation, 185
- microstructure evolutions during thermal exposure, 183–5
- thermally grown oxide stresses distributions, 183
- thermal conductivity, 177–9
- YSZ powders images, 178
- diffusion coatings, 55–61, 68
- aluminised coatings, 56–8
- chromised coatings, 58–9
- low temperature pack cementation, 59–61
- M–Cr–Al type, 59
- directed vapour deposition, 324–5
- dispersed spheroid microporosity, 167
- dissociation, 100
- dopant oxides, 319
- dopants, 318
- drag strength, 297
- DVD *see* directed vapour deposition
- e-beam multisource evaporation, 325
- EB–PVD *see* electron beam physical vapour deposition
- EB–PVD thermal barrier coatings, 133, 321–2

- failure mechanism under 3-D
 - thermal gradient coupled with mechanical loading, 233–40
- cross-sectional images along the radius direction, 235
- equivalent stress profiles along the axial direction, 237
- failure mechanism, 238, 240
- failure modes, 234–6
- failure modes along the direction perpendicular to loading, 235
- in-plane normal stress distribution, 239
- shear stress profiles, 239
- stress analysis, 236–8, 236–9
- stress distributions along the radial direction, 238
- failure mechanism under in-plane
 - thermal gradient with constant tensile loading, 221–6
- cross-sectional microstructure, 224
- failure modes during thermal shock testing, 222
- impedance spectra after thermomechanical loading, 225
- impedance spectroscopy
 - evaluation, 222, 225–6
- surface morphology, 223
- failure mechanism under in-plane
 - thermal gradient with cycling fatigue loading, 226–33
- failure mechanism, 233
- failure modes, 226–8
- impedance evaluation, 228
- impedance spectra at different positions, 229
- normal stress profile along the axial direction, 232
- sample images at different positions, 227
- shear stress profiles along the axial direction, 232
- simulated equivalent stress distribution profile, 230
- simulated temperature profile at TGO/TBC interface, 229
- stress analysis, 230–3
- stress profiles along radial direction, 231
- TGO growth, 228–30
- life prediction, 310–12
- manufacturing, 118–20
 - industrial production system, 118
 - multipurpose equipment, 119
- microstructure vs plasma-sprayed coatings, 120–5
 - conventional TBCs, 122–3
- EB-PVD coating and APS coating, 120
- EB-PVD YSZ coating feather-like microstructure, 122
- gradient thermal barrier coating, 124
- multi-layered and graded TBCs, 123–5
- YSZ coatings after heat treatment, 125
- processing, microstructures and properties, 115–28
- EB-PVD principle, 116–18
- hot-fatigue behaviour and failure mechanisms, 125–8
- edge effect, 162
- EDX *see* energy dispersive X-ray
- electrochemical impedance spectroscopy (EIS), 248, 251
- electron beam directed vapour deposition, 324–5
- electron beam physical vapour deposition, 170, 176, 198, 317
- gas turbine engines service environment simulation system establishment, 217–21
- experimental parameters, 219–21
- experimental parameters for thermomechanical loading test, 220
- Ni–Co–Cr–Al–Y bond coat parameters, 221
- sample description, 219
- standard tensile samples, 219
- super alloy parameters, 220
- TGO layer parameters, 221

- thermomechanical loading test system, 217–19
- YSZ top coat parameters, 221
- in-plane thermal gradient coupled with mechanical loading, 221–33
- industrial production system, 118
- multipurpose equipment, 119
- principle, 116–18
- TBCs processing, microstructures and properties, 115–28
 - EB–PVD TBC microstructure vs plasma-sprayed coatings, 120–5
 - hot-fatigue behaviour and failure mechanisms, 125–8
 - manufacturing of TBCs, 118–20
- technology and its equipment, 4–5
 - equipment, 5
- thermal barrier coatings, 3–20
 - factors affecting thermal cyclic behaviour, 11–16
 - failure mechanism, 19
 - gradient thermal barrier coatings preparation, 16–19
 - preparation process and parameters, 6–8
 - preparation processes of two-layered TBCs, 8–11
- Walker model for the top coat, 296–7
- electron probe microprobe analyser (EPMA), 272–6
- energy dispersive X-ray, 268, 282
- field emission electron probe microprobe analyser (FE–EPMA), 268
- field emission gun scanning electron microscope (FEG–SEM), 268, 282
- finite element analysis, 205
- flattening degree, 144
- fluorite lanthanum cerate ($\text{La}_2\text{Ce}_2\text{O}_7$), 319
- fluorite oxides, 319
- FORTTRAN, 302
- fracture toughness, 155
- fragmentation degree, 144
- functionally graded materials (FGM), 150
- functionally gradient material–TBC, 186
- gas turbine engines service environment simulation system establishment, 217–21
- thermal barrier coatings failure mechanism, 215–40
- graded TBCs, 123–5
- gradient thermal barrier coatings, 124
 - preparation, 16–19
 - as-deposited gradient coating, 18
 - diagram, 17
 - new investigations on bond coat, 18–19
 - new investigations on top coat, 19
 - transition layer in as-deposited gradient coating, 18
 - growth stresses, 149
- helium, 324–5
- hot corrosion, 194, 202–3
 - initiation stage, 203
 - propagation stage, 203
- hot-fatigue behaviour, 125–8
- hybrid coatings, 198
- hydroxyapatite, 105–7
 - apatite structure, 106
 - as-sprayed coating, 109
 - crystal structure, 106
 - decomposition after plasma spraying, 107–9
 - physical properties, 107
- impedance spectroscopy, 216, 250–1
- in vitro* testing, 109–11
- inductively coupled plasma mass spectrometry (ICPMS), 266
- infrared thermography, 247–8, 250
- INSTRON 8803, 221
- ionisation, 100
- kinetic oxidation model, 306
- Kyoto Protocol, 263

- lanthanum aluminates, 40–1
- lanthanum cerium oxide, 38
- lanthanum hexaluminat
 - (LaMgAl₁₁O₁₉, LHA), 320
- lanthanum phosphate, 41
- laser flash apparatus, 166
- LECO Carbon & Sulphur
 - Determinator, 266
- life prediction
 - EB-PVD thermal barrier coatings, 310–12
 - APS thermal fatigue data, 310
 - failure mode under thermal fatigue, 311
 - parameters for fatigue life model, 310
 - thermal fatigue data, 312
- finite element method calculation
 - and analysis, 302–5
 - cyclic behaviour under 900°C, 305
 - DZ40M superalloy simulation, 302–5
 - monotonic compressive curves under strain rate, 304
 - monotonic tensile curve under strain rate, 303
 - monotonic tensile stress-strain curve under 500°C, 304
 - stress-strain curve under strain rate dependency, 303
 - top coat simulation, 302
- material constitutive laws, 296–8
 - Chaboche model for the substrate, 297–8
 - Walker model for the top coat by EB-PVD, 296–7
 - William-Warnke model for the top coat by APS, 296
- material parameters under high temperature, 298–302
 - thermal conductivity evaluation for the top coat, 301–2
 - Young's modulus measurement for the top coat, 298–301
- model, 305–7
 - fatigue model based on damage mechanics, 307
 - fatigue model based on imperfections, 306–7
 - phenomenological fatigue life model, 305–6
 - plasma sprayed thermal barrier coatings, 307–10
 - APS TBC failure mode under thermal fatigue, 308
 - FEM model for TBC, 309
 - thermal barrier coatings, 294–315
 - future trends, 314
 - mechanical behaviour under evaluated temperatures, 295–305
 - vane with TBCs, 312–14
 - critical locations at leading and trailing edge, 313
 - critical locations cyclic behaviour, 313
- low pressure plasma spraying (LPPS), 136
- M–Cr–Al–Y bond coats, 67
- M–Cr–Al–Y overlay coatings, 61–4
- magnesium oxide stabilised zirconia, 31
- Manson–Coffin model, 305
- Mcperson model, 301
- mechanical interlocking, 154
- metal–glass composite (MGC), 43
- metallic bond coat, 120
- metallic coatings
 - bond coats for thermal barrier coatings, 64–7
 - EB-PVD TBC coating, 64
 - M–Cr–Al–Y bond coats, 67
 - platinum-modified aluminide bond coats, 65–6
 - rumpling of bond coat surface, 66
 - high-temperature oxidation resistance, 53–69
 - oxidation resistant coatings and their fabrication techniques, 55–64
 - chromised samples, 61
 - diffusion coatings, 55–61

- M–Cr–Al(–Y) overlay coatings,
 - 61–4
 - oxidation and hot corrosion resistance, 62
- Miner linear cumulative damage theory, 306
- Miner's law, 314
- mismatch stresses, 150
- modulus, 151–3
- mullite, 36
- multi-layered TBCs, 123–5
- nano-indentation technique, 152
- nanocrystalline coatings, 54
- nanocrystalline materials, 320–1
- nanostructured thermal barrier coatings, 75–93
 - creep strain
 - nanostructured samples at different temperatures, 86
 - nanostructured samples under different stresses, 85
 - mechanical properties, 82–7
 - activation energy calculation, 86
 - coefficients of thermal expansion, 84–5
 - creep, 85–7
 - hardness and elastic modulus, 82–4
 - phase composition and microstructure, 78–82
 - microstructure, 80–2
 - nano YSZ coatings, 81
 - phase composition, 78–80
 - porosity distribution, 82
 - primitive nano YSZ particles, 80
 - starting ZrO₂ powder and as-sprayed ZrO₂ coating, 79
 - spray parameters
 - elastic modulus–roughness relationship, 84
 - Knoop microhardness–roughness relationship, 84
 - PSZ coatings, 83
 - Vickers microhardness–roughness relationship, 83
 - spray-drying process making powders, 76–8
 - ceramics, 77
 - spray-dried powders, 78
 - thermophysical properties and failure behaviour, 87–92
 - buckling of nanostructured TBCs, 91
 - cumulative porosity variation, 92
 - failed conventional TBCs, 90
 - failed nanostructured TBCs, 89
 - failure mechanism, 88–91
 - kinetics during 1 h cycles at 1050 °C, 88
 - sintering of nanostructured Al₂O₃-YSZ coating, 91–2
 - thermal cycles, 89
 - thermal diffusivity, 87–8
- NASA's Hot Section Technology (HOST), 295
- neodymium cerate, 38
- non-destructive evaluation (NDE), 216
 - thermal barrier coatings failure, 243–58
 - failure inspection methods development, 247–58
 - future trends, 258
- octahedral tilting, 42
- overlay coatings, 61–4, 68
- oxides, 193
- pack cementation, 55, 59–61, 196
- Peclet number, 140
- perovskite oxides, 42–3
- phonon conductivity, 155
- photo-stimulated luminescence spectroscopy (PSLS), 179, 248, 252
- piezospectroscopy, 279
- plasma, 100–2
- plasma jet modelling, 139–40
- plasma spraying, 99–111, 317
 - applications, 104–11
 - biomaterials, 104–7
 - bonding of bone to implants, 108
 - decomposition and chemical changes, 107–9

- in vitro* tests, 109–11
- organisation of a typical bone, 105
- process, 102–4
 - building up a coating, 103
 - schematic, 102
- processing parameters, 137
- processing, microstructures and
 - properties of TBCs, 132–57
 - microstructures, 141–51
 - processing, 134–41
 - properties, 151–6
- plasma-sprayed thermal barrier
 - coatings (PS–TBCs), 121, 322
 - life prediction., 307–10
 - microstructures, 141–51
 - crack and fragment, 147–51
 - fracture surface, 146
 - porosity, 145–7
 - schematics, 142
 - splat formation, 142–5
 - processing, 134–41
 - air plasma spray, 135
 - method, 135–7
 - modelling, 139
 - parameters, 137–9
 - particle in flight modelling, 140
 - plasma jet modelling, 139–40
 - splat formation modelling, 140–1
 - processing, microstructures and
 - properties, 132–57
 - EB–PVD YSZ/M–Cr–Al–X TBC, 134
 - zirconia–yttria/M–Cr–Al–X TBC, 133
 - properties, 151–6
 - bonding strength, 154–5
 - four-point bend testers, 153
 - load–displacement curve, 153
 - modulus, 151–3
 - thermal conductivity, 155–6
 - with segmentation cracks, 161–72
 - future trends, 172
 - manufacturing, 162–5
 - TBCs microstructure, 165–6
 - thermal shock resistance and
 - associate failure mechanism, 167–72
 - thermophysical and mechanical
 - properties, 166–7
 - platinum–diffusion bond coat, 271, 289–90
 - platinum-modified aluminide bond
 - coats, 65–6, 196–7
 - pyrochlore oxides, 36–7
- Raleigh–Taylor instability, 144
- Raman spectroscopy, 179
- rare earth oxides, 33, 39–40
- ratcheting, 198
- reactive element effect (REE), 56
- recombination, 101
- Renishaw Raman optical microprobe
 - model 2000, 279
- residual stresses, 148–50
- Reynolds number, 140
- rumpling, 287
- Scherrer equation, 78–9
- segmented thermal barrier coatings,
 - 161–72
 - future trends, 172
 - manufacturing, 162–5
 - microstructure, 165–6
 - thermal shock resistance and
 - associate failure mechanism, 167–72
 - burner rig set-up for thermal
 - shock testing, 168
 - cross-section of segmented TBC
 - showing TGO morphology, 169
 - segmented TBC after thermal
 - shock resistance, 169
 - thin TBC cross-section
 - micrograph, 171
 - thermophysical and mechanical
 - properties, 166–7
 - YSZ coatings
 - cross-sections micrographs, 165
 - fracture cross-sections, 166
 - segmentation crack densities, 164
 - surface morphologies, 166
 - shot control method, 186
 - silicates, 38–9
 - sintering, 151

- Solatron 1260, 222
- solution precursor plasma spraying, 136–7, 322–3
- spallation, 198
- splats, 120–1, 135, 163
 - formation, 142–5
 - modelling, 140–1
- SPPS *see* solution precursor plasma spray
- spray-drying, 76–8
- stress concentration, 233, 240
- stress intensity factor (SIF), 155
- substrate related failure
 - coating cross-sections
 - characterisation, 268–71
 - bond coats cross-section microstructures, 268
 - Pt and Al EDX concentration line -profile, 269
 - Pt-diffusion coatings
 - microstructure, 269
 - TBC spallation life for cyclic oxidation testing, 270
- experimental details and background information, 266–8
 - alloys chemical compositions, 266
 - superalloys trace elements, 266
 - thermal cycling furnace, 267
- failure mechanism, 271–2
 - TBC interfacial spallation failure location, 271
 - TBC spallation life vs TGO thickness, 272
- high-resolution analysis and mapping by EPMA/WDX, 272–6
- TBC coated CMSX-4–Pt–diffusion system, 275
- TBC coated PWA1484–Pt–diffusion system, 274
- TBC coated SRR99–Pt–diffusion system, 273
- TBC coated TMS-82+–Pt–diffusion system, 274
- TBC coated TMS138A–Pt–diffusion system, 275
- TGO layers elemental compositions, 273
- thermal barrier coatings, 265–76
 - substrate temperature, 6–7
 - sulphates–vanadate, 205
 - suspension plasma spraying (SPS), 136
- TBC *see* thermal barrier coatings
- TGO *see* thermally grown oxide
- thermal barrier coatings, 54
 - advanced processing technologies, 322–5
 - electron beam directed vapour deposition, 324–5
 - solution precursor plasma spray, 322–3
 - SPPS process illustration, 323
 - SPPS TBC polished cross-sections micrographs, 323
 - alternate low thermal conductivity materials, 319–21
 - fluorite oxides, 319
 - lanthanum hexaluminate, 320
 - nanocrystalline materials, 320–1
 - zirconate pyrochlore oxides, 319–20
 - degradation mechanisms of systems exposed to deposits, 202–7
 - corrosion kinetics in NaCl vapour and NaCl plus water vapour, 207
 - hypothetical in-service failure regimens for APS YSZ TBCs, 204
 - TBC with TGO axial and radial stress distribution, 206
 - temperature effect on superalloy damage rate, 203
- detonation gun sprayed, 175–87
- electron beam physical vapour deposition, 3–20
 - failure mechanism under thermomechanical coupled loads, 215–40
 - schematic representation, 244
 - technology and its equipment, 4–5

- factors affecting thermal cyclic
 - behaviour, 11–16
 - bond coat surface roughness, 14–16
 - pre-oxide layer thickness, 11–14
 - pre-oxide layer thickness of TBCs as-deposited, 13
 - TBCs after thermal cycling testing, 14
 - TBCs after thermally cycled to spallation, 15
 - thermal cyclic weight gain curves, 16
- failure inspection methods
 - development, 247–58
 - crack or delamination, 248–9
 - EBPVD/Pt aluminide stress map, 255
 - effect of flame temperature and number of holes, 256
 - fluorescence spectrum
 - de-convolution, 254
 - in situ inspection by doping in YSZ, 254–8
 - Li₂O-doped TBCs emission intensity, 256
 - plasma-sprayed TBCs thermal cycling results at 1115°C, 257
 - plasma-sprayed TBCs thermal cycling results at 1150°C, 257
 - R1/R2 fluorescence spectra for chromium, 252
 - TGO and its interface with YSZ and bond coat, 251–4
 - YSZ thermal property change, 249–51
- failure mechanisms, 19–20, 198–202
 - APS TBC cracking mechanisms, 201
 - EB-PVD TBC cracking
 - mechanisms, 202
 - tensile stresses resulting from surface imperfection, 199
 - two-layered TBCs failure, 20
- failure summary, 245–7
 - application, 247
 - materials, 245–7
 - structure, 247
- gradient TBCs preparation, 16–19
 - as-deposited gradient coating, 18
 - diagram, 17
 - new investigations on bond coat, 18–19
 - new investigations on top coat, 19
 - transition layer in as-deposited gradient coating, 18
- life prediction, 294–315
 - future trends, 314
 - mechanical behaviour under
 - evaluated temperatures, 295–305
- metallic coatings as bond coats, 64–7
 - EB-PVD TBC coating, 64
 - M–Cr–Al–Y bond coats, 67
 - platinum-modified aluminide bond coats, 65–6
- microstructure modification, 321–2
 - electron beam physical vapour deposited thermal barrier coatings, 321–2
 - plasma sprayed TBCs, 322
- new materials, technologies and processes, 317–25
 - chemically modified yttria stabilised zirconia, 318–19
 - future trends, 325
- non-destructive evaluation of failure, 243–58
 - future trends, 258
- oxidation, 194–8
 - behaviour, 195–8
 - corrosion kinetics for Pt-Ir
 - aluminide coatings and aluminised substrate, 197
 - mechanisms of metals and alloys, 195
 - NiAl bond coat rumpling after thermal cycling, 196
 - specimens average surface roughness, 197
- oxidation and hot corrosion, 193–208

- plasma spraying processes and
 - applications, 99–111
 - applications, 104–11
 - basic plasma concepts, 100–2
 - plasma spraying, 102–4
- plasma-sprayed TBCs with
 - segmentation cracks, 161–72
- preparation process and parameters, 6–8
 - deposition rate, 8
 - substrate temperature, 6–7
 - substrate temperature and coating structure, 7
 - vacuum pressure, 6
- preparation processes of two-layered TBCs, 8–11
 - anneal for diffusion, 8
 - M–Cr–Al–Y preparation, 8
 - pre-oxide step, 9
 - shot peening, 8–9
 - substrate surface treatment, 8
 - top coat deposition, 9
- processing, microstructures and
 - properties by EB–PVD, 115–28
 - EB–PVD principle, 116–18
 - hot fatigue behaviour and failure mechanisms, 125–8
 - manufacturing, 118–20
 - microstructure and advantages over plasma-sprayed coatings, 120–5
- service environmental performance
 - simulation test system, 218
- structure, 5–6
 - two-layered, graded and multi-layered, 5
- substrate and bond coat related
 - failure, 263–90
 - bond coat effect on the TBC
 - degradation mechanisms, 286–8
 - bond coat related failure, 278–86
 - driving force and interfacial fracture toughness variation, 278
 - future trends, 288–90
 - nickel-based single-crystal
 - superalloys compatibility issues, 276–8
 - substrate related failure, 265–76
 - superalloys high-temperature capability evolution, 264
- traditional, 9–11
 - after thermal cycle testing, 11
 - alloy IC6 coated with M–Cr–Al–Y, 11
 - alloy IC6 isothermal oxidation curves, 10
 - oxidation, 10
 - typical microstructure of
 - conventional TBCs, 122–3
- thermal conductivity, 155–6, 167
- thermal cyclic behaviour, 11–16
- thermal cycling lifetime, 125
- thermal cycling tests, 9, 12, 319
- thermal emission spectroscopy, 250
- thermal plasma spraying, 99–100
 - see also* plasma spraying
- thermal spraying, 301
- thermally grown oxides, 9, 11–12, 53, 116, 126, 269
- thermomechanical loading test system, 217–19
- top coat, 19
 - atmospheric plasma spraying, 296
 - electron beam physical vapour deposition, 296–7
 - simulation, 302
 - thermal conductivity evaluation, 301–2
 - under high temperature, 302
 - Young's modulus measurement, 298–301
 - specimens for oxidation experiment, 300
 - testing system, 300
 - under different temperatures, 301
- transformation toughening effect, 148
- turbine inlet temperature (TIT), 317
- type I hot corrosion, 203
- type II hot corrosion, 203
- user-defined material model (UMAT), 302

- vanadates, 205
- Vickers microindentation technique, 152

- Walker model, 296–7
- wavelength dispersive spectrometry (WDS), 268, 272–6
- WaveMaker software, 218
- Weber number, 140
- William–Warnke flow surface, 295
- William–Warnke model, 296, 302

- X-ray fluorescence (XRF), 266

- YAG *see* yttrium aluminium garnet
- Young’s modulus, 152, 298–301, 306

- YSZ *see* yttria stabilised zirconia
- yttria stabilised hafnia, 35
- yttria stabilised zirconia, 26–30, 54, 68–9, 176, 194, 317
 - activation energy calculation, 86
 - insulation layer, 246–7
 - nanostructured coatings, 75–93
- yttrium, 63, 318
- yttrium aluminium garnet, 40

- zircon, 38–9
- zirconate pyrochlore oxides ($\text{RE}_2\text{Zr}_2\text{O}_7$), 319–20
- zirconia, 26, 31–5, 203–4
 - thermal diffusivity, 87
- Zview software, 222